SANDIA REPORT
SAND2026-22016
Printed June 3, 2026

Sandia National Laboratories

Library of Advanced Materials for Engineering (LAMÉ) 5.30

LAMÉ Team
Materials and Failure Modeling Department
Engineering Sciences Center

Prepared by
Sandia National Laboratories
Albuquerque, New Mexico 87185
Livermore, California 94550

Issued by Sandia National Laboratories, operated for the United States Department of Energy by National Technology & Engineering Solutions of Sandia, LLC.

NOTICE: This report was prepared as an account of work sponsored by an agency of the United States Government. Neither the United States Government, nor any agency thereof, nor any of their employees, nor any of their contractors, subcontractors, or their employees, make any warranty, express or implied, or assume any legal liability or responsibility for the accuracy, completeness, or usefulness of any information, apparatus, product, or process disclosed, or represent that its use would not infringe privately owned rights. Reference herein to any specific commercial product, process, or service by trade name, trademark, manufacturer, or otherwise, does not necessarily constitute or imply its endorsement, recommendation, or favoring by the United States Government, any agency thereof, or any of their contractors or subcontractors. The views and opinions expressed herein do not necessarily state or reflect those of the United States Government, any agency thereof, or any of their contractors.

Printed in the United States of America. This report has been reproduced directly from the best available copy.

Available to DOE and DOE contractors from

U.S. Department of Energy
Office of Scientific and Technical Information
P.O. Box 62
Oak Ridge, TN 37831

Telephone: (865) 576-8401
Facsimile: (865) 576-5728
E-Mail: reports@osti.gov
Online ordering: http://www.osti.gov/scitech

Available to the public from

U.S. Department of Commerce
National Technical Information Service
5301 Shawnee Road
Alexandria, VA 22312

Telephone: (800) 553-6847
Facsimile: (703) 605-6900
E-Mail: orders@ntis.gov
Online order: https://classic.ntis.gov/help/order-methods

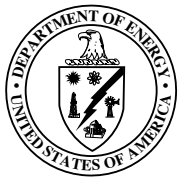

Abstract

Accurate and efficient constitutive modeling remains a cornerstone issue for solid mechanics analysis. Over the years, the LAMÉ advanced material model library has grown to address this challenge by implementing models capable of describing material systems spanning soft polymers to stiff ceramics including both isotropic and anisotropic responses. Inelastic behaviors including (visco)plasticity, damage, and fracture have all incorporated for use in various analyses. This multitude of options and flexibility, however, comes at the cost of many capabilities, features, and responses and the ensuing complexity in the resulting implementation. Therefore, to enhance confidence and enable the utilization of the LAMÉ library in application, this effort seeks to document and verify the various models in the LAMÉ library. Specifically, the broader strategy, organization, and interface of the library itself is first presented. The physical theory, numerical implementation, and user guide for a large set of models is then discussed. Importantly, a number of verification tests are performed with each model to not only have confidence in the model itself but also highlight some important response characteristics and features that may be of interest to end-users. Finally, in looking ahead to the future, approaches to add material models to this library and further expand the capabilities are presented.

Acknowledgements

This document, and the models contained with it, are the result of a longstanding commitment to material modeling at Sandia National Laboratories. As such, a number of people representing a wide set of expertise and discipline have all contributed in various forms. While the current LAMÉ manual is maintained by William Scherzinger and Brian Lester, it would not be possible without the contributions of numerous others. The list of people includes, but is not limited to, Lupe Arguello, Arthur Brown, Michael Buche, Bob Chambers, Jim Cox, Ken Cundiff, Arlo Fossum, Jay Foulk, Arne Gullerud, Jason Hales, Dan Hammerand, Sam Key, Kevin Long, Jeffery McGuire, Mike Neilsen, Pania Newell, Jake Ostien, Ben Reedlunn, Ben Spencer, Mike Stone, Chet Vignes, and Jerry Wellman.

Additionally, as LAMÉ is a part of Sierra/SolidMechanics the continued development of this document and the corresponding models would not be possible without the support of core development team for Sierra/SolidMechanics including, Frank N. Beckwith, Michael R. Buche, Gabriel J. de Frias, Scott O. Gampert, Kevin L. Manktelow, Mark T. Merewether, Scott T. Miller, Krishen J. Parmar, Matt G. Rand, Timothy R. Shelton, Jesse D. Thomas, Jeremy Trageser, Benjamin C. Treweek, Michael G. Veilleux, and Ellen B. Wagman.

Front Matter

Abstract 3

Acknowledgements 4

1. Introduction 25

2. Strategy 27
   2.1. Code Development 27
   2.2. Model Implementation 28
      2.2.1. Code Standards 29
      2.2.2. Testing Standards 29
      2.2.3. Documentation Standards 30
   2.3. Model Status 30

3. Interface 33

4. Material Models 35
   4.1. Hypoelastic Models 35
   4.2. Hyperelastic Models 37
   4.3. Elastic Model 38
      4.3.1. Theory 38
      4.3.2. Implementation 39
      4.3.3. Verification 39
      4.3.4. User Guide 46
   4.4. Elastic Three Dimensional Orthotropic Model 46
      4.4.1. Theory 46
      4.4.2. Implementation 48
      4.4.3. Verification 49
      4.4.4. User Guide 50
   4.5. Neo-Hookean Model 53
      4.5.1. Theory 53
      4.5.2. Implementation 53
      4.5.3. Verification 54
      4.5.4. User Guide 61
   4.6. Gent Model 61
      4.6.1. Theory 61
      4.6.2. Implementation 63
      4.6.3. Verification 64
      4.6.4. User Guide 68
   4.7. Elastic-Plastic Model 68
      4.7.1. Theory 68
      4.7.2. Implementation 71

4.7.3. Verification . . . 72
4.7.4. User Guide . . . 76
4.8. Elastic-Plastic Power Law Hardening Model . . . 79
4.8.1. Theory . . . 79
4.8.2. Implementation . . . 81
4.8.3. Verification . . . 81
4.8.4. User Guide . . . 86
4.9. Ductile Fracture Model . . . 87
4.9.1. Theory . . . 87
4.9.2. Implementation . . . 88
4.9.3. Verification . . . 89
4.9.4. User Guide . . . 91
4.10. Multilinear Elastic-Plastic Model . . . 95
4.10.1. Theory . . . 95
4.10.2. Implementation . . . 97
4.10.3. Verification . . . 97
4.10.4. User Guide . . . 102
4.11. Multilinear Elastic-Plastic Fail Model . . . 104
4.11.1. Theory . . . 104
4.11.2. Implementation . . . 104
4.11.3. Verification . . . 106
4.11.4. User Guide . . . 108
4.12. Johnson-Cook Model . . . 112
4.12.1. Theory . . . 112
4.12.2. Implementation . . . 114
4.12.3. Verification . . . 115
4.12.4. User Guide . . . 120
4.13. J_2 Plasticity Model . . . 122
4.13.1. Theory . . . 122
4.13.2. Implementation . . . 128
4.13.3. Verification . . . 129
4.13.4. User Guide . . . 133
4.14. Hosford Plasticity Model . . . 148
4.14.1. Theory . . . 148
4.14.2. Implementation . . . 152
4.14.3. Verification . . . 154
4.14.4. User Guide . . . 165
4.15. Hill Plasticity Model . . . 173
4.15.1. Theory . . . 173
4.15.2. Implementation . . . 180
4.15.3. Verification . . . 181
4.15.4. User Guide . . . 197
4.16. Barlat Plasticity Model . . . 210
4.16.1. Theory . . . 210
4.16.2. Implementation . . . 215

4.16.3. Verification . . . 217
4.16.4. User Guide . . . 228
4.17. Plane Stress Rate Plasticity Model . . . 246
4.17.1. Theory . . . 246
4.17.2. Implementation . . . 249
4.17.3. User Guide . . . 251
4.18. Modular Plane Stress Plasticity Model . . . 254
4.18.1. Theory . . . 254
4.18.2. Implementation . . . 260
4.18.3. Verification . . . 263
4.18.4. User Guide . . . 265
4.19. Power Law Creep Model . . . 269
4.19.1. Theory . . . 269
4.19.2. Implementation . . . 270
4.19.3. Verification . . . 271
4.19.4. User Guide . . . 273
4.20. Viscoplastic Model . . . 274
4.20.1. Theory . . . 274
4.20.2. Implementation . . . 276
4.20.3. Verification . . . 277
4.20.4. User Guide . . . 280
4.21. Munson-Dawson Viscoplastic Model . . . 282
4.21.1. Theory . . . 282
4.21.2. Implementation . . . 285
4.21.3. Verification . . . 286
4.21.4. User Guide . . . 294
4.22. Hyperfoam Model . . . 295
4.22.1. Theory . . . 295
4.22.2. Implementation . . . 296
4.22.3. Verification . . . 296
4.22.4. User Guide . . . 306
4.23. Hyperelastic Damage Model . . . 308
4.23.1. Theory . . . 308
4.23.2. Implementation . . . 310
4.23.3. Verification . . . 310
4.23.4. User Guide . . . 313
4.24. Soil and Foam Model . . . 314
4.24.1. Theory . . . 314
4.24.2. Implementation . . . 315
4.24.3. Verification . . . 316
4.24.4. User Guide . . . 316
4.25. Shape Memory Alloy Model . . . 320
4.25.1. Theory . . . 320
4.25.2. Implementation . . . 325
4.25.3. Verification . . . 326

4.25.4. User Guide . . . 328
4.26. Low Density Foam Model . . . 332
4.26.1. Theory . . . 332
4.26.2. Implementation . . . 333
4.26.3. Verification . . . 333
4.26.4. User Guide . . . 337
4.27. Foam Plasticity Model . . . 337
4.27.1. Theory . . . 337
4.27.2. Implementation . . . 339
4.27.3. Verification . . . 340
4.27.4. User Guide . . . 341
4.28. Viscoplastic Foam Model . . . 343
4.28.1. Theory . . . 343
4.28.2. Implementation . . . 345
4.28.3. Verification . . . 346
4.28.4. User Guide . . . 349
4.29. Foam Damage Model . . . 351
4.29.1. Theory . . . 351
4.29.2. Implementation . . . 354
4.29.3. Verification . . . 357
4.29.4. User Guide . . . 363
4.30. Orthotropic Crush Model . . . 365
4.30.1. Theory . . . 365
4.30.2. Implementation . . . 367
4.30.3. Verification . . . 368
4.30.4. User Guide . . . 369
4.31. Orthotropic Rate Model . . . 371
4.31.1. Theory . . . 371
4.31.2. Implementation . . . 373
4.31.3. Verification . . . 375
4.31.4. User Guide . . . 377
4.32. Universal Polymer Model . . . 380
4.32.1. Theory . . . 380
4.32.2. Implementation . . . 383
4.32.3. Verification . . . 385
4.32.4. User Guide . . . 389
4.33. Linear Thermoviscoelastic Model . . . 393
4.33.1. Theory . . . 393
4.33.2. Implementation . . . 396
4.33.3. Verification . . . 398
4.33.4. User Guide . . . 406
4.34. Wire Mesh Model . . . 409
4.34.1. Theory . . . 409
4.34.2. Implementation . . . 409
4.34.3. Verification . . . 410

4.34.4. User Guide . . . 413
4.35. Viscoplastic-viscoSCRAM Model . . . 415
4.35.1. Theory . . . 415
4.35.2. Implementation . . . 419
4.35.3. Verification . . . 421
4.35.4. User Guide . . . 435
4.36. Phase Field F^eF^p Model . . . 436
4.36.1. Theory . . . 437
4.36.2. Plastic Hardening . . . 440
4.36.3. Implementation . . . 444
4.36.4. Operator split scheme for explicit time integration . . . 447
4.36.5. Verification . . . 451
4.36.6. User Guide . . . 456
4.37. Phase Field F^eF^p Modular Model . . . 462
4.37.1. Theory . . . 463
4.37.2. Implementation . . . 466
4.37.3. Verification . . . 468
4.37.4. User Guide . . . 470
4.38. Modular Failure . . . 484
4.38.1. Tearing Parameter . . . 484
4.38.2. Johnson-Cook Failure . . . 485
4.38.3. Wilkins . . . 486
4.38.4. Modular Failure . . . 487
4.38.5. Modular BCJ Failure . . . 489
4.38.6. Anisotropic Failure . . . 491

A. Common Boundary Value Problems . . . 499
A.1 Uniaxial Stress . . . 499
A.2 Simple Shear . . . 499
A.3 Pure Shear . . . 500
A.4 Hydrostatic Compression . . . 500
A.5 Constant Equivalent Plastic Strain Rate . . . 500
A.5.1 Uniaxial Stress . . . 501
A.5.2 Pure Shear . . . 503

References . . . 507
Bibliography507

List of Tables

Table 4.1. The material properties for the elastic 3D orthotropic model used for the varying temperature, uniaxial stress tests. . . . 49
Table 4.2. The coordinate system rotations used with the elastic 3D orthotropic model for the uniaxial strain test. . . . 50
Table 4.3. The material properties for the neo-Hookean model used for both the uniaxial and simple shear tests. . . . 54
Table 4.4. The material properties for the Gent model used for uniaxial strain, simple shear, and hydrostatic compression tests. . . . 64
Table 4.5. State Variables for `ELASTIC PLASTIC` Model . . . 78
Table 4.6. State Variables for `ELASTIC PLASTIC` Model for Shells . . . 78
Table 4.7. State Variables for EP POWER HARD Model . . . 86
Table 4.8. State Variables for EP POWER HARD Model for Shells . . . 87
Table 4.9. State Variables for DUCTILE FRACTURE Model . . . 94
Table 4.10. State Variables for MULTILINEAR EP Model . . . 103
Table 4.11. State Variables for MULTILINEAR EP Model for Shells . . . 103
Table 4.12. State Variables for ML EP FAIL Model . . . 110
Table 4.13. State Variables for ML EP FAIL Model for Shells . . . 111
Table 4.14. The material properties and model parameters of the Johnson-Cook model used for verification testing . . . 115
Table 4.15. State Variables for JOHNSON COOK Model . . . 122
Table 4.16. The model parameters for the hardening verification tests used with the J_2 plasticity model during verification tests. Parameters for the rate *independent* hardening functions, $\tilde{\sigma}_y$, are also given and denoted with a $\tilde{}$ while the subscript refers to the functional form. . . . 129
Table 4.17. State Variables for J2 PLASTICITY Model . . . 148
Table 4.18. The model parameters for the hardening verification tests used with the Hosford plasticity model during verification tests. Parameters for the rate *independent* hardening functions, $\tilde{\sigma}_y$, are also given and denoted with a $\tilde{}$ while the subscript refers to the functional form. . . . 156
Table 4.19. State Variables for HOSFORD PLASTICITY Model . . . 172
Table 4.20. The model parameters for the hardening verification tests used with the Hill plasticity model during verification tests. Parameters for the rate *independent* hardening functions, $\tilde{\sigma}_y$, are also given and denoted with a $\tilde{}$ while the subscript refers to the functional form. . . . 190
Table 4.21. State Variables for HILL PLASTICITY Model . . . 209
Table 4.22. The material and model parameters for the Barlat plasticity model used for verification testing. The anisotropy coefficients correspond to 2090-T3 aluminum. . . 217
Table 4.23. The model parameters for the hardening verification tests used with the Barlat plasticity model during verification tests. Parameters for the rate *independent* hardening functions, $\tilde{\sigma}_y$, are also given and denoted with a $\tilde{}$ while the subscript refers to the functional form. . . . 225
Table 4.24. State Variables for BARLAT PLASTICITY Model . . . 246

Table 4.25. State Variables for PLANE STRESS RATE PLASTICITY Model 254
Table 4.26. Model parameters for verification tests used with the modular plane stress plasticity (MPSP) model. 263
Table 4.27. State Variables for MODULAR PLANE STRESS PLASTICITY Model 269
Table 4.28. The material properties and model parameters for the power law creep model used for the verification testing. 271
Table 4.29. State Variables for POWER LAW CREEP Model 274
Table 4.30. Material properties and model parameters used for isothermal, isotropic hardening/recovery creep and stress 277
Table 4.31. State Variables for VISCOPLASTIC Model 282
Table 4.32. State Variables for MD_VISCOPLASTIC Model 295
Table 4.33. The material properties for the hyperfoam model tested in uniaxial strain. 297
Table 4.34. The material properties for the hyperelastic damage model used for both the uniaxial and simple shear tests. 310
Table 4.35. State Variables for HYPERELASTIC DAMAGE Model 314
Table 4.36. State Variables for SOIL FOAM Model 319
Table 4.37. The material and model parameters for the shape memory alloy model used during verification test. 326
Table 4.38. State Variables for SHAPE MEMORY ALLOY Model 331
Table 4.39. Material properties and model parameters for the low density foam model used during verification testing. 334
Table 4.40. State Variables for LOW DENSITY FOAM Model 337
Table 4.41. Material properties and model parameters for the foam plasticity model used during verification testing. 340
Table 4.42. State Variables for FOAM PLASTICITY Model 343
Table 4.43. The material properties for the viscoplastic foam model tested in uniaxial stress. 347
Table 4.44. State Variables for VISCOPLASTIC FOAM Model 351
Table 4.45. Common material properties and model parameters for the foam damage model used during verification testing. 357
Table 4.46. State Variables for FOAM DAMAGE Model 364
Table 4.47. The material properties for the orthotropic crush model used for the uniaxial crush tests. 368
Table 4.48. State Variables for ORTHOTROPIC CRUSH Model 371
Table 4.49. Material and model parameters for the orthotropic rate model used for verification 375
Table 4.50. State Variables for ORTHOTROPIC RATE Model 380
Table 4.51. The material and model parameters for the Universal Polymer Model used for verification testing. Parameters are approximately based on a fit for 828DEA, but they represent a linear thermal-viscoelastic representation of the model. Both the shear and volumetric Prony series weights come from fitting these 4 relaxation times to stretched exponential series as discussed in that paper. The thermal relaxation and volumetric relaxation functions are the same in the UPM model. All other material and model parameters are unused and set to zero. 386
Table 4.52. State Variables for Universal Polymer Model 393
Table 4.53. Model parameters for the linear thermoviscoelastic model from Kuether. 398
Table 4.54. Viscoelastic strectra for the linear thermoviscoelastic model from Kuether. 398

Table 4.55. State Variables for LINEAR_THERMOVISCOELASTIC Model 408
Table 4.56. The material properties and model parameters of the wire mesh model used for verification testing 410
Table 4.57. State Variables for WIRE MESH Model 415
Table 4.58. The material properties for the viscoSCRAM model testing viscoelastic response. 422
Table 4.59. The shift factor model properties for the viscoSCRAM model testing viscoelastic response. 424
Table 4.60. The material properties for the viscoSCRAM model testing crack growth kinetics. 426
Table 4.61. The material properties for the viscoSCRAM model tested in uniaxial compression. 428
Table 4.62. The material properties for the viscoplastic model tested in uniaxial tension. . . . 430
Table 4.63. The material properties for the viscoplastic model tested in simple shear. 431
Table 4.64. State Variables for VISCOSCRAM EXPLICIT Model 436
Table 4.65. State Variables for PHASE_FIELD_FEFP Model 461
Table 4.66. Property Inputs for HENCKY_ELASTIC_POTENTIAL 475
Table 4.67. Property Inputs for LINEAR_PLASTIC_POTENTIAL 476
Table 4.68. Property Inputs for POWER_LAW_PLASTIC_POTENTIAL 476
Table 4.69. Property Inputs for POWER_LAW_SIMPLE_PLASTIC_POTENTIAL 476
Table 4.70. Property Inputs for VOCE_PLASTIC_POTENTIAL 476
Table 4.71. Property Inputs for JOHNSON_COOK_PLASTIC_POTENTIAL 477
Table 4.72. Property Inputs for GRADIENT_DAMAGE_POTENTIAL 478
Table 4.73. Property Inputs for CLASSICAL_GRADIENT_DAMAGE_POTENTIAL 478
Table 4.74. Property Inputs for WU_DAMAGE_POTENTIAL 478
Table 4.75. Property Inputs for POWER_LAW_PLASTIC_KINETIC_POTENTIAL 479
Table 4.76. Property Inputs for JOHNSON_COOK_PLASTIC_KINETIC_POTENTIAL . . . 479
Table 4.77. State Variables for POWER_LAW_BREAKDOWN_PLASTIC_KINETIC_POTENTIAL 479
Table 4.78. Property Inputs for TALAMINI_DEGRADATION_FUNCTION 479
Table 4.79. Property Inputs for LO_DEGRADATION_FUNCTION 480
Table 4.80. Property Inputs for WU_DEGRADATION_FUNCTION 480
Table 4.81. Property Inputs for STAR_CONVEX_TCS 480
Table 4.82. State Variables for HENCKY_ELASTIC_POTENTIAL 480
Table 4.83. State Variables for LINEAR_PLASTIC_POTENTIAL 481
Table 4.84. State Variables for POWER_LAW_PLASTIC_POTENTIAL 481
Table 4.85. State Variables for POWER_LAW_SIMPLE_PLASTIC_POTENTIAL 481
Table 4.86. State Variables for VOCE_PLASTIC_POTENTIAL 481
Table 4.87. State Variables for JOHNSON_COOK_PLASTIC_POTENTIAL 482
Table 4.88. State Variables for GRADIENT_DAMAGE_POTENTIAL 482
Table 4.89. State Variables for CLASSICAL_GRADIENT_DAMAGE_POTENTIAL 482
Table 4.90. State Variables for WU_DAMAGE_POTENTIAL 482
Table 4.91. State Variables for POWER_LAW_PLASTIC_KINETIC_POTENTIAL 483
Table 4.92. State Variables for JOHNSON_COOK_PLASTIC_KINETIC_POTENTIAL . . . 483
Table 4.93. State Variables for POWER_LAW_BREAKDOWN_PLASTIC_KINETIC_POTENTIAL 483
Table 4.94. State Variables for TALAMINI_DEGRADATION_FUNCTION 483
Table 4.95. State Variables for LO_DEGRADATION_FUNCTION 483
Table 4.96. State Variables for WU_DEGRADATION_FUNCTION 484

Table 4.97. State Variables for Anisotropic Failure Model 496

List of Figures

Fig. 4.1. The axial stress component σ_{11} in uniaxial stress using the elastic model. 40
Fig. 4.2. The lateral strain components ε_{22} and ε_{33} in uniaxial stress using the elastic model. 41
Fig. 4.3. The strain component ε_{33} in biaxial stress using the elastic model. 43
Fig. 4.4. The normal stress components σ_{11} and σ_{22} in biaxial stress using the elastic model. 44
Fig. 4.5. The shear stress component σ_{12} in pure shear using the elastic model. 45
Fig. 4.6. Analytical and numerical results of axial σ_{11} and transverse, σ_{22} and σ_{33}, as a function of the stretch λ_1. 50
Fig. 4.7. Analytical and numerical results of the stress state through a thermomechanical uniaxial strain loading as a function of the axial strain ε_{11}. 51
Fig. 4.8. Analytical and numerical results for the (a) uniaxial stress and (b) lateral strain. The green line gives the linear elastic response. 56
Fig. 4.9. Analytical and numerical results for the neo-Hookean model subjected to a pure shear strain. The solid lines are the analytical results and the boxes are results from Sierra/SM. 57
Fig. 4.10. Analytical and numerical results for the neo-Hookean model subjected to a pure shear stress. The curve gives the logarithmic strain component, $\varepsilon_{33} = \frac{1}{2} \ln B$. The solid lines are the analytical results and the boxes are results from Sierra/SM. 58
Fig. 4.11. Analytical and numerical results for the uniaxial stretch case. 60
Fig. 4.12. Analytical and numerical results for the simple shear case. 62
Fig. 4.13. Analytical and numerical results for the uniaxial stretch case. 65
Fig. 4.14. Analytical and numerical results for the simple shear case. 66
Fig. 4.15. Stress determined analytically and numerically for the Gent model during displacement controlled hydrostatic compression. 67
Fig. 4.16. Example von Mises yield surface (J_2) used by the elastic-plastic model presented in the deviatoric π-plane. In this case the surface is plotted for $\alpha_{ij} = 0$ and $\bar{\varepsilon}^p = 0$. 69
Fig. 4.17. Axial stress for loading in the x_1 direction for the elastic-plastic model with linear hardening. 74
Fig. 4.18. Lateral strains for uniaxial stress loading in the x_1 direction for the elastic-plastic model with linear hardening. 75
Fig. 4.19. Results are for shear in the x_1-x_2 plane, x_2-x_3 plane, and x_3-x_1 plane. 77
Fig. 4.20. Typical stress-strain response for the power-law hardening model. 80
Fig. 4.21. The axial stress as a function of axial strain for the elastic-plastic power-law hardening model. 83
Fig. 4.22. The lateral strain as a function of axial strain for the elastic-plastic power-law hardening model. 84
Fig. 4.23. The shear stress as a function of shear strain for the elastic-plastic power-law hardening model. 85
Fig. 4.24. The (a) tearing parameter, t_p, and (b) axial stress-strain response for the ductile fracture model in uniaxial stress. The post failure reduction in stress depends on the time discretization or step size. 90

Fig. 4.25. The tearing parameter, t_p, in pure shear. The maximum tearing parameter depends on the time discretization or step size. 92
Fig. 4.26. Shear stress vs. shear strain for the ductile fracture model in pure shear. The post failure reduction in stress depends on the time discretization or step size. . . 93
Fig. 4.27. An example of a multilinear elastic-plastic stress-strain curve. 96
Fig. 4.28. The axial stress as a function of axial strain for the multilinear elastic-plastic model with an analytical Voce law for the hardening model. 99
Fig. 4.29. The lateral strain as a function of axial strain for the multilinear elastic-plastic model with an analytical Voce law for the hardening model. 100
Fig. 4.30. The shear stress as a function of shear strain for the multilinear elastic-plastic model with an analytical Voce law for the hardening model. 101
Fig. 4.31. Analytical and numerical results of the tearing parameter and axial stress evolution through a uniaxial tension loading path as a function of the axial strain, ε_{11}. 107
Fig. 4.32. Analytical and numerical results of the tearing parameter and shear stress evolution through a pure shear loading path as a function of the shear strain, ε_{12}. . . . 108
Fig. 4.33. Semi-analytical and numerical (a) stress-strain and (b) damage evolutions of the Johnson-Cook model subjected to a uniaxial loading at three different applied strain rates. In these results, $\beta = 0$. 116
Fig. 4.34. Semi-analytical and numerical (a) stress-strain (b) damage and (c) temperature evolutions of the Johnson-Cook model subjected to a uniaxial loading with three different plastic work conversion ratios, β. The strain rate for all three cases is $\dot{\varepsilon} = 1\text{s}^{-1}$. 117
Fig. 4.35. Semi-analytical and numerical (a) stress-strain and (b) damage evolutions of the Johnson-Cook model subjected to a pure shear loading at three different applied strain rates. In these results, $\beta = 0$. 118
Fig. 4.36. Semi-analytical and numerical (a) stress-strain (b) damage and (c) temperature evolutions of the Johnson-Cook model subjected to a pure shear loading with three different plastic work conversion ratios, β. The strain rate for all three cases is $\dot{\varepsilon} = 1\text{s}^{-1}$. 119
Fig. 4.37. Analytical and numerical (Sierra) (a) uniaxial stress-strain and (b) pure shear responses of the J_2 plasticity model with linear, power-law, and Voce rate *independent* isotropic hardening. Solid lines are analytical while open symbols are numerical. 130
Fig. 4.38. Uniaxial stress-strain responses of the J_2 plasticity model with (a,b) linear, (c,d) power-law, and (e,f) Voce isotropic hardening with the (a,c,e) Johnson-Cook and (b,d,f) Power-law breakdown rate *dependent* hardening models. Solid lines are analytical while open symbols are numerical (Sierra). 131
Fig. 4.39. Pure shear responses of the J_2 plasticity model with (a,b) linear, (c,d) power-law, and (e,f) Voce isotropic hardening with the (a,c,e) Johnson-Cook and (b,d,f) Power-law breakdown rate *dependent* hardening models. Solid lines are analytical while open symbols are numerical (Sierra). 132

Fig. 4.40. Uniaxial stress-strain responses of the J_2 plasticity model using the flow-stress hardening model comprised of (a,b) linear, (c,d) power-law, and (e,f) Voce isotropic hardening, (a,c,e) Johnson-Cook and (b,d,f) power-law breakdown rate multipliers, and (a-f) Johnson-Cook temperature multipliers. Solid lines are analytical while open symbols are numerical (Sierra). 134
Fig. 4.41. Pure shear responses of the J_2 plasticity model using the flow-stress hardening model comprised of (a,b) linear, (c,d) power-law, and (e,f) Voce isotropic hardening, (a,c,e) Johnson-Cook and (b,d,f) Power-law breakdown rate multipliers and (a-f) Johnson-Cook temperature multipliers. Solid lines are analytical while open symbols are numerical (Sierra). 135
Fig. 4.42. Uniaxial stress-strain responses of the J_2 plasticity model using the decoupled flow-stress hardening model comprised of (a-c) linear ("L") and (d-f) power-law ("PL"), (a-f) temperature independent hardening, (a-f) Johnson-Cook type temperature multiplier for yield, (a,d) Johnson-Cook ("JC") and power-law breakdown ("PLB") type yield and hardening rate multipliers, respectively, (b,e) rate-independent (-) yield with Johnson-Cook type hardening rate dependence, and (c,f) power-law breakdown yield rate dependence with rate-independent hardening. Solid lines are analytical while open symbols are numerical (Sierra). 136
Fig. 4.43. Uniaxial stress-strain responses of the J_2 plasticity model using the decoupled flow-stress hardening model comprised of (a-c) Voce isotropic hardening ("V"), (a-c) temperature independent hardening, (a-c) Johnson-Cook type temperature multiplier for yield, (a) Johnson-Cook ("JC") and power-law breakdown ("PLB") type yield and hardening rate multipliers, respectively, (b) rate-independent (-) yield with Johnson-Cook type hardening rate dependence, and (c) power-law breakdown yield rate dependence with rate-independent hardening. Solid lines are analytical while open symbols are numerical (Sierra). 137
Fig. 4.44. Uniaxial stress-strain responses of the J_2 plasticity model using the decoupled flow-stress hardening model comprised of (a-c) linear ("L") and (d-f) power-law ("PL") hardening, (a-f) temperature independent yield, (a-f) Johnson-Cook type temperature multiplier for hardening, (a,d) power-law breakdown ("PLB") and Johnson-Cook ("JC") rate multipliers for yield and hardening, respectively (b,e) rate-independent (-)hardening with Johnson-Cook type yield rate dependence, and (c,f) power-law breakdown hardening rate dependence with rate-independent yield. Solid lines are analytical while open symbols are numerical (Sierra). 138
Fig. 4.45. Uniaxial stress-strain responses of the J_2 plasticity model using the decoupled flow-stress hardening model comprised of (a-c) Voce ("V") isotropic hardening, (a-c) temperature independent yield, (a-c) Johnson-Cook type temperature multiplier for hardening, (a) power-law breakdown ("PLB") and Johnson-Cook ("JC") rate multipliers for yield and hardening, respectively (b) rate-independent (-)hardening with Johnson-Cook type yield rate dependence, and (c) power-law breakdown hardening rate dependence with rate-independent yield. Solid lines are analytical while open symbols are numerical (Sierra). 139

Fig. 4.46. Example Hosford yield surfaces, $f\left(\sigma_{ij}, \bar{\varepsilon}^p = 0; a\right)$, presented in the deviatoric π-plane. The presented surfaces correspond to the different yield exponents $a = 4,\ 8$, and 100. 149
Fig. 4.47. Axial stress-strain (a) and lateral strain (b) results of the Hosford plasticity model determined analytically and numerically for the case of yield surface exponents $a = 4, 8$. 155
Fig. 4.48. Shear stress-strain results of the Hosford plasticity model determined analytically and numerically for the case of yield surface exponents $a = 4,\ 8$. 156
Fig. 4.49. Uniaxial stress-strain (a) and pure shear (b) responses of the Hosford plasticity model with rate *independent*, linear hardening. Solid line are analytical while open symbols are numerical. 157
Fig. 4.50. Uniaxial stress-strain (a) and pure shear (b) responses of the Hosford plasticity model with rate *independent*, power-law hardening. Solid line are analytical while open symbols are numerical. 158
Fig. 4.51. Uniaxial stress-strain (a) and pure shear (b) responses of the Hosford plasticity model with rate *independent*, Voce hardening. Solid line are analytical while open symbols are numerical. 158
Fig. 4.52. Uniaxial stress-strain response of the Hosford plasticity model ($a = 8$) with rate *dependent*, Johnson-Cook type hardening with (a) linear (b) power-law and (c) Voce rate *independent* hardening. Solid lines are analytical results while open symbols are numerical. 159
Fig. 4.53. Stress-strain response of the Hosford plasticity model with rate *dependent*, Johnson-Cook type hardening in pure shear with (a-c) linear (d-f) and power-law rate *independent* hardening. Solid lines are analytical results while open symbols are numerical. 160
Fig. 4.54. Stress-strain response of the Hosford plasticity model with rate *dependent*, Johnson-Cook type hardening in pure shear with (a-c) Voce rate *independent* hardening. Solid lines are analytical results while open symbols are numerical. . 161
Fig. 4.55. Uniaxial stress-strain response of the Hosford plasticity model ($a = 8$) with rate *dependent*, power-law breakdown type hardening with (a) linear (b) power-law and (c) Voce rate *independent* hardening. Solid lines are analytical results while open symbols are numerical. 162
Fig. 4.56. Stress-strain response of the Hosford plasticity model with rate *dependent*, power-law breakdown type hardening in pure shear with (a-c) linear and (d-f) power-law rate *independent* hardening. Solid lines are analytical results while open symbols are numerical. 163
Fig. 4.57. Stress-strain response of the Hosford plasticity model with rate *dependent*, power-law breakdown type hardening in pure shear with (a-c) Voce rate *independent* hardening. Solid lines are analytical results while open symbols are numerical. 164
Fig. 4.58. Example anisotropic Hill yield surface, $f_{Hill}\left(\sigma_{ij}, \bar{\varepsilon}^p = 0\right)$, presented in the deviatoric π-plane fit to 2090-T3 aluminum. Comparison von Mises (J_2) and Hosford (with $a = 8$) surfaces are also presented. 174
Fig. 4.59. Stresses when loading in the e_1, e_2, and e_3-directions using the Hill model with a Voce hardening law. 184

Fig. 4.60. Lateral strain as a function of axial strain for the Hill model of 2090-T3 aluminum. Loading is in the e_1-direction and the hardening law is a Voce law. 185
Fig. 4.61. Lateral strain as a function of axial strain for the Hill model of 2090-T3 aluminum. Loading is in the e_2-direction and the hardening law is a Voce law. 186
Fig. 4.62. Lateral strain as a function of axial strain for the Hill model of 2090-T3 aluminum. Loading is in the e_3-direction and the hardening law is a Voce law. 187
Fig. 4.63. Shear stress versus shear strain using the Hill model with a Voce hardening law. Results are for shear in the three orthogonal planes of the material coordinate system. 189
Fig. 4.64. Uniaxial stress-strain (a) and pure shear (b) responses of the Hill plasticity model with rate *independent*, linear hardening. Solid lines are analytical while open symbols are numerical. 191
Fig. 4.65. Uniaxial stress-strain (a) and pure shear (b) responses of the Hill plasticity model with rate *independent*, power-law hardening. Solid lines are analytical while open symbols are numerical. 191
Fig. 4.66. Uniaxial stress-strain (a) and pure shear (b) responses of the Hill plasticity model with rate *independent*, Voce hardening. Solid lines are analytical while open symbols are numerical. 192
Fig. 4.67. Uniaxial stress-strain response of the Hill plasticity model with rate *dependent*, Johnson-Cook type hardening with (a-c) linear and (d-f) power-law rate *independent* hardening. Solid lines are analytical results while open symbols are numerical. 193
Fig. 4.68. Uniaxial stress-strain response of the Hill plasticity model with rate *dependent*, Johnson-Cook type hardening with (a-c) Voce rate *independent* hardening. Solid lines are analytical results while open symbols are numerical. 194
Fig. 4.69. Stress-strain response of the Hill plasticity model with rate *dependent*, Johnson-Cook type hardening in pure shear with (a-c) linear and (d-f) power-law rate *independent* hardening. Solid lines are analytical results while open symbols are numerical. 195
Fig. 4.70. Stress-strain response of the Hill plasticity model with rate *dependent*, Johnson-Cook type hardening in pure shear with (a-c) Voce rate *independent* hardening. Solid lines are analytical results while open symbols are numerical. 196
Fig. 4.71. Uniaxial stress-strain response of the Hill plasticity model with rate *dependent*, power-law breakdown type hardening in with (a-c) linear and (d-f) power-law rate *independent* hardening. Solid lines are analytical results while open symbols are numerical. 198
Fig. 4.72. Uniaxial stress-strain response of the Hill plasticity model with rate *dependent*, power-law breakdown type hardening in with (a-c) Voce rate *independent* hardening. Solid lines are analytical results while open symbols are numerical. 199
Fig. 4.73. Stress-strain response of the Hill plasticity model with rate *dependent*, power-law breakdown type hardening in pure shear with (a-c) linear and (d-f) power-law rate *independent* hardening. Solid lines are analytical results while open symbols are numerical. 200

Fig. 4.74. Stress-strain response of the Hill plasticity model with rate *dependent*, power-law breakdown type hardening in pure shear with (a-c) Voce rate *independent* hardening. Solid lines are analytical results while open symbols are numerical. . 201
Fig. 4.75. Example Barlat yield surface, $f_{Barlat}\left(\sigma_{ij}, \bar{\varepsilon}^p = 0\right)$, of 2090-T3 aluminum presented in the deviatoric π-plane. Comparison von Mises (J_2), Hosford (with $a = 8$), and Hill surfaces are also presented for comparison. 212
Fig. 4.76. Axial stress-strain response determined analytically and numerically for 2090-T3 aluminum using the Barlat plasticity model with Voce hardening. 219
Fig. 4.77. Lateral strain as a function of axial strain of 2090-T3 aluminum with Voce hardening as determined by the Barlat plasticity model both analytically and numerically. 221
Fig. 4.78. Stress-strain (a) and lateral strain (b) responses of 2090-T3 aluminum with Voce hardening and the Barlat plasticity model. The material is rotated such that the loading is aligned with the 2 direction. 222
Fig. 4.79. Stress-strain (a) and lateral strain (b) responses of 2090-T3 aluminum with Voce hardening and the Barlat plasticity model. The material is rotated such that the loading is aligned with the 3 direction. 222
Fig. 4.80. Shear stress-strain results for 2090-T3 aluminum determined analytically and numerically by the Barlat plasticity model with Voce Hardening 224
Fig. 4.81. Uniaxial stress-strain (a) and pure shear (b) responses of the Barlat plasticity model with rate *independent*, linear hardening. Solid lines are analytical while open symbols are numerical 226
Fig. 4.82. Uniaxial stress-strain (a) and pure shear (b) responses of the Barlat plasticity model with rate *independent*, power-law hardening. Solid lines are analytical while open symbols are numerical. 227
Fig. 4.83. Uniaxial stress-strain (a) and pure shear (b) responses of the Barlat plasticity model with rate *independent*, Voce hardening. Solid lines are analytical while open symbols are numerical. 227
Fig. 4.84. Uniaxial stress-strain response of the Barlat plasticity model ($a = 8$) with rate *dependent*, Johnson-Cook type hardening with (a-c) linear and (d-f) power-law rate *independent* hardening. Solid lines are analytical results while open symbols are numerical. 229
Fig. 4.85. Uniaxial stress-strain response of the Barlat plasticity model ($a = 8$) with rate *dependent*, Johnson-Cook type hardening with (a-c) Voce rate *independent* hardening. Solid lines are analytical results while open symbols are numerical. . 230
Fig. 4.86. Stress-strain response of the Barlat plasticity model ($a = 8$) with rate *dependent*, Johnson-Cook type hardening in pure shear with (a-c) linear and (d-f) power-law rate *independent* hardening. Solid lines are analytical results while open symbols are numerical. 231
Fig. 4.87. Stress-strain response of the Barlat plasticity model ($a = 8$) with rate *dependent*, Johnson-Cook type hardening in pure shear with (a-c) Voce rate *independent* hardening. Solid lines are analytical results while open symbols are numerical. . 232

Fig. 4.88. Uniaxial stress-strain response of the Barlat plasticity model ($a = 8$) with rate *dependent*, power-law breakdown type hardening with (a-c) linear and (d-f) power-law rate *independent* hardening. Solid lines are analytical while open symbols are numerical. . . . 233
Fig. 4.89. Uniaxial stress-strain response of the Barlat plasticity model ($a = 8$) with rate *dependent*, power-law breakdown type hardening with (a-c) Voce rate *independent* hardening. Solid lines are analytical while open symbols are numerical. . . . 234
Fig. 4.90. Stress-strain response of the Barlat plasticity model ($a = 8$) with rate *dependent*, power-law breakdown type hardening in pure shear with (a-c) linear and (d-f) power-law rate *independent* hardening. Solid lines are analytical results while open symbols are numerical. . . . 235
Fig. 4.91. Stress-strain response of the Barlat plasticity model ($a = 8$) with rate *dependent*, power-law breakdown type hardening in pure shear with (a-c) Voce rate *independent* hardening. Solid lines are analytical results while open symbols are numerical. . . . 236
Fig. 4.92. Analytical and numerical constant equivalent plastic strain rate verification tests of the modular plane stress plasticity models with a uniaxial stress state and strain rates of (a) $\dot{\varepsilon}^p = 1 \times 10^{-3}\text{s}^{-1}$ and (b) $\dot{\varepsilon}^p = 1\text{s}^{-1}$ with linear, power-law, and voce isotropic hardening and power-law breakdown rate-dependence. Solid lines are analytical and open symbols are from finite element calculations. . . . 264
Fig. 4.93. Analytical and numerical constant equivalent plastic strain rate verification tests of the modular plane stress plasticity models with a balanced biaxial stress state and strain rates of (a) $\dot{\varepsilon}^p = 1 \times 10^{-3}\text{s}^{-1}$ and (b) $\dot{\varepsilon}^p = 1\text{s}^{-1}$ with linear, power-law, and voce isotropic hardening and power-law breakdown rate-dependence. Solid lines are analytical and open symbols are from finite element calculations. Positive valued stresses correspond to σ_{11} while negative values are σ_{22}. . . . 264
Fig. 4.94. Analytical and numerical constant equivalent plastic strain rate verification tests of the modular plane stress plasticity models with a pure shear stress state and strain rates of (a) $\dot{\varepsilon}^p = 1 \times 10^{-3}\text{s}^{-1}$ and (b) $\dot{\varepsilon}^p = 1\text{s}^{-1}$ with linear, power-law, and voce isotropic hardening and power-law breakdown rate-dependence. Solid lines are analytical and open symbols are from finite element calculations. . . . 265
Fig. 4.95. Semi-analytical and numerical results of (a) strain and (b) stress evolution during a creep test. . . . 272
Fig. 4.96. Semi-analytical and numerical results of the (a) strain and (b) stress evolution during a stress relaxation test. . . . 273
Fig. 4.97. Semi-analytical and numerical results of (a) strain and (b) external and internal, (D), stress evolution during a creep test with the viscoplastic model. . . . 279
Fig. 4.98. Semi-analytical and numerical results of (a) strain and (b) external and internal (D) stress evolution during a stress relaxation test with the viscoplastic model. . . 279
Fig. 4.99. Hosford equivalent stress surface in the π-plane. . . . 288
Fig. 4.100. Stress and temperature dependence of the transient strain limit for Calibration 3B. 288
Fig. 4.101. Stress and temperature dependence of the steady-state strain rate for Calibration 3B. . . . 289
Fig. 4.102. Triaxial Compression Verification Test . . . 290
Fig. 4.103. Pure Shear Verification Test . . . 291

Fig. 4.104. Unequal Biaxial Compression Verification Test 293
Fig. 4.105. The axial and lateral stresses for uniaxial strain in tension using the hyperfoam model. The results show agreement with the analytical results. The material properties for the model are given in Table 4.33 298
Fig. 4.106. The axial and lateral stresses for uniaxial strain in compression using the hyperfoam model. The results show agreement with the analytical results. The material properties for the model are given in Table 4.33. 299
Fig. 4.107. The axial and lateral stresses for uniaxial strain in both tension and compression using the hyperfoam model. The results show agreement with the analytical results and that the response of the material is very different in tension and compression. The material properties for the model are given in Table 4.33. 300
Fig. 4.108. The normal stresses for biaxial strain in tension using the hyperfoam model. The results show agreement with the analytical results. The material properties for the model are given in Table 4.33. 302
Fig. 4.109. The normal stresses for biaxial strain in compression using the hyperfoam model. The results show agreement with the analytical results. The material properties for the model are given in Table 4.33. 303
Fig. 4.110. The normal stresses for biaxial strain in both tension and compression using the hyperfoam model. The results show agreement with the analytical results and that the response of the material is very different in tension and compression. The material properties for the model are given in Table 4.33. 304
Fig. 4.111. The shear and normal stresses for the hyperfoam model in pure shear. The material properties for the model are given in Table 4.33. 305
Fig. 4.112. The shear and normal stresses for the hyperfoam model in simple shear. The material properties for the model are given in Table 4.33. 307
Fig. 4.113. Analytical and numerical results of the stress and damage state for the uniaxial stretch case. 312
Fig. 4.114. Analytical and numerical results of the stress and damage state for the simple shear case. 313
Fig. 4.115. Lateral strain, ε_{11} and ε_{33}, over the course of the prescribed triaxial loading path. 317
Fig. 4.116. Axial stress, σ_{22}, over the course of the prescribed triaxial loading path. 318
Fig. 4.117. Representative phase diagram of shape memory alloys highlighting characteristic loading paths ((A) and (B)), transformation surfaces, and phases. 321
Fig. 4.118. Axial stress-strain response (a) and martensitic volume fraction (b), ξ, evolution determined analytically and via adagio for three different ambient temperatures $\theta = 300,\ 320$ and 340 K. 327
Fig. 4.119. Axial stress-strain (a), lateral strain (b), and martensitic volume fraction (c), ξ, evolution as a function of temperature as determined analytically and numerically (Sierra/SM). Results are presented for three different applied bias stresses $\sigma = 100,\ 200$ and 300 MPa. 329
Fig. 4.120. Skeleton (a) stress and (b) strain determined analytically and numerically (with $N_{\text{air}} = 0$) with the low density foam model during a displacement controlled uniaxial compression test. 334

Fig. 4.121. Foam (a) stress and (b) strain determined analytically and numerically (with $N_{\text{air}} = 1$) with the load density foam model during a displacement controlled uniaxial compression test. 335
Fig. 4.122. Foam stress determined analytically and numerically for both $N_{\text{air}} = 0.0$ and $N_{\text{air}} = 1.0$ cases for the low density foam model during displacement controlled hydrostatic compression 336
Fig. 4.123. Pressure vs. engineering volume strain (ε_{V}) response of the foam plasticity model through a hydrostatic compression cycle. For convenience, pressure is defined as positive in compression in the figure. 341
Fig. 4.124. Verification of the viscoplastic foam model in uniaxial compression showing the axial stress as a function of thelogarithmic strain 347
Fig. 4.125. Pressure-engineering volume strain results of viscoplastic foam model subjected to a hydrostatic loading at both fast and slow rates determined semi-analytically and numerically. 348
Fig. 4.126. Axial stress (a) and maximum solid volume fraction (b), ϕ, evolution obtained as a function of applied compressive displacement and determined via the foam damage model considering both associated ($\beta = 0$) and radial($\beta = 1$) flow assumptions semi-analytically and numerically. 358
Fig. 4.127. Diagon strain evolution through a uniaxial displacement loading of the foam damage model considering (a) associated ($\beta = 0$) and (b) radial ($\beta = 1$) flow determined semi-analytically and numerically. 359
Fig. 4.128. Response of the foam damage model through a uniaxial stress, displacement controlled tension simulation. Stress in the loading direction, σ_{11}, and damage measure, w, against the applied displacement, λ_1, are shown. 360
Fig. 4.129. Pressure-engineering volume strain results of the foam damage model subjected to a hydrostatic loading at both fast and slow rates determined semi-analytically and numerically. 362
Fig. 4.130. Pressure and damage evolutions as function of engineering volume strain results of the foam damage model subject to a tensile hydrostatic loading determined analytically and numerically. Note, conventionally with this model pressure is defined positive in compression. 363
Fig. 4.131. An example of an input crush curve for an aluminum honeycomb. 366
Fig. 4.132. Input crush curves used for uniaxial crush analysis. 368
Fig. 4.133. Analytical and numerical results for uniaxial crush cases. 369
Fig. 4.134. Orientation of the T, L and W vectors for 38 pc aluminum honeycomb. 371
Fig. 4.135. Input strength/hardening curves, $f_{\beta\gamma}$, for use in verification tests of the orthotropic rate model. 376
Fig. 4.136. Axial and off-axis stresses determined analytically and numerically via the orthotropic rate model with constant, isotropic elastic properties. 377
Fig. 4.137. Axial and off-axis stresses determined analytically and numerically via the orthotropic rate model with constant, orthotropic elastic constants. The material coordinate systems is rotated in two different directions with the loading direction always aligned with x_1 378

Fig. 4.138. Time-temperature dependence of the shift factor, a, during cooling through the glass transition and then reheating back through it. The cooling/heating rate is 1°C per minute. FEA (circles) show the expected WLF (blue dashed line) behavior for $\theta - \theta_{\text{ref}} > 0$. The UPM model departs from WLF behavior below the reference temperature as expected, and continues to agree with an external to Sierra numerical scheme (solid line) to simulate this boundary value problem. 387
Fig. 4.139. Linear viscoelastic response to a two stage uniaxial strain boundary value problem with material and loading properties specified in Table 4.51. Symbols represent FEA simulations with the UPM model while solid lines are the analytic results. The three logarithmic strain rates of 0.1, 1.0, and 10.0 per second are shown, and all cease at 10% strain, and all cases are isothermal at the reference temperature so that the shift factor is unity. 390
Fig. 4.140. Verification results for the balanced biaxial creep problem for models with (a) WLF and (b) Arrhenius shift factors at 65°C and 75°C. Results labelled with (A), (UPM), and (SD) reflect solutions obtained from (4.157), the UNIVERSAL_POLYMER model, and Sierra/SD, respectively. Results from the LTVE model with user-defined, WLF, WLF_LAG, and Arrhenius shift factors are denoted, respectively, (UD), (WLF), (WLF-L), and (Arr). 400
Fig. 4.141. Verification results for the hydrostatic creep problem for models with (a) WLF and (b) Arrhenius shift factors at 65°C and 75°C. Results labelled with (A), (UPM), and (SD) reflect solutions obtained from (4.159), the UNIVERSAL_POLYMER model, and Sierra/SD, respectively. Results from the LTVE model with user-defined, WLF, WLF_LAG, and Arrhenius shift factors are denoted, respectively, (UD), (WLF), (WLF-L), and (Arr). 401
Fig. 4.142. Verification results for the pure shear, constant strain rate problem for LTVE model with (a) WLF, (b) WLF_Lag (c) user-defined (ud), (d) Arrhenius (Arr) shift factors and (e) UNIVERSAL_POLYMER model at 75∘C and shear strain rates of $\dot{\varepsilon}_{xy} = 1\times10^{-3},\ 1\times10^{-1}$, and 1×10^{1} s^{-1}. Solutions determined through the reduced in (4.160) are (A). 403
Fig. 4.143. Verification results for the no-load cooling problem for the LTVE model exhibiting analytical and numerical results for (a) $\log_{10}a$, (b) ε_{kk}, (c) J^1, and (d) J^3. Results are obtained (A) semi-analytically and with WLF, (UD) user-defined, and (Arr) Arrhenius shift factors. 404
Fig. 4.144. Verification results for the no-load cooling problem for the LTVE and UNIVERSAL_POLYMER models exhibiting analytical and numerical results for (a) $\log_{10}a$, (b) ε_{kk}, (c) J^1, and (d) J^3. The numbers in the legend indicate cooling rates of $\dot{T} = 0.2,\ 2$, and 20 K/min and results are obtained semi-analytically (A), numerically with the LTVE model (N), and numerically with the UNIVERSAL_POLYMER (UPM) model. 405
Fig. 4.145. Analytical and numerical results of the normal stress and strain components through a compressive uniaxial stress loading path as a function of the applied displacement, λ_1 411
Fig. 4.146. Analytical and numerical results of the normal stress and strain components through a tension uniaxial strain loading path as a function of the applied displacement, λ_1. 412

Fig. 4.147. Analytical and numerical pressure-volume strain response of the wire mesh model through a hydrostatic compression loading as a function of the applied displacement, λ_1. 414
Fig. 4.148. The axial and lateral stresses. 423
Fig. 4.149. The axial and lateral stresses with the shift factor models. (A) denotes the Arrhenius model and (UD) denotes the user defined model. 425
Fig. 4.150. Crack size 427
Fig. 4.151. Uniaxial compression 429
Fig. 4.152. Uniaxial tension 432
Fig. 4.153. Simple shear 434
Fig. 4.154. Approximation of sharp crack by smeared phase field. 437
Fig. 4.155. Effect of parameter γ in the rational degradation function. Graphs are shown for $\gamma = \{0, \frac{1}{3}, 1, 7\}$. Increasing γ makes the degradation function (and hence the stress) drop off more quickly with increasing phase value. 442
Fig. 4.156. Behavior of the model with the rational degradation function in homogeneous uniaxial tension. Data are shown for $\gamma = \{0, 1, 2\}$. The solid lines are for $\gamma = 0$. **(a)** Damage nucleates when the free energy density reaches the value of the model parameter ψ_c, regardless of the value of γ. The softening behavior is sensitive to γ. **(b)** The rate of damage with strain decreases as γ increases. 443
Fig. 4.157. Alternating minimization scheme behavior. **(a)** Schematic of alternating minimization scheme. At a new time step t_{n+1}, nonlinear solves for mechanics (M) and phase field (PF) are repeated until convergence achieved in both fields. Solver then proceeds to the next time step. **(b)** Force vs. displacement for a single element uniaxial tension problem with elastic material. The exact solution for the problem is shown with a dotted line. the curve marked "uncoupled" is solved with a single pass at each time step, leading to a solution that is out of equilibrium. The curve "ControlRxnDiff" is solved until convergence, indicating equilibrium. The equilibrium result is seen to agree with the exact solution. . 447
Fig. 4.158. Imagery showing the phase field solutions generated from the *1D PhaseBC FeFp* verification test, with the phase boundary condition placed at $x = 0.5$ and $\ell = 0.001$. 454

This page left blank

1 Introduction

Constitutive modeling is a fundamental aspect of solid mechanics modeling and simulation. The wide range of behaviors of solid materials requires a vast number of models capable of modeling all (or even some of) the different responses. This is in contrast to fluid mechanics, for example. As such, constitutive modeling is arguably the major problem in solid mechanics. A constitutive model is necessary for accurately predicting the state of a material. This determination includes both the stress state whose resolution is essential for many phenomena of interest like fracture and failure as well as capturing inelastic responses like damage or multiphysics couplings.

One aspect of obtaining an accurate resolution of the stress field is, in one sense, easy to understand. It is mesh discretization. More degrees of freedom in a simulation enables better resolution and results in a more accurate stress field if we look just at the mathematics. If all materials followed an elastic law, then mesh resolution on its own would be all that is needed to resolve the stress field. In reality, however, materials do not exhibit elastic responses except in very limited cases.

This leads us to a second aspect of calculating accurate stress fields, which is much harder to understand. This one concerns the physics. The specific behavior of a material depends on the physical processes specific to that material, and this must be included in a constitutive model in some form or another. The main goal of the Library of Advanced Materials for Engineering - LAMÉ - is to provide a simple means to implement the wide variety of models in a library that can be used by our solid mechanics application codes.

This page left blank

2 Strategy

As a third party library, the Library of Advanced Materials for Engineering (LAMÉ) is renewing a commitment to accurate, robust, and efficient constitutive modeling for solid mechanics. There are three distinct groups that require services from LAMÉ: constitutive model developers, application code developers, and analysts. Each group has different, but related, requirements on LAMÉ.

Constitutive modelers who develop the mathematical models describing the response of interest and the associated numerical methodologies require a framework for developing and implementing these models. This framework must be well documented so that these developers can easily develop and implement a model that can, when the model is sufficiently robust, be used reliably in production calculations.

Application code developers, on the other hand, require that the library of constitutive models share a common, simple interface. This requires that the conceptual division between a constitutive model and the application code be well understood. The application codes also require verified behavior of the models along with certain performance requirements as these models can be called billions of times in an analysis.

Analysts require constitutive models that are both verified and well documented. The responses of interest can very greatly depending on the material utilized and the conditions under which it is loaded. This accounts for the wide range and sheer volume of constitutive models in the literature. Furthermore, there may be nothing that affects the results of an analysis more then the constitutive model. Therefore, the analyst needs a thorough knowledge of the behavior of the models along with how to use it in an application code. Such an understanding is also essential for the accurate determination and calibration of different material and model parameters. In some cases, even subtle changes in a material specimen's history can lead to large variation in properties and responses. As such, a clear description and understanding of this input data is essential for appropriate utilization of different models.

Due to the varied requirements on LAMÉ, a strategy for supporting these various user groups has been developed. This strategy is described here.

2.1 Code Development

There are many strategies that can be employed for a code development process. The choice of such a procedure depends on what the overall project is creating. And even after a development process has been selected, it is often tailored to the needs of the specific code project.

The LAMÉ code development team has spent some time deciding on an appropriate process that reflects the needs of the project and its stakeholders.

Given that LAMÉ has two roles, as an interface to a host code that will supply a material model response and as a repository for constitutive models, this led us to consider two different code development processes: one for the interface and one for the constitutive models.

For the interface an *iterative* process was chosen. The iterative process allows us to plan and generate requirements, perform analysis and design, implement and deploy code changes and finally test and evaluate the code. This process can work well for the interface design where we implement the conceptual changes that we want to the interface. The models beneath the interface should be unaffected by these changes, and where they are affected it will be on the surface.

For the constitutive models a *waterfall* process was chosen. Generally the process of developing and implementing a constitutive model is a linear process that is followed by a single person. That person generates requirements, designs the solution, implements the solution as a piece of code, verifies the code and maintains the code. Much of the constitutive modeler's work involves formulating the model, which is a solid mechanics and applied mathematics problem first and foremost. This can be seen as either the gathering requirements phase or part of the design phase. The design and implementation phases are where the code development occur. All models are verified after they are implemented. However, model verification itself is quite complicated, so this step is not simple. Finally the model is maintained through documentation and user support. Bug fixes are also an aspect of code maintenance in this process.

2.2 Model Implementation

The key feature in LAMÉ that allows constitutive models to be implemented easily and application codes to be able to use those models is the interface. *The key concept to understand concerning the interface is that it defines what roles the constitutive models have, what roles the application codes have, and how the models and the codes transfer information.*

From the application code perspective we would like all of the constitutive models to look the same. Of course this is not the case. This is why, if we were to look at our legacy finite element codes, we see information regarding specific constitutive models show up in the application codes. Even a piece of information as simple as a material model ID will show up in the application code in order that the code call the correct model. Modern programming languages/styles allow us to avoid this confusion.

From a constitutive modeling perspective we would like a simple interface for implementing constitutive models. Constitutive modelers are only part-time code developers. They can have strengths in many areas in addition to code development, including physics, chemistry, continuum mechanics, applied mathematics, numerical methods and experimental mechanics. Having a code development environment that is useful for a constitutive model developer is necessary in the design of the constitutive model library.

2.2.1 Code Standards

The need to supply not only robust constitutive models, but also a robust constitutive modeling environment, requires strict adherence to code standards. Some code standards are stylistic. These are necessary to support the code (promoting readability) and to simplify the effort needed by the constitutive modeler to implement a model. Other code standards are necessary to support the code on various platforms and to prevent unintended behavior like memory leaks.

2.2.2 Testing Standards

Ensuring robust and reliable constitutive models also requires testing. There are two main concerns in providing constitutive modeling to an application code: accuracy and speed. Both of these concerns can be addressed to a large degree through testing. Toward this end two testing systems are developed: a verification test suite and a performance test suite.

2.2.2.1 Verification Testing

Constitutive models for the large deformation of materials can be extremely complex. This complexity is added to by the issues associated with implementing the model in the code. There are two questions associated with assessing this complexity. First, what is the expected result of the model, independent of its implementation? Second, does the implementation model that response?

2.2.2.2 Performance Testing

In a nonlinear solid mechanics analysis, the constitutive models are called often. For an explicit transient dynamics problem, the model is called once for each time step for each integration point in the finite element model. On the other hand, implicit quasi-static analyses call the model every iteration of every time step for each integration point in the finite element model.

Given the amount of time that a nonlinear solid mechanics finite element analysis spends calculating the stresses in a constitutive model, the performance of the constitutive model can have a large effect on the performance of the host code.

In order to ensure some measure of performance, a procedure for testing the performance of the models is proposed. First, a baseline set of performance data must be generated. Given that the CPU time used by the model can depend on many things, including the current loads on the machine where the test is being run, developing an approach for modeling the performance is not straightforward. If we call the various states of the machine “configurations”, then the best approach appears to be to generate a large set of data for the performance of the constitutive model that reflects the performance on a single machine over a large variety of its configurations.

Specifically, since we want to test only the speed of the constitutive model, we run tests that are fully prescribed strain paths. This eliminates any need for the material driver to solve an equilibrium state. We also want to test as many of the features of the constitutive model as possible. This requires a prescribed strain path that pushes the model into regimes of interest. For example, for an elastic-plastic model the performance test has to trigger plasticity, otherwise it will not reflect accurately on how the model performs in an analysis. We also want the strain path to push the plasticity model deep enough into the plastic range.

Determination of an appropriate strain path is not clear cut for all materials. Recognizing this, the performance tests should be documented clearly so that we know exactly what we are testing and we can go back and modify a test if there is some feature of the model that doesn't appear in the performance test.

2.2.3 Documentation Standards

In order to disseminate information about the models in LAMÉ, there must be a commitment to documentation. The theory behind the models and their implementation must be documented. Furthermore, much of the success of the verification and performance testing depends on documentation too. Finally, documentation must be generated for analysts that allows them to understand what materials and behavior the model can represent, along with the inputs necessary to use the model and the outputs that come from the model.

2.3 Model Status

As previously discussed, LAMÉ is structured to facilitate support of model and application developers as well as analysts. This means that models in various stages of development from initial research to robust analysis tools may be found in LAMÉ. For analysts and end users, this diverse model base could pose a challenge during model selection. To try and aid in this selection, the LAMÉ library has been split into two branches – *development* and *production*.

The *development* branch – as its name implies – is intended for any model that is currently being implemented, improved, or otherwise studied. New models not yet subject to full verification rigors are placed here. As such, the usage of *development* models in simulations supporting engineering decisions should be carefully considered and vetted. *Production* models have been subject to strong verification activities and meet further standards to help give credibility and credence to any simulation results.

To establish that a model is at a *production* state of readiness, the model must meet three criteria. The first is that it must have a minimum of one regression test but more tests are recommended. Given the diversity of model complexities and fidelities arriving at an alternative common baseline requirement is challenging. Second, the model must be sufficiently documented including underlying theory, discussion of numerical implementation, usage guides, and documentation of verification tests. Third, the verification tests and ensuing documentation must be peer-reviewed. This review should consider the appropriateness of the documentation and the

verification tests. Importantly, the alignment of verification tests to expected usage and model phenomenology should be assessed to ensure that the test basis is sufficient for model usage. This peer-review should be documented and retained.

Whereas the *production* status of a model is meant to establish a credibility basis with respect to verification, validation of a model requires consideration of the actual material of interest, the intended usage, and availability of experimental data. Thus, validation must be considered on a case-by-case basis and determinations in that context are out of scope of this manual. Importantly, a model being *production* status does not make any statement towards validation.

This page left blank

3 Interface

LAMÉ is designed to have a simple interface that allows the easy implementation of a wide range of constitutive models. This interface is between the application code (sometimes referred to as the "host code") and the constitutive model.

The interface has two main aspects: the data that is passed between the application code and the model, and the functions that pass this data. Given that the interface consists of data and functions, the most reasonable way to set up this interface is through a class.

The class that defines this interface is the `Material` class, which is declared in `include/interface/Material.h`.

There are two types of data that are passed between the application code and the model. The first is the material property information. This is done using an object in the `MatProps` class. This is used when constructing a material model at the beginning of an analysis.

The second type of data that is passed between the application code and the material model is the data that the material model uses during an analysis. This data is in the `MatParams` struct. This data consists of the stress, the kinematics, the time and time step, etc.

More detail can be found in [90].

This page left blank

4 Material Models

This section details the constitutive models that are implemented and supported in LAMÉ. The description of each model has four sections. First, a section discussing the *theory* of the model is found. This is the mathematical description of the model in a continuum mechanics framework, independent of its implementation in a computational code. As these models are intended for solid mechanics analysis, the following section describes the *numerical implementation* of the model. This delves into how the model is implemented in the code and any special numerical techniques that are used to integrate the model. The subsequent section presents the *verification* problems that are run for the model. Through the results of such problems, evidence is provided that, to the best of our understanding, the model is behaving as expected. Finally, documentation of the model *user inputs* and *user outputs* are given for analyst reference.

It is our belief that this collection of documentation is important for the use of our constitutive models, and it provides confidence that our models are implemented correctly for the capabilities that are tested.

What this documentation does not provide is guidance on how to use the models. Different materials behave differently, and it is the responsibility of the user to ensure that the material model chosen can accurately model the behavior of a particular material. Furthermore, even with a single material, many models might be capable of modeling the material depending on the loading in a given analysis. It is the responsibility of the analyst to ensure that the model they choose is the best model for their problem. Across the different models, parameters may also vary in value or have slight changes in interpretation. Care needs to undertaken to ensure that material and model parameters used accurately reflect the specific material being investigated (some parameters may vary with simple changes in processing route) and capture the behaviors that of interest. If emphasis needs to be placed on initial yield rather than failure, subtle differences in some parameters may be expected.

4.1 Hypoelastic Models

Many models presented in this report are derived starting with small deformation formulations. These models are implemented in finite deformation codes by substituting the rate of deformation for the strain rate (it should be noted that the rate of deformation is *not* the rate of any strain measure), and making the stress rate objective. There are many objective stress rates to choose from, the two most common being the Jaumann and the Green-McInnis.

Models that are implemented using the Jaumann or Green-McInnis stress rate are done so in an unrotated configuration. This means that the incremental constitutive relations are written in this configuration. The tensor components of the Cauchy stress, σ_{ij}, and the rate of deformation, D_{ij}, are unrotated using some orthogonal tensor, $Q_{ij}^{-1} = Q_{ji}$, such that

$$T_{ij} = Q_{ki}\sigma_{kl}Q_{lj} \quad ; \quad d_{ij} = Q_{ki}D_{kl}Q_{lj} \tag{4.1}$$

where T_{ij} and d_{ij} are the components of the unrotated stress and rate of deformation respectively. The choice of orthogonal tensor, Q_{ij}, depends on the objective stress rate. The incremental constitutive relation is then written as

$$T_{ij}^{n+1} = T_{ij}^{n} + f_{ij}\left(d_{kl}, \Delta t\right) \tag{4.2}$$

After the stress is updated in the unrotated configuration, it is rotated forward to the current configuration [29]. (The terminology used in describing the unrotated configuration with the rotations backward and forward is infinitely confusing. It is simply one of the many difficulties encountered using finite deformation hypoelastic models.)

If the Green-McInnis stress rate is used, then the unrotated configuration is found using the rotation tensor from the polar decomposition of the deformation gradient

$$dx_i^{n+1} = F_{ij} dX_j \quad ; \quad F_{ij} = R_{ik}U_{kj} = V_{ik}R_{kj} \quad ; \quad Q_{ij} = R_{ij}$$

If the Jaumann stress rate is used, then the unrotated configuration is found using the rotation tensor from the polar decomposition of the incremental deformation gradient

$$dx_i^{n+1} = \hat{F}_{ij} dx_j^{n} \quad ; \quad \hat{F}_{ij} = \hat{R}_{ik}\hat{U}_{kj} = \hat{V}_{ik}\hat{R}_{kj} \quad ; \quad Q_{ij} = \hat{R}_{ij}$$

Without loss of generality we will assume the Green-McInnis stress rate. The algorithm for the Jaumann stress rate can be recovered by substituting $\hat{F}_{ij}$ for F_{ij} and $\hat{R}_{ij}$ for R_{ij} in what follows.

Before updating the stress, the rotation is calculated from the deformation gradient in the *current* configuration, F_{ij}. The unrotated rate of deformation is then

$$d_{ij} = R_{ki}^{n+1} D_{kl} R_{lj}^{n+1}$$

and the unrotated stress is updated using (4.2). Then the stress is rotated to the current configuration, using the same rotation that we used to unrotate the rate of deformation

$$\sigma_{ij}^{n+1} = R_{ik}^{n+1} T_{kl}^{n+1} R_{jl}^{n+1}$$

The unrotated stress from the previous time step is simply $T_{ij}^{n} = R_{ki}^{n}\sigma_{kl}R_{lj}^{n}$. Furthermore, for the elastic model (Section 4.3) the stress update algorithm can be reduced to

$$\sigma_{ij}^{n+1} = R_{ik}^{n+1} R_{mk}^{n} \sigma_{mn} R_{nl}^{n} R_{jl}^{n+1} + \lambda\delta_{ij}\Delta t D_{kk} + 2\mu\Delta t D_{ij} \tag{4.3}$$

One final note about this algorithm. While it is convenient to use the rotation tensor R_{ij}^{n+1}, strictly this is not correct. Since the rate of deformation is most often computed at the mid-step configuration, the rotation used to unrotate the rate of deformation should be the rotation from the mid-step deformation gradient, i.e. the deformation gradient that relates the mid-step configuration to the reference configuration. Other consistency considerations should also be considered, but we will not discuss them here. Suffice it to say that the solutions all converge in the limit of infinitesimal time steps. In a future release of LAMÉ other options might be added.

4.2 Hyperelastic Models

Hyperelastic materials are in many ways easier to understand than hypoelastic materials, and are often considered more thermodynamically consistent. On the other hand, it may be difficult to consistently extend a small deformation model to the finite deformation regime in a hyperelastic framework. Regardless of the pluses and minuses of the two formulations, hyperelastic models are in LAMÉ and will be reviewed here.

Hyperelastic models generally assume a scalar valued strain energy density that is a function of invariants of the deformation through the deformation gradient, F_{ij}. Using the principle of material frame indifference, the strain energy density is written as a function of the symmetric right Cauchy-Green tensor, $C_{ij} = F_{ki}F_{kj}$

$$W = W\left(C_{ij}\right)$$

The stress, in particular the second Piola-Kirchhoff stress, is found by taking the derivative of W with respect to C_{ij}. This relation comes from the stress-power relations. From the second Piola-Kirchhoff stress, we can find the Cauchy stress

$$S_{ij} = 2\frac{\partial W}{\partial C_{ij}} \quad ; \quad \sigma_{ij} = \frac{1}{J}F_{ik}S_{kl}F_{jl}$$

Hyperelastic models are generally of two types. The most common are written in terms of the three invariants of C_{ij}: I_1, I_2, and I_3

$$I_1 = \mathrm{tr}\mathbf{C} = C_{ii} \quad ; \quad I_2 = \frac{1}{2}\left(C_{ii}C_{jj} - C_{ij}C_{ij}\right) \quad ; \quad I_3 = \det\mathbf{C}$$

The second Piola-Kirchhoff stress is then

$$S_{ij} = 2\left(\frac{\partial W}{\partial I_1}\frac{\partial I_1}{\partial C_{ij}} + \frac{\partial W}{\partial I_2}\frac{\partial I_2}{\partial C_{ij}} + \frac{\partial W}{\partial I_3}\frac{\partial I_3}{\partial C_{ij}}\right)$$

Evaluating this expression requires the derivatives of the invariants with respect to the components C_{ij}

$$\frac{\partial I_1}{\partial C_{ij}} = \delta_{ij} \quad ; \quad \frac{\partial I_2}{\partial C_{ij}} = I_1\delta_{ij} - C_{ij} \quad ; \quad \frac{\partial I_3}{\partial C_{ij}} = I_3C^{-1}_{ij}$$

Using this in the expression for the second Piola-Kirchhoff stress, and converting it to the Cauchy stress, we have

$$\sigma_{ij} = \frac{2}{J}\left\{\frac{\partial W}{\partial I_3}\delta_{ij} + \left(\frac{\partial W}{\partial I_1} + I_1\frac{\partial W}{\partial I_2}\right)B_{ij} - \frac{\partial W}{\partial I_2}B^2_{ij}\right\}$$

The majority of hyperelastic models calculate the stress in this manner.

Some hyperelastic models, however, have their strain energy densities written in terms of the principal stretches [79]. When this is the case the calculation of the stress is more complex. The right stretch can be written as

$$\mathbf{U} = \sum_{i=1}^{3}\lambda_i\bar{\mathbf{e}}_i \otimes \bar{\mathbf{e}}_i$$

where λ_i are the principal stretches, or eigenvalues, and $\bar{\mathbf{e}}_i$ are the principal directions, or eigenvectors. The strain energy density is $W(\lambda_i)$. We calculate the stress components of the second Piola-Kirchhoff stress, $\bar{S}_{ij}$, with respect to the principal directions

$$\mathbf{S} = \bar{S}_{ij}\bar{\mathbf{e}}_i \otimes \bar{\mathbf{e}}_j$$

This is done by calculating $\partial W/\partial \mathbf{C}$ in the following manner

$$\delta W = \frac{\partial W}{\partial \lambda_i}\delta\lambda_i = \frac{\partial W}{\partial \mathbf{C}} : \delta\mathbf{C} \tag{4.4}$$

Writing the right Cauchy-Green tensor with respect to the principal directions we have

$$\mathbf{C} = \sum_{i=1}^{3} \lambda_i^2\, \bar{\mathbf{e}}_i \otimes \bar{\mathbf{e}}_i \quad ; \quad \delta\mathbf{C} = \sum_{i=1}^{3} 2\lambda_i\delta\lambda_i\bar{\mathbf{e}}_i \otimes \bar{\mathbf{e}}_i + \lambda_i^2\delta\bar{\omega}_{ij}\left(\bar{\mathbf{e}}_i \otimes \bar{\mathbf{e}}_j + \bar{\mathbf{e}}_j \otimes \bar{\mathbf{e}}_i\right)$$

Equating terms on both sides of (4.4) we get

$$\bar{S}_{11} = \frac{1}{\lambda_1}\frac{\partial W}{\partial \lambda_1} \quad ; \quad \bar{S}_{22} = \frac{1}{\lambda_2}\frac{\partial W}{\partial \lambda_2} \quad ; \quad \bar{S}_{33} = \frac{1}{\lambda_3}\frac{\partial W}{\partial \lambda_3} \quad ; \quad \bar{S}_{ij} = 0 \quad \text{otherwise}$$

These calculations can also be checked by writing the invariants in terms of the principal stretches. For a hyperelastic model written in terms of the invariants the results should be the same.

The differences between hypoelastic and hyperelastic models should not matter for the analyst. For the constitutive modeler, however, the benefits and drawbacks of the two formulations must be considered.

4.3 Elastic Model

4.3.1 Theory

The elastic model is a hypoelastic extension of isotropic, small-strain, linear elasticity [63], [94], [107]. The stress-strain response for an isotropic, elastic material is

$$\sigma_{ij} = \lambda\delta_{ij}\varepsilon_{kk} + 2\mu\varepsilon_{ij}$$

where the Lamé constants, λ and μ, are given by

$$\lambda = \frac{E\nu}{(1+\nu)\,(1-2\nu)} \quad ; \quad \mu = \frac{E}{2\,(1+\nu)}$$

This model is extended to a finite-deformation, hypoelastic model by first making it a rate equation. Then the stress rate is replaced with an objective stress rate and the strain rate is replaced with the rate of deformation. This gives us

$$\overset{\circ}{\sigma}_{ij} = \lambda\delta_{ij}D_{kk} + 2\mu D_{ij}$$

The stress rate is arbitrary, as long as it is objective. Two objective stress rates are commonly used: the Jaumann rate and the Green-McInnis rate. For problems with fixed principal axes of deformation, these two rates give the same answers. For problems where the principal axes of deformation rotate during the deformation, the two rates can give different answers. Generally speaking there is no reason to pick one objective rate over another. Sierra/SM uses the Green-McInnis rate.

The fourth-order elastic moduli are used in many constitutive models. There are many equivalent representations for the elastic moduli. In index notation we present the following three representations

$$\overset{\circ}{\sigma}_{ij} = \mathbb{C}_{ijkl} D_{kl}$$

$$\mathbb{C}_{ijkl} = \frac{E}{1+\nu}\left[\frac{\nu}{1-2\nu}\delta_{ij}\delta_{kl} + \frac{1}{2}\left(\delta_{ik}\delta_{jl} + \delta_{il}\delta_{jk}\right)\right]$$

$$\mathbb{C}_{ijkl} = \lambda\delta_{ij}\delta_{kl} + \mu\left(\delta_{ik}\delta_{jl} + \delta_{il}\delta_{jk}\right)$$

$$\mathbb{C}_{ijkl} = K\delta_{ij}\delta_{kl} + \mu\left(\delta_{ik}\delta_{jl} + \delta_{il}\delta_{jk} - \frac{2}{3}\delta_{ij}\delta_{kl}\right)$$

where K is the elastic bulk modulus and is given by

$$K = \frac{E}{3\left(1-2\nu\right)}$$

4.3.2 Implementation

The elastic model is a hypoelastic model and is implemented using an unrotated configuration in order to preserve objectivity. Given an unrotated rate of deformation, d_{ij}, and the unrotated stress at time t_n, T^n_{ij}, the unrotated stress is updated by integrating the constant unrotated rate of deformation

$$T^{n+1}_{ij} = T^n_{ij} + \lambda\delta_{ij}\Delta t d_{kk} + 2\mu\Delta t d_{ij}$$

4.3.3 Verification

Three verification problems are run for the elastic model: uniaxial stress, pure shear, and biaxial stress. The results of these test problems serve as verification for the elastic model.

4.3.3.1 Uniaxial Stress

The elastic model was verified in uniaxial stress. The problem was run with a Young's modulus of 200 GPa and a Poisson's ratio of 0.3. The axial stress is simply

$$\sigma_{11} = E\varepsilon_{11}$$

The axial stress is shown in Fig. 4.1. The axial stress is linear with the axial strain and has a slope of $E = 200 \times 10^3$ MPa.

The lateral strains for uniaxial stress are

$$\varepsilon_{22} = \varepsilon_{33} = -\nu\varepsilon_{11}$$

The lateral strains are shown in Fig. 4.2.

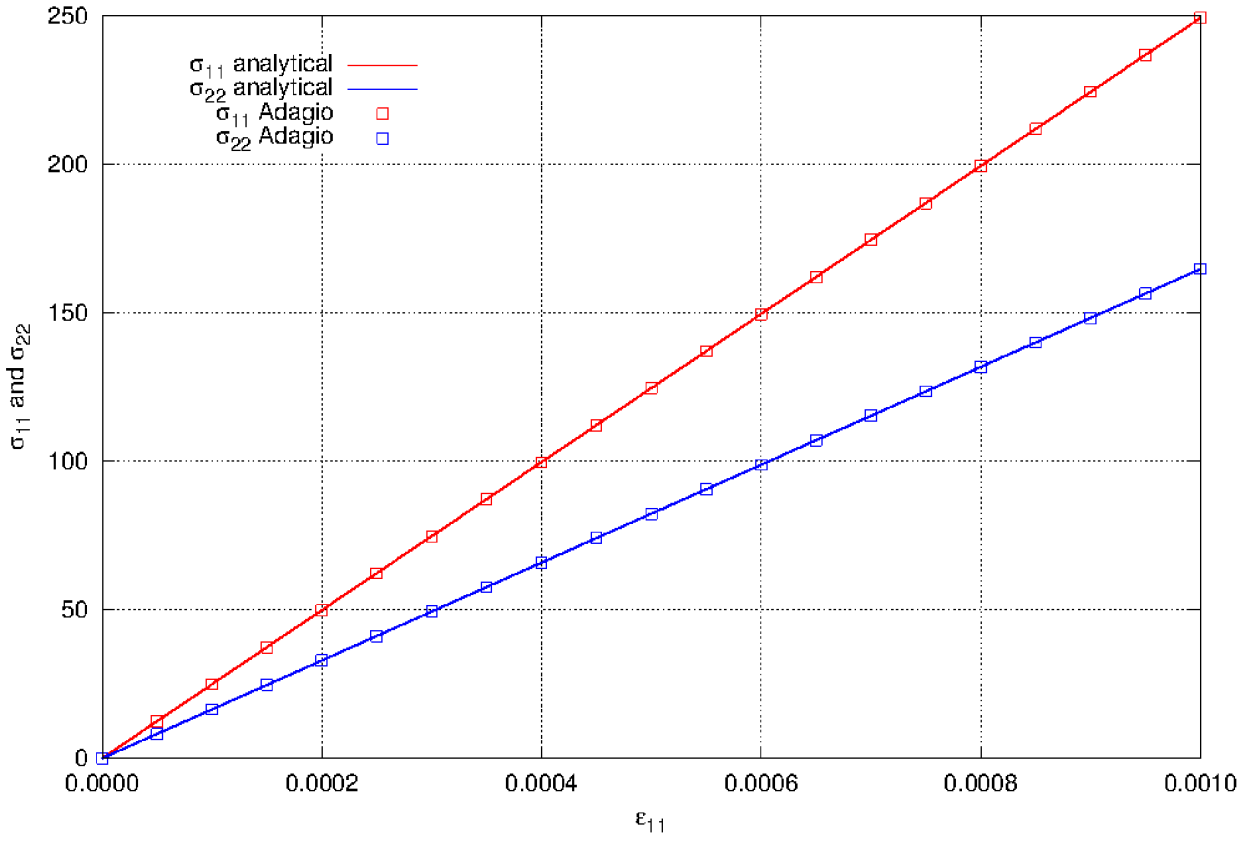

Fig. 4.1 The axial stress component σ_{11} in uniaxial stress using the elastic model.

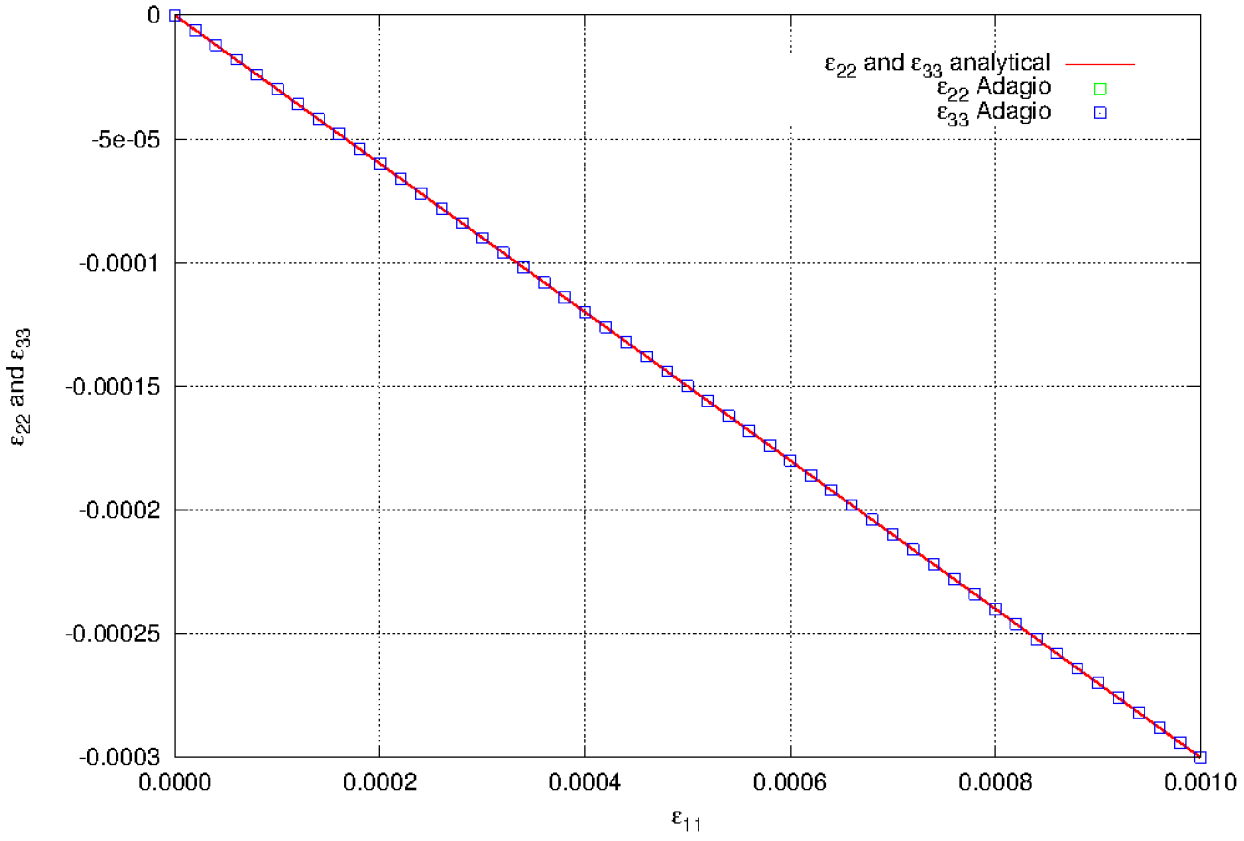

Fig. 4.2 The lateral strain components ε_{22} and ε_{33} in uniaxial stress using the elastic model.

4.3.3.2 Biaxial Stress

The elastic model is verified in biaxial stress. Biaxial stress is a plane stress state where $\sigma_{11} = \sigma_1$, $\sigma_{22} = \sigma_2$, and all other stress components are zero. The problem is displacement controlled in the x_1 and x_2 directions. If the applied strains are $\varepsilon_{11} = \varepsilon$ and $\varepsilon_{22} = \alpha\varepsilon$ where $\alpha \in [0, 1]$, then the applied displacements are

$$\begin{aligned} u_1 &= \lambda_1 - 1 \quad ; \quad \lambda_1 = \exp(\varepsilon) \\ u_2 &= \lambda_2 - 1 \quad ; \quad \lambda_2 = \exp(\alpha\varepsilon). \end{aligned}$$

In the following results, α will be taken to be 0.45. For the plane stress state, we have $\sigma_{33} = 0$, which allows us to solve for ε_{33}

$$\varepsilon_{33} = -\frac{\nu}{1-\nu}\,(1+\alpha)\,\varepsilon.$$

The component ε_{33} is shown in Fig. 4.3. The in-plane stress components are

$$\begin{aligned} \sigma_{11} &= \frac{E}{1-\nu^2}\,(1+\alpha\nu)\,\varepsilon \\ \sigma_{22} &= \frac{E}{1-\nu^2}\,(\alpha+\nu)\,\varepsilon. \end{aligned}$$

The in-plane stress components are shown in Fig. 4.4.

4.3.3.3 Pure Shear

The elastic model is verified in pure shear. Pure shear gives a stress state where σ_{12} is the only non-zero stress component. The problem is completely displacement controlled and the applied shear strain is $\varepsilon_{12} = \varepsilon(t)$.

The shear stress in the problem is

$$\sigma_{12} = 2\mu\varepsilon$$

The shear stress-strain response is shown in Fig. 4.5.

4.3.3.4 Performance

The performance of the elastic model was analyzed using the material point driver. The elastic model was run in uniaxial strain for 1 billion calculations and the CPU time was recorded using clock() method in the time.h header. The start and end times are found and the CPU time is calculated by dividing the difference by the variable CLOCKS_PER_SECOND.

Since the CPU times will depend on many things outside of the actual code, a set of times were generated as a baseline. For this task the 1 billion calculations were performed 100 times. With

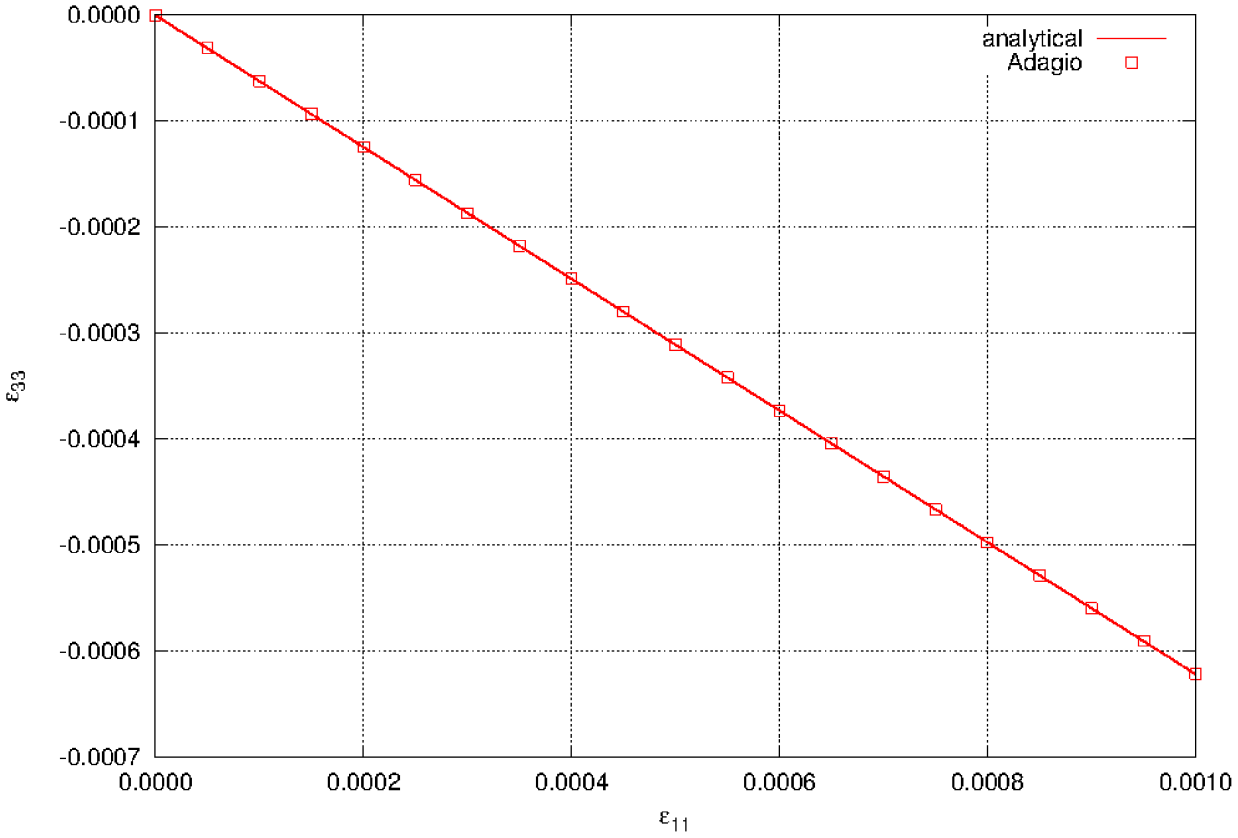

Fig. 4.3 The strain component ε_{33} in biaxial stress using the elastic model.

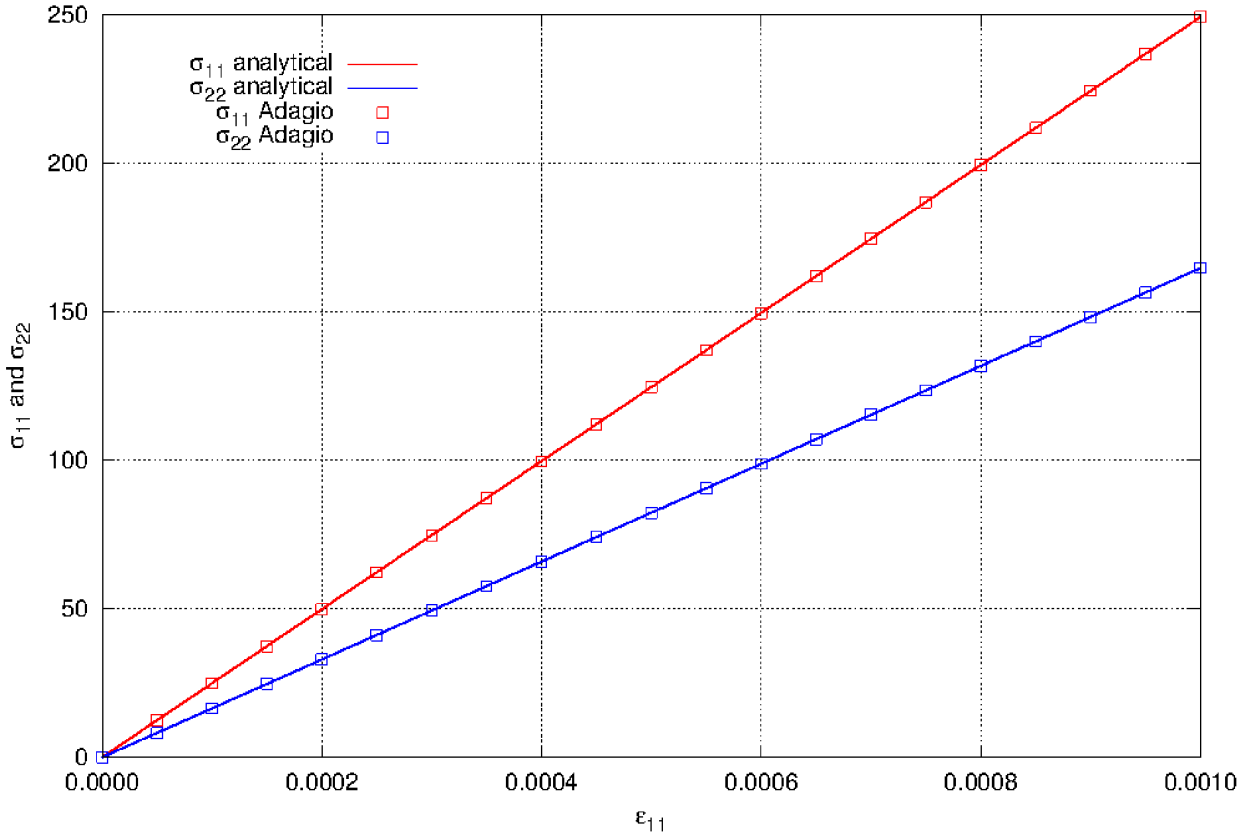

Fig. 4.4 The normal stress components σ_{11} and σ_{22} in biaxial stress using the elastic model.

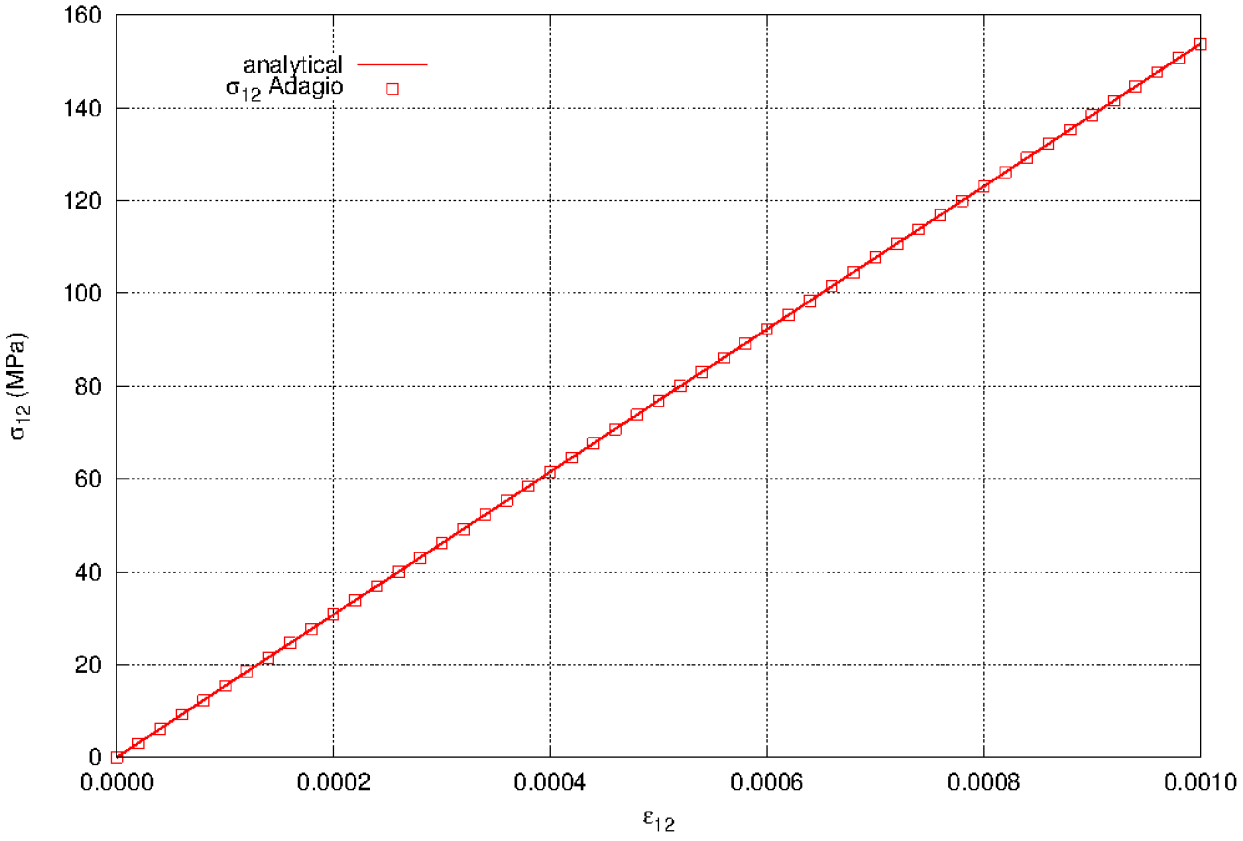

Fig. 4.5 The shear stress component σ_{12} in pure shear using the elastic model.

the 100 CPU times the mean and standard deviation were calculated. Next we assume a normal distribution of CPU times and the normal distribution is generated.

Subsequent performance tests involve generating 10 sets of the 1 billion calculations. This much smaller data set is used to generate its own mean and standard deviation. If this mean is within 3 standard deviations of the baseline mean, then the performance of the model is assumed to be identical to that of the baseline model.

4.3.4 User Guide

```
BEGIN PARAMETERS FOR MODEL ELASTIC
  #
  # Elastic constants
  #
  YOUNGS MODULUS = <real>
  POISSONS RATIO = <real>
  SHEAR MODULUS  = <real>
  BULK MODULUS   = <real>
  LAMBDA         = <real>
  TWO MU         = <real>
END [PARAMETERS FOR MODEL ELASTIC]
```

There are no output variables available for the elastic model. For information about the elastic model, consult [103].

4.4 Elastic Three Dimensional Orthotropic Model

4.4.1 Theory

The ELASTIC 3D ORTHOTROPIC model is an extension of the previously discussed ELASTIC routine and describes the linear elastic response of a material which exhibits orthotropic symmetry, where the orientation of the principal material directions can be arbitrary with respect to the global Cartesian axes as specified by the user.

First, a rectangular, cylindrical, or spherical reference coordinate system is defined. The material coordinate system can then be defined through two successive rotations about axes in the reference coordinate system. These principal axes are denoted as A, B, and C in the following. Thermal strains are also defined with respect to these principal material axes.

The elastic stiffness for an orthotropic material can be described in terms of the elastic compliance which relates the strain to the stress, $\varepsilon_{ij} = \mathbb{S}_{ijkl}\sigma_{kl}$. For a material with an orthogonal ABC

coordinate system, and written in that reference frame, the elastic compliance tensor is given by

$$\left[\tilde{\mathbb{S}}\right] = \begin{bmatrix} \frac{1}{E_{AA}} & -\frac{\nu_{BA}}{E_{BB}} & -\frac{\nu_{CA}}{E_{CC}} & 0 & 0 & 0 \\ -\frac{\nu_{AB}}{E_{AA}} & \frac{1}{E_{BB}} & -\frac{\nu_{CB}}{E_{CC}} & 0 & 0 & 0 \\ -\frac{\nu_{AC}}{E_{AA}} & -\frac{\nu_{BC}}{E_{BB}} & \frac{1}{E_{CC}} & 0 & 0 & 0 \\ 0 & 0 & 0 & \frac{1}{2G_{AB}} & 0 & 0 \\ 0 & 0 & 0 & 0 & \frac{1}{2G_{BC}} & 0 \\ 0 & 0 & 0 & 0 & 0 & \frac{1}{2G_{CA}} \end{bmatrix}, \tag{4.5}$$

where the $\tilde{\cdot}$ is used to denote a variable in the ABC material system.

From the definition (4.5), it can be seen that requiring symmetry leads to relations of the form,

$$\nu_{BA} = \nu_{AB}\frac{E_{BB}}{E_{AA}} \quad ; \quad \nu_{CB} = \nu_{BC}\frac{E_{CC}}{E_{BB}} \quad ; \quad \nu_{AC} = \nu_{CA}\frac{E_{AA}}{E_{CC}}.$$

Therefore, only 9 independent constants are needed to fully define the model behavior.

The orthotropic model is also formulated in a hypoelastic fashion, leading to a constitutive equation (in the ABC material frame) of,

$$\overset{\circ}{\tilde{\sigma}}_{ij} = \tilde{\mathbb{C}}_{ijkl}\left(\tilde{D}_{kl} - \tilde{D}^{th}_{kl}\right),$$

where $\tilde{D}^{th}_{ij}$ is the thermal strain rate.

The elastic stiffness tensor, $\tilde{\mathbb{C}}_{ijkl}$, is the inverse of the compliance, $\tilde{\mathbb{C}}_{ijkl} = \tilde{\mathbb{S}}^{-1}_{ijkl}$, and as such may be determined to be,

$$\left[\tilde{\mathbb{C}}\right] = \begin{bmatrix} \mathbb{C}_{AAAA} & \mathbb{C}_{AABB} & \mathbb{C}_{CCAA} & 0 & 0 & 0 \\ \mathbb{C}_{AABB} & \mathbb{C}_{BBBB} & \mathbb{C}_{BBCC} & 0 & 0 & 0 \\ \mathbb{C}_{CCAA} & \mathbb{C}_{BBCC} & \mathbb{C}_{CCCC} & 0 & 0 & 0 \\ 0 & 0 & 0 & 2G_{AB} & 0 & 0 \\ 0 & 0 & 0 & 0 & 2G_{BC} & 0 \\ 0 & 0 & 0 & 0 & 0 & 2G_{CA} \end{bmatrix}.$$

where

$$\mathbb{C}_{AAAA} = \frac{1-\nu_{BC}\nu_{CB}}{\Delta}E_{AA} \quad ; \quad \mathbb{C}_{BBBB} = \frac{1-\nu_{CA}\nu_{AC}}{\Delta}E_{BB} \quad ; \quad \mathbb{C}_{CCCC} = \frac{1-\nu_{AB}\nu_{BA}}{\Delta}E_{CC}$$

$$\mathbb{C}_{AABB} = \frac{\nu_{BA}+\nu_{CA}\nu_{BC}}{\Delta}E_{AA} \quad ; \quad \mathbb{C}_{BBCC} = \frac{\nu_{CB}+\nu_{AB}\nu_{CA}}{\Delta}E_{BB} \quad ; \quad \mathbb{C}_{CCAA} = \frac{\nu_{AC}+\nu_{BC}\nu_{AB}}{\Delta}E_{CC}$$

and $\Delta = 1 - \nu_{AB}\nu_{BA} - \nu_{BC}\nu_{CB} - \nu_{CA}\nu_{RT} - 2\nu_{AB}\nu_{BC}\nu_{CA}$.

[38] for more information about the elastic three-dimensional orthotropic model.

4.4.2 Implementation

Given the similarities in formulation, the 3D orthotropic and elastic models are integrated in a similar fashion. Section 4.3.2 discussed many of these issues in detail for the isotropic elastic formulation. As such, in this section, special attention is paid to the treatment of the complexity associated with the orthotropic model – namely, the multiple coordinate systems.

To implement the elastic 3D orthotropic model, two coordinate systems need to be considered – the local ABC material and global XYZ coordinate systems. The former is used in defining the material response and the latter refers to the larger boundary value problem being analyzed. To map between these configurations, a user-defined coordinate system is specified that can be rotated twice about one of its current axes to give the final, desired directions. A corresponding rotation tensor, $\tilde{Q}_{ij}$, may also be constructed in this way and used to transform various variables. Noting that the elastic stiffness tensor is constant throughout loading enables the transformation

$$\mathbb{C}_{ijkl} = \tilde{Q}_{ai}\tilde{Q}_{bj}\tilde{Q}_{ck}\tilde{Q}_{dl}\tilde{\mathbb{C}}_{abcd} \tag{4.6}$$

to be performed during initialization. The $\tilde{\cdot}$ is used with the rotation tensor Q_{ij} to emphasize that it does not map between the unrotated and rotated configurations (as defined in (4.1)) and is instead associated with transforming between the ABC and XYZ frames.

In the material coordinate system, the thermal strain tensor may be written as,

$$\tilde{\varepsilon}^{th}_{ij} = \varepsilon^{th}_{aa}(\theta)\,\delta_{ia}\delta_{ja} + \varepsilon^{th}_{bb}(\theta)\,\delta_{ib}\delta_{jb} + \varepsilon^{th}_{cc}(\theta)\,\delta_{ic}\delta_{jc},$$

where $\varepsilon^{th}_{aa}(\theta)$, $\varepsilon^{th}_{bb}(\theta)$, and $\varepsilon^{th}_{cc}(\theta)$ are the temperature (θ) dependent thermal strain functions in the A, B, and C principal material directions, respectively, and δ_{ij} is the Kronecker delta. Using the same constant transformation, $\tilde{Q}_{ij}$, the XYZ-system thermal strain tensor is determined to be,

$$\varepsilon^{th}_{ij}(\theta) = \tilde{Q}_{ai}\tilde{\varepsilon}^{th}_{ab}\tilde{Q}_{jb}. \tag{4.7}$$

Following (4.3), the updated Cauchy stress may then be found to be,

$$\sigma^{n+1}_{ij} = R^{n+1}_{ik}R^{n}_{mk}\sigma^{n}_{mn}R^{n}_{nl}R^{n+1}_{jl} + \mathbb{C}_{ijkl}\left(\Delta t D_{kl} - \left(\varepsilon^{th}_{kl}\left(\theta^{n+1}\right) - \varepsilon^{th}_{kl}\left(\theta^{n}\right)\right)\right),$$

where the time dependency in the thermal strains is accounted for through changes in the temperature field.

4.4.3 Verification

The elastic 3D orthotropic model is verified through both biaxial displacement and uniaxial strain tests. The first is performed with the material and global coordinate systems aligned to investigate anisotropy while the second is done with the material coordinate system misaligned with respect to the global system. The latter also incorporates a thermal loading component to test the thermal strain contributions. In this case, it is assumed that each of the thermal strain input functions have linear slopes of α_{aa}, α_{bb}, and α_{cc} for the A, B, and C principal material axes, respectively. A common zero strain reference temperature, T_0, is assumed for all three functions. The set of material properties used for these tests are given in Table 4.1.

Table 4.1 The material properties for the elastic 3D orthotropic model used for the varying temperature, uniaxial stress tests.

$E_{AA} = E$	10,000.0 ksi	G_{AB}	100.0 ksi
E_{BB}	200.0 ksi	G_{BC}	1,000.0 ksi
E_{CC}	10.0 ksi	G_{CA}	5.0 ksi
$\nu_{AB} = \nu$	0.25	α_{aa}	50 $\frac{\mu\varepsilon}{\mathrm{K}}$
ν_{BC}	0.2	α_{bb}	500 $\frac{\mu\varepsilon}{\mathrm{K}}$
ν_{CA}	0.003	α_{cc}	5 $\frac{\mu\varepsilon}{\mathrm{K}}$
		θ_0	293 K

4.4.3.1 Biaxial Displacement

First, to investigate anisotropic effects, the case of a biaxial applied displacement of the form,

$$u_i = \lambda_1 \delta_{1i} + \lambda_2 \delta_{2i},$$

is considered for a material which has its axes aligned with the global Cartesian system – $\alpha_1 = \alpha_2 = 0$ or the A, B, and C frame is the same as the $\hat{\mathrm{e}}_1$, $\hat{\mathrm{e}}_2$, and $\hat{\mathrm{e}}_3$. To simplify the problem, $\lambda_2 = \frac{1}{2}\lambda_1$ and it can be shown that (noting $\sigma_{33} = 0$ from a corresponding traction free condition),

$$\begin{aligned}
\varepsilon_{11} &= \ln\left(1 + \lambda_1\right), \\
\varepsilon_{22} &= \ln\left(1 + \frac{1}{2}\lambda_1\right) \\
\varepsilon_{33} &= -\frac{\nu_{AC} + \nu_{BC}\nu_{AB}}{1 - \nu_{AB}\nu_{BA}}\varepsilon_{11} - \frac{\nu_{BC} + \nu_{BA}\nu_{AC}}{1 - \nu_{AB}\nu_{BA}}\varepsilon_{22}.
\end{aligned}$$

With the strain state known, analytical stresses may be found via Hooke's law. The corresponding results of both the numerical and analytical results are presented below in Fig. 4.6. Numerical results are found through a single element test. Importantly, by comparing the results of Fig. 4.6(a) and Fig. 4.6(b) the expected and desired anisotropy may be clearly seen in the vast difference of stress magnitudes (as indicated by the figure scaling). Additionally, the matching results serves to verify the model under such conditions.

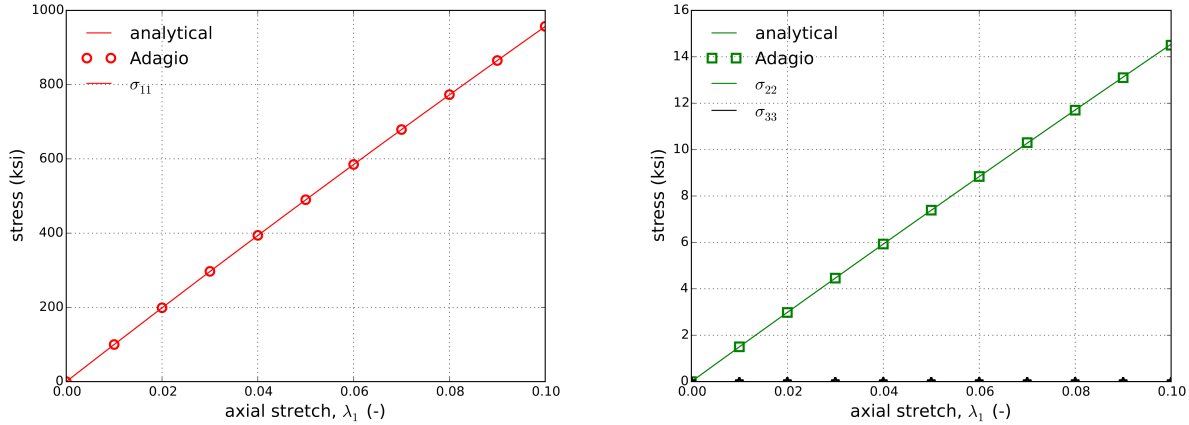

Fig. 4.6 Analytical and numerical results of axial σ_{11} and transverse, σ_{22} and σ_{33}, as a function of the stretch λ_1.

4.4.3.2 Uniaxial Strain

Secondly, the capabilities of this model under arbitrary rotations are explored. To be able to analytically consider this problem, a uniaxial strain ($\varepsilon_{ij} = \varepsilon_{11}\delta_{i1}\delta_{j1}$) loading is investigated. The material properties are rotated with the specified orientations per Equations (4.6) and (4.7) using the specified orientations in Table 4.2. A combined thermal-mechanical loading is considered. Specifically, the material is first stretched to the specified strain and that strain is then held fixed during a heating step (ΔT =400 K) to investigate the ability of the model to accurately incorporate anisotropic coefficients of thermal expansion. The results for both the analytical and numerical (from a corresponding single element simulation) analyses are shown in Fig. 4.7 with the normal and shear stresses presented in Fig. 4.7(a) and Fig. 4.7(b) respectively. Clear agreement may be seen during both the thermal and mechanical loading stages including the anisotropic effects further verifying model capabilities.

Table 4.2 The coordinate system rotations used with the elastic 3D orthotropic model for the uniaxial strain test.

α_1	30	Direction 1	3
α_2	60	Direction 2	1

4.4.4 User Guide

```
BEGIN PARAMETERS FOR MODEL ELASTIC_3D_ORTHOTROPIC
  #
  # Elastic constants
  #
  YOUNGS MODULUS = <real>
```

(continues on next page)

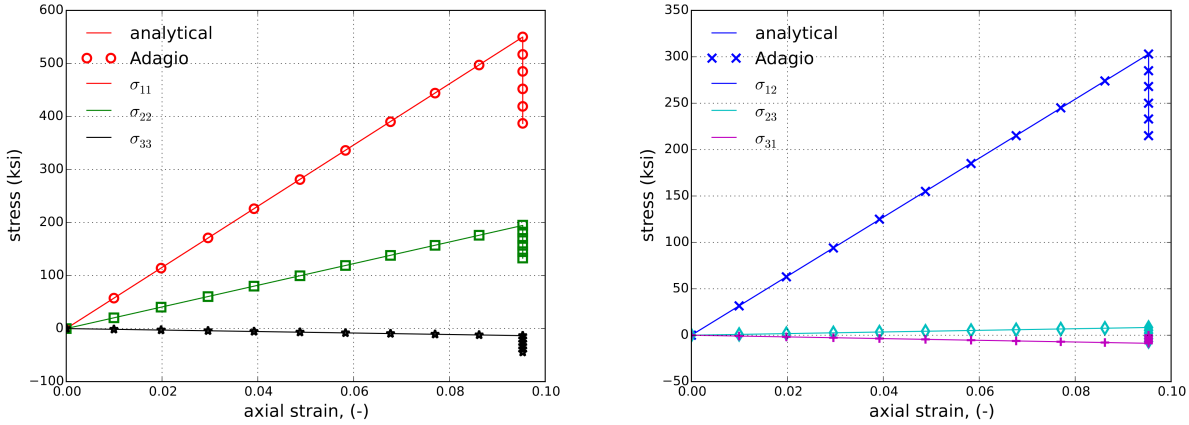

(a) Normal stresses **(b) Shear stresses**

Fig. 4.7 Analytical and numerical results of the stress state through a thermomechanical uniaxial strain loading as a function of the axial strain ε_{11}.

(continued from previous page)

```
POISSONS RATIO = <real>
SHEAR MODULUS  = <real>
BULK MODULUS   = <real>
LAMBDA         = <real>
TWO MU         = <real>
#
# Material coordinates system definition
#
COORDINATE SYSTEM             = <string> coordinate_system_name
DIRECTION FOR ROTATION        = <real>   1|2|3
ALPHA                         = <real>   (degrees)
SECOND DIRECTION FOR ROTATION = <real>   1|2|3
SECOND ALPHA                  = <real>   (degrees)
#
# Required parameters
#
YOUNGS MODULUS AA = <real>
YOUNGS MODULUS BB = <real>
YOUNGS MODULUS CC = <real>
POISSONS RATIO AB = <real>
POISSONS RATIO BC = <real>
POISSONS RATIO CA = <real>
SHEAR MODULUS AB  = <real>
SHEAR MODULUS BC  = <real>
SHEAR MODULUS CA  = <real>
#
# Thermal strain functions
```

(continues on next page)

(continued from previous page)

```
  #
  THERMAL STRAIN AA FUNCTION = <string>
  THERMAL STRAIN BB FUNCTION = <string>
  THERMAL STRAIN CC FUNCTION = <string>
  #
END [PARAMETERS FOR MODEL ELASTIC_3D_ORTHOTROPIC]
```

In the above command blocks all of the following are required inputs.

- Even though they are not used within the material model itself, elastic constants are still required input for hourglass control, certain preconditioners, and other various capabilities. After examining various test problems, it has been determined that using the mean of the orthotropic properties as the isotropic elastic constants yields the best results.
- The Young's moduli corresponding to the principal material axes A, B, and C are given by the `YOUNGS MODULUS AA`, `YOUNGS MODULUS BB`, and `YOUNGS MODULUS CC` command lines.
- The Poisson's ratio defining the BB normal strain when the material is subjected only to AA normal stress is given by the `POISSONS RATIO AB` command line.
- The Poisson's ratio defining the CC normal strain when the material is subjected only to BB normal stress is given by the `POISSONS RATIO BC` command line.
- The Poisson's ratio defining the AA normal strain when the material is subjected only to CC normal stress is given by the `POISSONS RATIO CA` command line.
- The remaining Poisson's ratios needed for the orthotropic elastic relations (i.e. the BA, CB, and AC Poisson's ratios) are calculated internally. They are calculated as usual from the given Poisson's ratios, given Young's moduli, and energy considerations, which provide expressions for these parameters from the resulting symmetry of the compliance tensor.
- The shear moduli for shear in the AB, BC, and CA planes are given by the `SHEAR MODULUS AB`, `SHEAR MODULUS BC`, and `SHEAR MODULUS CA` command lines, respectively.
- The thermal strain functions for normal thermal strains along the principal material directions are given by the `THERMAL STRAIN AA FUNCTION`, `THERMAL STRAIN BB FUNCTION`, and `THERMAL STRAIN CC FUNCTION` command lines.

Warning: The `ELASTIC_3D_ORTHOTROPIC` model cannot currently be used in conjunction with the control stiffness implicit solver block.

There are no output variables available for the Elastic Three-Dimensional Orthotropic material model.

4.5 Neo-Hookean Model

4.5.1 Theory

The neo-Hookean model is a hyperelastic generalization of isotropic, small-strain linear elasticity. The stress-strain response for the neo-Hookean model may be determined from a free energy function - in this case the strain energy density, W. The form of the strain energy density [93] is

$$W(C_{ij}) = \frac{1}{2}K\left[\frac{1}{2}\left(J^2 - 1\right) - \ln J\right] + \frac{1}{2}\mu\left(\bar{C}_{kk} - 3\right), \tag{4.8}$$

where K and μ are the bulk and shear moduli, respectively. The deformation measure is given by C_{ij}, the components of the right Cauchy-Green tensor, where $C_{ij} = F_{ki}F_{kj}$. The determinant of the deformation gradient is given by J and is a measure of the volumetric part of the deformation. $\bar{C}_{ij}$ provides the isochoric part of the deformation and is given by

$$\bar{C}_{ij} = \bar{F}_{ki}\bar{F}_{kj}, \quad \bar{F}_{ij} = J^{-1/3}F_{ij}. \tag{4.9}$$

The second Piola-Kirchoff stress, with components S_{ij}, may be determined by taking a derivative of the strain energy density and the Cauchy stress may be found by mapping from the second Piola-Kirchoff stress. The components of the Cauchy stress are

$$\sigma_{ij} = \frac{1}{2}K\left(J - \frac{1}{J}\right)\delta_{ij} + J^{-5/3}\mu\left(B_{ij} - \frac{1}{3}B_{kk}\delta_{ij}\right), \tag{4.10}$$

where $B_{ij} = F_{ik}F_{jk}$, are the components of the left Cauchy-Green tensor and δ_{ij} is the Kronecker delta.

Linearizing (4.10) we recover small strain linear elasticity

$$\begin{aligned}\sigma_{ij} &= \left(K - \frac{2}{3}\mu\right)u_{k,k}\delta_{ij} + \mu\left(u_{i,j} + u_{j,i}\right)\\ &= \left(K - \frac{2}{3}\mu\right)\varepsilon_{kk}\delta_{ij} + 2\mu\varepsilon_{ij}.\end{aligned}$$

The neo-Hookean model is used for the recoverable (elastic) part for a number of inelastic, finite deformation constitutive models.

4.5.2 Implementation

As a hyperelastic model, the current state of the material may be determined by the total deformation. To this end we use the polar decomposition of the deformation gradient,

$$F_{ij} = V_{ik}R_{kj}, \tag{4.11}$$

in which V_{ij} are the components of the left stretch tensor and R_{ij} is the corresponding rotation. Noting that,

$$B_{ij} = V_{ik}V_{kj},$$

and $J = \det\left(V_{ij}\right)$, the Cauchy stress (via (4.10)) is found. The unrotated stress, T_{ij}, which is needed for internal force calculations in Sierra/SM, is found using the transformation

$$T_{ij} = R_{ki}\sigma_{kl}R_{lj}.$$

4.5.3 Verification

It is possible to find closed form solutions for a number of loadings. Five problems are described here: uniaxial stress, pure shear strain, pure shear stress, uniaxial strain and simple shear. One set of material properties was used for all tests and they are given in Table 4.3. The elastic modulus and Poisson's ratio are given in addition to the bulk and shear moduli.

Table 4.3 The material properties for the neo-Hookean model used for both the uniaxial and simple shear tests.

K	0.5 MPa	μ	0.375 MPa
E	0.9 MPa	ν	0.2

4.5.3.1 Uniaxial Stress

For uniaxial stress we will assume, without loss of generality, that $\sigma_{11} \neq 0$. The deformation, in terms of the components of the left stretch tensor, for this stress state is

$$V_{11} = \lambda_1, \quad V_{22} = V_{33} = \lambda_2,$$

with all other components being zero.

The Cauchy stress is given by (4.10), however for simplicity we will use the Kirchhoff stress instead

$$\tau_{ij} = J\sigma_{ij},$$

where in what follows $\tau_{11} = \tau$. With the lateral stresses being zero we have two equations

$$\tau = \frac{K}{2}\left(J^2 - 1\right) + \frac{2}{3}\mu J^{-2/3}\left(\lambda_1^2 - \lambda_2^2\right)$$

$$0 = \frac{K}{2}\left(J^2 - 1\right) - \frac{1}{3}\mu J^{-2/3}\left(\lambda_1^2 - \lambda_2^2\right).$$

First, we solve for J by looking at the trace of the stress tensor. This gives us

$$\tau = \frac{3K}{2}\left(J^2 - 1\right) .J = \sqrt{1 + \frac{2\tau}{3K}}.$$

Once we have J we can write $\lambda_2^2 = J/\lambda_1$ and solve for λ_1 by looking at the deviatoric part of the Kirchhoff stress. For this we have

$$\tau = \mu J^{-2/3}\left(\lambda_1^2 - \frac{J}{\lambda_1}\right).$$

Rearranging we get a cubic equation for λ_1

$$\lambda_1^3 - \left(\frac{\tau}{\mu}J^{2/3}\right)\lambda_1 - J = 0.$$

A solution for this can be found with the following substitution

$$\lambda_1 = x + \frac{p}{3x}, \quad p = \frac{\tau}{\mu}J^{2/3}, \tag{4.12}$$

which gives a quadratic equation for x^3

$$x^6 - Jx^3 + \frac{p^3}{27} = 0.$$

The one meaningful solution to this polynomial is

$$x = \left[\frac{J}{2} + \sqrt{\left(\frac{J}{2}\right)^2 - \left(\frac{p}{3}\right)^3}\right]^{1/3},$$

with which we can substitute into (4.12) to get λ_1. With J and λ_1 we can solve for λ_2. Note that in this solution the axial Kirchhoff stress, τ, is the independent variable.

This solution is compared to the solution from a single element problem in Sierra/SM in Fig. 4.8(a) and Fig. 4.8(b). It should be noted that the response of the neo-Hookean model is *slightly* nonlinear. The linear elastic solution is given by the green line in each figure.

4.5.3.2 Pure Shear Strain

For pure shear strain the deformation gradient, which is symmetric, is

$$\left[F_{ij}\right] = \frac{1}{2}\begin{bmatrix} \left(\lambda + \lambda^{-1}\right) & \left(\lambda - \lambda^{-1}\right) & 0 \\ \left(\lambda - \lambda^{-1}\right) & \left(\lambda + \lambda^{-1}\right) & 0 \\ 0 & 0 & 2 \end{bmatrix},$$

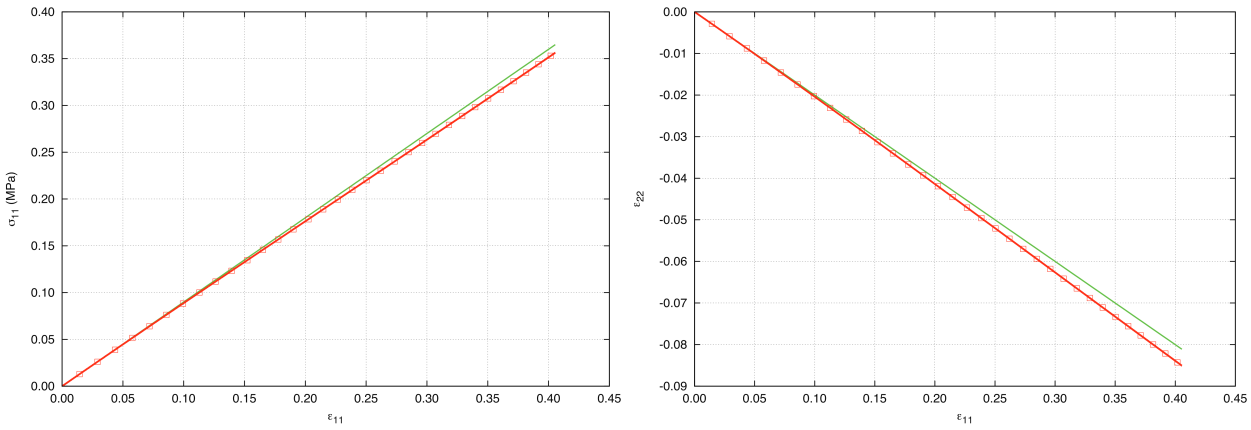

(a) Axial stress **(b) Lateral Strain**

Fig. 4.8 Analytical and numerical results for the (a) uniaxial stress and (b) lateral strain. The green line gives the linear elastic response.

which gives no volume change, $J = 1$. Since there is no volume chance, the Kirchhoff stress is equal to the Cauchy stress: $\boldsymbol{\tau} = \boldsymbol{\sigma}$. Using (4.10), the non-zero stress components are

$$\sigma_{12} = \frac{\mu}{2}\left(\lambda^2 - \lambda^{-2}\right)$$

$$\sigma_{11} = \sigma_{22} = \frac{\mu}{3}\left[\frac{1}{2}\left(\lambda^2 + \lambda^{-2}\right) - 1\right]$$

$$\sigma_{33} = \frac{\mu}{3}\left(2 - \lambda^2 + \lambda^{-2}\right).$$

The results of a single element problem in Sierra/SM are compared with the analytical solution in Fig. 4.9. It is interesting to note that the normal stresses, σ_{11}, σ_{22}, and σ_{33} are not equal to zero. This is a much different result than what we get for the linear hypoelastic model.

4.5.3.3 Pure Shear Stress

Since pure shear strain did not result in a pure shear stress state, we do not expect a pure shear stress state to result in a pure shear strain state. For pure shear stress the only non-zero stress component is

$$\sigma_{12} = \tau = \mu B_{12},$$

and using (4.10) it can be shown that $J = 1$. The deformation, in terms of the left Cauchy-Green deformation tensor, is

$$\left[B_{ij}\right] = \begin{bmatrix} B & B_{12} & 0 \\ B_{12} & B & 0 \\ 0 & 0 & B \end{bmatrix}.$$

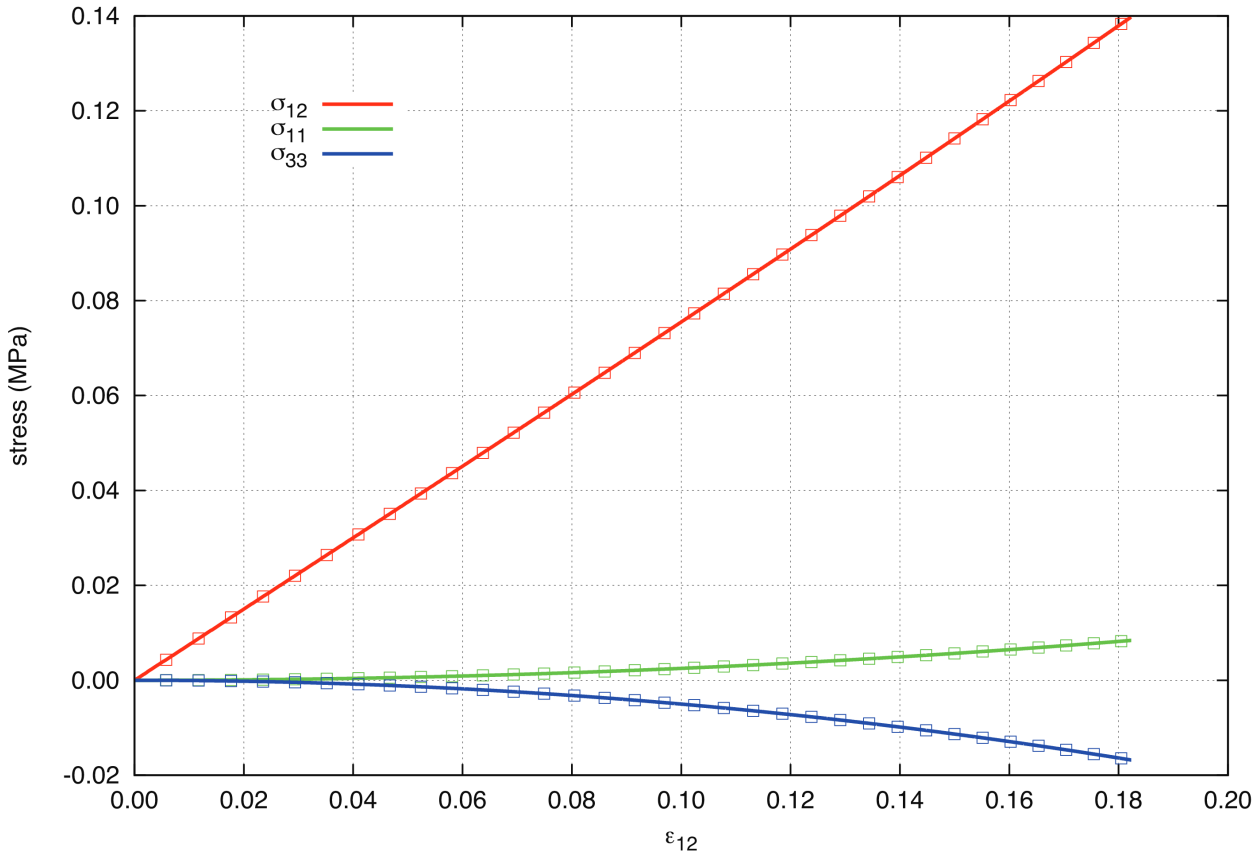

Fig. 4.9 Analytical and numerical results for the neo-Hookean model subjected to a pure shear strain. The solid lines are the analytical results and the boxes are results from Sierra/SM.

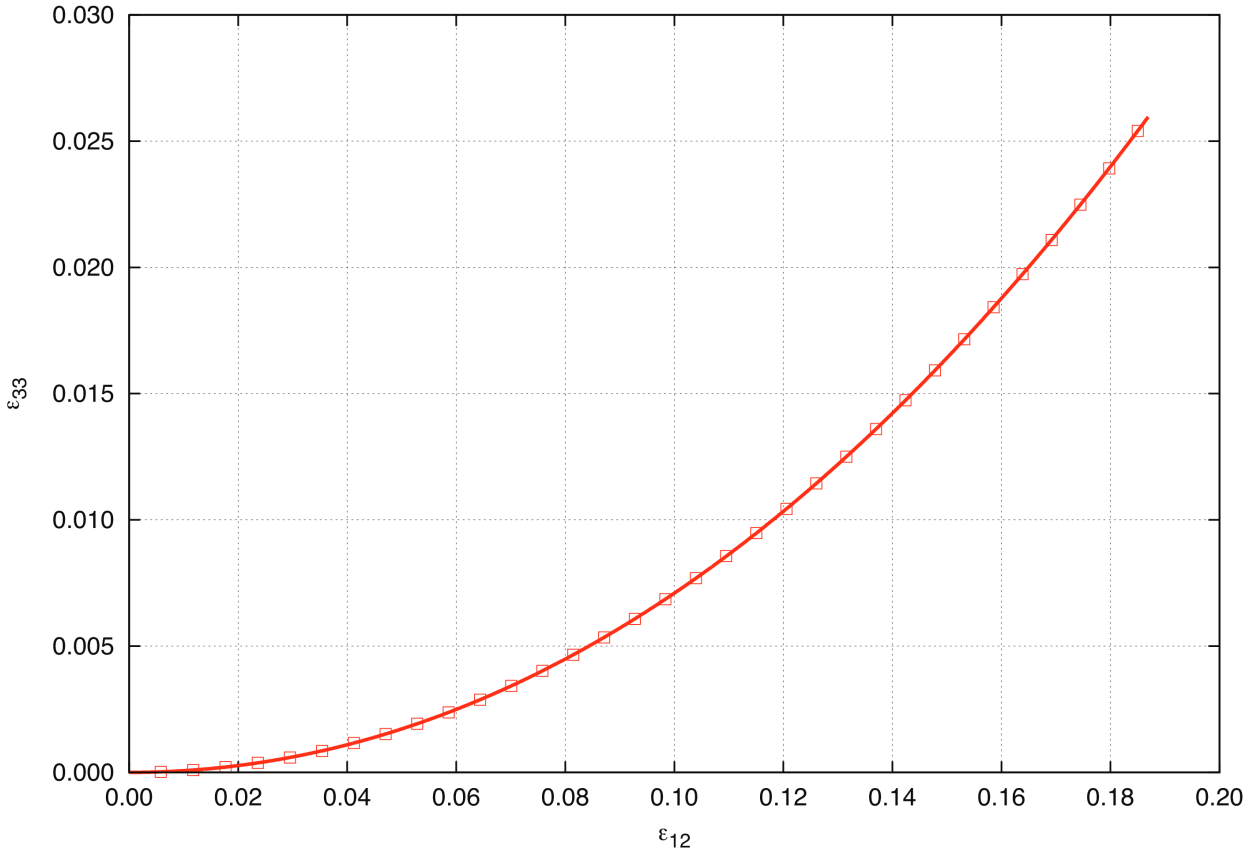

Fig. 4.10 Analytical and numerical results for the neo-Hookean model subjected to a pure shear stress. The curve gives the logarithmic strain component, $\varepsilon_{33} = \frac{1}{2}\ln B$. The solid lines are the analytical results and the boxes are results from Sierra/SM.

The equation we need to solve for the deformation is $\det \mathbf{B} = 1$. This gives us the cubic equation

$$B^3 - \left(\frac{\tau}{\mu}\right)^2 B - 1 = 0.$$

This is a cubic equation of the same form as that in the uniaxial stress problem. We make the substitution

$$B = x + \frac{p}{3x}, \; p = \left(\frac{\tau}{\mu}\right)^2. \tag{4.13}$$

This gives us a quadratic equation in x^3

$$x^6 - x^3 + \frac{p^3}{27} = 0,$$

which has the solution

$$x = \left[\frac{1}{2} + \frac{1}{2}\sqrt{1 - \frac{4p^3}{27}}\right]^{1/3}.$$

Substituting this solution into (4.13) gives B.

The results of a single element problem in Sierra/SM are compared with the analytical solution in Fig. 4.10. Of interest here is the fact that the normal strains, ε_{11}, ε_{22}, and ε_{33} are not equal to zero. Again, this is a different result than what we get for the linear hypoelastic model.

4.5.3.4 Uniaxial Strain

First, utilizing a displacement condition corresponding to uniaxial strain results in a deformation gradient of the form,

$$F_{ij} = \lambda \delta_{1i}\delta_{1j} + \delta_{2i}\delta_{2j} + \delta_{3i}\delta_{3j}.$$

By evaluating relation (4.10) with this deformation field produces stresses that may be written as

$$\sigma_{11} = \frac{1}{2}K\left(\lambda - \frac{1}{\lambda}\right) + \frac{2}{3}\mu\left(\lambda^2 - 1\right)\lambda^{-5/3},$$

$$\sigma_{22} = \sigma_{33} = \frac{1}{2}K\left(\lambda - \frac{1}{\lambda}\right) - \frac{1}{3}\mu\left(\lambda^2 - 1\right)\lambda^{-5/3}$$

with the shear stress components equal to zero. Both the corresponding analytical and numerical solutions are presented in Fig. 4.11.

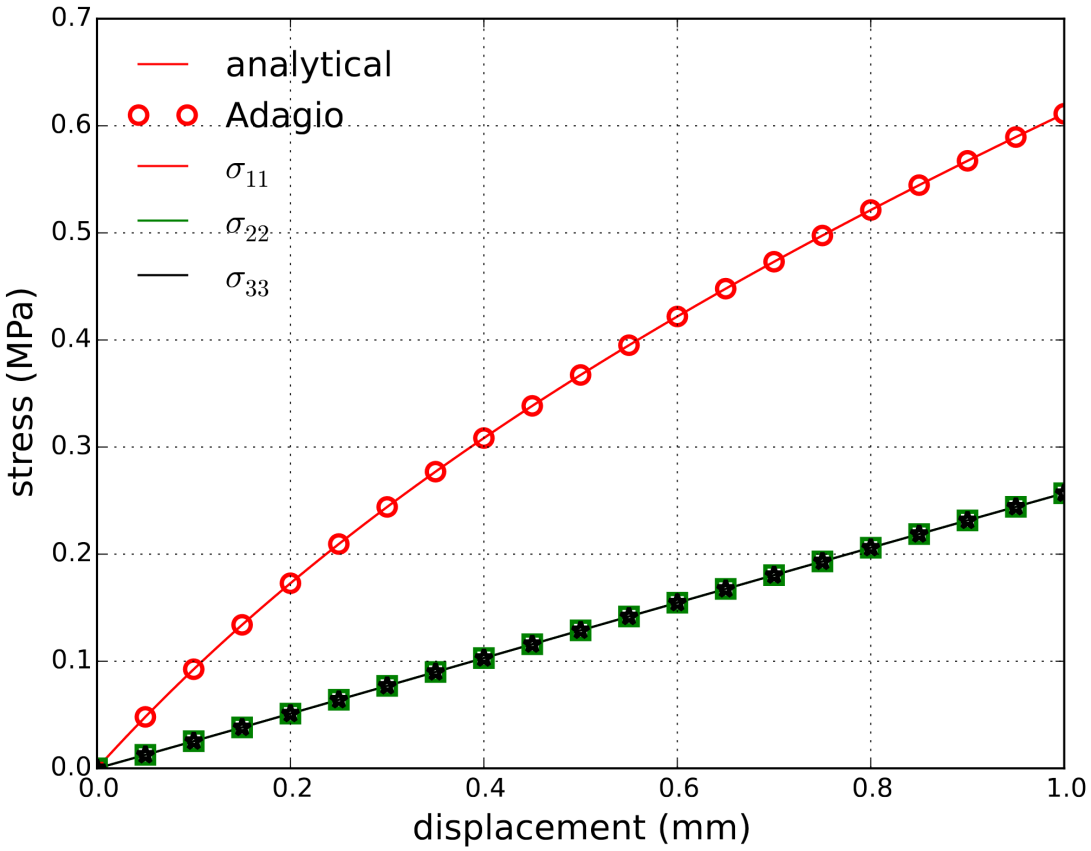

Fig. 4.11 Analytical and numerical results for the uniaxial stretch case.

4.5.3.5 Simple Shear

For the simple shear case, a deformation gradient of the form,

$$F_{ij} = \delta_{ij} + \gamma \delta_{1i} \delta_{2j},$$

is assumed. Noting this is a volume preserving deformation ($J = 1$) and again evaluating (4.10) produces stresses that may be written as,

$$\sigma_{11} = W \frac{2}{3} \mu \gamma^2$$

$$\sigma_{22} = \sigma_{33} = -\frac{1}{3} \mu \gamma^2$$

$$\sigma_{12} = \mu \gamma$$

Both the corresponding analytical and numerical solutions are presented in Fig. 4.12.

4.5.4 User Guide

```
BEGIN PARAMETERS FOR MODEL NEO_HOOKEAN
  #
  # Elastic constants
  #
  YOUNGS MODULUS = <real>
  POISSONS RATIO = <real>
  SHEAR MODULUS  = <real>
  BULK MODULUS   = <real>
  LAMBDA         = <real>
  TWO MU         = <real>
END [PARAMETERS FOR MODEL NEO_HOOKEAN]
```

There are no output variables available for the neo-Hookean model.

4.6 Gent Model

4.6.1 Theory

The Gent model is a hyperelastic model of rubber elasticity developed from phenomenological continuum mechanics approaches. Specifically, the model is based on the concept of limiting

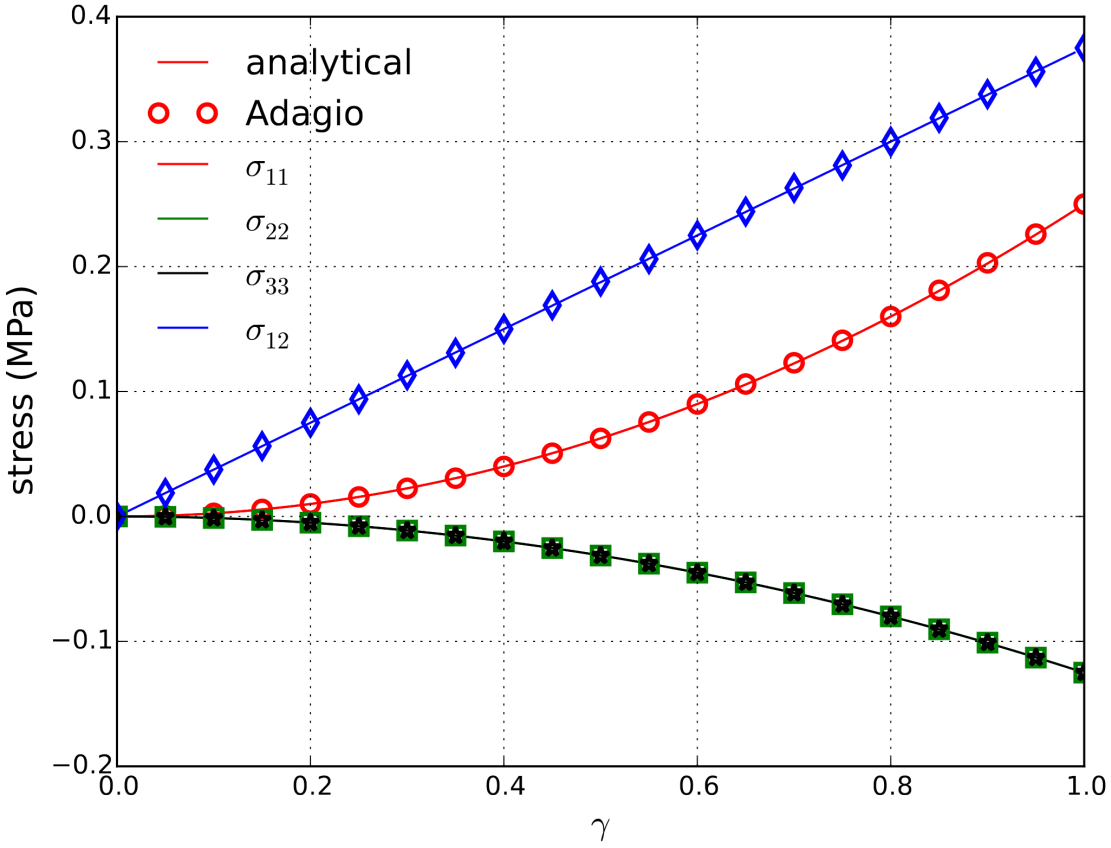

Fig. 4.12 Analytical and numerical results for the simple shear case.

chain extensibility and is an accurate approximation to the Arruda-Boyce model [6]. To determine the stress-strain response of the Gent model, a strain energy density of the form [35],

$$W(B_{ij}) = \frac{1}{2}K\left[\frac{1}{2}\left(J^2-1\right) - \ln J\right] + \frac{1}{2}\mu J_m \ln\left(1 - \frac{\bar{B}_{kk}-3}{J_m}\right), \tag{4.14}$$

is proposed with K and μ the bulk and shear moduli, J the determinant of the deformation gradient and J_m an input parameter for limiting the value of $\bar{B}_{kk} - 3$. J_m is the parameter effectively accounting for limiting chain extensibility. The deformation measure is given by B_{ij}, the components of the Left Cauchy Green tensor, where $B_{ij} = F_{ik}F_{jk}$. $\bar{B}_{kk}$ provides the isochoric part of the deformation and is given by

$$\bar{B}_{ij} = \bar{F}_{ik}\bar{F}_{jk} \; ; \; \bar{F}_{ij} = J^{-1/3}F_{ij}. \tag{4.15}$$

In the limit where $J_m \to \infty$ the Gent model reduces to the classical neo-Hookean model (see (4.8)). This can be seen by defining x to be $\frac{1}{J_m}$, taking a Taylor series expansion of $\ln\left(1 - (\bar{B}_{kk} - 3)x\right)$ about $x = 0$ and taking the limit as $x \to 0$.

The second Piola-Kirchoff stress, with components S_{ij}, may be determined by taking a derivative of the strain energy density. A mapping of the second Piola-Kirchoff may be used to determined the Cauchy stress. These relations produce components of the Cauchy stress, σ_{ij}, that are

$$\sigma_{ij} = \frac{1}{2}K\left(J - \frac{1}{J}\right)\delta_{ij} + \frac{J^{-5/3}\mu J_m\left(B_{ij} - \frac{1}{3}B_{kk}\delta_{ij}\right)}{J_m - \bar{B}_{kk} + 3}, \tag{4.16}$$

where δ_{ij} is the Kronecker delta.

The Gent model is a useful model for rubber elasticity as it is simple and provides similar predictions to comparatively complicated molecular models [6], [17]. It is also a practical model to use since analytic solutions to benchmark problems exist for this model.

4.6.2 Implementation

As a hyperelastic model, the current state of the material may be determined by the total deformation. To this end we use the polar decomposition of the deformation gradient,

$$F_{ij} = V_{ik}R_{kj}, \tag{4.17}$$

in which V_{ij} are the components of the left stretch tensor and R_{ij} is the corresponding rotation. Noting that,

$$B_{ij} = V_{ik}V_{kj},$$

and $J = \det\left(V_{ij}\right)$, the Cauchy stress (via (4.16)) is found. The unrotated stress, T_{ij}, which is needed for internal force calculations in Sierra/SM, is found using the transformation

$$T_{ij} = R_{ki}\sigma_{kl}R_{lj}.$$

4.6.3 Verification

It is possible to find closed form solutions for a number of loadings. Three problems are described here: uniaxial strain, simple shear, and hydrostatic compression. One set of material properties was used for all tests and they are given in Table 4.4. The elastic modulus and Poisson's ratio are given in addition to the bulk modulus, shear modulus, and limiting chain extensibility parameter, J_m.

Table 4.4 The material properties for the Gent model used for uniaxial strain, simple shear, and hydrostatic compression tests.

K	0.325 MPa	μ	0.15 MPa	J_m	13.125
E	0.39 MPa	ν	0.33		

4.6.3.1 Uniaxial Strain

First, utilizing a displacement condition corresponding to uniaxial strain results in a deformation gradient of the form,

$$F_{ij} = \lambda\delta_{1i}\delta_{1j} + \delta_{2i}\delta_{2j} + \delta_{3i}\delta_{3j}.$$

By evaluating relation (4.16) with this deformation field, we produce stresses that may be written as,

$$\sigma_{11} = \frac{1}{2}K\left(\lambda - \frac{1}{\lambda}\right) - \frac{2}{3}\frac{J_m\mu\left(\lambda^2 - 1\right)}{\lambda^3 - \left(J_m + 3\right)\lambda^{5/3} + 2\lambda}$$

$$\sigma_{22} = \sigma_{33} = \frac{1}{2}K\left(\lambda - \frac{1}{\lambda}\right) + \frac{1}{3}\frac{J_m\mu\left(\lambda^2 - 1\right)}{\lambda^3 - \left(J_m + 3\right)\lambda^{5/3} + 2\lambda},$$

with the shear stress components equal to zero. Both the corresponding analytical and numerical solutions are presented in Fig. 4.13.

4.6.3.2 Simple Shear

For the simple shear case, a deformation gradient of the form,

$$F_{ij} = \delta_{ij} + \gamma\delta_{1i}\delta_{2j},$$

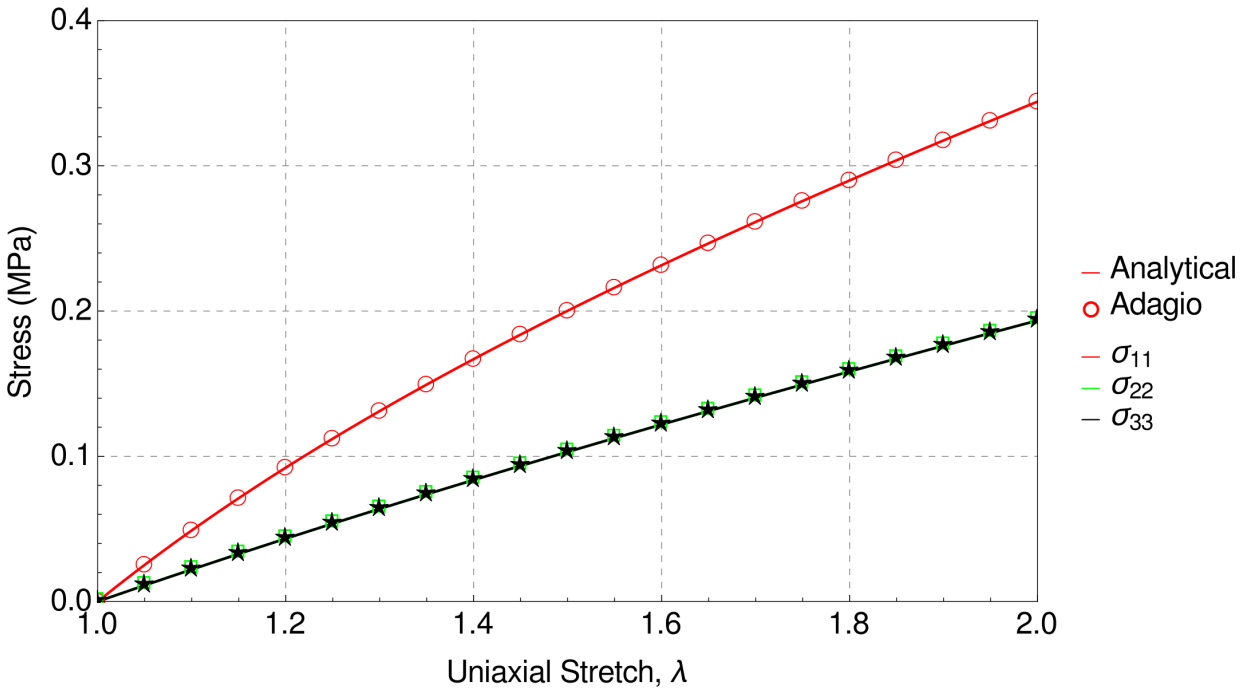

Fig. 4.13 Analytical and numerical results for the uniaxial stretch case.

is assumed. Noting this is a volume preserving deformation ($J = 1$) and again evaluating (4.16) produces stresses that may be written as,

$$\sigma_{11} = \frac{2}{3}\frac{J_m \mu \gamma^2}{J_m - \gamma^2}$$

$$\sigma_{22} = \sigma_{33} = -\frac{1}{3}\frac{J_m \mu \gamma^2}{J_m - \gamma^2}$$

$$\sigma_{12} = \frac{J_m \mu \gamma}{J_m - \gamma^2}$$

Both the corresponding analytical and numerical solutions are presented in Fig. 4.14.

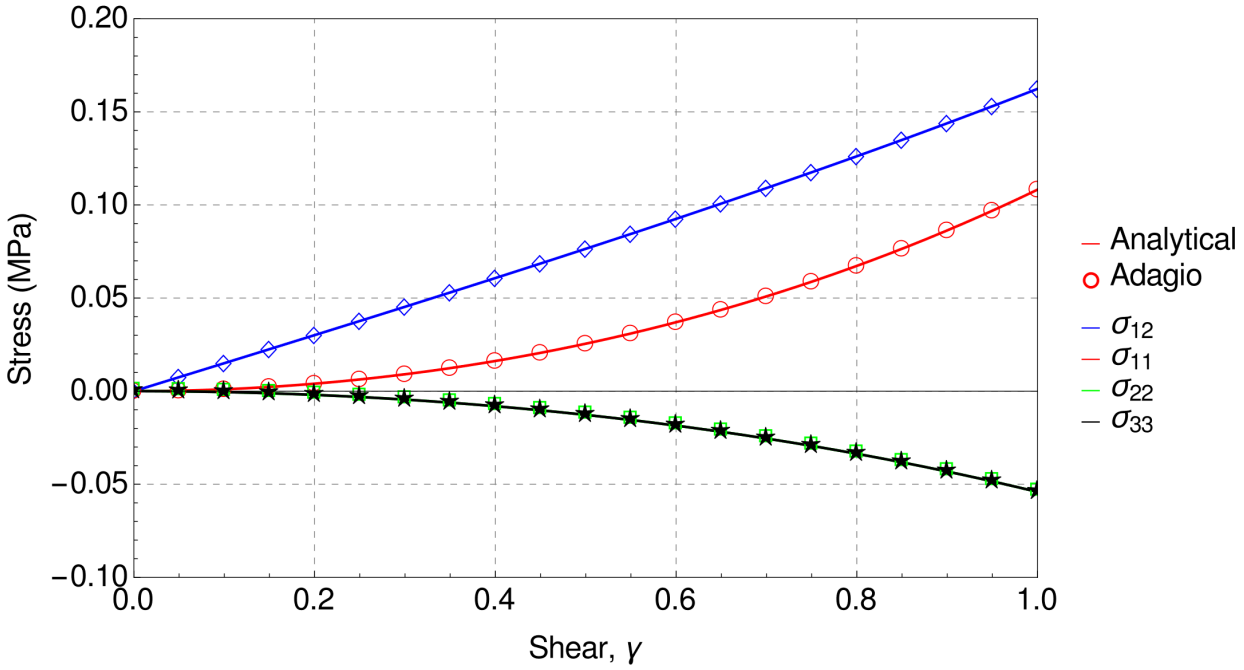

Fig. 4.14 Analytical and numerical results for the simple shear case.

4.6.3.3 Hydrostatic Compression

The volumetric deformation capabilities of the model are also investigated through displacement controlled hydrostatic compression. Specifically, hydrostatic compression results in a deformation gradient of the form,

$$F_{ij} = \lambda \delta_{ij},$$

where $0 < \lambda \leq 1$. As there is no deviatoric deformation, evaluation of (4.16) produces stresses that may be written as,

$$\sigma_{11} = \sigma_{22} = \sigma_{33} = \frac{1}{2} K \left(\lambda^3 - \frac{1}{\lambda^3} \right),$$

with the shear stress components equal to zero. Both the corresponding analytical and numerical solutions are presented in Fig. 4.15.

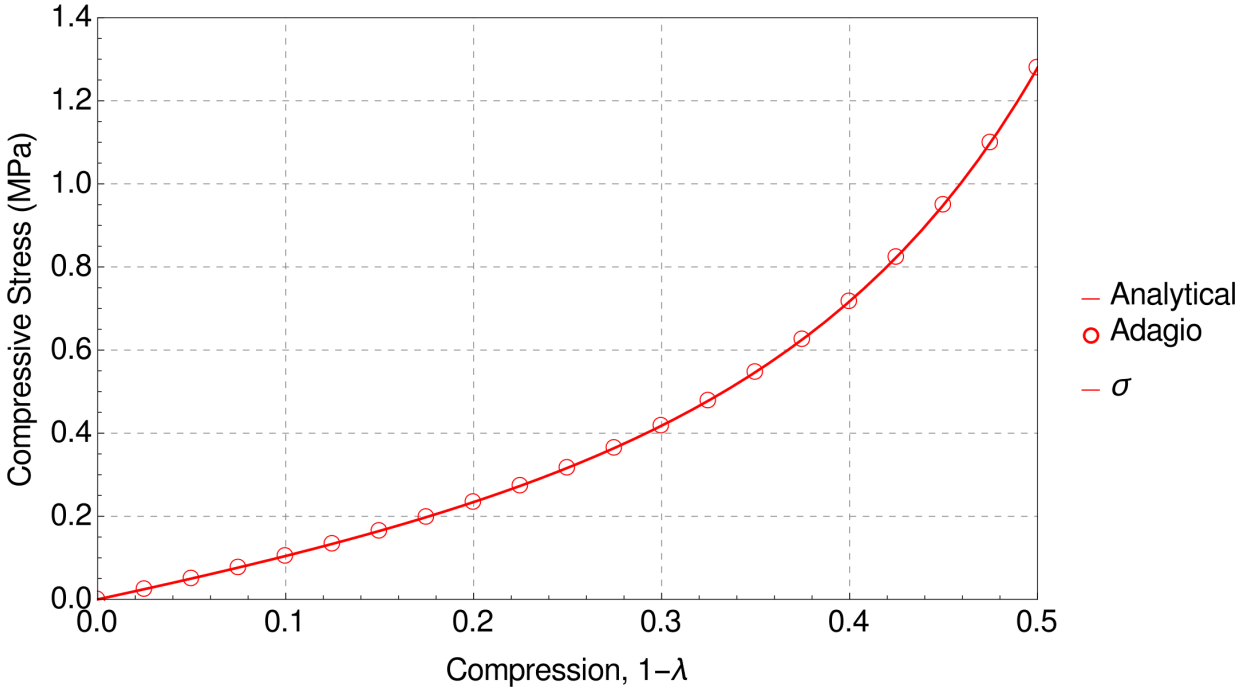

Fig. 4.15 Stress determined analytically and numerically for the Gent model during displacement controlled hydrostatic compression.

4.6.4 User Guide

```
BEGIN PARAMETERS FOR MODEL GENT
  #
  # Elastic constants
  #
  YOUNGS MODULUS = <real>
  POISSONS RATIO = <real>
  SHEAR MODULUS  = <real>
  BULK MODULUS   = <real>
  LAMBDA         = <real>
  TWO MU         = <real>
  #
  Jm Parameter  = <real>
END [PARAMETERS FOR MODEL GENT]
```

There are no output variables available for the Gent model.

4.7 Elastic-Plastic Model

4.7.1 Theory

The elastic-plastic model is a hypoelastic, rate-independent linear hardening plasticity model. The rate form of the constitutive equation assumes an additive split of the rate of deformation into an elastic and plastic part

$$D_{ij} = D^{\mathrm{e}}_{ij} + D^{\mathrm{p}}_{ij} \tag{4.18}$$

The stress rate only depends on the elastic strain rate in the problem

$$\overset{\circ}{\sigma}_{ij} = \mathbb{C}_{ijkl} D^{\mathrm{e}}_{kl} \tag{4.19}$$

where $\mathbb{C}_{ijkl}$ are the components of the fourth-order, isotropic elasticity tensor.

The key to the model is finding the plastic rate of deformation. For associated flow the plastic rate of deformation is in a direction normal to the yield surface. The yield surface is given by

$$f\left(\sigma_{ij}, \alpha_{ij}, \bar{\varepsilon}^{p}\right) = \phi\left(\sigma_{ij}, \alpha_{ij}\right) - \bar{\sigma}\left(\bar{\varepsilon}^{p}\right) = 0 \tag{4.20}$$

where ϕ is the effective stress, α_{ij} are the components of the back stress (used with kinematic hardening), and $\bar{\sigma}$ is the hardening function which is a function of an internal state variable, the equivalent plastic strain $\bar{\varepsilon}^{p}$. An example of such a yield surface (plotted in the deviatoric π-plane) is presented below in Fig. 4.16. The isotropy of the yield surface is clearly evident.

For the elastic plastic model a linear hardening law is assumed

$$\bar{\sigma} = \sigma_y + H' \bar{\varepsilon}^{p} \tag{4.21}$$

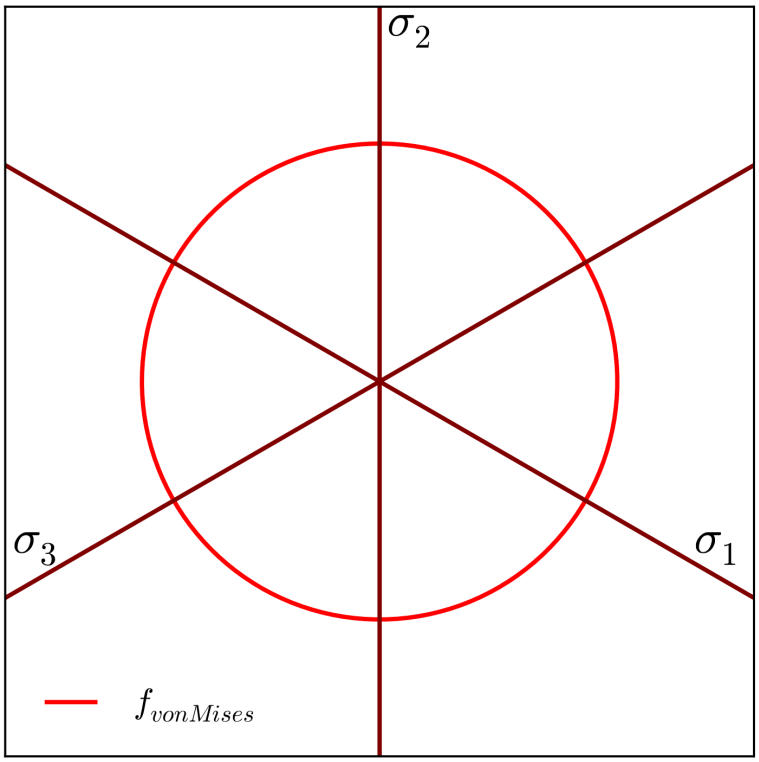

Fig. 4.16 Example von Mises yield surface (J_2) used by the elastic-plastic model presented in the deviatoric π-plane. In this case the surface is plotted for $\alpha_{ij} = 0$ and $\bar{\varepsilon}^p = 0$.

where σ_y is the yield stress and H' is the hardening modulus.

If the stress state is such that $f < 0$, the the behavior of the material is elastic; if the stress state is such that $f = 0$ and $\dot{f} < 0$, i.e. the strain rate brings the stress inside the yield surface, then the behavior of the material is elastic; if the stress state is such that $f = 0$ and $\dot{f} > 0$, i.e. the strain rate brings the stress outside the yield surface, then plastic deformation occurs.

We assume associated flow in this model, which gives the plastic rate of deformation

$$D_{ij}^{\mathrm{p}} = \dot{\gamma} \frac{\partial \phi}{\partial \sigma_{ij}} \tag{4.22}$$

where $\dot{\gamma}$ is the consistency parameter. For the elastic-plastic model the yield surface is assumed to be a von Mises yield surface with a back stress tensor to denote the center of the yield surface. The effective stress for a von Mises yield surface is

$$\phi\left(\sigma_{ij}\right) = \sqrt{\frac{3}{2}\xi_{ij}\xi_{ij}} \quad ; \quad \xi_{ij} = s_{ij} - \alpha_{ij} \tag{4.23}$$

where s_{ij} are the components of the deviatoric stress tensor

$$s_{ij} = \sigma_{ij} - \frac{1}{3}\delta_{ij}\sigma_{kk} \tag{4.24}$$

and α_{ij} are the components of the back stress tensor, another internal state variable.

The equivalent plastic strain is found through equating the rate of plastic work

$$\dot{W}^p = \sigma_{ij} D_{ij}^{\mathrm{p}} = \bar{\sigma}\dot{\bar{\varepsilon}}^p \quad \rightarrow \quad \dot{\bar{\varepsilon}}^p = \dot{\gamma}$$
$$\bar{\varepsilon}^p = \int_0^t \dot{\gamma} dt$$

Finally, the model allows for kinematic hardening through the back stress. The back stress is a symmetric, deviatoric rank two tensor that evolves in the following manner

$$\dot{\alpha}_{ij} = \frac{2}{3}\left(1 - \beta\right) H' D_{ij}^{\mathrm{p}} \tag{4.25}$$

The radius of the yield surface can be defined, $R = \sqrt{\xi_{ij}\xi_{ij}}$. The evolution of the radius of the yield surface is given by

$$\dot{R} = \sqrt{\frac{2}{3}}\beta H' \dot{\bar{\varepsilon}}^p \tag{4.26}$$

In (4.25) and (4.26) the parameter $\beta \in [0, 1]$ distributes the hardening between isotropic and kinematic hardening. If $\beta = 1$ the hardening is isotropic, if $\beta = 0$ the hardening is kinematic, and if β is between 0 and 1 the hardening is a combination of isotropic and kinematic.

4.7.2 Implementation

The elastic-plastic linear hardening model is implemented using a predictor-corrector algorithm. First, an elastic trial stress state is calculated. This is done by assuming that the rate of deformation is completely elastic

$$T_{ij}^{tr} = T_{ij}^{n} + \Delta t \left(\lambda \delta_{ij} d_{kk} + 2\mu d_{ij} \right)$$

The trial stress state can be decomposed into a pressure and a deviatoric stress

$$p^{tr} = \frac{1}{3} T_{kk}^{tr} \quad ; \quad s_{ij}^{tr} = T_{ij}^{tr} - p^{tr} \delta_{ij}$$

The difference between the deviatoric trial stress state and the back stress is compared to the current radius of the yield surface

$$\xi_{ij}^{tr} = s_{ij}^{tr} - \alpha_{ij}^{n} \quad ; \quad \xi_{tr}^{2} = \xi_{ij}^{tr} \xi_{ij}^{tr}$$

If $\xi_{tr}^{2} < R^{2}$ then the strain rate is elastic and the stress update is finished. If $\xi_{tr}^{2} > R^{2}$ then plastic deformation has occurred. The algorithm then needs to determine the extent of plastic deformation.

The normal to the yield surface, N_{ij} is assumed to lie in the direction of the trial stress state. This gives us the following expression for N_{ij}

$$N_{ij} = \frac{\xi_{ij}^{tr}}{\| \xi_{ij}^{tr} \|}$$

In what follows the change in the yield surface is assumed to be a linear combination of isotropic and kinematic hardening, i.e. the yield surface grows and or moves. Using a backward Euler algorithm the final deviatoric stress state is

$$s_{ij}^{n+1} = s_{ij}^{tr} - \Delta t \, 2\mu d_{ij}^{\mathrm{p}}$$

where the plastic strain increment is

$$\Delta t \, d_{ij}^{p} = \sqrt{\frac{3}{2}} \Delta \bar{\varepsilon}^{p} N_{ij}$$

The updated back stress is

$$\alpha_{ij}^{n+1} = \alpha_{ij}^{n} + \sqrt{\frac{2}{3}} \left(1 - \beta\right) \left(H' \Delta \bar{\varepsilon}^{p}\right) N_{ij}$$

and the updated radius of the yield surface is

$$R^{n+1} = R^{n} + \beta \sqrt{\frac{2}{3}} \left(H' \Delta \bar{\varepsilon}^{p}\right)$$

Combining these expressions we get an equation for the change in the equivalent plastic strain over the load step

$$\left(3\mu + H'\right) \Delta \bar{\varepsilon}^{p} = \sqrt{\frac{3}{2}} \left(\| \xi_{ij}^{tr} \| - R^{n} \right) \quad ; \quad \xi_{ij}^{tr} = s_{ij}^{tr} - \alpha_{ij}^{n}$$

With $\Delta \bar{\varepsilon}^{p}$ we can update the stress and the internal state variables.

4.7.3 Verification

The elastic-plastic material model is verified for a number of loading conditions. The elastic properties used in these analyses are $E = 70$ GPa and $\nu = 0.25$. The hardening parameters are $\sigma_y = 200$ MPa, $H' = 500$ MPa, and $\beta = 1$. By setting $\beta = 1$ the hardening is isotropic.

4.7.3.1 Uniaxial Stress

The elastic-plastic model is tested in uniaxial tension. The test looks at the stress, strain, and equivalent plastic strain and compares these values against analytical results for the same problem. The model is tested in uniaxial stress in the x (x_1), directions.

For the uniaxial stress problem, the only non-zero stress component is σ_{11}. In the analysis that follows $\sigma_{11} = \sigma$. There are three non-zero strain components, ε_{11}, ε_{22}, and ε_{33}. In the analysis that follows $\varepsilon_{11} = \varepsilon$. Furthermore, the axial elastic stress, $\varepsilon^{\mathrm{e}}_{11} = \sigma/E$ will be denoted by ε^{e}.

Axial Stresses

The uniaxial stress calculated by the model in Adagio is compared to an analytical solution. For uniaxial loading in the x_1 direction, the effective stress is

$$\phi = \sigma$$

If the stress state is on the yield surface, then $\phi = \bar{\sigma}\,(\bar{\varepsilon}^p)$, so the axial stress, as a function of the hardening function, is

$$\sigma = \bar{\sigma}\,(\bar{\varepsilon}^p) = \sigma_y + H'\bar{\varepsilon}^p \tag{4.27}$$

The stress state can be calculated from the hardening law and the anisotropy parameters.

To evaluate the axial stress we need the equivalent plastic strain as a function of the axial strain. If we equate the rate of plastic work we get

$$\bar{\sigma}\dot{\bar{\varepsilon}}^p = \sigma\,(\dot{\varepsilon} - \dot{\varepsilon}^{\mathrm{e}}) \quad \rightarrow \quad \dot{\bar{\varepsilon}}^p = \dot{\varepsilon} - \dot{\varepsilon}^{\mathrm{e}}$$

which, when integrated, gives us an equation for the equivalent plastic strain

$$\bar{\varepsilon}^p = \frac{E\varepsilon - \sigma_y}{E + H'} \tag{4.28}$$

The equivalent plastic strain can then be used in (4.45) to find the axial stress, σ

$$\sigma = \frac{\sigma_y + H'\varepsilon}{1 + H'/E} \tag{4.29}$$

The axial stresses is shown in Fig. 4.17.

Lateral Strains

For the lateral strains we need the plastic strains and therefore the normal to the yield surface. The components of the normal to the yield surface are

$$\frac{\partial \phi}{\partial \sigma_{11}} = 1 \quad ; \quad \frac{\partial \phi}{\partial \sigma_{22}} = \frac{\partial \phi}{\partial \sigma_{33}} = -\frac{1}{2}$$

The elastic axial and lateral strain components are

$$\varepsilon^{\mathrm{e}}_{11} = \frac{\sigma}{E} = \varepsilon^{\mathrm{e}} \quad ; \quad \varepsilon^{\mathrm{e}}_{22} = \varepsilon^{\mathrm{e}}_{33} = -\nu \frac{\sigma}{E} = -\nu \varepsilon^{\mathrm{e}}$$

The plastic axial strain component is

$$\varepsilon^{\mathrm{p}}_{11} = \varepsilon_{11} - \frac{\sigma}{E} = \varepsilon - \varepsilon^{\mathrm{e}}$$

which comes from the additive decomposition of the strain rates. Using the equivalent plastic strain (4.46) we can find the lateral plastic strain components

$$\varepsilon^{\mathrm{p}}_{22} = \varepsilon^{\mathrm{p}}_{33} = -\frac{1}{2}\left(\varepsilon - \varepsilon^{\mathrm{e}}\right)$$

The lateral {em total} stain components prior to yield are $\varepsilon_{22} = \varepsilon_{33} = -\nu\varepsilon$. After yield they are

$$\varepsilon_{22} = \varepsilon_{33} = -\nu \varepsilon^{\mathrm{e}} - \frac{1}{2}\bar{\varepsilon}^{p}$$

where $\varepsilon^{\mathrm{e}} = \sigma / E$.

Results are shown in Fig. 4.18.

4.7.3.2 Pure Shear

The shear stress calculated by the elastic-plastic model in Adagio is compared to analytical solutions. Considering pure shear with respect to the x_1-x_2 axes, the only non-zero shear stress is σ_{12}, and the only non-zero shear strain will be ε_{12} For pure shear with respect to the x_1-x_2 axes, the effective stress is

$$\phi = \sqrt{3}\,\sigma_{12}$$

If the stress state is on the yield surface, then $\phi = \bar{\sigma}\,(\bar{\varepsilon}^{p})$, so the shear stress is

$$\sigma_{12} = \frac{\bar{\sigma}\,(\bar{\varepsilon}^{p})}{\sqrt{3}} \tag{4.30}$$

Using this, the pure shear stress state can be calculated from the hardening law and the anisotropy parameters.

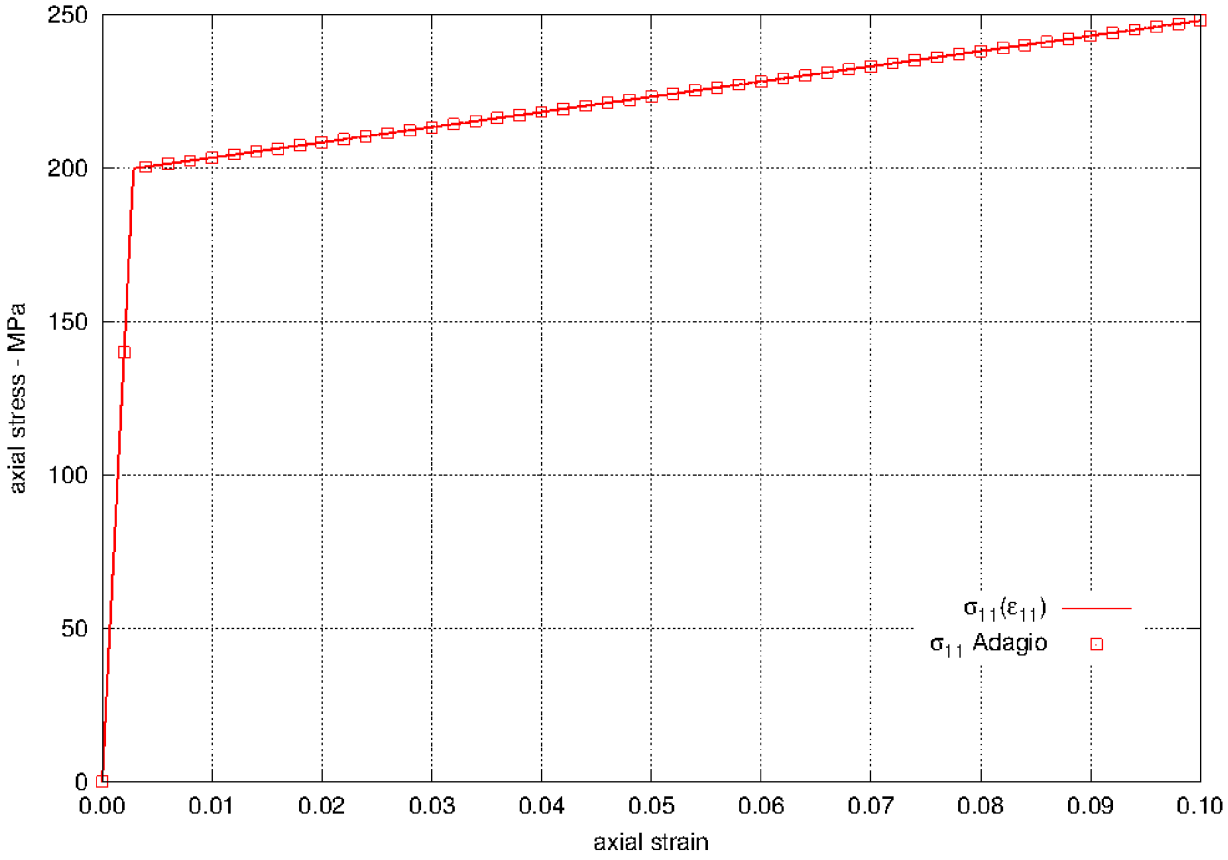

Fig. 4.17 Axial stress for loading in the x_1 direction for the elastic-plastic model with linear hardening.

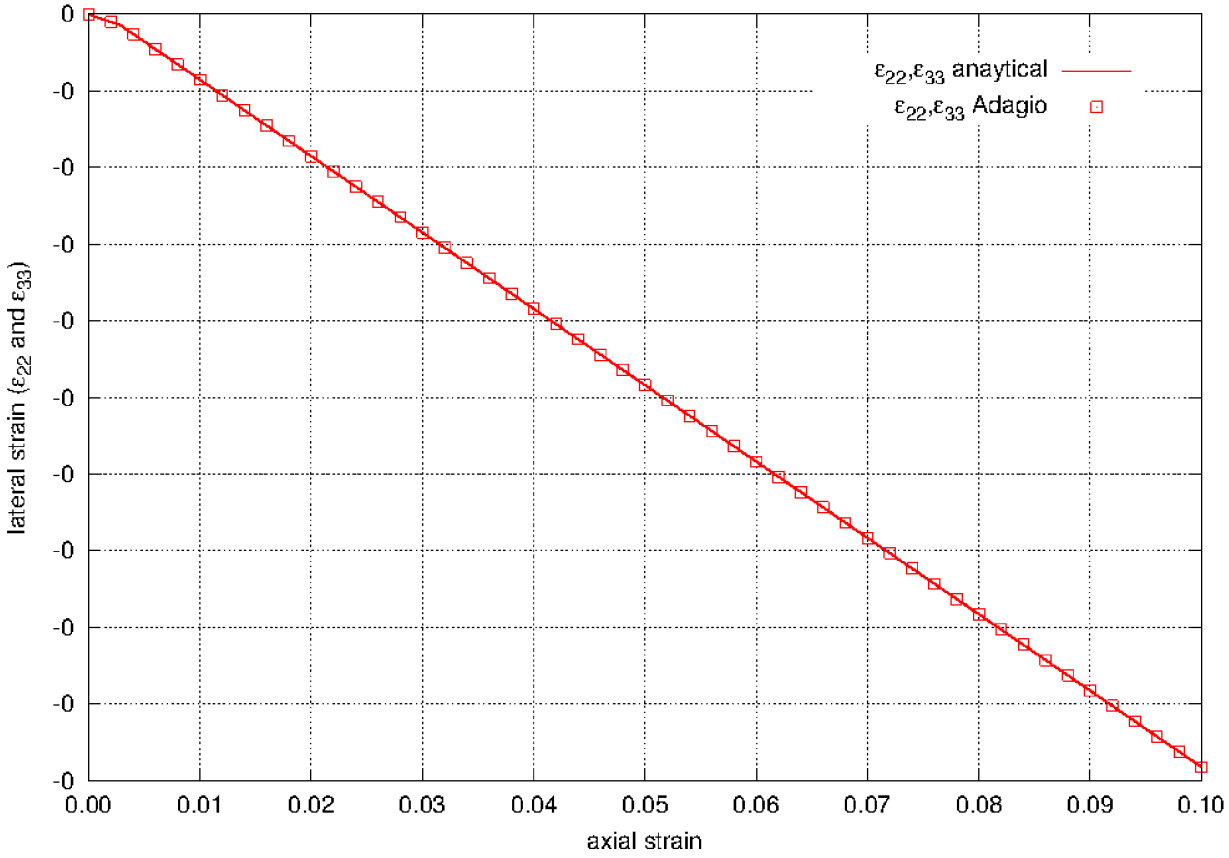

Fig. 4.18 Lateral strains for uniaxial stress loading in the x_1 direction for the elastic-plastic model with linear hardening.

To evaluate the shear stress we need the equivalent plastic strain as a function of the shear strain. If we equate the rate of plastic work we get

$$\bar{\sigma}\dot{\bar{\varepsilon}}^p = 2\sigma_{12}\left(\dot{\varepsilon}_{12} - \dot{\varepsilon}^e_{12}\right) \quad \rightarrow \quad \dot{\bar{\varepsilon}}^p = \frac{2}{\sqrt{3}}\left(\dot{\varepsilon}_{12} - \dot{\varepsilon}^e_{12}\right)$$

which, when integrated, gives us an implicit equation for the equivalent plastic strain

$$\bar{\varepsilon}^p = \frac{2}{\sqrt{3}}\left(\varepsilon_{12} - \frac{\bar{\sigma}\left(\bar{\varepsilon}^p\right)}{\sqrt{3}\,G}\right)$$

The equivalent plastic strain can now be used to find the shear stress.

Boundary Conditions for Pure Shear

The deformation gradient that gives pure shear for loading relative to the x_1-x_2 axes is

$$[\mathbf{F}] = \begin{bmatrix} \frac{1}{2}\left(\lambda + \lambda^{-1}\right) & \frac{1}{2}\left(\lambda - \lambda^{-1}\right) & 0 \\ \frac{1}{2}\left(\lambda - \lambda^{-1}\right) & \frac{1}{2}\left(\lambda + \lambda^{-1}\right) & 0 \\ 0 & 0 & 1 \end{bmatrix} \quad \rightarrow \quad [\boldsymbol{\varepsilon}] = \begin{bmatrix} 0 & \varepsilon & 0 \\ \varepsilon & 0 & 0 \\ 0 & 0 & 0 \end{bmatrix} \quad ; \quad \varepsilon = \ln\lambda$$

For loading relative to the x_2-x_3 axes and the x_3-x_1 axes the boundary conditions are modified appropriately.

Results

The results for the elastic-plastic model loaded in pure shear are shown in Fig. 4.19. We see that the stress strain curves in pure shear as calculated by Adagio follow the expected stress strain curves. All other stress and strain components for the three problems are zero.

4.7.4 User Guide

```
BEGIN PARAMETERS FOR MODEL ELASTIC_PLASTIC
  #
  # Elastic constants
  #
  YOUNGS MODULUS = <real>
  POISSONS RATIO = <real>
  SHEAR MODULUS  = <real>
  BULK MODULUS   = <real>
  LAMBDA         = <real>
```

(continues on next page)

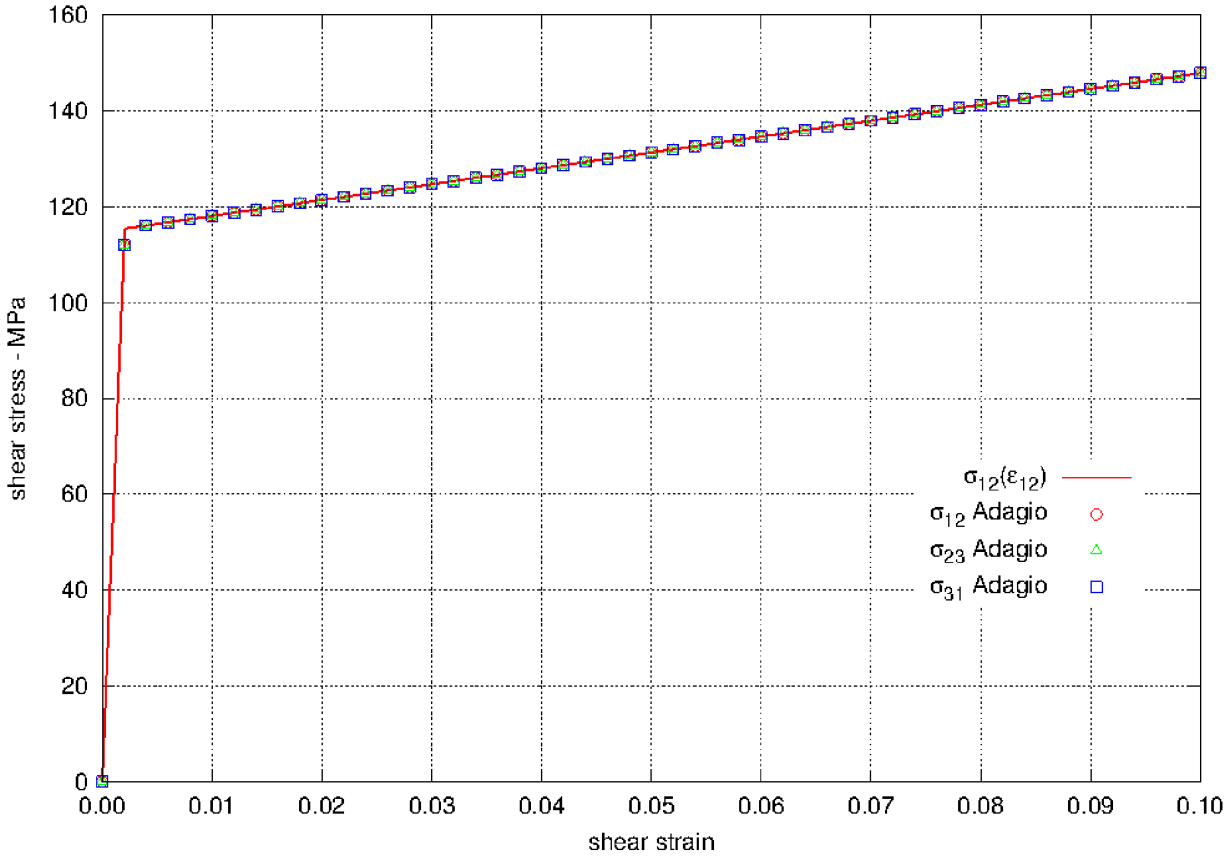

Fig. 4.19 Results are for shear in the x_1-x_2 plane, x_2-x_3 plane, and x_3-x_1 plane.

(continued from previous page)

```
  TWO MU          = <real>
  #
  # Hardening Behavior
  #
  YIELD STRESS      = <real>
  BETA              = <real>
  HARDENING MODULUS = <real>
END [PARAMETERS FOR MODEL ELASTIC_PLASTIC]
```

In the above command blocks:

- The elastic constants describe both the pre-yield behavior of the model and the slope of post yield unloading.
- The yield stress, the stress at which yield first initiates, is defined with the `YIELD STRESS` command line.
- The hardening modulus, the slope of the post yield hardening curve, is defined with the `HARDENING MODULUS` command line.
- The beta parameter defines if hardening is isotropic or kinematic.

Output variables available for this model are listed in Table 4.5 and Table 4.6. For information about the elastic-plastic model, consult [103].

Table 4.5 State Variables for `ELASTIC PLASTIC` Model

Name	Description
EQPS	equivalent plastic strain, $\bar{\varepsilon}^p$
RADIUS	radius of the yield surface, R
BACK_STRESS	back stress (symmetric tensor), α_{ij}

Table 4.6 State Variables for `ELASTIC PLASTIC` Model for Shells

Name	Description
EQPS	equivalent plastic strain, $\bar{\varepsilon}^p$
TENSILE_EQPS	equivalent plastic strain only accumulated when the material is in tension (trace of stress tensor is positive)
RADIUS	radius of the yield surface, R
BACK_STRESS	back stress (symmetric tensor), α_{ij}
ITERATIONS	radial return iterations
ERROR	error in plane stress iterations
PS_ITER	plane stress iterations
TSTRAIN	integrated thickness strain

4.8 Elastic-Plastic Power Law Hardening Model

4.8.1 Theory

The elastic-plastic power law hardening model is a hypoelastic, rate-independent plasticity model with power law hardening [102]. The rate form of the constitutive equation assumes an additive split of the rate of deformation into an elastic and plastic part

$$D_{ij} = D_{ij}^{\mathrm{e}} + D_{ij}^{\mathrm{p}}$$

The stress rate only depends on the elastic strain rate in the problem

$$\overset{\circ}{\sigma}_{ij} = \mathbb{C}_{ijkl} D_{kl}^{\mathrm{e}}$$

where $\mathbb{C}_{ijkl}$ are the components of the fourth-order, isotropic elasticity tensor.

The key to integrating the model is finding the plastic rate of deformation. For associated flow the plastic rate of deformation is in a direction normal to the yield surface. The yield surface is given by

$$f\left(\sigma_{ij}, \bar{\varepsilon}^{p}\right) = \phi\left(\sigma_{ij}\right) - \bar{\sigma}\left(\bar{\varepsilon}^{p}\right) = 0 \tag{4.31}$$

where ϕ is the equivalent stress and $\bar{\sigma}$ is the hardening function which is a function of the equivalent plastic strain $\bar{\varepsilon}^{p}$. For this model the hardening function uses a power law

$$\bar{\sigma}\left(\bar{\varepsilon}^{p}\right) = \sigma_{y} + A\left\langle \bar{\varepsilon}^{p} - \varepsilon_{L} \right\rangle^{n}$$

which is shown in Fig. 4.20. The yield stress is σ_{y}, the hardening constant is A, the hardening exponent is n, and the Lüders strain is ε_{L}. The bracket $< \cdot >$ is the Macaulay bracket defined as

$$\langle x \rangle = \begin{cases} 0, & \text{if } x \leq 0 \\ x, & \text{if } x > 0. \end{cases}$$

By assuming associated plastic flow, the plastic rate of deformation can be written as

$$D_{ij}^{\mathrm{p}} = \dot{\gamma} \frac{\partial \phi}{\partial \sigma_{ij}}. \tag{4.32}$$

For this model the yield surface is chosen to be a von Mises yield surface, so

$$\phi\left(\sigma_{ij}\right) = \sqrt{\frac{3}{2} s_{ij} s_{ij}}$$

where s_{ij} are the components of the deviatoric stress

$$s_{ij} = \sigma_{ij} - \frac{1}{3} \delta_{ij} \sigma_{kk}$$

Unlike the elastic-plastic model Section 4.7, the power-law hardening model does not allow for kinematic hardening, so there is no back stress.

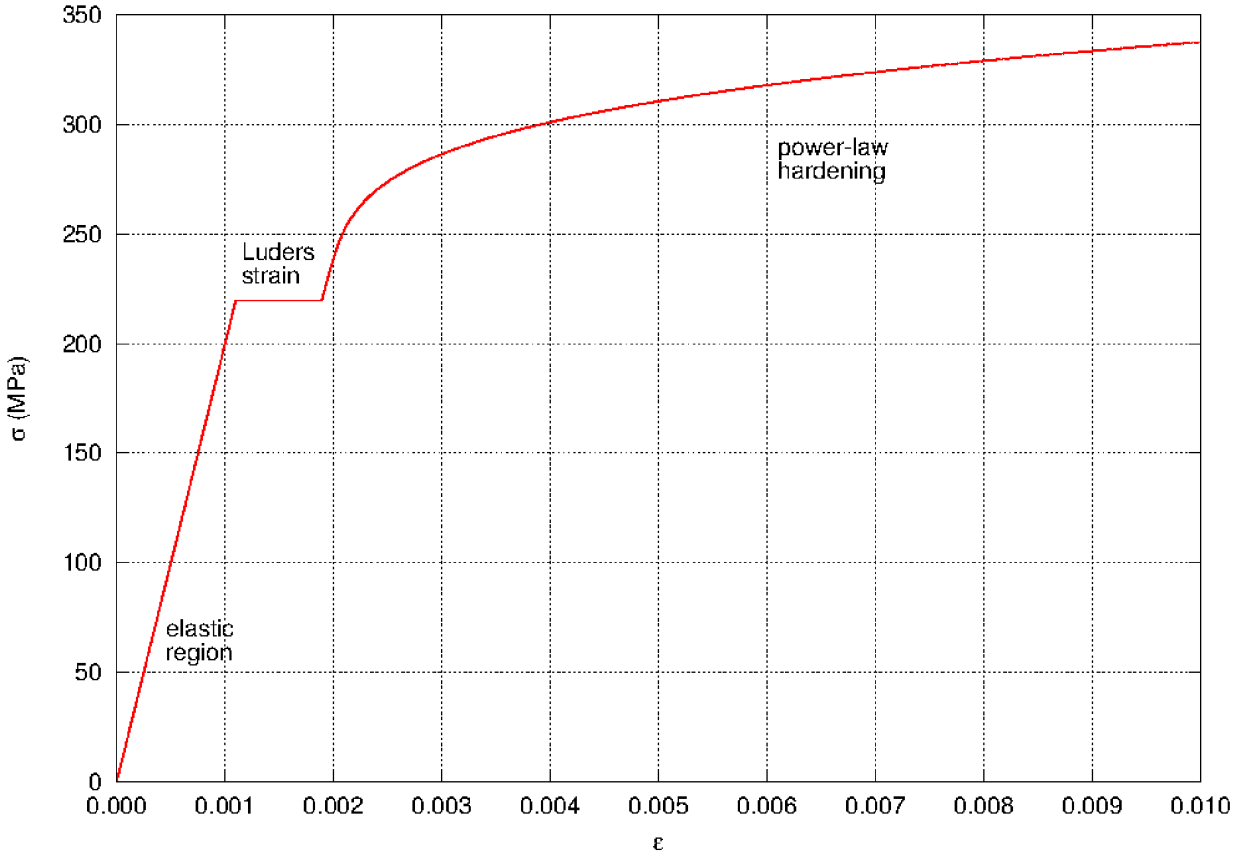

Fig. 4.20 Typical stress-strain response for the power-law hardening model.

4.8.2 Implementation

The elastic-plastic power-law hardening model is implemented using a predictor-corrector algorithm. First, an elastic trial stress state is calculated. This is done by assuming that the rate of deformation is completely elastic

$$T_{ij}^{tr} = T_{ij}^{n} + \Delta t \left(\lambda \delta_{ij} d_{kk} + 2\mu d_{ij} \right)$$

The trial stress state is decomposed into a pressure and a deviatoric stress

$$p^{tr} = \frac{1}{3} T_{kk}^{tr} \quad ; \quad s_{ij}^{tr} = T_{ij}^{tr} - p^{tr} \delta_{ij}$$

The effective trial stress is calculated and and used in the yield function (4.31).

$$f\left(s_{ij}^{tr}, \bar{\varepsilon}^{p}\right) = \phi\left(s_{ij}^{tr}\right) - \bar{\sigma}\left(\bar{\varepsilon}^{p}\right)$$

If $f \leq 0$ then the strain rate is elastic and the stress update is finished. If $f > 0$ then plastic deformation has occurred and a radial return algorithm determines the extent of plastic deformation.

The normal to the yield surface is assumed to lie in the direction of the trial stress state. This gives us the following expression for N_{ij}

$$N_{ij} = \frac{s_{ij}^{tr}}{\| s_{ij}^{tr} \|}$$

Using a backward Euler algorithm, the final deviatoric stress state is

$$s_{ij}^{n+1} = s_{ij}^{tr} - \Delta t 2\mu d_{ij}^{\mathrm{p}}$$

where the plastic strain increment is

$$\Delta d_{ij}^{\mathrm{p}} = \sqrt{\frac{3}{2}} \Delta \bar{\varepsilon}^{p} N_{ij}$$

The equation for the change in the equivalent plastic strain over the load step is found as the solution to

$$3\mu \Delta \bar{\varepsilon}^{p} + \bar{\sigma}\left(\bar{\varepsilon}_{n} + \Delta \bar{\varepsilon}^{p}\right) - \phi^{tr} + f_{n} = 0$$

4.8.3 Verification

The elastic-plastic power-law hardening model is verified for uniaxial stress and pure shear. The elastic properties used in these analyses are $E = 70$ GPa and $\nu = 0.25$. The hardening law used for the model is

$$\bar{\sigma}\left(\bar{\varepsilon}^{p}\right) = \sigma_{y} + A \left\langle \bar{\varepsilon}^{p} - \varepsilon_{L} \right\rangle^{n}$$

For these calculations $\sigma_{y} = 200$ MPa, $A = 400$ MPa, $n = 0.25$, and $\varepsilon_{L} = 0.008$.

4.8.3.1 Uniaxial Stress

The elastic-plastic power-law hardening model is tested in uniaxial tension. The test looks at the axial stress and the lateral strain and compares these values against analytical results for the same problem. In this verification problem only the normal strains/stresses are needed, and the shear terms are not exercised.

For the uniaxial stress problem, the only non-zero stress component is σ_{11}. In the analysis that follows $\sigma_{11} = \sigma$. There are three non-zero strain components, ε_{11}, ε_{22}, and ε_{33}. In the analysis that follows $\varepsilon_{11} = \varepsilon$ and $\varepsilon_{22} = \varepsilon_{33}$. Furthermore, the axial elastic strain, $\varepsilon^{\mathrm{e}}_{11} = \sigma/E$ will be denoted by ε^{e}.

The equivalent plastic strain, $\bar{\varepsilon}^{\mathrm{p}}$, for this model is equivalent to $\varepsilon^{\mathrm{p}}_{11}$, and is

$$\bar{\varepsilon}^{\mathrm{p}} = \varepsilon - \frac{\bar{\sigma}\left(\bar{\varepsilon}^{\mathrm{p}}\right)}{E}$$

This allows us, after yield, to parameterize the problem with the equivalent plastic strain.

For the lateral strains we need the lateral plastic strain. Plastic incompressibility ($\varepsilon^{\mathrm{p}}_{kk} = 0$) gives us

$$\varepsilon^{\mathrm{p}}_{22} = -\frac{1}{2}\bar{\varepsilon}^{\mathrm{p}}$$

Combined with the lateral elastic strains we have the lateral strain as a function of the equivalent plastic strain

$$\varepsilon_{22} = -\nu\frac{\bar{\sigma}\left(\bar{\varepsilon}^{\mathrm{p}}\right)}{E} - \frac{1}{2}\bar{\varepsilon}^{\mathrm{p}}$$

The results are shown in Fig. 4.21 and Fig. 4.22 and show agreement between the model in Adagio and the analytical results.

4.8.3.2 Pure Shear

The elastic-plastic power-law hardening model is tested in pure shear. The test looks at the shear stress as a function of the shear strain and compares these values against analytical results for the same problem. For the pure shear problem, the only non-zero strain component is ε_{12} and the only non-zero stress component is σ_{12}.

After yield, the shear stress as a function of the hardening curve is $\sigma_{12} = \bar{\sigma}\left(\bar{\varepsilon}^{\mathrm{p}}\right)/\sqrt{3}$. The elastic shear strain is $\varepsilon^{\mathrm{e}}_{12} = \sigma_{12}/2G$; the plastic shear strain is $\varepsilon^{\mathrm{p}}_{12} = \sqrt{3}\bar{\varepsilon}^{\mathrm{p}}/2$. Using this, the shear stress and strain are given as functions of the equivalent plastic strain

$$\sigma_{12} = \frac{\bar{\sigma}\left(\bar{\varepsilon}^{\mathrm{p}}\right)}{\sqrt{3}} \quad ; \quad \varepsilon_{12} = \frac{\sqrt{3}}{2}\bar{\varepsilon}^{\mathrm{p}} + \frac{1}{\sqrt{3}}\frac{\bar{\sigma}\left(\bar{\varepsilon}^{\mathrm{p}}\right)}{2\mu}$$

This allows us, after yield, to parameterize the problem with $\bar{\varepsilon}^{\mathrm{p}}$.

The results are shown in Fig. 4.23 and show agreement between the model in Adagio and the analytical results.

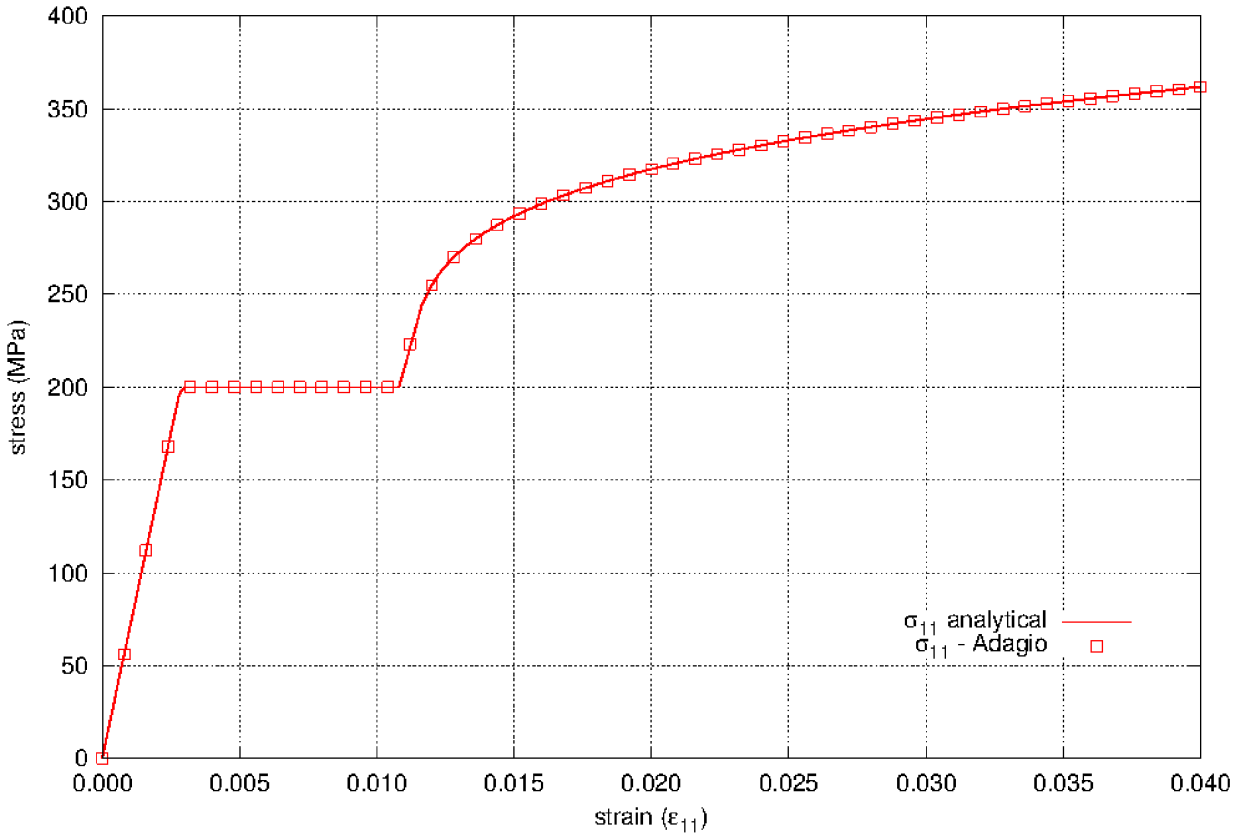

Fig. 4.21 The axial stress as a function of axial strain for the elastic-plastic power-law hardening model.

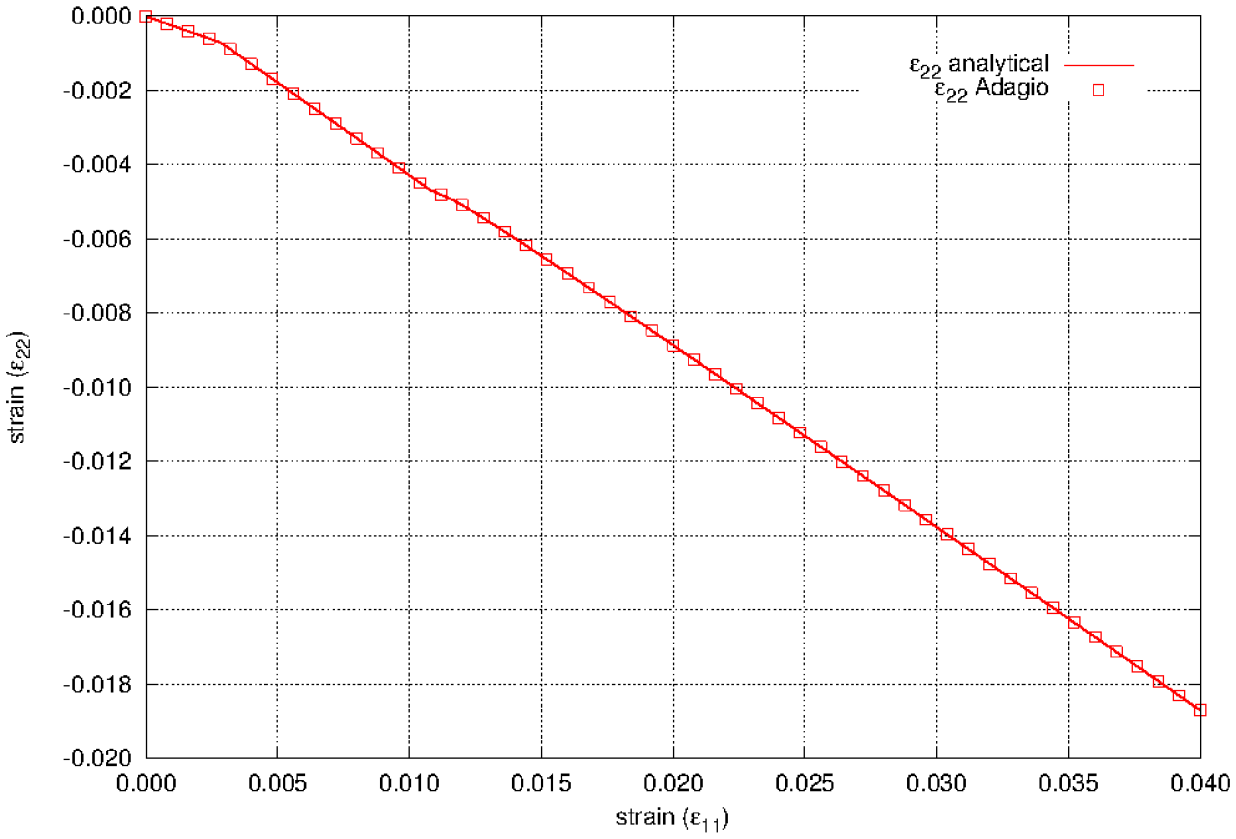

Fig. 4.22 The lateral strain as a function of axial strain for the elastic-plastic power-law hardening model.

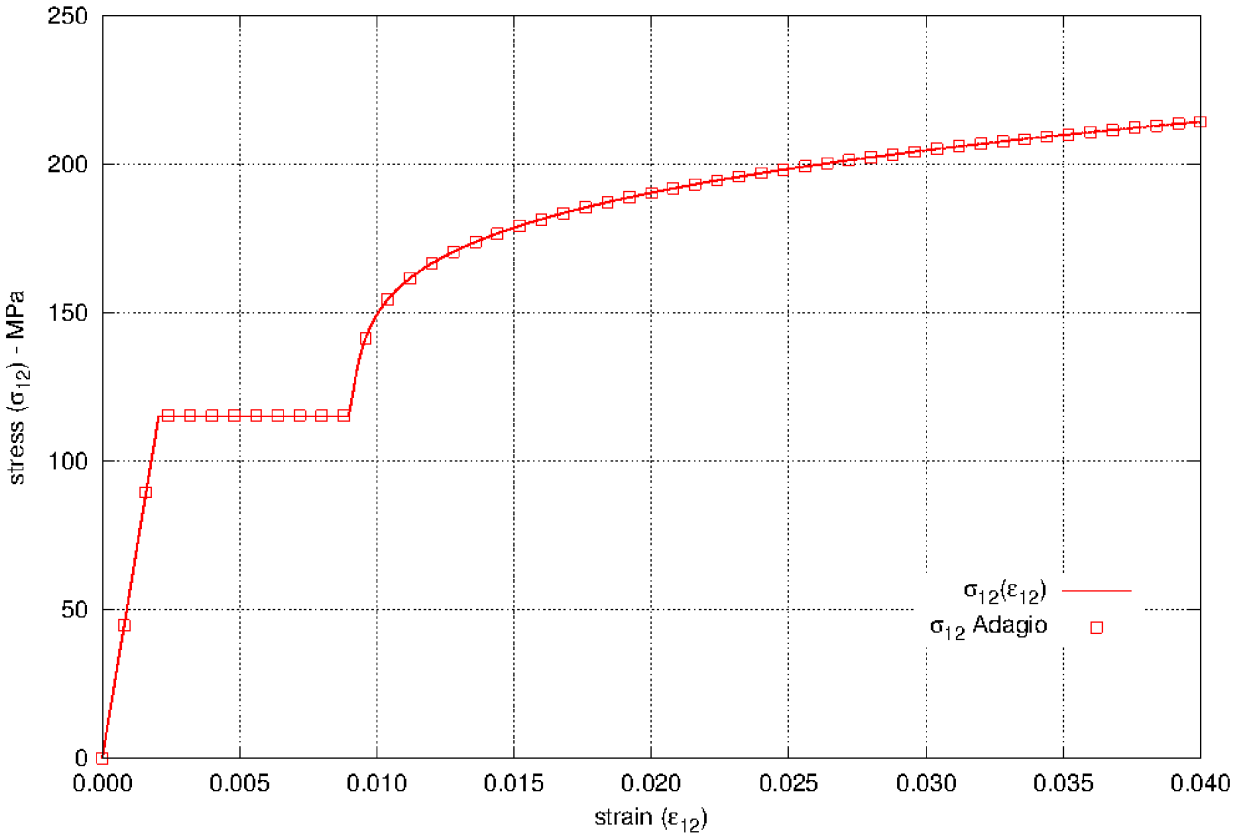

Fig. 4.23 The shear stress as a function of shear strain for the elastic-plastic power-law hardening model.

4.8.4 User Guide

```
BEGIN PARAMETERS FOR MODEL EP_POWER_HARD
  #
  # Elastic constants
  #
  YOUNGS MODULUS = <real>
  POISSONS RATIO = <real>
  SHEAR MODULUS  = <real>
  BULK MODULUS   = <real>
  LAMBDA         = <real>
  TWO MU         = <real>
  #
  # Hardening behavior
  #
  YIELD STRESS       = <real>
  HARDENING CONSTANT = <real>
  HARDENING EXPONENT = <real>
  LUDERS STRAIN      = <real>
END [PARAMETERS FOR MODEL EP_POWER_HARD]
```

In the above command blocks:

- The `YIELD STRESS` is the stress at which the plastic power law yielding and hardening model takes effect. See Fig. 4.20.
- The `LUDERS STRAIN` defines a regime of zero hardening modulus prior to onset of the power law hardening. A small Luder band is seen in the hardening behavior or many metals. See Fig. 4.20 for details.
- The `HARDENING CONSTANT` command line and `HARDENING EXPONENT` command define the power law hardening curve. Past the Luder strain the hardened yield surface radius is given by the `HARDENING CONSTANT` times plastic strain to the `HARDENING EXPONENT` power.

Output variables available for this model are listed in Table 4.7 and Table 4.8. For information about the elastic-plastic power-law hardening model, consult [103].

Table 4.7 State Variables for EP POWER HARD Model

Name	Description
EQPS	equivalent plastic strain, $\bar{\varepsilon}^p$
TEN-SILE_EQPS	equivalent plastic strain only accumulated when the material is in tension (trace of stress tensor is positive)
RADIUS	radius of yield surface, R
ITERA-TIONS	number of radial return iterations

Table 4.8 State Variables for EP POWER HARD Model for Shells

Name	Description
EQPS	equivalent plastic strain, $\bar{\varepsilon}^p$
TEN-SILE_EQPS	equivalent plastic strain only accumulated when the material is in tension (trace of stress tensor is positive)
RADIUS	radius of yield surface, R
ITERA-TIONS	number of radial return iterations
ERROR	error in plane stress iterations
PS_ITER	plane stress iterations

4.9 Ductile Fracture Model

4.9.1 Theory

The ductile fracture model is identical to the elastic-plastic power-law hardening model with the addition of a failure criterion and an isotropic decay of the stress to zero during the failure process within the constitutive model. To accomplish this task, the tearing parameter, t_p, proposed by Wellman [110] is introduced and the functional form as given as

$$t_p = \int_0^{\varepsilon} \left\langle \frac{2\sigma_{\max}}{3\left(\sigma_{\max} - \sigma_m\right)} \right\rangle^4 d\bar{\varepsilon}^p \tag{4.33}$$

where $\sigma_{\max}$ is the maximum principal stress, and σ_m is the mean stress. It can also be noted that the tearing parameter evolves during the plastic deformation regime as indicated by integrating over the effective plastic strain, $\bar{\varepsilon}^p$. The angle brackets denoting the Macaulay brackets, where

$$\langle x \rangle = \begin{cases} 0 & \text{if } x \leq 0 \\ x & \text{if } x > 0 \end{cases},$$

are used to ensure that the failure process occurs only with tensile stress states and prevent "damage healing". The failure process then initiates at a critical tearing parameter, t_p^{crit}, and the corresponding stress decay occurs over a strain interval corresponding to the *critical crack opening strain*, $\varepsilon_{\text{ccos}}$. Importantly, the $\varepsilon_{\text{ccos}}$ serves a dual role in that it may also be used to control the energy dissipated during failure. With respect to the latter point, careful selection of the critical crack opening strain may be used to ensure consistent energy is dissipated through different meshes. This decay process is isotropic and linear with the current damage value being equivalent to the ratio of crack opening strain in the direction of the maximum principal stress to the critical value.

4.9.2 Implementation

The ductile fracture model seeks to capture both the nonlinear elastic-plastic and fracture responses of a ductile metal. Independently, each of these requirements necessitates the use of a nonlinear solution algorithm and the combination of the two is even more complex. This consideration is compounded by the relaxation and softening observed during the failure process that introduces additional complications for the global finite element solver. For this discussion, however, the focus is solely on the underlying numerical treatment of the failure process at the constitutive level. The solution of the elastic-plastic constitutive problem was discussed in detail in Section 4.8.2 while details of the implications at the global finite element problem are found in the Sierra/SM User's Manual [115]. With respect to the latter, it is important to note that in quasistatic cases the ductile fracture model is tightly integrated with the multilevel `CONTROL FAILURE` capabilities although details of this coupling are left to [110], [115].

Prior to fracture initiation – while $t_p^{n+1} < t_p^{\text{crit}}$ – the ductile fracture model is exactly that of the elastic-plastic power law. Through this process the tearing parameter is continually calculated at the plastically converged state. When fracture initiation is first detected – $t_p^{n+1} \geq t_p^{\text{crit}}$ – the direction of the maximum principal stress, denoted by the normalized vector n_i^{cr}, is determined and stored. Regardless of loading path, this vector does not change during the unloading process. Additionally, for this first initial failure step, the unrotated stress tensor, T_{ij} must be set equal to its maximum value, T_{ij}^{crit} before any unloading may be performed. This maximum value is simply given by,

$$T_{ij}^{\text{crit}} = T_{ij}^n + \left(T_{ij}^{tr} - T_{ij}^n\right) \frac{t_p^{\text{crit}} - t_p^n}{t_p^{n+1} - t_p^n}$$

with T_{ij}^{tr} being the elastic trial stress. As alluded to in the prior section, a linear decay based on the crack opening strain in the direction of maximum stress, ε_{cos}, is utilized. To determine this decay value, the crack opening strain increment is first found via

$$d\varepsilon_{\text{cos}}^{n+1} =< \beta n_i^{cr} d_{ij}^{n+1} n_j^{cr} >,$$

where d_{ij}^{n+1} is the total unrotated rate of deformation and β is a partitioning factor between plastic and crack opening strains and takes the value of 1 for all loading steps emph{except} the initiation step. The $< \cdot >$ are the Macaulay brackets. During the first fracture step,

$$\beta = \frac{t_p^{n+1} - t_p^{\text{crit}}}{t_p^{n+1} - t_p^n}.$$

The current crack opening strain is then simply,

$$\varepsilon_{\text{cos}}^{n+1} = \varepsilon_{\text{cos}}^n + d\varepsilon_{\text{cos}}^{n+1} \Delta t$$

and the decay value, α^{n+1}, is then found as,

$$\alpha^{n+1} = \max\left[0, \frac{\varepsilon_{\text{ccos}} - \varepsilon_{\text{cos}}^{n+1}}{\varepsilon_{\text{ccos}}}\right].$$

To perform the actual stress decay, the hardening and yield values are proportionally decayed via,

$$\bar{\sigma}^{n+1}\left(\bar{\varepsilon}^{p}\right) = \alpha^{n+1}\bar{\sigma}^{f}; \qquad \beta_{ij}^{n+1} = \alpha^{n+1}\beta_{ij}^{n},$$

with $\bar{\sigma}^{f} = \phi\left(T_{ij}^{\text{crit}}\right)$ being the critical yield stress associated with the yield surface, ϕ, and β_{ij} is the backstress tensor used with kinematic hardening. The decayed stress is then found by radially returning to the reduced yield stress, $\bar{\sigma}^{n+1}\left(\bar{\varepsilon}\right)$. As a J_2 deviatoric yield stress is used for the plastic response, the hydrostatic component of the stress tensor is similarly decayed.

4.9.3 Verification

The ductile fracture model is tested in uniaxial stress and pure shear. For these test problems, the Young's modulus and Poisson's ratio are $E = 70$ GPa and $\nu = 0.25$. The yield stress is taken to be $\sigma_y = 200$ MPa while the hardening constant and exponent are $A = 400$ MPa and $n = 0.25$, respectively, and the Luders strain is 0.008. To describe failure, the critical tearing parameter is $t_p^{\text{crit}} = 0.025$ and the critical crack opening strain is $\varepsilon_{\text{ccos}} = 0.001$.

4.9.3.1 Uniaxial Stress

For loading in uniaxial stress the only non-zero stress component is σ_{11}. All other stress components are zero. If the stress state is on the yield surface then this stress is

$$\sigma_{11} = \bar{\sigma}(\bar{\varepsilon}^{p}),$$

with $\bar{\sigma}$ being the yield stress including any hardening effects associated with the evolution of the effective plastic strain, $\bar{\varepsilon}^{p}$. To evaluate the axial stress we need the equivalent plastic strain as a function of the axial strain, ε_{11}. If we equate the rate of plastic work we get

$$\bar{\sigma}\dot{\bar{\varepsilon}}^{p} = \sigma_{11}\left(\dot{\varepsilon}_{11} - \dot{\varepsilon}_{11}^{\text{e}}\right) \quad \rightarrow \quad \dot{\bar{\varepsilon}}^{p} = \dot{\varepsilon}_{11} - \dot{\varepsilon}_{11}^{\text{e}} = \dot{\varepsilon}_{11}^{p}$$

which, when integrated, gives us an implicit equation for the equivalent plastic strain

$$\bar{\varepsilon}^{p} = \left(\varepsilon_{11} - \frac{\bar{\sigma}(\bar{\varepsilon}^{p})}{E}\right).$$

Alternatively, we write the axial strain as a function of the equivalent plastic strain, which allows us to parameterize the problem with $\bar{\varepsilon}^{p}$

$$\varepsilon_{11} = \bar{\varepsilon}^{p} + \frac{\bar{\sigma}(\bar{\varepsilon}^{p})}{E}.$$

In uniaxial stress the pressure is $\sigma_{11}/3$ and the maximum principal stress is $\sigma_{\text{max}} = \sigma_{11}$. Using this in (4.33) we get

$$t_p = \bar{\varepsilon}^{p}$$

i.e. the tearing parameter is equal to the equivalent plastic strain. This result is shown in Fig. 4.24(a). The final value for the tearing parameter is a function of the number of steps, or the step size. The smaller the step size the closer the final value is to t_p^{crit}.

The axial stress as a function of axial strain is shown in Fig. 4.24(b). The axial stress depends on the elastic-plastic response until the critical tearing parameter is reached. As with the tearing parameter results, this point is time step dependent. Once the critical tearing parameter is reached the stress decay occurs over the critical crack opening strain.

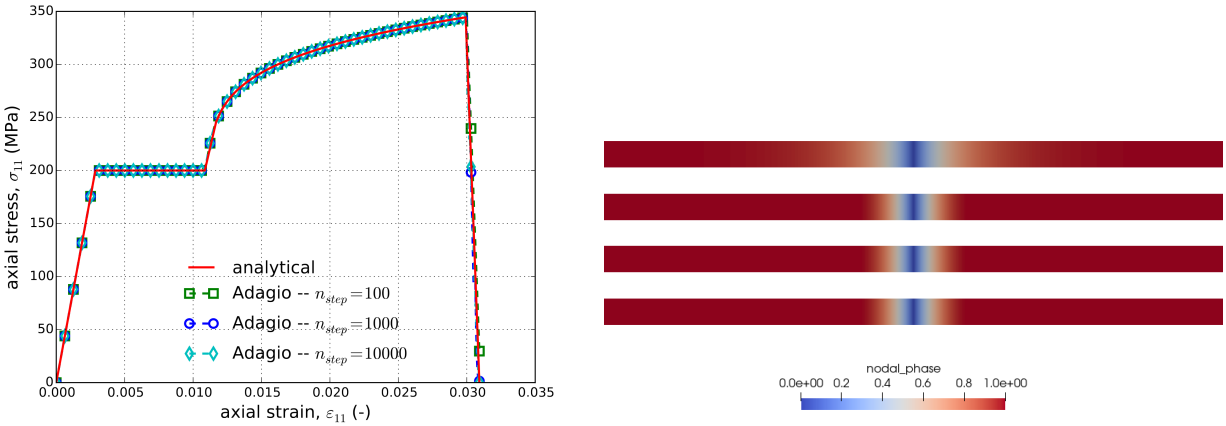

(a) Tearing parameter **(b) Axial stress**

Fig. 4.24 The (a) tearing parameter, t_p, and (b) axial stress-strain response for the ductile fracture model in uniaxial stress. The post failure reduction in stress depends on the time discretization or step size.

4.9.3.2 Pure Shear

For loading in pure shear the only non-zero stress component is σ_{12}. All other stress components are zero. If the stress state is on the yield surface then the shear stress is

$$\sigma_{12} = \frac{\bar{\sigma}(\bar{\varepsilon}^p)}{\sqrt{3}}.$$

To evaluate the shear stress we need the equivalent plastic strain as a function of the shear strain. If we equate the rate of plastic work we get

$$\bar{\sigma}\dot{\bar{\varepsilon}}^p = 2\sigma_{12}\left(\dot{\varepsilon}_{12} - \dot{\varepsilon}_{12}^{\text{e}}\right) \quad \rightarrow \quad \dot{\bar{\varepsilon}}^p = \frac{2}{\sqrt{3}}\left(\dot{\varepsilon}_{12} - \dot{\varepsilon}_{12}^{\text{e}}\right)$$

which, when integrated, gives us an implicit equation for the equivalent plastic strain

$$\bar{\varepsilon}^p = \frac{2}{\sqrt{3}}\left(\varepsilon_{12} - \frac{\bar{\sigma}(\bar{\varepsilon}^p)}{\sqrt{3}G}\right).$$

Alternatively, we write the shear strain, ε_{12} as a function of the equivalent plastic strain, which allows us to parameterize the problem with $\bar{\varepsilon}^p$

$$\varepsilon_{12} = \frac{\sqrt{3}}{2}\bar{\varepsilon}^p + \frac{\bar{\sigma}(\bar{\varepsilon}^p)}{\sqrt{3}G}.$$

In pure shear the pressure is zero, and the maximum principal stress is $\sigma_{\max} = \sigma_{12}$. Using this in (4.33) we get

$$t_p = \left(\frac{2}{3}\right)^4 \bar{\varepsilon}^p.$$

This result is shown in Fig. 4.25, where the tearing parameter is a function of the shear strain. The final value for the tearing parameter is a function of the number of steps, or the step size. The smaller the step size the closer the final value is to t_p^{crit}.

The shear stress as a function of shear strain is shown in Fig. 4.26. The shear stress depends on the elastic-plastic response until the critical tearing parameter is reached. As with the tearing parameter results, this point is time step dependent. Once the critical tearing parameter is reached the stress decay occurs over the critical crack opening strain.

4.9.4 User Guide

```
BEGIN PARAMETERS FOR MODEL DUCTILE_FRACTURE
  #
  # Elastic constants
  #
  YOUNGS MODULUS = <real>
  POISSONS RATIO = <real>
  SHEAR MODULUS  = <real>
  BULK MODULUS   = <real>
  LAMBDA         = <real>
  TWO MU         = <real>
  #
  # Yield surface parameters
  #
  YIELD STRESS       = <real>
  HARDENING CONSTANT = <real>
  HARDENING EXPONENT = <real>
  LUDERS STRAIN      = <real>
  #
  # Failure parameters
  #
  CRITICAL TEARING PARAMETER    = <real>
  CRITICAL CRACK OPENING STRAIN = <real>
END [PARAMETERS FOR MODEL DUCTILE_FRACTURE]
```

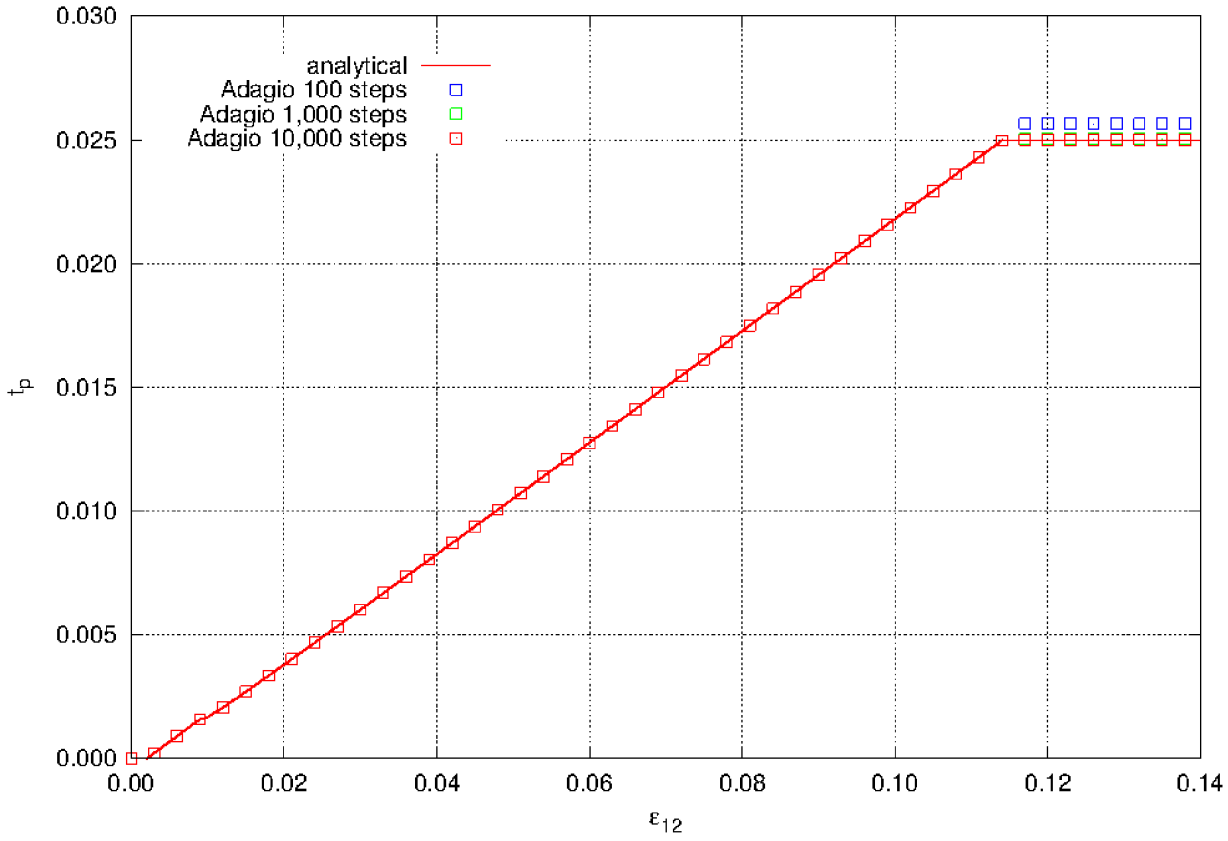

Fig. 4.25 The tearing parameter, t_p, in pure shear. The maximum tearing parameter depends on the time discretization or step size.

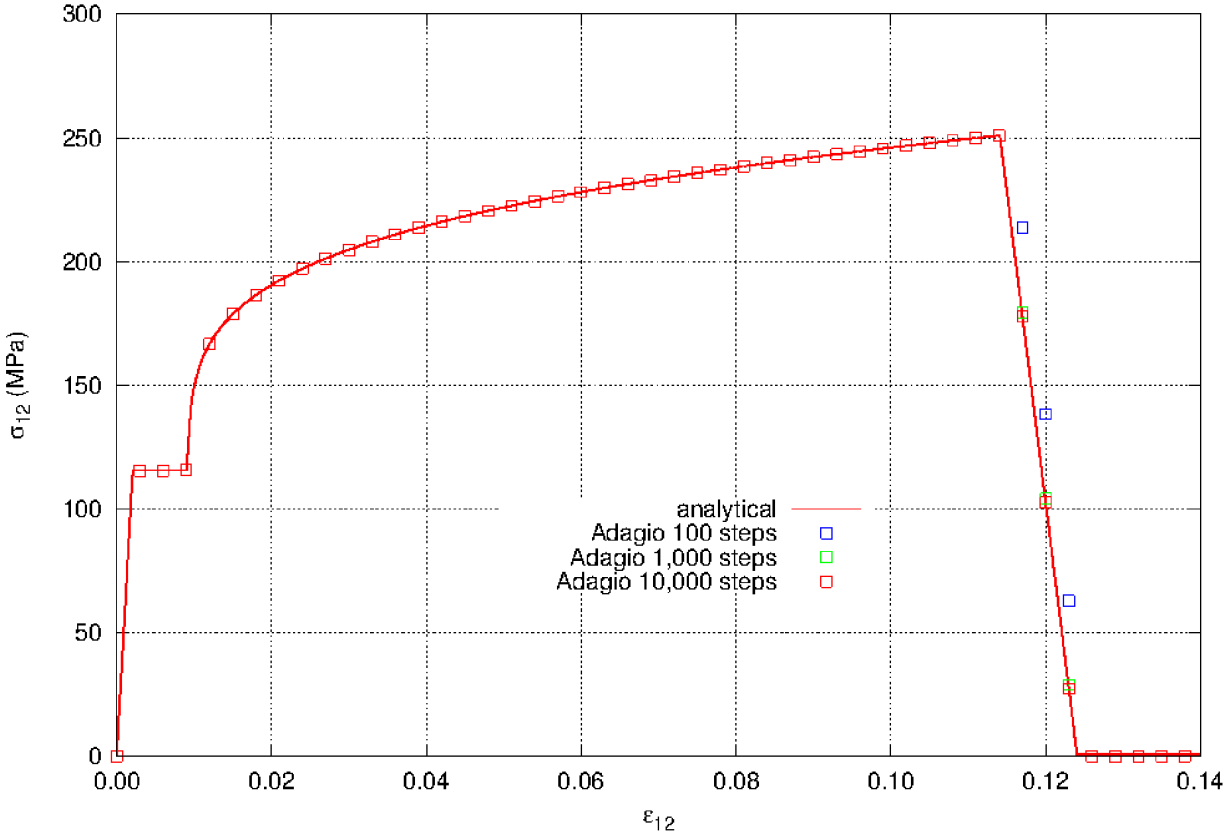

Fig. 4.26 Shear stress vs. shear strain for the ductile fracture model in pure shear. The post failure reduction in stress depends on the time discretization or step size.

In the above command blocks:

- The `YIELD STRESS` is the stress at which the plastic power load yielding and hardening model takes effect. See Fig. 4.20.
- The `LUDERS STRAIN` defines a regime of zero hardening modulus prior to onset of the power law hardening. A small Luder band is seen in the hardening behavior or many metals. See Fig. 4.20 for details.
- The `HARDENING CONSTANT` command line and `HARDENING EXPONENT` command define the power law hardening curve. Past the Luder strain the hardened yield surface radius is given by the `HARDENING CONSTANT` times plastic strain to the `HARDENING EXPONENT` power.
- `CRITICAL TEARING PARAMETER` defines the t_p value at which fracture and subsequent decay of stress will occur.
- When the model undergoes additionally strain after reaching the critical tearing parameter the stress in the model will decay to zero. The amount strain over which the stress decays to zero is defined with the `CRITICAL CRACK OPENING STRAIN` command line. The relevant opening strain is the component of strain that is aligned with the maximum-principal-stress direction at initial failure.

Output variables available for this model are listed in Table 4.9. For information about the ductile fracture material model, consult [110].

Table 4.9 State Variables for DUCTILE FRACTURE Model

Name	Description
EQPS	equivalent plastic strain, $\bar{\varepsilon}^p$
RADIUS	radius of yield surface, R
BACK_STRESS	back stress - tensor α_{ij}
TEARING_PARAMETER	Current value of the integrated tearing parameter
CRACK_OPENING_STRAIN	Current value of the crack opening strain. Will be zero prior to reaching the maximum tearing parameter.
FAILURE_DIRECTION	Crack opening direction (maximum principal stress direction at failure) - vector
DF_STRAIN_XX	XX component of current strain
DF_STRAIN_YY	YY component of current strain
DF_STRAIN_ZZ	ZZ component of current strain
DF_STRAIN_XY	XY component of current strain
DF_STRAIN_YZ	YZ component of current strain
DF_STRAIN_ZX	ZX component of current strain
MAX_RADIUS	Yield surface radius at failure
MAX_PRESS	Stress pressure norm at failure

4.10 Multilinear Elastic-Plastic Model

4.10.1 Theory

The multilinear elastic-plastic model is a generalization of the standard rate independent plasticity models already presented - the linear and power law hardening models. However, rather than having a specific functional form, the multilinear hardening model allows the user to input a piecewise linear function for the hardening curve. The rate form of the constitutive equation assumes an additive split of the rate of deformation into an elastic and plastic part such that

$$D_{ij} = D^{\mathrm{e}}_{ij} + D^{\mathrm{p}}_{ij}.$$

The stress rate only depends on the elastic strain rate so that,

$$\overset{\circ}{\sigma}_{ij} = \mathbb{C}_{ijkl} D^{\mathrm{e}}_{kl},$$

where $\mathbb{C}_{ijkl}$ are the components of the fourth-order, isotropic elasticity tensor.

The key to the model is finding the plastic rate of deformation. For associated flow, the plastic rate of deformation is in the direction normal to the yield surface. With a yield surface given by

$$\phi\left(\sigma_{ij}\right) - \bar{\sigma}\left(\bar{\varepsilon}^{p}\right) = 0$$

then the plastic rate of deformation can be written as

$$D^{\mathrm{p}}_{ij} = \dot{\gamma} \frac{\partial \phi}{\partial \sigma_{ij}}. \tag{4.34}$$

For this model the yield surface is taken to be a von Mises yield surface, such that

$$\phi\left(\sigma_{ij}\right) = \sqrt{\frac{3}{2} s_{ij} s_{ij}}$$

where s_{ij} are the components of the deviatoric stress

$$s_{ij} = \sigma_{ij} - \frac{1}{3}\delta_{ij}\sigma_{kk}.$$

For simplicity it is easier to write (4.34) in terms of the normal to the yield surface

$$D^{\mathrm{p}}_{ij} = \dot{\gamma} N_{ij} \quad ; \quad N_{ij} = \frac{\partial \phi}{\partial \sigma_{ij}} \Big/ \left\| \frac{\partial \phi}{\partial \sigma_{ij}} \right\|$$

The model also incorporates temperature dependence in that the elastic properties and the yield stress can be functions of temperature. This is not as general as having the yield curves depend on temperature. For that behavior the thermoelastic-plastic model can be used.

An example stress vs. plastic strain hardening curve is shown in Fig. 4.27. This curve was generated for a loading case of uniaxial strain. In this case, the effective stress is the same as the uniaxial. Therefore, for use with the multilinear elastic-plastic model this curve would simply have to be discretized and used as input.

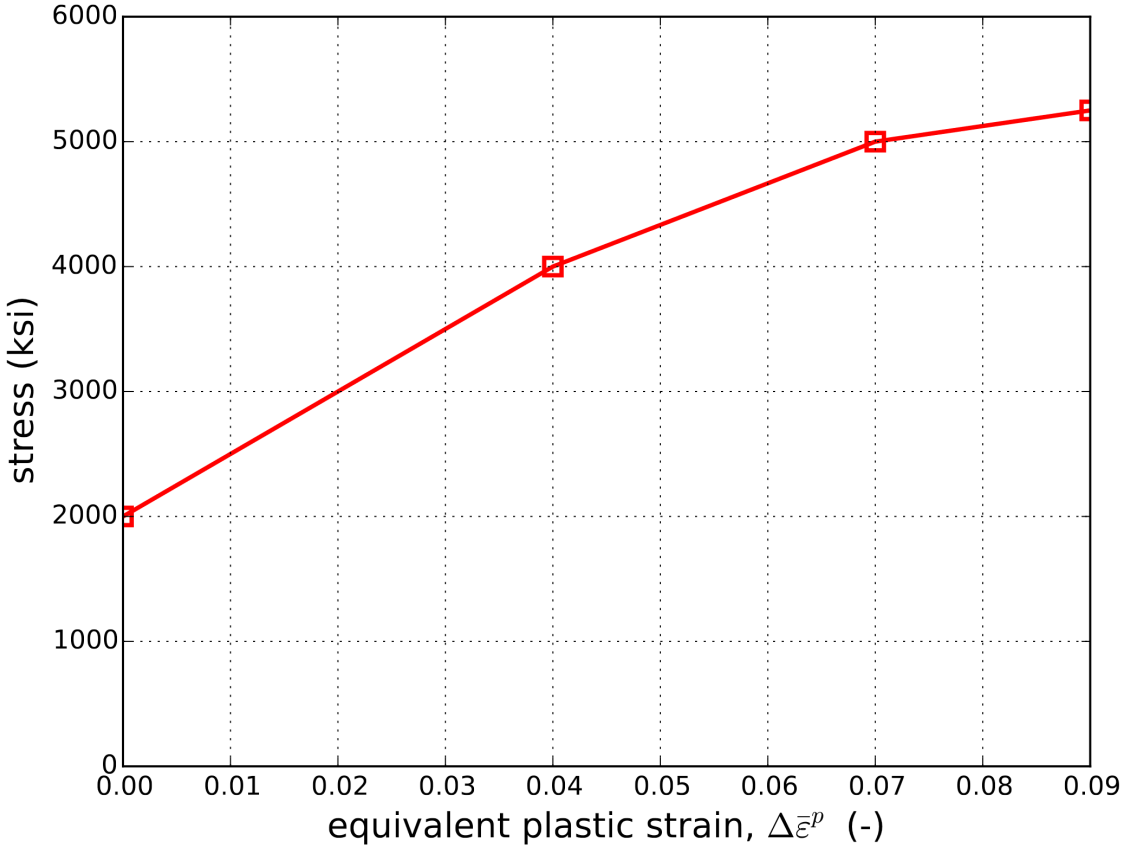

Fig. 4.27 An example of a multilinear elastic-plastic stress-strain curve.

4.10.2 Implementation

The multilinear elastic-plastic model is implemented using a predictor-corrector algorithm. First, an elastic trial stress state is calculated. This is done in the unrotated configuration (see Section 4.1) by assuming that the rate of deformation is completely elastic

$$T_{ij}^{tr} = T_{ij}^{n} + \Delta t \left(\lambda \delta_{ij} d_{kk} + 2\mu d_{ij}\right).$$

The trial stress state is decomposed into a pressure and a deviatoric stress

$$p^{tr} = \frac{1}{3} T_{kk}^{tr} \quad ; \quad s_{ij}^{tr} = T_{ij}^{tr} - p^{tr} \delta_{ij}$$

The effective trial stress is calculated and used with the yield function (4.31),

$$f\left(s_{ij}^{tr}, \bar{\varepsilon}^{p}\right) = \phi\left(s_{ij}^{tr}\right) - \bar{\sigma}\left(\bar{\varepsilon}^{p}\right).$$

If $f \leq 0$ then the response is elastic and the stress update is finished. If $f > 0$ then plastic deformation has occurred and a radial return algorithm is used to determine the extent of this behavior.

The model assumes associated flow such that the normal to the yield surface lies in the direction of the trial stress state. This leads to the following expression for the normal, N_{ij},

$$N_{ij} = \frac{s_{ij}^{tr}}{\| s_{ij}^{tr} \|}.$$

Using a backward Euler algorithm, the final deviatoric stress state may be written as

$$s_{ij}^{n+1} = s_{ij}^{tr} - \Delta t 2\mu d_{ij}^{\mathrm{p}}$$

where the plastic strain increment, $\Delta d_{ij}^{\mathrm{p}}$, is

$$\Delta d_{ij}^{\mathrm{p}} = \sqrt{\frac{3}{2}} \Delta \bar{\varepsilon}^{p} N_{ij}.$$

Thus, to determine the response of the material the increment of the effective plastic strain, $\Delta \bar{\varepsilon}^{p}$, needs to be determined. This may be done by solving the linearized consistency equation over the load step that is written as,

$$3\mu \Delta \bar{\varepsilon}^{p} + \bar{\sigma}\left(\bar{\varepsilon}_{n} + \Delta \bar{\varepsilon}^{p}\right) - \phi^{tr} + f_{n} = 0.$$

4.10.3 Verification

The multilinear elastic-plastic material model is verified for uniaxial stress and pure shear. The elastic properties used in these analyses are $E = 70$ GPa and $\nu = 0.25$. In order to appropriately

verify this model, the hardening curve must have a functional form to appropriately determine an analytical solution. Here, the hardening law used for the model is a Voce law with the following form

$$\bar{\sigma}\left(\bar{\varepsilon}^{p}\right) = \sigma_{y} + A\left(1 - \exp(-n\bar{\varepsilon}^{p})\right).$$

In the numerical analyses, this expression is discretized at a series of plastic strain values and used as input. For these calculations $\sigma_y = 200$ MPa, $A = 200$ MPa, and $n = 20$.

4.10.3.1 Uniaxial Stress

The multilinear elastic-plastic model is tested in uniaxial tension. The test looks at the axial stress and the lateral strain and compares these values against analytical results for the same problem. In this verification problem only the normal strains/stresses are needed, and the shear terms are not exercised.

For the uniaxial stress problem, the only non-zero stress component is σ_{11}. In the analysis that follows $\sigma_{11} = \sigma$. There are three non-zero strain components, ε_{11}, ε_{22}, and ε_{33}. In the analysis that follows $\varepsilon_{11} = \varepsilon$ and $\varepsilon_{22} = \varepsilon_{33}$. Furthermore, the axial elastic strain, $\varepsilon^{\mathrm{e}}_{11} = \sigma/E$ will be denoted by ε^{e}.

The equivalent plastic strain, $\bar{\varepsilon}^{\mathrm{p}}$, for this model is equivalent to $\varepsilon^{\mathrm{p}}_{11}$, and is

$$\bar{\varepsilon}^{\mathrm{p}} = \varepsilon - \frac{\bar{\sigma}\left(\bar{\varepsilon}^{\mathrm{p}}\right)}{E}$$

This allows us, after yield, to parameterize the problem with the equivalent plastic strain.

For the lateral strains we need the lateral plastic strain. Incompressibility gives us

$$\bar{\varepsilon}^{\mathrm{p}}_{22} = -\frac{1}{2}\bar{\varepsilon}^{\mathrm{p}}$$

Combined with the lateral elastic strains we have the lateral strain as a function of the equivalent plastic strain

$$\varepsilon_{22} = -\nu\frac{\bar{\sigma}\left(\bar{\varepsilon}^{\mathrm{p}}\right)}{E} - \frac{1}{2}\bar{\varepsilon}^{\mathrm{p}}$$

The results are shown in Fig. 4.28 and Fig. 4.29 and show agreement between the model in Adagio and the analytical results.

4.10.3.2 Pure Shear

The multilinear elastic-plastic model is tested in pure shear. The test looks at the shear stress as a function of the shear strain and compares these values against analytical results for the same problem. For the pure shear problem, the only non-zero strain component is ε_{12} and the only non-zero stress component is σ_{12}.

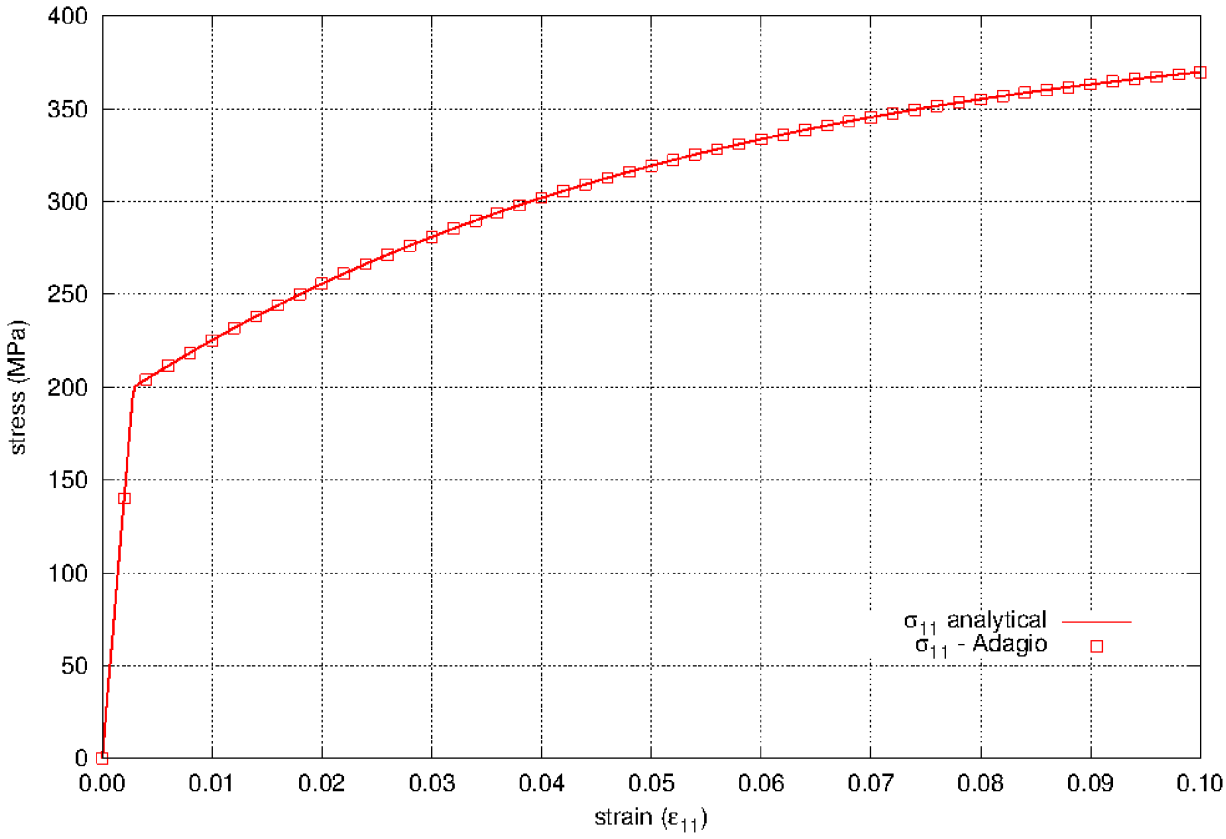

Fig. 4.28 The axial stress as a function of axial strain for the multilinear elastic-plastic model with an analytical Voce law for the hardening model.

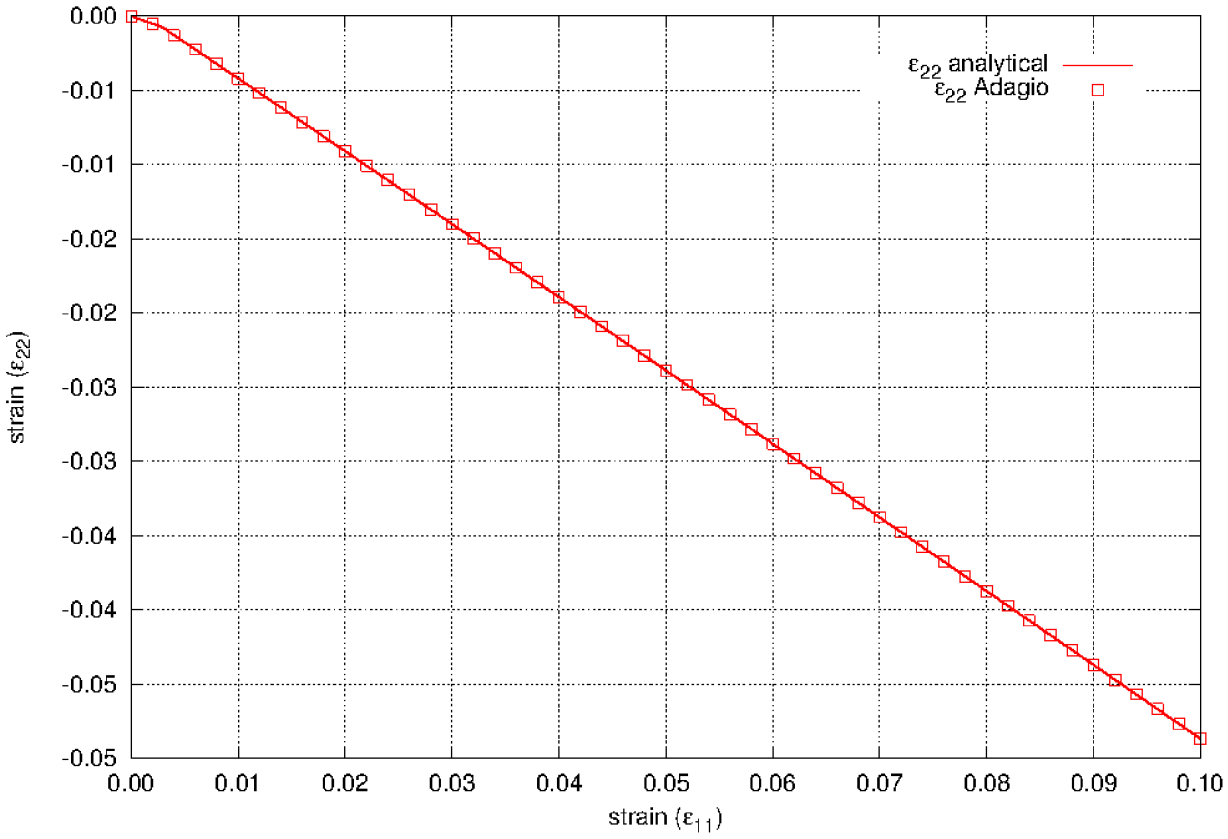

Fig. 4.29 The lateral strain as a function of axial strain for the multilinear elastic-plastic model with an analytical Voce law for the hardening model.

After yield, the shear stress as a function of the hardening curve is $\sigma_{12} = \bar{\sigma}\,(\bar{\varepsilon}^{p})\,/\sqrt{3}$. The elastic shear strain is $\varepsilon_{12}^{e} = \sigma_{12}/2G$; the plastic shear strain is $\varepsilon_{12}^{p} = \sqrt{3}\bar{\varepsilon}^{p}/2$. Using this, the shear stress and strain are given as functions of the equivalent plastic strain

$$\sigma_{12} = \frac{\bar{\sigma}\,(\bar{\varepsilon}^{p})}{\sqrt{3}} \quad ; \quad \varepsilon_{12} = \frac{\sqrt{3}}{2}\bar{\varepsilon}^{p} + \frac{1}{\sqrt{3}}\frac{\bar{\sigma}\,(\bar{\varepsilon}^{p})}{2G}$$

This allows us, after yield, to parameterize the problem with $\bar{\varepsilon}^{p}$.

The results are shown in Fig. 4.30 and show agreement between the model in Adagio and the analytical results.

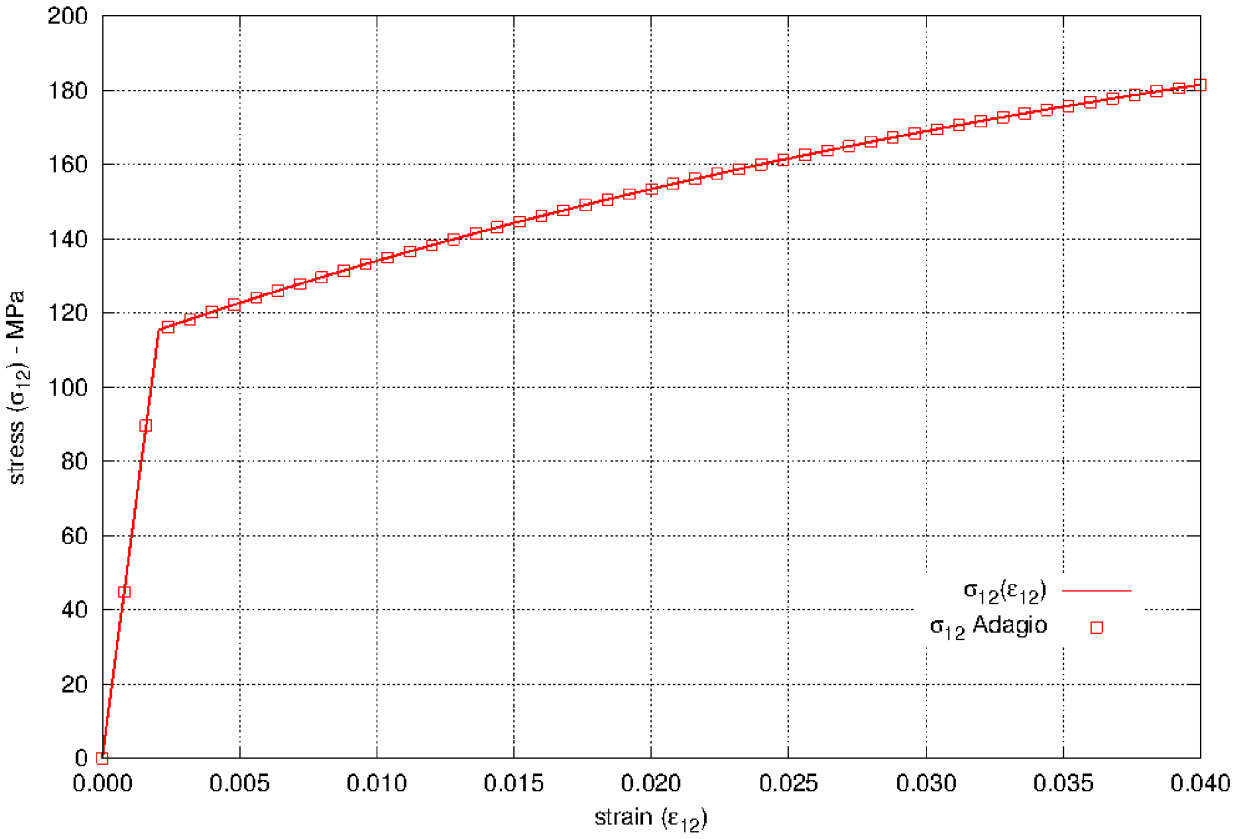

Fig. 4.30 The shear stress as a function of shear strain for the multilinear elastic-plastic model with an analytical Voce law for the hardening model.

4.10.4 User Guide

```
 BEGIN PARAMETERS FOR MODEL MULTILINEAR_EP
  #
  # Elastic constants
  #
  YOUNGS MODULUS = <real>
  POISSONS RATIO = <real>
  SHEAR MODULUS  = <real>
  BULK MODULUS   = <real>
  LAMBDA         = <real>
  TWO MU         = <real>
  #
  # Hardening behavior
  #
  YIELD STRESS       = <real>
  BETA               = <real> (1.0)
  HARDENING FUNCTION = <string> hardening_function_name
  #
  # Functions
  #
  YOUNGS MODULUS FUNCTION = <string> ym_function_name
  POISSONS RATIO FUNCTION = <string> pr_function_name
  YIELD STRESS FUNCTION   = <string> yield_stress_function_name
END [PARAMETERS FOR MODEL MULTILINEAR_EP]
```

In the above command blocks:

- The beta parameter defines if hardening is isotropic or kinematic.
- `YIELD STRESS` defines the stress where plastic yielding first occurs.
- The `HARDENING FUNCTION` command line references the name of a function defined in a `FUNCTION` command line in the SIERRA scope. The function describes the hardening behavior of the material as stress versus equivalent plastic strain. The x values of the function should be values of equivalent plastic strain while the y values of the function can be either the increment of stress over the yield stress or the actual stress at the corresponding equivalent plastic strain. Note the hardening function can have its first point defined at (0,0), or at (0, `YIELD_STRESS`). Either function definition behaves the same as only the slope of the hardening function between two strains is used by the model.
- The `YOUNGS MODULUS FUNCTION` command line references the name of a function defined in a `FUNCTION` command line in the SIERRA scope that describes a scale factor on Young's modulus as a function of temperature.
- The `POISSONS RATIO FUNCTION` command line references the name of a function defined in a `FUNCTION` command line in the SIERRA scope that describes a scale factor on Poisson's ratio as a function of temperature.

- The `YIELD STRESS FUNCTION` command line references the name of a function defined in a `FUNCTION` command line in the SIERRA scope that describes a scale factor on the yield stress as a function of temperature.

Output variables available for this model are listed in Table 4.10 and Table 4.11.

Table 4.10 State Variables for MULTILINEAR EP Model

Name	Description
EQPS	equivalent plastic strain
TEN-SILE_EQPS	equivalent plastic strain only accumulated when the material is in tension (trace of stress tensor is positive)
RADIUS	radius of yield surface
BACK_STRESS	back stress (symmetric tensor)
YOUNGS_MODULUS	the current Young's modulus as a function of temperature
POIS-SONS_RATIO	the current Poisson's ratio as a function of temperature
YIELD_STRESS	the current yield stress as a function of temperature
ITERATIONS	radial return iterations
YIELD_FLAG	inside (0) or on (1) the yield surface

Table 4.11 State Variables for MULTILINEAR EP Model for Shells

Name	Description
EQPS	equivalent plastic strain
TEN-SILE_EQPS	equivalent plastic strain only accumulated when the material is in tension (trace of stress tensor is positive)
RADIUS	radius of yield surface
BACK_STRESS	back stress (symmetric tensor)
YOUNGS_MODULUS	the current Young's modulus as a function of temperature
POIS-SONS_RATIO	the current Poisson's ratio as a function of temperature
YIELD_STRESS	the current yield stress as a function of temperature
ITERATIONS	radial return iterations
ERROR	error in plane stress iterations
PS_ITER	plane stress iterations

4.11 Multilinear Elastic-Plastic Fail Model

4.11.1 Theory

Like the ductile fracture model, the multilinear elastic-plastic fail model is an extension of an existing plasticity model (multilinear elastic-plastic) to include a ductile failure criteria. Again, the tearing parameter criterion and failure propagation model of Wellman [110] is selected. Specifically, this approach uses a failure criterion (the tearing parameter, t_p) that is based on the history of the plastic strain and stress states. Most failure criteria for ductile failure involve some form of the stress triaxiality, or the ratio of the pressure and the effective (shear) stress. The tearing parameter, however, is slightly different in that it depends on the pressure and the maximum principal stress and is given as,

$$t_p = \int_0^{\varepsilon} \left\langle \frac{2\sigma_{\max}}{3\left(\sigma_{\max} - \sigma_m\right)} \right\rangle^m d\varepsilon_p, \tag{4.35}$$

with $\sigma_{\max}$ and σ_m being the maximum principal and mean stresses, respectively. The exponent m is typically taken to be 4 while the $\langle \cdot \rangle$ are Macaulay brackets defined as,

$$\langle x \rangle = \begin{cases} 0 & x \leq 0 \\ x & x > 0 \end{cases},$$

and introduced so that failure only occurs and propagates under tensile stress states. Failure then initiates when the tearing parameter, t_p, reaches a critical value, t_p^{crit}. After this point, the stress decays (to 0) in a linear fashion according to the ratio of the crack opening strain in the maximum principal stress direction to its critical value, $\varepsilon_{\text{ccos}}$. Modification and control of this latter parameter is important as it may be used to ensure consistent energy is dissipated through different meshes.

4.11.2 Implementation

The multilinear elastic-plastic fail model seeks to capture both the nonlinear elastic-plastic and fracture responses of a ductile metal. Independently, each of these requirements necessitates the use of a nonlinear solution algorithm and the combination of the two is even more complex. This consideration is compounded by the relaxation and softening observed during the failure process that introduces additional complications for the global finite element solver. For this discussion, however, the focus is solely on the underlying numerical treatment of the failure process at the constitutive level. The solution of the elastic-plastic constitutive problem was discussed in detail in Section 4.10.2 while details of the implications at the global finite element problem are found in the Sierra/SM User's Manual [115]. With respect to the latter, it is important to note that the ductile fracture model is tightly integrated with the multilevel `CONTROL FAILURE` capabilities although details of this coupling are left to [110], [115].

Prior to fracture initiation – while $t_p^{n+1} < t_p^{\text{crit}}$ – the multilinear elastic-plastic fail model is the same as the "normal" multilinear elastic-plastic model. Through this process the tearing

parameter is continually calculated at the plastically converged state. When fracture initiation is first detected – $t_p^{n+1} \geq t_p^{\text{crit}}$ – the crack direction (assumed aligned with the maximum principal stress), denoted by the normalized vector n_i^{cr}, is determined and stored. Regardless of loading path, this vector does not change during the unloading process. Additionally, for this first initial failure step, the unrotated stress tensor, T_{ij} must be updated to its maximum value, T_{ij}^{crit} before any unloading may be performed. This is done simply by,

$$T_{ij}^{\text{crit}} = T_{ij}^n + \left(T_{ij}^{tr} - T_{ij}^n\right) \frac{t_p^{\text{crit}} - t_p^n}{t_p^{n+1} - t_p^n},$$

with T_{ij}^{tr} being the elastic trial stress. As alluded to in the prior section, a linear decay based on the crack opening strain in the direction of maximum stress, $\varepsilon_{\cos}$, is utilized. To determine this decay value, the crack opening strain increment is first found via

$$d\varepsilon_{\cos}^{n+1} =< \gamma n_i^{cr} d_{ij}^{n+1} n_j^{cr} >,$$

where d_{ij}^{n+1} is the unrotated rate of deformation and γ is a partitioning factor between plastic and crack opening strains and takes the value of 1 for all loading steps *except* the initiation step and the "$< \cdot >$" are the Macaulay brackets. During the first fracture step,

$$\gamma = \frac{t_p^{n+1} - t_p^{\text{crit}}}{t_p^{n+1} - t_p^n}.$$

The current crack opening strain is then simply,

$$\varepsilon_{\cos}^{n+1} = \varepsilon_{\cos}^n + d\varepsilon_{\cos}^{n+1} \Delta t.$$

and the decay factor, α, may be written as

$$\alpha^{n+1} = \max\left[0, \frac{\varepsilon_{\text{ccos}} - \varepsilon_{\cos}^{n+1}}{\varepsilon_{\text{ccos}}}\right].$$

Given the temperature dependence, stress decay is slightly more complicated than in the ductile fracture case. This task is primarily accomplished by decreasing the yield stress (radius) proportionally with the decay factor,

$$\bar{\sigma}^{n+1}\left(\bar{\varepsilon}^{\text{p}}\right) = \alpha^{n+1} \bar{\sigma}^f,$$

where $\bar{\sigma}^f = \phi\left(T^{\text{crit}}\right)$ is the yield stress at failure. The decayed stress is then found by radially returning to this reduced yield stress. Similarly, the hydrostatic and von Mises effective stress at failure (σ_m^f and $\bar{\sigma}_{vM}^f$, respectively) are also calculated and stored to appropriately constrain the stress state. An additional check is then performed to ensure (and if necessary modify) the decayed stress to ensure that,

$$\sigma_m \leq \alpha \sigma_m^f; \qquad \bar{\sigma}_{vM} \leq \alpha \bar{\sigma}_{vM}^f.$$

4.11.3 Verification

The multilinear elastic-plastic model with failure has been tested with a number of verification tests. Specifically, uniaxial stress and uniaxial strain loadings are considered. For the elastic-plastic response, the same material properties as those in Section 4.10.3 are again considered. To this end, the Young's modulus and Poisson ratio are $E = 70$ GPa and $\nu = 0.25$, respectively, and a Voce hardening model of the form,

$$\bar{\sigma}\left(\bar{\varepsilon}^p\right) = \sigma_y + A\left(1 - \exp\left(-n\bar{\varepsilon}^p\right)\right),$$

is discretized and used. In this case, $\sigma_y = 200$ MPa, $A = 200$ MPa, and $n = 20$.

In terms of failure, the critical tearing parameter, t_p^{crit} is taken to be .04, the critical crack opening strain, $\varepsilon_{\text{ccos}}$, is .005 and $m = 4.0$.

4.11.3.1 Uniaxial Stress

To consider the uniaxial response, displacement controlled deformations are applied such that the only non-zero stress is the axial component, σ_{11}. Through such a loading path, three distinct regimes result. The first is the elastic domain with $t_p = 0$. Second is the plastic domain. During this stage,

$$\sigma_{11} = \bar{\sigma}\left(\bar{\varepsilon}^p\right),$$

and by considering the rate of plastic work and integrating yields the implicit (in terms of equivalent plastic strain) relation,

$$\bar{\varepsilon}^p = \left(\varepsilon_{11} - \frac{\bar{\sigma}\left(\bar{\varepsilon}^p\right)}{E}\right).$$

By rearranging, the axial strain may be found in terms of the plastic strain as,

$$\varepsilon_{11} = \bar{\varepsilon}^p + \frac{\bar{\sigma}\left(\bar{\varepsilon}^p\right)}{E}.$$

With this stress state ($\sigma_{ij} = \sigma_{11}\delta_{i1}\delta_{j1}$), the pressure is simply $\sigma_{11}/3$ and the maximum principal stress is $\sigma_{\text{max}} = \sigma_{11}$. From (4.35), the tearing parameter is then

$$t_p = \bar{\varepsilon}^p.$$

The final stage of deformation corresponds to the failure process in which the axial stress is,

$$\sigma_{11} = \alpha\sigma_{\text{peak}},$$

and

$$\alpha = \frac{\varepsilon_{\text{ccos}} - \left(\varepsilon_{11} - \varepsilon_{\text{peak}}\right)}{\varepsilon_{\text{ccos}}}.$$

In the preceding relations, σ_{peak} and $\varepsilon_{\text{peak}}$ are the axial stress and strain, respectively, at failure initiation. The former is simply $\sigma_{\text{peak}} = \bar{\sigma}\left(t_p^{\text{crit}}\right)$ and $\varepsilon_{\text{peak}} = t_p^{\text{crit}} + \sigma_{\text{peak}}/E$.

The tearing parameter and axial stress evolution as a function of axial strain are presented in Fig. 4.31(a) and Fig. 4.31(b), respectively. Good agreement is observed between the results verifying the model capability under such a loading. Three different numerical load incrementations were considered in this analysis and some dependence on load step is noted in the post-failure response of Fig. 4.31(b). Even with this observation, the resulting agreement between the different responses is still quite good.

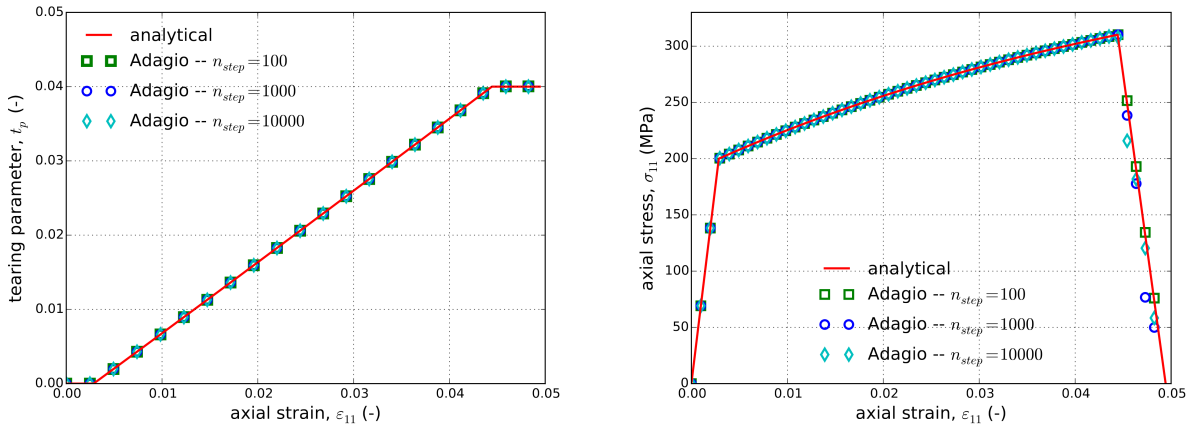

Fig. 4.31 Analytical and numerical results of the tearing parameter and axial stress evolution through a uniaxial tension loading path as a function of the axial strain, ε_{11}.

4.11.3.2 Pure Shear

The analysis of the pure shear loading path follows closely with that of the ductile fracture model (Section 4.9.3.2). In this case, pure shear deformations are applied such that the only non-zero stress and strain are σ_{12} and ε_{12}, respectively. Therefore, during plastic loading

$$\sigma_{12} = \frac{\bar{\sigma}}{\sqrt{3}},$$

and by comparing the plastic rate of work,

$$\varepsilon_{12} = \frac{\sqrt{3}}{2}\bar{\varepsilon}^p + \frac{\bar{\sigma}\left(\bar{\varepsilon}^p\right)}{\sqrt{3}\mu}.$$

Additionally, as the stress state is purely in shear there is no hydrostatic stress and the maximum principal stress is simply $\sigma_{\text{max}} = \sigma_{12}$ leading to an expression for the tearing parameter of the form,

$$t_p = \left(\frac{2}{3}\right)^4 \bar{\varepsilon}^p.$$

The stress then simply decays after the critical tearing parameter is reached. Numerical (from Adagio) and analytical results are presented in Fig. 4.32. Specifically, the tearing parameter and shear stress evolutions are presented in Fig. 4.32(a) and Fig. 4.32(b), respectively. Clear agreement is noted indicating the ability of the model to capture the response over a variety of loading paths.

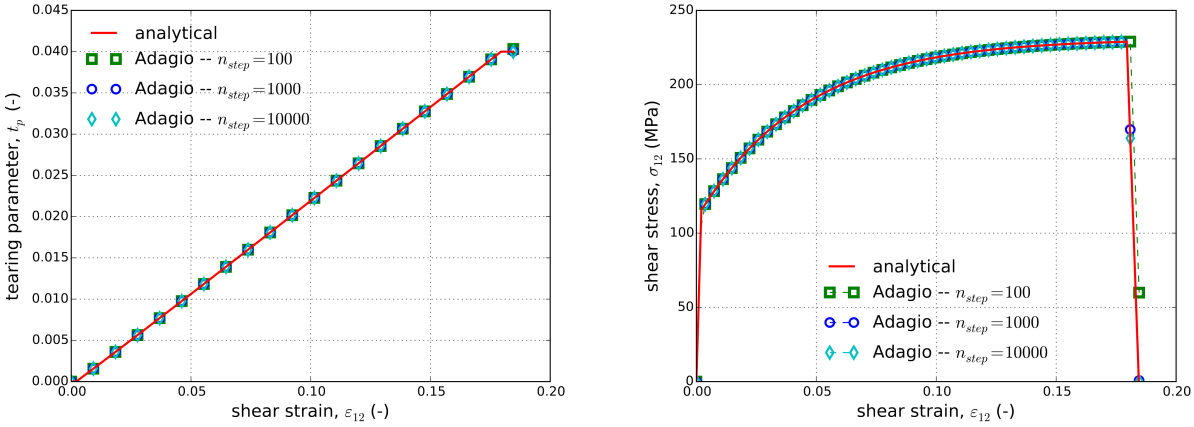

Fig. 4.32 Analytical and numerical results of the tearing parameter and shear stress evolution through a pure shear loading path as a function of the shear strain, ε_{12}.

4.11.4 User Guide

```
BEGIN PARAMETERS FOR MODEL ML_EP_FAIL
  #
  # Elastic constants
  #
  YOUNGS MODULUS = <real>
  POISSONS RATIO = <real>
  SHEAR MODULUS  = <real>
  BULK MODULUS   = <real>
  LAMBDA         = <real>
  TWO MU         = <real>
  #
  # Hardening behavior
  #
  YIELD STRESS       = <real>
  BETA               = <real> (1.0)
  HARDENING FUNCTION = <string> hardening_function_name
  #
  # Functions
  #
  YOUNGS MODULUS FUNCTION = <string> ym_function_name
```

(continues on next page)

(continued from previous page)

```
  POISSONS RATIO FUNCTION = <string> pr_function_name
  YIELD STRESS FUNCTION   = <string> yield_stress_function_name
  #
  # Failure parameters
  #
  CRITICAL TEARING PARAMETER    = <real>
  CRITICAL CRACK OPENING STRAIN = <real>
  CRITICAL BIAXIALITY RATIO     = <real> critical_ratio(0.0)
  FAILURE EXPONENT              = <real> (4.0)
END [PARAMETERS FOR MODEL ML_EP_FAIL]
```

In the above command blocks:

- The beta parameter defines if hardening is isotropic or kinematic.
- `YIELD STRESS` defines the stress for onset of yielding and plasticity.
- The `HARDENING FUNCTION` command line references the name of a function defined in a `FUNCTION` command line in the SIERRA scope. The function describes the hardening behavior of the material as stress versus equivalent plastic strain. The x values of the function should be values of equivalent plastic strain while the y values of the function can be either the increment of stress over the yield stress or the actual stress at the corresponding equivalent plastic strain. Note the hardening function can have its first point defined at (0,0), or at (0, `YIELD_STRESS`). Either function definition behaves the same as only the slope of the hardening function between two strains is used by the model.
- The `YOUNGS MODULUS FUNCTION` command line references the name of a function defined in a `FUNCTION` command line in the SIERRA scope that describes a scale factor on Young's modulus as a function of temperature.
- The `POISSONS RATIO FUNCTION` command line references the name of a function defined in a `FUNCTION` command line in the SIERRA scope that describes a scale factor on Poisson's ratio as a function of temperature.
- The `YIELD STRESS FUNCTION` command line references the name of a function defined in a `FUNCTION` command line in the SIERRA scope that describes a scale factor on the yield stress as a function of temperature.
- `CRITICAL TEARING PARAMETER` defines the t_p value at which fracture and subsequent decay of stress will occur.
- When the model undergoes additionally strain after reaching the critical tearing parameter the stress in the model will decay to zero. The amount strain over which the stress decays to zero is defined with the `CRITICAL CRACK OPENING STRAIN` command line. The relevant opening strain is the component of strain that is aligned with the maximum-principal-stress direction at initial failure.
- The `CRITICAL BIAXIALITY RATIO` command line should only be used under highly

specific conditions and with extreme caution. It is intended only for the special case where the stress state is nearly biaxial, resulting in nearly identical principal strains. In this case, the eigenvector computation can give unreliable results for the direction vectors for the principal strains. If the ratio of the difference between two principal strains divided by their magnitude is less that the value specified by the `CRITICAL BIAXIALITY RATIO` command, the direction of the vector defining the crack opening strain will be given equal weight in each of the principal directions associated with those strains. The default value for the critical ratio is 0.0, which means that the principal directions will be accepted directly from the eigenvector computation. This command should only be used as a last resort if the loading is nearly biaxial and the default value has been demonstrated to lead to elements with high strains that are not failing long after reaching the critical tearing parameter.

- The `FAILURE EXPONENT` command line specifies the exponent on the tearing parameter, the *m* parameter in (4.35). This exponent defaults to 4.0.

Output variables available for this model are listed in Table 4.12 and Table 4.13.

Table 4.12 State Variables for ML EP FAIL Model

Name	Description
EQPS	Equivalent plastic strain
RADIUS	Radius of yield surface
BACK_STRESS	back stress - tensor
BACK_STRESS_XX	back stress - xx component
BACK_STRESS_YY	back stress - yy component
BACK_STRESS_ZZ	back stress - zz component
BACK_STRESS_XY	back stress - xy component
BACK_STRESS_YZ	back stress - yz component
BACK_STRESS_ZX	back stress - zx component
YOUNGS_MODULUS	Current Young's modulus as a function of temperature
POISSONS_RATIO	Current Poisson's ratio as a function of temperature
YIELD_STRESS	Current Yield stress as a function of temperature
TENSILE_EQPS	equivalent plastic strain only accumulated when the material is in tension (trace of stress tensor is positive)
ITERATIONS	radial return iterations
YIELD_FLAG	inside(0) or on(1) yield surface
TEARING_PARAMETER	Current integrated value of the tearing parameter. Zero until yield is reached
CRACK_OPENING_STRAIN	Current value of the crack opening strain. Zero until the critical tearing parameter is reached
FAILURE_DIRECTION	crack opening direction at failure - vector
FAIL-URE_DIRECTION_X	crack opening direction at failure - x component
FAIL-URE_DIRECTION_Y	crack opening direction at failure - y component
FAIL-URE_DIRECTION_Z	crack opening direction at failure - z component
MAX_RADIUS	maximum radius at initial failure
MAX_PRESSURE	maximum stress pressure norm at initial failure
CRITI-CAL_CRACK_OPENING_STRAIN	
CRITI-CAL_TEARING_PARAMETER	

Table 4.13 State Variables for ML EP FAIL Model for Shells

Name	Description
EQPS	equivalent plastic strain
RADIUS	radius of yield surface
BACK_STRESS	back stress - tensor
BACK_STRESS_XX	back stress - xx component
BACK_STRESS_YY	back stress - yy component
BACK_STRESS_ZZ	back stress - zz component
BACK_STRESS_XY	back stress - xy component
BACK_STRESS_YZ	back stress - yz component
BACK_STRESS_ZX	back stress - zx component
YOUNGS_MODULUS	Current Young's modulus as a function of temperature
POISSONS_RATIO	Current Poisson's ratio as a function of temperature
YIELD_STRESS	Current Yield stress as a function of temperature
ITER	radial return iterations
ERROR	Error in plane stress iterations
PS_ITER	Plane stress iterations
TEARING_PARAMETER	Current integrated value of the tearing parameter. Zero until yield is reached
CRACK_OPENING_STRAIN	Current value of the crack opening strain. Zero until the critical tearing parameter is reached
FAILURE_DIRECTION	crack opening direction at failure - vector
FAILURE_DIRECTION_X	crack opening direction at failure - x component
FAILURE_DIRECTION_Y	crack opening direction at failure - y component
FAILURE_DIRECTION_Z	crack opening direction at failure - z component
RADIUS_MAX	maximum radius at initial failure
TENSILE_EQPS	equivalent plastic strain only accumulated when the material is in tension (trace of stress tensor is positive)

4.12 Johnson-Cook Model

4.12.1 Theory

The Johnson-Cook model [48], [49] is an isotropic, hypoelastic plasticity model. Unlike the previously discussed models, the Johnson-Cook formulation is rate-dependent and as such is often considered for high-rate, finite strain simulations like those for impact. The viscoplastic response is phenomenological in that the form of the model is not derived from any physical mechanisms like other viscoplastic models, e.g. Zerilli-Armstrong [114], Steinberg-Guinan-Lund [96], [97],

BCJ [16], and the MTS model [30], [31] to name a few. Like most other rate-dependent models, the current formulation utilizes an effective plastic strain rate, $\dot{\bar{\varepsilon}}^p$, to capture rate dependence.

As with other hypoelastic plasticity models, an additive decomposition of of the total rate of deformation such that,

$$D_{ij} = D^{\mathrm{e}}_{ij} + D^{\mathrm{p}}_{ij},$$

is used such that an objective stress rate of the form,

$$\overset{\circ}{\sigma}_{ij} = \mathbb{C}_{ijkl} D^{\mathrm{e}}_{kl},$$

with $\mathbb{C}_{ijkl}$ being the fourth-order, isotropic elasticity tensor, may be used.

With respect to the yield behavior, the Johnson-Cook model incorporates both strain rate and temperature, θ, dependence. This leads to a yield function of the form,

$$f\left(\sigma_{ij}, \bar{\varepsilon}^p, \dot{\bar{\varepsilon}}^p, \theta\right) = \phi\left(\sigma_{ij}\right) - \bar{\sigma}\left(\bar{\varepsilon}^p, \dot{\bar{\varepsilon}}^p, \theta\right),$$

in which $\phi\left(\sigma_{ij}\right)$ is the effective stress – the von Mises effective stress is used – and $\bar{\sigma}$ is the isotropic hardening function. Incorporating the temperature and rate dependency, the hardening function is written as,

$$\bar{\sigma}\left(\bar{\varepsilon}^p, \dot{\bar{\varepsilon}}^p, \theta\right) = \left[A + B\left(\bar{\varepsilon}^p\right)^N\right]\left[1 + C\left\langle \ln \dot{\bar{\varepsilon}}^{p*} \right\rangle\right]\left[1 - \theta^{*M}\right] \tag{4.36}$$

where $\bar{\varepsilon}^p$ is the equivalent plastic strain, $\dot{\bar{\varepsilon}}^{p*} = \dot{\bar{\varepsilon}}^p / \dot{\bar{\varepsilon}}_0$ is a dimensionless plastic strain rate, and θ^* is the homologous temperature. The quantities A, B, C, $\dot{\bar{\varepsilon}}_0$, N, and M are material parameters. The Macaulay brackets in (4.36) ensure that $\bar{\sigma}$ is equal to the static flow stress $\bar{\sigma}_{\mathrm{s}} = \left[A + B\left(\bar{\varepsilon}^p\right)^N\right]\left[1 - \theta^{*M}\right]$ when $\dot{\bar{\varepsilon}}^p < \dot{\bar{\varepsilon}}_0$. The homologous temperature is defined as,

$$\theta^* = \frac{\theta - \theta_{\mathrm{ref}}}{\theta_{\mathrm{melt}} - \theta_{\mathrm{ref}}}, \tag{4.37}$$

with θ, θ_{ref}, and θ_{melt} being the current, reference, and melt temperatures. Note, the temperature used internal to the Johnson-Cook model is NOT the standard prescribed "temperature" field. Instead, the material temperature is initialized by a model input as θ_0. By assuming adiabatic thermal conditions, subsequent plastic work raises the material temperature via,

$$\dot{\theta} = \frac{\beta}{\rho C_v} \bar{\sigma} \dot{\bar{\varepsilon}}^p,$$

where ρ is the materials density, C_v is the specific heat, and β ($0 \leq \beta \leq 1$) is the fraction of plastic work that is converted to heat.

The Johnson-Cook model also has a failure criterion. The Johnson-Cook damage model [49] has a failure strain that is given by:

$$\varepsilon^f = \left(D_1 + D_2 \exp\left(D_3 \eta\right)\right)\left(1 + D_4 \ln \dot{\bar{\varepsilon}}^{p*}\right)\left(1 + D_5 \theta^*\right)$$

with D_1, D_2, D_3, D_4, and D_5 being material parameters and η is the triaxiality ($\eta = (1/3)\,\sigma_{kk}/\bar{\sigma}_{vM}$). The damage in the model is accumulated over time using:

$$D = \int_0^t \frac{\dot{\bar{\varepsilon}}^p}{\varepsilon^f} dt. \tag{4.38}$$

When $D = 1$, the material has failed. For the default behavior of the Johnson-Cook model, the fracture behavior is not active.

4.12.2 Implementation

The implementation of the Johnson-Cook model requires the effective strain rate to be used for calculating the rate effects on yield. This is done through a predictor-corrector return mapping algorithm. In what follows the temperature dependence is not included; this will be addressed later.

The initial response is assumed to be elastic and a trial stress state is calculated

$$T_{ij}^{\text{tr}} = T_{ij}^n + \mathbb{C}_{ijkl}\,\Delta t d_{kl}$$

Since the plastic response is independent of pressure we can use the deviatoric stress

$$s_{ij} = T_{ij} - \frac{1}{3}\delta_{ij} T_{kk}$$
$$s_{ij}^{\text{tr}} = s_{ij}^n + 2\mu\,\Delta t d'_{ij},$$

with d'_{ij} being the total deviatoric rate of deformation – $d'_{ij} = d_{ij} - (1/3)\,\delta_{ij} d_{kk}$.

If this gives a von Mises stress that is greater then the effective stress, i.e.

$$\phi^{\text{tr}} = \sqrt{\frac{3}{2} s_{ij}^{\text{tr}} s_{ij}^{\text{tr}}} > A + B\left(\bar{\varepsilon}^{p(n)}\right)^N,$$

then plastic deformation occurs and we solve the following nonlinear equation for $\dot{\bar{\varepsilon}}^p$,

$$\left[A + B\left(\bar{\varepsilon}_{p(n)} + \Delta t \dot{\bar{\varepsilon}}^p\right)^N\right]\left[1 + C\ln\left(\max\left(1, \dot{\bar{\varepsilon}}^p/\dot{\bar{\varepsilon}}_0\right)\right)\right] = \phi^{\text{tr}} - 3\mu\Delta t\dot{\bar{\varepsilon}}^p. \tag{4.39}$$

This simple equation comes from the radial return algorithm

$$s_{ij}^{n+1} = s_{ij}^{\text{tr}} - 3\mu\,\Delta t\,\dot{\bar{\varepsilon}}^p \frac{s_{ij}^{\text{tr}}}{\phi^{\text{tr}}} \quad \rightarrow \quad s_{ij}^{n+1} = \left(\phi^{\text{tr}} - 3\mu\,\Delta t\,\dot{\bar{\varepsilon}}^p\right)\frac{s_{ij}^{\text{tr}}}{\phi^{\text{tr}}}$$

Taking the inner product of both sides gives (4.39).

4.12.3 Verification

The Johnson-Cook model is verified through a series of uniaxial stress and pure shear tests. Given the emphasis on the strain-rate and temperature dependent nature of the model a series of these tests are performed at different loading conditions. The material properties and model parameters used for these tests are given in Table 4.14 and come from the work of Corona and Orient [26]. Note, in this case a modified reference plastic strain rate is used ($\dot{\bar{\varepsilon}}_0 = 1 \times 10^{-4}\text{s}^{-1}$) as the one reported in [26] was selected based on calibration conditions. Here the value is selected to better investigate and highlight strain rate dependency.

Table 4.14 The material properties and model parameters of the Johnson-Cook model used for verification testing

E	71.7 GPa	ν	0.33
A	217 MPa	B	405 MPa
C	0.0075	$\dot{\bar{\varepsilon}}_0$	1×10^{-4} s^{-1}
θ_{ref}	293 K	θ_{melt}	750 K
N	0.41	M	1.1
ρ	2810 kg/m^3	C_v	960 J/(kg-K)
D_1	0.015	D_2	0.24
D_3	-1.5	D_4	-0.039
D_5	8.0		

4.12.3.1 Uniaxial Stress

To determine a (semi)-analytical expression of the Johnson-Cook model, the equivalency of plastic work for uniaxial loading is recalled such that,

$$\bar{\sigma}\dot{\bar{\varepsilon}}^p = \sigma\left(\dot{\varepsilon} - \dot{\varepsilon}^{\text{e}}\right), \tag{4.40}$$

with σ, $\dot{\varepsilon}$, and $\dot{\varepsilon}^{\text{e}}$ being the uniaxial stress, total strain rate, and elastic strain rate, respectively. Assuming $\dot{\bar{\varepsilon}}^p \geq \dot{\bar{\varepsilon}}_0$, and noting that $\dot{\varepsilon}^p = \dot{\varepsilon} - \dot{\varepsilon}^{\text{e}}$, the expression for the flow stress (4.36), the definition of the homologous temperature (4.37), and the dimensionless strain rate, the plastic work expression (4.40) may be rearranged as

$$\dot{\bar{\varepsilon}}^p = \dot{\bar{\varepsilon}}_0 \exp\left[\frac{\sigma}{C\left[A + B\left(\bar{\varepsilon}^p\right)^N\right]\left[1 - \theta^{*M}\right]} - \frac{1}{C}\right]. \tag{4.41}$$

Given the implicit nature (in terms of effective plastic strain) of (4.41), a semi-analytical approach is used to evaluate the Johnson-Cook model. Specifically, a simple forward Euler integration scheme is adopted to solve (4.41) and then update the remaining state variables. Using such an approach, Fig. 4.33 presents the stress-strain and corresponding damage evolution of the Johnson-Cook determined at three strain rates. A constant total logarithmic strain rate is applied by utilizing an applied displacement of the form,

$$u_i\left(t\right) = \left(\text{e}^{\omega t} - 1\right)\delta_{i1},$$

where ω is the considered strain rate. Here rates corresponding to a slow quasistatic ($\omega = 1 \times 10^{-3}\text{s}^{-1}$), medium ($\omega = 1\text{s}^{-1}$), and high rate ($\omega = 1 \times 10^{3}\text{s}^{-1}$) loading are considered to explore a variety of regimes. Temperature effects are not addressed in Fig. 4.33 ($\beta = 0$) to first investigate the purely mechanical response. The damage evolution is evaluated by simply integrating expression (4.38) and noting that for a uniaxial loading $\eta = 1/3$. In this case, as the constitutive behavior is being probed the material does not degrade when $D \geq 1$.

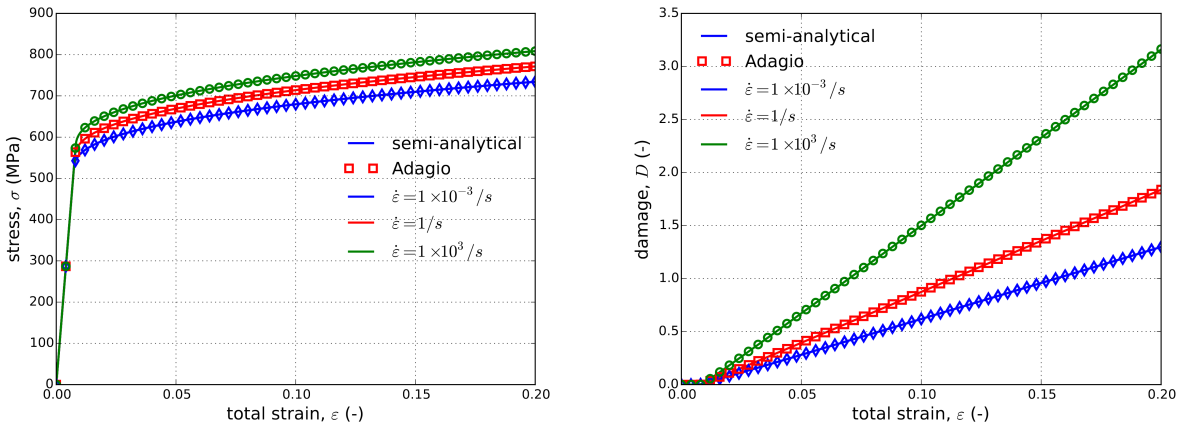

(a) Stress-strain **(b) Damage**

Fig. 4.33 Semi-analytical and numerical (a) stress-strain and (b) damage evolutions of the Johnson-Cook model subjected to a uniaxial loading at three different applied strain rates. In these results, $\beta = 0$.

From the results of Fig. 4.33 clear agreement is observed between the numerical and semi-analytical response verifying the model behavior in a variety of conditions. Next, to explore the thermomechanical coupling, three different plastic work conversion ratios ($\beta = 0.00,\ 0.50$ and 1.0) are considered for the medium strain rate ($\omega = 1\text{s}^{-1}$). The stress, damage, and temperature evolutions are all presented in Fig. 4.34 as a function of axial strains.

From Fig. 4.34 the influence of the thermomechanical coupling may be clearly observed. For instance, a roughly 50 K increase in material temperature over the loading range may be seen in the $\beta = 1$ case leading to a roughly 25% decrease in the damage metric and approximately 10% drop in final stress. Additionally, clear agreement between the semi-analytical and numerical responses providing additional verification of the coupled capabilities of the model.

4.12.3.2 Pure Shear

For the pure shear case, a loading like that described in *Appendix A* is utilized. Specifically, displacements producing a deformation gradient of,

$$F_{ij} = \frac{1}{2}\left(\lambda + \lambda^{-1}\right)\left(\delta_{i1}\delta_{j1} + \delta_{i2}\delta_{j2}\right) + \frac{1}{2}\left(\lambda - \lambda^{-1}\right)\left(\delta_{i1}\delta_{j2} + \delta_{i2}\delta_{j1}\right) + \delta_{i3}\delta_{j3},$$

are considered with $\lambda = \lambda(t) = \text{e}^{\omega t}$. This loading leads to a logarithmic shear strain rate of $\dot{\varepsilon}_{12} = \omega$ that is constant in time enabling the study of strain rate effects.

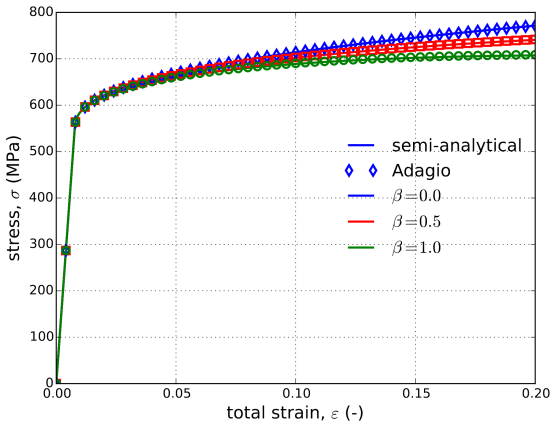

(a) Stress-strain

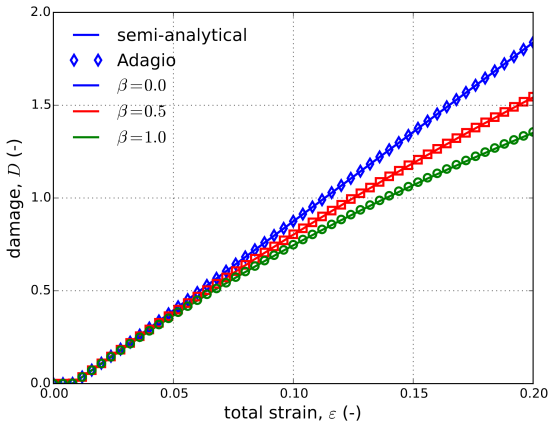

(b) Damage

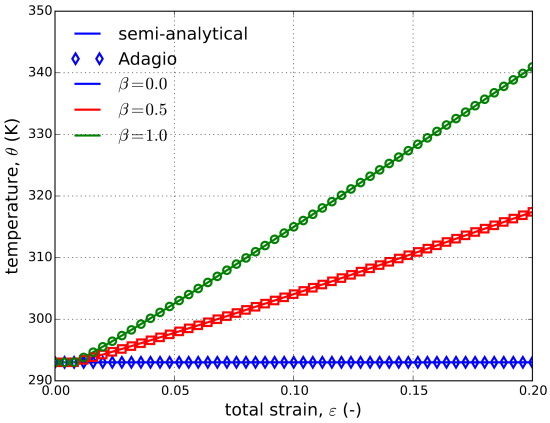

(c) Temperature

Fig. 4.34 Semi-analytical and numerical (a) stress-strain (b) damage and (c) temperature evolutions of the Johnson-Cook model subjected to a uniaxial loading with three different plastic work conversion ratios, β. The strain rate for all three cases is $\dot{\varepsilon} = 1\mathrm{s}^{-1}$.

In the shear stress case, the plastic work equivalency is written as,

$$\bar{\sigma}\dot{\bar{\varepsilon}}^p = 2\sigma_{12}\dot{\varepsilon}^p_{12}.$$

Like the uniaxial stress case, the definition of the effective stress may be used with the fact that $\dot{\varepsilon}^p_{12} = \frac{\sqrt{3}}{2}\dot{\bar{\varepsilon}}^p$ to find the following form of the effective plastic strain rate when $\dot{\bar{\varepsilon}}^p > \dot{\bar{\varepsilon}}_0$,

$$\dot{\bar{\varepsilon}}^p = \dot{\bar{\varepsilon}}_0 \exp\left[\frac{\sqrt{3}\sigma_{12}}{C\left[A + B\left(\bar{\varepsilon}^p\right)^N\right]\left[1 - \theta^{*M}\right]} - \frac{1}{C}\right].$$

A simple forward Euler scheme is then used to integrate the model at three different strain rates – $\omega = .001\text{s}^{-1}$, 1s^{-1} and 1000s^{-1}. The stress-strain and damage evolution responses of these cases are presented in Fig. 4.35 for the purely mechanical case ($\beta = 0$). With respect to the damage evolution, it is noted that for pure shear responses $\eta = 0$.

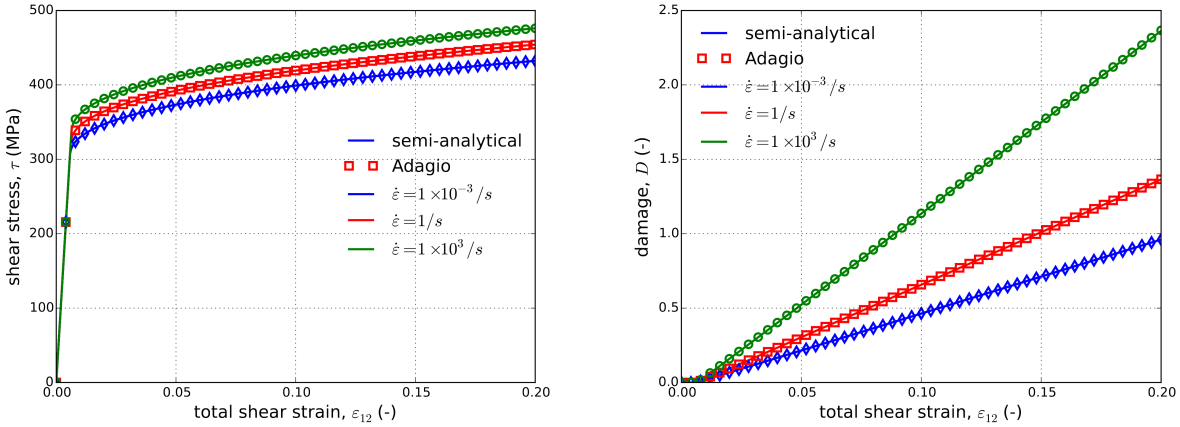

(a) Stress-strain **(b) Damage**

Fig. 4.35 Semi-analytical and numerical (a) stress-strain and (b) damage evolutions of the Johnson-Cook model subjected to a pure shear loading at three different applied strain rates. In these results, $\beta = 0$.

The effect of plastic work is considered for $\omega = 1\text{s}^{-1}$ in Fig. 4.36. Similar influences like those reported in the uniaxial stress case are observed. A larger increase in temperature through plastic loading is noted however. Regardless in both the results of Figures Fig. 4.35 and Fig. 4.36 clear agreement between numerical and semi-analytical is observed further verifying the current implementation of the Johnson-Cook model.

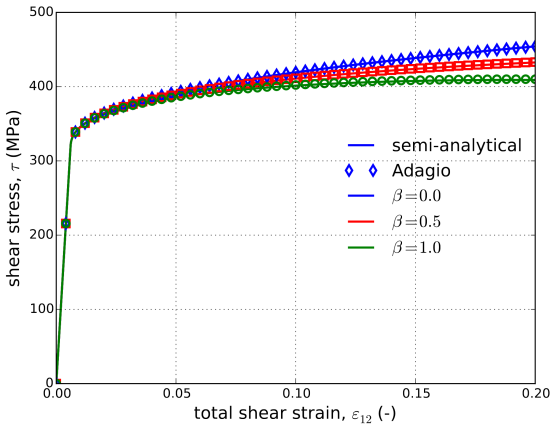

(a) Stress-strain

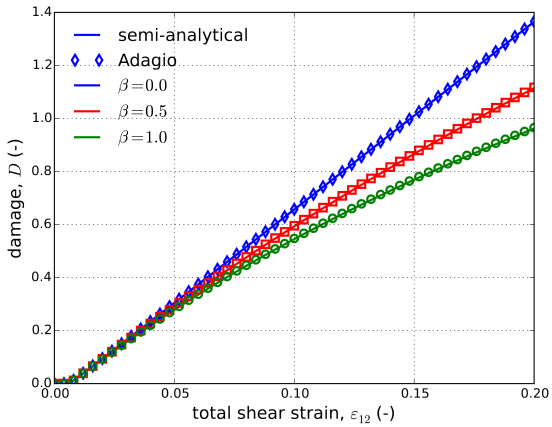

(b) Damage

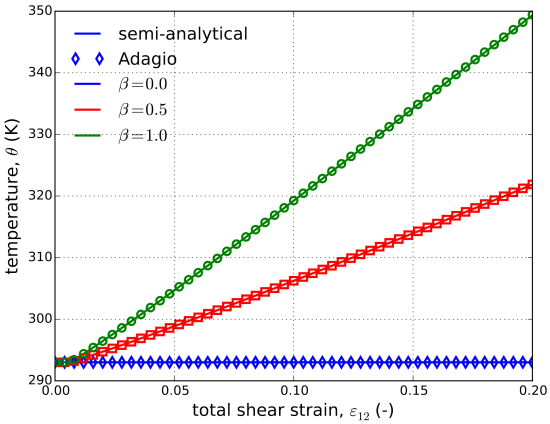

(c) Temperature

Fig. 4.36 Semi-analytical and numerical (a) stress-strain (b) damage and (c) temperature evolutions of the Johnson-Cook model subjected to a pure shear loading with three different plastic work conversion ratios, β. The strain rate for all three cases is $\dot{\varepsilon} = 1\mathrm{s}^{-1}$.

4.12.4 User Guide

```
BEGIN PARAMETERS FOR MODEL JOHNSON_COOK
  #
  # Elastic constants
  #
  YOUNGS MODULUS = <real>
  POISSONS RATIO = <real>
  SHEAR MODULUS  = <real>
  BULK MODULUS   = <real>
  LAMBDA         = <real>
  TWO MU         = <real>
  #
  # Yield surface parameters
  #
  YIELD STRESS       = <real>
  HARDENING CONSTANT = <real>
  HARDENING EXPONENT = <real>
  RATE CONSTANT      = <real>
  REFERENCE RATE     = <real> (0.001)
  EDOT_REF           = <real> (0.0)
  #
  # Failure strain parameters
  #
  D1 = <real> (0.0)
  D2 = <real> (0.0)
  D3 = <real> (0.0)
  D4 = <real> (0.0)
  D5 = <real> (0.0)
  #
  # Temperature softening commands
  #
  RHOCV                 = <real>
  BETA                  = <real>
  THERMAL EXPONENT      = <real>
  REFERENCE TEMPERATURE = <real>
  MELT TEMPERATURE      = <real>
  INITIAL TEMPERATURE   = <real>
  #
  FORMULATION = <int> (0)
  #
END [PARAMETERS FOR MODEL JOHNSON_COOK]
```

In the command blocks that define the Johnson-Cook model:

- The `YIELD STRESS` defines the stress for onset of yield and the plasticity.
- The `HARDENING CONSTANT` command line defines B.

- The `HARDENING EXPONENT` command line defines N
- The `RHOCV` command line defines ρC_v which is the product of material density and specific heat.
- The material initial temperature is defined by the `INITIAL TEMPERATURE` command line. Note, the Johnson Cook material model temperature is NOT linked to the standard model "temperature" field that is set from `BEGIN PRESCRIBED TEMPERATURE` command blocks.
- The thermal exponent M is defined with the `THERMAL EXPONENT` command line. This exponent must be greater than zero.
- The reference temperature θ_{ref} is defined with the `REFERENCE TEMPERATURE` command line.
- The melt temperature θ_{melt} is defined with the `MELT TEMPERATURE` command line.
- The reference strain rate, $\dot{\varepsilon}_0$, is defined with the `REFERENCE RATE` command line. The default is 0.001 s^{-1}.
- The fraction of plastic work that is converted to heat, β, is defined with the `BETA` command line. The default is 0.95.
- The fracture coefficient D_1 is defined with the `D1` command line. The default is 0.0.
- The fracture coefficient D_2 is defined with the `D2` command line. The default is 0.0.
- The fracture coefficient D_3 is defined with the `D3` command line. The default is 0.0.
- The fracture coefficient D_4 is defined with the `D4` command line. The default is 0.0.
- The fracture coefficient D_5 is defined with the `D5` command line. The default is 0.0.
- The failure model – and corresponding coefficients – are only valid for solid (3D) elements. Specifying the values for 2D elements (e.g. shell) will result in an error as the damage model is not implemented. A possible alternative is the J_2 Plasticity Model specified with Johnson-Cook hardening and failure.
- `FORMULATION` controls the strain rate source term. A `FORMULATION` of `0` is the default which is to use the total strain rate. A `FORMULATION` of `1` means use the plastic strain rate. The plastic strain rate is monotonic and changes a much lower frequency than the total strain rate, thus use of the plastic strain rate may be more stable.

4.12.4.1 Warnings and Usage Guidelines

Warning: Strongly rate dependent models may fare poorly in implicit quasistatic solution. In implicit the rate term used to evaluate the current load step is the rate seen by the model in the previous load step. Potentially this can cause the solution to jump back and forth between a high right and low rate equilibrium state from step to step.

Output variables available for this model are listed in Table 4.15.

Table 4.15 State Variables for JOHNSON COOK Model

Name	Description
RADIUS	radius of yield surface
EQPS	equivalent plastic strain
THETA	temperature
EQDOT	effective total strain rate
ITER	
EFAIL	failure strain, ε^f
DAMAGE	damage, D
YIELD_STRESS	yield stress

4.13 J_2 Plasticity Model

4.13.1 Theory

The J_2 plasticity model is a generic implementation of a von Mises yield surface with kinematic and isotropic hardening features. Unlike other models (*e.g.* Elastic-Plastic, Elastic-Plastic Power Law) more flexible, general hardening forms are implemented enabling different isotropic hardening descriptions and some rate and/or temperature dependence.

As is common to other plasticity models in LAMÉ, the J_2 plasticity model uses a hypoelastic formulation. As such, the total rate of deformation is additively decomposed into an elastic and plastic part such that

$$D_{ij} = D^{\mathrm{e}}_{ij} + D^{\mathrm{p}}_{ij}.$$

The objective stress rate, depending only on the elastic deformation, may then be written as,

$$\overset{\circ}{\sigma}_{ij} = \mathbb{C}_{ijkl} D^{\mathrm{e}}_{kl},$$

where $\mathbb{C}_{ijkl}$ is the fourth-order elastic, isotropic stiffness tensor.

The yield surface for the J_2 plasticity model, f, may be written,

$$f\left(\sigma_{ij}, \alpha_{ij}, \bar{\varepsilon}^p, \dot{\bar{\varepsilon}}^p, \theta\right) = \phi\left(\sigma_{ij}, \alpha_{ij}\right) - \bar{\sigma}\left(\bar{\varepsilon}^p, \dot{\bar{\varepsilon}}^p, \theta\right), \tag{4.42}$$

in which α_{ij}, $\bar{\varepsilon}^p$, $\dot{\bar{\varepsilon}}^p$, and θ are the kinematic backstress, equivalent plastic strain, equivalent plastic strain rate, and absolute temperature, respectively, while ϕ and $\bar{\sigma}$ are the effective stress and a generic form of the flow stress. Broadly speaking, the effective stress describes the shape of the yield surface and kinematic effects while the flow stress gives the size of the current yield surface. It should also be noted that in writing the yield surface in this way, the dependence on the state variables is split between the effective stress and flow stress functions.

For J_2 plasticity, the effective stress is given as,

$$\phi^2\left(\sigma_{ij}, \alpha_{ij}\right) = \frac{3}{2}\left(s_{ij} - \alpha_{ij}\right)\left(s_{ij} - \alpha_{ij}\right),$$

with s_{ij} being the deviatoric stress defined as $s_{ij} = \sigma_{ij} - (1/3)\sigma_{kk}\delta_{ij}$. For the flow stress, a general representation of the form,

$$\bar{\sigma}\left(\bar{\varepsilon}^p, \dot{\bar{\varepsilon}}^p, \theta\right) = \sigma_y \hat{\sigma}_{\mathrm{y}}\left(\dot{\bar{\varepsilon}}^p\right) \breve{\sigma}_{\mathrm{y}}\left(\theta\right) + K\left(\bar{\varepsilon}^p\right) \hat{\sigma}_{\mathrm{h}}\left(\dot{\bar{\varepsilon}}^p\right) \breve{\sigma}_{\mathrm{h}}\left(\theta\right),$$

is allowed. In this fashion, the effects of rate ($\hat{\sigma}_{\mathrm{y,h}}$) and temperature ($\breve{\sigma}_{\mathrm{y,h}}$) dependence on yield ($\sigma_y$) and isotropic hardening ($K\left(\bar{\varepsilon}^p\right)$) are decomposed. Separate temperature and rate dependencies may be be specified for yield (subscript y) and hardening (h). This assumption is an extension of the multiplicative decomposition of the Johnson-Cook model [48], [49]. It should be noted that not all effects need to be included and the default parameterization of the hardening classes is such that the response is rate and temperature independent. The following section on plastic hardening will go into more detail on possible choices for functional representations.

An associated flow rule is utilized such that the plastic rate of deformation is normal to the yield surface and is given by,

$$D^{\mathrm{p}}_{ij} = \dot{\gamma}\frac{\partial \phi}{\partial \sigma_{ij}} = \dot{\gamma}\frac{3}{2\phi}s_{ij},$$

where $\dot{\gamma}$ is the consistency multiplier enforcing $f = 0$ during plastic deformation. Given the form of f, it can also be shown that $\dot{\gamma} = \dot{\bar{\varepsilon}}^p$.

Additional discussion on options for failure models and adiabatic heating may be found in [61], [62] and [60], respectively.

4.13.1.1 Plastic Hardening

Plastic hardening refers to increases in the flow stress, $\bar{\sigma}$, with plastic deformation. As such, hardening is described via a functional relationship between the flow stress and isotropic hardening variable (effective plastic strain), $\bar{\sigma}\left(\bar{\varepsilon}^p\right)$. Over the course of nearly a century of work in metal plasticity, a variety of relationships have been proposed to describe the interactions

associated with different physical interpretations, deformation mechanisms, and materials. To enable the utilization of the same plasticity models for different material systems, a modular implementation of plastic hardening has been adopted such that the analyst may select different hardening models from the input deck thereby avoiding any code changes or user subroutines. In this section, additional details are given for the different models to enable the user to select the appropriate choice of model. Note, the models being discussed here are only for *isotropic* hardening in which the yield surface expands. *Kinematic* hardening in which the yield surface translates in stress-space with deformation and *distortional* hardening where the shape of the yield surface changes shape with deformation are not treated. For a larger discussion of the phenomenology and history of different hardening types, the reader is referred to [42], [57], [64].

Given the ubiquitous nature of these hardening laws in computational plasticity, some (if not most) of this material may be found elsewhere in this manual. Nonetheless, the discussion is repeated here for the convenience of the reader.

Linear

Linear hardening is conceptually the simplest model available in LAMÉ. As the name implies, a linear relationship is assumed between the hardening variable, $\bar{\varepsilon}^p$, and flow stress. The hardening modulus, H', is a constant giving the rate of change of flow stress with plastic flow. The flow stress expression may therefore be written,

$$\bar{\sigma} = \sigma_y + H'\bar{\varepsilon}^p.$$

The simplicity of the model is its main feature as the constant slope,

$$\frac{d\bar{\sigma}}{d\bar{\varepsilon}^p} = H',$$

makes the model attractive for analytical models and cheap for computational implementations (*e.g.* radial return algorithms require only a single correction step). Unfortunately, the simplicity of the representation also means that it has limited predictive capabilities and can lead to overly stiff responses.

Power Law

Another common expression for isotropic hardening is the power-law hardening model. Due to its prevalence, a dedicated `ELASTIC-PLASTIC POWER LAW HARDENING` model may be found in LAMÉ (see Section 4.8.1). This expression is given as,

$$\bar{\sigma} = \sigma_y + A < \bar{\varepsilon}^p - \varepsilon_L >^n,$$

in which $< \cdot >$ are Macaulay brackets, ε_L is the Luders strain, A is a fitting constant, and n is an exponent typically taken such that $0 < n \leq 1$. The Luders strain is a positive, constant strain value

(defaulted to zero) giving an initially perfectly plastic response in the plastic deformation domain (see Fig. 4.20). The derivative is then simply,

$$\frac{d\bar{\sigma}}{d\bar{\varepsilon}^p} = nA < \bar{\varepsilon}^p - \varepsilon_L >^{(n-1)} .$$

Note, one difficulty in such an implementation is that when the effective equivalent plastic strain is zero, numerical difficulties may arise in evaluating the derivative and necessitate special treatment of the case.

Voce

The Voce hardening model (sometimes referred to as a saturation model) uses a decaying exponential function of the equivalent plastic strain such that the hardening eventually saturates to a specified value (thus the name). Such a relationship has been observed in some structural metals giving rise to the popularity of the model. The hardening response is given as,

$$\bar{\sigma} = \sigma_y + A\left(1 - \exp\left(-n\bar{\varepsilon}^p\right)\right),$$

in which A is a fitting constant and n is a fitting exponent controlling how quickly the hardening saturates. Importantly, the derivative is written as,

$$\frac{d\bar{\sigma}}{d\bar{\varepsilon}^p} = nA\exp\left(-n\bar{\varepsilon}^p\right),$$

and is well defined everywhere giving the selected form an advantage over the aforementioned power law model.

Johnson-Cook

The Johnson-Cook hardening model is a variant of the classical Johnson-Cook [48], [49] expression. In this instance, the temperature-dependence is neglected to focus on the *rate-dependent* capabilities while allowing for arbitrary isotropic hardening forms via the use of a user-defined hardening function. With these assumptions, the flow stress may be written as,

$$\bar{\sigma} = \tilde{\sigma}_y\left(\bar{\varepsilon}^p\right)\left[1 + C\left\langle \ln\left(\frac{\dot{\bar{\varepsilon}}^p}{\dot{\varepsilon}_0}\right)\right\rangle\right],$$

in which $\tilde{\sigma}_y\left(\bar{\varepsilon}^p\right)$ is the user-specified rate-independent hardening function, C is a fitting constant and $\dot{\varepsilon}_0$ is a reference strain rate. The Macaulay brackets ensure the material behaves in a rate independent fashion when $\dot{\bar{\varepsilon}}^p < \dot{\varepsilon}_0$.

Power Law Breakdown

Like the Johnson-Cook formulation, the power-law breakdown model is also rate-dependent. Again, a multiplicative decomposition is assumed between isotropic hardening and the corresponding rate-dependence dependent. In this case, however, the functional form is derived from the analysis of Frost and Ashby [33] in which power-law relationships like those of the Johnson-Cook model cease to appropriately capture the physical response. The form used here is similar to the expression used by Brown and Bammann [16] and is written as,

$$\bar{\sigma} = \tilde{\sigma}_y\left(\bar{\varepsilon}^p\right)\left[1 + \operatorname{asinh}\left(\left(\frac{\dot{\bar{\varepsilon}}^p}{g}\right)^{(1/m)}\right)\right],$$

with $\tilde{\sigma}_y\left(\bar{\varepsilon}^p\right)$ being the user supplied rate independent expression, g is a model parameter related to the activation energy required to transition from climb to glide-controlled deformation, and m dictates the strength of the dependence.

4.13.1.2 Flow Stress

Unlike the previously described models, the flow-stress hardening method is less a specific physical representation and more a generalization of hardening behaviors to allow greater flexibility in separately describing isotropic hardening, rate-dependence, and temperature dependence. As such, the generic flow-stress definition of

$$\bar{\sigma}\left(\bar{\varepsilon}^p, \dot{\bar{\varepsilon}}^p, \theta\right) = \tilde{\sigma}_y\left(\bar{\varepsilon}^p\right)\hat{\sigma}\left(\dot{\bar{\varepsilon}}^p\right)\breve{\sigma}\left(\theta\right),$$

is used in which $\hat{\sigma}$ and $\breve{\sigma}$ are rate and temperature multipliers, respectively, that by default are unity (such that the response is rate and temperature independent). The isotropic hardening component, $\tilde{\sigma}_y$, is specified as,

$$\tilde{\sigma}_y = \sigma_y + K\left(\bar{\varepsilon}^p\right),$$

with σ_y being the constant yield stress and K is the isotropic hardening that is initially zero and a function of the equivalent plastic strain. A multiplicative decomposition such as this mirrors the general structure used by Johnson and Cook [48], [49] although greater flexibility is allowed in terms of the specific form of the rate and temperature multipliers.

Given the aforementioned defaults for rate and temperature dependence, the corresponding multipliers need not be specified. A representation for the isotropic hardening, however, *must* be specified and can be defined via linear, power-law, Voce, or user-defined representations. For the user-defined case, an *isotropic* hardening function is required and it must be highlighted that the interpretation differs from the general user-defined hardening model. *In this case, as the specified function represents the isotropic hardening, it should start from zero – not yield.*

Although the flow-stress hardening model defaults to rate and temperature independent, a multiplier may be defined for either (or both) of the terms. For rate-dependence, either the

previously discussed Johnson-Cook or power-law breakdown models or a user-defined multiplier may be used. For the user-defined capability, the multiplier should be input as a strictly positive function of the equivalent plastic strain rate with a value of one in the rate-independent limit.

In terms of temperature dependence, the multiplier may be specified given a Johnson-Cook dependency [48], [49],

$$\breve{\sigma}\left(\theta\right) = 1 - \left(\frac{\theta - \theta_{\text{ref}}}{\theta_{\text{melt}} - \theta_{\text{ref}}}\right)^{M},$$

with θ_{ref}, θ_{melt} and M being the reference temperature, melting temperature, and temperature exponent. The temperature multiplier may also be specified via a user defined function.

4.13.1.3 Decoupled Flow Stress

Like the flow-stress hardening method, the decoupled flow-stress hardening implementation is a generalization of the hardening behaviors to allow greater flexibility. In differentiating the two, for the decoupled model the rate and temperature dependence may be separately specified for the yield and hardening portions of the flow stress. As such, the generic flow-stress definition of

$$\bar{\sigma}\left(\bar{\varepsilon}^{p}, \dot{\bar{\varepsilon}}^{p}, \theta\right) = \sigma_{y}\hat{\sigma}_{\text{y}}\left(\dot{\bar{\varepsilon}}^{p}\right)\breve{\sigma}_{\text{y}}\left(\theta\right) + K\left(\bar{\varepsilon}^{p}\right)\hat{\sigma}_{\text{h}}\left(\dot{\bar{\varepsilon}}^{p}\right)\breve{\sigma}_{\text{h}}\left(\theta\right),$$

is used in which $\hat{\sigma}$ and $\breve{\sigma}$ are rate and temperature multipliers, respectively, that by default are unity (such that the response is rate and temperature independent) with subscripts y and h denoting functions associated with yield and hardening. The isotropic hardening is described by $K\left(\bar{\varepsilon}^{p}\right)$ and σ_{y} is the constant initial yield stress. It may also be seen that if the yield and hardening dependencies are the same ($\hat{\sigma}_{\text{y}} = \hat{\sigma}_{\text{h}}$ and $\breve{\sigma}_{\text{y}} = \breve{\sigma}_{\text{h}}$) the decoupled flow stress model reduces to that of the flow stress case and mirrors the general structure of the Johnson-Cook model [48], [49].

Given the aforementioned defaults for rate and temperature dependence, the corresponding multipliers need not be specified. A representation for the isotropic hardening, however, *must* be specified and can be defined via linear, power-law, Voce, or user-defined representations. For the user-defined case, an *isotropic* hardening function should be used and it must be highlighted that the interpretation differs from the general user-defined hardening model. *In this case, as the specified function represents the isotropic hardening, it should start from zero – not yield.*

Although the decoupled flow-stress hardening model defaults to rate and temperature independent, a multiplier may be defined for any of the terms. For rate-dependence, either the previously discussed Johnson-Cook or power-law breakdown models or a user-defined multiplier may be used. For the user-defined capability, the multiplier should be input as a strictly positive function of the equivalent plastic strain rate with a value of one in the rate-independent limit.

In terms of temperature dependence, the multiplier may be specified given a Johnson-Cook dependency [48], [49],

$$\breve{\sigma}\left(\theta\right) = 1 - \left(\frac{\theta - \theta_{\text{ref}}}{\theta_{\text{melt}} - \theta_{\text{ref}}}\right)^{M},$$

where θ_{ref}, θ_{melt}, and M are the reference temperature, melting temperature, and temperature exponent. A temperature multiplier may also be specified via a user defined function.

4.13.2 Implementation

The J_2 plasticity model is implemented using a radial return predictor-corrector algorithm. First, an elastic trial stress state is calculated. This is done by assuming that the rate of deformation is completely elastic,

$$T_{ij}^{tr} = T_{ij}^{n} + \Delta t \left(\lambda \delta_{ij} d_{kk} + 2\mu d_{ij} \right).$$

The trial stress state is decomposed into a pressure and a deviatoric stress

$$p^{tr} = \frac{1}{3} T_{kk}^{tr} \quad ; \quad s_{ij}^{tr} = T_{ij}^{tr} - p^{tr} \delta_{ij}.$$

A trial yield function value, f^{tr}, is calculated by assuming purely thermoelastic deformations ($\dot{\bar{\varepsilon}}^{p} = 0, \bar{\varepsilon}_{tr}^{p} = \bar{\varepsilon}_{n}^{p}$) such that,

$$f^{tr}\left(s_{ij}^{tr}, \alpha_{ij}^{n}, \bar{\varepsilon}_{n}^{p}, \dot{\bar{\varepsilon}}_{tr}^{p} = 0, \theta_{n+1} \right) = \phi^{tr}\left(s_{ij}^{tr}, \alpha_{ij}^{n} \right) - \bar{\sigma}\left(\bar{\varepsilon}_{n}^{p}, \dot{\bar{\varepsilon}}_{tr}^{p} = 0, \theta_{n+1} \right).$$

If $f^{tr} \leq 0$ then the strain rate is elastic and the stress update is finished. If $f^{tr} > 0$ then plastic deformation has occurred and a radial return algorithm determines the extent of plastic deformation.

The normal to the yield surface is assumed to lie in the direction of the trial stress state. This gives the following expression for N_{ij},

$$N_{ij} = \frac{\left(s_{ij}^{tr} - \alpha_{ij}^{n} \right)}{\| \left(s_{ij}^{tr} - \alpha_{ij}^{n} \right) \|}.$$

Using a backward Euler algorithm, the final deviatoric stress state is

$$s_{ij}^{n+1} = s_{ij}^{tr} - \Delta t 2\mu d_{ij}^{\text{p}},$$

where the plastic strain increment is

$$\Delta d_{ij}^{\text{p}} = \sqrt{\frac{3}{2}} \Delta \bar{\varepsilon}^{p} N_{ij}.$$

The equation for the change in the equivalent plastic strain over the load step is found as the solution to

$$3\mu \Delta \bar{\varepsilon}^{p} + \bar{\sigma}\left(\bar{\varepsilon}_{n} + \Delta \bar{\varepsilon}^{p}, \Delta t, \theta_{n+1} \right) - \phi^{tr} + f_{n} = 0,$$

in which the plastic strain rate is approximated as, $\dot{\bar{\varepsilon}}^{p} = \Delta \bar{\varepsilon}^{p} / \Delta t$.

4.13.3 Verification

The J_2 plasticity model is verified through a series of uniaxial stress and pure shear tests considering a variety of hardening models. Specifically, the boundary value problems of *Appendix A* are used. Throughout these tests, the elastic properties are maintained as $E = 70$ GPa and $\nu = 0.25$.

Additional verification exercises for the various failure models and adiabatic heating capabilities may be found in [61], [62] and [60], respectively.

4.13.3.1 Plastic Hardening

For the verification of the J_2 model, a series of tests using different rate *independent*, rate *dependent*, and combinations of these hardening models are investigated for both uniaxial stress and pure shear. For these cases, by imposing a constant plastic strain rate as described in *Appendix A* the model response may be analytically determined as a function of time. For the rate *independent* cases, a constant rate of $\dot{\bar{\varepsilon}}^p = 1 \times 10^{-4}\text{s}^{-1}$ is used to replicate quasi-static conditions.

The various rate *dependent* and rate *independent* hardening coefficients are found in Table 4.16 while the remaining model parameters are unchanged from the previous verification exercises. For the current verification exercises, the rate *independent* hardening models (linear, Voce, and power-law) and rate *dependent* forms (Johnson-Cook, power-law breakdown) are examined.

Table 4.16 The model parameters for the hardening verification tests used with the J_2 plasticity model during verification tests. Parameters for the rate *independent* hardening functions, $\tilde{\sigma}_y$, are also given and denoted with a $\tilde{}$ while the subscript refers to the functional form.

C	0.1	$\dot{\varepsilon}_0$	1×10^{-4} s^{-1}
g	0.21 s^{-1}	m	16.4
$\tilde{H}_{\text{Linear}}$	200 MPa		
$\tilde{A}_{\text{PL}}$	400 MPa	$\tilde{n}_{\text{PL}}$	0.25
$\tilde{A}_{\text{Voce}}$	200 MPa	$\tilde{n}_{\text{Voce}}$	20
σ_y	200 MPa		

Rate-Independent

First, the ability of the built-in rate *independent* hardening models is assessed in both uniaxial stress and pure shear. Specifically, the linear, power-law, and Voce hardening models are considered and the results determined analytically and numerically via Sierra are presented in Fig. 4.37. As expected, excellent agreement is noted between the two sets of results. Importantly, as the responses of all three rate *independent* isotropic hardening models are presented in the same figures, the corresponding behaviors can be seen. Note, the given parameterizations are not selected for any form of equivalency. Nonetheless, the linear post-yielding behavior of the linear

model can be seen and compared to the non-linear responses of the Voce and power-law implementations. The critical difference between the latter two being that the Voce response saturates at a stress level while the power-law continues to grow.

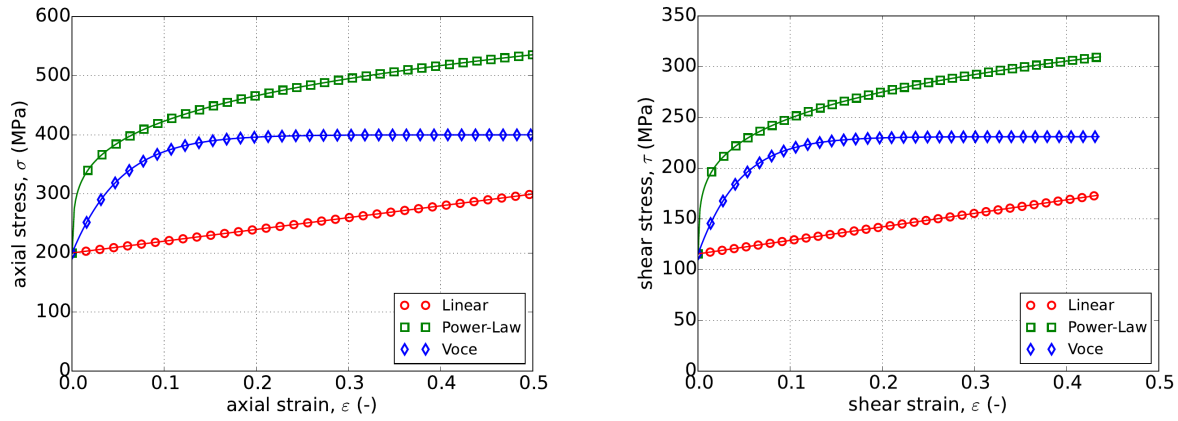

(a) Uniaxial Stress **(b) Pure Shear**

Fig. 4.37 Analytical and numerical (Sierra) (a) uniaxial stress-strain and (b) pure shear responses of the J_2 plasticity model with linear, power-law, and Voce rate *independent* isotropic hardening. Solid lines are analytical while open symbols are numerical.

Rate-Dependent

With the performance of the model under rate *independent* conditions established, next the capabilities of the rate *dependent* (Johnson-Cook and power-law breakdown) formulations are considered. Note, the flow-stress and decoupled flow-stress models that incorporate more flexible descriptions of isotropic hardening and rate and temperature dependence are left to later sections. With the current Johnson-Cook and power-law breakdown models, user-defined analytic functions are used for each of the specified rate *independent* hardening functions.

The uniaxial stress-strain responses are interrogated for the Johnson-Cook and power-law breakdown rate *dependent* hardening models considering linear, power-law, and Voce isotropic hardening in Fig. 4.38. Five decades of plastic strain rates $\dot{\bar{\varepsilon}}^p = 1 \times 10^{-3} \rightarrow 1 \times 10^{1} \mathrm{s}^{-1}$ are considered. In comparing the analytical and numerical results between all of the cases exceptional agreement is noted between every case.

Similarly, the pure shear responses of the six hardening combinations over the five plastic strain rates are given in Fig. 4.39 for both analytical and numerical approaches. As with the normal cases, outstanding agreement is noted between the various results. Thus, between the plethora of problems presented in Fig. 4.38 and Fig. 4.39 the performance of the rate-dependent models may be considered verified.

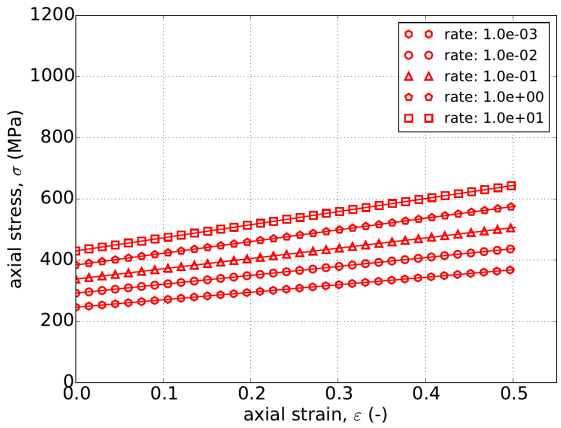

(a) Linear, Johnson-Cook

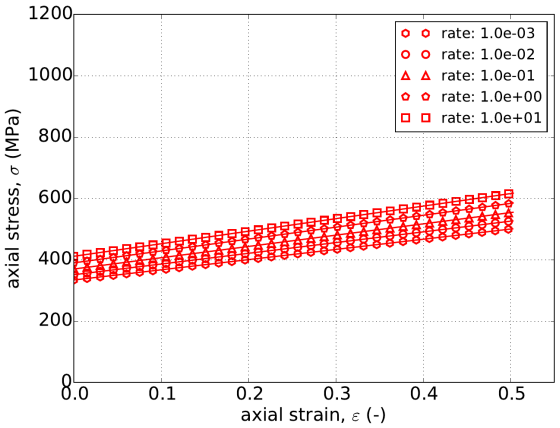

(b) Linear, Power-Law Breakdown

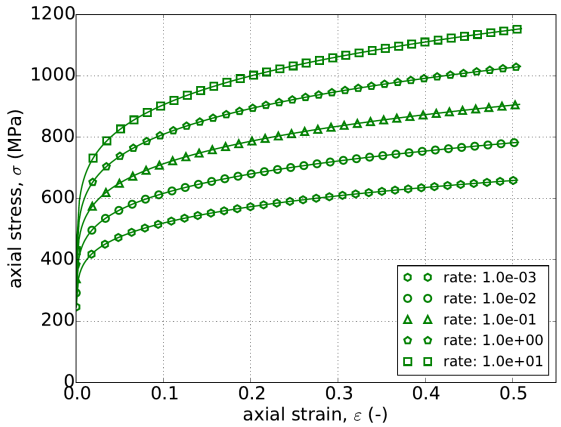

(c) Power-Law, Johnson-Cook

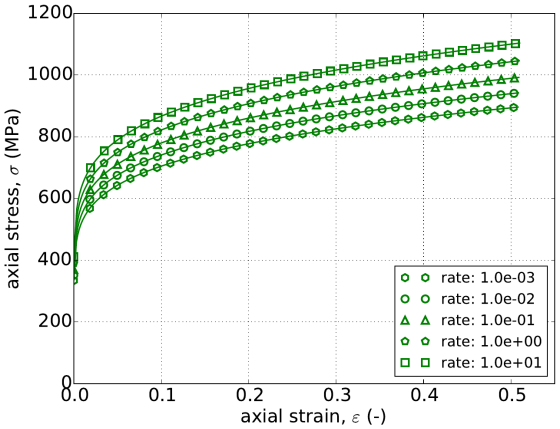

(d) Power-Law, Power-Law Breakdown

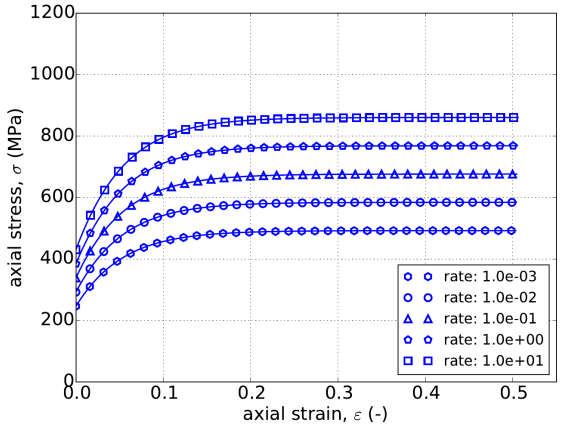

(e) Voce, Johnson-Cook

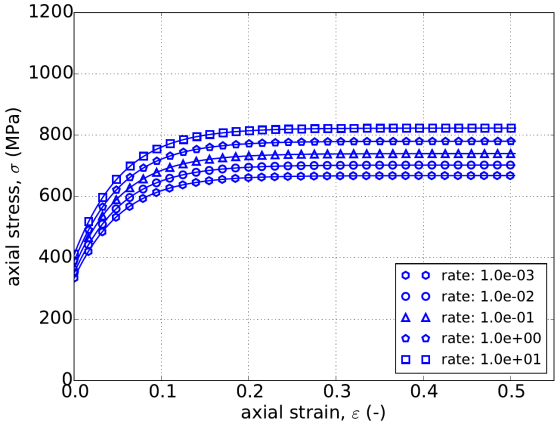

(f) Voce, Power-Law Breakdown

Fig. 4.38 Uniaxial stress-strain responses of the J_2 plasticity model with (a,b) linear, (c,d) power-law, and (e,f) Voce isotropic hardening with the (a,c,e) Johnson-Cook and (b,d,f) Power-law breakdown rate *dependent* hardening models. Solid lines are analytical while open symbols are numerical (Sierra).

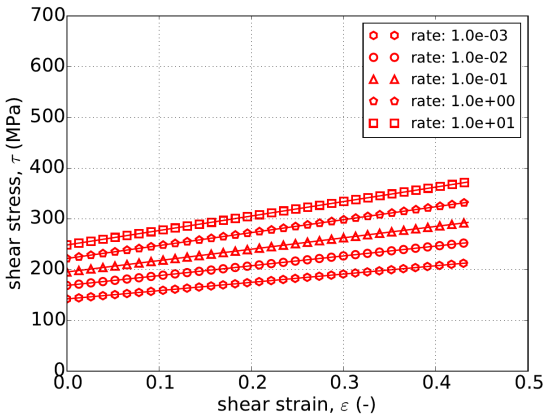

(a) Linear, Johnson-Cook

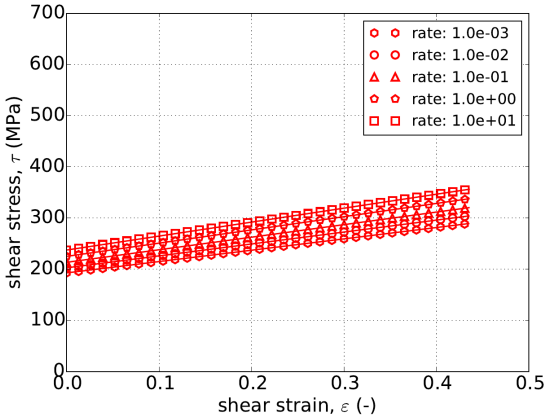

(b) Linear, Power-Law Breakdown

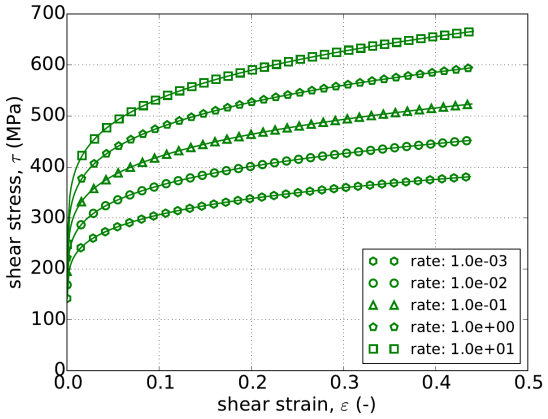

(c) Power-Law, Johnson-Cook

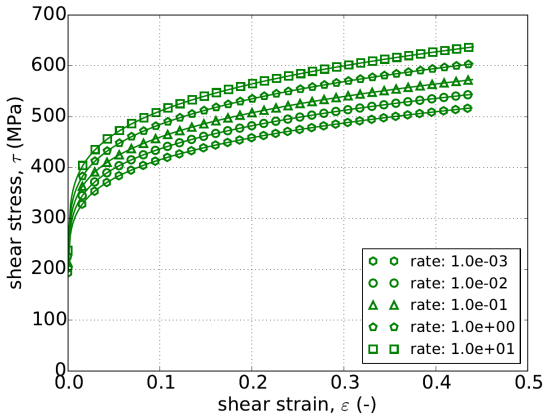

(d) Power-Law, Power-Law Breakdown

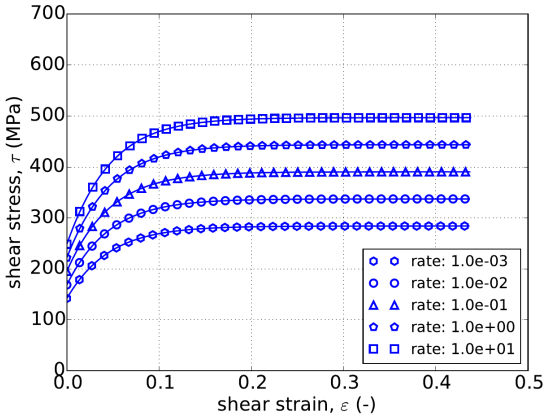

(e) Voce, Johnson-Cook

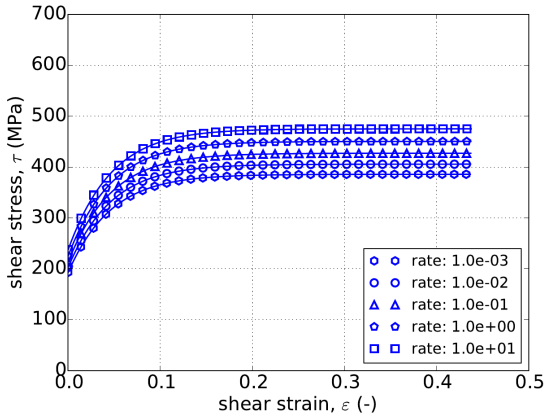

(f) Voce, Power-Law Breakdown

Fig. 4.39 Pure shear responses of the J_2 plasticity model with (a,b) linear, (c,d) power-law, and (e,f) Voce isotropic hardening with the (a,c,e) Johnson-Cook and (b,d,f) Power-law breakdown rate *dependent* hardening models. Solid lines are analytical while open symbols are numerical (Sierra).

Flow Stress

As a next step in verification, the capabilities of the *flow-stress* hardening model incorporating rate- and temperature-dependence is assessed. To this end, Fig. 4.40 presents uniaxial stress-strain responses considering linear, power-law, and Voce isotropic hardening models with both Johnson-Cook and power-law breakdown rate dependent multipliers and Johnson-Cook type temperature dependence. Five decades of strain rates along with temperatures spanning 180 K are considered in the various figures. In all of the results, agreement is noted between analytical and numerical results.

To complement the uniaxial results, pure shear results are given in Fig. 4.41. These results consider the same combinations of linear, power-law, and Voce isotropica hardening multiplier, Johnson-Cook and power-law breakdown rate multipliers, and Johnson-Cook temperature dependence. The same ranges of rates and temperatures are considered. As with the uniaxial cases, good agreement is noted between the analytical and numerical results.

Decoupled Flow Stress

As a further extension, the verification of the *decoupled flow-stress* model is explored. To this end, Fig. 4.42 and Fig. 4.43 present uniaxial stress-strain results of various combinations of linear, power-law, and Voce isotropic hardening functions with rate-independent, Johnson-Cook, and power-law breakdown rate multipliers applied in different combinations to yield and hardening. Hardening is taken to be temperature-independent while yield has a Johnson-Cook temperature multiplier. The considered cases span five decades of applied strain rates and a range of temperatures. In these cases, the various analytical and numerical results are in agreement.

While the previous results considered temperature-dependence on yield only, the temperature dependence on hardening is examined in Fig. 4.44 and Fig. 4.45. As with the previous case, linear, power-law, and Voce isotropic hardening laws are considered in conjunction with different combinations of Johnson-Cook, power-law breakdown, and rate-independent rate multipliers spanning large ranges of strain rates and temperatures. Once again, excellent agreement is noted between analytical and numerical results.

4.13.4 User Guide

```
BEGIN PARAMETERS FOR MODEL J2_PLASTICITY
  #
  # Elastic constants
  #
  YOUNGS MODULUS = <real>
  POISSONS RATIO = <real>
  SHEAR MODULUS  = <real>
  BULK MODULUS   = <real>
```

(continues on next page)

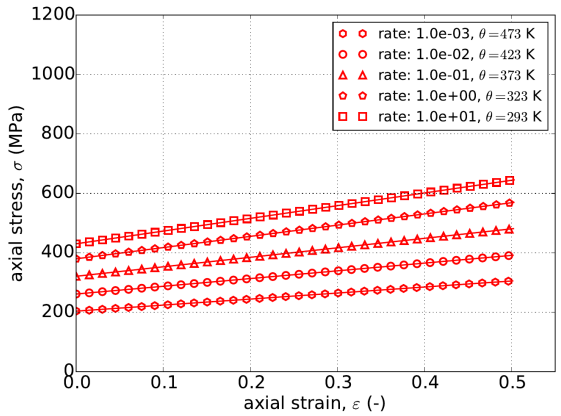

(a) Linear, Johnson-Cook

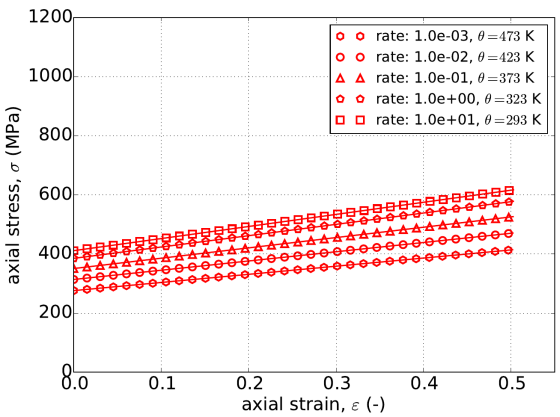

(b) Linear, Power-Law Breakdown

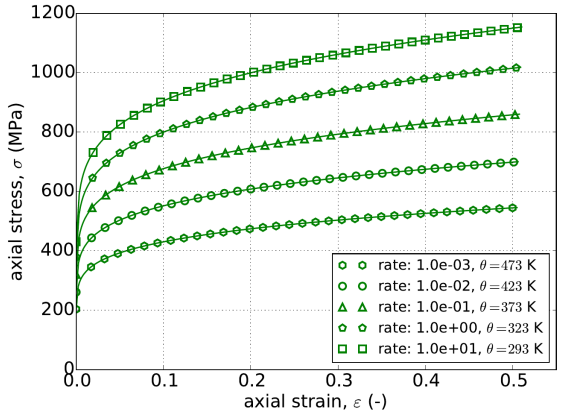

(c) Power-Law, Johnson-Cook

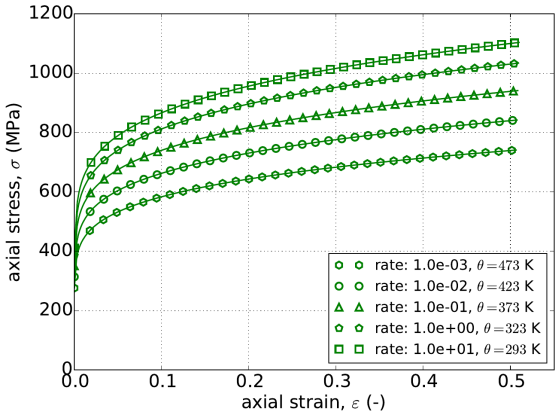

(d) Power-Law, Power-Law Breakdown

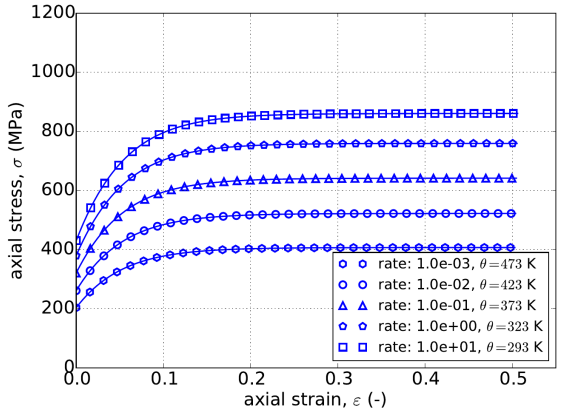

(e) Voce, Johnson-Cook

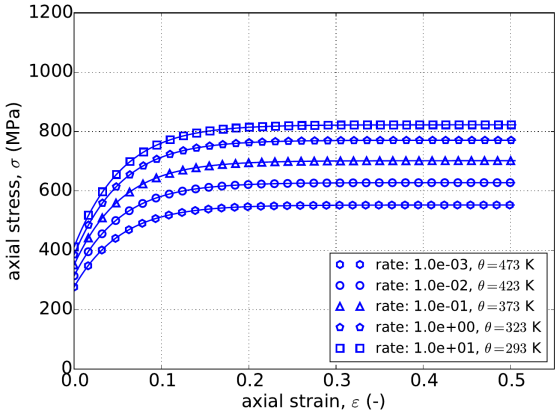

(f) Voce, Power-Law Breakdown

Fig. 4.40 Uniaxial stress-strain responses of the J_2 plasticity model using the flow-stress hardening model comprised of (a,b) linear, (c,d) power-law, and (e,f) Voce isotropic hardening, (a,c,e) Johnson-Cook and (b,d,f) power-law breakdown rate multipliers, and (a-f) Johnson-Cook temperature multipliers. Solid lines are analytical while open symbols are numerical (Sierra).

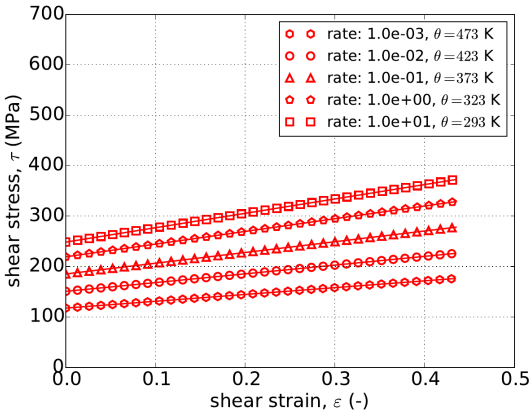

(a) Linear, Johnson-Cook

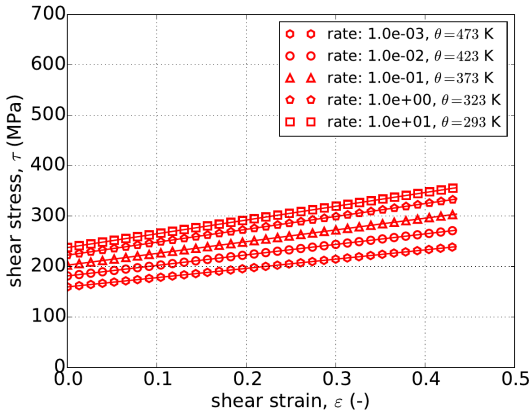

(b) Linear, Power-Law Breakdown

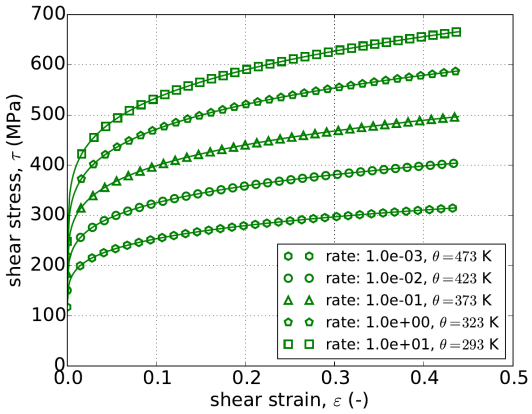

(c) Power-Law, Johnson-Cook

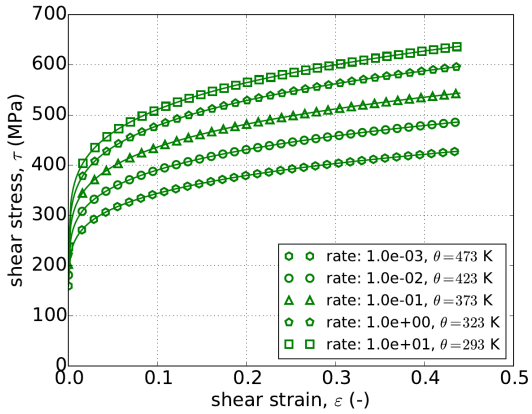

(d) Power-Law, Power-Law Breakdown

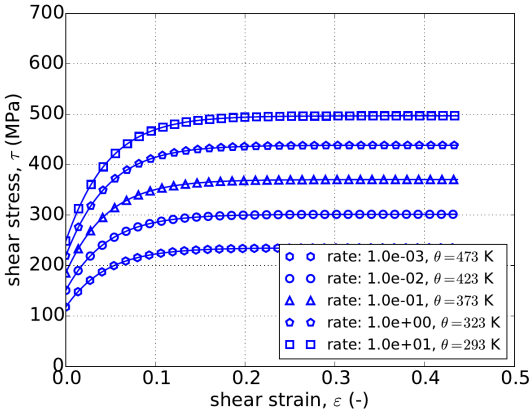

(e) Voce, Johnson-Cook

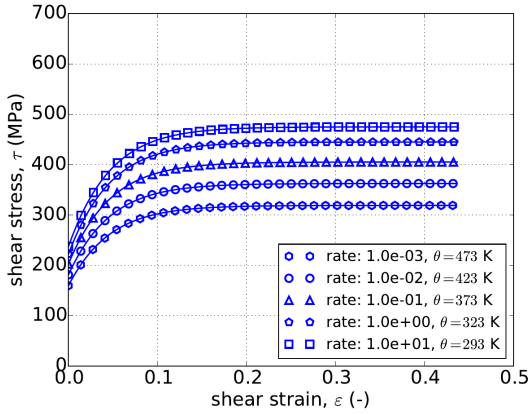

(f) Voce, Power-Law Breakdown

Fig. 4.41 Pure shear responses of the J_2 plasticity model using the flow-stress hardening model comprised of (a,b) linear, (c,d) power-law, and (e,f) Voce isotropic hardening, (a,c,e) Johnson-Cook and (b,d,f) Power-law breakdown rate multipliers and (a-f) Johnson-Cook temperature multipliers. Solid lines are analytical while open symbols are numerical (Sierra).

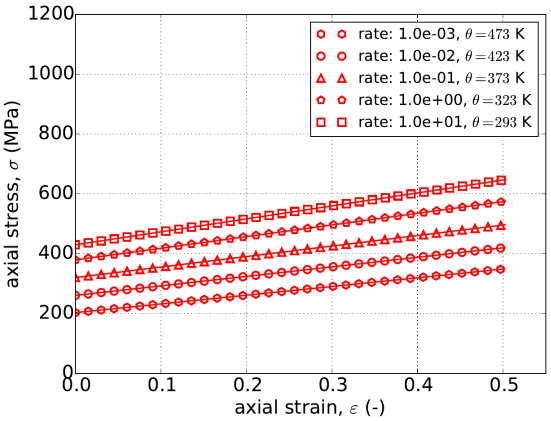

(a) (L), Yield (JC) Hardening (PLB)

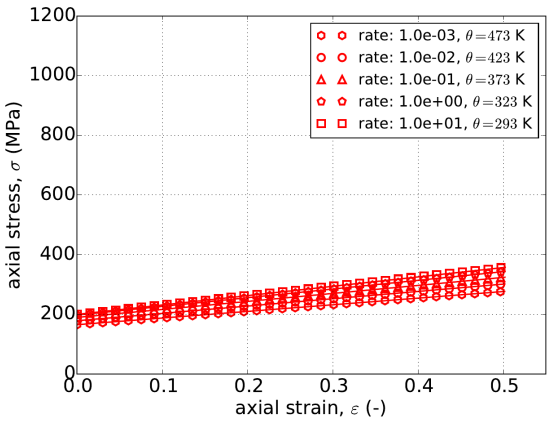

(b) (L), Yield (-) Hardening (JC)

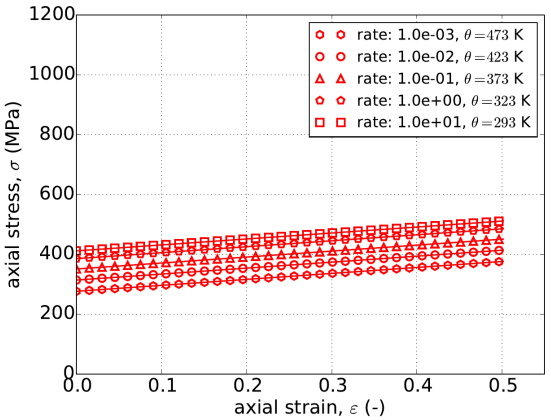

(c) (L), Yield (PLB) Hardening (-)

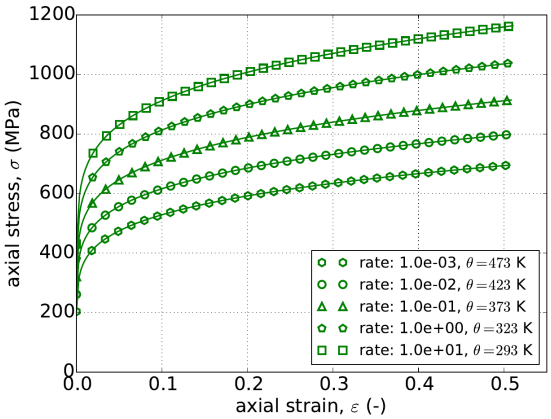

(d) (PL), Yield (JC) Hardening (PLB)

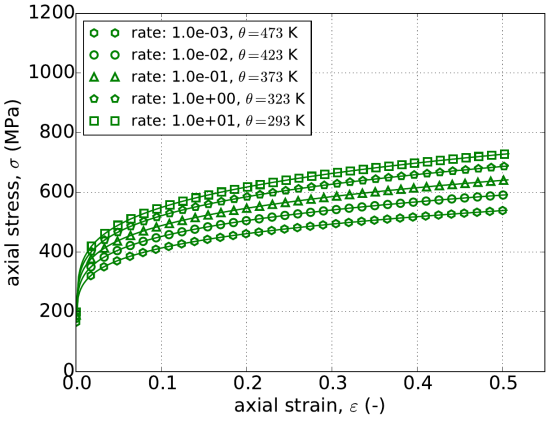

(e) (PL), Yield (-) Hardening (JC)

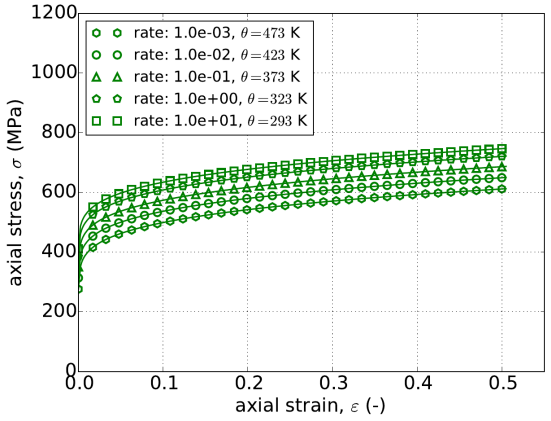

(f) (PL), Yield (PLB) Hardening (-)

Fig. 4.42 Uniaxial stress-strain responses of the J_2 plasticity model using the decoupled flow-stress hardening model comprised of (a-c) linear ("L") and (d-f) power-law ("PL"), (a-f) temperature independent hardening, (a-f) Johnson-Cook type temperature multiplier for yield, (a,d) Johnson-Cook ("JC") and power-law breakdown ("PLB") type yield and hardening rate multipliers, respectively, (b,e) rate-independent (-) yield with Johnson-Cook type hardening rate dependence, and (c,f) power-law breakdown yield rate dependence with rate-independent hardening. Solid lines are analytical while open symbols are numerical (Sierra).

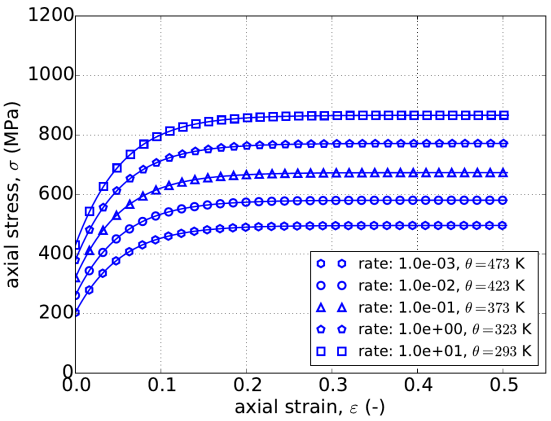

(a) (V), Yield (JC) Hardening (PLB)

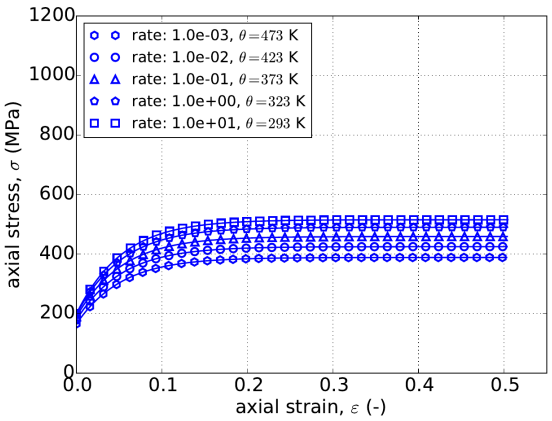

(b) (V), Yield (-) Hardening (JC)

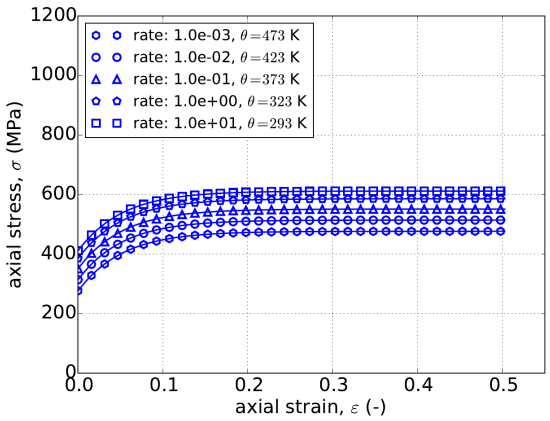

(c) (V), Yield (PLB) Hardening (i)

Fig. 4.43 Uniaxial stress-strain responses of the J_2 plasticity model using the decoupled flow-stress hardening model comprised of (a-c) Voce isotropic hardening ("V"), (a-c) temperature independent hardening, (a-c) Johnson-Cook type temperature multiplier for yield, (a) Johnson-Cook ("JC") and power-law breakdown ("PLB") type yield and hardening rate multipliers, respectively, (b) rate-independent (-) yield with Johnson-Cook type hardening rate dependence, and (c) power-law breakdown yield rate dependence with rate-independent hardening. Solid lines are analytical while open symbols are numerical (Sierra).

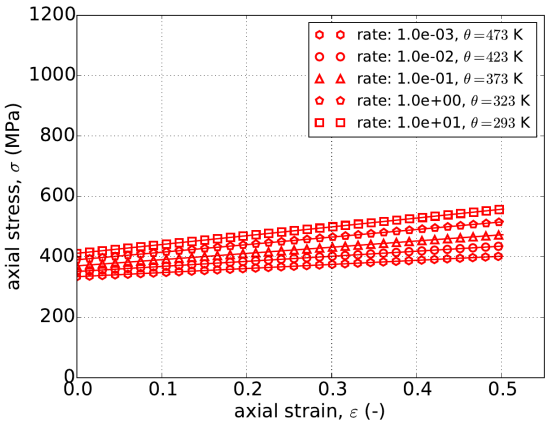

(a) (L), Yield (JC) Hardening (PLB)

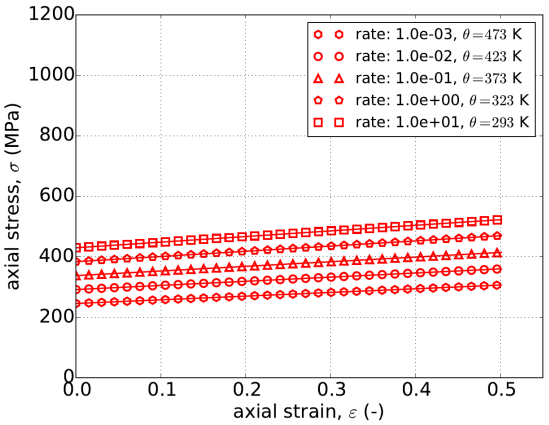

(b) (L), Yield (-) Hardening (JC)

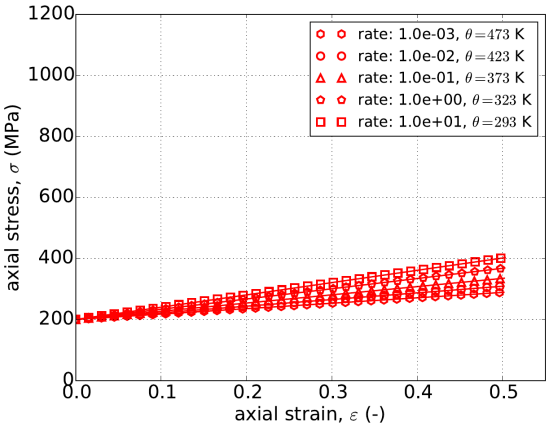

(c) (L), Yield (PLB) Hardening (-)

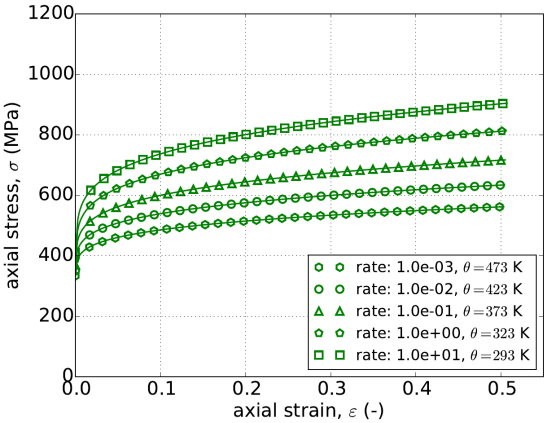

(d) (PL), Yield (JC) Hardening (PLB)

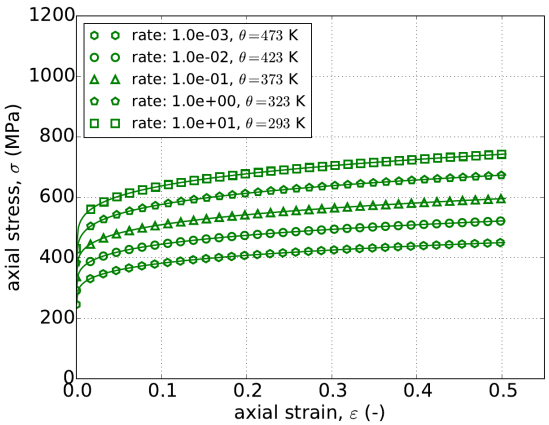

(e) (PL), Yield (-) Hardening (JC)

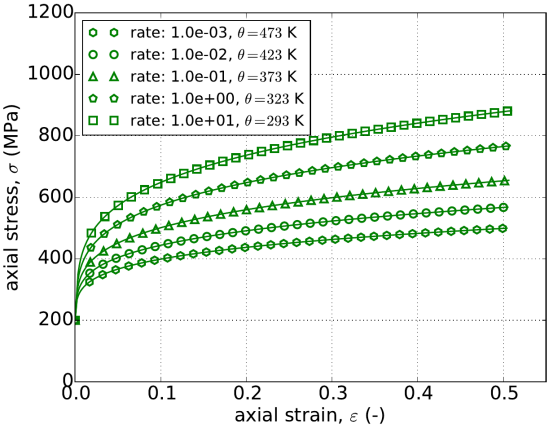

(f) (PL), Yield (PLB) Hardening (-)

Fig. 4.44 Uniaxial stress-strain responses of the J_2 plasticity model using the decoupled flow-stress hardening model comprised of (a-c) linear ("L") and (d-f) power-law ("PL") hardening, (a-f) temperature independent yield, (a-f) Johnson-Cook type temperature multiplier for hardening, (a,d) power-law breakdown ("PLB") and Johnson-Cook ("JC") rate multipliers for yield and hardening, respectively (b,e) rate-independent (-)hardening with Johnson-Cook type yield rate dependence, and (c,f) power-law breakdown hardening rate dependence with rate-independent yield. Solid lines are analytical while open symbols are numerical (Sierra).

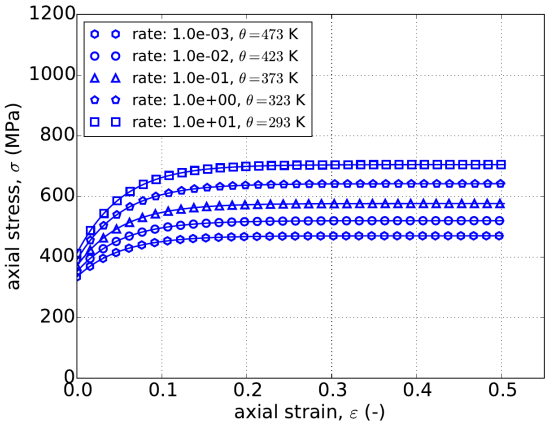

(a) (V), Yield (JC) Hardening (PLB)

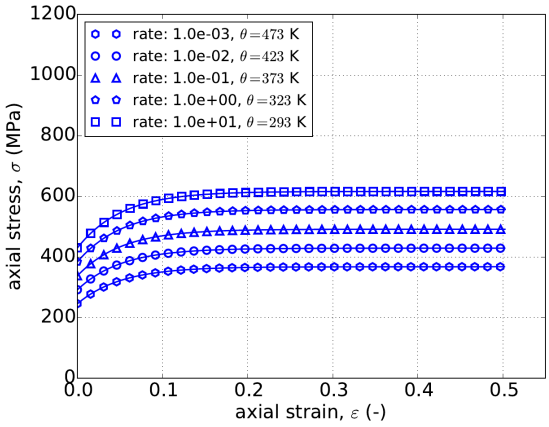

(b) (V), Yield (-) Hardening (JC)

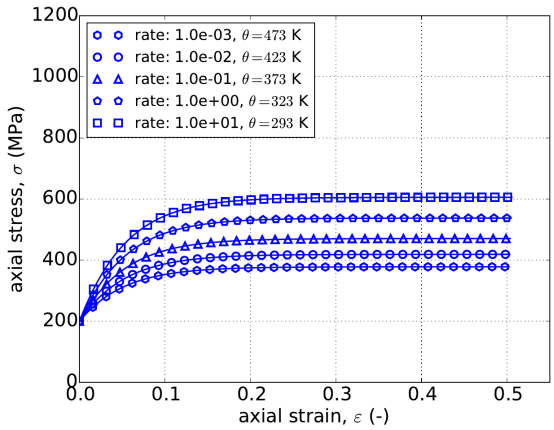

(c) (V), Yield (PLB) Hardening (i)

Fig. 4.45 Uniaxial stress-strain responses of the J_2 plasticity model using the decoupled flow-stress hardening model comprised of (a-c) Voce ("V") isotropic hardening, (a-c) temperature independent yield, (a-c) Johnson-Cook type temperature multiplier for hardening, (a) power-law breakdown ("PLB") and Johnson-Cook ("JC") rate multipliers for yield and hardening, respectively (b) rate-independent (-)hardening with Johnson-Cook type yield rate dependence, and (c) power-law breakdown hardening rate dependence with rate-independent yield. Solid lines are analytical while open symbols are numerical (Sierra).

(continued from previous page)

```
  LAMBDA          = <real>
  TWO MU          = <real>
  #
  # Yield surface parameters
  #
  YIELD STRESS = <real>
  BETA         = <real> (1.0)
```

```
#
  #
  # Hardening model
  #
  HARDENING MODEL = LINEAR | POWER_LAW | VOCE | USER_DEFINED |
  FLOW_STRESS | DECOUPLED_FLOW_STRESS | JOHNSON_COOK |
  POWER_LAW_BREAKDOWN
  #
  # Linear hardening
  #
  HARDENING MODULUS = <real>
  #
  # Power-law hardening
  #
  HARDENING CONSTANT = <real>
  HARDENING EXPONENT = <real> (0.5)
  LUDERS STRAIN      = <real> (0.0)
  #
  # Voce hardening
  #
  HARDENING MODULUS       = <real>
  EXPONENTIAL COEFFICIENT = <real>
  #
  # Johnson-Cook hardening
  #
  HARDENING FUNCTION = <string>hardening_function_name
  RATE CONSTANT      = <real>
  REFERENCE RATE     = <real>
  #
  # Power law breakdown hardening
  #
  HARDENING FUNCTION = <string>hardening_function_name
  RATE COEFFICIENT   = <real>
  RATE EXPONENT      = <real>
  # User defined hardening
  #
  HARDENING FUNCTION = <string>hardening_function_name
```

(continues on next page)

(continued from previous page)

```
  #
```

```
#
  #
  # Following Commands Pertain to Flow_Stress Hardening Model
  #
  #    -  Isotropic Hardening model
  #
  ISOTROPIC HARDENING MODEL = LINEAR | POWER_LAW | VOCE |
                              USER_DEFINED
  #
  # Specifications for Linear, Power-law, and Voce same as above
  #
  # User defined hardening
  #
  ISOTROPIC HARDENING FUNCTION = <string>iso_hardening_fun_name
  #
  #     - Rate dependence
  #
  RATE MULTIPLIER = JOHNSON_COOK | POWER_LAW_BREAKDOWN |
     USER_DEFINED | RATE_INDEPENDENT (RATE_INDEPENDENT)
  #
  # Specifications for Johnson-Cook, Power-law-breakdown
  #     same as before EXCEPT no need to specify a
  #     hardening function
  #
  # User defined rate multiplier
  #
  RATE MULTIPLIER FUNCTION = <string> rate_mult_function_name
  #
  #     - Temperature dependence
  #
  TEMPERATURE MULTIPLIER = JOHNSON_COOK | USER_DEFINED |
     TEMPERATURE_INDEPENDENT (TEMPERATURE_INDEPENDENT)
  #
  #  Johnson-Cook temperature dependence
  #
  MELTING TEMPERATURE   = <real>
  REFERENCE TEMPERATURE = <real>
  TEMPERATURE EXPONENT  = <real>
  #
  #  User-defined temperature dependence
  TEMPERATURE MULTIPLIER FUNCTION = <string>temp_mult_function_name
  #
  # Following Commands Pertain to Decoupled_Flow_Stress Hardening Model
```

(continues on next page)

(continued from previous page)

```
  #
  #     -  Isotropic Hardening model
  #
  ISOTROPIC HARDENING MODEL = LINEAR | POWER_LAW | VOCE | USER_DEFINED
  #
  # Specifications for Linear, Power-law, and Voce same as above
  #
  # User defined hardening
  #
  ISOTROPIC HARDENING FUNCTION = <string>isotropic_hardening_function_
↪name
  #
  #     - Rate dependence
  #
  YIELD RATE MULTIPLIER = JOHNSON_COOK | POWER_LAW_BREAKDOWN |
              USER_DEFINED | RATE_INDEPENDENT (RATE_INDEPENDENT)
  #
  # Specifications for Johnson-Cook, Power-law-breakdown same as before
  #     EXCEPT no need to specify a hardening function
  #     AND should be preceded by YIELD
  #
  #     As an example for Johnson-Cook yield rate dependence,
  #
  YIELD RATE CONSTANT  = <real>
  YIELD REFERENCE RATE = <real>
  #
  # User defined rate multiplier
  #
  YIELD RATE MULTIPLIER FUNCTION = <string>yield_rate_mult_function_
↪name
  #
  HARDENING_RATE MULTIPLIER = JOHNSON_COOK | POWER_LAW_BREAKDOWN |
              USER_DEFINED | RATE_INDEPENDENT (RATE_INDEPENDENT)
  #
  #     Syntax same as for yield parameters but with a HARDENING prefix
  #
  #     - Temperature dependence
  #
  YIELD TEMPERATURE MULTIPLIER = JOHNSON_COOK | USER_DEFINED |
            TEMPERATURE_INDEPENDENT (TEMPERATURE_INDEPENDENT)
  #
  #  Johnson-Cook temperature dependence
  #
  YIELD MELTING TEMPERATURE   = <real>
  YIELD REFERENCE TEMPERATURE = <real>
```

(continues on next page)

(continued from previous page)

```
  YIELD TEMPERATURE EXPONENT  = <real>
  #
  #  User-defined temperature dependence
  YIELD TEMPERATURE MULTIPLIER FUNCTION = <string>yield_temp_mult_fun_
↪name
  #
  HARDENING TEMPERATURE MULTIPLIER = JOHNSON_COOK | USER_DEFINED |
            TEMPERATURE_INDEPENDENT (TEMPERATURE_INDEPENDENT)
  #
  #   Syntax for hardening constants same as for yield but
  #             with HARDENING prefix
```

```
#
  #
  # Optional Failure Definitions
  #    Following only need to be defined if intend to use failure model
  #
  FAILURE MODEL = TEARING_PARAMETER | JOHNSON_COOK_FAILURE | WILKINS
                  | MODULAR_FAILURE | MODULAR_BCJ_FAILURE

  CRITICAL FAILURE PARAMETER = <real>
  #
  # TEARING_PARAMETER Failure model definitions
  #
  TEARING PARAMETER EXPONENT = <real>
  #
  # JOHNSON_COOK_FAILURE Failure model definitions
  #
  JOHNSON COOK D1       = <real>
  JOHNSON COOK D2       = <real>
  JOHNSON COOK D3       = <real>
  JOHNSON COOK D4       = <real>
  JOHNSON COOK D5       = <real>
  #
  #Following Johnson-Cook parameters can only be defined once.  As␣
↪such, only
  #  needed if not previously defined via Johnson-Cook multipliers
  #  w/ flow-stress hardening.  Does need to be defined
  #  w/ Decoupled Flow Stress
  #
  REFERENCE RATE        = <real>
  REFERENCE TEMPERATURE = <real>
  MELTING TEMPERATURE   = <real>
  #
  # WILKINS Failure model definitions
```

(continues on next page)

(continued from previous page)

```
  #
  WILKINS ALPHA    = <real>
  WILKINS BETA     = <real>
  WILKINS PRESSURE = <real>
  #
  #  MODULAR_FAILURE Failure model definitions
  #
  PRESSURE MULTIPLIER         = PRESSURE_INDEPENDENT | WILKINS
                                | USER_DEFINED (PRESSURE_INDEPENDENT)
  LODE ANGLE MULTIPLIER       = LODE_ANGLE_INDEPENDENT |
                                WILKINS (LODE_ANGLE_INDEPENDENT)
  TRIAXIALITY MULTIPLIER      = TRIAXIALITY_INDEPENDENT | JOHNSON_COOK
                                | USER_DEFINED (TRIAXIALITY_
↪INDEPENDENT)
  RATE FAIL MULTIPLIER        = RATE_INDEPENDENT | JOHNSON_COOK
                                | USER_DEFINED (RATE_INDEPENDENT)
  TEMPERATURE FAIL MULTIPLIER = TEMPERATURE_INDEPENDENT | JOHNSON_COOK
                                | USER_DEFINED (TEMPERATURE_
↪INDEPENDENT)
  #
  # Individual multiplier definitions
  #
  PRESSURE MULTIPLIER = WILKINS
  WILKINS ALPHA       = <real>
  WILKINS PRESSURE    = <real>
  #
  PRESSURE MULTIPLIER = USER_DEFINED
  PRESSURE MULTIPLIER FUNCTION = <string> pressure_multiplier_fun_name
  #
  LODE ANGLE MULTIPLIER = WILKINS
  WILKINS BETA          = <real>
  #
  TRIAXIALITY MULTIPLIER = JOHNSON_COOK
  JOHNSON COOK D1        = <real>
  JOHNSON COOK D2        = <real>
  JOHNSON COOK D3        = <real>
  #
  TRIAXIALITY MULTIPLIER = USER_DEFINED
  TRIAXIALITY MULTIPLIER FUNCTION = <string> triaxiality_multiplier_
↪fun_name
  #
  RATE FAIL MULTIPLIER = JOHNSON_COOK
  JOHNSON COOK D4      = <real>
  # REFERENCE RATE should only be added if not previously defined
  REFERENCE RATE       = <real>
```

(continues on next page)

(continued from previous page)

```
  #
  RATE FAIL MULTIPLIER = USER_DEFINED
  RATE FAIL MULTIPLIER FUNCTION = <string> rate_fail_multiplier_fun_
↪name
  #
  TEMPERATURE FAIL MULTIPLIER = JOHNSON_COOK
  JOHNSON COOK D5             = <real>
  # JC Temperatures should only be defined if not previously given
  REFERENCE TEMPERATURE       = <real>
  MELTING TEMPERATURE         = <real>
  #
  TEMPERATURE FAIL MULTIPLIER          = USER_DEFINED
  TEMPERATURE FAIL MULTIPLIER FUNCTION = <string> temp_multiplier_fun_
↪name
  #
  # MODULAR_BCJ_FAILURE Failure model definitions
  #
  INITIAL DAMAGE    = <real>
  INITIAL VOID SIZE = <real>
  DAMAGE BETA       = <real> (0.5)
  GROWTH MODEL      = COCKS_ASHBY | NO_GROWTH (NO_GROWTH)
  NUCLEATION MODEL  = HORSTEMEYER_GOKHALE | CHU_NEEDLEMAN_STRAIN
                      | NO_NUCLEATION (NO_NUCLEATION)
  #
  GROWTH RATE FAIL MULTIPLIER        = JOHNSON_COOK | USER_DEFINED
                                       | RATE_INDEPENDENT
                                       (RATE_INDEPENDENT)
  GROWTH TEMPERATURE FAIL MULTIPLIER = JOHNSON_COOK | USER_DEFINED
                                       | TEMPERATURE_INDEPENDENT
                                       (TEMPERATURE_INDEPENDENT)
  #
  NUCLEATION RATE FAIL MULTIPLIER        = JOHNSON_COOK | USER_DEFINED
                                           | RATE_INDEPENDENT
                                           (RATE_INDEPENDENT)
  NUCLEATION TEMPERATURE FAIL MULTIPLIER = JOHNSON_COOK | USER_DEFINED
                                           | TEMPERATURE_INDEPENDENT
                                           (TEMPERATURE_INDEPENDENT)
  #
  # Definitions for individual growth and nucleation models
  #
  GROWTH MODEL = COCKS_ASHBY
  DAMAGE EXPONENT = <real> (0.5)
  #
  NUCLEATION MODEL      = HORSTEMEYER_GOKHALE
  NUCLEATION PARAMETER1 = <real> (0.0)
```

(continues on next page)

(continued from previous page)

```
  NUCLEATION PARAMETER2 = <real> (0.0)
  NUCLEATION PARAMETER3 = <real> (0.0)
  #
  NUCLEATION MODEL          = CHU_NEEDLEMAN_STRAIN
  NUCLEATION AMPLITUDE      = <real>
  MEAN NUCLEATION STRAIN    = <real>
  NUCLEATION STRAIN STD DEV = <real>
  #
  # Definitions for rate and temperature fail multiplier
  #   Note: only showing definitions for growth.
  #    Nucleation terms are the same just with NUCLEATION instead
  #    of GROWTH
  #
  GROWTH RATE FAIL MULTIPLIER = JOHNSON_COOK
  GROWTH JOHNSON COOK D4      = <real>
  GROWTH REFERENCE RATE       = <real>
  #
  GROWTH RATE FAIL MULTIPLIER          = USER_DEFINED
  GROWTH RATE FAIL MULTIPLIER FUNCTION = <string> growth_rate_fail_
↪mult_func
  #
  GROWTH TEMPERATURE FAIL MULTIPLIER = JOHNSON_COOK
  GROWTH JOHNSON COOK D5             = <real>
  GROWTH REFERENCE TEMPERATURE       = <real>
  GROWTH MELTING TEMPERATURE         = <real>
  #
  GROWTH TEMPERATURE FAIL MULTIPLIER          = USER_DEFINED
  GROWTH TEMPERATURE FAIL MULTIPLIER FUNCTION = <string> temp_fail_
↪mult_func
  #
```

```
#
  #
  # Optional Adiabatic Heating/Thermal Softening  Definitions
  #    Following only need to be defined if intend to use failure model
  #
  THERMAL SOFTENING MODEL = ADIABATIC | COUPLED
  #
  SPECIFIC HEAT = <real> # not needed for COUPLED
  BETA_TQ       = <real>
```

```
END [PARAMETERS FOR MODEL J2_PLASTICITY]
```

In the command blocks that define the J_2 plasticity model:

- The reference nominal yield stress, $\bar{\sigma}$, is defined with the `YIELD STRESS` command line.

- The beta parameter defines if hardening is isotropic.
- The type of hardening law is defined with the `HARDENING MODEL` command line, other hardening commands then define the specific shape of that hardening curve.
- The hardening modulus for a linear hardening model is defined with the `HARDENING MODULUS` command line.
- The hardening constant for a power law hardening model is defined with the `HARDENING CONSTANT` command line.
- The hardening exponent for a power law hardening model is defined with the `HARDENING EXPONENT` command line.
- The Luders strain for a power law hardening model is defined with the `LUDERS STRAIN` command line.
- The hardening function for a user defined hardening model is defined with the `HARDENING FUNCTION` command line.
- The shape of the spline for the spline based hardening is defined by the `CUBIC SPLINE TYPE`, `CARDINAL PARAMETER`, `KNOT EQPS`, and `KNOT STRESS` command lines.
- The isotropic hardening model for the flow stress hardening model is defined with the `ISOTROPIC HARDENING MODEL` command line.
- The function name of a user-defined isotropic hardening model is defined via the `ISOTROPIC HARDENING FUNCTION` command line.
- The optional rate multiplier for the flow stress hardening model is defined with the `RATE MULTIPLIER` command line.
- The optional temperature multiplier for the flow stress hardening model is defined via the `TEMPERATURE MULTIPLIER` command line.
- The function name of a user-defined temperature multiplier is defined with the `TEMPERATURE MULTIPLIER FUNCTION` command line.
- For a Johnson-Cook temperature multiplier, the melting temperature, θ_{melt}, is defined via the `MELTING TEMPERATURE` command line.
- For a Johnson-Cook temperature multiplier, the reference temperature, θ_{ref}, is defined via the `REFERENCE TEMPERATURE` command line.
- For a Johnson-Cook temperature multiplier, the temperature exponent, M, is defined via the `TEMPERATURE EXPONENT` command line.
- The optional rate multiplier for the yield stress for the decoupled flow stress hardening model is defined with the `YIELD RATE MULTIPLIER` command line.
- The optional rate multiplier for the hardening for the decoupled flow stress hardening model is defined with the `HARDENING RATE MULTIPLIER` command line.

- The optional temperature multiplier for the yield stress for the decoupled flow stress hardening model is defined with the `YIELD TEMPERATURE MULTIPLIER` command line.
- The optional temperature multiplier for the hardening for the decoupled flow stress hardening model is defined via the `HARDENING TEMPERATURE MULTIPLIER` command line.

Output variables available for this model are listed in Table 4.17.

Table 4.17 State Variables for J2 PLASTICITY Model

Name	Description
`EQPS`	equivalent plastic strain, $\bar{\varepsilon}^p$
`EQDOT`	equivalent plastic strain rate, $\dot{\bar{\varepsilon}}^p$
`SEFF`	effective stress, ϕ
`TENSILE_EQPS`	tensile equivalent plastic strain, $\bar{\varepsilon}_t^p$
`DAMAGE`	damage, ϕ
`VOID_COUNT`	void count, η
`VOID_SIZE`	void size, υ
`DAMAGE_DOT`	damage rate, $\dot{\phi}$
`VOID_COUNT_DOT`	void count rate, $\dot{\eta}$
`PLASTIC_WORK_HEAT_RATE`	plastic work heat rate, $\dot{Q}^p$

4.14 Hosford Plasticity Model

4.14.1 Theory

Like other elastic-plastic models in LAMÉ, the Hosford plasticity model is a rate-independent hypoelastic formulation. Unlike the Hill and other more complex plasticity models, it is isotropic. In a similar fashion to those models, the total rate of deformation is additively decomposed into an elastic and plastic part such that

$$D_{ij} = D_{ij}^{\mathrm{e}} + D_{ij}^{\mathrm{p}}.$$

The objective stress rate, depending only on the elastic deformation, may then be written as,

$$\overset{\circ}{\sigma}_{ij} = \mathbb{C}_{ijkl} D_{kl}^{\mathrm{e}}.$$

The Hosford plasticity model utilizes a yield surface first put forth by W. F. Hosford in the 1970's [45] that is isotropic but non-quadratic. This specific form was proposed due to experimental observations of biaxial stretching in which neither the Tresca or J_2 yield surfaces could describe the results. In contrast to many of the yield surfaces proposed for similar purposes, only two parameters are utilized. Even with these limited terms, the developed model is quite versatile and

can be reduced to von Mises or Tresca conditions as well as capturing responses in between. This yield surface is given as,

$$f\left(\sigma_{ij}, \bar{\varepsilon}^p\right) = \phi\left(\sigma_{ij}\right) - \bar{\sigma}\left(\bar{\varepsilon}^p\right) = 0,$$

in which $\phi\left(\sigma_{ij}\right)$ is the Hosford effective stress and $\bar{\sigma}\left(\bar{\varepsilon}^p\right)$ is the current yield stress that may depend on rate and/or temperature. The Hosford effective stress is a non-quadratic function of the principal stresses ($\sigma_i, \quad i = 1, 2, 3$) and is given as

$$\phi\left(\sigma_{ij}\right) = \left[\frac{|\sigma_1 - \sigma_2|^a + |\sigma_2 - \sigma_3|^a + |\sigma_1 - \sigma_3|^a}{2}\right]^{1/a}$$

in which a is the yield surface exponent. Interestingly, if $a = 2$ or 4 the yield surface reduces to that of a J_2 von Mises surface while $a = 1$ or as $a \to \infty$ produces a Tresca like shape. If the value of a is above 4 the yield surface takes a position between the Tresca and J_2 limits. Typical values are $a = 6$ or $a = 8$ for *bcc* and *fcc* metals, respectively [37]. To highlight this variability the yield surface is plotted below in Fig. 4.46 for three values of $a - a = 4, 8$, and 100.

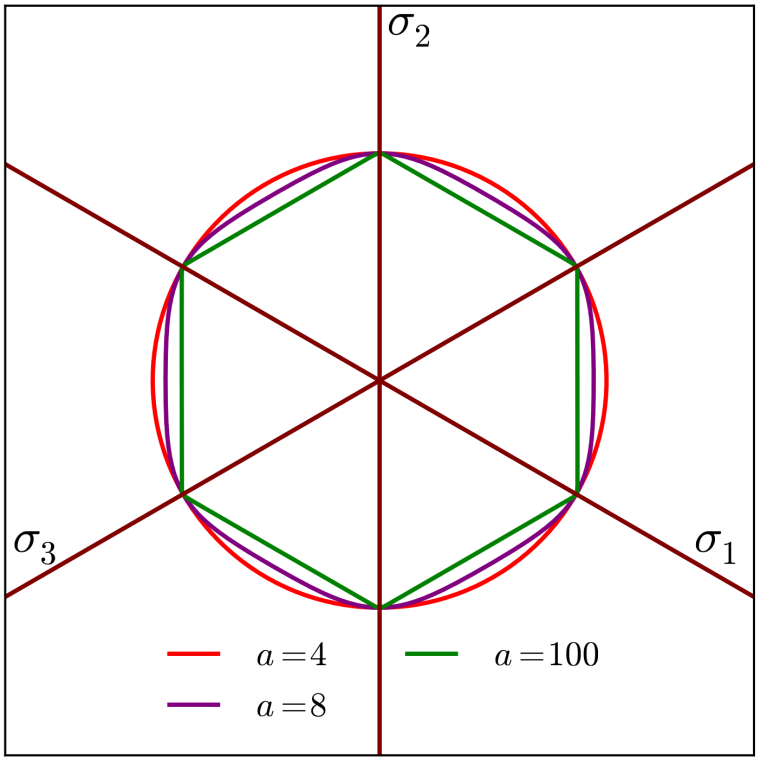

Fig. 4.46 Example Hosford yield surfaces, $f\left(\sigma_{ij}, \bar{\varepsilon}^p = 0; a\right)$, presented in the deviatoric π-plane. The presented surfaces correspond to the different yield exponents $a = 4, 8,$ and 100.

For the hardening function, $\bar{\sigma}\ (\bar{\varepsilon}^p)$, a variety of forms including linear, power law, or a more general user defined function may be used.

An associated flow rule is utilized such that the plastic rate of deformation is normal to the yield surface and is given by,

$$\dot{D}^{\mathrm{p}}_{ij} = \dot{\gamma}\frac{\partial \phi}{\partial \sigma_{ij}},$$

where $\dot{\gamma}$ is the consistency multiplier enforcing $f = 0$ during plastic deformation. Given the form of f, it can also be shown that $\dot{\gamma} = \dot{\bar{\varepsilon}}^p$.

For details on the plasticity model, please see [88]. Additional details on failure models and adiabatic heating capabilities may be found in [61], [62] and [60], respectively.

4.14.1.1 Plastic Hardening

Plastic hardening refers to increases in the flow stress, $\bar{\sigma}$, with plastic deformation. As such, hardening is described via a functional relationship between the flow stress and isotropic hardening variable (effective plastic strain), $\bar{\sigma}\ (\bar{\varepsilon}^p)$. Over the course of nearly a century of work in metal plasticity, a variety of relationships have been proposed to describe the interactions associated with different physical interpretations, deformation mechanisms, and materials. To enable the utilization of the same plasticity models for different material systems, a modular implementation of plastic hardening has been adopted such that the analyst may select different hardening models from the input deck thereby avoiding any code changes or user subroutines. In this section, additional details are given for the different models to enable the user to select the appropriate choice of model. Note, the models being discussed here are only for *isotropic* hardening in which the yield surface expands. *Kinematic* hardening in which the yield surface translates in stress-space with deformation and *distortional* hardening where the shape of the yield surface changes shape with deformation are not treated. For a larger discussion of the phenomenology and history of different hardening types, the reader is referred to [42], [57], [64].

Given the ubiquitous nature of these hardening laws in computational plasticity, some (if not most) of this material may be found elsewhere in this manual. Nonetheless, the discussion is repeated here for the convenience of the reader.

Linear

Linear hardening is conceptually the simplest model available in LAMÉ. As the name implies, a linear relationship is assumed between the hardening variable, $\bar{\varepsilon}^p$, and flow stress. The hardening modulus, H', is a constant giving the rate of change of flow stress with plastic flow. The flow stress expression may therefore be written,

$$\bar{\sigma} = \sigma_y + H'\bar{\varepsilon}^p.$$

The simplicity of the model is its main feature as the constant slope,

$$\frac{d\bar{\sigma}}{d\bar{\varepsilon}^p} = H',$$

makes the model attractive for analytical models and cheap for computational implementations (*e.g.* radial return algorithms require only a single correction step). Unfortunately, the simplicity of the representation also means that it has limited predictive capabilities and can lead to overly stiff responses.

Power Law

Another common expression for isotropic hardening is the power-law hardening model. Due to its prevalence, a dedicated `ELASTIC-PLASTIC POWER LAW HARDENING` model may be found in LAMÉ (see Section 4.8.1). This expression is given as,

$$\bar{\sigma} = \sigma_y + A < \bar{\varepsilon}^p - \varepsilon_L >^n,$$

in which $< \cdot >$ are Macaulay brackets, ε_L is the Luders strain, A is a fitting constant, and n is an exponent typically taken such that $0 < n \leq 1$. The Luders strain is a positive, constant strain value (defaulted to zero) giving an initially perfectly plastic response in the plastic deformation domain (see Fig. 4.20). The derivative is then simply,

$$\frac{d\bar{\sigma}}{d\bar{\varepsilon}^p} = nA < \bar{\varepsilon}^p - \varepsilon_L >^{(n-1)} .$$

Note, one difficulty in such an implementation is that when the effective equivalent plastic strain is zero, numerical difficulties may arise in evaluating the derivative and necessitate special treatment of the case.

Voce

The Voce hardening model (sometimes referred to as a saturation model) uses a decaying exponential function of the equivalent plastic strain such that the hardening eventually saturates to a specified value (thus the name). Such a relationship has been observed in some structural metals giving rise to the popularity of the model. The hardening response is given as,

$$\bar{\sigma} = \sigma_y + A \left(1 - \exp\left(-n\bar{\varepsilon}^p\right)\right),$$

in which A is a fitting constant and n is a fitting exponent controlling how quickly the hardening saturates. Importantly, the derivative is written as,

$$\frac{d\bar{\sigma}}{d\bar{\varepsilon}^p} = nA \exp\left(-n\bar{\varepsilon}^p\right),$$

and is well defined everywhere giving the selected form an advantage over the aforementioned power law model.

Johnson-Cook

The Johnson-Cook hardening model is a variant of the classical Johnson-Cook [48], [49] expression. In this instance, the temperature-dependence is neglected to focus on the *rate-dependent* capabilities while allowing for arbitrary isotropic hardening forms via the use of a user-defined hardening function. With these assumptions, the flow stress may be written as,

$$\bar{\sigma} = \tilde{\sigma}_y\left(\bar{\varepsilon}^p\right)\left[1 + C\left\langle \ln\left(\frac{\dot{\bar{\varepsilon}}^p}{\dot{\varepsilon}_0}\right)\right\rangle\right],$$

in which $\tilde{\sigma}_y\left(\bar{\varepsilon}^p\right)$ is the user-specified rate-independent hardening function, C is a fitting constant and $\dot{\varepsilon}_0$ is a reference strain rate. The Macaulay brackets ensure the material behaves in a rate independent fashion when $\dot{\bar{\varepsilon}}^p < \dot{\varepsilon}_0$.

Power Law Breakdown

Like the Johnson-Cook formulation, the power-law breakdown model is also rate-dependent. Again, a multiplicative decomposition is assumed between isotropic hardening and the corresponding rate-dependence dependent. In this case, however, the functional form is derived from the analysis of Frost and Ashby [33] in which power-law relationships like those of the Johnson-Cook model cease to appropriately capture the physical response. The form used here is similar to the expression used by Brown and Bammann [16] and is written as,

$$\bar{\sigma} = \tilde{\sigma}_y\left(\bar{\varepsilon}^p\right)\left[1 + \operatorname{asinh}\left(\left(\frac{\dot{\bar{\varepsilon}}^p}{g}\right)^{(1/m)}\right)\right],$$

with $\tilde{\sigma}_y\left(\bar{\varepsilon}^p\right)$ being the user supplied rate independent expression, g is a model parameter related to the activation energy required to transition from climb to glide-controlled deformation, and m dictates the strength of the dependence.

4.14.2 Implementation

The Hosford plasticity model is implicitly integrated using a closest point projection (CPP) return mapping algorithm (RMA). The resulting nonlinear equations are solved via a line search augmented Newton-Raphson method and the stress update routine is very similar to that of the Hill plasticity model. The key difference between the two is the isotropy. Specifically, given that the Hosford yield surface is isotropic and the functional form is given in terms of principal stresses, the stress update routine is performed in *principal stress* space and then converted to global Cartesian values.

For a loading step, a trial stress state, T_{ij}^{tr}, may be computed by knowing the rate of deformation, d_{ij}, and time step as,

$$T_{ij}^{tr} = T_{ij}^{n} + \Delta t \mathbb{C}_{ijkl} d_{kl}.$$

The principal stresses, T_i^{tr}, may then be used to determine the trial yield function value, $\phi^{tr} = \phi\left(T_i^{tr}, \bar{\varepsilon}^{p(n)}\right)$. If $\phi^{tr} < 0$, the elastic trial solution is acceptable. On the other hand, if the trial solution is inadmissible, the aforementioned CPP-RMA problem is solved in principal stress space. The crux of this algorithm is the simultaneous solution of two nonlinear equations – (*i*) the flow rule and (*ii*) consistency condition. The former leads to a residual, R_i, of the form (again in principal stress space),

$$R_i = \Delta d_i^p - \Delta\gamma \frac{\partial \phi}{\partial T_i} = 0,$$

while the latter is enforced by the yield function,

$$f = \phi\left(T_i\right) - \bar{\sigma}\left(\bar{\varepsilon}^p\right) = 0,$$

and its derivative ($\dot{f}$) being zero. This system is solved via a Newton-Raphson type approach in which the state variables (stress, T_i, and consistency multiplier, γ) are iteratively corrected until the residuals are satisfied. Using $(k+1)$ and (k) to denote the next and current iterations, this updating takes the form,

$$\begin{aligned} \Delta\gamma^{(k+1)} &= \Delta\gamma^{(k)} + \Delta\left(\Delta\gamma\right), \\ T_i^{(k+1)} &= T_i^{(k)} + \Delta T_i, \end{aligned}$$

in which $T^{(0)} = T_i^{tr}$ and $\Delta\gamma^{(0)} = 0$. Consistent linearization of the two equations can be solved to give correction increments of the form,

$$\begin{aligned} \Delta\left(\Delta\gamma\right) &= \frac{f^{(k)} - R_i^{(k)} \mathcal{L}_{ij}^{(k)} \frac{\partial \phi^{(k)}}{\partial T_j}}{\frac{\partial \phi^{(k)}}{\partial T_i} \mathcal{L}_{ij}^{(k)} \frac{\partial \phi^{(k)}}{\partial T_j} + H'^{(k)}}, \\ \Delta T_i &= -\mathcal{L}_{ij}^{(k)} \left(R_j^{(k)} + \Delta\left(\Delta\gamma\right) \frac{\partial \phi^{(k)}}{\partial T_j}\right), \end{aligned}$$

with $\mathcal{L}_{ij}^{(k)}$ being the Hessian of the CPP-RMA problem and $H'^{(k)}$ is the slope of the hardening curve.

Previous studies have indicated that the Newton-Raphson method alone may be insufficient to guarantee convergence with arbitrary stress states in the case of non-quadratic yield surfaces [5], [83], [88]. To address this, a *line search* method is adopted. In such an approach, the incrementation rule (4.43) is modified such that,

$$\begin{aligned} \Delta\gamma^{(k+1)} &= \Delta\gamma^{(k)} + \alpha\Delta\left(\Delta\gamma\right), \\ T_i^{(k+1)} &= T_i^{(k)} + \alpha\Delta T_i, \end{aligned}$$

where $\alpha \in (0, 1]$ is the step magnitude. This parameter enforces that the solution be converging and is determined via various convergence criteria. The $\alpha = 1$ case corresponds to the Newton-Raphson method. Utilization of this approach has been shown to greatly increase the robustness of this algorithm under large trial stresses [88].

Finally, upon convergence of the algorithm, the Cartesian stress are found from the principal stresses via,

$$T_{ij}^{n+1} = \sum_{k=1}^{3} T_k^{n+1} \hat{e}_i^k \hat{e}_j^k,$$

in which $\hat{e}_i^k$ is the eigenvector of the k^{th} principal stress.

Details of this implementation and the line search algorithm may be found in the work of Scherzinger [88].

4.14.3 Verification

The Hosford plasticity material model is verified through a variety of loading and material conditions. For these cases, the elastic properties corresponding to 2090-T3 aluminum [9] given in Section 4.15.3 are utilized. Additional verification exercises for the various failure models and adiabatic heating capabilities may be found in [61], [62] and [60], respectively.

The elastic properties are $E = 70$ GPa and $\nu = 0.25$ while a linear hardening law of the form,

$$\bar{\sigma}\left(\bar{\varepsilon}^p\right) = \sigma_y + K\bar{\varepsilon}^p,$$

with $\sigma_y = 200$ MPa and $K = E/200$ is assumed. For these studies, two different yield surface exponents will be used, $a = 4,\ 8$. The former corresponds to the J_2 surface while the latter is a common value for aluminum.

4.14.3.1 Uniaxial Stress

In the case of uniaxial stress (σ), it is trivial to note that the corresponding principal stress state is simply $\sigma_1 = \sigma,\ \sigma_2 = \sigma_3 = 0$. As such, regardless of a,

$$\phi = |\sigma_1|.$$

With the aforementioned linear hardening, this case reduces to that discussed in Section 4.7.3.1. Corresponding analytical and numerical results (both with $a = 4$ and 8) of the axial stress and lateral strain are presented in Fig. 4.47(a) and Fig. 4.47(b), respectively. In these figures, the invariance of response on yield surface exponent through this loading is clearly observed.

4.14.3.2 Pure Shear

To explore the impact of the yield exponent a, the case of pure shear is considered. Specifically, the only shear component shall be in the Cartesian $e_1 - e_2$ direction such that $\sigma_{12} = \tau$ and ε_{12} are

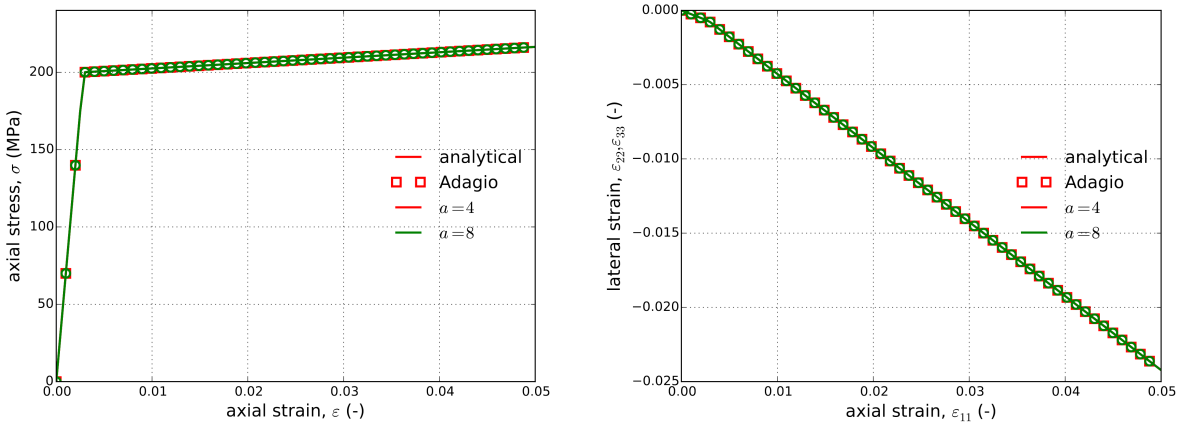

(a) Uniaxial Stress **(b) Lateral Strain**

Fig. 4.47 Axial stress-strain (a) and lateral strain (b) results of the Hosford plasticity model determined analytically and numerically for the case of yield surface exponents $a = 4, 8$.

the only non-zero components. Noting that the three principal stresses are $\tau, 0, -\tau$, the yield condition simplifies to

$$\phi = \left[1 + 2^{a-1}\right]^{1/a} \tau.$$

The equivalent plastic strain may then be found as a function of ε_{12} in the same way as presented in Section 4.15.3.2. Shear stress-strain results for both $a = 4,\ 8$ are presented in Fig. 4.48 as determined both by adagio and analytically. The boundary conditions for this loading are given in *Appendix A*. In these results, the effect of the yield surface exponent, a, may clearly be seen.

4.14.3.3 Plastic Hardening

To verify the capabilities of the hardening models, rate *independent* and rate *dependent* alike, the constant equivalent plastic strain rate, $\dot{\bar{\varepsilon}}^p$, uniaxial stress and pure shear verification tests described in *Appendix A* are utilized. In these simplified loading cases, the material state may be found explicitly as a function of time knowing the prescribed equivalent strain rate. For the rate *independent* cases, a strain rate of $\dot{\bar{\varepsilon}}^p = 1 \times 10^{-4}\text{s}^{-1}$ is used for ease in simulations although the selected rate does not affect the results. Through this testing protocol, the hardening models are not only tested at different rates but also different yield surface shapes. In the current Hosford case, multiple yield surface exponents, a, are considered to probe this effect. Additionally, the rate *dependent* models are tested for a wide range of strain rates (over five decades) and with all three rate *independent* hardening functions ($\tilde{\sigma}_y$ in the previous theory section). Although linear, Voce, and power-law rate *independent* representations are utilized in the rate *dependent* tests, in those cases the hardening models are prescribed via user-defined analytic functions. The rate *independent* verification exercises, on the other hand, examine the built-in hardening models. This distinction necessitates the different considerations and treatments.

The various rate *dependent* and rate *independent* hardening coefficients are found in Table 4.18

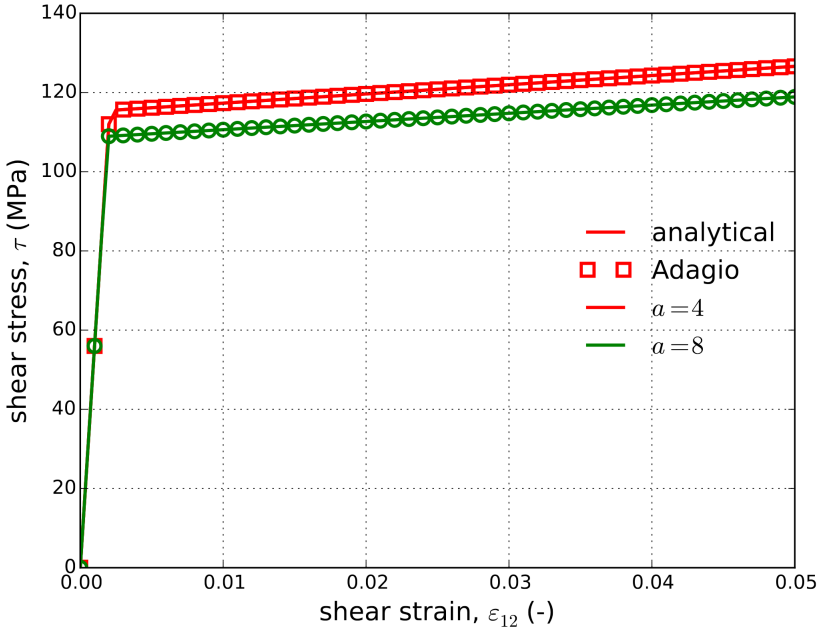

Fig. 4.48 Shear stress-strain results of the Hosford plasticity model determined analytically and numerically for the case of yield surface exponents $a = 4,\ 8$.

while the remaining model parameters are unchanged from the previous verification exercises. For the current verification exercises, the rate *independent* hardening models (linear, Voce, and power-law) will first be considered and then the rate *dependent* forms (Johnson-Cook, power-law breakdown).

Table 4.18 The model parameters for the hardening verification tests used with the Hosford plasticity model during verification tests. Parameters for the rate *independent* hardening functions, $\tilde{\sigma}_y$, are also given and denoted with a $\tilde{}$ while the subscript refers to the functional form.

C	0.1	$\dot{\varepsilon}_0$	1×10^{-4} s^{-1}
g	0.21 s^{-1}	m	16.4
$\tilde{H}_{\text{Linear}}$	200 MPa		
$\tilde{A}_{\text{PL}}$	400 MPa	$\tilde{n}_{\text{PL}}$	0.25
$\tilde{A}_{\text{Voce}}$	200 MPa	$\tilde{n}_{\text{Voce}}$	20

Linear

The aforementioned verification exercises from *Appendix A* are used to investigate the numerical implementation of the rate *independent* linear hardening model. Results from uniaxial stress and pure shear exercises determined analytically and numerically are given in Fig. 4.49 for three different exponents $a = 4,\ 8$, and 20. The first exponent produces a J_2 like response with the latter increasing the curvature of the yield surface. As discussed in Section 4.14.3.1, a purely uniaxial response is independent of exponent thus producing the collapsed results in Fig. 4.49. In both the uniaxial stress and pure shear cases, clear agreement is noted between the two sets of results. The linear slope (tangent modulus) giving the model its name is also observable in the results of Fig. 4.49.

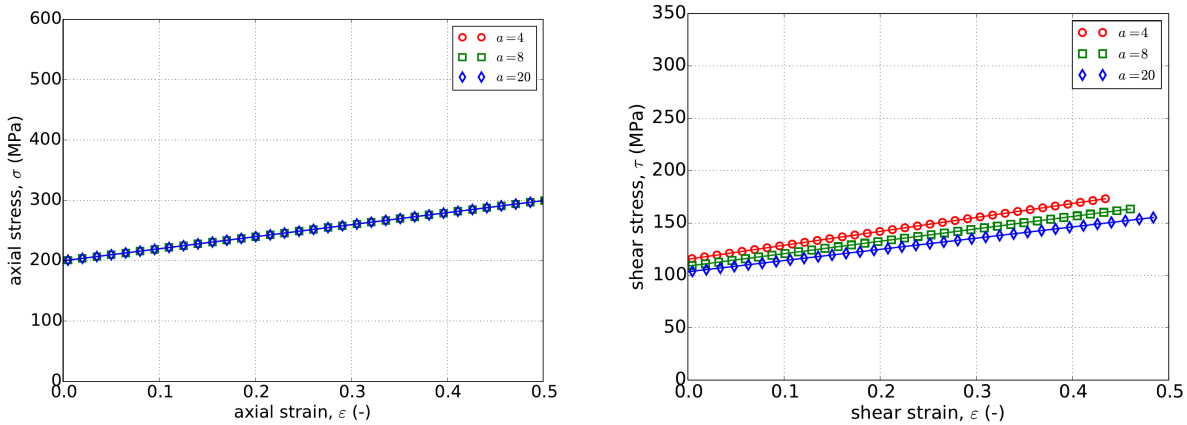

(a) Uniaxial Stress **(b) Pure Shear**

Fig. 4.49 Uniaxial stress-strain (a) and pure shear (b) responses of the Hosford plasticity model with rate *independent*, linear hardening. Solid line are analytical while open symbols are numerical.

Power-Law

To consider the performance of the common power-law hardening model with the Hosford yield surface, the uniaxial stress and pure shear exercises of *Appendix A* are solved analytically and numerically. These results are presented in Fig. 4.50 for three different Hosford exponents – $a = 4,\ 8$ and 20. As expected from previous discussions the uniaxial stress results in Fig. 4.50(a) are independent of a. For both the uniaxial stress and pure shear results, the desired agreement between analytical and numerical solutions is apparent. These results also highlight the initial curved response during plastic-deformation eventually transitioning into a more linear type response.

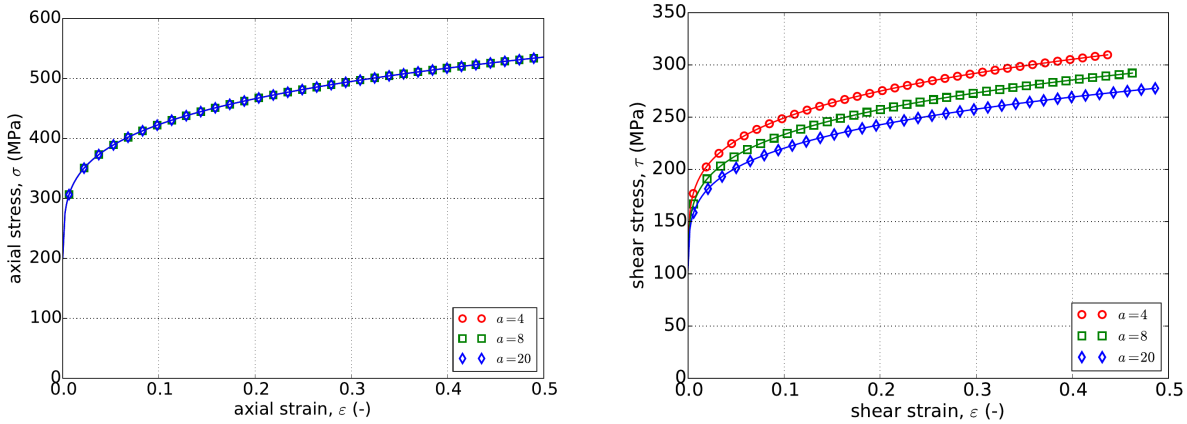

(a) Uniaxial Stress **(b) Pure Shear**

Fig. 4.50 Uniaxial stress-strain (a) and pure shear (b) responses of the Hosford plasticity model with rate *independent*, power-law hardening. Solid line are analytical while open symbols are numerical.

Voce

For the rate *independent* Voce hardening model, the problems of *Appendix A* are used to verify the model response. Specifically, results for the uniaxial stress and pure shear analyses are presented in Fig. 4.51 as determined analytically and numerically for three different values of $a - a = 4, 8,$ and 20. From these results, clear agreement is noted between the two sets of results; including the invariance of the uniaxial stress case to a (Fig. 4.51a). Additionally, the results of Fig. 4.51 also exemplify the saturation nature of the Voce hardening model as the stress-strain response eventually asymptotes.

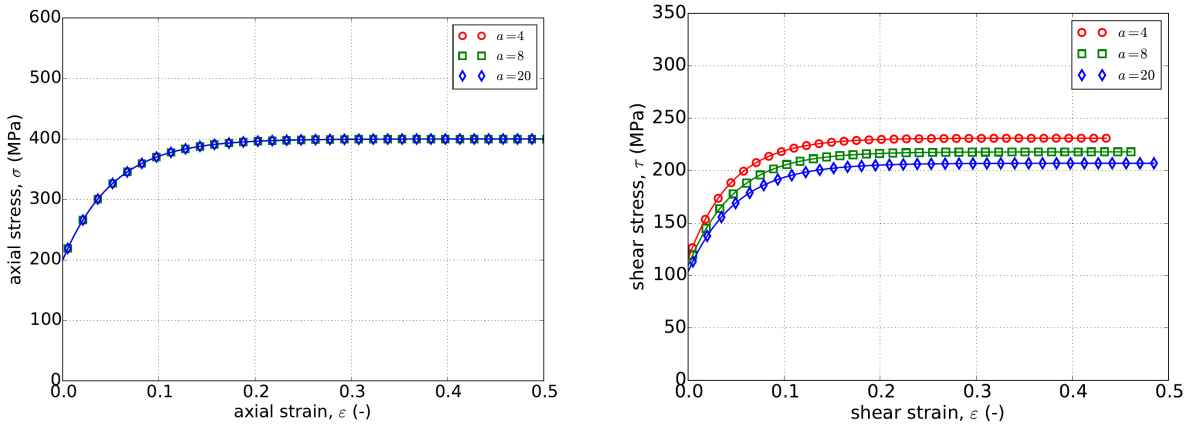

(a) Uniaxial Stress **(b) Pure Shear**

Fig. 4.51 Uniaxial stress-strain (a) and pure shear (b) responses of the Hosford plasticity model with rate *independent*, Voce hardening. Solid line are analytical while open symbols are numerical.

Johnson-Cook

As noted in Section 4.14.3.1, the uniaxial stress response is independent of a. This is also reflected *Appendix A* in which the stress weighting coefficients (Γ) for the Hosford uniaxial case are one. As such in Fig. 4.52 the results of the constant equivalent plastic strain rate uniaxial stress test are presented with $a = 8$ and using the linear (Fig. 4.52a), power-law (Fig. 4.52b), and Voce (Fig. 4.52c) rate *independent* hardening models for five different rates – $\dot{\bar{\varepsilon}}^p = 1 \times 10^{-3},\ 1 \times 10^{-2},\ 1 \times 10^{-1},\ 1 \times 10^{0}$ and 1×10^{1} s^{-1}. In all cases in Fig. 4.52 excellent agreement is observed between the results.

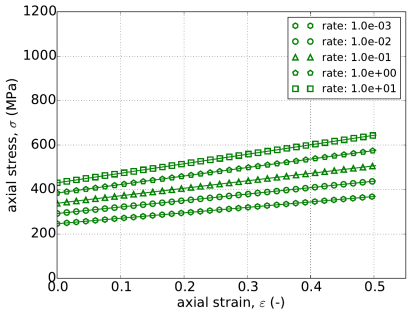

(a) Linear Hardening

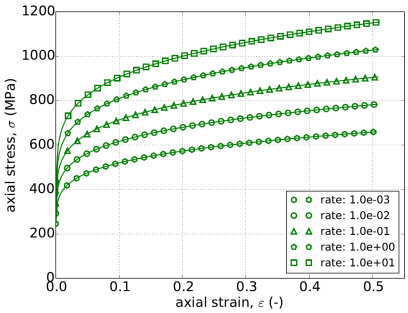

(b) Power-Law Hardening

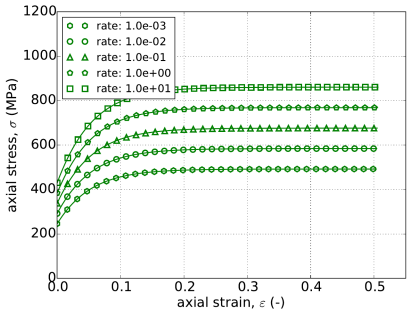

(c) Voce Hardening

Fig. 4.52 Uniaxial stress-strain response of the Hosford plasticity model ($a = 8$) with rate *dependent*, Johnson-Cook type hardening with (a) linear (b) power-law and (c) Voce rate *independent* hardening. Solid lines are analytical results while open symbols are numerical.

Unlike the uniaxial stress case, for pure shear the response depends on the exponent a. Therefore, in addition to the three hardening models, results are also presented for three different exponent values – $a = 4,\ 8$, and 20. The results for all nine cases are presented in Fig. 4.53 and Fig. 4.54 and again excellent agreement is noted in all instances.

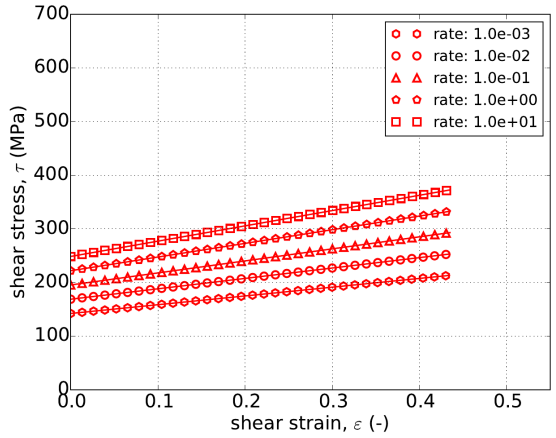

(a) Linear Hardening a=4

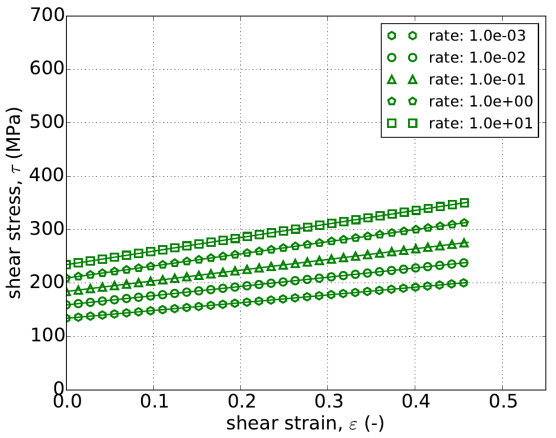

(b) Linear Hardening, a=8

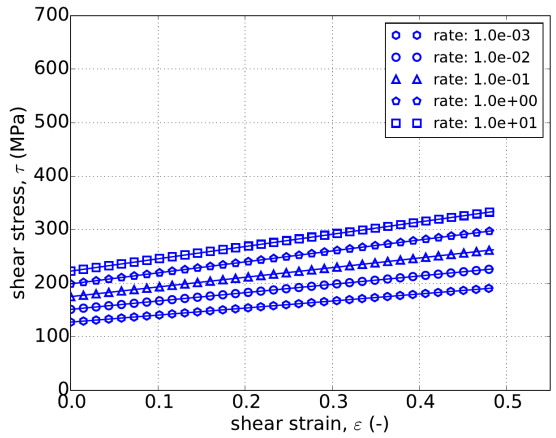

(c) Linear Hardening, a=20

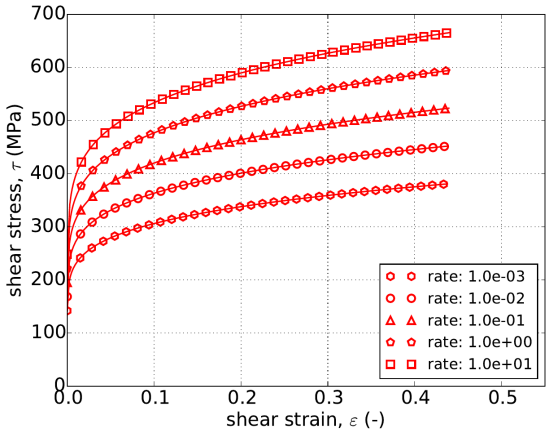

(d) Power-Law Hardening, a=4

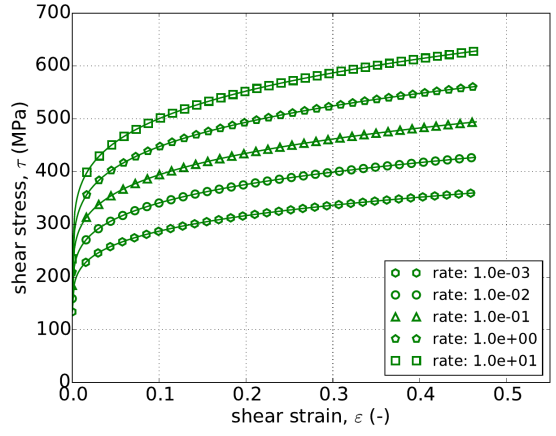

(e) Power-Law Hardening, a=8

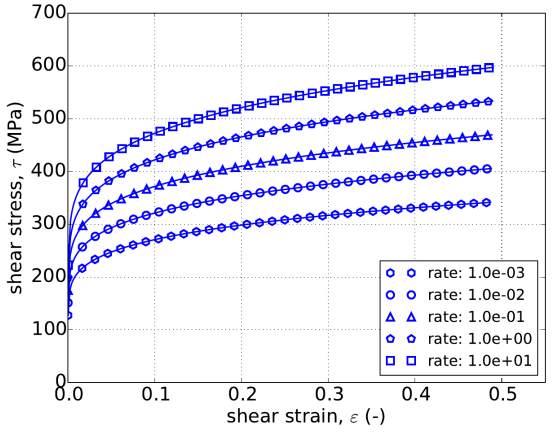

(f) Power-Law Hardening, a=20

Fig. 4.53 Stress-strain response of the Hosford plasticity model with rate *dependent*, Johnson-Cook type hardening in pure shear with (a-c) linear (d-f) and power-law rate *independent* hardening. Solid lines are analytical results while open symbols are numerical.

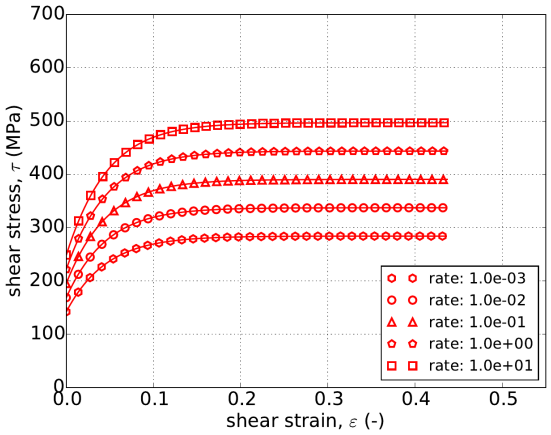

(a) Power-Law Hardening, a=4

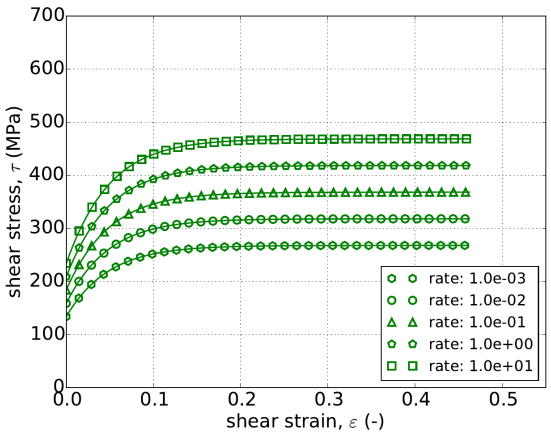

(b) Power-Law Hardening, a=8

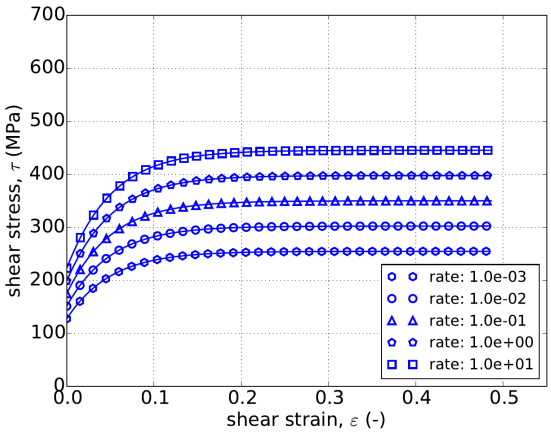

(c) Power-Law Hardening, a=20

Fig. 4.54 Stress-strain response of the Hosford plasticity model with rate *dependent*, Johnson-Cook type hardening in pure shear with (a-c) Voce rate *independent* hardening. Solid lines are analytical results while open symbols are numerical.

Power-Law Breakdown

As mentioned in the previous Johnson-Cook section, for the Hosford model under uniaxial stress the response is independent of yield surface exponent, a. Therefore, Fig. 4.55 presents the results of the constant equivalent plastic strain rate verification test of *Appendix A* for strain rates spanning five decades – $\dot{\bar{\varepsilon}}^p = 1 \times 10^{-3},\ 1 \times 10^{-2},\ 1 \times 10^{-1},\ 1 \times 10^{0}$ and 1×10^{1} s^{-1}. The tests are performed for each rate- *independent* hardening model. In all fifteen cases excellent agreement is noted between numerical and analytical results.

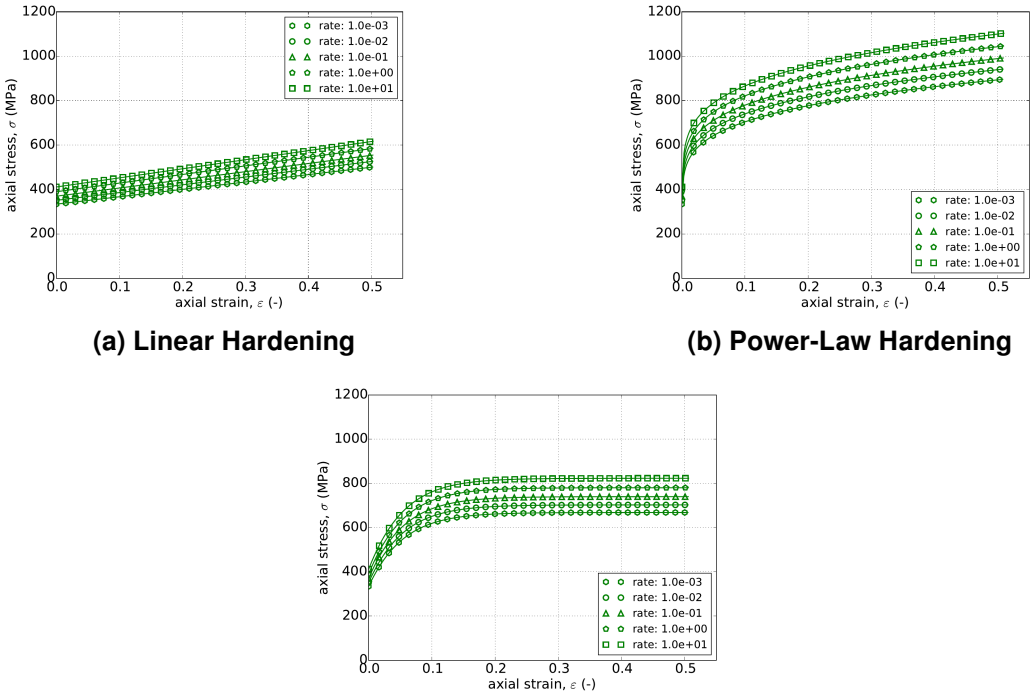

(a) Linear Hardening

(b) Power-Law Hardening

(c) Voce Hardening

Fig. 4.55 Uniaxial stress-strain response of the Hosford plasticity model ($a = 8$) with rate *dependent*, power-law breakdown type hardening with (a) linear (b) power-law and (c) Voce rate *independent* hardening. Solid lines are analytical results while open symbols are numerical.

Similarly, Fig. 4.56 and Fig. 4.57 gives the results of the pure shear variant of the constant equivalent plastic strain rate verification test of *Appendix A*. The same five rates used in the uniaxial stress case are again utilized although in this instance as the pure shear response does depend on a the results are given for three yield surface exponents – $a =$ 4, 8 and 20. In the forty-five cases shown in Fig. 4.56 and Fig. 4.57 quite acceptable agreement is noted verifying the capabilities of the rate *dependent* Hosford implementation.

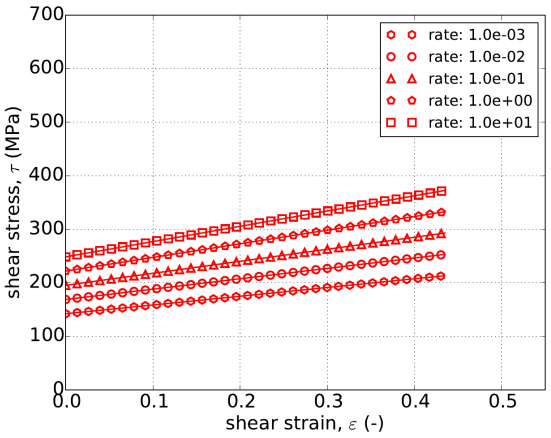

(a) Linear Hardening, a=4

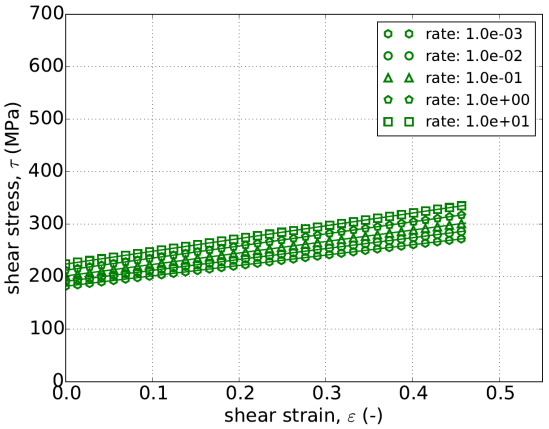

(b) Linear Hardening, a=8

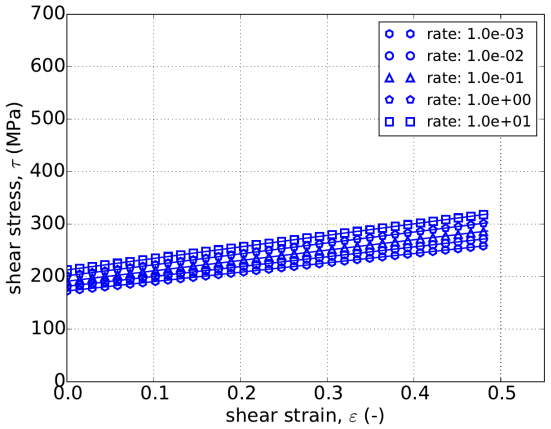

(c) Linear Hardening, a=20

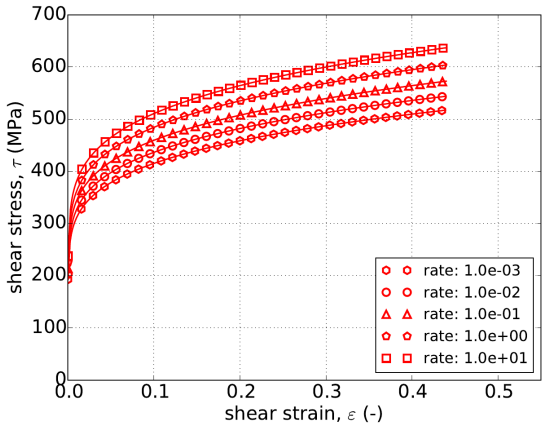

(d) Power-Law Hardening, a=4

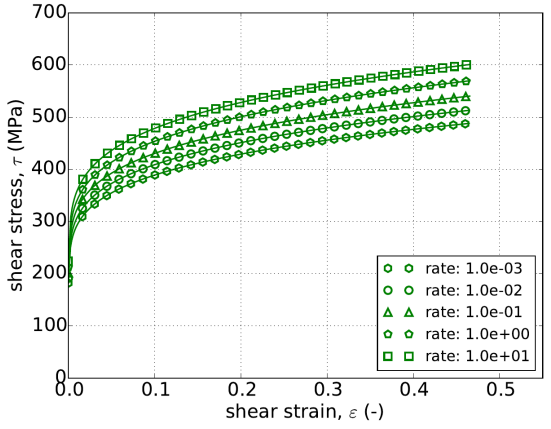

(e) Power-Law Hardening, a=8

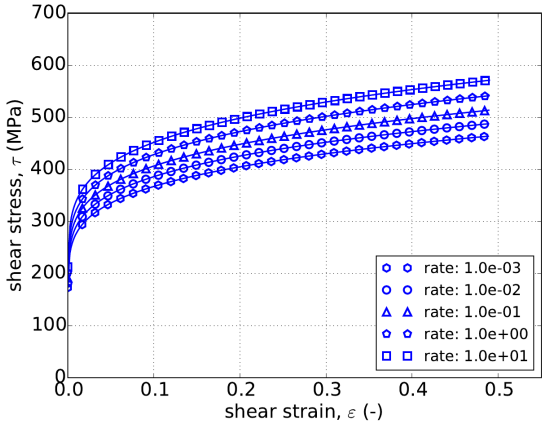

(f) Power-Law Hardening, a=20

Fig. 4.56 Stress-strain response of the Hosford plasticity model with rate *dependent*, power-law breakdown type hardening in pure shear with (a-c) linear and (d-f) power-law rate *independent* hardening. Solid lines are analytical results while open symbols are numerical.

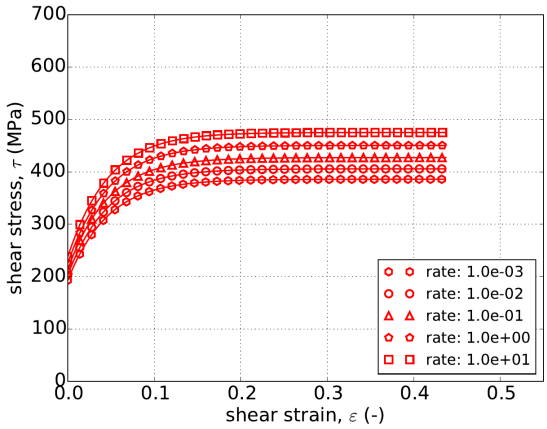

(a) Power-Law Hardening, a=4

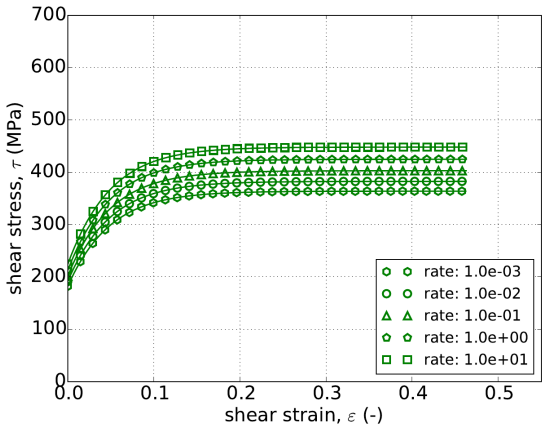

(b) Power-Law Hardening, a=8

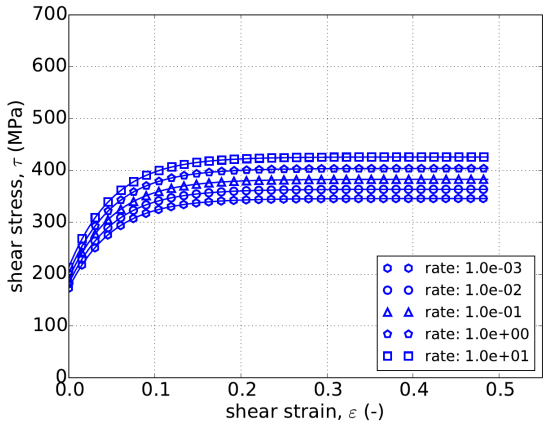

(c) Power-Law Hardening, a=20

Fig. 4.57 Stress-strain response of the Hosford plasticity model with rate *dependent*, power-law breakdown type hardening in pure shear with (a-c) Voce rate *independent* hardening. Solid lines are analytical results while open symbols are numerical.

4.14.4 User Guide

```
BEGIN PARAMETERS FOR MODEL HOSFORD_PLASTICITY
  #
  # Elastic constants
  #
  YOUNGS MODULUS = <real>
  POISSONS RATIO = <real>
  SHEAR MODULUS  = <real>
  BULK MODULUS   = <real>
  LAMBDA         = <real>
  TWO MU         = <real>
  #
  # Yield surface parameters
  #
  YIELD STRESS = <real>
  A            = <real> (4.0)
```

```
#
  #
  # Hardening model
  #
  HARDENING MODEL = LINEAR | POWER_LAW | VOCE | USER_DEFINED |
  FLOW_STRESS | DECOUPLED_FLOW_STRESS | JOHNSON_COOK |
  POWER_LAW_BREAKDOWN
  #
  # Linear hardening
  #
  HARDENING MODULUS = <real>
  #
  # Power-law hardening
  #
  HARDENING CONSTANT = <real>
  HARDENING EXPONENT = <real> (0.5)
  LUDERS STRAIN      = <real> (0.0)
  #
  # Voce hardening
  #
  HARDENING MODULUS       = <real>
  EXPONENTIAL COEFFICIENT = <real>
  #
  # Johnson-Cook hardening
  #
  HARDENING FUNCTION = <string>hardening_function_name
  RATE CONSTANT      = <real>
  REFERENCE RATE     = <real>
```

(continues on next page)

(continued from previous page)

```
  #
  # Power law breakdown hardening
  #
  HARDENING FUNCTION = <string>hardening_function_name
  RATE COEFFICIENT   = <real>
  RATE EXPONENT      = <real>
  # User defined hardening
  #
  HARDENING FUNCTION = <string>hardening_function_name
  #
```

```
#
  #
  # Following Commands Pertain to Flow_Stress Hardening Model
  #
  #    -  Isotropic Hardening model
  #
  ISOTROPIC HARDENING MODEL = LINEAR | POWER_LAW | VOCE |
                              USER_DEFINED
  #
  # Specifications for Linear, Power-law, and Voce same as above
  #
  # User defined hardening
  #
  ISOTROPIC HARDENING FUNCTION = <string>iso_hardening_fun_name
  #
  #     - Rate dependence
  #
  RATE MULTIPLIER = JOHNSON_COOK | POWER_LAW_BREAKDOWN |
     USER_DEFINED | RATE_INDEPENDENT (RATE_INDEPENDENT)
  #
  # Specifications for Johnson-Cook, Power-law-breakdown
  #     same as before EXCEPT no need to specify a
  #     hardening function
  #
  # User defined rate multiplier
  #
  RATE MULTIPLIER FUNCTION = <string> rate_mult_function_name
  #
  #     - Temperature dependence
  #
  TEMPERATURE MULTIPLIER = JOHNSON_COOK | USER_DEFINED |
     TEMPERATURE_INDEPENDENT (TEMPERATURE_INDEPENDENT)
  #
  #  Johnson-Cook temperature dependence
```

(continues on next page)

(continued from previous page)

```
  #
  MELTING TEMPERATURE   = <real>
  REFERENCE TEMPERATURE = <real>
  TEMPERATURE EXPONENT  = <real>
  #
  #  User-defined temperature dependence
  TEMPERATURE MULTIPLIER FUNCTION = <string>temp_mult_function_name
  #
  # Following Commands Pertain to Decoupled_Flow_Stress Hardening Model
  #
  #    -  Isotropic Hardening model
  #
  ISOTROPIC HARDENING MODEL = LINEAR | POWER_LAW | VOCE | USER_DEFINED
  #
  # Specifications for Linear, Power-law, and Voce same as above
  #
  # User defined hardening
  #
  ISOTROPIC HARDENING FUNCTION = <string>isotropic_hardening_function_
↪name
  #
  #     - Rate dependence
  #
  YIELD RATE MULTIPLIER = JOHNSON_COOK | POWER_LAW_BREAKDOWN |
              USER_DEFINED | RATE_INDEPENDENT (RATE_INDEPENDENT)
  #
  # Specifications for Johnson-Cook, Power-law-breakdown same as before
  #     EXCEPT no need to specify a hardening function
  #     AND should be preceded by YIELD
  #
  #     As an example for Johnson-Cook yield rate dependence,
  #
  YIELD RATE CONSTANT  = <real>
  YIELD REFERENCE RATE = <real>
  #
  # User defined rate multiplier
  #
  YIELD RATE MULTIPLIER FUNCTION = <string>yield_rate_mult_function_
↪name
  #
  HARDENING_RATE MULTIPLIER = JOHNSON_COOK | POWER_LAW_BREAKDOWN |
              USER_DEFINED | RATE_INDEPENDENT (RATE_INDEPENDENT)
  #
  #     Syntax same as for yield parameters but with a HARDENING prefix
  #
```

(continues on next page)

(continued from previous page)

```
  #     - Temperature dependence
  #
  YIELD TEMPERATURE MULTIPLIER = JOHNSON_COOK | USER_DEFINED |
            TEMPERATURE_INDEPENDENT (TEMPERATURE_INDEPENDENT)
  #
  #  Johnson-Cook temperature dependence
  #
  YIELD MELTING TEMPERATURE   = <real>
  YIELD REFERENCE TEMPERATURE = <real>
  YIELD TEMPERATURE EXPONENT  = <real>
  #
  #  User-defined temperature dependence
  YIELD TEMPERATURE MULTIPLIER FUNCTION = <string>yield_temp_mult_fun_
↪name
  #
  HARDENING TEMPERATURE MULTIPLIER = JOHNSON_COOK | USER_DEFINED |
            TEMPERATURE_INDEPENDENT (TEMPERATURE_INDEPENDENT)
  #
  #   Syntax for hardening constants same as for yield but
  #            with HARDENING prefix
```

```
#
  #
  # Optional Failure Definitions
  #    Following only need to be defined if intend to use failure model
  #
  FAILURE MODEL = TEARING_PARAMETER | JOHNSON_COOK_FAILURE | WILKINS
                  | MODULAR_FAILURE | MODULAR_BCJ_FAILURE

  CRITICAL FAILURE PARAMETER = <real>
  #
  # TEARING_PARAMETER Failure model definitions
  #
  TEARING PARAMETER EXPONENT = <real>
  #
  # JOHNSON_COOK_FAILURE Failure model definitions
  #
  JOHNSON COOK D1       = <real>
  JOHNSON COOK D2       = <real>
  JOHNSON COOK D3       = <real>
  JOHNSON COOK D4       = <real>
  JOHNSON COOK D5       = <real>
  #
  #Following Johnson-Cook parameters can only be defined once.  As␣
↪such, only
```

(continues on next page)

(continued from previous page)

```
  #  needed if not previously defined via Johnson-Cook multipliers
  #  w/ flow-stress hardening.  Does need to be defined
  #  w/ Decoupled Flow Stress
  #
  REFERENCE RATE        = <real>
  REFERENCE TEMPERATURE = <real>
  MELTING TEMPERATURE   = <real>
  #
  # WILKINS Failure model definitions
  #
  WILKINS ALPHA    = <real>
  WILKINS BETA     = <real>
  WILKINS PRESSURE = <real>
  #
  #  MODULAR_FAILURE Failure model definitions
  #
  PRESSURE MULTIPLIER         = PRESSURE_INDEPENDENT | WILKINS
                                | USER_DEFINED (PRESSURE_INDEPENDENT)
  LODE ANGLE MULTIPLIER       = LODE_ANGLE_INDEPENDENT |
                                WILKINS (LODE_ANGLE_INDEPENDENT)
  TRIAXIALITY MULTIPLIER      = TRIAXIALITY_INDEPENDENT | JOHNSON_COOK
                                | USER_DEFINED (TRIAXIALITY_
↪INDEPENDENT)
  RATE FAIL MULTIPLIER        = RATE_INDEPENDENT | JOHNSON_COOK
                                | USER_DEFINED (RATE_INDEPENDENT)
  TEMPERATURE FAIL MULTIPLIER = TEMPERATURE_INDEPENDENT | JOHNSON_COOK
                                | USER_DEFINED (TEMPERATURE_
↪INDEPENDENT)
  #
  # Individual multiplier definitions
  #
  PRESSURE MULTIPLIER = WILKINS
  WILKINS ALPHA       = <real>
  WILKINS PRESSURE    = <real>
  #
  PRESSURE MULTIPLIER = USER_DEFINED
  PRESSURE MULTIPLIER FUNCTION = <string> pressure_multiplier_fun_name
  #
  LODE ANGLE MULTIPLIER = WILKINS
  WILKINS BETA          = <real>
  #
  TRIAXIALITY MULTIPLIER = JOHNSON_COOK
  JOHNSON COOK D1        = <real>
  JOHNSON COOK D2        = <real>
  JOHNSON COOK D3        = <real>
```

(continues on next page)

(continued from previous page)

```
  #
  TRIAXIALITY MULTIPLIER = USER_DEFINED
  TRIAXIALITY MULTIPLIER FUNCTION = <string> triaxiality_multiplier_
↪fun_name
  #
  RATE FAIL MULTIPLIER = JOHNSON_COOK
  JOHNSON COOK D4      = <real>
  # REFERENCE RATE should only be added if not previously defined
  REFERENCE RATE       = <real>
  #
  RATE FAIL MULTIPLIER = USER_DEFINED
  RATE FAIL MULTIPLIER FUNCTION = <string> rate_fail_multiplier_fun_
↪name
  #
  TEMPERATURE FAIL MULTIPLIER = JOHNSON_COOK
  JOHNSON COOK D5             = <real>
  # JC Temperatures should only be defined if not previously given
  REFERENCE TEMPERATURE       = <real>
  MELTING TEMPERATURE         = <real>
  #
  TEMPERATURE FAIL MULTIPLIER          = USER_DEFINED
  TEMPERATURE FAIL MULTIPLIER FUNCTION = <string> temp_multiplier_fun_
↪name
  #
  # MODULAR_BCJ_FAILURE Failure model definitions
  #
  INITIAL DAMAGE    = <real>
  INITIAL VOID SIZE = <real>
  DAMAGE BETA       = <real> (0.5)
  GROWTH MODEL      = COCKS_ASHBY | NO_GROWTH (NO_GROWTH)
  NUCLEATION MODEL  = HORSTEMEYER_GOKHALE | CHU_NEEDLEMAN_STRAIN
                    | NO_NUCLEATION (NO_NUCLEATION)
  #
  GROWTH RATE FAIL MULTIPLIER        = JOHNSON_COOK | USER_DEFINED
                                     | RATE_INDEPENDENT
                                     (RATE_INDEPENDENT)
  GROWTH TEMPERATURE FAIL MULTIPLIER = JOHNSON_COOK | USER_DEFINED
                                     | TEMPERATURE_INDEPENDENT
                                     (TEMPERATURE_INDEPENDENT)
  #
  NUCLEATION RATE FAIL MULTIPLIER        = JOHNSON_COOK | USER_DEFINED
                                         | RATE_INDEPENDENT
                                         (RATE_INDEPENDENT)
  NUCLEATION TEMPERATURE FAIL MULTIPLIER = JOHNSON_COOK | USER_DEFINED
                                         | TEMPERATURE_INDEPENDENT
```

(continues on next page)

(continued from previous page)

```
                                                    (TEMPERATURE_INDEPENDENT)
  #
  # Definitions for individual growth and nucleation models
  #
  GROWTH MODEL = COCKS_ASHBY
  DAMAGE EXPONENT = <real> (0.5)
  #
  NUCLEATION MODEL      = HORSTEMEYER_GOKHALE
  NUCLEATION PARAMETER1 = <real> (0.0)
  NUCLEATION PARAMETER2 = <real> (0.0)
  NUCLEATION PARAMETER3 = <real> (0.0)
  #
  NUCLEATION MODEL          = CHU_NEEDLEMAN_STRAIN
  NUCLEATION AMPLITUDE      = <real>
  MEAN NUCLEATION STRAIN    = <real>
  NUCLEATION STRAIN STD DEV = <real>
  #
  # Definitions for rate and temperature fail multiplier
  #   Note: only showing definitions for growth.
  #    Nucleation terms are the same just with NUCLEATION instead
  #    of GROWTH
  #
  GROWTH RATE FAIL MULTIPLIER = JOHNSON_COOK
  GROWTH JOHNSON COOK D4      = <real>
  GROWTH REFERENCE RATE       = <real>
  #
  GROWTH RATE FAIL MULTIPLIER          = USER_DEFINED
  GROWTH RATE FAIL MULTIPLIER FUNCTION = <string> growth_rate_fail_
↪mult_func
  #
  GROWTH TEMPERATURE FAIL MULTIPLIER = JOHNSON_COOK
  GROWTH JOHNSON COOK D5             = <real>
  GROWTH REFERENCE TEMPERATURE       = <real>
  GROWTH MELTING TEMPERATURE         = <real>
  #
  GROWTH TEMPERATURE FAIL MULTIPLIER          = USER_DEFINED
  GROWTH TEMPERATURE FAIL MULTIPLIER FUNCTION = <string> temp_fail_
↪mult_func
  #
```

```
#
  #
  # Optional Adiabatic Heating/Thermal Softening  Definitions
  #    Following only need to be defined if intend to use failure model
  #
```

(continues on next page)

(continued from previous page)

```
  THERMAL SOFTENING MODEL = ADIABATIC | COUPLED
  #
  SPECIFIC HEAT = <real> # not needed for COUPLED
  BETA_TQ       = <real>
```

```
END [PARAMETERS FOR MODEL HOSFORD_PLASTICITY]
```

In the command blocks that define the Hosford plasticity model:

- The reference nominal yield stress, $\bar{\sigma}$, is defined with the `YIELD STRESS` command line.
- The yield surface exponent, a, is defined with the `A` command line.
- The type of hardening law is defined with the `HARDENING MODEL` command line, other hardening commands then define the specific shape of that hardening curve.
- The hardening modulus for a linear hardening model is defined with the `HARDENING MODULUS` command line.
- The hardening constant for a power law hardening model is defined with the `HARDENING CONSTANT` command line.
- The hardening exponent for a power law hardening model is defined with the `HARDENING EXPONENT` command line.
- The Luders strain for a power law hardening model is defined with the `LUDERS STRAIN` command line.
- The hardening function for a user defined hardening model is defined with the `HARDENING FUNCTION` command line.
- The shape of the spline for the spline based hardening is defined by the `CUBIC SPLINE TYPE`, `CARDINAL PARAMETER`, `KNOT EQPS`, and `KNOT STRESS` command lines.

Output variables available for this model are listed in Table 4.19.

Table 4.19 State Variables for HOSFORD PLASTICITY Model

Name	Description
EQPS	equivalent plastic strain, $\bar{\varepsilon}^p$
EQDOT	equivalent plastic strain rate, $\dot{\bar{\varepsilon}}^p$
SEFF	effective stress, ϕ
TENSILE_EQPS	tensile equivalent plastic strain, $\bar{\varepsilon}_t^p$
DAMAGE	damage, ϕ
VOID_COUNT	void count, η
VOID_SIZE	void size, υ
DAMAGE_DOT	damage rate, $\dot{\phi}$
VOID_COUNT_DOT	void count rate, $\dot{\eta}$
PLASTIC_WORK_HEAT_RATE	plastic work heat rate, $\dot{Q}^p$

4.15 Hill Plasticity Model

4.15.1 Theory

The Hill plasticity model is similar to other plasticity models except that it is not isotropic. It is a hypoelastic, rate-independent plasticity model. The rate form of the equation assumes an additive split of the rate of deformation into an elastic and plastic part

$$D_{ij} = D^{\mathrm{e}}_{ij} + D^{\mathrm{p}}_{ij}$$

The stress rate only depends on the elastic rate of deformation

$$\overset{\circ}{\sigma}_{ij} = \mathbb{C}_{ijkl} D^{\mathrm{e}}_{kl}$$

where $\mathbb{C}_{ijkl}$ are the components of the fourth-order, isotropic elasticity tensor.

The Hill plasticity model has an orthotropic yield surface that assumes orthogonal principal material directions. An example of this yield surface is presented below in Fig. 4.58 along with examples of two isotropic surfaces – the von Mises (J_2) and Hosford (with $a = 8$). The various surface parameters correspond to 2090-T3 aluminum and the specific Hill strengths are found in [88]. By comparing the Hill surface to the two isotropic surfaces, the impact of the anisotropy is clear. Additionally, substantial differences to the normals of the yield surfaces at points of intersection highlight the impact of the yield function selection on the resulting flow directions.

Like other plasticity models, the Hill yield surface, f, is written,

$$f\left(\sigma_{ij}, \bar{\varepsilon}^{p}\right) = \phi\left(\sigma_{ij}\right) - \bar{\sigma}\left(\bar{\varepsilon}^{p}\right) = 0,$$

with ϕ being the effective stress and $\bar{\sigma}$ is the current yield stress that may be dependent on rate and/or temperature. The Hill effective stress is essentially an orthotropic extension of the von Mises function. After accounting for plastic incompressibility and related constraints, there are six individual yield stresses: σ^{y}_{11}, σ^{y}_{22}, σ^{y}_{33}, τ^{y}_{12}, τ^{y}_{23}, and τ^{y}_{31}. These yield stresses correspond to 3 normal and 3 shear yield stresses. Written in terms of the components, the effective stress has the form,

$$\begin{aligned}\phi^2\left(\sigma_{ij}\right) = {} & F\left(\hat{\sigma}_{22} - \hat{\sigma}_{33}\right)^2 + G\left(\hat{\sigma}_{33} - \hat{\sigma}_{11}\right)^2 + H\left(\hat{\sigma}_{11} - \hat{\sigma}_{22}\right)^2 \\ & + 2L\hat{\sigma}^2_{23} + 2M\hat{\sigma}^2_{31} + 2N\hat{\sigma}^2_{12}.\end{aligned}$$

The coefficients F, G, H, L, M, and N were introduced by Hill. In terms of the yield stresses they are:

$$F = \frac{(\bar{\sigma})^2}{2}\left[\frac{1}{\left(\sigma^{y}_{22}\right)^2} + \frac{1}{\left(\sigma^{y}_{33}\right)^2} - \frac{1}{\left(\sigma^{y}_{11}\right)^2}\right] \quad ; \quad L = \frac{(\bar{\sigma})^2}{2}\left[\frac{1}{\left(\tau^{y}_{23}\right)^2}\right]$$

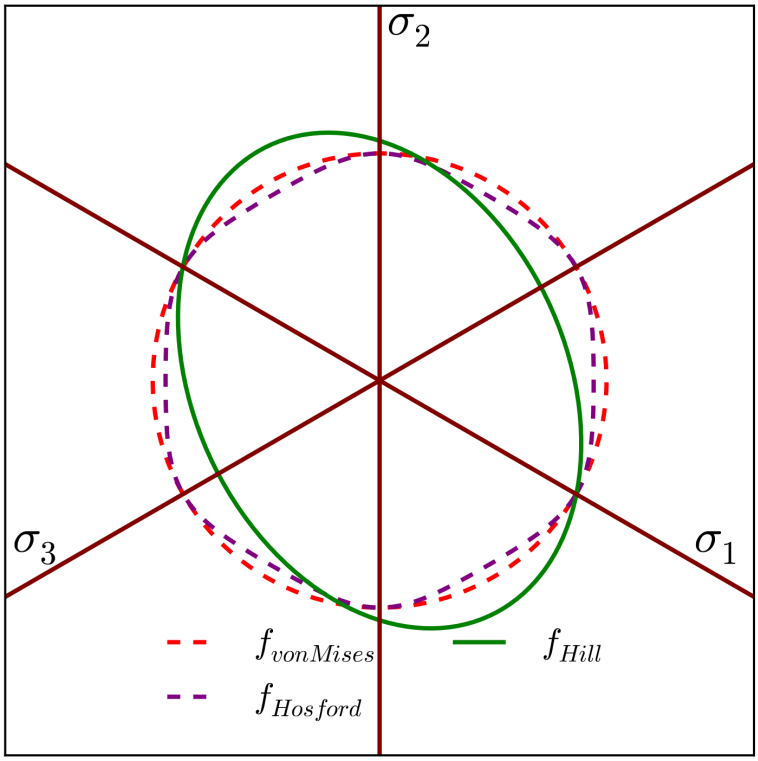

Fig. 4.58 Example anisotropic Hill yield surface, $f_{Hill}\left(\sigma_{ij}, \bar{\varepsilon}^p = 0\right)$, presented in the deviatoric π-plane fit to 2090-T3 aluminum. Comparison von Mises (J_2) and Hosford (with $a = 8$) surfaces are also presented.

$$G = \frac{(\bar{\sigma})^2}{2}\left[\frac{1}{\left(\sigma^y_{33}\right)^2} + \frac{1}{\left(\sigma^y_{11}\right)^2} - \frac{1}{\left(\sigma^y_{22}\right)^2}\right] \quad ; \quad M = \frac{(\bar{\sigma})^2}{2}\left[\frac{1}{\left(\tau^y_{31}\right)^2}\right]$$
$$H = \frac{(\bar{\sigma})^2}{2}\left[\frac{1}{\left(\sigma^y_{11}\right)^2} + \frac{1}{\left(\sigma^y_{22}\right)^2} - \frac{1}{\left(\sigma^y_{33}\right)^2}\right] \quad ; \quad N = \frac{(\bar{\sigma})^2}{2}\left[\frac{1}{\left(\tau^y_{12}\right)^2}\right]. \tag{4.43}$$

where $\bar{\sigma}$ is a reference yield stress.

Rather than input the six independent yield stresses, the ratios of the yield stresses to some reference yield stress are generally used as input. These ratios are

$$\begin{aligned} R_{11} &= \frac{\sigma^y_{11}}{\bar{\sigma}} \quad ; \quad R_{12} = \sqrt{3}\frac{\tau^y_{12}}{\bar{\sigma}} \\ R_{22} &= \frac{\sigma^y_{22}}{\bar{\sigma}} \quad ; \quad R_{23} = \sqrt{3}\frac{\tau^y_{23}}{\bar{\sigma}} \\ R_{33} &= \frac{\sigma^y_{33}}{\bar{\sigma}} \quad ; \quad R_{31} = \sqrt{3}\frac{\tau^y_{31}}{\bar{\sigma}}. \end{aligned} \tag{4.44}$$

These ratios are set up so that if $R_{ij} = 1$ then the yield surface is isotropic.

The orientation of the principal material axes with respect to the global Cartesian axes may be specified by the user. First, a rectangular or cylindrical reference coordinate system is defined. *Spherical coordinate systems are not currently implemented for the Hill model.* The material coordinate system can then be defined through two successive rotations about axes in the reference rectangular or cylindrical coordinate system. In the case of the cylindrical coordinate system this allows the principal material axes to vary point-wise in a given element block.

The plastic rate of deformation, as with the isotropic models, assumes associated flow

$$D^{\mathrm{p}}_{ij} = \dot{\gamma}\frac{\partial \phi}{\partial \sigma_{ij}}.$$

Given the form for ϕ, the consistency parameter, $\dot{\gamma}$ is equal to the rate of the equivalent plastic strain, $\dot{\bar{\varepsilon}}^p$.

For more information about the Hill plasticity model, consult [42]. Additional discussion on options for failure models and adiabatic heating may be found in [61], [62] and [60], respectively.

4.15.1.1 Plastic Hardening

Plastic hardening refers to increases in the flow stress, $\bar{\sigma}$, with plastic deformation. As such, hardening is described via a functional relationship between the flow stress and isotropic hardening variable (effective plastic strain), $\bar{\sigma}\left(\bar{\varepsilon}^p\right)$. Over the course of nearly a century of work in metal plasticity, a variety of relationships have been proposed to describe the interactions associated with different physical interpretations, deformation mechanisms, and materials. To enable the utilization of the same plasticity models for different material systems, a modular implementation of plastic hardening has been adopted such that the analyst may select different hardening models from the input deck thereby avoiding any code changes or user subroutines. In this section, additional details are given for the different models to enable the user to select the appropriate choice of model. Note, the models being discussed here are only for *isotropic* hardening in which the yield surface expands. *Kinematic* hardening in which the yield surface translates in stress-space with deformation and *distortional* hardening where the shape of the yield surface changes shape with deformation are not treated. For a larger discussion of the phenomenology and history of different hardening types, the reader is referred to [42], [57], [64].

Given the ubiquitous nature of these hardening laws in computational plasticity, some (if not most) of this material may be found elsewhere in this manual. Nonetheless, the discussion is repeated here for the convenience of the reader.

Linear

Linear hardening is conceptually the simplest model available in LAMÉ. As the name implies, a linear relationship is assumed between the hardening variable, $\bar{\varepsilon}^p$, and flow stress. The hardening modulus, H', is a constant giving the rate of change of flow stress with plastic flow. The flow stress expression may therefore be written,

$$\bar{\sigma} = \sigma_y + H'\bar{\varepsilon}^p.$$

The simplicity of the model is its main feature as the constant slope,

$$\frac{d\bar{\sigma}}{d\bar{\varepsilon}^p} = H',$$

makes the model attractive for analytical models and cheap for computational implementations (*e.g.* radial return algorithms require only a single correction step). Unfortunately, the simplicity of the representation also means that it has limited predictive capabilities and can lead to overly stiff responses.

Power Law

Another common expression for isotropic hardening is the power-law hardening model. Due to its prevalence, a dedicated `ELASTIC-PLASTIC POWER LAW HARDENING` model may be found in LAMÉ (see Section 4.8.1). This expression is given as,

$$\bar{\sigma} = \sigma_y + A < \bar{\varepsilon}^p - \varepsilon_L >^n,$$

in which $< \cdot >$ are Macaulay brackets, ε_L is the Luders strain, A is a fitting constant, and n is an exponent typically taken such that $0 < n \leq 1$. The Luders strain is a positive, constant strain value (defaulted to zero) giving an initially perfectly plastic response in the plastic deformation domain (see Fig. 4.20). The derivative is then simply,

$$\frac{d\bar{\sigma}}{d\bar{\varepsilon}^p} = nA < \bar{\varepsilon}^p - \varepsilon_L >^{(n-1)} .$$

Note, one difficulty in such an implementation is that when the effective equivalent plastic strain is zero, numerical difficulties may arise in evaluating the derivative and necessitate special treatment of the case.

Voce

The Voce hardening model (sometimes referred to as a saturation model) uses a decaying exponential function of the equivalent plastic strain such that the hardening eventually saturates to a specified value (thus the name). Such a relationship has been observed in some structural metals giving rise to the popularity of the model. The hardening response is given as,

$$\bar{\sigma} = \sigma_y + A \left(1 - \exp\left(-n\bar{\varepsilon}^p\right)\right),$$

in which A is a fitting constant and n is a fitting exponent controlling how quickly the hardening saturates. Importantly, the derivative is written as,

$$\frac{d\bar{\sigma}}{d\bar{\varepsilon}^p} = nA \exp\left(-n\bar{\varepsilon}^p\right),$$

and is well defined everywhere giving the selected form an advantage over the aforementioned power law model.

Johnson-Cook

The Johnson-Cook hardening model is a variant of the classical Johnson-Cook [48], [49] expression. In this instance, the temperature-dependence is neglected to focus on the *rate-dependent* capabilities while allowing for arbitrary isotropic hardening forms via the use of a user-defined hardening function. With these assumptions, the flow stress may be written as,

$$\bar{\sigma} = \tilde{\sigma}_y \left(\bar{\varepsilon}^p\right) \left[1 + C \left\langle \ln\left(\frac{\dot{\bar{\varepsilon}}^p}{\dot{\varepsilon}_0}\right) \right\rangle\right],$$

in which $\tilde{\sigma}_y\left(\bar{\varepsilon}^p\right)$ is the user-specified rate-independent hardening function, C is a fitting constant and $\dot{\varepsilon}_0$ is a reference strain rate. The Macaulay brackets ensure the material behaves in a rate independent fashion when $\dot{\bar{\varepsilon}}^p < \dot{\varepsilon}_0$.

Power Law Breakdown

Like the Johnson-Cook formulation, the power-law breakdown model is also rate-dependent. Again, a multiplicative decomposition is assumed between isotropic hardening and the corresponding rate-dependence dependent. In this case, however, the functional form is derived from the analysis of Frost and Ashby [33] in which power-law relationships like those of the Johnson-Cook model cease to appropriately capture the physical response. The form used here is similar to the expression used by Brown and Bammann [16] and is written as,

$$\bar{\sigma} = \tilde{\sigma}_y\left(\bar{\varepsilon}^p\right)\left[1 + \operatorname{asinh}\left(\left(\frac{\dot{\bar{\varepsilon}}^p}{g}\right)^{(1/m)}\right)\right],$$

with $\tilde{\sigma}_y\left(\bar{\varepsilon}^p\right)$ being the user supplied rate independent expression, g is a model parameter related to the activation energy required to transition from climb to glide-controlled deformation, and m dictates the strength of the dependence.

4.15.1.2 Flow Stress

Unlike the previously described models, the flow-stress hardening method is less a specific physical representation and more a generalization of hardening behaviors to allow greater flexibility in separately describing isotropic hardening, rate-dependence, and temperature dependence. As such, the generic flow-stress definition of

$$\bar{\sigma}\left(\bar{\varepsilon}^p, \dot{\bar{\varepsilon}}^p, \theta\right) = \tilde{\sigma}_y\left(\bar{\varepsilon}^p\right)\hat{\sigma}\left(\dot{\bar{\varepsilon}}^p\right)\breve{\sigma}\left(\theta\right),$$

is used in which $\hat{\sigma}$ and $\breve{\sigma}$ are rate and temperature multipliers, respectively, that by default are unity (such that the response is rate and temperature independent). The isotropic hardening component, $\tilde{\sigma}_y$, is specified as,

$$\tilde{\sigma}_y = \sigma_y + K\left(\bar{\varepsilon}^p\right),$$

with σ_y being the constant yield stress and K is the isotropic hardening that is initially zero and a function of the equivalent plastic strain. A multiplicative decomposition such as this mirrors the general structure used by Johnson and Cook [48], [49] although greater flexibility is allowed in terms of the specific form of the rate and temperature multipliers.

Given the aforementioned defaults for rate and temperature dependence, the corresponding multipliers need not be specified. A representation for the isotropic hardening, however, *must* be specified and can be defined via linear, power-law, Voce, or user-defined representations. For the user-defined case, an *isotropic* hardening function is required and it must be highlighted that the

interpretation differs from the general user-defined hardening model. *In this case, as the specified function represents the isotropic hardening, it should start from zero – not yield.*

Although the flow-stress hardening model defaults to rate and temperature independent, a multiplier may be defined for either (or both) of the terms. For rate-dependence, either the previously discussed Johnson-Cook or power-law breakdown models or a user-defined multiplier may be used. For the user-defined capability, the multiplier should be input as a strictly positive function of the equivalent plastic strain rate with a value of one in the rate-independent limit.

In terms of temperature dependence, the multiplier may be specified given a Johnson-Cook dependency [48], [49],

$$\breve{\sigma}\left(\theta\right) = 1 - \left(\frac{\theta - \theta_{\text{ref}}}{\theta_{\text{melt}} - \theta_{\text{ref}}}\right)^{M},$$

with θ_{ref}, θ_{melt} and M being the reference temperature, melting temperature, and temperature exponent. The temperature multiplier may also be specified via a user defined function.

4.15.1.3 Decoupled Flow Stress

Like the flow-stress hardening method, the decoupled flow-stress hardening implementation is a generalization of the hardening behaviors to allow greater flexibility. In differentiating the two, for the decoupled model the rate and temperature dependence may be separately specified for the yield and hardening portions of the flow stress. As such, the generic flow-stress definition of

$$\bar{\sigma}\left(\bar{\varepsilon}^{p}, \dot{\bar{\varepsilon}}^{p}, \theta\right) = \sigma_{y}\hat{\sigma}_{\text{y}}\left(\dot{\bar{\varepsilon}}^{p}\right)\breve{\sigma}_{\text{y}}\left(\theta\right) + K\left(\bar{\varepsilon}^{p}\right)\hat{\sigma}_{\text{h}}\left(\dot{\bar{\varepsilon}}^{p}\right)\breve{\sigma}_{\text{h}}\left(\theta\right),$$

is used in which $\hat{\sigma}$ and $\breve{\sigma}$ are rate and temperature multipliers, respectively, that by default are unity (such that the response is rate and temperature independent) with subscripts y and h denoting functions associated with yield and hardening. The isotropic hardening is described by $K\left(\bar{\varepsilon}^{p}\right)$ and σ_{y} is the constant initial yield stress. It may also be seen that if the yield and hardening dependencies are the same ($\hat{\sigma}_{\text{y}} = \hat{\sigma}_{\text{h}}$ and $\breve{\sigma}_{\text{y}} = \breve{\sigma}_{\text{h}}$) the decoupled flow stress model reduces to that of the flow stress case and mirrors the general structure of the Johnson-Cook model [48], [49].

Given the aforementioned defaults for rate and temperature dependence, the corresponding multipliers need not be specified. A representation for the isotropic hardening, however, *must* be specified and can be defined via linear, power-law, Voce, or user-defined representations. For the user-defined case, an *isotropic* hardening function should be used and it must be highlighted that the interpretation differs from the general user-defined hardening model. *In this case, as the specified function represents the isotropic hardening, it should start from zero – not yield.*

Although the decoupled flow-stress hardening model defaults to rate and temperature independent, a multiplier may be defined for any of the terms. For rate-dependence, either the previously discussed Johnson-Cook or power-law breakdown models or a user-defined multiplier may be used. For the user-defined capability, the multiplier should be input as a strictly positive function of the equivalent plastic strain rate with a value of one in the rate-independent limit.

In terms of temperature dependence, the multiplier may be specified given a Johnson-Cook dependency [48], [49],

$$\breve{\sigma}\left(\theta\right) = 1 - \left(\frac{\theta - \theta_{\text{ref}}}{\theta_{\text{melt}} - \theta_{\text{ref}}}\right)^{M},$$

where θ_{ref}, θ_{melt}, and M are the reference temperature, melting temperature, and temperature exponent. A temperature multiplier may also be specified via a user defined function.

4.15.2 Implementation

The Hill plasticity model uses a predictor-corrector algorithm for integrating the constitutive model. Given a rate of deformation, ifindex d_{ij}else **d**fi, and a time step, Δt, a trial stress state is calculated based on an elastic response

$$T_{ij}^{tr} = T_{ij}^{n} + \Delta t\, \mathbb{C}_{ijkl} d_{kl}$$

If the trial stress state lies outside the yield surface, i.e. if ifindex $\phi(T_{ij}^{tr}) > \bar{\sigma}$else $\phi(\mathbf{T}^{tr}) > \bar{\sigma}$fi, then the model uses a backward Euler algorithm to return the stress to the yield surface. There are two equations that need to be solved. To ensure that the plastic strain increment is in the correct direction we have

$$R_{ij}^{p} = \Delta t\, d_{ij}^{p} - \Delta\gamma \frac{\partial \phi}{\partial T_{ij}} = 0$$

while to ensure that the stress state is on the yield surface we require

$$f = \phi\left(T_{ij}\right) - \bar{\sigma}\left(\bar{\varepsilon}^{p}\right) = 0$$

The primary algorithm for solving these equations is a Newton-Raphson algorithm. Using $\Delta\gamma$ (which is equal to $\Delta\bar{\varepsilon}^{p}$) and ifindex T_{ij}else **T**fi as the solution variables, we set up an iterative algorithm where

$$\Delta\gamma^{(k+1)} = \Delta\gamma^{(k)} + \Delta\left(\Delta\gamma\right)$$

$$T_{ij}^{(k+1)} = T_{ij}^{(k)} + \Delta T_{ij}$$

where $\Delta\gamma^{(0)} = 0$ and ifindex $T_{ij}^{(0)} = T_{ij}^{tr}$else $\mathbf{T}^{(0)} = \mathbf{T}^{tr}$fi and

$$\Delta t\, d_{ij}^{p} = \mathbb{C}_{ijkl}^{-1}\left(T_{kl}^{tr} - T_{kl}\right)$$

The Newton-Raphson algorithm gives

$$\Delta\left(\Delta\gamma\right) = \frac{f^{(k)} - R_{ij}^{(k)}\, \mathcal{L}_{ijkl}^{(k)} \dfrac{\partial \phi^{(k)}}{\partial T_{kl}}}{\dfrac{\partial \phi^{(k)}}{\partial T_{ij}}\, \mathcal{L}_{ijkl}^{(k)} \dfrac{\partial \phi^{(k)}}{\partial T_{kl}} + H'^{(k)}}$$

$$\Delta T_{ij} = -\mathcal{L}_{ijkl}^{(k)}\left(R_{kl}^{(k)} + \Delta\left(\Delta\gamma\right)\frac{\partial \phi^{(k)}}{\partial T_{kl}}\right)$$

A straightforward Newton-Raphson algorithm does not always converge, so the return mapping algorithm is augmented with a line search algorithm

$$\Delta\gamma^{(k+1)} = \Delta\gamma^{(k)} + \alpha\Delta\left(\Delta\gamma\right)$$

$$T_{ij}^{(k+1)} = T_{ij}^{(k)} + \alpha\Delta T_{ij}$$

where $\alpha \in (0, 1]$ is the line search parameter which is determined from certain convergence considerations. If $\alpha = 1$ then the Newton-Raphson algorithm is recovered. The line search algorithm greatly increases the reliability of the return mapping algorithm.

4.15.3 Verification

The Hill plasticity material model is verified for a number of loading conditions.

Additional verification exercises for the various failure models and adiabatic heating capabilities may be found in [61], [62] and [60], respectively.

The elastic properties used in these analyses are $E = 70$ GPa and $\nu = 0.25$. The parameters that are used to define the yield surface are

$$R_{11} = 1.000680 \quad ; \quad R_{12} = 0.909194$$

$$R_{22} = 0.906397 \quad ; \quad R_{23} = 0.851434$$

$$R_{33} = 1.027380 \quad ; \quad R_{31} = 0.799066$$

These parameters correspond to a parameterization of the Barlat model for 2090-T3 aluminum [9] that is fit to the Hill model. The hardening law used for the model is a Voce law with the following form

$$\bar{\sigma}\left(\bar{\varepsilon}^{p}\right) = \sigma_{y} + A\left(1 - \exp(-n\bar{\varepsilon}^{p})\right)$$

For these calculations $\sigma_y = 200$ MPa, $A = 200$ MPa, and $n = 20$. Finally, the coordinate system used in these calculations is a rectangular coordinate system with the e_1, e_2, e_3 axes aligned with the x, y, z axes.

4.15.3.1 Uniaxial Stress

The Hill plasticity model is tested in uniaxial tension along the three orthogonal principal material directions. The tests looks at the stress, the strain, and the equivalent plastic strain and compares these values against analytical results for the same problem. In this verification problem only the normal stresses are needed, and the shear terms are not exercised. Therefore, the parameters R_{12},

R_{23}, and R_{31} are not used in the problem and a separate verification test will be needed for shear response.

The model is tested in uniaxial stress in the x, y, and z directions, giving three test problems. Each problem can be formulated exactly the same. For the description of the test we will only look at loading in the x direction (x_1 direction).

For the uniaxial stress problem, the only non-zero stress component is σ_{11}. In the analysis that follows $\sigma_{11} = \sigma$. There are three non-zero strain components, ε_{11}, ε_{22}, and ε_{33}. In the analysis that follows $\varepsilon_{11} = \varepsilon$. Furthermore, the axial elastic strain, $\varepsilon^{\mathrm{e}}_{11} = \sigma/E$ will be denoted by ε^{e}.

Axial Stresses

The uniaxial stress calculated by the model in Adagio is compared to analytical solutions. For uniaxial loading in the e_1 direction, the effective stress is

$$\phi = \frac{\sigma}{R_{11}}$$

If the stress state is on the yield surface, then $\phi = \bar{\sigma}\,(\bar{\varepsilon}^p)$, so the axial stress, as a function of the hardening function, is

$$\sigma = R_{kk}\bar{\sigma}\,(\bar{\varepsilon}^p) \tag{4.45}$$

This shows that the stress state can be calculated from the hardening law and the anisotropy parameters.

To evaluate the axial stress we need the equivalent plastic strain as a function of the axial strain. If we equate the rate of plastic work we get

$$\bar{\sigma}\dot{\bar{\varepsilon}}^p = \sigma\,(\dot{\varepsilon} - \dot{\varepsilon}^{\mathrm{e}}) \quad \rightarrow \quad \dot{\bar{\varepsilon}}^p = R_{11}\,(\dot{\varepsilon} - \dot{\varepsilon}^{\mathrm{e}})$$

which, when integrated, gives us an implicit equation for the equivalent plastic strain

$$\bar{\varepsilon}^p = R_{11}\left(\varepsilon - R_{11}\frac{\bar{\sigma}(\bar{\varepsilon}^p)}{E}\right) \tag{4.46}$$

The equivalent plastic strain can then be used in (4.45) to find the axial stress, σ.

The axial stresses for loading in the other directions can be found the same way. The axial stresses for loading in the e_1, e_2, and e_3 directions are shown in Fig. 4.59.

Lateral Strains

For the lateral strains we need the plastic strains and therefore the normal to the yield surface. The components of the normal to the yield surface are

$$\frac{\partial\phi}{\partial\sigma_{11}} = \frac{1}{R_{11}} \quad ; \quad \frac{\partial\phi}{\partial\sigma_{22}} = -HR_{11} \quad ; \quad \frac{\partial\phi}{\partial\sigma_{33}} = -GR_{11}$$

The elastic axial and lateral strain components are

$$\varepsilon^{\mathrm{e}}_{11} = \frac{\sigma}{E} = \varepsilon^{\mathrm{e}} \quad ; \quad \varepsilon^{\mathrm{e}}_{22} = \varepsilon^{\mathrm{e}}_{33} = -\nu\frac{\sigma}{E} = -\nu\varepsilon^{\mathrm{e}}$$

The plastic axial strain component is

$$\varepsilon^{\mathrm{p}}_{11} = \varepsilon_{11} - \frac{\sigma}{E} = \varepsilon - \varepsilon^{\mathrm{e}}$$

which comes from the additive decomposition of the strain rates. Using the equivalent plastic strain (4.46) we can find the lateral plastic strain components

$$\varepsilon^{\mathrm{p}}_{22} = -\left(\varepsilon - \varepsilon^{\mathrm{e}}\right) HR^2_{11} \quad ; \quad \varepsilon^{\mathrm{p}}_{33} = -\left(\varepsilon - \varepsilon^{\mathrm{e}}\right) GR^2_{11}$$

The lateral *total* stain components prior to yield are $\varepsilon_{22} = \varepsilon_{33} = -\nu\varepsilon$. After yield they are

$$\varepsilon_{22} = -\nu\varepsilon^{\mathrm{e}} - HR_{11}\bar{\varepsilon}^p$$

$$\varepsilon_{33} = -\nu\varepsilon^{\mathrm{e}} - GR_{11}\bar{\varepsilon}^p$$

where $\varepsilon^{\mathrm{e}} = \sigma/E$.

For loading in the y direction, a similar analysis leads to the lateral strains, after yield

$$\varepsilon_{33} = -\nu\varepsilon^{\mathrm{e}} - FR_{22}\bar{\varepsilon}^p$$

$$\varepsilon_{11} = -\nu\varepsilon^{\mathrm{e}} - HR_{22}\bar{\varepsilon}^p$$

For loading in the z direction, a similar analysis leads to the lateral strains, after yield

$$\varepsilon_{11} = -\nu\varepsilon^{\mathrm{e}} - GR_{33}\bar{\varepsilon}^p$$

$$\varepsilon_{22} = -\nu\varepsilon^{\mathrm{e}} - FR_{33}\bar{\varepsilon}^p$$

Results for all three loadings are shown in Fig. 4.60, Fig. 4.61, and Fig. 4.62.

4.15.3.2 Pure Shear

The shear stress calculated by the Hill plasticity model in Adagio is compared to analytical solutions. Without loss of generality we will look at solutions for pure shear with respect to the e_1-e_2 axes. Solutions for shear with respect to the other axes will be similar. In what follows, the only non-zero shear stress will be σ_{12}, and the only non-zero shear strain will be ε_{12} In general, for pure shear with respect to the e_1-e_2 axes, the effective stress is

$$\phi = \sqrt{3}\,\frac{\sigma_{12}}{R_{12}}$$

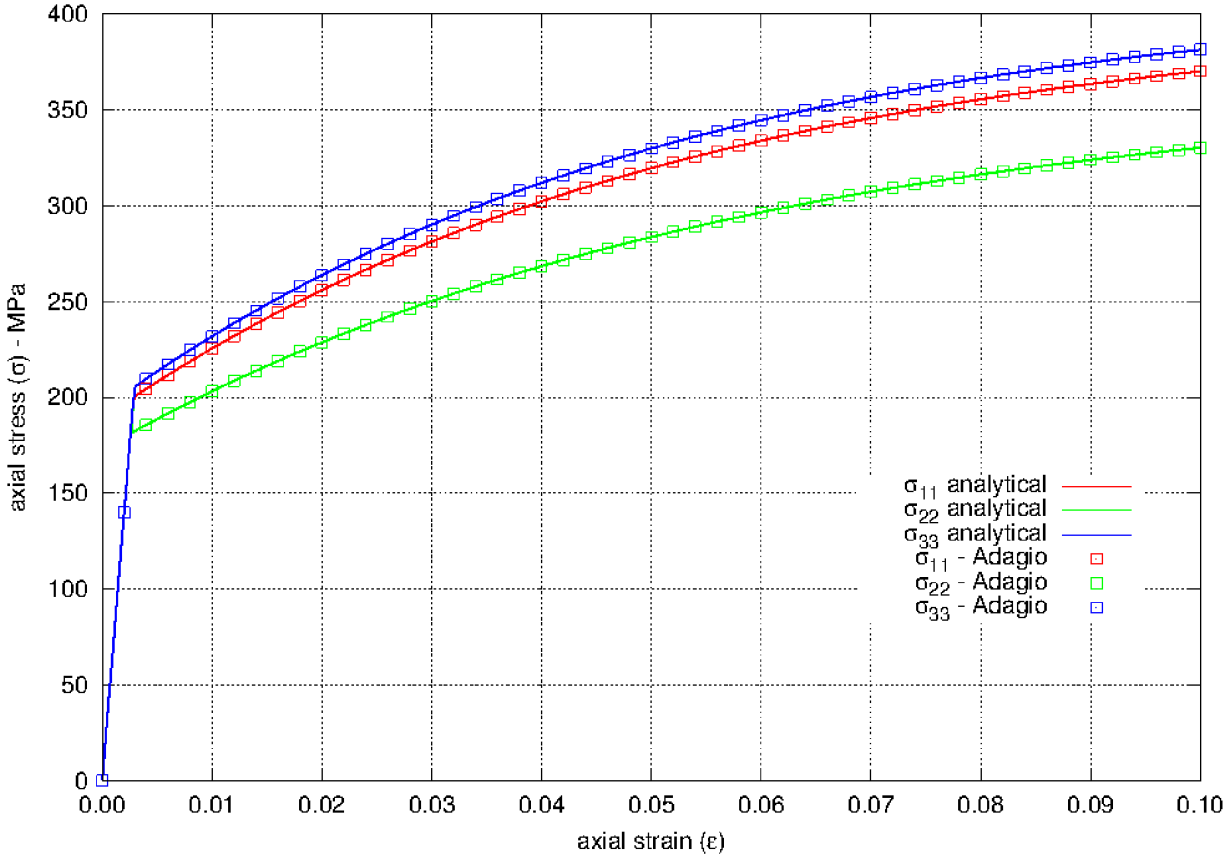

Fig. 4.59 Stresses when loading in the e_1, e_2, and e_3-directions using the Hill model with a Voce hardening law.

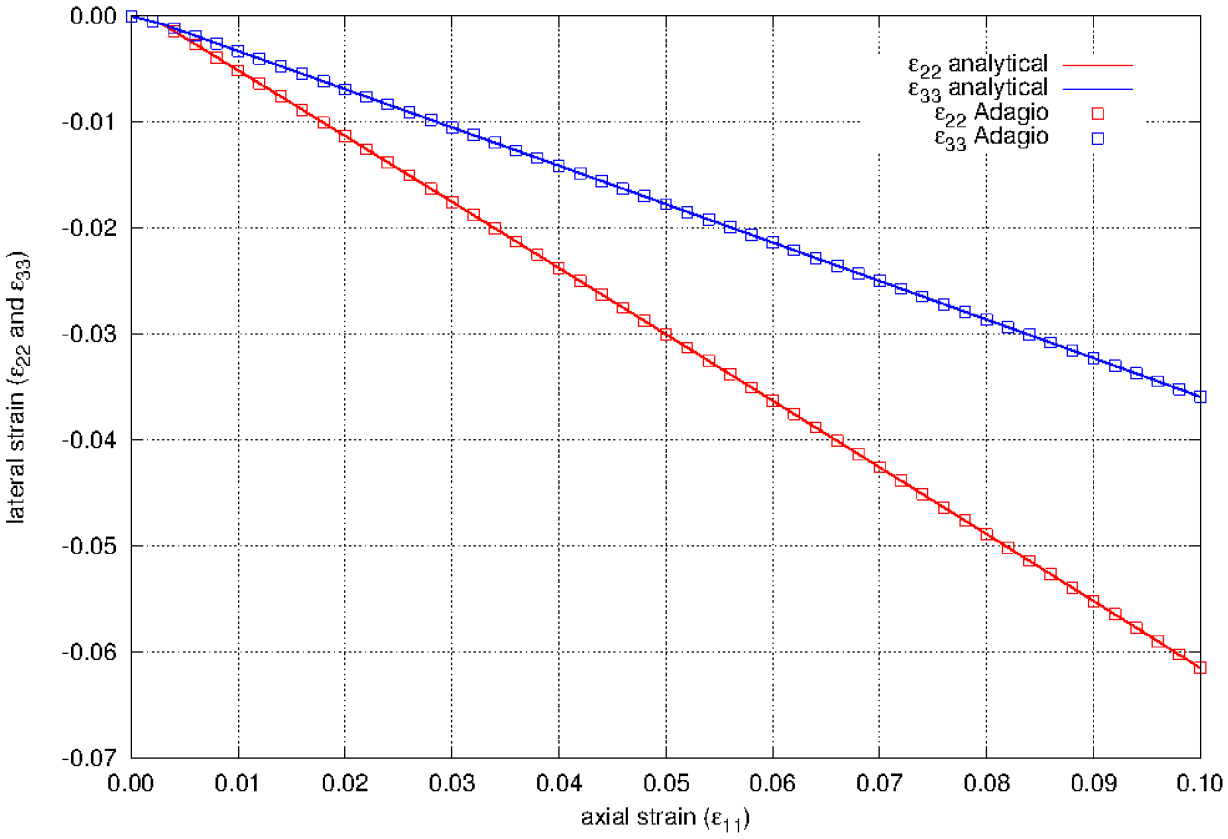

Fig. 4.60 Lateral strain as a function of axial strain for the Hill model of 2090-T3 aluminum. Loading is in the e_1-direction and the hardening law is a Voce law.

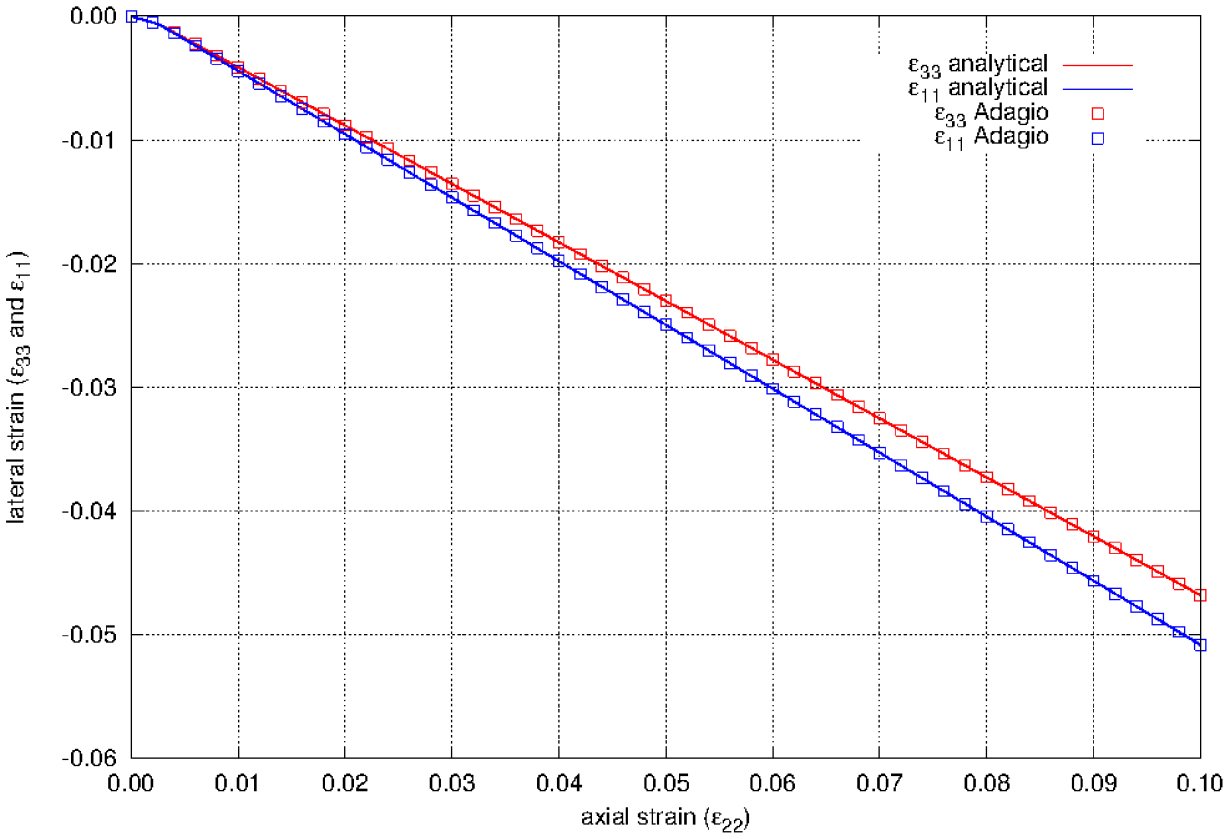

Fig. 4.61 Lateral strain as a function of axial strain for the Hill model of 2090-T3 aluminum. Loading is in the e_2-direction and the hardening law is a Voce law.

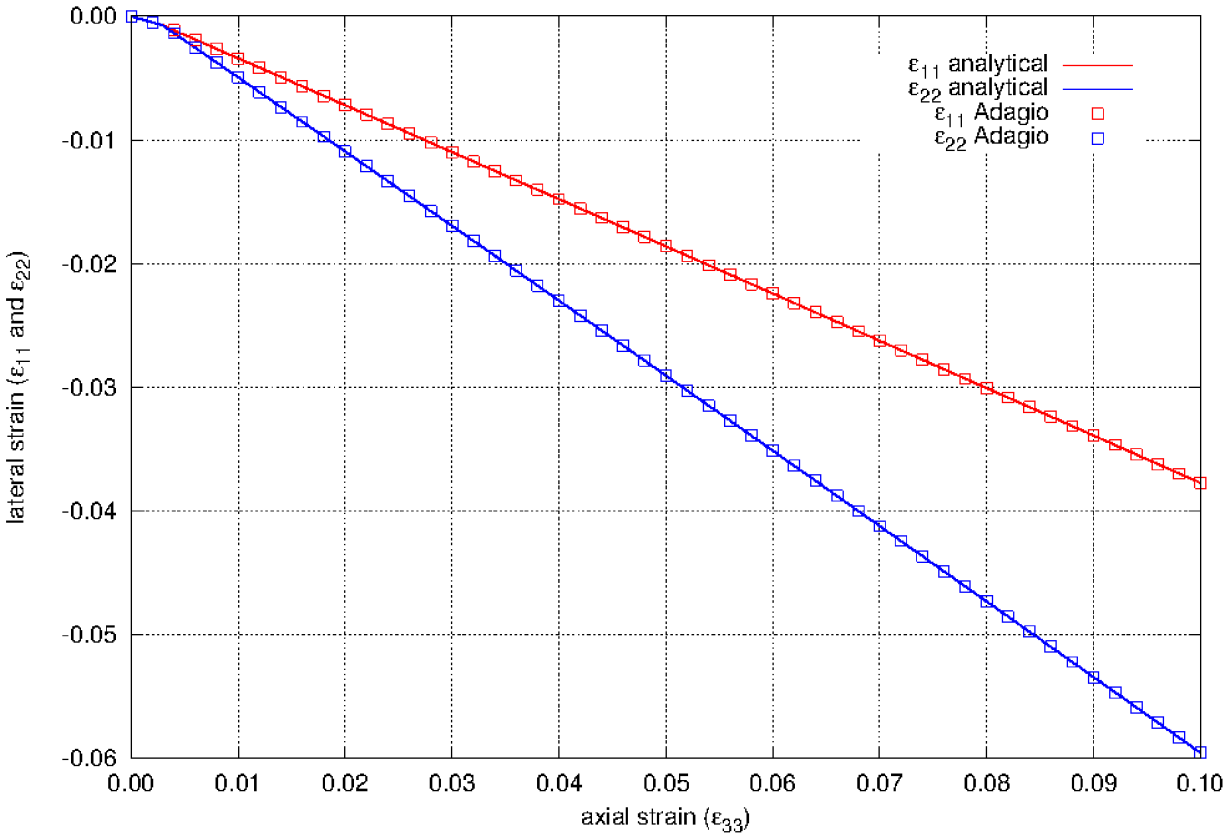

Fig. 4.62 Lateral strain as a function of axial strain for the Hill model of 2090-T3 aluminum. Loading is in the e_3-direction and the hardening law is a Voce law.

If the stress state is on the yield surface, then $\phi = \bar{\sigma}\left(\bar{\varepsilon}^p\right)$, so the shear stress is

$$\sigma_{12} = \frac{R_{12}}{\sqrt{3}}\bar{\sigma}\left(\bar{\varepsilon}^p\right) \tag{4.47}$$

This shows that the pure shear stress state can be calculated from the hardening law and the anisotropy parameters.

To evaluate the shear stress we need the equivalent plastic strain as a function of the shear strain. If we equate the rate of plastic work we get

$$\bar{\sigma}\dot{\bar{\varepsilon}}^p = 2\sigma_{12}\left(\dot{\varepsilon}_{12} - \dot{\varepsilon}^{\mathrm{e}}_{12}\right) \quad \rightarrow \quad \dot{\bar{\varepsilon}}^p = \frac{2R_{12}}{\sqrt{3}}\left(\dot{\varepsilon}_{12} - \dot{\varepsilon}^{\mathrm{e}}_{12}\right)$$

which, when integrated, gives us an implicit equation for the equivalent plastic strain

$$\bar{\varepsilon}^p = \frac{2R_{12}}{\sqrt{3}}\left(\varepsilon_{12} - \frac{R_{12}}{\sqrt{3}}\frac{\bar{\sigma}\left(\bar{\varepsilon}^p\right)}{2\,G}\right)$$

If we define $\hat{R}_{12} = R_{12}/\sqrt{3}$ then we get a form similar to what we had for uniaxial stress

$$\bar{\varepsilon}^p = 2\hat{R}_{12}\left(\varepsilon_{12} - \hat{R}_{12}\frac{\bar{\sigma}\left(\bar{\varepsilon}^p\right)}{2\,G}\right)$$

The equivalent plastic strain can now be used to find the shear stress.

Boundary Conditions for Pure Shear

The deformation gradient that gives pure shear for loading relative to the e_1-e_2 axes is

$$[\mathbf{F}] = \begin{bmatrix} \frac{1}{2}\left(\lambda + \lambda^{-1}\right) & \frac{1}{2}\left(\lambda - \lambda^{-1}\right) & 0 \\ \frac{1}{2}\left(\lambda - \lambda^{-1}\right) & \frac{1}{2}\left(\lambda + \lambda^{-1}\right) & 0 \\ 0 & 0 & 1 \end{bmatrix} \quad \rightarrow \quad [\boldsymbol{\varepsilon}] = \begin{bmatrix} 0 & \varepsilon & 0 \\ \varepsilon & 0 & 0 \\ 0 & 0 & 0 \end{bmatrix} \quad ; \quad \varepsilon = \ln\lambda$$

For loading relative to the e_2-e_3 axes and the e_3-e_1 axes the boundary conditions are modified appropriately.

Results

The results for the Hill plasticity model loaded in pure shear are shown in Fig. 4.63. We see that the stress strain curves in pure shear as calculated by Adagio follow the expected stress strain curves. All other stress and strain components for the three problems are zero.

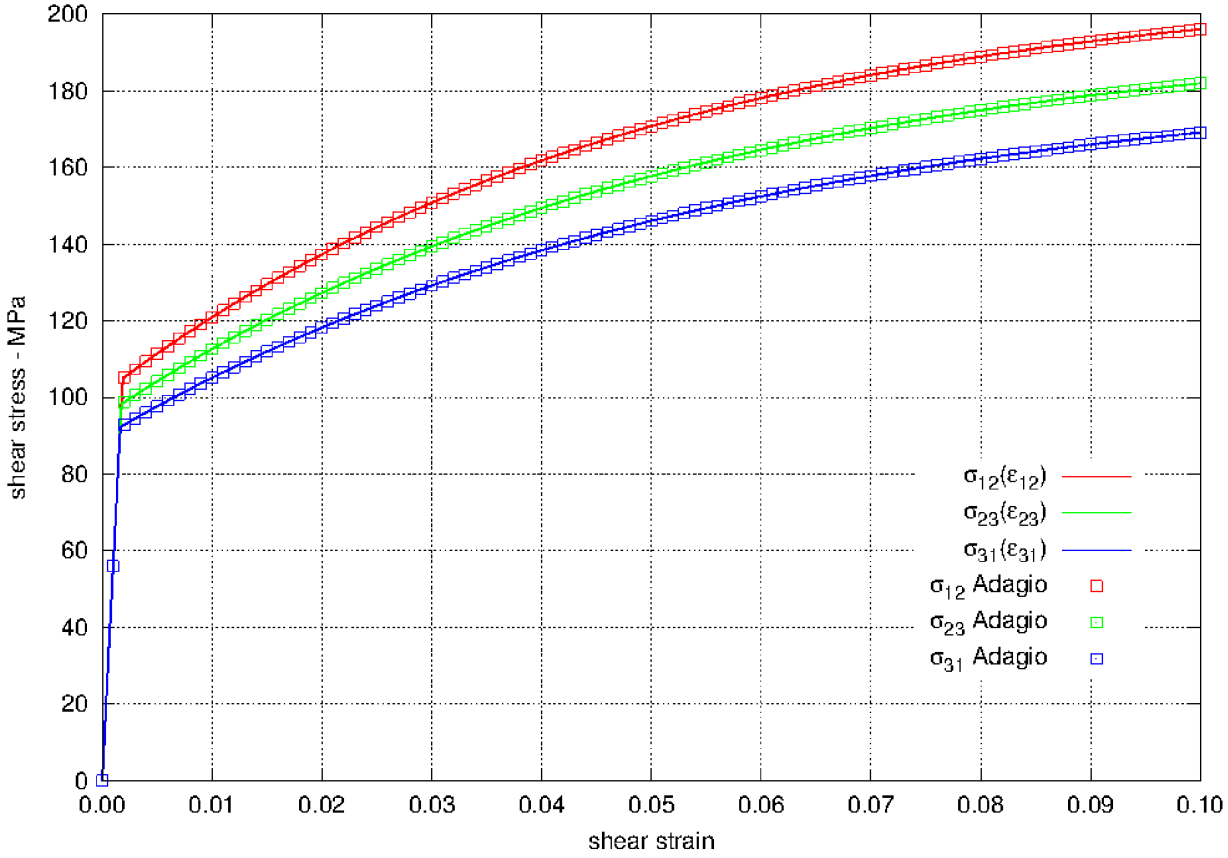

Fig. 4.63 Shear stress versus shear strain using the Hill model with a Voce hardening law. Results are for shear in the three orthogonal planes of the material coordinate system.

4.15.3.3 Plastic Hardening

To verify the capabilities of the hardening models, rate *independent* and rate *dependent* alike, the constant equivalent plastic strain rate, $\dot{\bar{\varepsilon}}^p$, uniaxial stress and pure shear verification tests described in *Appendix A* are utilized. In these simplified loading cases, the material state may be found explicitly as a function of time knowing the prescribed equivalent strain rate. For the rate *independent* cases, a strain rate of $\dot{\bar{\varepsilon}}^p = 1 \times 10^{-4} \text{s}^{-1}$ is used for ease in simulations although the selected rate does not affect the results. Through this testing protocol, the hardening models are not only tested at different rates but also in different principal material directions to consider the anisotropy of the Hill yield surface. Additionally, the rate *dependent* models are tested for a wide range of strain rates (over five decades) and with all three rate *independent* hardening functions ($\tilde{\sigma}_y$ in the previous theory section). Although linear, Voce, and power-law rate *independent* representations are utilized in the rate *dependent* tests, in those cases the hardening models are prescribed via user-defined analytic functions. The rate *independent* verification exercises, on the other hand, examine the built in hardening models. This distinction necessitates the different considerations and treatments.

The various rate *dependent* and rate *independent* hardening coefficients are found in Table 4.20 while the remaining model parameters are unchanged from the previous verification exercises. For the current verification exercises, the rate *independent* hardening models (linear, Voce, and power-law) will first be considered and then the rate *dependent* forms (Johnson-Cook, power-law breakdown).

Table 4.20 The model parameters for the hardening verification tests used with the Hill plasticity model during verification tests. Parameters for the rate *independent* hardening functions, $\tilde{\sigma}_y$, are also given and denoted with a $\tilde{}$ while the subscript refers to the functional form.

C	0.1	$\dot{\varepsilon}_0$	1×10^{-4} s^{-1}
g	0.21 s^{-1}	m	16.4
$\tilde{H}_{\text{Linear}}$	200 MPa		
$\tilde{A}_{\text{PL}}$	400 MPa	$\tilde{n}_{\text{PL}}$	0.25
$\tilde{A}_{\text{Voce}}$	200 MPa	$\tilde{n}_{\text{Voce}}$	20

Linear

To examine the performance of the rate *independent* linear hardening model, the verification exercises from *Appendix A* are used. In this case, as the Hill yield surface is being considered, the responses are determined numerically and analytically in the uniaxial stress case with loading in three different principal material directions and three different shear planes for the pure shear case. These results are presented in Fig. 4.64. From these responses, superb agreement between the analytical and numerical results is noted. Additionally, the constant linear stress-strain response during plastic deformations clearly demonstrates the behavior giving this model its name.

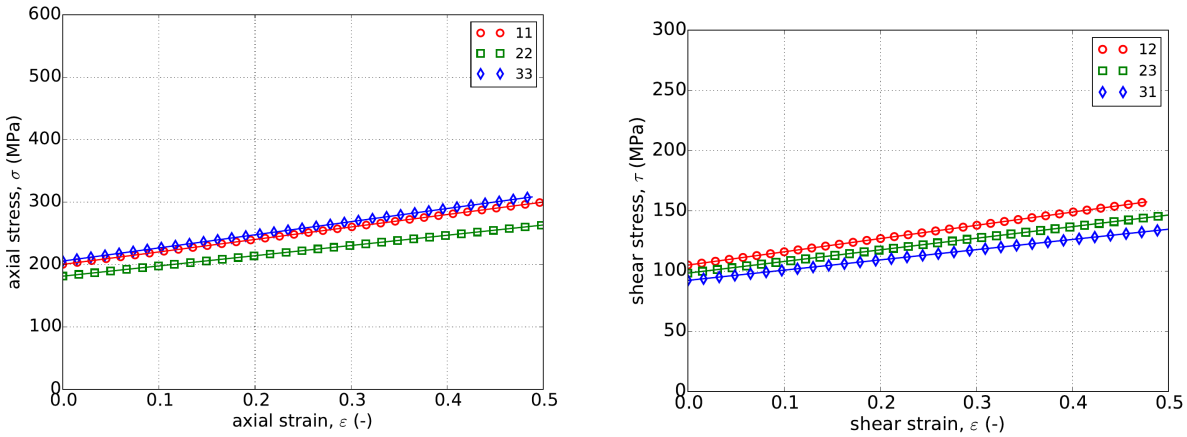

(a) Uniaxial Stress **(b) Pure Shear**

Fig. 4.64 Uniaxial stress-strain (a) and pure shear (b) responses of the Hill plasticity model with rate *independent*, linear hardening. Solid lines are analytical while open symbols are numerical.

Power-Law

The rate *independent* power-law hardening model is verified by using the uniaxial stress and pure shear problems of *Appendix A*. Results of these endeavors determined analytically and numerically are presented in Fig. 4.65 in which the uniaxial stress problem is presented for loading aligned with the three different principal material directions and three different shear planes for the pure shear case. From these results, outstanding agreement is noted between both numerical and analytical results sets verifying the model. Also, the initially stiff hardening decreasing to a lower linear tangent modulus characteristic of power-law hardening models is clearly evident in the various result sets of Fig. 4.65.

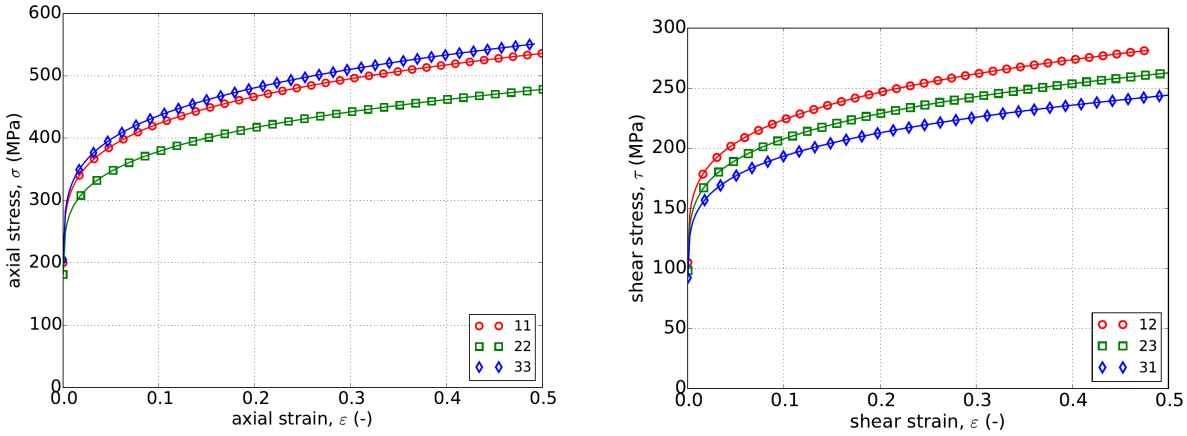

(a) Uniaxial Stress **(b) Pure Shear**

Fig. 4.65 Uniaxial stress-strain (a) and pure shear (b) responses of the Hill plasticity model with rate *independent*, power-law hardening. Solid lines are analytical while open symbols are numerical.

Voce

Verification of the rate *independent* Voce hardening model is pursued by considering both the uniaxial stress and pure shear approaches of *Appendix A*. The results of these investigations determined analytically and numerically are shown in Fig. 4.66. For the uniaxial stress cases, loadings in each of the three principal material directions is presented while complementary results from the three shear planes are shown for the pure shear case. In each of these six instances, exemplary agreement is observed between the different results sets. Additionally, such stress-strain results also show the saturation behavior associated with Voce models in which at some equivalent plastic strain the material no longer hardens.

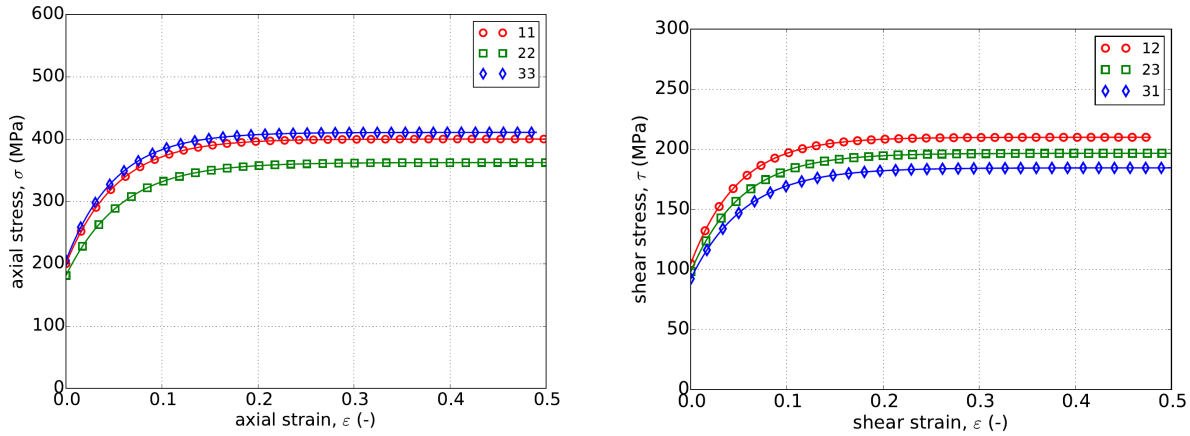

(a) Uniaxial Stress **(b) Pure Shear**

Fig. 4.66 Uniaxial stress-strain (a) and pure shear (b) responses of the Hill plasticity model with rate *independent*, Voce hardening. Solid lines are analytical while open symbols are numerical.

Johnson-Cook

As noted in *Appendix A*, the uniaxial stress response depends on the yield surface anisotropy coefficients (for the Hill model the $R's$). The respective coefficients are given in the aforementioned appendix while Fig. 4.67 and Fig. 4.68 present the results of forty-five different verification exercises corresponding to different combinations of the three material principal directions ($\hat{e}_1$, $\hat{e}_2$, and $\hat{e}_3$), five equivalent plastic strain rates(1×10^{-3}, 1×10^{-2}, 1×10^{-1}, 1×10^{0} and 1×10^{1} s^{-1}), and three rate *independent* hardening models (linear, power-law, and Voce). For each combination, the analytical and numerical results match to within acceptably small numerical differences.

For the pure shear case, the problem discussed in *Appendix A* is considered. The results still depend on the Hill R coefficients and forty-five different loadings are presented in Fig. 4.69 and Fig. 4.70. In this instance, three different shearing planes are used in lieu of the principal directions. Nonetheless, for these results the key result remains the same – analytical matches numerical further verifying rate dependent capabilities.

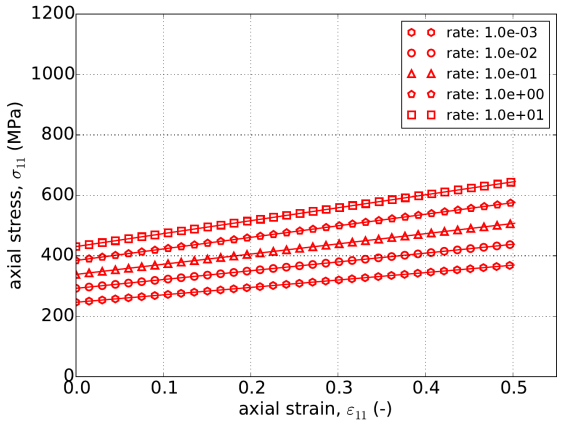

(a) Linear Hardening -- 11

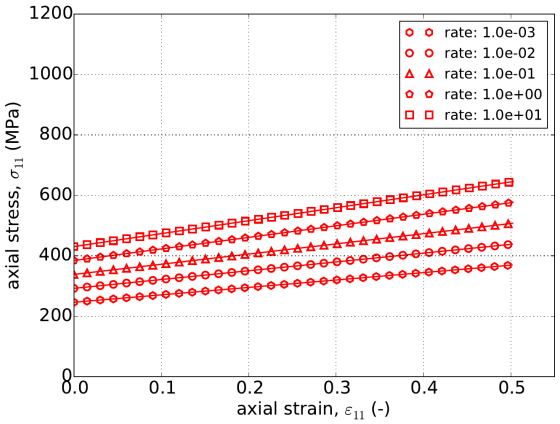

(b) Linear Hardening -- 22

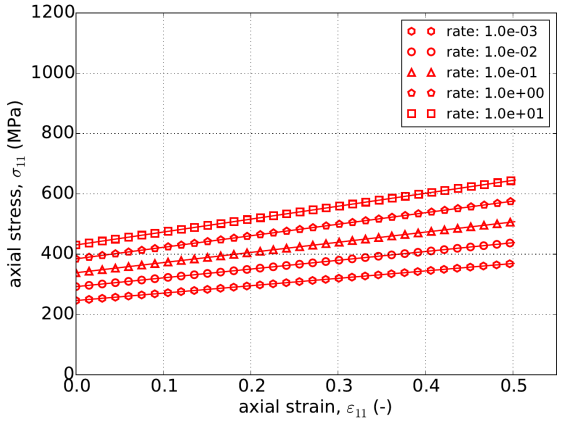

(c) Linear Hardening -- 33

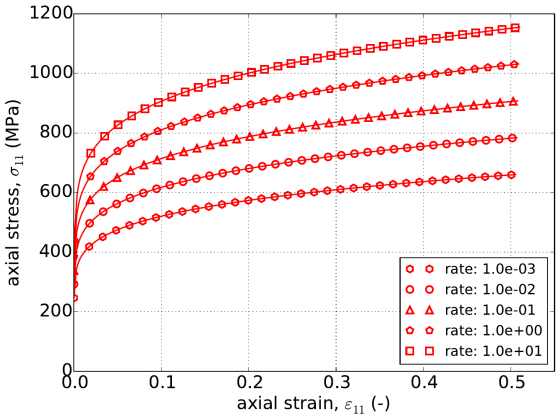

(d) Power-Law Hardening -- 11

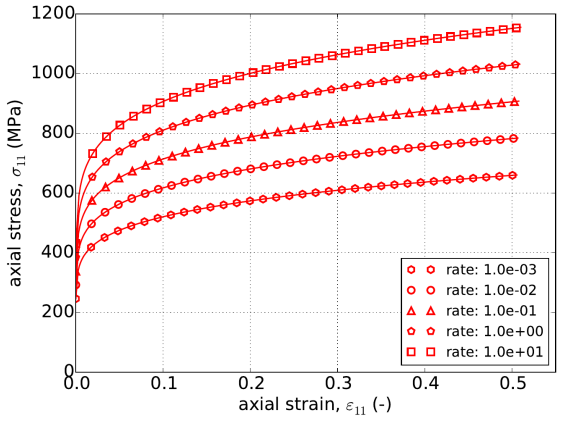

(e) Power-Law Hardening -- 22

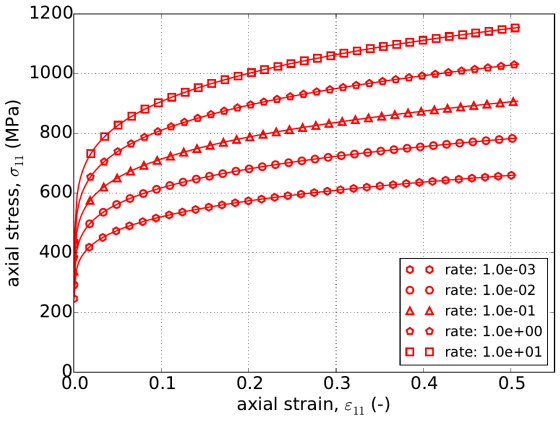

(f) Power-Law Hardening -- 33

Fig. 4.67 Uniaxial stress-strain response of the Hill plasticity model with rate *dependent*, Johnson-Cook type hardening with (a-c) linear and (d-f) power-law rate *independent* hardening. Solid lines are analytical results while open symbols are numerical.

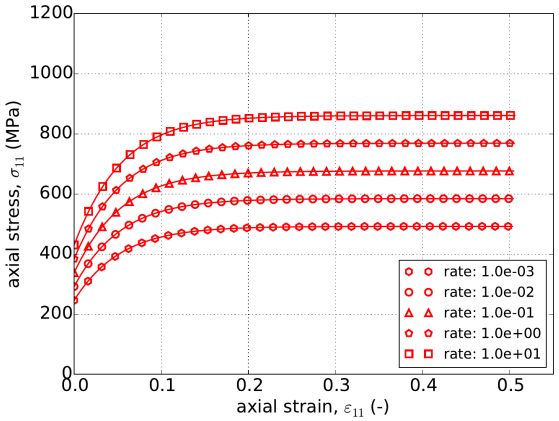

(a) Voce Hardening -- 11

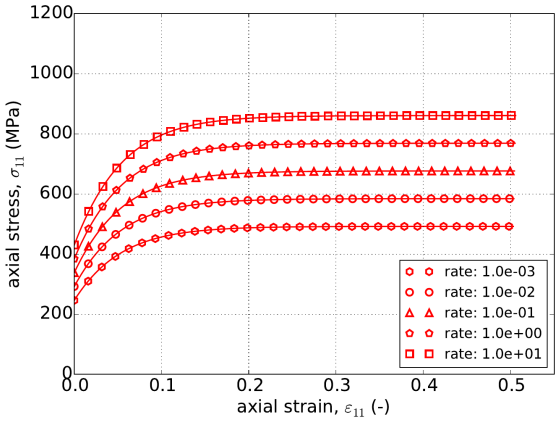

(b) Voce Hardening -- 22

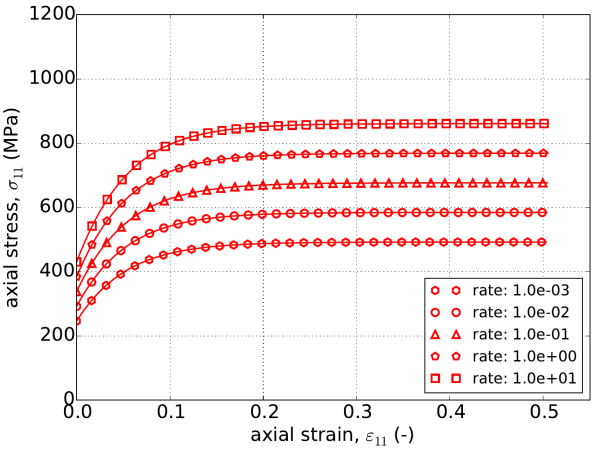

(c) Voce Hardening -- 33

Fig. 4.68 Uniaxial stress-strain response of the Hill plasticity model with rate *dependent*, Johnson-Cook type hardening with (a-c) Voce rate *independent* hardening. Solid lines are analytical results while open symbols are numerical.

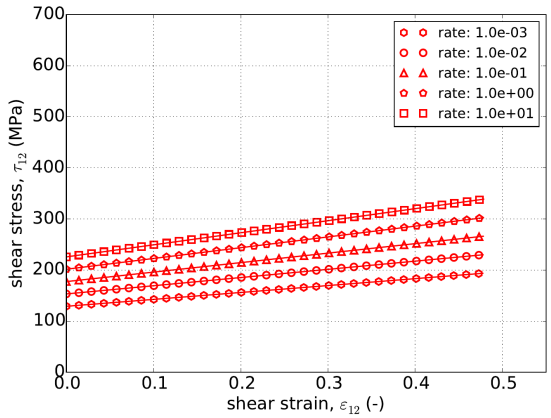

(a) Linear Hardening -- 11

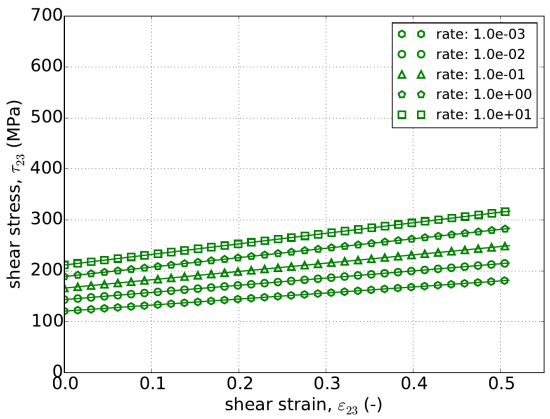

(b) Linear Hardening -- 22

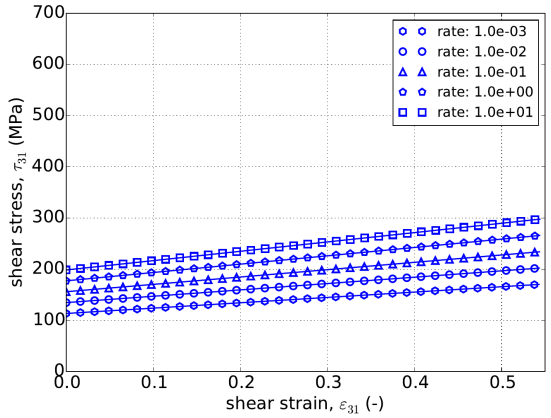

(c) Linear Hardening -- 33

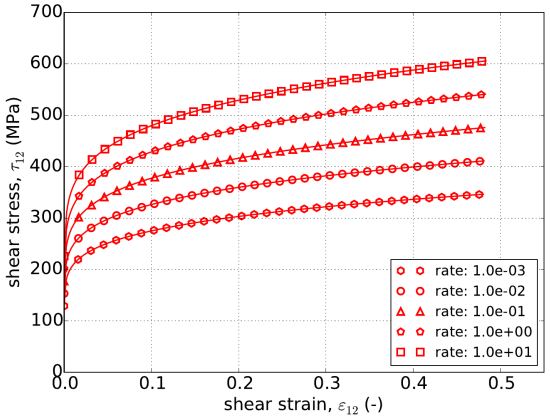

(d) Power-Law Hardening -- 11

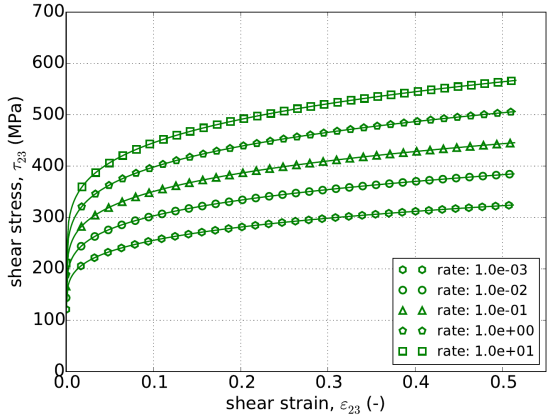

(e) Power-Law Hardening -- 22

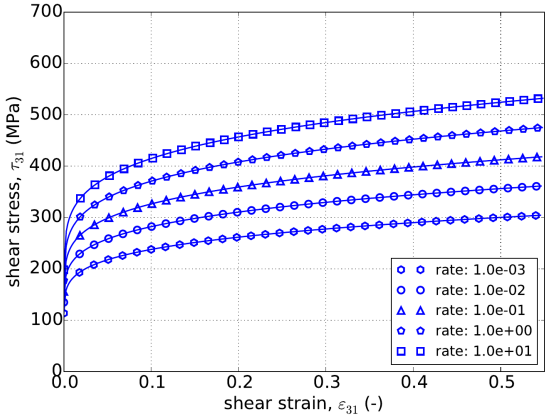

(f) Power-Law Hardening -- 33

Fig. 4.69 Stress-strain response of the Hill plasticity model with rate *dependent*, Johnson-Cook type hardening in pure shear with (a-c) linear and (d-f) power-law rate *independent* hardening. Solid lines are analytical results while open symbols are numerical.

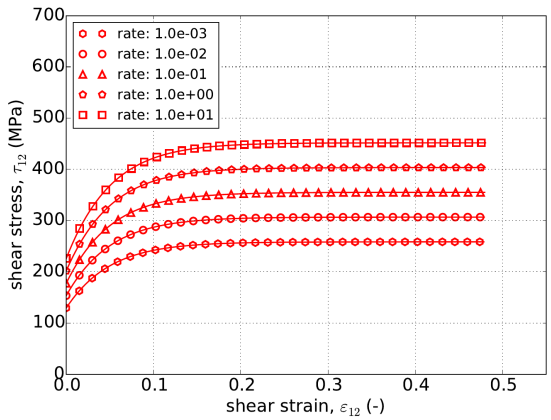

(a) Voce Hardening -- 11

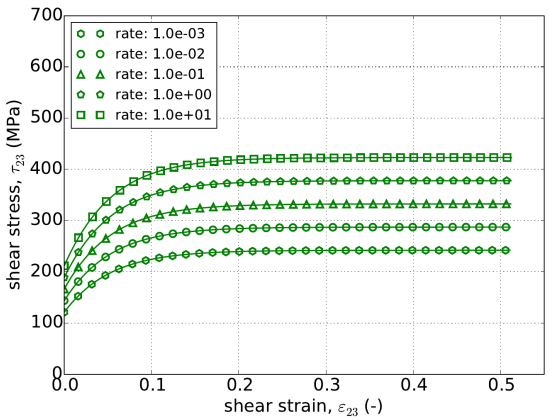

(b) Voce Hardening -- 22

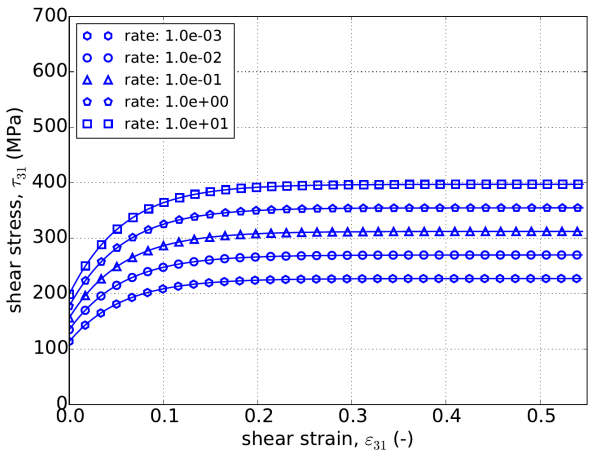

(c) Voce Hardening -- 33

Fig. 4.70 Stress-strain response of the Hill plasticity model with rate *dependent*, Johnson-Cook type hardening in pure shear with (a-c) Voce rate *independent* hardening. Solid lines are analytical results while open symbols are numerical.

Power-Law Breakdown

For the power-law breakdown model, the same forty-five cases discussed in the previous section (three directions, five rates, three hardening models) are again solved via the approach of *Appendix A* in Fig. 4.71 and Fig. 4.72. Although the impact of rate on the responses differs due to the assumed representation of the rate-dependent hardening, excellent agreement is still noted between analytical and numerical results.

To expand on the uniaxial stress results, the response through pure shear is also probed via the method of *Appendix A*. Again forty-five different cases are investigated and their results are presented in Fig. 4.73 and Fig. 4.74. Once again, the results aligning thereby verifying the capability of the model and producing additional credibility.

4.15.4 User Guide

```
BEGIN PARAMETERS FOR MODEL HILL_PLASTICITY
  #
  # Elastic constants
  #
  YOUNGS MODULUS = <real>
  POISSONS RATIO = <real>
  SHEAR MODULUS  = <real>
  BULK MODULUS   = <real>
  LAMBDA         = <real>
  TWO MU         = <real>
  #
  # Material coordinates system definition
  #
  COORDINATE SYSTEM             = <string> coordinate_system_name
  DIRECTION FOR ROTATION        = <real> 1|2|3
  ALPHA                         = <real> (degrees)
  SECOND DIRECTION FOR ROTATION = <real> 1|2|3
  SECOND ALPHA                  = <real> (degrees)
  #
  # Yield surface parameters
  #
  YIELD STRESS = <real>
  R11 = <real> (1.0)
  R22 = <real> (1.0)
  R33 = <real> (1.0)
  R12 = <real> (1.0)
  R23 = <real> (1.0)
  R31 = <real> (1.0)
```

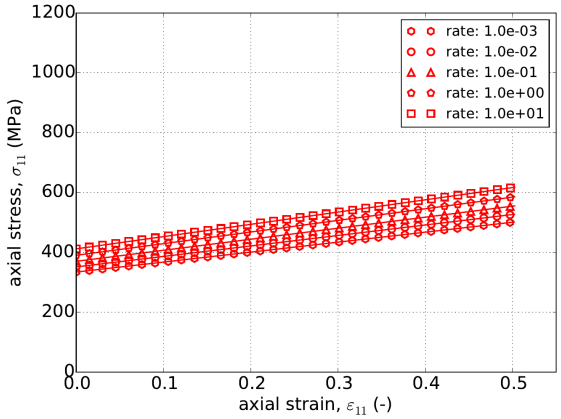

(a) Linear Hardening -- 11

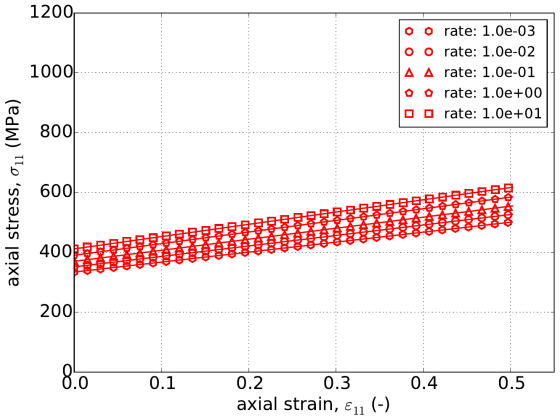

(b) Linear Hardening -- 22

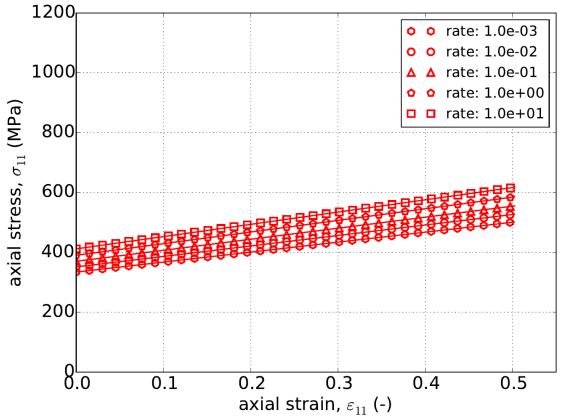

(c) Linear Hardening -- 33

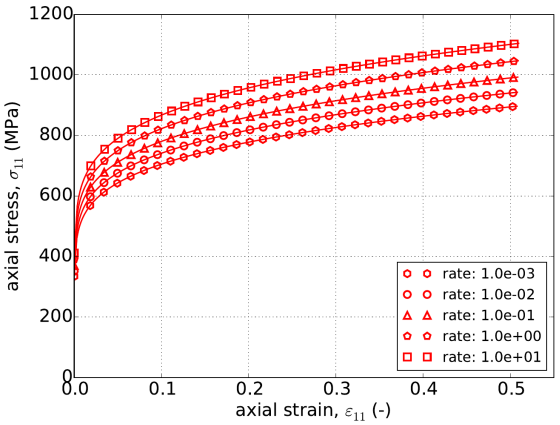

(d) Power-Law Hardening -- 11

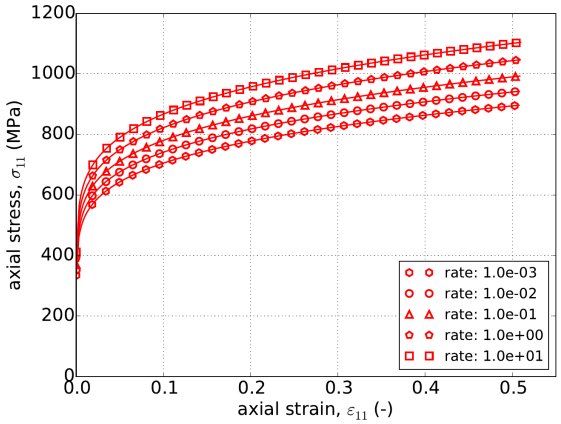

(e) Power-Law Hardening -- 22

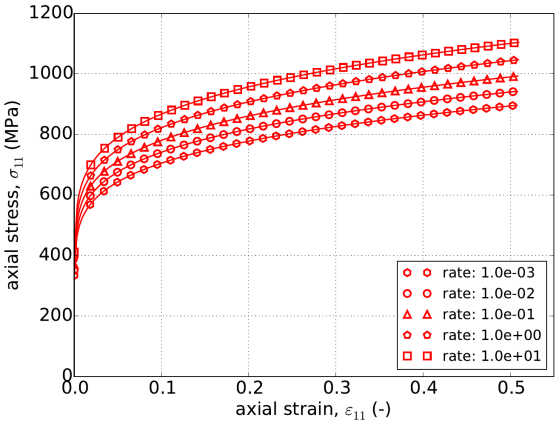

(f) Power-Law Hardening -- 33

Fig. 4.71 Uniaxial stress-strain response of the Hill plasticity model with rate *dependent*, power-law breakdown type hardening in with (a-c) linear and (d-f) power-law rate *independent* hardening. Solid lines are analytical results while open symbols are numerical.

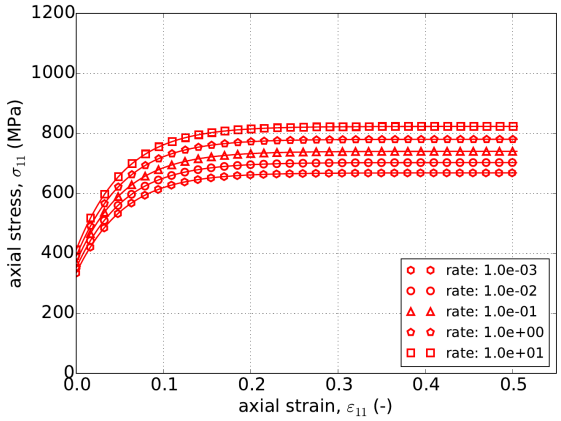

(a) Voce Hardening -- 11

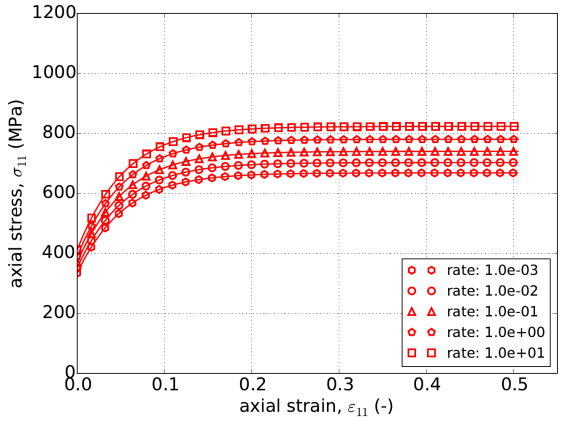

(b) Voce Hardening -- 22

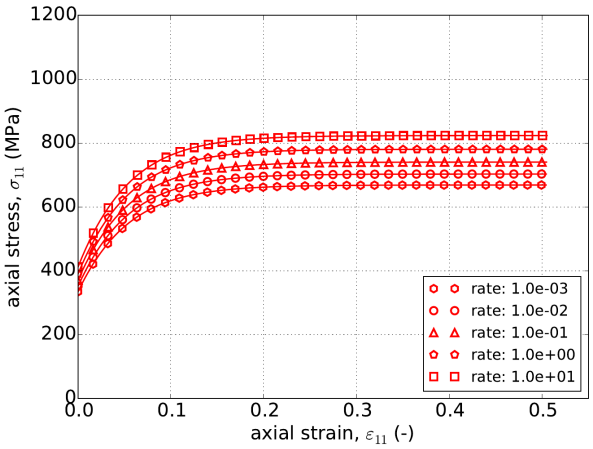

(c) Voce Hardening -- 33

Fig. 4.72 Uniaxial stress-strain response of the Hill plasticity model with rate *dependent*, power-law breakdown type hardening in with (a-c) Voce rate *independent* hardening. Solid lines are analytical results while open symbols are numerical.

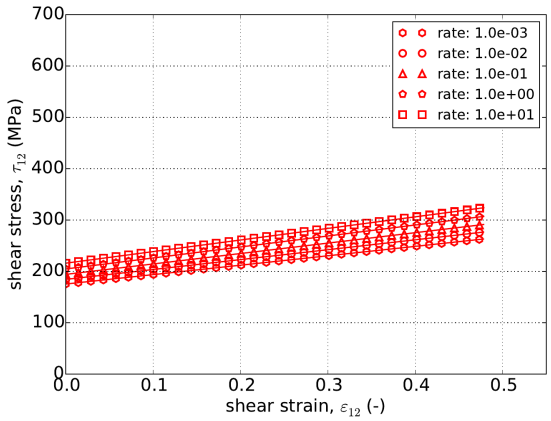

(a) Linear Hardening -- 11

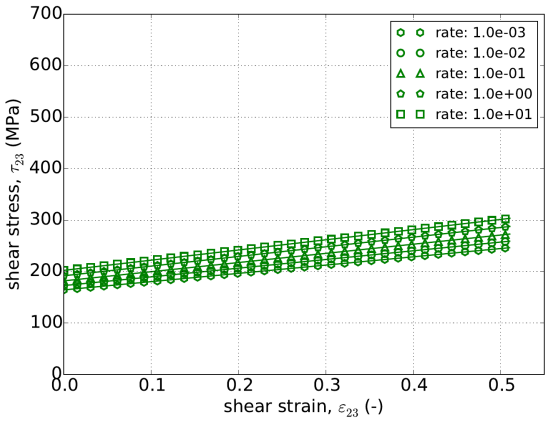

(b) Linear Hardening -- 22

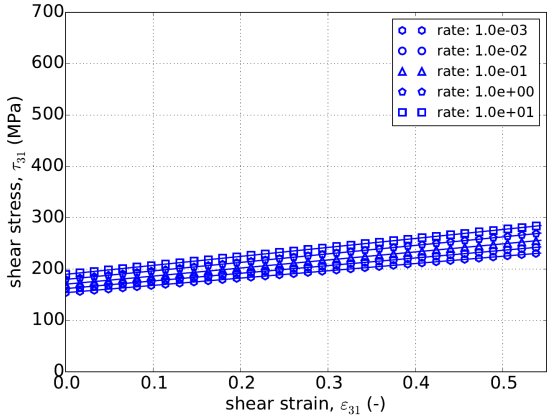

(c) Linear Hardening -- 33

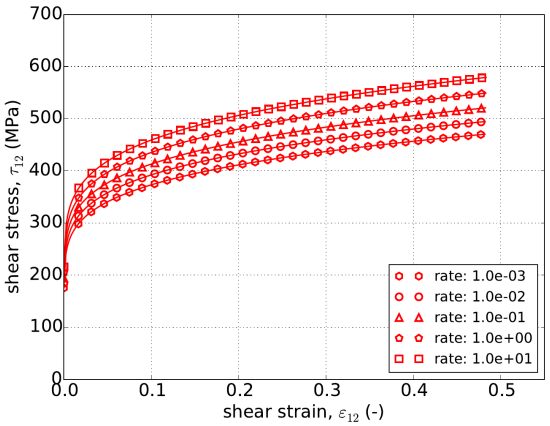

(d) Power-Law Hardening -- 11

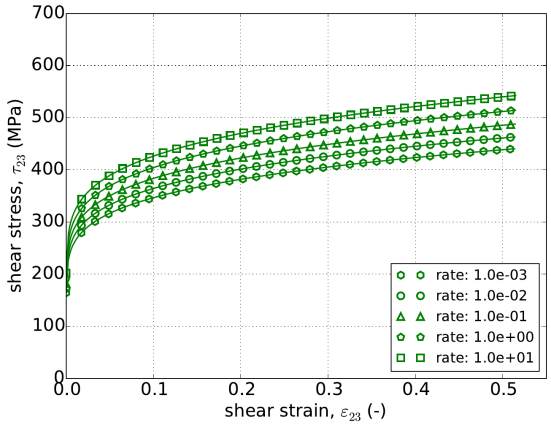

(e) Power-Law Hardening -- 22

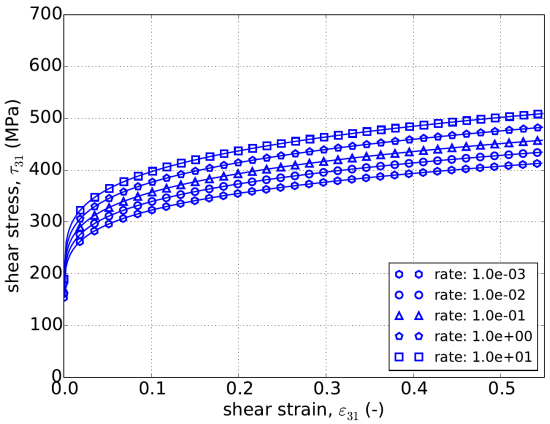

(f) Power-Law Hardening -- 33

Fig. 4.73 Stress-strain response of the Hill plasticity model with rate *dependent*, power-law breakdown type hardening in pure shear with (a-c) linear and (d-f) power-law rate *independent* hardening. Solid lines are analytical results while open symbols are numerical.

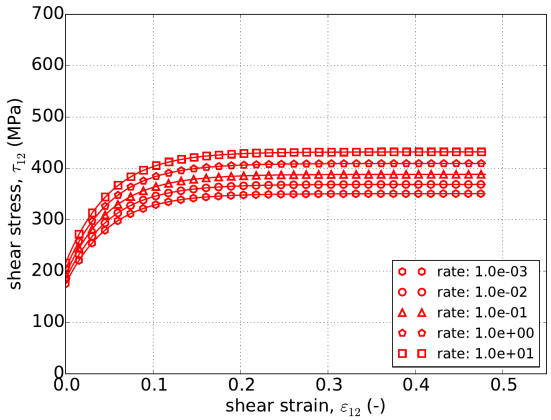

(a) Voce Hardening -- 11

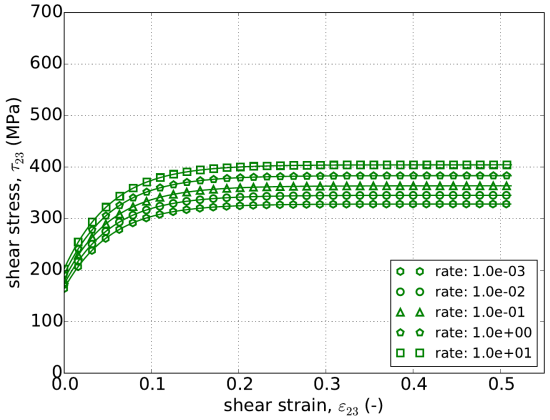

(b) Voce Hardening -- 22

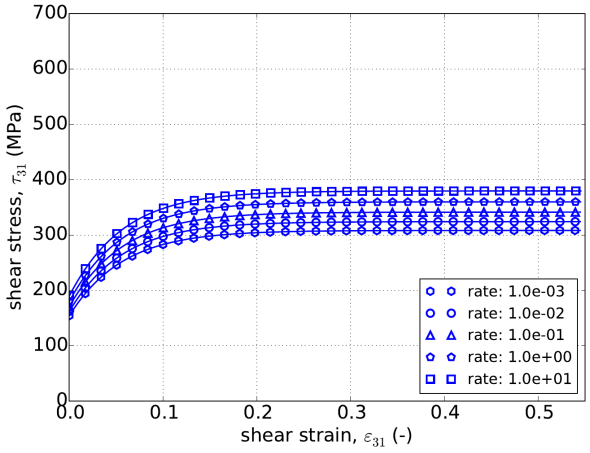

(c) Voce Hardening -- 33

Fig. 4.74 Stress-strain response of the Hill plasticity model with rate *dependent*, power-law breakdown type hardening in pure shear with (a-c) Voce rate *independent* hardening. Solid lines are analytical results while open symbols are numerical.

```
#
  #
  # Hardening model
  #
  HARDENING MODEL = LINEAR | POWER_LAW | VOCE | USER_DEFINED |
  FLOW_STRESS | DECOUPLED_FLOW_STRESS | JOHNSON_COOK |
  POWER_LAW_BREAKDOWN
  #
  # Linear hardening
  #
  HARDENING MODULUS = <real>
  #
  # Power-law hardening
  #
  HARDENING CONSTANT = <real>
  HARDENING EXPONENT = <real> (0.5)
  LUDERS STRAIN      = <real> (0.0)
  #
  # Voce hardening
  #
  HARDENING MODULUS       = <real>
  EXPONENTIAL COEFFICIENT = <real>
  #
  # Johnson-Cook hardening
  #
  HARDENING FUNCTION = <string>hardening_function_name
  RATE CONSTANT      = <real>
  REFERENCE RATE     = <real>
  #
  # Power law breakdown hardening
  #
  HARDENING FUNCTION = <string>hardening_function_name
  RATE COEFFICIENT   = <real>
  RATE EXPONENT      = <real>
  # User defined hardening
  #
  HARDENING FUNCTION = <string>hardening_function_name
  #
```

```
#
  #
  # Following Commands Pertain to Flow_Stress Hardening Model
  #
  #    -  Isotropic Hardening model
  #
  ISOTROPIC HARDENING MODEL = LINEAR | POWER_LAW | VOCE |
```

(continues on next page)

(continued from previous page)

```
                                USER_DEFINED
#
# Specifications for Linear, Power-law, and Voce same as above
#
# User defined hardening
#
ISOTROPIC HARDENING FUNCTION = <string>iso_hardening_fun_name
#
#     - Rate dependence
#
RATE MULTIPLIER = JOHNSON_COOK | POWER_LAW_BREAKDOWN |
   USER_DEFINED | RATE_INDEPENDENT (RATE_INDEPENDENT)
#
# Specifications for Johnson-Cook, Power-law-breakdown
#     same as before EXCEPT no need to specify a
#     hardening function
#
# User defined rate multiplier
#
RATE MULTIPLIER FUNCTION = <string> rate_mult_function_name
#
#     - Temperature dependence
#
TEMPERATURE MULTIPLIER = JOHNSON_COOK | USER_DEFINED |
   TEMPERATURE_INDEPENDENT (TEMPERATURE_INDEPENDENT)
#
#  Johnson-Cook temperature dependence
#
MELTING TEMPERATURE   = <real>
REFERENCE TEMPERATURE = <real>
TEMPERATURE EXPONENT  = <real>
#
#  User-defined temperature dependence
TEMPERATURE MULTIPLIER FUNCTION = <string>temp_mult_function_name
#
# Following Commands Pertain to Decoupled_Flow_Stress Hardening Model
#
#    -  Isotropic Hardening model
#
ISOTROPIC HARDENING MODEL = LINEAR | POWER_LAW | VOCE | USER_DEFINED
#
# Specifications for Linear, Power-law, and Voce same as above
#
# User defined hardening
#
```

(continues on next page)

(continued from previous page)

```
  ISOTROPIC HARDENING FUNCTION = <string>isotropic_hardening_function_
↪name
  #
  #     - Rate dependence
  #
  YIELD RATE MULTIPLIER = JOHNSON_COOK | POWER_LAW_BREAKDOWN |
              USER_DEFINED | RATE_INDEPENDENT (RATE_INDEPENDENT)
  #
  # Specifications for Johnson-Cook, Power-law-breakdown same as before
  #     EXCEPT no need to specify a hardening function
  #     AND should be preceded by YIELD
  #
  #     As an example for Johnson-Cook yield rate dependence,
  #
  YIELD RATE CONSTANT  = <real>
  YIELD REFERENCE RATE = <real>
  #
  # User defined rate multiplier
  #
  YIELD RATE MULTIPLIER FUNCTION = <string>yield_rate_mult_function_
↪name
  #
  HARDENING_RATE MULTIPLIER = JOHNSON_COOK | POWER_LAW_BREAKDOWN |
              USER_DEFINED | RATE_INDEPENDENT (RATE_INDEPENDENT)
  #
  #     Syntax same as for yield parameters but with a HARDENING prefix
  #
  #     - Temperature dependence
  #
  YIELD TEMPERATURE MULTIPLIER = JOHNSON_COOK | USER_DEFINED |
            TEMPERATURE_INDEPENDENT (TEMPERATURE_INDEPENDENT)
  #
  #  Johnson-Cook temperature dependence
  #
  YIELD MELTING TEMPERATURE   = <real>
  YIELD REFERENCE TEMPERATURE = <real>
  YIELD TEMPERATURE EXPONENT  = <real>
  #
  #  User-defined temperature dependence
  YIELD TEMPERATURE MULTIPLIER FUNCTION = <string>yield_temp_mult_fun_
↪name
  #
  HARDENING TEMPERATURE MULTIPLIER = JOHNSON_COOK | USER_DEFINED |
            TEMPERATURE_INDEPENDENT (TEMPERATURE_INDEPENDENT)
  #
```

(continues on next page)

(continued from previous page)

```
  #   Syntax for hardening constants same as for yield but
  #            with HARDENING prefix
```

```
#
  #
  # Optional Failure Definitions
  #    Following only need to be defined if intend to use failure model
  #
  FAILURE MODEL = TEARING_PARAMETER | JOHNSON_COOK_FAILURE | WILKINS
                  | MODULAR_FAILURE | MODULAR_BCJ_FAILURE

  CRITICAL FAILURE PARAMETER = <real>
  #
  # TEARING_PARAMETER Failure model definitions
  #
  TEARING PARAMETER EXPONENT = <real>
  #
  # JOHNSON_COOK_FAILURE Failure model definitions
  #
  JOHNSON COOK D1       = <real>
  JOHNSON COOK D2       = <real>
  JOHNSON COOK D3       = <real>
  JOHNSON COOK D4       = <real>
  JOHNSON COOK D5       = <real>
  #
  #Following Johnson-Cook parameters can only be defined once.  As␣
↪such, only
  #  needed if not previously defined via Johnson-Cook multipliers
  #  w/ flow-stress hardening.  Does need to be defined
  #  w/ Decoupled Flow Stress
  #
  REFERENCE RATE        = <real>
  REFERENCE TEMPERATURE = <real>
  MELTING TEMPERATURE   = <real>
  #
  # WILKINS Failure model definitions
  #
  WILKINS ALPHA    = <real>
  WILKINS BETA     = <real>
  WILKINS PRESSURE = <real>
  #
  #  MODULAR_FAILURE Failure model definitions
  #
  PRESSURE MULTIPLIER         = PRESSURE_INDEPENDENT | WILKINS
                                | USER_DEFINED (PRESSURE_INDEPENDENT)
```

(continues on next page)

(continued from previous page)

```
  LODE ANGLE MULTIPLIER       = LODE_ANGLE_INDEPENDENT |
                                WILKINS (LODE_ANGLE_INDEPENDENT)
  TRIAXIALITY MULTIPLIER      = TRIAXIALITY_INDEPENDENT | JOHNSON_COOK
                                | USER_DEFINED (TRIAXIALITY_
↪INDEPENDENT)
  RATE FAIL MULTIPLIER        = RATE_INDEPENDENT | JOHNSON_COOK
                                | USER_DEFINED (RATE_INDEPENDENT)
  TEMPERATURE FAIL MULTIPLIER = TEMPERATURE_INDEPENDENT | JOHNSON_COOK
                                | USER_DEFINED (TEMPERATURE_
↪INDEPENDENT)
  #
  # Individual multiplier definitions
  #
  PRESSURE MULTIPLIER = WILKINS
  WILKINS ALPHA       = <real>
  WILKINS PRESSURE    = <real>
  #
  PRESSURE MULTIPLIER = USER_DEFINED
  PRESSURE MULTIPLIER FUNCTION = <string> pressure_multiplier_fun_name
  #
  LODE ANGLE MULTIPLIER = WILKINS
  WILKINS BETA          = <real>
  #
  TRIAXIALITY MULTIPLIER = JOHNSON_COOK
  JOHNSON COOK D1        = <real>
  JOHNSON COOK D2        = <real>
  JOHNSON COOK D3        = <real>
  #
  TRIAXIALITY MULTIPLIER = USER_DEFINED
  TRIAXIALITY MULTIPLIER FUNCTION = <string> triaxiality_multiplier_
↪fun_name
  #
  RATE FAIL MULTIPLIER = JOHNSON_COOK
  JOHNSON COOK D4      = <real>
  # REFERENCE RATE should only be added if not previously defined
  REFERENCE RATE       = <real>
  #
  RATE FAIL MULTIPLIER = USER_DEFINED
  RATE FAIL MULTIPLIER FUNCTION = <string> rate_fail_multiplier_fun_
↪name
  #
  TEMPERATURE FAIL MULTIPLIER = JOHNSON_COOK
  JOHNSON COOK D5             = <real>
  # JC Temperatures should only be defined if not previously given
  REFERENCE TEMPERATURE       = <real>
```

(continues on next page)

(continued from previous page)

```
  MELTING TEMPERATURE         = <real>
  #
  TEMPERATURE FAIL MULTIPLIER          = USER_DEFINED
  TEMPERATURE FAIL MULTIPLIER FUNCTION = <string> temp_multiplier_fun_
↪name
  #
  # MODULAR_BCJ_FAILURE Failure model definitions
  #
  INITIAL DAMAGE    = <real>
  INITIAL VOID SIZE = <real>
  DAMAGE BETA       = <real> (0.5)
  GROWTH MODEL      = COCKS_ASHBY | NO_GROWTH (NO_GROWTH)
  NUCLEATION MODEL  = HORSTEMEYER_GOKHALE | CHU_NEEDLEMAN_STRAIN
                      | NO_NUCLEATION (NO_NUCLEATION)
  #
  GROWTH RATE FAIL MULTIPLIER        = JOHNSON_COOK | USER_DEFINED
                                       | RATE_INDEPENDENT
                                       (RATE_INDEPENDENT)
  GROWTH TEMPERATURE FAIL MULTIPLIER = JOHNSON_COOK | USER_DEFINED
                                       | TEMPERATURE_INDEPENDENT
                                       (TEMPERATURE_INDEPENDENT)
  #
  NUCLEATION RATE FAIL MULTIPLIER        = JOHNSON_COOK | USER_DEFINED
                                           | RATE_INDEPENDENT
                                           (RATE_INDEPENDENT)
  NUCLEATION TEMPERATURE FAIL MULTIPLIER = JOHNSON_COOK | USER_DEFINED
                                           | TEMPERATURE_INDEPENDENT
                                           (TEMPERATURE_INDEPENDENT)
  #
  # Definitions for individual growth and nucleation models
  #
  GROWTH MODEL = COCKS_ASHBY
  DAMAGE EXPONENT = <real> (0.5)
  #
  NUCLEATION MODEL      = HORSTEMEYER_GOKHALE
  NUCLEATION PARAMETER1 = <real> (0.0)
  NUCLEATION PARAMETER2 = <real> (0.0)
  NUCLEATION PARAMETER3 = <real> (0.0)
  #
  NUCLEATION MODEL          = CHU_NEEDLEMAN_STRAIN
  NUCLEATION AMPLITUDE      = <real>
  MEAN NUCLEATION STRAIN    = <real>
  NUCLEATION STRAIN STD DEV = <real>
  #
  # Definitions for rate and temperature fail multiplier
```

(continues on next page)

(continued from previous page)

```
  #   Note: only showing definitions for growth.
  #    Nucleation terms are the same just with NUCLEATION instead
  #    of GROWTH
  #
  GROWTH RATE FAIL MULTIPLIER = JOHNSON_COOK
  GROWTH JOHNSON COOK D4      = <real>
  GROWTH REFERENCE RATE       = <real>
  #
  GROWTH RATE FAIL MULTIPLIER          = USER_DEFINED
  GROWTH RATE FAIL MULTIPLIER FUNCTION = <string> growth_rate_fail_
↪mult_func
  #
  GROWTH TEMPERATURE FAIL MULTIPLIER = JOHNSON_COOK
  GROWTH JOHNSON COOK D5             = <real>
  GROWTH REFERENCE TEMPERATURE       = <real>
  GROWTH MELTING TEMPERATURE         = <real>
  #
  GROWTH TEMPERATURE FAIL MULTIPLIER          = USER_DEFINED
  GROWTH TEMPERATURE FAIL MULTIPLIER FUNCTION = <string> temp_fail_
↪mult_func
  #
```

```
#
  #
  # Optional Adiabatic Heating/Thermal Softening  Definitions
  #    Following only need to be defined if intend to use failure model
  #
  THERMAL SOFTENING MODEL = ADIABATIC | COUPLED
  #
  SPECIFIC HEAT = <real> # not needed for COUPLED
  BETA_TQ       = <real>
```

```
END [PARAMETERS FOR MODEL HILL_PLASTICITY]
```

In the command blocks that define the Hill plasticity model:

- The reference nominal yield stress, $\bar{\sigma}$, is defined with the `YIELD STRESS` command line.
- The ratio of the normal yield stress in the $\bar{\mathbf{e}}_1\bar{\mathbf{e}}_1$ material direction is defined with the `R11` command line. The default is 1.0.
- The ratio of the normal yield stress in the $\bar{\mathbf{e}}_2\bar{\mathbf{e}}_2$ material direction is defined with the `R22` command line. The default is 1.0.
- The ratio of the normal yield stress in the $\bar{\mathbf{e}}_3\bar{\mathbf{e}}_3$ material direction is defined with the `R33` command line. The default is 1.0.

- The ratio of the shear yield stress in the $\bar{\mathbf{e}}_1\bar{\mathbf{e}}_2$ material direction is defined with the `R12` command line. The default is 1.0.
- The ratio of the shear yield stress in the $\bar{\mathbf{e}}_2\bar{\mathbf{e}}_3$ material direction is defined with the `R23` command line. The default is 1.0.
- The ratio of the shear yield stress in the $\bar{\mathbf{e}}_3\bar{\mathbf{e}}_1$ material direction is defined with the `R31` command line. The default is 1.0.
- The type of hardening law is defined with the `HARDENING MODEL` command line, other hardening commands then define the specific shape of that hardening curve.
- The hardening modulus for a linear hardening model is defined with the `HARDENING MODULUS` command line.
- The hardening constant for a power law hardening model is defined with the `HARDENING CONSTANT` command line.
- The hardening exponent for a power law hardening model is defined with the `HARDENING EXPONENT` command line.
- The Luders strain for a power law hardening model is defined with the `LUDERS STRAIN` command line.
- The hardening function for a user defined hardening model is defined with the `HARDENING FUNCTION` command line.
- The shape of the spline for the spline based hardening is defined by the `CUBIC SPLINE TYPE`, `CARDINAL PARAMETER`, `KNOT EQPS`, and `KNOT STRESS` command lines.

Output variables available for this model are listed in Table 4.21.

Table 4.21 State Variables for HILL PLASTICITY Model

Name	Description
`EQPS`	equivalent plastic strain, $\bar{\varepsilon}^p$
`EQDOT`	equivalent plastic strain rate, $\dot{\bar{\varepsilon}}^p$
`SEFF`	effective stress, ϕ
`TENSILE_EQPS`	tensile equivalent plastic strain, $\bar{\varepsilon}_t^p$
`DAMAGE`	damage, ϕ
`VOID_COUNT`	void count, η
`VOID_SIZE`	void size, υ
`DAMAGE_DOT`	damage rate, $\dot{\phi}$
`VOID_COUNT_DOT`	void count rate, $\dot{\eta}$
`PLASTIC_WORK_HEAT_RATE`	plastic work heat rate, $\dot{Q}^p$

4.16 Barlat Plasticity Model

4.16.1 Theory

The Barlat plasticity model is a hypoelastic, rate-independent plasticity model. The underlying yield surface is both anisotropic and non-quadratic [9]. With respect to the former, linear transformations of the deviatoric stress are used to capture texture and anisotropy effects. The rate form of this model assumes an additive split of the rate of deformation into an elastic and plastic part

$$D_{ij} = D^{\mathrm{e}}_{ij} + D^{\mathrm{p}}_{ij}.$$

The stress rate only depends on the elastic rate of deformation

$$\overset{\circ}{\sigma}_{ij} = \mathbb{C}_{ijkl} D^{\mathrm{e}}_{kl}$$

where $\mathbb{C}_{ijkl}$ are the components of the fourth-order, isotropic elasticity tensor.

To describe anisotropy in the yield-behavior, two linear transformation tensors, C'_{ijkl} and C''_{ijkl}, are introduced such that,

$$s'_{ij} = C'_{ijkl} s_{kl} \qquad ; \qquad s''_{ij} = C''_{ijkl} s_{kl},$$

with s_{ij} being the deviatoric stress tensor ($s_{ij} = \sigma_{ij} - 1/3\sigma_{kk}\delta_{ij}$) and s'_{ij} and s''_{ij} being transformed stresses. Two transformations are used to capture both the anisotropy of the yield surface and flow rule. In Voigt notation the two transformation tensors are given as,

$$[C'] = \begin{bmatrix} 0 & -c'_{12} & -c'_{13} & 0 & 0 & 0 \\ -c'_{21} & 0 & -c'_{23} & 0 & 0 & 0 \\ -c'_{31} & -c'_{32} & 0 & 0 & 0 & 0 \\ 0 & 0 & 0 & c'_{44} & 0 & 0 \\ 0 & 0 & 0 & 0 & c'_{55} & 0 \\ 0 & 0 & 0 & 0 & 0 & c'_{66} \end{bmatrix}$$

$$[C''] = \begin{bmatrix} 0 & -c''_{12} & -c''_{13} & 0 & 0 & 0 \\ -c''_{21} & 0 & -c''_{23} & 0 & 0 & 0 \\ -c''_{31} & -c''_{32} & 0 & 0 & 0 & 0 \\ 0 & 0 & 0 & c''_{44} & 0 & 0 \\ 0 & 0 & 0 & 0 & c''_{55} & 0 \\ 0 & 0 & 0 & 0 & 0 & c''_{66} \end{bmatrix}.$$

Alternatively, the transformed stresses may be written in terms of the Cauchy stress tensor as,

$$s'_{ij} = L'_{ijkl} \sigma_{kl} \qquad ; \qquad s''_{ij} = L''_{ijkl} \sigma_{kl},$$

where $L'_{ijkl} = C'_{ijmn} I_{mnkl}$ and $L''_{ijkl} = C''_{ijmn} I_{mnkl}$. In this case, I_{ijkl} is the symmetric deviatoric projection tensor and takes the form of,

$$I_{ijkl} = \frac{1}{2}\left(\delta_{ik}\delta_{jl} + \delta_{il}\delta_{jk}\right) - \frac{1}{3}\delta_{ij}\delta_{kl}.$$

In reduced form,

$$[L'] = \frac{1}{3}\begin{bmatrix} c'_{12}+c'_{13} & -2c'_{12}+c'_{13} & c'_{12}-2c'_{13} & 0 & 0 & 0 \\ -2c'_{21}+c'_{23} & c'_{21}+c'_{23} & c'_{21}-2c'_{23} & 0 & 0 & 0 \\ -2c'_{31}+c'_{32} & c'_{31}-2c'_{32} & c'_{31}+c'_{32} & 0 & 0 & 0 \\ 0 & 0 & 0 & 3c'_{44} & 0 & 0 \\ 0 & 0 & 0 & 0 & 3c'_{55} & 0 \\ 0 & 0 & 0 & 0 & 0 & 3c'_{66} \end{bmatrix},$$

and an analogous expression may be written for L''_{ijkl}.

The yield surface, f, is given as,

$$f\left(\sigma_{ij}, \bar{\varepsilon}^p\right) = \phi\left(\sigma_{ij}\right) - \bar{\sigma}\left(\bar{\varepsilon}^p\right) = 0,$$

in which $\phi\left(\sigma_{ij}\right)$ is the effective stress and $\bar{\sigma}\left(\bar{\varepsilon}^p\right)$ is the current yield stress that may depend on rate and/or temperature. The effective stress is written in terms of the principal transformed stresses (s'_i and s''_i, respectively) and the yield surface exponent, a, as,

$$\begin{aligned}\phi\left(\sigma_{ij}\right) = \Bigg\{ \frac{1}{4}\Big[& |s'_1 - s''_1|^a + |s'_1 - s''_2|^a + |s'_1 - s''_3|^a \\ & + |s'_2 - s''_1|^a + |s'_2 - s''_2|^a + |s'_2 - s''_3|^a \\ & + |s'_3 - s''_1|^a + |s'_3 - s''_2|^a + |s'_3 - s''_3|^a \Big] \Bigg\}^{1/a}.\end{aligned}$$

An example of such a yield surface is given in Fig. 4.75 along with examples of previously presented (von Mises, Hosford, Hill) surfaces. The presented Barlat surface corresponds to that of 2090-T3 aluminum first characterized by Barlat *et al.* [9]. In Fig. 4.75, both the anisotropy and non-quadratic nature of the yield surface is evident leading to differing strengths and flow directions at various stresses from any of the other models.

The orientation of the principal material axes with respect to the global Cartesian axes may be specified by the user. First, a rectangular or cylindrical reference coordinate system is defined. *Spherical coordinate systems are not currently implemented for the Barlat model.* The material coordinate system can then be defined through two successive rotations about axes in the reference rectangular or cylindrical coordinate system. In the case of the cylindrical coordinate system this allows the principal material axes to vary point-wise in a given element block.

The plastic rate of deformation, as with the isotropic models, assumes associated flow

$$D^{\mathrm{p}}_{ij} = \dot{\gamma}\frac{\partial \phi}{\partial \sigma_{ij}},$$

in which $\dot{\gamma}$ is the consistency multiplier. Given the form for ϕ, $\dot{\gamma}$ is equal to the rate of the equivalent plastic strain, $\dot{\bar{\varepsilon}}^p$. As the yield surface is cast in transformed stress space, determining the flow direction in Cartesian space may be done via the chain rule (details may be found in [88]) leading to an expression of the form,

$$\frac{\partial \phi}{\partial \sigma_{ij}} = \sum_{k=1}^{3}\left(\frac{\partial \phi}{\partial s'_k}\frac{\partial s'_k}{\partial s'_{mn}}L'_{mnij} + \frac{\partial \phi}{\partial s''_k}\frac{\partial s''_k}{\partial s''_{mn}}L''_{mnij}\right). \tag{4.48}$$

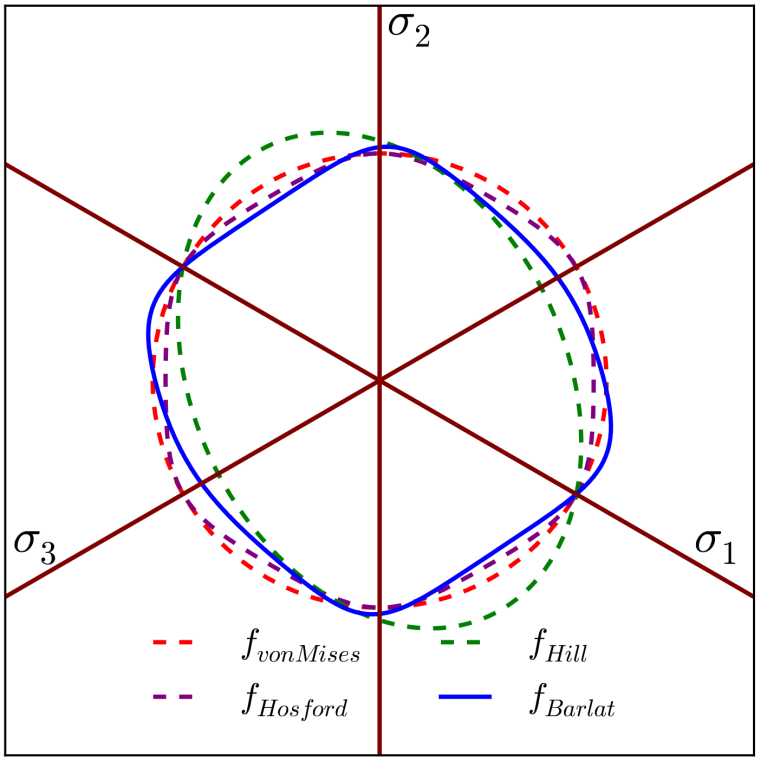

Fig. 4.75 Example Barlat yield surface, $f_{Barlat}\left(\sigma_{ij}, \bar{\varepsilon}^p = 0\right)$, of 2090-T3 aluminum presented in the deviatoric π-plane. Comparison von Mises (J_2), Hosford (with $a = 8$), and Hill surfaces are also presented for comparison.

For more information about the Barlat plasticity model, consult [9], [88]. Additional discussion on options for failure models and adiabatic heating may be found in [61], [62] and [60], respectively.

4.16.1.1 Plastic Hardening

Plastic hardening refers to increases in the flow stress, $\bar{\sigma}$, with plastic deformation. As such, hardening is described via a functional relationship between the flow stress and isotropic hardening variable (effective plastic strain), $\bar{\sigma}\left(\bar{\varepsilon}^p\right)$. Over the course of nearly a century of work in metal plasticity, a variety of relationships have been proposed to describe the interactions associated with different physical interpretations, deformation mechanisms, and materials. To enable the utilization of the same plasticity models for different material systems, a modular implementation of plastic hardening has been adopted such that the analyst may select different hardening models from the input deck thereby avoiding any code changes or user subroutines. In this section, additional details are given for the different models to enable the user to select the appropriate choice of model. Note, the models being discussed here are only for *isotropic* hardening in which the yield surface expands. *Kinematic* hardening in which the yield surface translates in stress-space with deformation and *distortional* hardening where the shape of the yield surface changes shape with deformation are not treated. For a larger discussion of the phenomenology and history of different hardening types, the reader is referred to [42], [57], [64].

Given the ubiquitous nature of these hardening laws in computational plasticity, some (if not most) of this material may be found elsewhere in this manual. Nonetheless, the discussion is repeated here for the convenience of the reader.

Linear

Linear hardening is conceptually the simplest model available in LAMÉ. As the name implies, a linear relationship is assumed between the hardening variable, $\bar{\varepsilon}^p$, and flow stress. The hardening modulus, H', is a constant giving the rate of change of flow stress with plastic flow. The flow stress expression may therefore be written,

$$\bar{\sigma} = \sigma_y + H'\bar{\varepsilon}^p.$$

The simplicity of the model is its main feature as the constant slope,

$$\frac{d\bar{\sigma}}{d\bar{\varepsilon}^p} = H',$$

makes the model attractive for analytical models and cheap for computational implementations (*e.g.* radial return algorithms require only a single correction step). Unfortunately, the simplicity of the representation also means that it has limited predictive capabilities and can lead to overly stiff responses.

Power Law

Another common expression for isotropic hardening is the power-law hardening model. Due to its prevalence, a dedicated `ELASTIC-PLASTIC POWER LAW HARDENING` model may be found in LAMÉ (see Section 4.8.1). This expression is given as,

$$\bar{\sigma} = \sigma_y + A < \bar{\varepsilon}^p - \varepsilon_L >^n,$$

in which $< \cdot >$ are Macaulay brackets, ε_L is the Luders strain, A is a fitting constant, and n is an exponent typically taken such that $0 < n \leq 1$. The Luders strain is a positive, constant strain value (defaulted to zero) giving an initially perfectly plastic response in the plastic deformation domain (see Fig. 4.20). The derivative is then simply,

$$\frac{d\bar{\sigma}}{d\bar{\varepsilon}^p} = nA < \bar{\varepsilon}^p - \varepsilon_L >^{(n-1)} .$$

Note, one difficulty in such an implementation is that when the effective equivalent plastic strain is zero, numerical difficulties may arise in evaluating the derivative and necessitate special treatment of the case.

Voce

The Voce hardening model (sometimes referred to as a saturation model) uses a decaying exponential function of the equivalent plastic strain such that the hardening eventually saturates to a specified value (thus the name). Such a relationship has been observed in some structural metals giving rise to the popularity of the model. The hardening response is given as,

$$\bar{\sigma} = \sigma_y + A \left(1 - \exp\left(-n\bar{\varepsilon}^p\right)\right),$$

in which A is a fitting constant and n is a fitting exponent controlling how quickly the hardening saturates. Importantly, the derivative is written as,

$$\frac{d\bar{\sigma}}{d\bar{\varepsilon}^p} = nA \exp\left(-n\bar{\varepsilon}^p\right),$$

and is well defined everywhere giving the selected form an advantage over the aforementioned power law model.

Johnson-Cook

The Johnson-Cook hardening model is a variant of the classical Johnson-Cook [48], [49] expression. In this instance, the temperature-dependence is neglected to focus on the *rate-dependent* capabilities while allowing for arbitrary isotropic hardening forms via the use of a user-defined hardening function. With these assumptions, the flow stress may be written as,

$$\bar{\sigma} = \tilde{\sigma}_y \left(\bar{\varepsilon}^p\right) \left[1 + C \left\langle \ln\left(\frac{\dot{\bar{\varepsilon}}^p}{\dot{\varepsilon}_0}\right) \right\rangle\right],$$

in which $\tilde{\sigma}_y\left(\bar{\varepsilon}^p\right)$ is the user-specified rate-independent hardening function, C is a fitting constant and $\dot{\varepsilon}_0$ is a reference strain rate. The Macaulay brackets ensure the material behaves in a rate independent fashion when $\dot{\bar{\varepsilon}}^p < \dot{\varepsilon}_0$.

Power Law Breakdown

Like the Johnson-Cook formulation, the power-law breakdown model is also rate-dependent. Again, a multiplicative decomposition is assumed between isotropic hardening and the corresponding rate-dependence dependent. In this case, however, the functional form is derived from the analysis of Frost and Ashby [33] in which power-law relationships like those of the Johnson-Cook model cease to appropriately capture the physical response. The form used here is similar to the expression used by Brown and Bammann [16] and is written as,

$$\bar{\sigma} = \tilde{\sigma}_y\left(\bar{\varepsilon}^p\right)\left[1 + \operatorname{asinh}\left(\left(\frac{\dot{\bar{\varepsilon}}^p}{g}\right)^{(1/m)}\right)\right],$$

with $\tilde{\sigma}_y\left(\bar{\varepsilon}^p\right)$ being the user supplied rate independent expression, g is a model parameter related to the activation energy required to transition from climb to glide-controlled deformation, and m dictates the strength of the dependence.

4.16.2 Implementation

Like the Hill and Hosford models, the Barlat plasticity model uses a elastic predictor-inelastic corrector closest point projection (CPP) return mapping algorithm (RMA) for integration. Details of the numerical scheme and forms of the necessary derivatives may be found in the work of Scherzinger [88]. For this approach, given a rate of deformation, d_{ij}, and a time step, Δt, a trial stress state is calculated based on an elastic response

$$T_{ij}^{tr} = T_{ij}^{n} + \Delta t\, \mathbb{C}_{ijkl} d_{kl}.$$

If the trial stress state lies outside the yield surface, i.e. if $\phi(T_{ij}^{tr}) > \bar{\sigma}$, then the model uses an implicit, backward Euler algorithm to return the stress to the yield surface. To perform this task, two nonlinear equations need to be solved. The first is associated with the satisfaction of the flow-rule and ensures that the plastic strain increment is in the correct direction. Such a relation leads to a residual of the form,

$$R_{ij} = \Delta d_{ij}^{\mathrm{p}} - \Delta\gamma \frac{\partial \phi}{\partial T_{ij}} = 0. \tag{4.49}$$

while the second equation to be addressed enforces that the converged stress state is on the yield surface and is written as,

$$f = \phi\left(T_{ij}\right) - \bar{\sigma}\left(\bar{\varepsilon}^p\right) = 0. \tag{4.50}$$

The primary method for solving these equations is a Newton-Raphson algorithm. With $\Delta\gamma$ (which is equal to $\Delta\bar{\varepsilon}^p$) and T_{ij} being the solution variables, an iterative algorithm is utilized such that

$$\Delta\gamma^{(k+1)} = \Delta\gamma^{(k)} + \Delta\left(\Delta\gamma\right)$$

$$T_{ij}^{(k+1)} = T_{ij}^{(k)} + \Delta T_{ij},$$

with $\Delta\gamma^{(0)} = 0$ and $T_{ij}^{(0)} = T_{ij}^{tr}$. The plastic rate of deformation correction is then simply

$$\Delta d_{ij}^{\mathrm{p}} = \mathbb{C}_{ijkl}^{-1}\left(T_{kl}^{tr} - T_{kl}\right).$$

After linearizing the residual and consistency equations (Equations (4.49) and (4.50)), the set of nonlinear equations may be solved for the correction increments leading to expressions of the form,

$$\Delta\left(\Delta\gamma\right) = \frac{f^{(k)} - R_{ij}^{(k)}\,\mathcal{L}_{ijkl}^{(k)}\,\dfrac{\partial\phi^{(k)}}{\partial T_{kl}}}{\dfrac{\partial\phi^{(k)}}{\partial T_{ij}}\,\mathcal{L}_{ijkl}^{(k)}\,\dfrac{\partial\phi^{(k)}}{\partial T_{kl}} + H'^{(k)}}$$

$$\Delta T_{ij} = -\mathcal{L}_{ijkl}^{(k)}\left(R_{kl}^{(k)} + \Delta\left(\Delta\gamma\right)\frac{\partial\phi^{(k)}}{\partial T_{kl}}\right),$$

and $\mathcal{L}_{ijkl}^{(k)}$ is the Hessian of the RMA problem (*not* the yield surface) and is given as,

$$\mathcal{L}_{ijkl}^{(k)} = \left(\mathbb{S}_{ijkl} + \Delta\gamma^{(k)}\frac{\partial^2\phi^{(k)}}{\partial\sigma_{ij}\partial\sigma_{kl}}\right)^{-1},$$

and $\mathbb{S}_{ijkl} = \mathbb{C}_{ijkl}^{-1}$.

Unfortunately, a straightforward Newton-Raphson algorithm does not always converge, so the RMA is augmented with a line search algorithm producing modified incrementation relations with

$$\Delta\gamma^{(k+1)} = \Delta\gamma^{(k)} + \alpha\Delta\left(\Delta\gamma\right),$$

$$T_{ij}^{(k+1)} = T_{ij}^{(k)} + \alpha\Delta T_{ij},$$

where $\alpha \in (0, 1]$ is the line search parameter which is determined from certain convergence considerations. If $\alpha = 1$ then the Newton-Raphson algorithm is recovered. The line search algorithm greatly increases the reliability of the return mapping algorithm.

4.16.3 Verification

To verify the Barlat plasticity model a similar approach to that used for the Hill plasticity model (Section 4.15.3) is utilized.

Additional verification exercises for the various failure models and adiabatic heating capabilities may be found in [61], [62] and [60], respectively.

Specifically, both uniaxial stress and pure shear loadings are considered. To this end, the response of a 2090-T3 aluminum [9] with Voce hardening of the form,

$$\bar{\sigma}\left(\bar{\varepsilon}^{p}\right) = \sigma_{y} + A\left(1 - \exp\left(-b\bar{\varepsilon}^{p}\right)\right),$$

is used. The corresponding elastic, plastic, and anisotropy model parameters are given in Table 4.22.

Table 4.22 The material and model parameters for the Barlat plasticity model used for verification testing. The anisotropy coefficients correspond to 2090-T3 aluminum.

E	70 GPa	ν	0.25
a	8	σ_y	200 MPa
A	200 MPa	b	20
c'_{12}	-0.069888	c''_{12}	0.981171
c'_{13}	0.936408	c''_{13}	0.476741
c'_{21}	0.079143	c''_{21}	0.575316
c'_{23}	1.003060	c''_{23}	0.866827
c'_{31}	0.524741	c''_{31}	1.145010
c'_{32}	1.363180	c''_{32}	-0.079294
c'_{44}	1.023770	c''_{44}	1.051660
c'_{55}	1.069060	c''_{55}	1.147100
c'_{66}	0.954322	c''_{66}	1.404620

Finally, the coordinate system used in these calculations is a rectangular coordinate system with the e_i^1, e_i^2, e_i^3 axes aligned with the x, y, z axes.

4.16.3.1 Uniaxial Stress

First, the response of the material subject to a uniaxial stress is considered. As such, the Cauchy stress tensor takes the form $\sigma_{ij} = \sigma\delta_{i1}\delta_{j1}$. In the transformed stress space, this uniaxial tensor

becomes,

$$s'_{ij} = \frac{1}{3}\sigma \begin{bmatrix} c'_{12} + c'_{13} & 0 & 0 \\ 0 & -2c'_{21} + c'_{23} & 0 \\ 0 & 0 & -2c'_{31} + c'_{32} \end{bmatrix}$$

$$s''_{ij} = \frac{1}{3}\sigma \begin{bmatrix} c''_{12} + c''_{13} & 0 & 0 \\ 0 & -2c''_{21} + c''_{23} & 0 \\ 0 & 0 & -2c''_{31} + c''_{32} \end{bmatrix}.$$

It is noted from (4.51) the that two transformed stress tensors are purely diagonal and therefore in a principal state. The actual ordering of the components into the corresponding principal stresses depends on the anisotropy coefficients. By inspection of Table 4.22 it is clear in this instance that tensors are already ordered ($s'_1 = s'_{11},\ s''_1 = s''_{11}$ *etc.*). With this observation, the effective stress may be reduced to,

$$\phi\left(\sigma_{ij}\right) = \omega|\sigma|,$$

where ω is a constant dependent on model parameters and is written as,

$$\begin{aligned}\omega =& \frac{1}{3}\left\{\frac{1}{4}\left[|c'_{12} + c'_{13} - c''_{12} - c''_{13}|^a + |c'_{12} + c'_{13} + 2c''_{21} - c''_{23}|^a + |c'_{12} + c'_{13} + 2c''_{31} - c''_{32}|^a \right.\right. \\ &+ |c'_{23} - 2c'_{21} - c''_{12} - c''_{13}|^a + |c'_{23} - 2c'_{21} + 2c''_{21} - c''_{23}|^a + |c'_{23} - 2c'_{21} + 2c''_{31} - c''_{32}|^a \\ &\left.\left. + |c'_{32} - 2c'_{31} - c''_{12} - c''_{13}|^a + |c'_{32} - 2c'_{31} + 2c''_{21} - c''_{23}|^a + |c'_{32} - 2c'_{31} + 2c''_{31} - c''_{32}|^a\right]\right\}^{1/a}.\end{aligned}$$

Axial Stresses

To determine the axial stress, it is first noted that during plastic deformation,

$$\phi\left(\sigma_{ij}\right) = \omega\sigma = \bar{\sigma}\left(\bar{\varepsilon}^p\right),$$

where the fact that a tensile loading will be investigated ($\sigma > 0$) is leveraged. The stress is then simply,

$$\sigma = \frac{\bar{\sigma}\left(\bar{\varepsilon}^p\right)}{\omega}. \tag{4.51}$$

This shows that during plastic deformation the stress state can be calculated from the hardening law and anisotropy parameters.

To evaluate the axial stress, a relationship between the equivalent plastic strain and axial strain is needed. By noting the uniaxial stress state and equating the rate of plastic work, it is evident that,

$$\bar{\sigma}\dot{\bar{\varepsilon}}^p = \sigma\left(\dot{\varepsilon} - \dot{\varepsilon}^{\mathrm{e}}\right) \quad \rightarrow \quad \dot{\bar{\varepsilon}}^p = \frac{1}{\omega}\left(\dot{\varepsilon} - \dot{\varepsilon}^{\mathrm{e}}\right)$$

which, when integrated, gives an implicit equation for the equivalent plastic strain that is written as

$$\bar{\varepsilon}^p = \frac{1}{\omega}\left(\varepsilon - \frac{\bar{\sigma}(\bar{\varepsilon}^p)}{\omega E}\right). \tag{4.52}$$

The equivalent plastic strain can then be used in (4.51) to find the axial stress, σ. Corresponding stress-strain results determined analytically in this fashion and numerically via Adagio are presented below in Fig. 4.76.

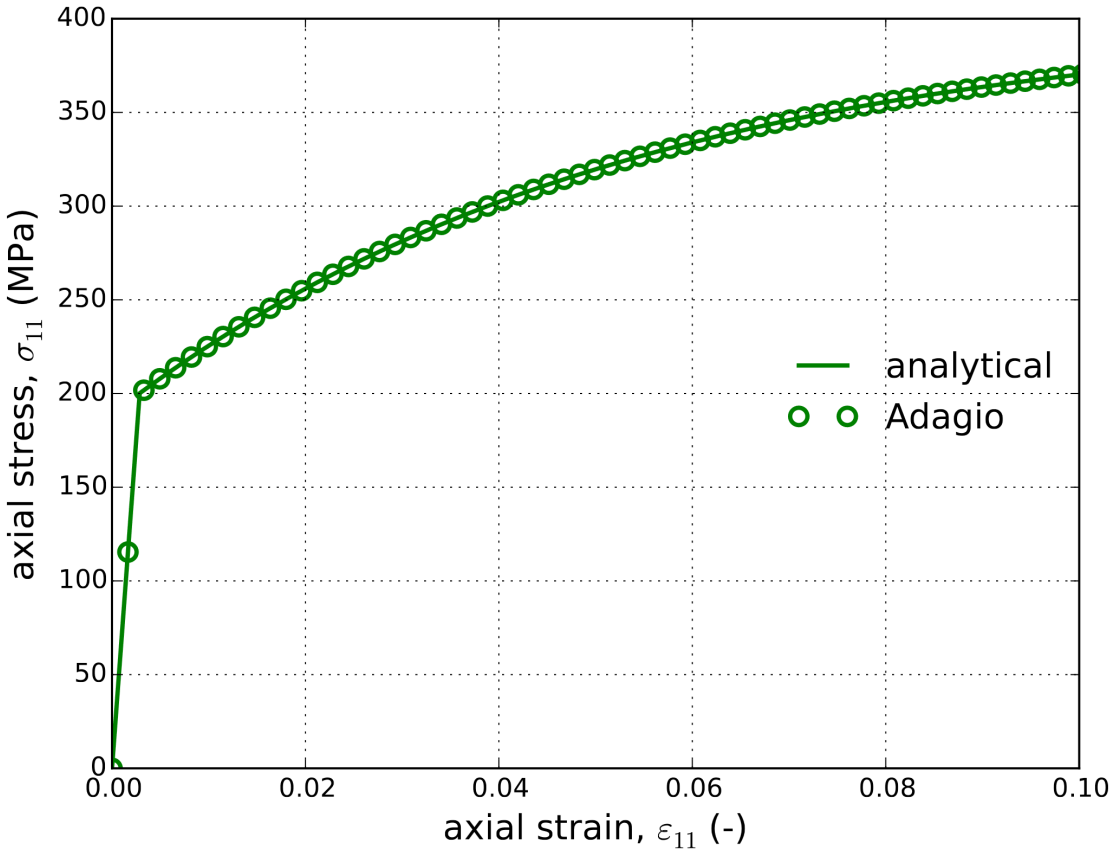

Fig. 4.76 Axial stress-strain response determined analytically and numerically for 2090-T3 aluminum using the Barlat plasticity model with Voce hardening.

Lateral Strains

To determine the plastic strain, the derivatives of the yield surface with respect to the Cauchy stress ($\partial\phi/\partial\sigma_{ij}$) are needed. From (4.48) it can be seen that these relations are quite complex and the reader is referred to [88] for a detailed discussion of how to rigorously evaluate these derivatives under arbitrary conditions. In this effort, the fact that the principal directions of the transformed stresses ($\hat{e}_i^{k\prime}$ and $\hat{e}_i^{k\prime\prime}$) are aligned with the global coordinate system ($\hat{e}_i^{1\prime} = e_i^1$ *etc.*) simplifies the problem sufficiently to allow for an analytical treatments. In this case,

$$\frac{\partial s'_k}{\partial s'_{ij}} = e_i^k e_j^k.$$

With this observation, the lateral flow directions may be written as,

$$\begin{aligned}\frac{\partial\phi}{\partial\sigma_{22}} =& \frac{1}{3}\Big[\frac{\partial\phi}{\partial s'_1}\left(c'_{13}-2c'_{12}\right)+\frac{\partial\phi}{\partial s'_2}\left(c'_{21}+c'_{23}\right)+\frac{\partial\phi}{\partial s'_3}\left(c'_{31}-2c'_{32}\right)\\ &+\frac{\partial\phi}{\partial s''_1}\left(c''_{13}-2c''_{12}\right)+\frac{\partial\phi}{\partial s''_2}\left(c''_{21}+c''_{23}\right)+\frac{\partial\phi}{\partial s''_3}\left(c''_{31}-2c''_{32}\right)\Big]\\ \frac{\partial\phi}{\partial\sigma_{33}} =& \frac{1}{3}\Big[\frac{\partial\phi}{\partial s'_1}\left(c'_{12}-2c'_{13}\right)+\frac{\partial\phi}{\partial s'_2}\left(c'_{21}-2c'_{23}\right)+\frac{\partial\phi}{\partial s'_3}\left(c'_{31}+c'_{32}\right)\\ &+\frac{\partial\phi}{\partial s''_1}\left(c''_{12}-2c''_{13}\right)+\frac{\partial\phi}{\partial s''_2}\left(c''_{21}-2c''_{23}\right)+\frac{\partial\phi}{\partial s''_3}\left(c''_{31}+c''_{32}\right)\Big],\end{aligned}$$

in which the various $\partial\phi/\partial s'_i$ derivatives are functions of the anisotropy coefficients and explicit forms may be found in [88].

The total strain is written simply as,

$$\varepsilon_{ij} = \varepsilon^{\mathrm{e}}_{ij} + \varepsilon^{\mathrm{p}}_{ij},$$

with the elastic strain being

$$\varepsilon^{\mathrm{e}}_{22} = \varepsilon^{\mathrm{e}}_{33} = -\nu\frac{\sigma}{E},$$

and the plastic strains found via the flow rules as,

$$\varepsilon^{\mathrm{p}}_{22} = \bar{\varepsilon}^p\frac{\partial\phi}{\partial\sigma_{22}} \qquad ; \qquad \varepsilon^{\mathrm{p}}_{33} = \bar{\varepsilon}^p\frac{\partial\phi}{\partial\sigma_{33}}.$$

The flow directions were given previously in (4.53) and (4.53) while the equivalent plastic strain may be found via (4.52). Fig. 4.77 presents the lateral strains as a function of the axial. Clear agreement may be observed both in Fig. 4.76 and Fig. 4.77 verifying the model. Additionally, the effect of the anisotropy is plainly evident in Fig. 4.77 in which the two lateral strains differ by approximately a factor of four.

To test the other directions and further examine the anisotropic character of the model, the coordinate system rotation input options are used to align the 2 and 3 directions of the material

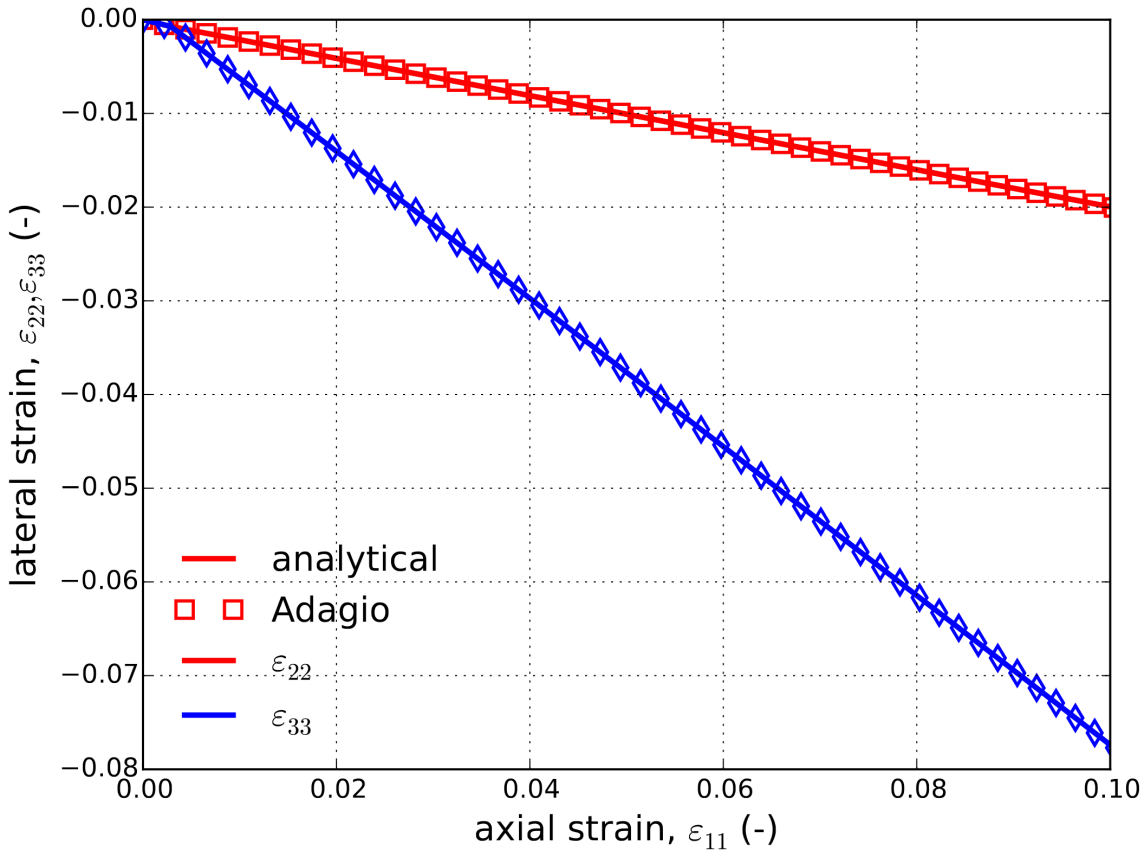

Fig. 4.77 Lateral strain as a function of axial strain of 2090-T3 aluminum with Voce hardening as determined by the Barlat plasticity model both analytically and numerically.

with the applied load. Analytical expressions may be determined by similarly rotating the coefficients in the previous expressions, although these are not repeated here for brevity. The corresponding results for the loading aligned with the 2 and 3 directions are presented in Fig. 4.78 and Fig. 4.79, respectively. All of the results are given with respect to the original coordinate system to avoid confusion. Clear agreement between analytical and simulation results is noted in both cases further verifying the capabilities of the model. Importantly, by comparing the various stress-strain and lateral strain curves, the influence of the material and model anisotropy on the responses may readily be observed.

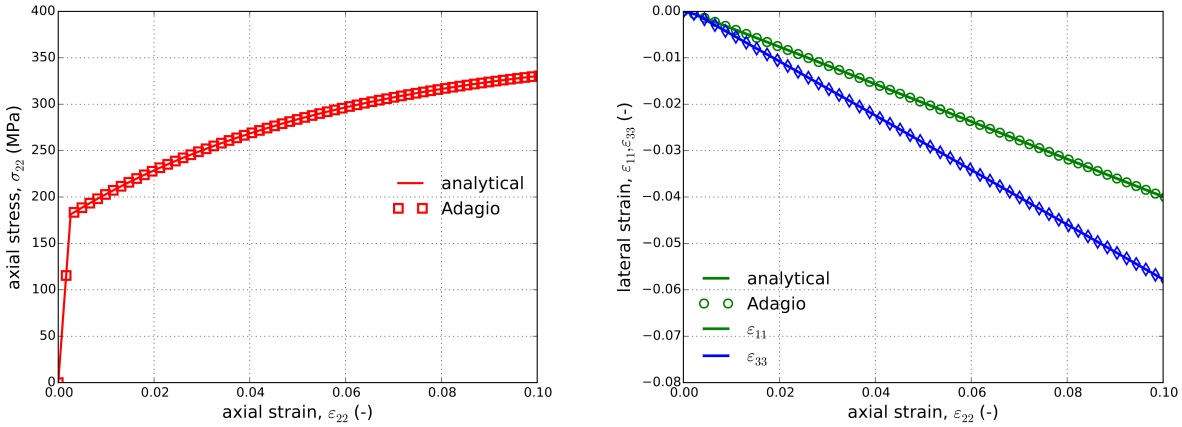

(a) Stress-strain **(b) Lateral strains**

Fig. 4.78 Stress-strain (a) and lateral strain (b) responses of 2090-T3 aluminum with Voce hardening and the Barlat plasticity model. The material is rotated such that the loading is aligned with the 2 direction.

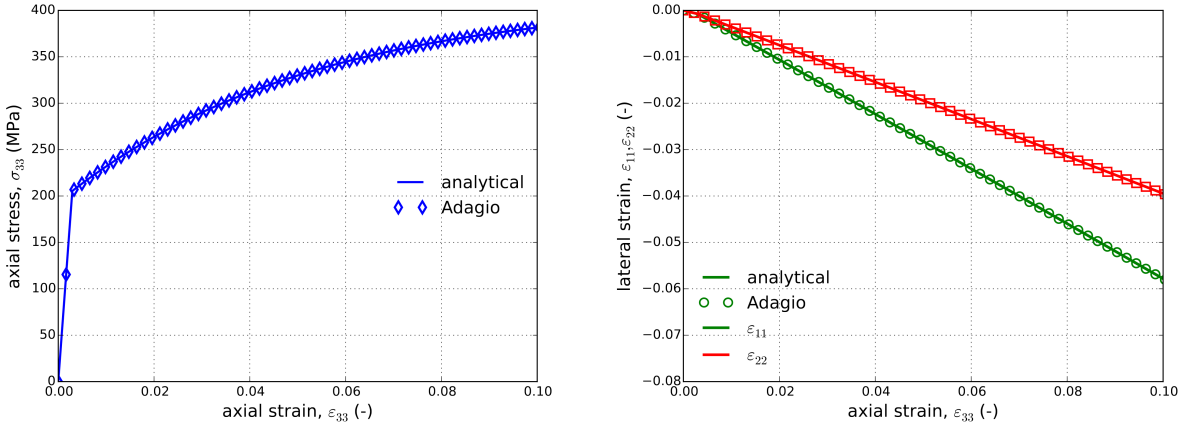

(a) Stress-strain **(b) Lateral strains**

Fig. 4.79 Stress-strain (a) and lateral strain (b) responses of 2090-T3 aluminum with Voce hardening and the Barlat plasticity model. The material is rotated such that the loading is aligned with the 3 direction.

4.16.3.2 Pure Shear

In this section, the pure shear response of the Barlat model is interrogated to assess its performance under such conditions. Before proceeding, it is important to recall the ordering of the shear stresses in Sierra/SM. Specifically, the σ_{12}, σ_{23}, and σ_{31} stresses are associated with the 44, 55, and 66, respectively, anisotropy coefficients.

To explore the shear performance of the Barlat plasticity model, a stress tensor of the form $\sigma_{ij} = \tau\left(\delta_{i1}\delta_{j2} + \delta_{i2}\delta_{j1}\right)$ is considered. The ordered principal stresses of the transformed stress tensors are,

$$s'_i = \begin{bmatrix} c'_{44}\tau \\ 0 \\ -c'_{44}\tau \end{bmatrix} \quad ; \quad s''_i = \begin{bmatrix} c''_{44}\tau \\ 0 \\ -c''_{44}\tau \end{bmatrix}, \tag{4.53}$$

thereby simplifying the effective stress to,

$$\phi\left(\sigma_{ij}\right) = \tau\zeta,$$

with

$$\zeta = \left\{\frac{1}{2}\left[|c'_{44} - c''_{44}|^a + |c'_{44} + c''_{44}|^a + |c'_{44}|^a + |c''_{44}|^a\right]\right\}^{1/a}.$$

During plastic flow,

$$\phi = \tau\zeta = \bar{\sigma}\left(\bar{\varepsilon}^p\right),$$

producing an expression for the stress in terms of equivalent plastic strain as,

$$\tau = \frac{1}{\zeta}\bar{\sigma}\left(\bar{\varepsilon}^p\right).$$

A relationship between the equivalent plastic and axial strains may be determined by first considering the equivalency of plastic work,

$$\bar{\sigma}\dot{\bar{\varepsilon}}^p = 2\tau\left(\dot{\varepsilon}_{12} - \dot{\varepsilon}^{\mathrm{e}}_{12}\right) \qquad \rightarrow \qquad \dot{\bar{\varepsilon}}^p = \frac{2}{\zeta}\left(\dot{\varepsilon}_{12} - \dot{\varepsilon}^{\mathrm{e}}\right).$$

Integrating leads to an implicit expression of the form,

$$\bar{\varepsilon}^p = \frac{2}{\zeta}\left(\varepsilon_{12} - \frac{\bar{\sigma}\left(\bar{\varepsilon}^p\right)}{\zeta G}\right). \tag{4.54}$$

The preceding relations may be used to analytically determine the shear stress-strain response. Corresponding results, along with those produced by Adagio, are presented in Fig. 4.80. Shear responses are also presented for stress tensors of the form $\sigma_{ij} = \tau\left(\delta_{2i}\delta_{3j} + \delta_{3i}\delta_{2j}\right)$ (23) and $\sigma_{ij} = \tau\left(\delta_{1i}\delta_{3j} + \delta_{3i}\delta_{1j}\right)$ (31). Analytically, these results were determined by substituting the relevant anisotropy coefficients in (4.53)-(4.54). For the results from Adagio, the coordinate system input commands were used to rotate the material coordinate system accordingly.

In all the cases presented in Fig. 4.80 excellent agreement is noted. This not only verifies the performance of the current model under pure shear loadings but also demonstrates the impact of the anisotropy and exercises the coordinate system rotation capabilities.

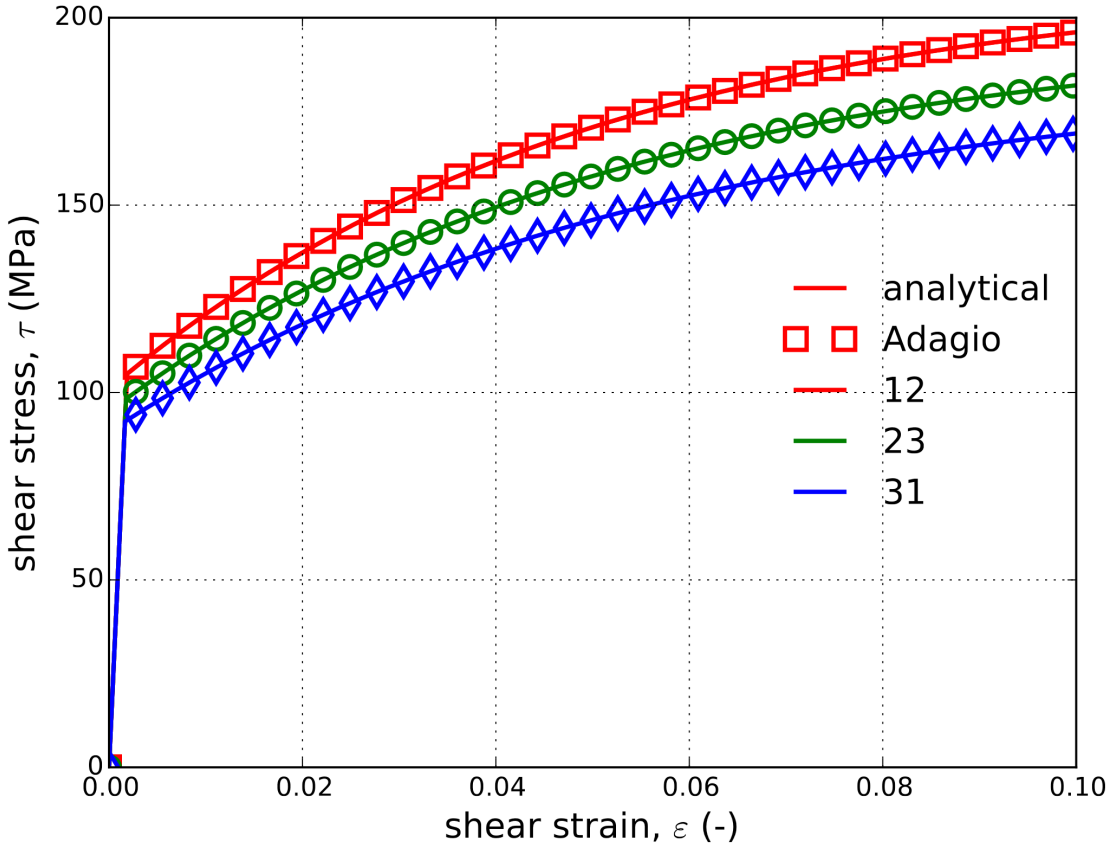

Fig. 4.80 Shear stress-strain results for 2090-T3 aluminum determined analytically and numerically by the Barlat plasticity model with Voce Hardening

4.16.3.3 Plastic Hardening

To verify the capabilities of the hardening models, rate *independent* and rate *dependent* alike, the constant equivalent plastic strain rate, $\dot{\bar{\varepsilon}}^p$, uniaxial stress and pure shear verification tests described in *Appendix A* are utilized. In these simplified loading cases, the material state may be found explicitly as a function of time knowing the prescribed equivalent strain rate. For the rate *independent* cases, a strain rate of $\dot{\bar{\varepsilon}}^p = 1 \times 10^{-4} \mathrm{s}^{-1}$ is used for ease in simulations although the selected rate does note affect the results. Through this testing protocol, the hardening models are not only tested at different rates but also in different principal material directions to consider the anisotropy of the Barlat yield surface. Additionally, the rate *dependent* models are tested for a wide range of strain rates (over five decades) with all three rate *independent* hardening functions ($\tilde{\sigma}_y$ in the previous theory section). Although linear, Voce, and power-law rate *independent* representations are utilized in the rate *dependent* tests, in those cases the hardening models are prescribed via user-defined analytic functions. The rate *independent* verification exercises, on the other hand, examine the built-in hardening models. This distinction necessitates the different considerations and treatments.

The rate *dependent* and rate *independent* hardening coefficients are found in Table 4.23 while the remaining model parameters are unchanged from the previous verification exercises. For the current verification exercise, the rate *independent* hardening models (linear, Voce, and power-law) will first be considered and then the rate *dependent* forms (Johnson-Cook, power-law breakdown).

Table 4.23 The model parameters for the hardening verification tests used with the Barlat plasticity model during verification tests. Parameters for the rate *independent* hardening functions, $\tilde{\sigma}_y$, are also given and denoted with a $\tilde{\cdot}$ while the subscript refers to the functional form.

C	0.1	$\dot{\varepsilon}_0$	1×10^{-4} s^{-1}
g	0.21 s^{-1}	m	16.4
$\tilde{H}_{\mathrm{Linear}}$	200 MPa	•	•
$\tilde{A}_{\mathrm{PL}}$	400 MPa	$\tilde{n}_{\mathrm{PL}}$	0.25
$\tilde{A}_{\mathrm{Voce}}$	200 MPa	$\tilde{n}_{\mathrm{Voce}}$	20

Linear

For the rate *independent* linear hardening model, verification is considered via the uniaxial stress and pure shear exercises of *Appendix A*. As the anisotropic Barlat yield surface is being used for this examination, the uniaxial stress response is determined for loading in three different principal material planes while the pure shear response is found along three shear planes. Results determined analytically and numerically are presented in Fig. 4.81. Clear agreement is evident between the dual solution approaches. Additionally, the linear response and constant tangent modulus during plastic deformation highlights the characteristic feature of the current model.

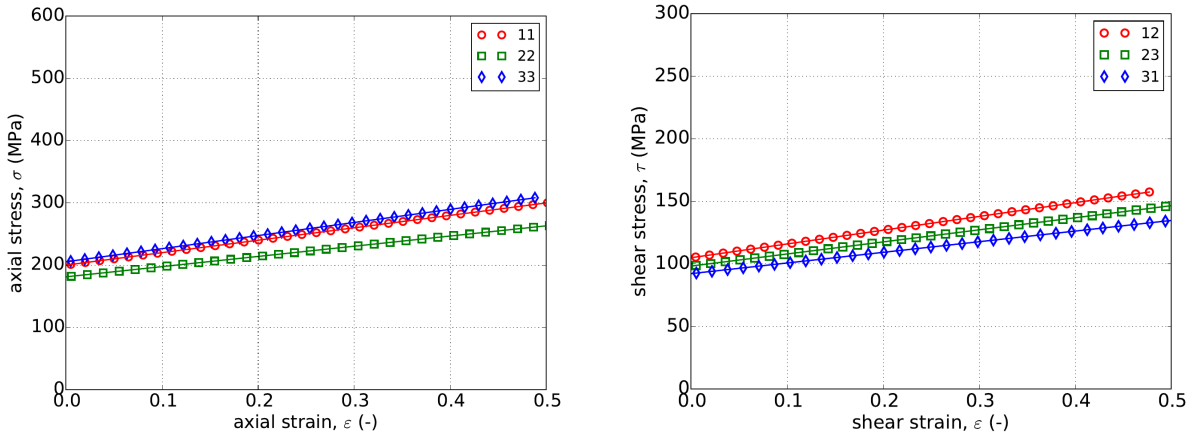

(a) Stress-strain **(b) Lateral strains**

Fig. 4.81 Uniaxial stress-strain (a) and pure shear (b) responses of the Barlat plasticity model with rate *independent*, linear hardening. Solid lines are analytical while open symbols are numerical

Power-Law

To probe the power-law rate *independent* hardening model, analytical and numerical results to the uniaxial stress and pure shear problems of *Appendix A* are determined. Given the anisotropic nature of the current model, responses are determined along the three principal and three shearing planes for the uniaxial stress and pure shear cases and all six cases are shown in Fig. 4.82. In considering Fig. 4.82, it is apparent that the numerical and analytical responses agree quite well verifying this specific response. These cases also highlight the initially stiff plastic response that eventually evolves into a more compliant linear like response that is associated with a power-law hardening model.

Voce

Verifying the Voce model is addressed through the methods of *Appendix A*. To this end, analytical and numerical uniaxial stress and pure shear responses are determined along three different principal directions and shear planes, respectively. The results for these various cases are presented in Fig. 4.83 and unambiguous agreement is readily seen between the analytical and numerical results providing further credence to hardening model capabilities. Responses in Fig. 4.83 also exhibit the clear saturation of hardening with sufficient plastic strain that is usually associated with the Voce model.

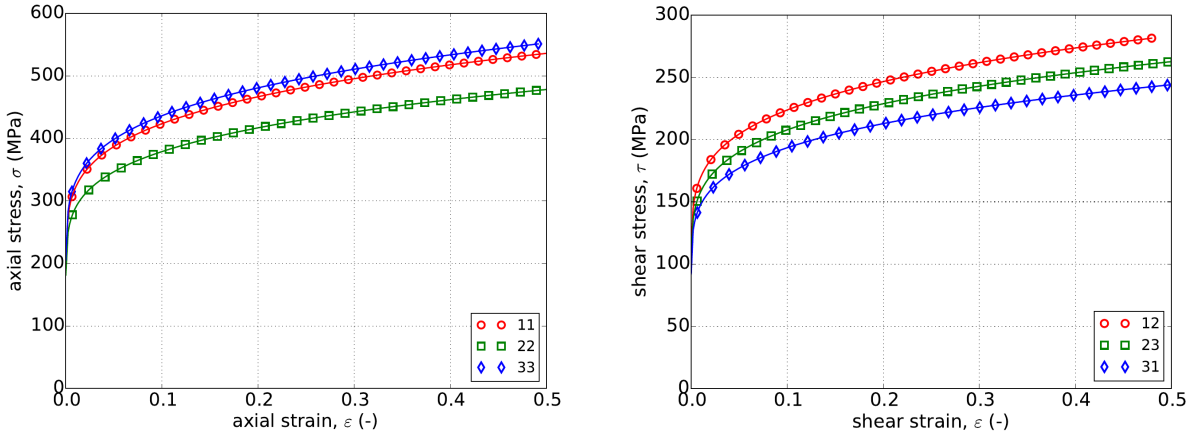

(a) Stress-strain **(b) Lateral strains**

Fig. 4.82 Uniaxial stress-strain (a) and pure shear (b) responses of the Barlat plasticity model with rate *independent*, power-law hardening. Solid lines are analytical while open symbols are numerical.

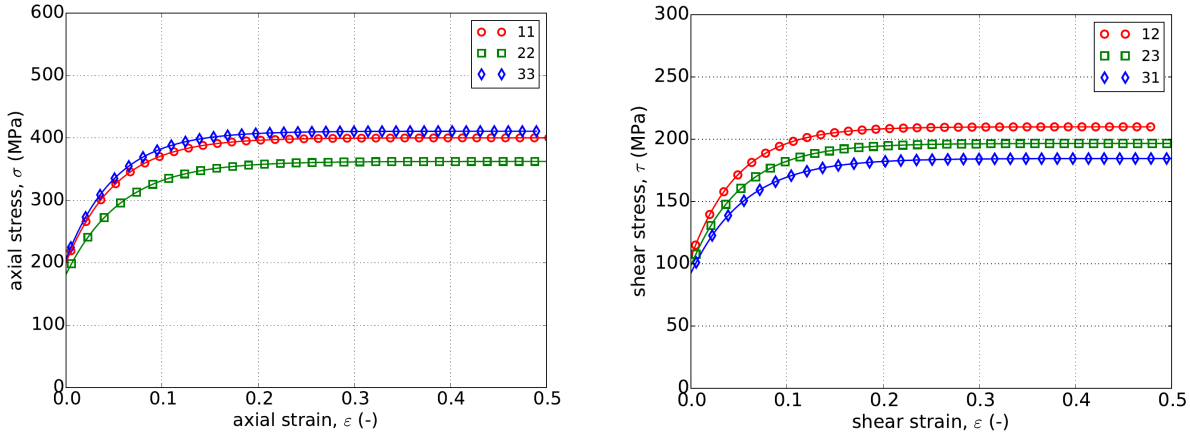

(a) Stress-strain **(b) Lateral strains**

Fig. 4.83 Uniaxial stress-strain (a) and pure shear (b) responses of the Barlat plasticity model with rate *independent*, Voce hardening. Solid lines are analytical while open symbols are numerical.

Johnson-Cook

To investigate the uniaxial response of the Johnson-Cook rate *dependent* hardening model, the problem discussed in *Appendix A* is considered. In this analysis, the response depends only on time and the various c_i' and c_i'' Barlat yield surface coefficients. For a full-spectrum verification, forty-five different cases are evaluated using three different material principal directions ($\hat{e}_1$, $\hat{e}_2$, and $\hat{e}_3$), five different rates ($\dot{\bar{\varepsilon}}^p = 1 \times 10^{-3},\ 1 \times 10^{-2},\ 1 \times 10^{-1},\ 1 \times 10^{0}$ and 1×10^{1} s^{-1}), and three different rate *independent* hardening models (linear, Voce, and power-law). All forty-five analytical and numerical results are presented in Fig. 4.84 and Fig. 4.85 and quite notable agreement is observed in each instance.

For the pure shear case, the forty-five different permutations are again explored. The same five rates and three hardening models are used although three different shearing planes are used instead of the three principal directions. The solution of the pure shear problem is described in *Appendix A* and the analytical and numerical results are presented in Fig. 4.86 and Fig. 4.87. As with the uniaxial stress response excellent correspondence is noted between the two sets of results.

Power-Law Breakdown

In the case of the power-law Breakdown model, verification is again pursued through the problem of *Appendix A* and using the same forty-five cases discussed with the Johnson-Cook model. Corresponding results are given in Fig. 4.88 and Fig. 4.89 and as with the preceding results substantial convergence is noted between the analytical and numerical results giving further credence to the hardening models.

As with the uniaxial stress case, the pure shear capabilities are interrogated through the procedure of *Appendix A* using the same forty-five cases outlined in the Johnson-Cook discussion. The analytical and numerical results are presented in Fig. 4.90 and Fig. 4.91. Again, the two result sets align beautifully enabling further capability credibility.

4.16.4 User Guide

```
BEGIN PARAMETERS FOR MODEL BARLAT_PLASTICITY
  #
  # Elastic constants
  #
  YOUNGS MODULUS = <real>
  POISSONS RATIO = <real>
  SHEAR MODULUS  = <real>
  BULK MODULUS   = <real>
  LAMBDA         = <real>
  TWO MU         = <real>
  #
```

(continues on next page)

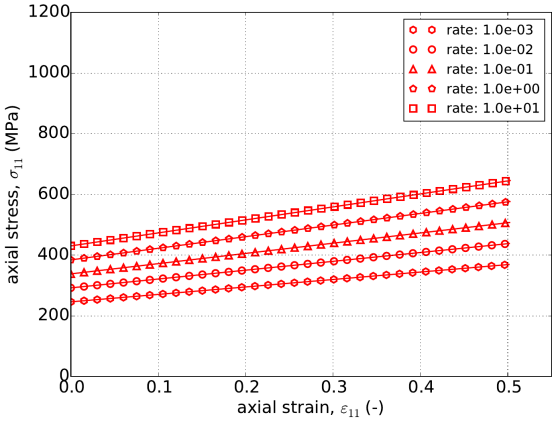

(a) Linear Hardening -- 11

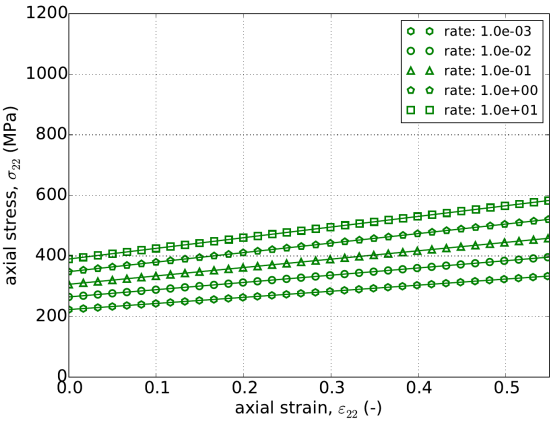

(b) Linear Hardening -- 22

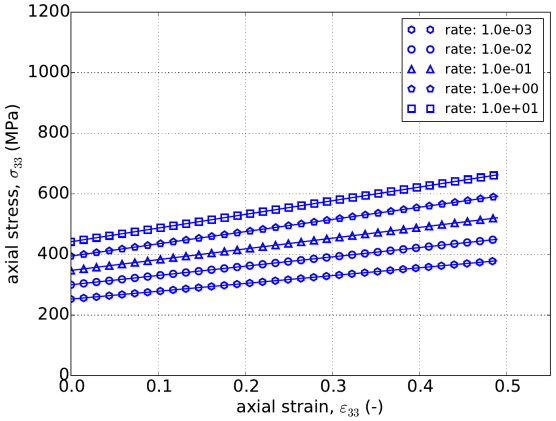

(c) Linear Hardening -- 33

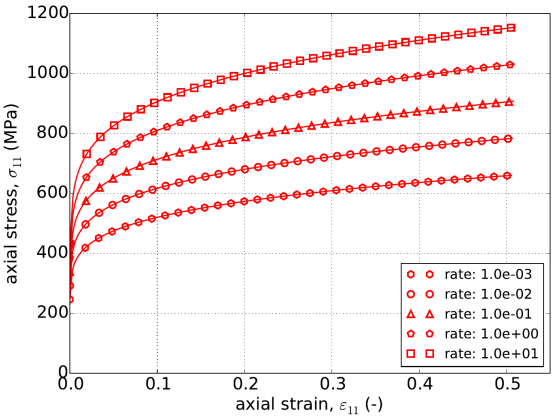

(d) Power-Law Hardening -- 11

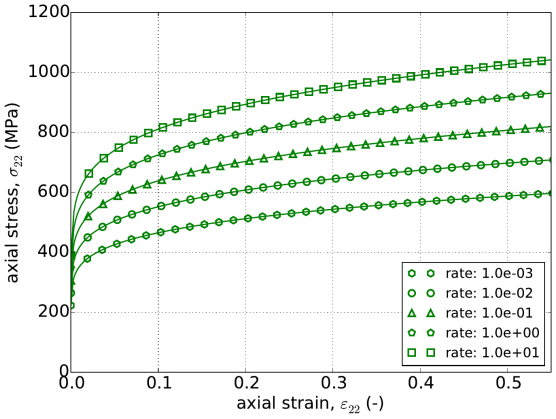

(e) Power-Law Hardening -- 22

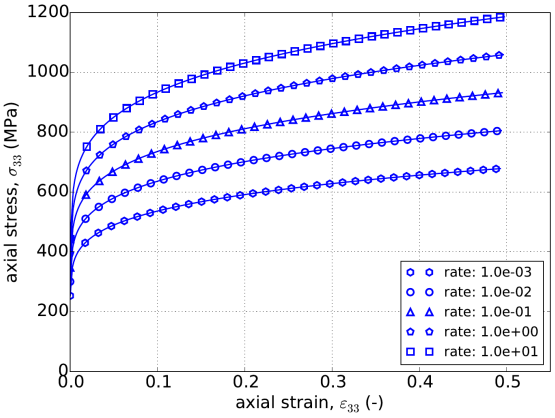

(f) Power-Law Hardening -- 33

Fig. 4.84 Uniaxial stress-strain response of the Barlat plasticity model ($a = 8$) with rate *dependent*, Johnson-Cook type hardening with (a-c) linear and (d-f) power-law rate *independent* hardening. Solid lines are analytical results while open symbols are numerical.

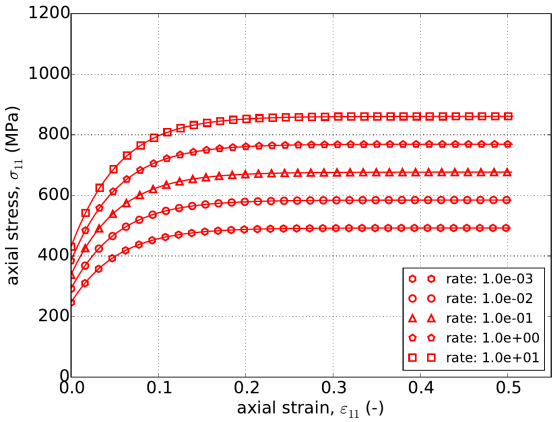

(a) Voce Hardening -- 11

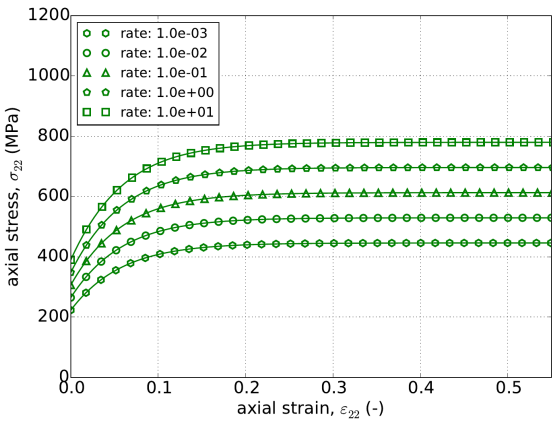

(b) Voce Hardening -- 22

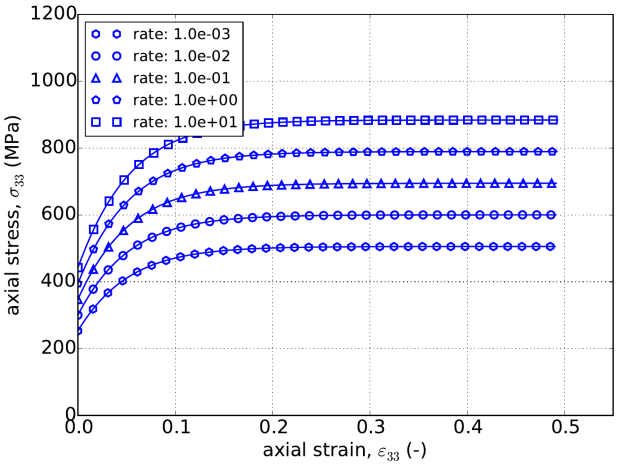

(c) Voce Hardening -- 33

Fig. 4.85 Uniaxial stress-strain response of the Barlat plasticity model ($a = 8$) with rate *dependent*, Johnson-Cook type hardening with (a-c) Voce rate *independent* hardening. Solid lines are analytical results while open symbols are numerical.

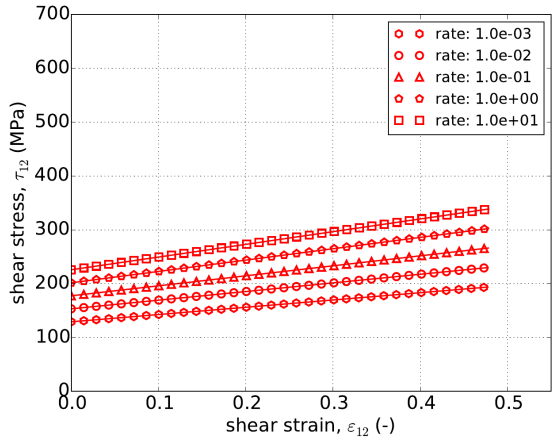

(a) Linear Hardening -- 11

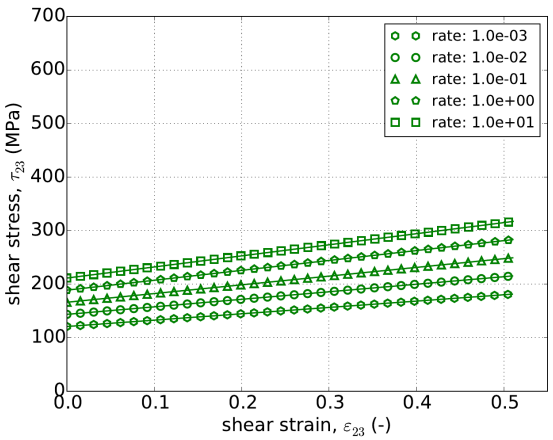

(b) Linear Hardening -- 22

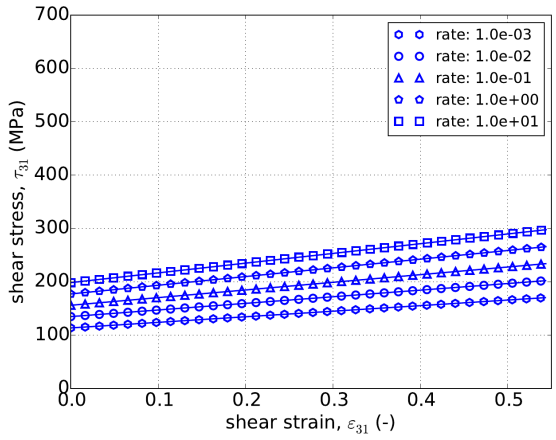

(c) Linear Hardening -- 33

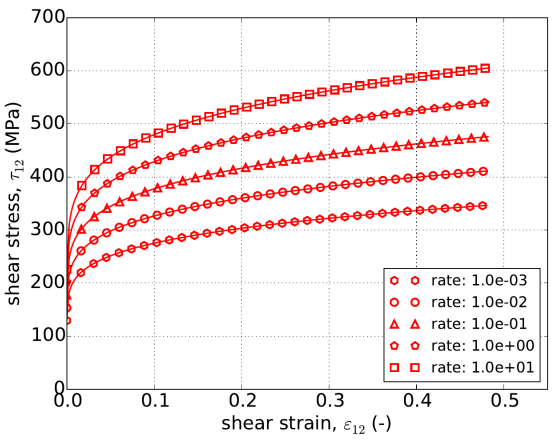

(d) Power-Law Hardening -- 11

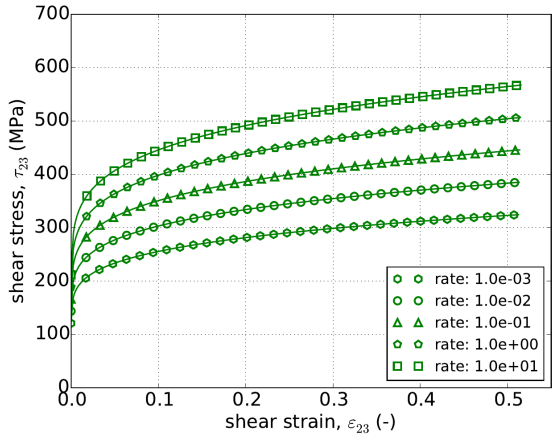

(e) Power-Law Hardening -- 22

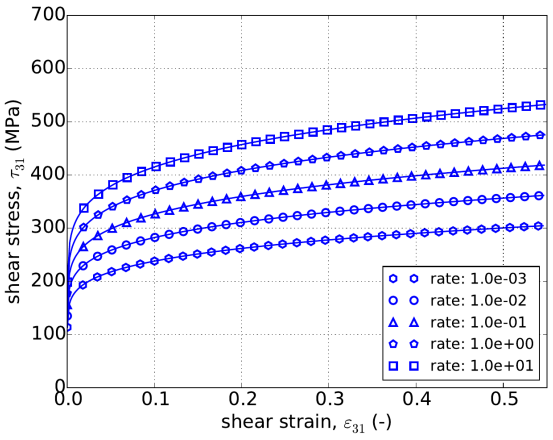

(f) Power-Law Hardening -- 33

Fig. 4.86 Stress-strain response of the Barlat plasticity model ($a = 8$) with rate *dependent*, Johnson-Cook type hardening in pure shear with (a-c) linear and (d-f) power-law rate *independent* hardening. Solid lines are analytical results while open symbols are numerical.

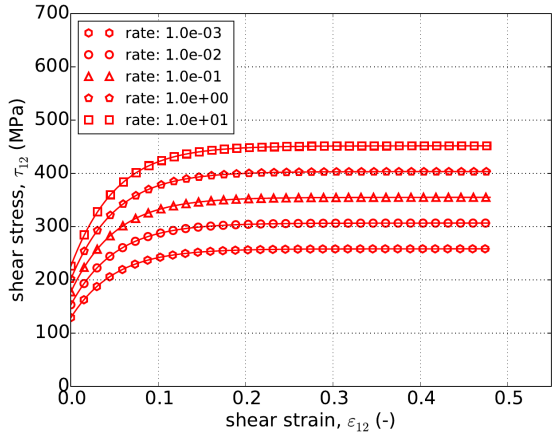

(a) Voce Hardening -- 11

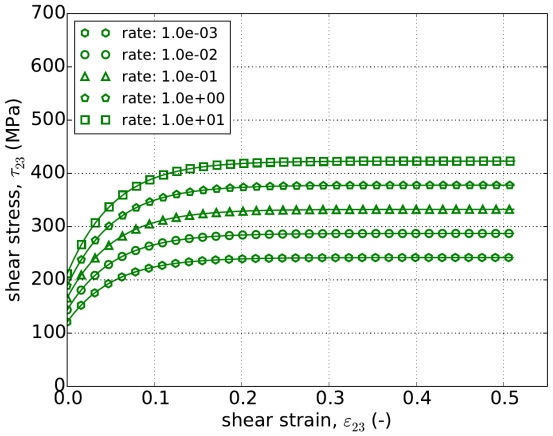

(b) Voce Hardening -- 22

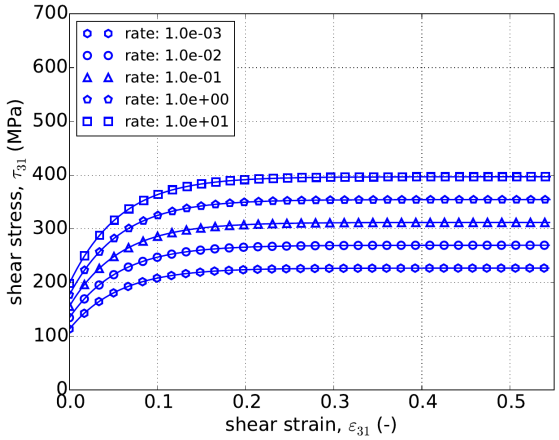

(c) Voce Hardening -- 33

Fig. 4.87 Stress-strain response of the Barlat plasticity model ($a = 8$) with rate *dependent*, Johnson-Cook type hardening in pure shear with (a-c) Voce rate *independent* hardening. Solid lines are analytical results while open symbols are numerical.

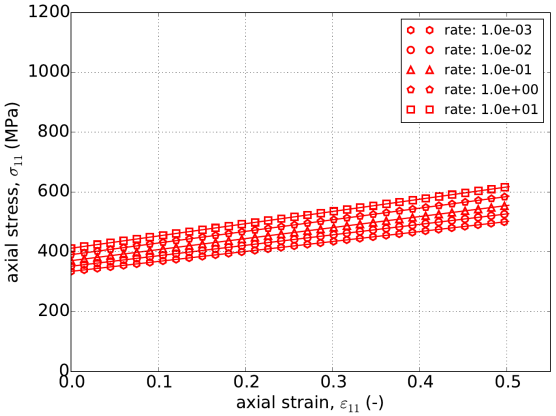

(a) Linear Hardening -- 11

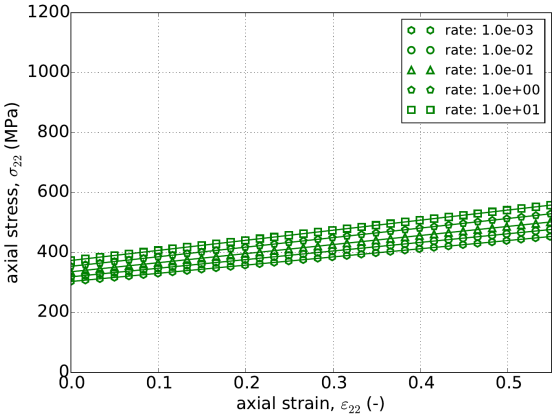

(b) Linear Hardening -- 22

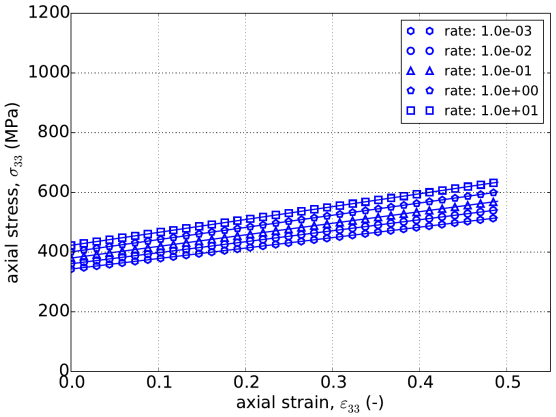

(c) Linear Hardening -- 33

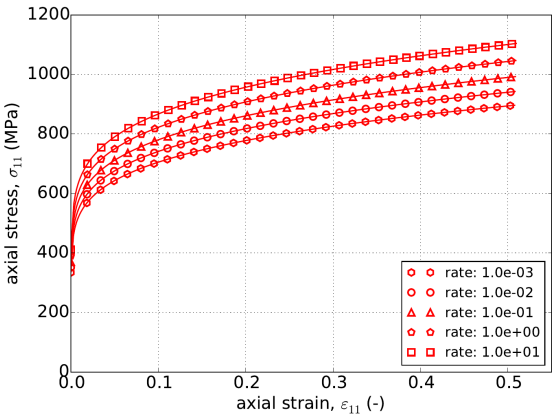

(d) Power-Law Hardening -- 11

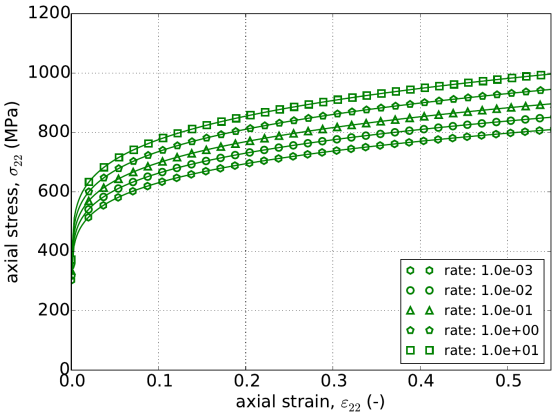

(e) Power-Law Hardening -- 22

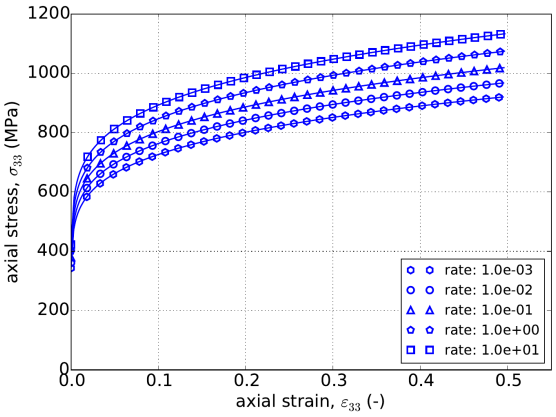

(f) Power-Law Hardening -- 33

Fig. 4.88 Uniaxial stress-strain response of the Barlat plasticity model ($a = 8$) with rate *dependent*, power-law breakdown type hardening with (a-c) linear and (d-f) power-law rate *independent* hardening. Solid lines are analytical while open symbols are numerical.

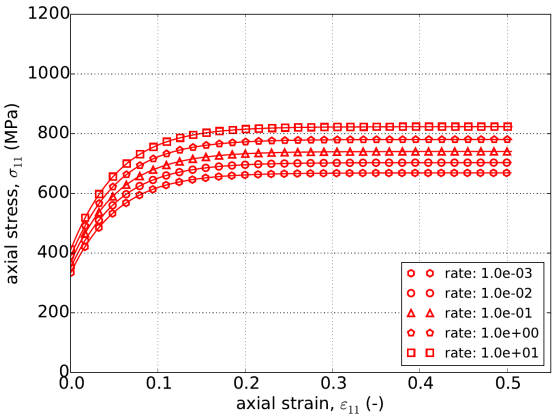

(a) Voce Hardening -- 11

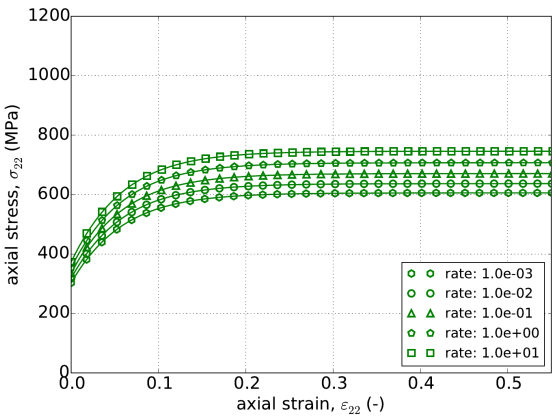

(b) Voce Hardening -- 22

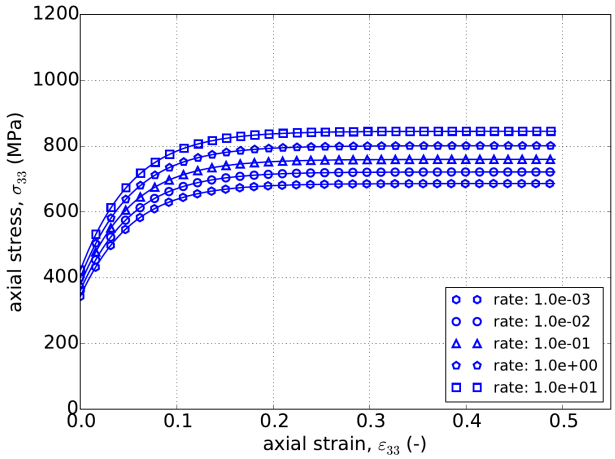

(c) Voce Hardening -- 33

Fig. 4.89 Uniaxial stress-strain response of the Barlat plasticity model ($a = 8$) with rate *dependent*, power-law breakdown type hardening with (a-c) Voce rate *independent* hardening. Solid lines are analytical while open symbols are numerical.

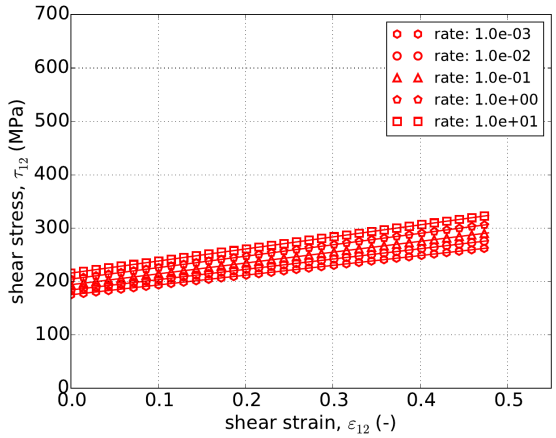

(a) Linear Hardening -- 11

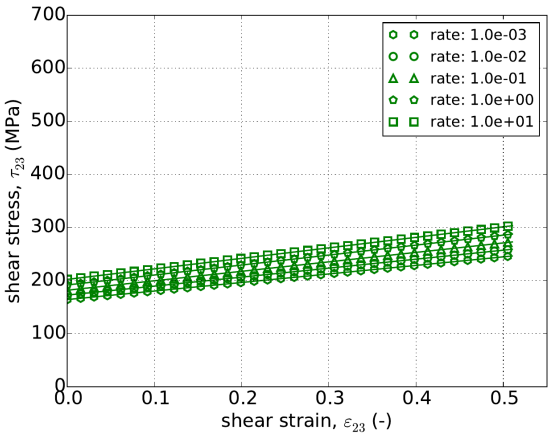

(b) Linear Hardening -- 22

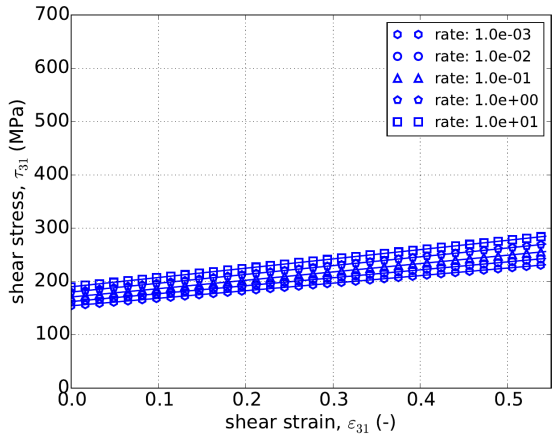

(c) Linear Hardening -- 33

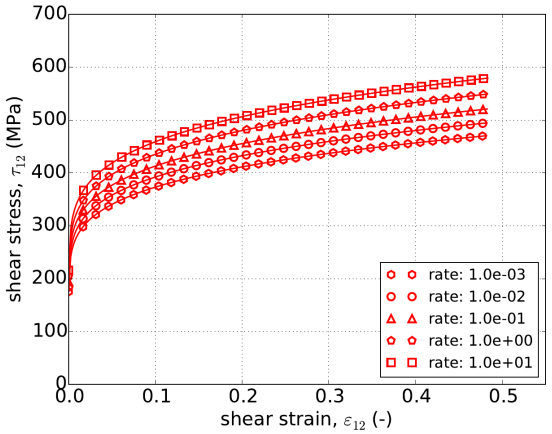

(d) Power-Law Hardening -- 11

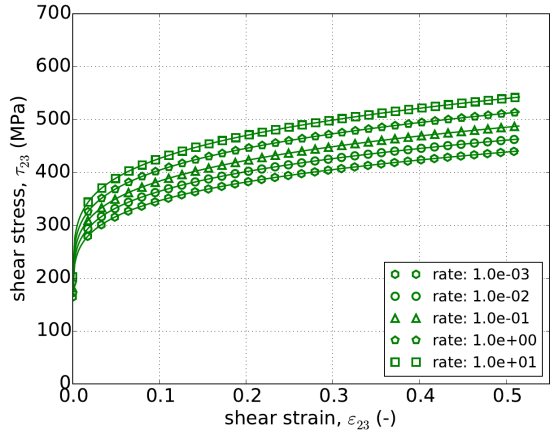

(e) Power-Law Hardening -- 22

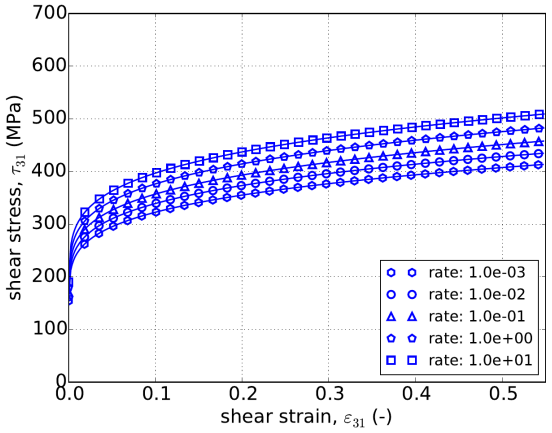

(f) Power-Law Hardening -- 33

Fig. 4.90 Stress-strain response of the Barlat plasticity model ($a = 8$) with rate *dependent*, power-law breakdown type hardening in pure shear with (a-c) linear and (d-f) power-law rate *independent* hardening. Solid lines are analytical results while open symbols are numerical.

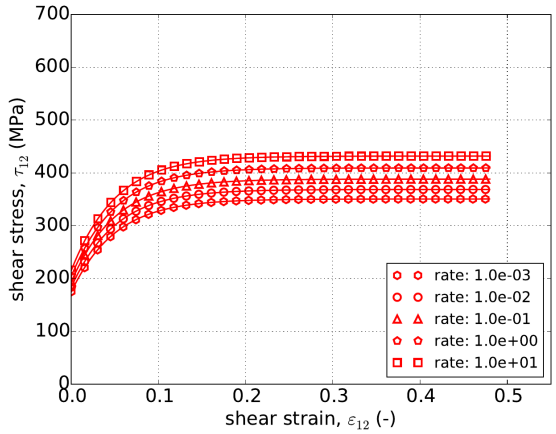

(a) Voce Hardening -- 11

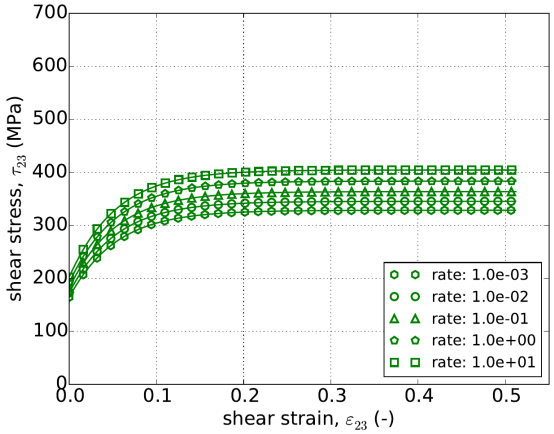

(b) Voce Hardening -- 22

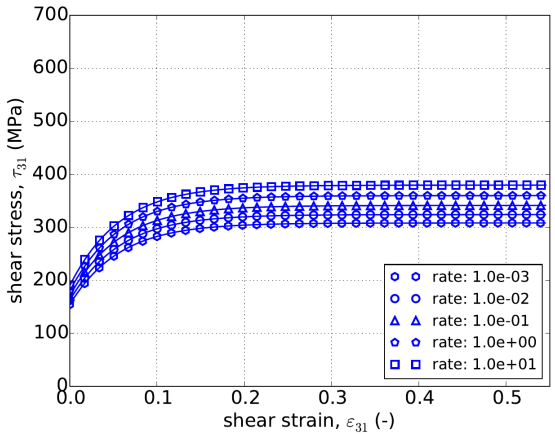

(c) Voce Hardening -- 33

Fig. 4.91 Stress-strain response of the Barlat plasticity model ($a = 8$) with rate *dependent*, power-law breakdown type hardening in pure shear with (a-c) Voce rate *independent* hardening. Solid lines are analytical results while open symbols are numerical.

(continued from previous page)

```
  # Material coordinates system definition
  #
  COORDINATE SYSTEM              = <string> coordinate_system_name
  DIRECTION FOR ROTATION         = <real> 1|2|3
  ALPHA                          = <real> (degrees)
  SECOND DIRECTION FOR ROTATION = <real> 1|2|3
  SECOND ALPHA                   = <real> (degrees)
  #
  # Yield surface parameters
  #
  YIELD STRESS = <real>
  A            = <real> (4.0)
  CP12         = <real> (1.0)
  CP13         = <real> (1.0)
  CP21         = <real> (1.0)
  CP23         = <real> (1.0)
  CP31         = <real> (1.0)
  CP32         = <real> (1.0)
  CP44         = <real> (1.0)
  CP55         = <real> (1.0)
  CP66         = <real> (1.0)
  CPP12        = <real> (1.0)
  CPP13        = <real> (1.0)
  CPP21        = <real> (1.0)
  CPP23        = <real> (1.0)
  CPP31        = <real> (1.0)
  CPP32        = <real> (1.0)
  CPP44        = <real> (1.0)
  CPP55        = <real> (1.0)
  CPP66        = <real> (1.0)
```

```
#
  #
  # Hardening model
  #
  HARDENING MODEL = LINEAR | POWER_LAW | VOCE | USER_DEFINED |
  FLOW_STRESS | DECOUPLED_FLOW_STRESS | JOHNSON_COOK |
  POWER_LAW_BREAKDOWN
  #
  # Linear hardening
  #
  HARDENING MODULUS = <real>
  #
  # Power-law hardening
  #
```

(continues on next page)

(continued from previous page)

```
  HARDENING CONSTANT = <real>
  HARDENING EXPONENT = <real> (0.5)
  LUDERS STRAIN      = <real> (0.0)
  #
  # Voce hardening
  #
  HARDENING MODULUS       = <real>
  EXPONENTIAL COEFFICIENT = <real>
  #
  # Johnson-Cook hardening
  #
  HARDENING FUNCTION = <string>hardening_function_name
  RATE CONSTANT      = <real>
  REFERENCE RATE     = <real>
  #
  # Power law breakdown hardening
  #
  HARDENING FUNCTION = <string>hardening_function_name
  RATE COEFFICIENT   = <real>
  RATE EXPONENT      = <real>
  # User defined hardening
  #
  HARDENING FUNCTION = <string>hardening_function_name
  #
```

```
#
  #
  # Following Commands Pertain to Flow_Stress Hardening Model
  #
  #    -  Isotropic Hardening model
  #
  ISOTROPIC HARDENING MODEL = LINEAR | POWER_LAW | VOCE |
                              USER_DEFINED
  #
  # Specifications for Linear, Power-law, and Voce same as above
  #
  # User defined hardening
  #
  ISOTROPIC HARDENING FUNCTION = <string>iso_hardening_fun_name
  #
  #     - Rate dependence
  #
  RATE MULTIPLIER = JOHNSON_COOK | POWER_LAW_BREAKDOWN |
     USER_DEFINED | RATE_INDEPENDENT (RATE_INDEPENDENT)
  #
```

(continues on next page)

(continued from previous page)

```
  # Specifications for Johnson-Cook, Power-law-breakdown
  #     same as before EXCEPT no need to specify a
  #     hardening function
  #
  # User defined rate multiplier
  #
  RATE MULTIPLIER FUNCTION = <string> rate_mult_function_name
  #
  #     - Temperature dependence
  #
  TEMPERATURE MULTIPLIER = JOHNSON_COOK | USER_DEFINED |
     TEMPERATURE_INDEPENDENT (TEMPERATURE_INDEPENDENT)
  #
  #  Johnson-Cook temperature dependence
  #
  MELTING TEMPERATURE   = <real>
  REFERENCE TEMPERATURE = <real>
  TEMPERATURE EXPONENT  = <real>
  #
  #  User-defined temperature dependence
  TEMPERATURE MULTIPLIER FUNCTION = <string>temp_mult_function_name
  #
  # Following Commands Pertain to Decoupled_Flow_Stress Hardening Model
  #
  #    -  Isotropic Hardening model
  #
  ISOTROPIC HARDENING MODEL = LINEAR | POWER_LAW | VOCE | USER_DEFINED
  #
  # Specifications for Linear, Power-law, and Voce same as above
  #
  # User defined hardening
  #
  ISOTROPIC HARDENING FUNCTION = <string>isotropic_hardening_function_
↪name
  #
  #     - Rate dependence
  #
  YIELD RATE MULTIPLIER = JOHNSON_COOK | POWER_LAW_BREAKDOWN |
              USER_DEFINED | RATE_INDEPENDENT (RATE_INDEPENDENT)
  #
  # Specifications for Johnson-Cook, Power-law-breakdown same as before
  #     EXCEPT no need to specify a hardening function
  #     AND should be preceded by YIELD
  #
  #     As an example for Johnson-Cook yield rate dependence,
```

(continues on next page)

(continued from previous page)

```
  #
  YIELD RATE CONSTANT  = <real>
  YIELD REFERENCE RATE = <real>
  #
  # User defined rate multiplier
  #
  YIELD RATE MULTIPLIER FUNCTION = <string>yield_rate_mult_function_
↪name
  #
  HARDENING_RATE MULTIPLIER = JOHNSON_COOK | POWER_LAW_BREAKDOWN |
              USER_DEFINED | RATE_INDEPENDENT (RATE_INDEPENDENT)
  #
  #     Syntax same as for yield parameters but with a HARDENING prefix
  #
  #     - Temperature dependence
  #
  YIELD TEMPERATURE MULTIPLIER = JOHNSON_COOK | USER_DEFINED |
           TEMPERATURE_INDEPENDENT (TEMPERATURE_INDEPENDENT)
  #
  #  Johnson-Cook temperature dependence
  #
  YIELD MELTING TEMPERATURE   = <real>
  YIELD REFERENCE TEMPERATURE = <real>
  YIELD TEMPERATURE EXPONENT  = <real>
  #
  #  User-defined temperature dependence
  YIELD TEMPERATURE MULTIPLIER FUNCTION = <string>yield_temp_mult_fun_
↪name
  #
  HARDENING TEMPERATURE MULTIPLIER = JOHNSON_COOK | USER_DEFINED |
           TEMPERATURE_INDEPENDENT (TEMPERATURE_INDEPENDENT)
  #
  #   Syntax for hardening constants same as for yield but
  #            with HARDENING prefix
```

```
#
  #
  # Optional Failure Definitions
  #    Following only need to be defined if intend to use failure model
  #
  FAILURE MODEL = TEARING_PARAMETER | JOHNSON_COOK_FAILURE | WILKINS
                  | MODULAR_FAILURE | MODULAR_BCJ_FAILURE

  CRITICAL FAILURE PARAMETER = <real>
  #
```

(continues on next page)

(continued from previous page)

```
  # TEARING_PARAMETER Failure model definitions
  #
  TEARING PARAMETER EXPONENT = <real>
  #
  # JOHNSON_COOK_FAILURE Failure model definitions
  #
  JOHNSON COOK D1       = <real>
  JOHNSON COOK D2       = <real>
  JOHNSON COOK D3       = <real>
  JOHNSON COOK D4       = <real>
  JOHNSON COOK D5       = <real>
  #
  #Following Johnson-Cook parameters can only be defined once.  As␣
↪such, only
  #  needed if not previously defined via Johnson-Cook multipliers
  #  w/ flow-stress hardening.  Does need to be defined
  #  w/ Decoupled Flow Stress
  #
  REFERENCE RATE        = <real>
  REFERENCE TEMPERATURE = <real>
  MELTING TEMPERATURE   = <real>
  #
  # WILKINS Failure model definitions
  #
  WILKINS ALPHA    = <real>
  WILKINS BETA     = <real>
  WILKINS PRESSURE = <real>
  #
  #  MODULAR_FAILURE Failure model definitions
  #
  PRESSURE MULTIPLIER         = PRESSURE_INDEPENDENT | WILKINS
                                | USER_DEFINED (PRESSURE_INDEPENDENT)
  LODE ANGLE MULTIPLIER       = LODE_ANGLE_INDEPENDENT |
                                WILKINS (LODE_ANGLE_INDEPENDENT)
  TRIAXIALITY MULTIPLIER      = TRIAXIALITY_INDEPENDENT | JOHNSON_COOK
                                | USER_DEFINED (TRIAXIALITY_
↪INDEPENDENT)
  RATE FAIL MULTIPLIER        = RATE_INDEPENDENT | JOHNSON_COOK
                                | USER_DEFINED (RATE_INDEPENDENT)
  TEMPERATURE FAIL MULTIPLIER = TEMPERATURE_INDEPENDENT | JOHNSON_COOK
                                | USER_DEFINED (TEMPERATURE_
↪INDEPENDENT)
  #
  # Individual multiplier definitions
  #
```

(continues on next page)

(continued from previous page)

```
  PRESSURE MULTIPLIER = WILKINS
  WILKINS ALPHA       = <real>
  WILKINS PRESSURE    = <real>
  #
  PRESSURE MULTIPLIER = USER_DEFINED
  PRESSURE MULTIPLIER FUNCTION = <string> pressure_multiplier_fun_name
  #
  LODE ANGLE MULTIPLIER = WILKINS
  WILKINS BETA          = <real>
  #
  TRIAXIALITY MULTIPLIER = JOHNSON_COOK
  JOHNSON COOK D1        = <real>
  JOHNSON COOK D2        = <real>
  JOHNSON COOK D3        = <real>
  #
  TRIAXIALITY MULTIPLIER = USER_DEFINED
  TRIAXIALITY MULTIPLIER FUNCTION = <string> triaxiality_multiplier_
↪fun_name
  #
  RATE FAIL MULTIPLIER = JOHNSON_COOK
  JOHNSON COOK D4      = <real>
  # REFERENCE RATE should only be added if not previously defined
  REFERENCE RATE       = <real>
  #
  RATE FAIL MULTIPLIER = USER_DEFINED
  RATE FAIL MULTIPLIER FUNCTION = <string> rate_fail_multiplier_fun_
↪name
  #
  TEMPERATURE FAIL MULTIPLIER = JOHNSON_COOK
  JOHNSON COOK D5             = <real>
  # JC Temperatures should only be defined if not previously given
  REFERENCE TEMPERATURE       = <real>
  MELTING TEMPERATURE         = <real>
  #
  TEMPERATURE FAIL MULTIPLIER          = USER_DEFINED
  TEMPERATURE FAIL MULTIPLIER FUNCTION = <string> temp_multiplier_fun_
↪name
  #
  # MODULAR_BCJ_FAILURE Failure model definitions
  #
  INITIAL DAMAGE    = <real>
  INITIAL VOID SIZE = <real>
  DAMAGE BETA       = <real> (0.5)
  GROWTH MODEL      = COCKS_ASHBY | NO_GROWTH (NO_GROWTH)
  NUCLEATION MODEL  = HORSTEMEYER_GOKHALE | CHU_NEEDLEMAN_STRAIN
```

(continues on next page)

(continued from previous page)

```
                      | NO_NUCLEATION (NO_NUCLEATION)
  #
  GROWTH RATE FAIL MULTIPLIER        = JOHNSON_COOK | USER_DEFINED
                                       | RATE_INDEPENDENT
                                       (RATE_INDEPENDENT)
  GROWTH TEMPERATURE FAIL MULTIPLIER = JOHNSON_COOK | USER_DEFINED
                                       | TEMPERATURE_INDEPENDENT
                                       (TEMPERATURE_INDEPENDENT)
  #
  NUCLEATION RATE FAIL MULTIPLIER        = JOHNSON_COOK | USER_DEFINED
                                           | RATE_INDEPENDENT
                                           (RATE_INDEPENDENT)
  NUCLEATION TEMPERATURE FAIL MULTIPLIER = JOHNSON_COOK | USER_DEFINED
                                           | TEMPERATURE_INDEPENDENT
                                           (TEMPERATURE_INDEPENDENT)
  #
  # Definitions for individual growth and nucleation models
  #
  GROWTH MODEL = COCKS_ASHBY
  DAMAGE EXPONENT = <real> (0.5)
  #
  NUCLEATION MODEL      = HORSTEMEYER_GOKHALE
  NUCLEATION PARAMETER1 = <real> (0.0)
  NUCLEATION PARAMETER2 = <real> (0.0)
  NUCLEATION PARAMETER3 = <real> (0.0)
  #
  NUCLEATION MODEL          = CHU_NEEDLEMAN_STRAIN
  NUCLEATION AMPLITUDE      = <real>
  MEAN NUCLEATION STRAIN    = <real>
  NUCLEATION STRAIN STD DEV = <real>
  #
  # Definitions for rate and temperature fail multiplier
  #   Note: only showing definitions for growth.
  #    Nucleation terms are the same just with NUCLEATION instead
  #    of GROWTH
  #
  GROWTH RATE FAIL MULTIPLIER = JOHNSON_COOK
  GROWTH JOHNSON COOK D4      = <real>
  GROWTH REFERENCE RATE       = <real>
  #
  GROWTH RATE FAIL MULTIPLIER          = USER_DEFINED
  GROWTH RATE FAIL MULTIPLIER FUNCTION = <string> growth_rate_fail_
↪mult_func
  #
  GROWTH TEMPERATURE FAIL MULTIPLIER = JOHNSON_COOK
```

(continues on next page)

(continued from previous page)

```
  GROWTH JOHNSON COOK D5              = <real>
  GROWTH REFERENCE TEMPERATURE        = <real>
  GROWTH MELTING TEMPERATURE          = <real>
  #
  GROWTH TEMPERATURE FAIL MULTIPLIER          = USER_DEFINED
  GROWTH TEMPERATURE FAIL MULTIPLIER FUNCTION = <string> temp_fail_
↪mult_func
  #
```

```
#
  #
  # Optional Adiabatic Heating/Thermal Softening  Definitions
  #    Following only need to be defined if intend to use failure model
  #
  THERMAL SOFTENING MODEL = ADIABATIC | COUPLED
  #
  SPECIFIC HEAT = <real> # not needed for COUPLED
  BETA_TQ       = <real>
```

```
END [PARAMETERS FOR MODEL BARLAT_PLASTICITY]
```

In the command blocks that define the Barlat plasticity model:

- The reference nominal yield stress, $\bar{\sigma}$, is defined with the `YIELD STRESS` command line.
- The exponent for the yield surface description, a, is defined with the `A` command line.
- The transformation coefficient, c'_{12}, is defined with the `CP12` command line. It is defaulted to 1.0.
- The transformation coefficient, c'_{13}, is defined with the `CP13` command line. It is defaulted to 1.0.
- The transformation coefficient, c'_{21}, is defined with the `CP21` command line. It is defaulted to 1.0.
- The transformation coefficient, c'_{23}, is defined with the `CP23` command line. It is defaulted to 1.0.
- The transformation coefficient, c'_{31}, is defined with the `CP31` command line. It is defaulted to 1.0.
- The transformation coefficient, c'_{32}, is defined with the `CP32` command line. It is defaulted to 1.0.
- The transformation coefficient, c'_{44}, is defined with the `CP44` command line. It is defaulted to 1.0.

- The transformation coefficient, c'_{55}, is defined with the CP55 command line. It is defaulted to 1.0.
- The transformation coefficient, c'_{66}, is defined with the CP66 command line. It is defaulted to 1.0.
- The transformation coefficient, c''_{12}, is defined with the CPP12 command line. It is defaulted to 1.0.
- The transformation coefficient, c''_{13}, is defined with the CPP13 command line. It is defaulted to 1.0.
- The transformation coefficient, c''_{21}, is defined with the CPP21 command line. It is defaulted to 1.0.
- The transformation coefficient, c''_{23}, is defined with the CPP23 command line. It is defaulted to 1.0.
- The transformation coefficient, c''_{31}, is defined with the CPP31 command line. It is defaulted to 1.0.
- The transformation coefficient, c''_{32}, is defined with the CPP32 command line. It is defaulted to 1.0.
- The transformation coefficient, c''_{44}, is defined with the CPP44 command line. It is defaulted to 1.0.
- The transformation coefficient, c''_{55}, is defined with the CPP55 command line. It is defaulted to 1.0.
- The transformation coefficient, c''_{66}, is defined with the CPP66 command line. It is defaulted to 1.0.
- The type of hardening law is defined with the HARDENING MODEL command line, other hardening commands then define the specific shape of that hardening curve.
- The hardening modulus for a linear hardening model is defined with the HARDENING MODULUS command line.
- The hardening constant for a power law hardening model is defined with the HARDENING CONSTANT command line.
- The hardening exponent for a power law hardening model is defined with the HARDENING EXPONENT command line.
- The Luders strain for a power law hardening model is defined with the LUDERS STRAIN command line.
- The hardening function for a user defined hardening model is defined with the HARDENING FUNCTION command line.
- The shape of the spline for the spline based hardening is defined by the CUBIC SPLINE TYPE, CARDINAL PARAMETER, KNOT EQPS, and KNOT STRESS command lines.

Output variables available for this model are listed in Table 4.24.

Table 4.24 State Variables for BARLAT PLASTICITY Model

Name	Description
EQPS	equivalent plastic strain, $\bar{\varepsilon}^p$
EQDOT	equivalent plastic strain rate, $\dot{\bar{\varepsilon}}^p$
SEFF	effective stress, ϕ
TENSILE_EQPS	tensile equivalent plastic strain, $\bar{\varepsilon}_t^p$
DAMAGE	damage, ϕ
VOID_COUNT	void count, η
VOID_SIZE	void size, υ
DAMAGE_DOT	damage rate, $\dot{\phi}$
VOID_COUNT_DOT	void count rate, $\dot{\eta}$
PLASTIC_WORK_HEAT_RATE	plastic work heat rate, $\dot{Q}^p$

4.17 Plane Stress Rate Plasticity Model

4.17.1 Theory

The plane stress rate plasticity model is the plane stress formulation of a J_2 plasticity model given by Simo and Taylor [92] (and described again in Simo and Hughes [93]) extended to include rate-dependent hardening and a failure model for use with shell elements.

Like other plasticity models, the components of the objective stress rate, $\overset{\circ}{\sigma}_{ij}$, are written as,

$$\overset{\circ}{\sigma}_{ij} = \mathbb{C}_{ijkl} D^{\mathrm{e}}_{kl}$$

where $\mathbb{C}_{ijkl}$ are the components of the fourth-order, isotropic elasticity tensor and D^{e}_{ij} are the components of the elastic part of the total rate of deformation tensor. An additive split of the total rate of deformation tensor into elastic and plastic contributions is assumed such that,

$$D_{ij} = D^{\mathrm{e}}_{ij} + D^{\mathrm{p}}_{ij}.$$

The plane stress formulation recasts the three-dimensional problem into a constrained subspace with plane stress conditions acting as the constraints. To do this, the plane stress rate plasticity model follows the approach of Simo and Taylor [92] to enforce $\sigma_{13} = \sigma_{23} = \sigma_{33} = 0$ and related conditions.

For the plasticity portion of the model, the formulation of Simo and Taylor [92] is used (In the work of Simo and Taylor [92] and later Simo and Hughes [93], hardening is assumed to be rate and temperature independent. Here, such terms are included but do not materially change the formulation. Similarly, the earlier works also introduce kinematic hardening which is not used in the current model.) in which a traditional three-dimensional J_2 plasticity model is recast in

reduced subspace. To do this, it is recalled that in three-dimensions the von Mises effective stress, ϕ, is written,

$$\phi^2 = \frac{3}{2} s_{ij} s_{ij},$$

with $s_{ij} = \sigma_{ij} - (1/3)\sigma_{kk}\delta_{ij}$ the deviatoric stress. To write an equivalent expression in the reduced subspace, the vector, $\underline{\sigma}$, and matrix, $\underline{\underline{\bar{P}}}$, are introduced as (Note, here the $\underline{x}$ and $\underline{\underline{X}}$ notations are introduced for vector and matrix objects, respectively, to clearly distinguish that these variables are *not* tensors. This results from operating in the constrained stress subspace and means that these terms do not have properties of a tensor and act on each other as traditional matrices and vectors.),

$$\underline{\sigma} = \begin{bmatrix} \sigma_{11} \\ \sigma_{22} \\ \sigma_{12} \end{bmatrix}, \qquad ; \qquad \underline{\underline{\bar{P}}} = \frac{1}{3} \begin{bmatrix} 2 & -1 & 0 \\ -1 & 2 & 0 \\ 0 & 0 & 3 \end{bmatrix},$$

such that,

$$\underline{s} = \begin{bmatrix} s_{11} \\ s_{22} \\ s_{12} \end{bmatrix} = \underline{\underline{\bar{P}}}\, \underline{\sigma}.$$

In the reduced plane-stress subspace, an alternative effective stress, $\bar{\phi}$, is given as,

$$\bar{\phi}^2 = \underline{\sigma}^T \underline{\underline{P}}\, \underline{\sigma} = \frac{2}{3}\phi^2,$$

where

$$\underline{\underline{P}} = \frac{1}{3} \begin{bmatrix} 2 & -1 & 0 \\ -1 & 2 & 0 \\ 0 & 0 & 6 \end{bmatrix},$$

in which $\underline{\underline{P}}$ and $\underline{\underline{\bar{P}}}$ differ by a two in the shear term to reflect Voigt corrections.

A yield function, f, is introduced as,

$$f = \bar{\phi}^2 - R^2, \tag{4.55}$$

with,

$$R = \sqrt{\frac{2}{3}} \bar{\sigma} \left(\bar{\varepsilon}^p, \dot{\bar{\varepsilon}}^p, \theta \right),$$

where $\bar{\varepsilon}^p$ and $\dot{\bar{\varepsilon}}^p$ are the equivalent plastic strain (isotropic hardening variable) and its rate, respectively. Various hardening options may be used with this model. In general, the current flow stress is written as,

$$\bar{\sigma} \left(\bar{\varepsilon}^p, \dot{\bar{\varepsilon}}^p, \theta \right) = \left(\sigma_y + K \left(\bar{\varepsilon}^p \right) \right) \hat{\sigma} \left(\dot{\bar{\varepsilon}}^p \right) \left(1 - \left(\frac{\theta - \theta_{\text{ref}}}{\theta_{\text{melt}} - \theta_{\text{ref}}} \right)^M \right), \tag{4.56}$$

in which σ_y is the original yield stress, K is the isotropic hardening function that may take linear, power-law, or multilinear form, $\hat{\sigma}$ the rate multiplier whose specification will be defined later, and the right-most term is the Johnson-Cook temperature dependence term that may be optionally used to give temperature dependence of the flow-stress.

To complete the theoretical formulation, the flow rules are specified as,

$$d\underline{\varepsilon}^p = \lambda \underline{\underline{P}}\, \underline{\sigma},$$
$$d\bar{\varepsilon}^p = \dot{\bar{\varepsilon}}^p \Delta t = \lambda \sqrt{\frac{2}{3}} \phi,$$

where λ is the consistency multiplier enforcing $f = 0$ during plastic deformation and $d\underline{\varepsilon}^p$ is the plastic strain increment in the constrained subspace. It is emphasized here that the yield surface described in (4.55) is *not* homogeneous of degree one like in other three-dimensional formulations presented in this manual. As such, the consistency multiplier and equivalent plastic strain increment are not equivalent. As an example of this, by consideration of the preceding relations, it is apparent that λ has units of one over stress.

The specification of the rate dependence, $\hat{\sigma}$, is important as it enables the consideration of two different model responses. These behaviors are controlled via the `USER RATE DEPENDENCE` command. If this input parameter is zero, then either an analytical or user-defined rate-dependence may be given. Importantly, in this case failure is *not* modeled. For the analytical case, the Johnson-Cook [48], [49] rate-multiplier is used such that,

$$\hat{\sigma}\left(\dot{\bar{\varepsilon}}^p\right) = \begin{cases} 1 + C \ln\left(\frac{\dot{\bar{\varepsilon}}^p}{\dot{\varepsilon}_0}\right) & \dot{\bar{\varepsilon}}^p > \dot{\varepsilon}_0 \\ 1 & \dot{\bar{\varepsilon}}^p \leq \dot{\varepsilon}_0 \end{cases},$$

with C being the rate dependence multiplier and $\dot{\varepsilon}_0$ is a reference rate. Note, while other models allow user specification of the reference rate, the plane stress rate plasticity model uses the value set in the original work of Johnson-Cook [48] such that $\dot{\varepsilon}_0 = 1\text{s}^{-1}$. Alternatively, a user function may be specified for the rate multiplier, $\hat{\sigma}$.

If `USER RATE DEPENDENCE` is set to one, both rate dependence and failure may be modeled. With respect to the rate dependence, (4.56) is rewritten,

$$\bar{\sigma}\left(\bar{\varepsilon}^p, \dot{\bar{\varepsilon}}^p, \theta\right) = \tilde{\sigma}\left(\bar{\varepsilon}^p, \dot{\bar{\varepsilon}}^p\right)\left(1 - \left(\frac{\theta - \theta_{\text{ref}}}{\theta_{\text{melt}} - \theta_{\text{ref}}}\right)^M\right),$$

in which both isotropic hardening and rate dependence are described via definition of $\tilde{\sigma}$. In this case, $\tilde{\sigma}$ cannot be specified through analytical expressions and must instead be given as a series of isotropic hardening curves; each at a different strain rate. For rates not explicitly given, interpolation is performed between relevant curves. Note, no extrapolation is performed with respect to the rates. If a rate is determined outside any specified curves, the hardening is calculated with respect to the bounding curve.

For failure, a failure parameter, α, is calculated as

$$\alpha = \int_0^t \frac{1}{\varepsilon_f\left(\eta, \dot{\bar{\varepsilon}}^p\right)} \dot{\bar{\varepsilon}}^p dt = \sum_{t_0}^{t} \frac{d\bar{\varepsilon}^p}{\varepsilon_f\left(\eta, \dot{\bar{\varepsilon}}^p\right)}, \tag{4.57}$$

in which the summation is used to imply the discrete calculation of the damage variable over a series of loadsteps and ε_f is the rate and triaxiality, η, dependent failure strain. The failure strain, ε_f, is specified in a fashion similar to $\tilde{\sigma}$. Specifically, a series of triaxiality dependent functions are defined each at a given strain rate. Interpolation is used at rates between those specified. Extrapolation outside the defined bounds is not done and the extremum curves are instead used.

The onset of damage is assumed to occur when $\alpha = 1$ and the current failure strain is taken to be the critical one such that $\varepsilon_f^{cr} = \varepsilon_f \left(t = t_{cr}\right)$ with t_{cr} being the time at which $\alpha = 1$. Subsequent damage calculation is performed via,

$$\alpha \left(t > t_{cr}\right) = \int_0^{t_{cr}} \frac{1}{\varepsilon_f \left(\eta, \dot{\bar{\varepsilon}}^p\right)} \dot{\bar{\varepsilon}}^p dt + \int_{t_{cr}}^{t} \frac{1}{\varepsilon_f^{cr}} \dot{\bar{\varepsilon}}^p dt. \tag{4.58}$$

After the critical failure parameter has been reached, an exponential decay relation is used to decrease the strength of the material. In this fashion, a decay relation of the form,

$$\bar{\sigma} = \bar{\sigma} e^{C_1 (1-\alpha)}, \tag{4.59}$$

is used in which C_1 is the decay coefficient.

For more information about the plane stress rate plasticity model, consult [92], [93].

4.17.2 Implementation

The plane stress rate plasticity model encapsulates both a plasticity and failure model. These features are implemented in a decoupled, sequential sense. As such, the implementation of these features will also be presented and discussed in a sequential fashion.

For the plasticity portion, the approach of Simo and Taylor [92] (and Simo and Hughes [93]) in developing a single scalar equation to solve is adopted. As will be discussed, a slightly different approach will be used to solve this equation versus that used previously. To get to this single scalar equation, an elastic-predictor inelastic corrector scheme is adopted. In this scheme, an elastic predictor is calculated by assuming all deformation is elastic such that,

$$\underline{\sigma}^{tr} = \underline{\sigma}^n + \Delta t \underline{\underline{\bar{C}}}\, d\underline{\varepsilon}^{n+1}, \tag{4.60}$$

in which n and n+1 denote the material states at $t = t_n$ and $t = t_{n+1}$, respectively, with $\Delta t = t_{n+1} - t_n$. The plane stress stiffness matrix, $\underline{\underline{\bar{C}}}$, is given as,

$$\underline{\underline{\bar{C}}} = \frac{E}{1-\nu^2} \begin{bmatrix} 1 & \nu & 0 \\ \nu & 1 & 0 \\ 0 & 0 & \frac{1-\nu}{2} \end{bmatrix},$$

with E and ν being the Youngs Modulus and Poisson's ratio, respectively, and $d\underline{\varepsilon}^{n+1}$ is the plane stress total strain increment that is written,

$$d\underline{\varepsilon} = \Delta t \begin{bmatrix} d_{11} \\ d_{22} \\ 2d_{12} \end{bmatrix},$$

where d_{ij} are the components of the rate of deformation tensor.

The stress at time $t = t_{n+1}$ may be given as,

$$\underline{\sigma}_{n+1} = \underline{\underline{\bar{C}}} \left[\underline{\varepsilon}^{n+1} - \underline{\varepsilon}^{\mathrm{p}} \right],$$

which noting the definition of the trial stress in (4.60) may be implicitly rewritten,

$$\underline{\sigma}^{n+1} = \underline{\sigma}^{tr} - \lambda \underline{\underline{\bar{C}}}\, \underline{\underline{P}}\, \underline{\sigma}^{n+1}.$$

Rearranging yields,

$$\left[\underline{\underline{I}} + \lambda \underline{\underline{\bar{C}}}\, \underline{\underline{P}} \right] \underline{\sigma}^{n+1} = \underline{\sigma}^{tr}, \tag{4.61}$$

with $\underline{\underline{I}}$ the identity matrix. Importantly, by noting that $\underline{\sigma}^{tr}$ is known it is clear that (4.61) is an equation for the updated stress vector in terms of only the unknown scalar consistency parameter, λ. To further simplify the problem, it can be shown that $\underline{\underline{\bar{C}}}$ and $\underline{\underline{P}}$ share the same principal subspaces such that (see Simo and Hughes [93] for details),

$$\underline{\underline{P}} = \underline{\underline{Q}}\, \underline{\underline{\Lambda}}^{P} \underline{\underline{Q}}^{T}, \qquad ; \qquad \underline{\underline{\bar{C}}} = \underline{\underline{Q}}\, \underline{\underline{\Lambda}}^{C} \underline{\underline{Q}}^{T},$$

where $\underline{\underline{Q}}^{T}$ is an orthogonal matrix such that $\underline{\underline{Q}}^{T} = \underline{\underline{Q}}^{-1}$ and the matrices $\underline{\underline{Q}}$, $\underline{\underline{\Lambda}}^{P}$ and $\underline{\underline{\Lambda}}^{C}$ are given as,

$$\underline{\underline{\Lambda}}^{P} = \begin{bmatrix} 1/3 & 0 & 0 \\ 0 & 1 & 0 \\ 0 & 0 & 2 \end{bmatrix}, \; ; \; \underline{\underline{\Lambda}}^{C} = \begin{bmatrix} E/(1-\nu) & 0 & 0 \\ 0 & 2\mu & 0 \\ 0 & 0 & 2\mu \end{bmatrix}$$

$$\underline{\underline{Q}} = \frac{1}{\sqrt{2}} \begin{bmatrix} 1 & -1 & 0 \\ 1 & 1 & 0 \\ 0 & 0 & \sqrt{2} \end{bmatrix}.$$

By introducing a transformed stress vector in the principal space of $\underline{\underline{\bar{C}}}$ and $\underline{\underline{P}}$, η, such that,

$$\underline{\eta} = \begin{bmatrix} \eta_{11} \\ \eta_{12} \\ \eta_{12} \end{bmatrix} = \underline{\underline{Q}}^{T} \underline{\sigma},$$

the effective stress may be rewritten,

$$\bar{\phi}^2 = \underline{\eta}^{T} \underline{\underline{\Lambda}}^{P} \underline{\eta}.$$

By rewriting (4.61) in the transformed space the premultiplying matrix on the left-hand side can be analytically inverted such that,

$$\underline{\eta}^{n+1} = \begin{bmatrix} \frac{\eta_{11}^{tr}}{1+\lambda \frac{E}{3(1-\nu)}} \\ \frac{\eta_{22}^{tr}}{1+\lambda 2\mu} \\ \frac{\eta_{12}^{tr}}{1+\lambda 2\mu} \end{bmatrix},$$

and the effective stress may be written as a scalar function of λ,

$$\bar{\phi}^2(\lambda) = \frac{\frac{1}{3}\left(\eta_{11}^{tr}\right)^2}{\left[1+\lambda\frac{E}{2(1-\nu)}\right]^2}\frac{\left(\eta_{22}^{tr}\right)^2+2\left(\eta_{12}^{tr}\right)^2}{\left[1+\lambda 2\mu\right]^2}.$$

Noting that the equivalent plastic strain and rate may be written,

$$\bar{\varepsilon}^{p(n+1)} = \bar{\varepsilon}^{p(n)} + \lambda\sqrt{\frac{2}{3}}\phi, \qquad ; \qquad \dot{\bar{\varepsilon}}^{p} = \frac{\lambda}{\Delta t}\sqrt{\frac{2}{3}}\phi,$$

means determining the updated states reduces to solving the scalar consistency equation,

$$f(\lambda) = \bar{\phi}^2(\lambda) - \bar{\sigma}(\lambda),$$

for λ. This is done iteratively by using a line-search augmented Newton-Raphson method like that described in [88].

Failure is handled separately from plasticity and in a straight-forward fashion. Specifically, if $\alpha^n > 1$ (above the critical value) then a decay coefficient, β^{n+1}, is calculated via

$$\beta^{n+1} = e^{C_1(1-\alpha^n)},$$

and the yield stress is scaled accordingly such that,

$$\bar{\sigma} = \beta\bar{\sigma}.$$

Such corrections are done *prior* to performing the plasticity calculation. Updating the damage variable, α^{n+1}, is done via relations (4.57) (or (4.58)) *after* convergence is achieved for the inelastic correction.

4.17.3 User Guide

```
BEGIN PARAMETERS FOR MODEL PLANE_STRESS_RATE_PLASTICITY
   #
   # Elastic constants
   #
   YOUNGS MODULUS = <real>
   POISSONS RATIO = <real>
   SHEAR MODULUS  = <real>
   BULK MODULUS   = <real>
   LAMBDA         = <real>
   TWO MU         = <real>
   #
   # Optional parameters related to inelastic correction criteria
   #
```

(continues on next page)

(continued from previous page)

```
   TOLERANCE          = <real> tolerance (1.0e-10)
   MAX_INEL_CORR_ITER = <int> maximum_correction_iterations (100)
   MAX_LS_CORR_ITER   = <int> maximum_line_search_cutbacks  (20)
   #
   USER RATE DEPENDENCE = 0|1(0)
   YIELD STRESS         = <real>
   #
   FORMULATION          = <int> formulation (1)
   #
   # Input Options for USER RATE DEPENDENCE = 0
   #
   # linear hardening
   HARDENING MODULUS = <real> hardening_modulus
   # power law hardening
   HARDENING CONSTANT = <real> hardening_constant
   HARDENING EXPONENT = <real> hardening_exponent (0.5)
   # multilinear hardening
   HARDENING FUNCTION = <string>
   #
   # Rate dependence
   #
   # Johnson-Cook rate dependence
   RATE CONSTANT = <real>
   # multilinear rate dependence
   RATE FUNCTION = <string> rate_function_name
   #
   # Input Options for USER RATE DEPENDENCE = 1
   #
   # rate-dependent yield
   YIELD STRAIN RATES = <real_list> yield_strain_rates
   YIELD CURVES       = <string_list> yield_function_names
   # rate-dependent damage
   FRACTURE STRAIN RATES = <real_list> fracture_strain_rates
   FRACTURE CURVES       = <string_list> fracture_function_names
   DECAY COEFFICIENT     = <real> (1.0)
   #
   # Thermal softening commands (Johnson-Cook)
   INITIAL TEMPERATURE   = <real>
   MELT TEMPERATURE      = <real>
   REFERENCE TEMPERATURE = <real>
   THERMAL EXPONENT      = <real>
   #
END [PARAMETERS FOR MODEL PLANE_STRESS_RATE_PLASTICITY]
```

In the command blocks that define the Plane Stress Rate Plasticity model:

- TOLERANCE specifies the numerical value used for assessing convergence of the plastic correction routine.
- Optionally, the user can specify the maximum number of inelastic correction iterations for the plasticity inelastic correction routines. By default this value is 100.
- Optionally, the user can specify the maximum number of line search cutbacks in the plasticity correction routine. By default this value is 20 and only impacts the formulation not equal to 0 (plastic strain rate) case.
- The reference nominal yield stress, $\bar{\sigma}$, is defined with the YIELD STRESS command line.
- The formulation parameter defines whether the total strain rate (formulation = 0) or equivalent plastic strain rate (anything else) is used for calculating rate dependence.
- INITIAL TEMPERATURE defines the initial temperature at $t = 0$.
- MELT TEMPERATURE defines T_{melt} in (4.56).
- REFERENCE TEMPERATURE defines T_{ref} in (4.56).
- THERMAL EXPONENT defines M in (4.56).
- The USER RATE DEPENDENCE is used to control the way hardening may be specified and whether or not failure is calculated.
  - For USER RATE DEPENDENCE = 0, plastic hardening may be specified as linear, power-law, OR multilinear. Failure cannot be used with USER RATE DEPENDENCE = 0:
    - For linear hardening, a non-zero HARDENING MODULUS should be specified. Do not give if using power-law or multilinear hardening.
    - For power-law hardening, the HARDENING CONSTANT should be specified. Optionally, the HARDENING EXPONENT parameter should be specified if the default value (0.5) is not to be used. Do not give for linear or multilinear hardening.
    - For multilinear hardening, a function name should be given for HARDENING FUNCTION command. Do not specify for linear or power-law hardening.
    - For Johnson-Cook rate-dependence, a rate constant must be specified via the RATE CONSTANT command. Do not use if using functionally specified rate-dependence.
    - For functionally defined rate-dependence, a function name should be given via the RATE FUNCTION command. Do not specify if using Johnson-Cook type rate dependence.
  - For USER RATE DEPENDENCE = 1, plastic hardening is specified through a series of user functions. Failure can be modeled

* Rate-dependent plastic hardening is specified jointly via the `YIELD STRAIN RATES` and `YIELD CURVES` commands. `YIELD STRAIN RATES` is a list of strain rates corresponding one-to-one to functions specified in the `YIELD CURVES` list of strings giving user-defined function names. Each `YIELD CURVES` function should give the plastic isotropic plastic hardening curve at the corresponding rate given in `YIELD STRAIN RATES`.
* Failure strains used in calculating damage are specified via the `FRACTURE STRAIN RATES` and `FRACTURE CURVES` commands. Similarly to the plastic hardening, a list of strain rates should be given with the `FRACTURE STRAIN RATES` input. Each rate should correspond one-to-one with a user function listed via `FRACTURE CURVES`. These functions are specified as a function of triaxiality and should give the failure strain at the specified rate.
* The decay coefficient, C_1, that controls the exponential decay of the yield stress related to failure should be specified via the `DECAY COEFFICIENT` command.

Output variables available for this model are listed in Table 4.25.

Table 4.25 State Variables for PLANE STRESS RATE PLASTICITY Model

Name	Description
`EQPS`	equivalent plastic strain, $\bar{\varepsilon}^p$
`EQDOT`	equivalent plastic strain rate, $\dot{\bar{\varepsilon}}^p$
`SEFF`	effective stress, ϕ

4.18 Modular Plane Stress Plasticity Model

4.18.1 Theory

Like the plane stress plasticity model of Section 4.17, the modular plane stress plasticity (MPSP) model is a plane stress implementation of a J_2 plasticity formulation largely following and motivated by the works of Simo and Taylor [92] and Simo and Hughes [93]. However, the modular plane stress plasticity model differs from those prior works and the aforementioned plane stress plasticity formulation via its specification of the hardening. Specifically, in the current case kinematic hardening is neglected and expanded isotropic hardening and rate-dependence are considered by leveraging various modular hardening capabilities used with a variety of solid plasticity models (*i.e.* the J_2 plasticity model in Section 4.13).

Like other plasticity models, the components of the objective stress rate, $\overset{\circ}{\sigma}_{ij}$, are written as,

$$\overset{\circ}{\sigma}_{ij} = \mathbb{C}_{ijkl} D^{\mathrm{e}}_{kl}$$

where $\mathbb{C}_{ijkl}$ are the components of the fourth-order, isotropic elasticity tensor and D^{e}_{ij} are the components of the elastic part of the total rate of deformation tensor. An additive split of the total

rate of deformation tensor into elastic and plastic contributions is assumed such that,

$$D_{ij} = D^{\mathrm{e}}_{ij} + D^{\mathrm{p}}_{ij}.$$

With a J_2 plasticity model, the effective stress measure, ϕ, may be written,

$$\phi^2 = \frac{3}{2} s_{ij} s_{ij} \qquad ; \qquad s_{ij} = \sigma_{ij} - \frac{1}{3}\sigma_{kk}\delta_{ij},$$

with s_{ij} begin the deviatoric stress tensor. After enforcing the plane-stress conditions ($\sigma_{13} = \sigma_{23} = \sigma_{33} = 0$), there are only three non-zero stress components. As such, the problem may be simplified by introducing the projection matrix, $\underline{\underline{\bar{P}}}$, of Simo and Taylor [92],

$$\underline{\underline{\bar{P}}} = \frac{1}{3}\begin{bmatrix} 2 & -1 & 0 \\ -1 & 2 & 0 \\ 0 & 0 & 3 \end{bmatrix},$$

so that,

$$\underline{s} = \underline{\underline{\bar{P}}}\,\underline{\sigma}$$

where,

$$\underline{\sigma} = \begin{bmatrix} \sigma_{11} \\ \sigma_{22} \\ \sigma_{12} \end{bmatrix} \qquad ; \qquad \underline{s} = \begin{bmatrix} s_{11} \\ s_{22} \\ s_{12} \end{bmatrix}.$$

Note, in the previous and following relations an explicit matrix notation is used to denote variables in the projected stress space to reinforce that these terms are not tensors. To this end, a single underline ($\underline{x}$) is used for a vector while a twice underlined variable ($\underline{\underline{X}}$) is a matrix.

The projected effective stress measure, $\bar{\phi}$, may then be taken to be,

$$\bar{\phi}^2 = \underline{\sigma}^T \underline{\underline{P}}\,\underline{\sigma},$$

in which a superscript T denotes transpose and,

$$\underline{\underline{P}} = \frac{1}{3}\begin{bmatrix} 2 & -1 & 0 \\ -1 & 2 & 0 \\ 0 & 0 & 6 \end{bmatrix}.$$

Written in this fashion, there is a small difference between the projected effective stress ($\bar{\phi}$) and the traditional 3D form (ϕ) associated with a constant premultiplier. This is due to subtle differences in notation used by the plane-stress references [92], [93] and is accounted for in the definition of the yield surface radius, R, ensuring equivalence in forms.

A corresponding yield function, f, is introduced such that,

$$f = \bar{\phi}\left(\underline{\sigma}\right) - R^2\left(\bar{\varepsilon}^p, \dot{\bar{\varepsilon}}^p\right),$$

where R is the yield surface radius in the deviatoric π-plane that isotropically hardens via dependencies on the equivalent plastic strain (isotropic hardening variable) and its rate that are denoted $\bar{\varepsilon}^p$ and $\dot{\bar{\varepsilon}}^p$, respectively. The radius may be related to the current yield stress, $\bar{\sigma}$, via,

$$R = \sqrt{\frac{2}{3}}\bar{\sigma}\left(\bar{\varepsilon}^p, \dot{\bar{\varepsilon}}^p\right).$$

The distinguishing feature of the modular plane stress plasticity model is a flexible definition of the isotropic hardening in which the current yield stress is generically written,

$$\bar{\sigma} = \sigma_y \hat{\sigma}_y\left(\dot{\bar{\varepsilon}}^p\right) + K\left(\bar{\varepsilon}^p\right)\hat{\sigma}_h\left(\dot{\bar{\varepsilon}}^p\right),$$

with σ_y, K, and $\hat{\sigma}_{y,h}$ being the constant initial yield stress, isotropic hardening, and separate rate multipliers for yield and hardening, respectively. A variety of different forms may be assumed as described below.

To complete the theoretical formulation, the flow rules are specified as,

$$d\underline{\varepsilon}^p = \lambda \underline{\underline{P}}\,\underline{\sigma},$$
$$d\bar{\varepsilon}^p = \lambda\sqrt{\frac{2}{3}}\bar{\phi},$$

where λ is the consistency multiplier enforcing $f = 0$ during plastic deformation and $d\underline{\varepsilon}^p$ is the plastic strain increment in the constrained subspace. It is emphasized here that the current yield function described in is *not* homogeneous of degree one like in other three-dimensional formulations presented in this manual. As such, the consistency multiplier and equivalent plastic strain increment are not equivalent. As an example of this, by consideration of the preceding relations, it is apparent that λ has units of one over stress.

For more information about the modular plane stress plasticity model, consult [92], [93].

4.18.1.1 Plastic Hardening

Plastic hardening refers to increases in the flow stress, $\bar{\sigma}$, with plastic deformation. As such, hardening is described via a functional relationship between the flow stress and isotropic hardening variable (effective plastic strain), $\bar{\sigma}\left(\bar{\varepsilon}^p\right)$. Over the course of nearly a century of work in metal plasticity, a variety of relationships have been proposed to describe the interactions associated with different physical interpretations, deformation mechanisms, and materials. To enable the utilization of the same plasticity models for different material systems, a modular implementation of plastic hardening has been adopted such that the analyst may select different hardening models from the input deck thereby avoiding any code changes or user subroutines. In this section, additional details are given for the different models to enable the user to select the appropriate choice of model. Note, the models being discussed here are only for *isotropic* hardening in which the yield surface expands. *Kinematic* hardening in which the yield surface translates in stress-space with deformation and *distortional* hardening where the shape of the yield surface changes shape with deformation are not treated. For a larger discussion of the

phenomenology and history of different hardening types, the reader is referred to [42], [57], [64].

Given the ubiquitous nature of these hardening laws in computational plasticity, some (if not most) of this material may be found elsewhere in this manual. Nonetheless, the discussion is repeated here for the convenience of the reader.

Linear

Linear hardening is conceptually the simplest model available in LAMÉ. As the name implies, a linear relationship is assumed between the hardening variable, $\bar{\varepsilon}^p$, and flow stress. The hardening modulus, H', is a constant giving the rate of change of flow stress with plastic flow. The flow stress expression may therefore be written,

$$\bar{\sigma} = \sigma_y + H'\bar{\varepsilon}^p.$$

The simplicity of the model is its main feature as the constant slope,

$$\frac{d\bar{\sigma}}{d\bar{\varepsilon}^p} = H',$$

makes the model attractive for analytical models and cheap for computational implementations (*e.g.* radial return algorithms require only a single correction step). Unfortunately, the simplicity of the representation also means that it has limited predictive capabilities and can lead to overly stiff responses.

Power Law

Another common expression for isotropic hardening is the power-law hardening model. Due to its prevalence, a dedicated `ELASTIC-PLASTIC POWER LAW HARDENING` model may be found in LAMÉ (see Section 4.8.1). This expression is given as,

$$\bar{\sigma} = \sigma_y + A < \bar{\varepsilon}^p - \varepsilon_L >^n,$$

in which $< \cdot >$ are Macaulay brackets, ε_L is the Luders strain, A is a fitting constant, and n is an exponent typically taken such that $0 < n \leq 1$. The Luders strain is a positive, constant strain value (defaulted to zero) giving an initially perfectly plastic response in the plastic deformation domain (see Fig. 4.20). The derivative is then simply,

$$\frac{d\bar{\sigma}}{d\bar{\varepsilon}^p} = nA < \bar{\varepsilon}^p - \varepsilon_L >^{(n-1)}.$$

Note, one difficulty in such an implementation is that when the effective equivalent plastic strain is zero, numerical difficulties may arise in evaluating the derivative and necessitate special treatment of the case.

Voce

The Voce hardening model (sometimes referred to as a saturation model) uses a decaying exponential function of the equivalent plastic strain such that the hardening eventually saturates to a specified value (thus the name). Such a relationship has been observed in some structural metals giving rise to the popularity of the model. The hardening response is given as,

$$\bar{\sigma} = \sigma_y + A\left(1 - \exp\left(-n\bar{\varepsilon}^p\right)\right),$$

in which A is a fitting constant and n is a fitting exponent controlling how quickly the hardening saturates. Importantly, the derivative is written as,

$$\frac{d\bar{\sigma}}{d\bar{\varepsilon}^p} = nA\exp\left(-n\bar{\varepsilon}^p\right),$$

and is well defined everywhere giving the selected form an advantage over the aforementioned power law model.

Johnson-Cook

The Johnson-Cook hardening model is a variant of the classical Johnson-Cook [48], [49] expression. In this instance, the temperature-dependence is neglected to focus on the *rate-dependent* capabilities while allowing for arbitrary isotropic hardening forms via the use of a user-defined hardening function. With these assumptions, the flow stress may be written as,

$$\bar{\sigma} = \tilde{\sigma}_y\left(\bar{\varepsilon}^p\right)\left[1 + C\left\langle \ln\left(\frac{\dot{\bar{\varepsilon}}^p}{\dot{\varepsilon}_0}\right)\right\rangle\right],$$

in which $\tilde{\sigma}_y\left(\bar{\varepsilon}^p\right)$ is the user-specified rate-independent hardening function, C is a fitting constant and $\dot{\varepsilon}_0$ is a reference strain rate. The Macaulay brackets ensure the material behaves in a rate independent fashion when $\dot{\bar{\varepsilon}}^p < \dot{\varepsilon}_0$.

Power Law Breakdown

Like the Johnson-Cook formulation, the power-law breakdown model is also rate-dependent. Again, a multiplicative decomposition is assumed between isotropic hardening and the corresponding rate-dependence dependent. In this case, however, the functional form is derived from the analysis of Frost and Ashby [33] in which power-law relationships like those of the Johnson-Cook model cease to appropriately capture the physical response. The form used here is similar to the expression used by Brown and Bammann [16] and is written as,

$$\bar{\sigma} = \tilde{\sigma}_y\left(\bar{\varepsilon}^p\right)\left[1 + \operatorname{asinh}\left(\left(\frac{\dot{\bar{\varepsilon}}^p}{g}\right)^{(1/m)}\right)\right],$$

with $\tilde{\sigma}_y\left(\bar{\varepsilon}^p\right)$ being the user supplied rate independent expression, g is a model parameter related to the activation energy required to transition from climb to glide-controlled deformation, and m dictates the strength of the dependence.

4.18.1.2 Flow Stress

Unlike the previously described models, the flow-stress hardening method is less a specific physical representation and more a generalization of the hardening behaviors to allow greater flexibility in separately describing isotropic hardening and rate-dependence. As such, the generic flow-stress definition of

$$\bar{\sigma}\left(\bar{\varepsilon}^p, \dot{\bar{\varepsilon}}^p\right) = \tilde{\sigma}_y\left(\bar{\varepsilon}^p\right) \hat{\sigma}\left(\dot{\bar{\varepsilon}}^p\right),$$

is used in which $\hat{\sigma}$ is the rate multiplier that by default is unity (such that the response is rate independent) and $\tilde{\sigma}_y$ is the isotropic hardening component that may also be specified as,

$$\tilde{\sigma}_y = \sigma_y + K\left(\bar{\varepsilon}^p\right),$$

with σ_y being the constant yield stress and K is the isotropic hardening that is initially zero and a function of the equivalent plastic strain. A multiplicative decomposition such as this mirrors the general structure used by Johnson and Cook [48], [49] although greater flexibility is allowed in terms of the specific form of the rate multiplier.

Given the aforementioned default for rate-dependence, the corresponding multiplier need not be specified. A representation for the isotropic hardening, however, *must* be specified and can be defined via linear, power-law, Voce, or user-defined representations. For the user-defined case, an *isotropic* hardening function is required and it must be highlighted that the interpretation differs from the general user-defined hardening model. *In this case, as the specified function represents the isotropic hardening, it should start from zero – not yield.*

Although the flow-stress hardening model defaults to rate independent, a multiplier may be defined. For rate-dependence, either the previously discussed Johnson-Cook or power-law breakdown models or a user-defined multiplier may be used. For the user-defined capability, the multiplier should be input as a strictly positive function of the equivalent plastic strain rate with a value of one in the rate-independent limit.

4.18.1.3 Decoupled Flow Stress

Like the flow-stress hardening method, the decoupled flow-stress hardening implementation is a generalization of the hardening behaviors to allow greater flexibility. In differentiating the two, for the decoupled model the rate dependence may be separately specified for the yield and hardening portions of the flow stress. As such, the generic flow-stress definition of

$$\bar{\sigma}\left(\bar{\varepsilon}^p, \dot{\bar{\varepsilon}}^p\right) = \sigma_y \hat{\sigma}_{\mathrm{y}}\left(\dot{\bar{\varepsilon}}^p\right) + K\left(\bar{\varepsilon}^p\right) \hat{\sigma}_{\mathrm{h}}\left(\dot{\bar{\varepsilon}}^p\right),$$

is used in which $\hat{\sigma}$ are rate multipliers that by default are unity (such that the response is rate independent) with subscripts y and h denoting functions associated with yield and hardening. The isotropic hardening is described by $K\left(\bar{\varepsilon}^p\right)$ and σ_y is the constant initial yield stress. It may also be seen that if the yield and hardening dependencies are the same ($\hat{\sigma}_{\mathrm{y}} = \hat{\sigma}_{\mathrm{h}}$) the decoupled flow

stress model reduces to that of the flow stress case and mirrors the general structure of the Johnson-Cook model [48], [49].

Given the aforementioned default to rate dependence, the corresponding multiplier need not be specified. A representation for the isotropic hardening, however, *must* be specified and can be defined via linear, power-law, Voce, or user-defined representations. For the user-defined case, an *isotropic* hardening function should be used and it must be highlighted that the interpretation differs from the general user-defined hardening model. *In this case, as the specified function represents the isotropic hardening, it should start from zero – not yield.*

Although the decoupled flow-stress hardening model defaults to rate independent, a multiplier may be defined. For rate-dependence, either the previously discussed Johnson-Cook or power-law breakdown models or a user-defined multiplier may be used. For the user-defined capability, the multiplier should be input as a strictly positive function of the equivalent plastic strain rate with a value of one in the rate-independent limit.

4.18.2 Implementation

The integration approach for the modular plane stress plasticity model follows largely from the elastic-predictor/inelastic-corrector radial return approaches of Simo and Taylor [92] (and Simo and Hughes [93]) with the exception of an extra line-search step and slightly modified treatment for the hardening. To this end, the total strain increment $\underline{d\varepsilon} = \underline{\dot{\varepsilon}}\Delta t$ is given as,

$$\underline{d\varepsilon} = \Delta t \begin{bmatrix} d_{11} \\ d_{22} \\ 2d_{12} \end{bmatrix}$$

where $\Delta t = t_{n+1} - t_n$ in which $t = t_n$ and $t = t_{n+1}$ are a completely known state and the state to be determined. The trial stress may then be written,

$$\underline{\sigma}^{tr} = \underline{\underline{\bar{C}}} \left[\underline{\varepsilon}_n + \underline{d\varepsilon} - \underline{\varepsilon}_n^{\mathrm{p}} \right] \tag{4.62}$$

with

$$\underline{\underline{\bar{C}}} = \frac{E}{1-\nu^2} \begin{bmatrix} 1 & \nu & 0 \\ \nu & 1 & 0 \\ 0 & 0 & \frac{1-\nu}{2} \end{bmatrix}$$

and E and ν being the elastic modulus and Poisson's ratio, respectively. The trial yield function is then simply,

$$f^{tr} = \bar{\phi}^2 \left(\underline{\sigma}^{tr} \right) - R^2 \left(\bar{\varepsilon}_n^{\mathrm{p}}, 0 \right).$$

For the case of plastic loading, if a fully implicit backward Euler scheme is adopted the plastic strain flow rules are,

$$\underline{\varepsilon}_{n+1}^{\mathrm{p}} = \underline{\varepsilon}_n^{\mathrm{p}} + \lambda \underline{\underline{P}}\, \underline{\sigma}_{n+1}, \tag{4.63}$$

$$\bar{\varepsilon}^{\mathrm{p}}_{n+1} = \bar{\varepsilon}^{\mathrm{p}}_{n} + \lambda\sqrt{\frac{2}{3}}\bar{\phi}_{n+1}. \tag{4.64}$$

By introducing,

$$\underline{\sigma}_{n+1} = \underline{\underline{\bar{C}}}\left(\underline{\varepsilon}_{n+1} - \underline{\varepsilon}^{\mathrm{p}}_{n+1}\right),$$

and using relations (4.62) and (4.63), the updated stress may be shown to be,

$$\left[\underline{\underline{I}} + \lambda\underline{\underline{\bar{C}}}\,\underline{\underline{P}}\right]\underline{\sigma}_{n+1} = \underline{\sigma}^{tr}, \tag{4.65}$$

with $\underline{\underline{I}}$ being the identity matrix. As noted by Simo and Taylor [92], $\underline{\underline{\bar{C}}}$ and $\underline{\underline{P}}$ share characteristic subspaces $\underline{\underline{Q}}$ enabling a principle decomposition such that,

$$\underline{\underline{P}} = \underline{\underline{Q}}\,\underline{\underline{\Lambda}}^{\mathrm{P}}\,\underline{\underline{Q}}^{T}, \qquad ; \qquad \underline{\underline{\bar{C}}} = \underline{\underline{Q}}\,\underline{\underline{\Lambda}}^{\mathrm{C}}\,\underline{\underline{Q}}^{T},$$

in which,

$$\underline{\underline{Q}}^{T} = \frac{1}{\sqrt{2}}\begin{bmatrix} 1 & 1 & 0 \\ -1 & 1 & 0 \\ 0 & 0 & \sqrt{2} \end{bmatrix} \; ; \; \underline{\underline{\Lambda}}^{\mathrm{P}} = \begin{bmatrix} \frac{1}{3} & 0 & 0 \\ 0 & 1 & 0 \\ 0 & 0 & 2 \end{bmatrix} \; ; \; \underline{\underline{\Lambda}}^{\mathrm{C}} = \begin{bmatrix} \frac{E}{1-\nu} & 0 & 0 \\ 0 & 2\mu & 0 \\ 0 & 0 & \mu \end{bmatrix}.$$

In this space, a transformed stress, $\underline{\eta}$, may be given as,

$$\underline{\eta} = \underline{\underline{Q}}^{T}\,\underline{\sigma},$$

which, when substituted into (4.65) yields,

$$\left[\underline{\underline{I}} + \lambda\underline{\underline{\Lambda}}^{\mathrm{C}}\,\underline{\underline{\Lambda}}^{\mathrm{P}}\right]\underline{\eta}_{n+1} = \underline{\eta}^{tr}. \tag{4.66}$$

Importantly, in (4.66) the matrix on the left-hand side is diagonal and easily inverted. The updated transformed stress is thus a function of the consistency multiplier alone. Substituting the corresponding evaluation of the stress into the definition of the effective stress produces a scalar function of λ such that,

$$\bar{\phi}^2 = \frac{\frac{1}{3}\left(\eta^{tr}_{11}\right)^2}{\left[1 + \lambda\frac{E}{3(1-\nu)}\right]^2} + \frac{\left(\eta^{tr}_{22}\right)^2 + 2\left(\eta^{tr}_{12}\right)^2}{\left[1 + \lambda 2\mu\right]^2}.$$

With the effective stress written as a function of λ alone and the flow rules in (4.63) and (4.64) only an appropriate approximation for the effective plastic strain rate is needed to arrive at the single scalar consistency equation to be solve. To that end, using (4.64), the effective plastic strain rate is taken to be,

$$\dot{\bar{\varepsilon}}^{\mathrm{p}}(\lambda) \approx \frac{\bar{\varepsilon}^{\mathrm{p}}_{n+1} - \bar{\varepsilon}^{\mathrm{p}}_{n}}{\Delta t} = \frac{\lambda}{\Delta t}\sqrt{\frac{2}{3}}\bar{\phi}_{n+1}(\lambda).$$

The updated yield function is now written as,

$$f_{n+1}(\lambda) = \bar{\phi}^2_{n+1}(\lambda) - R^2(\lambda) = 0.$$

This non-linear equation may be readily solved via a line-search augmented Newton-Raphson approach (see [88]) by recasting the consistency condition as a residual,

$$r^f(\lambda) = f(\lambda) = 0.$$

Which, when linearized as,

$$r^f_{k+1} = r^f_k + \frac{df}{d\lambda}\Delta\lambda,$$

with k being the non-linear correction iteration and $\Delta\lambda$ is the consistency increment yields the solution (with $r^f_{k+1} = 0$),

$$\Delta\lambda = \frac{-r^f_k}{\frac{df}{d\lambda}}.$$

The derivative is simply given as,

$$\frac{df}{d\lambda} = \frac{d}{d\lambda}\left(\bar{\phi}^2\right) - \frac{d}{d\lambda}\left(R^2\right),$$

where

$$\frac{d}{d\lambda}\left(\bar{\phi}^2\right) = -2\left[\frac{E}{3(1-\nu)}\frac{\frac{1}{3}\left(\eta^{tr}_{11}\right)^2}{\left[1+\lambda\frac{E}{3(1-\nu)}\right]^3} + 2\mu\frac{\left(\eta^{tr}_{22}\right)^2 + 2\left(\eta^{tr}_{12}\right)^2}{\left[1+\lambda 2\mu\right]^3}\right],$$

and

$$\frac{d}{d\lambda}\left(R^2\right) = \frac{4}{3}\left(\sigma_y\hat{\sigma}_y + K\hat{\sigma}_h\right)\left[\hat{\sigma}_h\frac{dK}{d\bar{\varepsilon}^{\mathrm{p}}}\frac{d\bar{\varepsilon}^{\mathrm{p}}}{d\lambda} + \frac{d\dot{\bar{\varepsilon}}^{\mathrm{p}}}{d\lambda}\left(\sigma_y\frac{d\hat{\sigma}_y}{d\dot{\bar{\varepsilon}}^{\mathrm{p}}} + K\frac{d\hat{\sigma}_h}{d\dot{\bar{\varepsilon}}^{\mathrm{p}}}\right)\right],$$

in which

$$\frac{d\bar{\varepsilon}^{\mathrm{p}}}{d\lambda} = \sqrt{\frac{2}{3}}\left(\phi + \lambda\frac{d\phi}{d\lambda}\right),$$
$$\frac{d\dot{\bar{\varepsilon}}^{\mathrm{p}}}{d\lambda} = \frac{1}{\Delta t}\sqrt{\frac{2}{3}}\left(\phi + \lambda\frac{d\phi}{d\lambda}\right).$$

As only a single equation needs to be solved, a merit function, ψ, is simply given as,

$$\psi(\lambda) = \frac{1}{2}\left(\frac{r^f}{\sigma^2_y}\right)^2$$

which may be solved via the quadratic approximation line-search scheme of [88].

4.18.3 Verification

Given the modular nature of the modular plane stress plasticity (MPSP) model, a variety of tests are constructed to ascertain performance under different loadings and and combinations of hardening models. The model parameters needed for such tests are given below in Table 4.26. While a large number of combinations of the hardening and/or rate multipliers have been tested under different conditions (>100 tests), here, for brevity only a sampling of these tests are presented.

Table 4.26 Model parameters for verification tests used with the modular plane stress plasticity (MPSP) model.

E	70 GPa	ν	0.33 (-)
σ_y	200 MPa	H'	500 MPa
A_{PL}	400 MPa	n_{PL}	0.25 (-)
A_{Voce}	200 MPa	n_{Voce}	20 (-)
C	0.1 (-)	$\dot{\varepsilon}_0$	1×10^{-4} s^{-1}
g	0.21 s^{-1}	m	16.4 (-)

4.18.3.1 Uniaxial stress

For the uniaxial stress tests, the constant equivalent plastic strain boundary value problem of *Appendix A* is used. Although that discussion is for 3D formulations, the plane stress assumptions agree with the assumed boundary conditions (*e.g.* traction free out-of-plane stress) enabling the same results to be used here. Results for such tests and their corresponding analytical solutions are shown in Fig. 4.92 for constant strain rates of $\dot{\bar{\varepsilon}}^p = 1 \times 10^{-3}\text{s}^{-1}$ (Fig. 4.92(a)) and $\dot{\bar{\varepsilon}}^p = 1\text{s}^{-1}$ (Fig. 4.92(b)).

4.18.3.2 Balanced Biaxial

To assess performance of the model with multiple stress components, a constant equivalent plastic strain rate balanced biaxial test is considered. For this test, a stress-state (in the projected plane stress space) of

$$\underline{\sigma}\left(t\right) = \begin{bmatrix} \sigma\left(t\right) \\ -\sigma\left(t\right) \\ 0 \end{bmatrix}$$

is assumed. Note, such a loading is equivalent to a pure shear loading in a rotated frame of reference. As such, many of the pure shear results of *Appendix A* may be leveraged. To that end, if elasticity effects are included the total strain, $\varepsilon\left(t\right)$, may be found to be

$$\varepsilon\left(t\right) = \frac{1}{\sqrt{3}} \frac{\sigma_y + \hat{\sigma}_h K\left(\dot{\bar{\varepsilon}}^p\left(t - t^{\text{el}}\right)\right)}{2\mu} + \frac{\sqrt{3}}{2}\dot{\bar{\varepsilon}}^p\left(t - t^{\text{el}}\right),$$

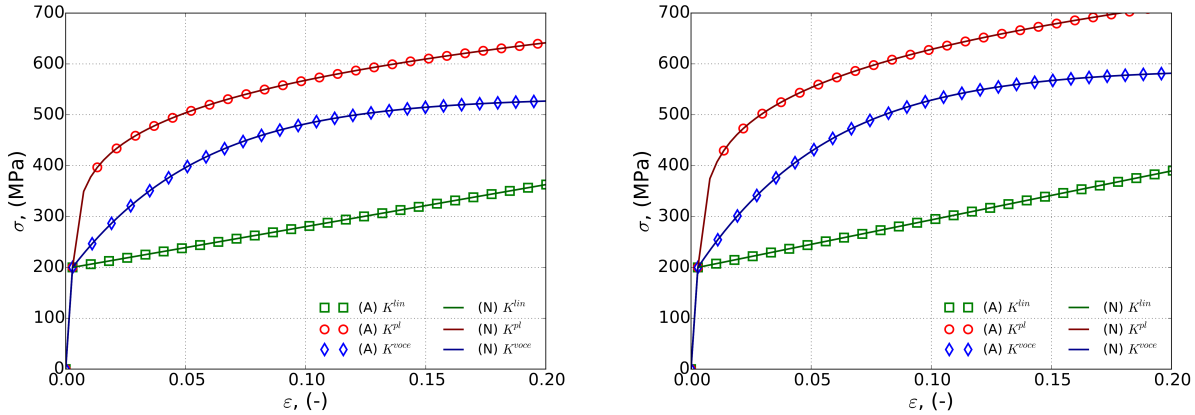

Fig. 4.92 Analytical and numerical constant equivalent plastic strain rate verification tests of the modular plane stress plasticity models with a uniaxial stress state and strain rates of (a) $\dot{\varepsilon}^p = 1 \times 10^{-3}\mathbf{s}^{-1}$ and (b) $\dot{\varepsilon}^p = 1\mathbf{s}^{-1}$ with linear, power-law, and voce isotropic hardening and power-law breakdown rate-dependence. Solid lines are analytical and open symbols are from finite element calculations.

with t^{el} being the time at yield (elastic limit). To produce the desired stress state, the corrresponding displacements are $u_1(t) = \exp(\varepsilon(t)) - 1$ and $u_2(t) = \exp(-\varepsilon(t)) - 1$. Results of such tests and their corresponding analytical solutions are presented below in Fig. 4.93 with constant strain rates of $\dot{\bar{\varepsilon}}^p = 1 \times 10^{-3}\text{s}^{-1}$ (Fig. 4.93(a)) and $\dot{\bar{\varepsilon}}^p = 1\text{s}^{-1}$ (Fig. 4.93(b)).

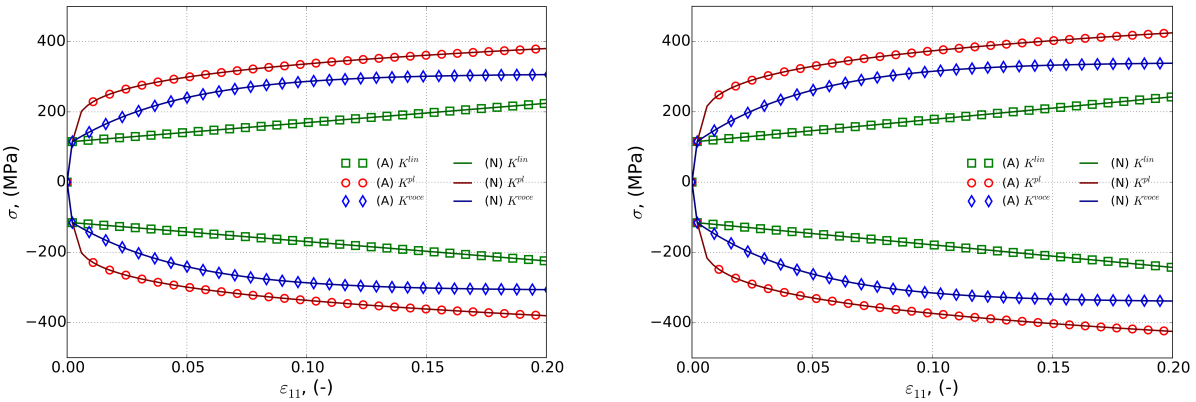

Fig. 4.93 Analytical and numerical constant equivalent plastic strain rate verification tests of the modular plane stress plasticity models with a balanced biaxial stress state and strain rates of (a) $\dot{\varepsilon}^p = 1\times10^{-3}\mathbf{s}^{-1}$ and (b) $\dot{\varepsilon}^p = 1\mathbf{s}^{-1}$ with linear, power-law, and voce isotropic hardening and power-law breakdown rate-dependence. Solid lines are analytical and open symbols are from finite element calculations. Positive valued stresses correspond to σ_{11} while negative values are σ_{22}.

4.18.3.3 Biaxial Shear

As a final set of tests, the pure shear response is probed. To accomplish this loading, the previous balanced biaxial test is reconsidered with the geometry rotated 45° about the out of plane direction producing a stress state of,

$$\underline{\sigma}\left(t\right) = \begin{bmatrix} 0 \\ 0 \\ \sigma_{xy}\left(t\right) \end{bmatrix}.$$

The previous results from Section 4.18.3.2 regarding the solution for the balanced biaxial problem may again be used with $\sigma_{xy}\left(t\right) = \sigma\left(t\right)$. Result for this case, both analytical and finite element, are given in Fig. 4.93 with constant applied strain rates of $\dot{\bar{\varepsilon}}^p = 1 \times 10^{-3}\text{s}^{-1}$ and $\dot{\bar{\varepsilon}}^p = 1\text{s}^{-1}$ in Fig. 4.94(a) and Fig. 4.94(b), respectively.

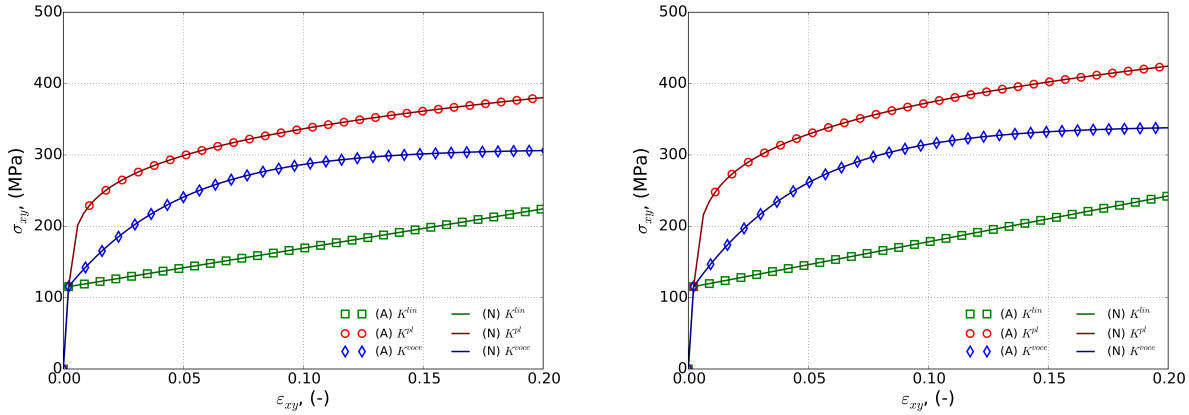

Fig. 4.94 Analytical and numerical constant equivalent plastic strain rate verification tests of the modular plane stress plasticity models with a pure shear stress state and strain rates of (a) $\dot{\varepsilon}^p = 1 \times 10^{-3}\mathbf{s}^{-1}$ and (b) $\dot{\varepsilon}^p = 1\mathbf{s}^{-1}$ with linear, power-law, and voce isotropic hardening and power-law breakdown rate-dependence. Solid lines are analytical and open symbols are from finite element calculations.

4.18.4 User Guide

```
BEGIN PARAMETERS FOR MODEL MODULAR_PLANE_STRESS_PLASTICITY
   #
   # Elastic constants
   #
   YOUNGS MODULUS  = <real>
   POISSONS RATIO  = <real>
   SHEAR MODULUS   = <real>
   BULK MODULUS    = <real>
   LAMBDA          = <real>
```

(continues on next page)

(continued from previous page)

```
  TWO MU          = <real>
  #
  YIELD STRESS    = <real>
  #
```

```
#
  #
  # Hardening model
  #
  HARDENING MODEL = LINEAR | POWER_LAW | VOCE | USER_DEFINED |
  FLOW_STRESS | DECOUPLED_FLOW_STRESS | JOHNSON_COOK |
  POWER_LAW_BREAKDOWN
  #
  # Linear hardening
  #
  HARDENING MODULUS = <real>
  #
  # Power-law hardening
  #
  HARDENING CONSTANT = <real>
  HARDENING EXPONENT = <real> (0.5)
  LUDERS STRAIN      = <real> (0.0)
  #
  # Voce hardening
  #
  HARDENING MODULUS       = <real>
  EXPONENTIAL COEFFICIENT = <real>
  #
  # Johnson-Cook hardening
  #
  HARDENING FUNCTION = <string>hardening_function_name
  RATE CONSTANT      = <real>
  REFERENCE RATE     = <real>
  #
  # Power law breakdown hardening
  #
  HARDENING FUNCTION = <string>hardening_function_name
  RATE COEFFICIENT   = <real>
  RATE EXPONENT      = <real>
  # User defined hardening
  #
  HARDENING FUNCTION = <string>hardening_function_name
  #
```

```
#
  #
  # Following Commands Pertain to Flow_Stress Hardening Model
  #
  #    -  Isotropic Hardening model
  #
  ISOTROPIC HARDENING MODEL = LINEAR | POWER_LAW | VOCE |
                              USER_DEFINED
  #
  # Specifications for Linear, Power-law, and Voce same as above
  #
  # User defined hardening
  #
  ISOTROPIC HARDENING FUNCTION = <string>iso_hardening_fun_name
  #
  #     - Rate dependence
  #
  RATE MULTIPLIER = JOHNSON_COOK | POWER_LAW_BREAKDOWN |
     RATE_INDEPENDENT (RATE_INDEPENDENT)
  #
  # Specifications for Johnson-Cook, Power-law-breakdown
  #     same as before EXCEPT no need to specify a
  #     hardening function
  #
  # User defined rate multiplier
  #
  RATE MULTIPLIER FUNCTION = <string> rate_mult_function_name
  #
  #
  # Following Commands Pertain to Decoupled_Flow_Stress Hardening Model
  #
  #    -  Isotropic Hardening model
  #
  ISOTROPIC HARDENING MODEL = LINEAR | POWER_LAW | VOCE | USER_DEFINED
  #
  # Specifications for Linear, Power-law, and Voce same as above
  #
  # User defined hardening
  #
  ISOTROPIC HARDENING FUNCTION = <string>isotropic_hardening_function_
↪name
  #
  #     - Rate dependence
  #
  YIELD RATE MULTIPLIER = JOHNSON_COOK | POWER_LAW_BREAKDOWN |
              RATE_INDEPENDENT (RATE_INDEPENDENT)
```

(continues on next page)

(continued from previous page)

```
  #
  # Specifications for Johnson-Cook, Power-law-breakdown same as before
  #     EXCEPT no need to specify a hardening function
  #     AND should be preceded by YIELD
  #
  #     As an example for Johnson-Cook yield rate dependence,
  #
  YIELD RATE CONSTANT  = <real>
  YIELD REFERENCE RATE = <real>
  #
  # User defined rate multiplier
  #
  YIELD RATE MULTIPLIER FUNCTION = <string>yield_rate_mult_function_
↪name
  #
  HARDENING_RATE MULTIPLIER = JOHNSON_COOK | POWER_LAW_BREAKDOWN |
              RATE_INDEPENDENT (RATE_INDEPENDENT)
  #
  #     Syntax same as for yield parameters but with a HARDENING prefix
  #
```

```
END [PARAMETERS FOR MODEL MODULAR_PLANE_STRESS_PLASTICITY]
```

In the command blocks that define the Modular Plane Stress Plasticity model:

- The reference nominal yield stress, $\bar{\sigma}$, is defined with the `YIELD STRESS` command line.
- The type of hardening law is defined with the `HARDENING MODEL` command line, other hardening commands then define the specific shape of that hardening curve.
- The hardening modulus for a linear hardening model is defined with the `HARDENING MODULUS` command line.
- The hardening constant for a power law hardening model is defined with the `HARDENING CONSTANT` command line.
- The hardening exponent for a power law hardening model is defined with the `HARDENING EXPONENT` command line.
- The Luders strain for a power law hardening model is defined with the `LUDERS STRAIN` command line.
- The hardening function for a user defined hardening model is defined with the `HARDENING FUNCTION` command line.
- The shape of the spline for the spline based hardening is defined by the `CUBIC SPLINE TYPE`, `CARDINAL PARAMETER`, `KNOT EQPS`, and `KNOT STRESS` command lines.

- The isotropic hardening model for the flow stress hardening model is defined with the `ISOTROPIC HARDENING MODEL` command line.
- The function name of a user-defined isotropic hardening model is defined via the `ISOTROPIC HARDENING FUNCTION` command line.
- The optional rate multiplier for the flow stress hardening model is defined with the `RATE MULTIPLIER` command line.
- The optional rate multiplier for the yield stress for the decoupled flow stress hardening model is defined with the `YIELD RATE MULTIPLIER` command line.
- The optional rate multiplier for the hardening for the decoupled flow stress hardening model is defined with the `HARDENING RATE MULTIPLIER` command line.

Output variables available for this model are listed in Table 4.27.

Table 4.27 State Variables for MODULAR PLANE STRESS PLASTICITY Model

Name	Description
`RADIUS`	yield surface radius in deviatoric π-plane, R
`EQPS`	equivalent plastic strain, $\bar{\varepsilon}^p$
`EQDOT`	equivalent plastic strain rate, $\dot{\bar{\varepsilon}}^p$
`TENSILE_EQPS`	tensile equivalent plastic strain, $\bar{\varepsilon}_t^p$

4.19 Power Law Creep Model

4.19.1 Theory

The power law creep model describes the secondary (or steady-state) creep and is useful in capturing the time-dependent behavior of metals, brazes, or solder at high homologous temperatures. It may also be used as a simple model for the time-dependent behavior of geologic materials such as salt. A general discussion of such creep behaviors and the associated modeling may be found in the texts of [57], [78] while the specific implementation used here is discussed in [103].

In the power law creep model, the effective creep strain rate is taken to be explicitly a function of stress and temperature. A power law relation is used for the stress dependence while an Arrhenius like expression is used to capture thermal effects. As such, the effective creep strain rate is written as,

$$\dot{\bar{\varepsilon}}^{\mathrm{c}} = A\bar{\sigma}_{vM}^{m} \exp\left(\frac{-Q}{R\theta}\right), \tag{4.67}$$

where $\dot{\bar{\varepsilon}}^{\mathrm{c}}$ is the effective creep strain rate, $\bar{\sigma}_{vM}$ is the von Mises stress, A is the creep constant, m is the creep exponent, Q is the activation energy, R is the universal gas constant (1.987 cal/mole

K), and θ is the absolute temperature. As a slip based mechanism, it is assumed that the creep strains are deviatoric leading to a 3D evolution law of the form,

$$D^{\mathrm{c}}_{ij} = \dot{\bar{\varepsilon}}^{\mathrm{c}} \frac{3}{2} \frac{s_{ij}}{\bar{\sigma}_{vM}},$$

with s_{ij} being the deviatoric stress. The corresponding incremental constitutive equation for this model is then given as,

$$\overset{\circ}{\sigma}_{ij} = \mathbb{C}_{ijkl} \left(D_{kl} - D^{\mathrm{c}}_{kl} \right). \tag{4.68}$$

4.19.2 Implementation

Given the time-dependent nature of the model response, an explicit, forward Euler scheme is used to integrate the routine. Prior analysis [103] has shown that this implementation is conditionally stable and found an expression of the form

$$\Delta t_{\mathrm{st}} < \frac{4\,(1+\nu)}{3EA \exp\left(\frac{-Q}{R\theta}\right) m \bar{\sigma}^{m-1}_{vM}}$$

for the critical time step for stability, Δt_{st}. This time step is calculated using the previously determined material state (state n) and compared to the input time step. If necessary, the time step is cut back to meet this critical limit.

To determine the updated material state (state $n+1$) it is first noted that the creep process is purely deviatoric. Therefore, the stress may be decomposed as,

$$T^n_{ij} = -p^n \delta_{ij} + s^n_{ij}$$

where p is the pressure ($p^n = -\,(1/3)\,T^n_{kk}$) and T_{ij} is the unrotated stress. Given the decoupled nature of the hydrostatic and deviatoric components, the updated pressure may be found as,

$$p^{n+1} = p^n - K d_{kk} \Delta t,$$

with d_{ij} being the unrotated rate of deformation. By similarly decomposing the rate of deformation,

$$d_{ij} = \frac{1}{3} d_{kk} \delta_{ij} + \hat{d}_{ij},$$

with $\hat{d}_{ij}$ being the deviatoric part of the rate of deformation, the updated deviatoric stress is

$$s^{n+1}_{ij} = s^n_{ij} + 2\mu \left(\hat{d}_{ij} - \frac{3}{2} A \exp\left(\frac{-Q}{R\theta^n}\right) \left(\bar{\sigma}^n_{vM}\right)^{m-1} s^n_{ij} \right).$$

The updated stress is then simply,

$$T^{n+1}_{ij} = -p^{n+1} \delta_{ij} + s^{n+1}_{ij}.$$

4.19.3 Verification

The power law creep model is verified through two, time-dependent tests – creep and stress relaxation. It is noted that given the strong time dependency and form of the differential constitutive equations, a closed form analytical expression for the response is not readily available. Semi-analytical approaches in which simple numerical integration is used to solve the underlying differential equation, however, are well suited to such efforts and are used here to verify the numerical responses. The set of material properties and model parameters used for these tests are taken from [91] and are given in Table 4.28 and it is assumed that there are no thermal strains.

Table 4.28 The material properties and model parameters for the power law creep model used for the verification testing.

E	90.68 MPa	ν	0.39
A	5.12 x 10^{-5}	m	4.51
Q/R	19,853.50 K	θ	673.00 K

4.19.3.1 Creep

To consider the creep response, the model response is determined both numerically and semi-analytically. Through such a response, the stress tensor is $\sigma_{ij} = \sigma\left(t\right)\delta_{i1}\delta_{j1}$ where $\sigma\left(t\right)$ is a prescribed boundary condition. For this investigation, $\sigma\left(t\right)$ ramps linearly from 0 to σ_{max} over the interval $t = [0, 100\text{ s}]$ and $\sigma_{max} = 300$ MPa. The stress is then held constant ($\dot{\sigma} = 0$) for the next 900 s. Inverting the constitutive law (4.68) for the strain rate yields,

$$D_{ij} = \mathbb{S}_{ijkl}\dot{\sigma}_{kl} + D^{\mathrm{c}}_{ij}.$$

Furthermore, given the stress tensor form above, the creep deformation rate is,

$$D^{\mathrm{c}}_{ij} = A\bar{\sigma}^{m}_{vM}\exp\left(\frac{-Q}{R\theta}\right)\left[\delta_{i1}\delta_{j1} - \frac{1}{2}\left(\delta_{i2}\delta_{j2} + \delta_{i3}\delta_{j3}\right)\right], \tag{4.69}$$

and

$$\mathbb{S}_{ijkl}\dot{\sigma}_{kl} = \dot{\sigma}\mathbb{S}_{ij11}.$$

The total deformation rate may then be determined and easily integrated to find an analytical response for the strain. To this end, both the semi-analytical and numerical strain and stress responses (as a function of time) are presented in Fig. 4.95(a) and Fig. 4.95(b), respectively.

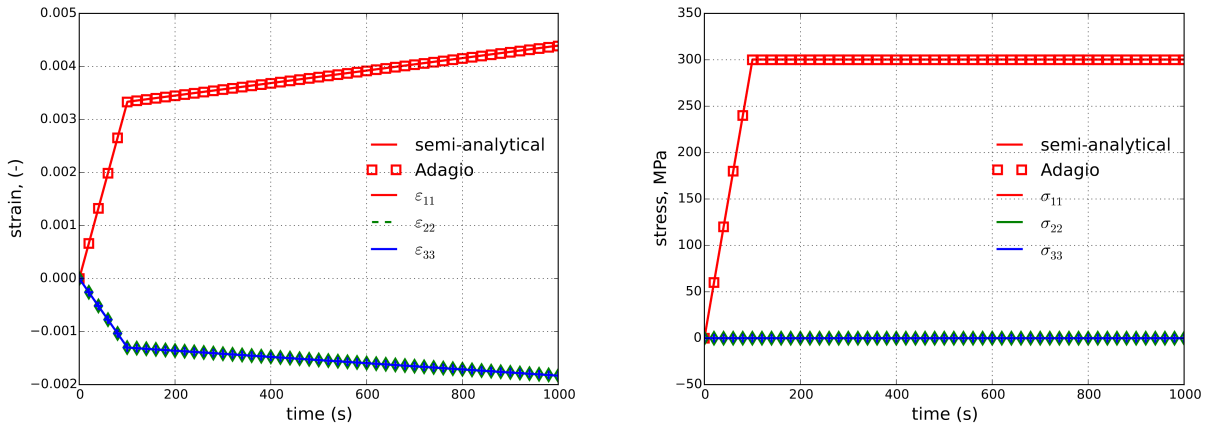

(a) Strain **(b) Stress**

Fig. 4.95 Semi-analytical and numerical results of (a) strain and (b) stress evolution during a creep test.

4.19.3.2 Stress Relaxation

The stress relaxation response of the considered model is evaluated both numerically and semi-analytically. Specifically, a displacement controlled loading of $u_1 = \lambda(t)$ is investigated. The other displacement degrees of freedom are not constrained so that a uniaxial stress state results – $\sigma_{ij}(t) = \sigma(t)\,\delta_{i1}\delta_{j1}$. The displacement is prescribed such that it scales linearly from $u_1 = 0$ at $t = 0$ to $u_1 = .01$ at $t = 100$ s and then held fixed for 900 s. Initially the considered element is of unit length.

To determine the material response, it is noted that: (emph{i}) $\sigma_{22} = \sigma_{33} = 0$; (emph{ii}) $D^{\mathrm{e}}_{22} = D^{\mathrm{e}}_{33}$ due to isotropy; and (emph{iii}) the creep deformation rate takes the form (4.69). With these observations, the elastic deformation rate in the direction of loading (D^{e}_{11}) becomes,

$$D^{\mathrm{e}}_{11} = \frac{\dot{\lambda}(t)}{1+\lambda(t)} - A\bar{\sigma}^{m}_{vM}\exp\left(\frac{-Q}{R\theta}\right). \tag{4.70}$$

Additionally, from (emph{i}) and (emph{ii}) above, it may be found that,

$$D^{\mathrm{e}}_{22} = D^{\mathrm{e}}_{33} = -\nu D^{\mathrm{e}}_{11}, \tag{4.71}$$

leading to an equation for the stress in the direction of loading of,

$$\dot{\sigma}_{11} = \left(\mathbb{C}_{1111} - 2\nu\mathbb{C}_{1122}\right) D^{\mathrm{e}}_{11}.$$

Additionally, as $D_{ij} = D^{\mathrm{e}}_{ij} + D^{\mathrm{c}}_{ij}$ the strains may easily integrated by using relations (4.69), (4.70), and (4.71). The resultant numerical and semi-analytical strain and stress responses are shown in Fig. 4.96(a) and Fig. 4.96(b), respectively.

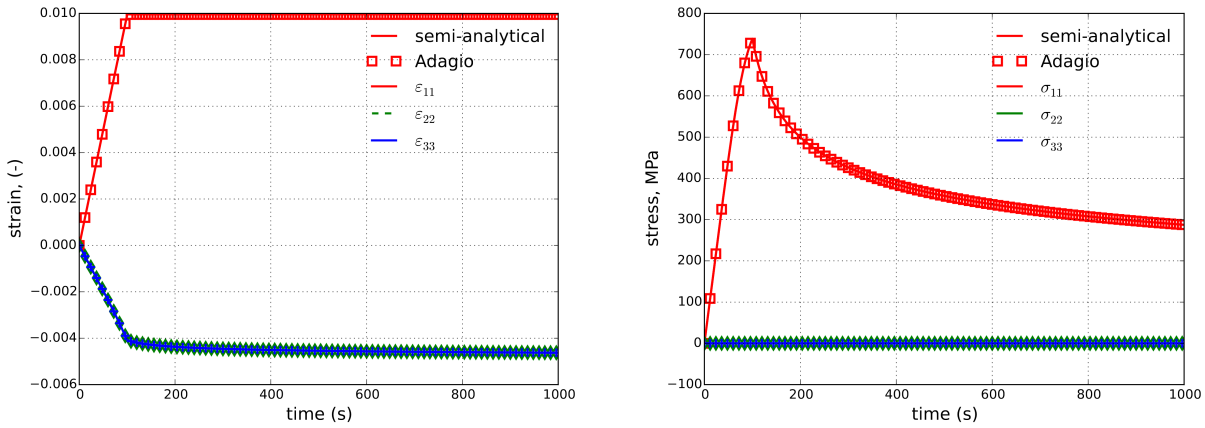

(a) Strain **(b) Stress**

Fig. 4.96 Semi-analytical and numerical results of the (a) strain and (b) stress evolution during a stress relaxation test.

4.19.4 User Guide

```
BEGIN PARAMETERS FOR MODEL POWER_LAW_CREEP
  #
  # Elastic constants
  #
  YOUNGS MODULUS = <real>
  POISSONS RATIO = <real>
  SHEAR MODULUS  = <real>
  BULK MODULUS   = <real>
  LAMBDA         = <real>
  TWO MU         = <real>
  #
  # Viscoplastic parameters
  #
  CREEP CONSTANT    = <real>
  CREEP EXPONENT    = <real>
  THERMAL CONSTANT  = <real>
  MAX SUBINCREMENTS = <integer> (100)
END [PARAMETERS FOR MODEL POWER_LAW_CREEP]
```

In the above command blocks:

- The creep constant, A, in (4.67) is defined with the `CREEP CONSTANT` command line.
- The creep exponent, m, in (4.67) is defined with the `CREEP EXPONENT` command line.
- The thermal constant, Q/R in (4.67) is defined with the `THERMAL CONSTANT` command line.

- Time step sub incrementation within the material model may be used to accurately calculate the true creep stress. The maximum sub-increments in a load step is defined with the `MAX SUBINCREMENTS` command line. The default is 100. A larger number of steps can potentially improve accuracy if a large amount of creep happens in a single step. A smaller number of steps can sometimes improve analysis speed.

Output variables available for this model are listed in Table 4.29.

Table 4.29 State Variables for POWER LAW CREEP Model

Name	Description
ECREEP	equivalent creep strain
SEQDOT	equivalent stress rate

4.20 Viscoplastic Model

4.20.1 Theory

The viscoplastic model is a rate dependent plasticity model that is useful for modeling solders and brazes and was developed by Neilsen et al. [74]. This model is formulated in terms of the stress rate for the material. Like many inelastic models, the rate of deformation, D_{ij}, is additively decomposed into an elastic, D^{e}_{ij}, and an inelastic, D^{in}_{ij} part such that,

$$D_{ij} = D^{\mathrm{e}}_{ij} + D^{\mathrm{in}}_{ij}.$$

The elastic rate of deformation is the only part that contributes to the stress rate and it does so through the elastic moduli, $\mathbb{C}_{ijkl}$, in a linear fashion leading to the relation,

$$\overset{\circ}{\sigma}_{ij} = \mathbb{C}_{ijkl} D^{\mathrm{e}}_{kl}, \tag{4.72}$$

where $\mathbb{C}_{ijkl}$ are the components of the fourth-order, isotropic elasticity tensor. The stress rate is arbitrary, as long as it is objective. Two objective stress rates are commonly used: the Jaumann rate and the Green-McInnis rate. For problems with fixed principal axes of deformation, these two rates give the same answers. For problems where the principal axes of deformation rotate during the deformation, the two rates can give different answers. Generally speaking there is no reason to pick one objective rate over another.

The inelastic strain rate is a function of the stress state, σ_{ij}, the temperature, θ, and a number of internal state variables including both scalar isotropic, D, and tensorial kinematic, B_{ij}, hardening variables. With these dependencies defined, a general form for the evolution of the inelastic deformation may be given by,

$$D^{\mathrm{in}}_{ij} = \frac{3}{2}\gamma\left(\sigma_{ij}, \theta; D, B_{ij}\right) n_{ij},$$

where n_{ij} is the direction of inelastic deformation and is defined as,

$$n_{ij} = \frac{1}{\tau}\left(s_{ij} - \frac{2}{3}B_{ij}\right), \tag{4.73}$$

and

$$\tau = \sqrt{\frac{3}{2}\left(s_{ij} - \frac{2}{3}B_{ij}\right)\left(s_{ij} - \frac{2}{3}B_{ij}\right)},$$

with s_{ij} being the deviatoric stress tensor. The inelastic strain rate, γ, is defined via a hyperbolic sin law,

$$\gamma = f(\theta)\left[\sinh\left(\frac{\tau}{\alpha(\theta)D}\right)\right]^{p(\theta)}, \tag{4.74}$$

where $f(\theta) = \exp(g(\theta))$. The expressions $g(\theta)$, $\alpha(\theta)$, and $p(\theta)$ are model parameters that are functions of temperature.

The evolution laws for the state variables D and B_{ij} are,

$$\dot{D} = \frac{A_1}{(D - D_0)^{A_3}}\gamma - A_2\left(D - D_0\right)^2, \tag{4.75}$$

and

$$\dot{B}_{ij} = \frac{A_4}{b^{A_6}}D_{ij}^{\text{in}} - A_5 b B_{ij}, \tag{4.76}$$

where

$$b = \sqrt{\frac{2}{3}B_{ij}B_{ij}}.$$

The parameters D_0, A_1, A_2, A_3, A_4, A_5 and A_6 are model parameters. The parameters A_1, A_2, A_4 and A_5 are also functions of temperature. The model can be simplified with the appropriate choice of these parameters.

The following material parameters are functions of temperature and have the following form

$$G(\theta) = G_0 h_G(\theta) \quad ; \quad K(\theta) = K_0 h_K(\theta)$$

$$g(\theta) = g_0 h_g(\theta) \quad ; \quad p(\theta) = p_0 h_p(\theta) \quad ; \quad \alpha(\theta) = \alpha_0 h_\alpha(\theta)$$

$$A_1(\theta) = A_1^0 h_1(\theta) \quad ; \quad A_2(\theta) = A_2^0 h_2(\theta)$$

$$A_4(\theta) = A_4^0 h_4(\theta) \quad ; \quad A_5(\theta) = A_5^0 h_5(\theta)$$

where the functions $h_*(\theta)$ are normalized functions of temperature and the values $(*)_0$ or $(*)^0$ are the reference values that are input in the command block.

4.20.2 Implementation

An explicit, forward Euler scheme is used to integrate the viscoplastic model. First, during initialization, the isotropic hardening variable D is set to $1.001D_0$. This is done to avoid a singularity in (4.75). Additionally, the kinematic variable is set to zero ($B_{ij} = 0$).

Like the power law creep model that is integrated in a similar fashion, the chosen numerical scheme is conditionally stable. As detailed in [74], a critical stability time step of,

$$\Delta t_{n+1} \leq \frac{2\alpha\left(\theta\right) D}{3Gf\left(\theta\right) p\left(\theta\right) \sinh^{p(\theta)-1}\left(\frac{\tau}{\alpha(\theta)D}\right) \cosh\left(\frac{\tau}{\alpha(\theta)D}\right)},$$

may be determined. For convince, in the following the dependence of f, p, and α will be assumed and not explicitly written. Instead, f^{n+1} will be used to refer to $f\left(\theta^{n+1}\right)$. Two additional limits are also imposed to ensure accurate integration of the state variables. Specifically,

$$\Delta t_{n+1} \leq \sqrt{\frac{2\delta D_0 \Delta t_n}{|\dot{D}_n - \dot{D}_{n-1}|}},$$

and

$$\Delta t_{n+1} \leq \sqrt{\frac{2\delta D_0 \Delta t_n}{|\dot{b}_n - \dot{b}_{n-1}|}},$$

where δ is an allowable error measure (here, $1.0x10^{-3}$) and $\dot{x}_n$ refers to the time rate of change of variable x at time step n. The current time step is checked to ensure it meets those criteria or else it is scaled back to ensure accurate integration.

After assessing the acceptability of the time step, the new material state at time $t = t_{n+1}$ is determined. If the time step needs to be cut back, multiple sub-increments are used. To elaborate, let k denote a specific sub-increment and N represent the total number of sub-increments. Each k^{th} interval evaluates the numerical routine over a step size δt^k where $\Delta t = \sum_{k=0}^{N} \delta t^k$. In such cases, temperature dependent variables are linearly interpolated between their values at t_n and t_{n+1}. For example,

$$G^k = G_n + \frac{\Delta t^k}{\Delta t}\left(G_{n+1} - G_n\right),$$

where Δt^k is the current sub-increment time, $\Delta t^k = \sum_{r=0}^{k} \delta t^r$. For simplicity and clarity of presentation, in the discussion below it is assumed that the input time step is acceptable and only a single increment is needed. If additional sub-increments were needed, the below steps would be repeated N times with time intervals of δt^k.

It is first noted that the unrotated stress, T_{ij}, and deformation rate, d_{ij}, may be decomposed as,

$$T_{ij}^n = -p^n \delta_{ij} + s_{ij}^n,$$
$$d_{ij}^n = \frac{1}{3} d_{kk}^n \delta_{ij} + \hat{d}_{ij}^n,$$

with p being the pressure ($p = -\frac{1}{3}T_{kk}$) and $\hat{d}_{ij}$ being the rate of deviatoric deformation. As the inelastic deformation flows in a deviatoric direction, the hydrostatic and deviatoric components may be evaluated separately. With this in mind, the pressure may be easily integrated via,

$$p^{n+1} = p^n \frac{K^{n+1}}{K^n} + \frac{1}{2}\left(K^n + K^{n+1}\right) d_{kk}\Delta t,$$

where K^n is abbreviated notation for $K\left(\theta^n\right)$. The inelastic deformation rate is then determined as,

$$D_{ij}^{\text{in}} = \frac{3}{2}\gamma\left(\sigma_{ij}^n, \theta^n; D^n, B_{ij}^n\right) n_{ij}^n,$$

by evaluating expressions (4.73)-(4.74) at $t = t_n$ and $\theta = \theta^n$. The internal state variables may then be similar evolved via (4.75) and (4.76). With the inelastic state determined, the updated deviatoric stress may be found via,

$$s_{ij}^{n+1} = \frac{G^{n+1}}{G^n} s_{ij}^n + 2\Delta t G^n\left(\hat{d}_{ij} - D_{ij}^{\text{in}}\right),$$

with the updated stress being,

$$T_{ij}^{n+1} = -p^{n+1}\delta_{ij} + s_{ij}^{n+1}.$$

4.20.3 Verification

The viscoplastic model is verified through two, time-dependent tests – creep and stress relaxation. To simplify the problem for verification purposes, the isothermal response only considering isotropic hardening and recovery is investigated. It is noted, however, that given the stress dependence and evolving internal state variable in the inelastic strain rate, a closed-form analytical solution may not be found. Semi-analytical approaches numerically integrating the differential equations are easily obtainable and used for comparison purposes. The considered test temperature is 450°‘$C(: math$: ‘723 K) and material properties and model parameters are those of CusilABA taken from Table 3 of [74] and are reproduced for convenience below in Table 4.30.

Table 4.30 Material properties and model parameters used for isothermal, isotropic hardening/recovery creep and stress

E	77.8 GPa	ν	0.375
g	-13.88	p	2.589
A_1	$3x10^4$ MPa$^{A_3+1}$	A_2	$2.07x10^{-5}$ $\frac{1}{\text{MPa s}}$
A_3	1.746	D_0	50.0 MPa
A_4	0 MPa$^{A_6+1}$	A_5	0.0 $\frac{1}{\text{MPa s}}$
A_6	0.0	α	1.0

4.20.3.1 Creep

The creep response of the viscoplastic model is investigated both numerically and semi-analytically. For such a loading, the stress tensor is $\sigma_{ij} = \sigma(t)\,\delta_{i1}\delta_{j1}$ with $\sigma(t)$ being a prescribed quantity. For this study, $\sigma(t)$ ramps linearly from 0 to σ_{max} over the interval $t = [0, 100\text{ s}]$ with $\sigma_{max} = 300$ MPa. That magnitude is then maintained for the next 900 s.

To analytically determine the model response, the constitutive law (4.72) is inverted to yield

$$D_{ij} = \mathbb{S}_{ijkl}\dot{\sigma}_{kl} + D^{\text{in}}_{ij}, \tag{4.77}$$

and it is trivial to determine that

$$\mathbb{S}_{ijkl}\dot{\sigma}_{kl} = \dot{\sigma}\mathbb{S}_{11kl}. \tag{4.78}$$

For the inelastic response, for the purely isotropic case it is noted that $\tau = \sigma(t)$ and therefore $n_{ij} = \frac{2}{3}\left[\delta_{i1}\delta_{j1} - \frac{1}{2}\left(\delta_{i2}\delta_{j2} + \delta_{i3}\delta_{j3}\right)\right]$. Additionally, the inelastic strain rate reduces to,

$$\gamma = f\left[\sinh\left(\frac{\sigma(t)}{\alpha D}\right)\right]^p \tag{4.79}$$

producing a rate of inelastic deformation of,

$$D^{\text{in}}_{ij} = \gamma\left[\delta_{i1}\delta_{j1} - \frac{1}{2}\left(\delta_{i2}\delta_{j2} + \delta_{i3}\delta_{j3}\right)\right]. \tag{4.80}$$

Expressions (4.77), (4.78), (4.80), and (4.75) can be easily integrated (via forward Euler or Runge-Kutta) to determine a semi-analytical response. Both the numerical and semi-analytical responses of the strain and stress (including flow stress, D) are presented below in Fig. 4.97(a) and Fig. 4.97(b), respectively.

4.20.3.2 Stress Relaxation

The model response through a stress relaxation type loading is considered here both numerically and semi-analytically. For this purpose, a displacement controlled loading, $u_1 = \lambda(t)$, is employed. The other displacement degrees of freedom are not prescribed to ensure that a uniaxial stress state ($\sigma_{ij} = \sigma(t)\,\delta_{i1}\delta_{j1}$) develops. Specifically, the displacement is set to scale linearly over 100 s (from $t = 0$ to $t = 100$ s) obtaining a maximum of $u_1 = 0.01$ at $t = 100$ s. Initially, a unit length is assumed. This displacement is held fixed over the next 900 s to investigate the stress relaxation characteristics of the model.

A similar procedure to the power law creep model (Section 4.19.3.2) is employed here. Specifically, by noting the elastic isotropy, uniaxial stress state, and (4.80) the elastic deformation rate in the direction of loading (D^{e}_{11}) is found to be,

$$D^{\text{e}}_{11} = \frac{\dot{\lambda}(t)}{1 + \lambda(t)} - \gamma,$$

where an expression for γ is given in (4.79). By noting $\dot{\sigma}_{ij} = \mathbb{C}_{ijkl}D^{\text{e}}_{kl}$ and $D_{ij} = D^{\text{e}}_{ij} + D^{\text{in}}_{ij}$, the material state may easily be found via numerical integration. The result strain and stress evolutions are given in Fig. 4.98(a) and Fig. 4.98(b), respectively.

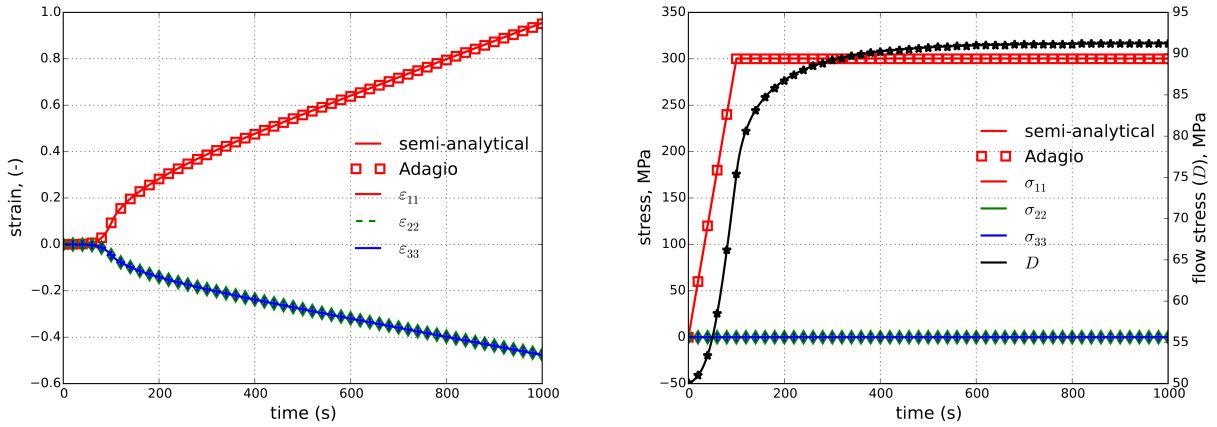

(a) Strain **(b) Stress**

Fig. 4.97 Semi-analytical and numerical results of (a) strain and (b) external and internal, (D), stress evolution during a creep test with the viscoplastic model.

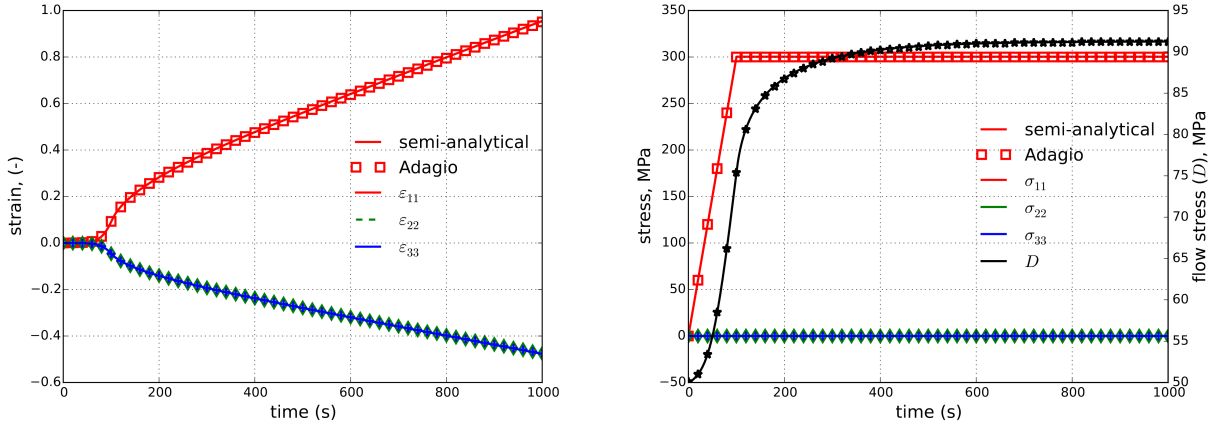

(a) Strain **(b) Stress**

Fig. 4.98 Semi-analytical and numerical results of (a) strain and (b) external and internal (D) stress evolution during a stress relaxation test with the viscoplastic model.

4.20.4 User Guide

```
BEGIN PARAMETERS FOR MODEL VISCOPLASTIC
  #
  # Elastic constants
  #
  YOUNGS MODULUS = <real>
  POISSONS RATIO = <real>
  SHEAR MODULUS  = <real>
  BULK MODULUS   = <real>
  LAMBDA         = <real>
  TWO MU         = <real>

  FLOW RATE     = <real>
  SINH EXPONENT = <real>
  ALPHA         = <real>
  ISO HARDENING = <real>
  ISO RECOVERY  = <real>
  ISO EXPONENT  = <real>
  KIN HARDENING = <real>
  KIN RECOVERY  = <real>
  KIN EXPONENT  = <real>
  FLOW STRESS   = <real>

  SHEAR FUNCTION    = <string>
  BULK FUNCTION     = <string>
  RATE FUNCTION     = <string>
  EXPONENT FUNCTION = <string>
  ALPHA FUNCTION    = <string>
  IHARD FUNCTION    = <string>
  IREC FUNCTION     = <string>
  KHARD FUNCTION    = <string>
  KREC FUNCTION     = <string>
  MAX SUBINCREMENTS = <int> itmax (2000)
END [PARAMETERS FOR MODEL VISCOPLASTIC]
```

In the above command blocks:

- Since the model requires functions to describe the temperature dependence of the bulk and shear modulus, it is recommended that one inputs the bulk and shear modulus at some reference temperature. However, any two of the elastic constants can be used for input.
- The reference value in the equation for the flow rate, ln f_0, is defined with the `FLOW RATE` command line.
- The reference value for the exponent on the sinh function, p_0, is defined with the `SINH EXPONENT` command line.

- The reference value $alpha_0$ is defined with the `ALPHA` command line.
- The reference value for the isotropic hardening parameter, A_1^0, is defined with the `ISO HARDENING` command line.
- The reference value for the isotropic recovery parameter, A_2^0, is defined with the `ISO RECOVERY` command line.
- The value for the isotropic hardening exponent parameter, A_3, is defined with the `ISO EXPONENT` command line.
- The reference value for the kinematic hardening parameter, A_4^0, is defined with the `KIN HARDENING` command line.
- The reference value for the kinematic recovery parameter, A_5^0, is defined with the `KIN RECOVERY` command line.
- The value for the kinematic hardening exponent parameter, A_6, is defined with the `KIN EXPONENT` command line.
- The value for the flow stress, D_0, is defined with the `FLOW STRESS` command line.
- The user-defined and normalized function that gives the shear modulus as a function of temperature, $h_G(\theta)$, is defined with the `SHEAR FUNCTION` command line.
- The user-defined and normalized function that gives the bulk modulus as a function of temperature, $h_K(\theta)$, is defined with the `BULK FUNCTION` command line.
- The user-defined and normalized function that gives the flow rate as a function of temperature, $h_g(\theta)$, is defined with the `RATE FUNCTION` command line.
- The user-defined and normalized function that gives the sinh exponent as a function of temperature, $h_p(\theta)$, is defined with the `EXPONENT FUNCTION` command line.
- The user-defined and normalized function that gives α as a function of temperature, $h_\alpha(\theta)$, is defined with the `ALPHA FUNCTION` command line.
- The user-defined and normalized function that gives A_1 as a function of temperature, $h_1(\theta)$, is defined with the `IHARD FUNCTION` command line.
- The user-defined and normalized function that gives A_2 as a function of temperature, $h_2(\theta)$, is defined with the `IREC FUNCTION` command line.
- The user-defined and normalized function that gives A_4 as a function of temperature, $h_4(\theta)$, is defined with the `KHARD FUNCTION` command line.
- The user-defined and normalized function that gives A_5 as a function of temperature, $h_5(\theta)$, is defined with the `KREC FUNCTION` command line.
- The Viscoplastic model may need to take sub-increments to solve for the plastic flow over the current time step. The maximum number of steps that may be taken on a step prior to issuing an error can be set by the `MAX SUBINCREMENTS` command line. This value defaults to 2000.

Output variables available for this model are listed in Table 4.31.

More information on the model can be found in the report by Neilsen, et. al. [74].

Table 4.31 State Variables for VISCOPLASTIC Model

Name	Description
EQPS	equivalent plastic strain
SVB	kinematic hardening variable, $\mathbf{B}$
SVB_XX	kinematic hardening variable - xx component, B_{xx}
SVB_YY	kinematic hardening variable - yy component, B_{yy}
SVB_ZZ	kinematic hardening variable - zz component, B_{zz}
SVB_XY	kinematic hardening variable - xy component, B_{xy}
SVB_YZ	kinematic hardening variable - yz component, B_{yz}
SVB_ZX	kinematic hardening variable - zx component, B_{zx}
SVD	isotropic hardening variable, D
EQDOT	inelastic strain rate, γ
COUNT	number of sub-increments
SHEAR	shear modulus, $G(\theta)$
BULK	bulk modulus, $K(\theta)$
RATE	$g(\theta)$ (see (4.74))
EXP	$p(\theta)$ (see (4.74))
ALPHA	$\alpha(\theta)$ (see (4.74))
A1	isotropic hardening parameter, $A_1(\theta)$
A2	isotropic recovery parameter, $A_2(\theta)$
A4	kinematic hardening parameter, $A_4(\theta)$
A5	kinematic recovery parameter, $A_5(\theta)$

4.21 Munson-Dawson Viscoplastic Model

4.21.1 Theory

The Munson-Dawson (MD) model was originally defined in [69], [70], [71], but several changes were made in [86]. This section presents the current model in a small strain setting. (Section 4.21.2 briefly mentions how the model is extended into the finite deformation realm.) Note that compressive stresses and strains are treated as positive in this section, as is common in the geomechanics literature.

The MD model is an isotropic, hypoelastic, unified viscoplastic, material model. The total strain rate $\dot{\varepsilon}_{ij}$ is decomposed into an elastic strain rate $\dot{\varepsilon}^{\text{el}}_{ij}$, a thermal strain rate $\dot{\varepsilon}^{\text{th}}_{ij}$, and a viscoplastic strain rate $\dot{\varepsilon}^{\text{vp}}_{ij}$:

$$\dot{\varepsilon}_{ij} = \dot{\varepsilon}^{\text{el}}_{ij} + \dot{\varepsilon}^{\text{th}}_{ij} + \dot{\varepsilon}^{\text{vp}}_{ij}. \tag{4.81}$$

The elastic portion of the MD model utilizes the following simple linear relationship between $\dot{\varepsilon}^{\text{el}}_{kl}$ and the stress rate $\dot{\sigma}_{ij}$,

$$\dot{\sigma}_{ij} = \mathbb{C}_{ijkl}\dot{\varepsilon}^{\text{el}}_{kl} = \mathbb{C}_{ijkl}\left(\dot{\varepsilon}_{kl} - \dot{\varepsilon}^{\text{th}}_{kl} - \dot{\varepsilon}^{\text{vp}}_{kl}\right) \tag{4.82}$$

$$\mathbb{C}_{ijkl} = (B - 2/3\,\mu)\,\delta_{ij}\,\delta_{kl} + \mu\,\left(\delta_{ik}\,\delta_{jl} + \delta_{il}\,\delta_{jk}\right), \tag{4.83}$$

where $\mathbb{C}_{ijkl}$ is the elastic stiffness, which is composed of the bulk modulus B, the shear modulus μ, and the Kronecker Delta δ_{ij}. The thermal strain portion of the model is simply

$$\dot{\varepsilon}^{\text{th}}_{ij} = -\alpha\,\dot{\theta}\,\delta_{ij} \tag{4.84}$$

where α is the coefficient of thermal expansion, and θ is the temperature. Sierra/SM also offers thermal strain functions for adding thermal strain effects to any given model. If $\alpha \neq 0$, then MD model users should not specify a thermal strain function, otherwise thermal strains will be applied twice.

Plastic deformation is assumed to be isochoric and only occurs in the presence of shear stress. The MD model utilizes the Hosford stress as its equivalent shear stress measure $\bar{\sigma}$. The Hosford stress is

$$\bar{\sigma} = \left\{\frac{1}{2}\left[|\sigma_1 - \sigma_2|^a + |\sigma_2 - \sigma_3|^a + |\sigma_1 - \sigma_3|^a\right]\right\}^{1/a}, \tag{4.85}$$

where σ_i are the principal stresses and a is a material parameter. This definition for $\bar{\sigma}$ was proposed in [45] because it encompasses the Tresca stress ($a = 1$), the von Mises stress ($a = 2$), and a range of behaviors in-between ($1 < a < 2$). One can also reproduce the Tresca stress with $a = \infty$, the von Mises stress with $a = 4$, and behaviors in-between with $4 < a < \infty$. This second range avoids potential singularities in the first and second derivatives of (4.85), so the exponent is restricted to $a \geq 4$.

The viscoplastic strain evolves according to an associated flow rule

$$\dot{\varepsilon}^{\text{vp}}_{ij} = \dot{\bar{\varepsilon}}^{\text{vp}}\frac{\partial\bar{\sigma}}{\partial\sigma_{ij}}, \tag{4.86}$$

where $\dot{\bar{\varepsilon}}^{\text{vp}}$ is the equivalent viscoplastic strain rate. It can be decomposed into two components

$$\dot{\bar{\varepsilon}}^{\text{vp}} = \dot{\bar{\varepsilon}}^{\text{tr}} + \dot{\bar{\varepsilon}}^{\text{ss}}, \tag{4.87}$$

where $\dot{\bar{\varepsilon}}^{\text{tr}}$ is the transient equivalent viscoplastic strain rate and $\dot{\bar{\varepsilon}}^{\text{ss}}$ is the steady state equivalent viscoplastic strain rate.

The MD model decomposes the steady state behavior into four mechanisms:

$$\begin{aligned}
\dot{\bar{\varepsilon}}^{\text{ss}} &= \sum_{i=0}^{3}\dot{\bar{\varepsilon}}^{\text{ss}}_i \\
\dot{\bar{\varepsilon}}^{\text{ss}}_i &= A_i\,\exp\left(-\frac{Q_i}{R\,\theta}\right)\left(\frac{\bar{\sigma}}{\mu}\right)^{n_i} \quad \text{for } i = 0,\,1,\,\text{and } 2 \\
\dot{\bar{\varepsilon}}^{\text{ss}}_3 &= H(\bar{\sigma} - \bar{\sigma}_{\text{g}})\sum_{i=0}^{2}B_i\,\exp\left(-\frac{Q_i}{R\,\theta}\right)\,\sinh\left(q\frac{(\bar{\sigma} - \bar{\sigma}_{\text{g}})}{\mu}\right),
\end{aligned}$$

The variables A_i, B_i, Q_i, n_i, $\bar{\sigma}_g$, and q are all model parameters. All four mechanisms have an Arrhenius temperature dependence, where Q_i is an activation energy and $R = 8.314\text{J/(K mol)}$ is the universal gas constant. Mechanism 3 is only activated when $\bar{\sigma}$ exceeds $\bar{\sigma}_g$, as reflected in the heaviside function $H(\bar{\sigma} - \bar{\sigma}_g)$. Typically, the parameters B_i are chosen to produce a smooth transition to mechanism 3 at $\bar{\sigma}_g$.

The simple functional forms of (4.88) suffice for the steady-state behavior, but the transient behavior is somewhat more complex. During work hardening under constant stress, $\dot{\bar{\varepsilon}}^{tr}$ approaches the transient strain limit $\dot{\bar{\varepsilon}}^{tr*}$ from below, and the total viscoplastic strain rate slows down over time. During recovery under constant stress, $\dot{\bar{\varepsilon}}^{tr}$ approaches $\dot{\bar{\varepsilon}}^{tr*}$ from above, and the total viscoplastic strain rate speeds up over time. The rate that $\dot{\bar{\varepsilon}}^{tr}$ approaches $\dot{\bar{\varepsilon}}^{tr*}$ is governed by

$$\dot{\bar{\varepsilon}}^{tr} = (F - 1)\ \dot{\bar{\varepsilon}}^{ss}, \tag{4.88}$$

where

$$F = \exp\left[\text{sign}\ (\dot{\bar{\varepsilon}}^{tr*} - \dot{\bar{\varepsilon}}^{tr})\ \kappa\ \left(1 - \frac{\dot{\bar{\varepsilon}}^{tr}}{\dot{\bar{\varepsilon}}^{tr*}}\right)^2\right]. \tag{4.89}$$

and κ is a quantity that depends on whether the material is work hardening or recovering. These two behaviors are captured in the following equations

$$\kappa = \begin{cases} \alpha_h + \beta_h\ \log_{10}\left(\dfrac{\bar{\sigma}}{\mu}\right) & \dot{\bar{\varepsilon}}^{tr} \le \dot{\bar{\varepsilon}}^{tr*} \\ \alpha_r + \beta_r\ \log_{10}\left(\dfrac{\bar{\sigma}}{\mu}\right) & \dot{\bar{\varepsilon}}^{tr} > \dot{\bar{\varepsilon}}^{tr*}. \end{cases} \tag{4.90}$$

where α_j and β_j are model parameters. Note that the parameter κ must be non-negative, otherwise (4.88) produces a negative/positive $\dot{\bar{\varepsilon}}^{tr}$ when $\dot{\bar{\varepsilon}}^{tr}$ is below/above $\dot{\bar{\varepsilon}}^{tr*}$. (Such behavior occurs during reverse creep, but the MD model is only designed to model forward creep.) To enforce this, (4.90) is calculated first, and then

$$\kappa \leftarrow \max(\kappa, 0)$$

is applied.

The MD model uses two mechanisms to endow $\dot{\bar{\varepsilon}}^{tr*}$ with stress and temperature dependence:

$$\dot{\bar{\varepsilon}}^{tr*} = \sum_{i=0}^{1} \dot{\bar{\varepsilon}}_i^{tr*}$$
$$\dot{\bar{\varepsilon}}_i^{tr*} = K_i\ \exp(c_i\,\theta)\left(\frac{\bar{\sigma}}{\mu}\right)^{m_i},$$

where K_i, c_i, and m_i are parameters to be calibrated against experimental results.

4.21.2 Implementation

The full details of the MD model's numerical implementation are published in [86]. This section discusses several salient points for the typical MD model user and to define all the input parameters in Section 4.21.4.

- As discussed in Section 4.21.3, one can obtain an analytical solution to the MD model's ordinary differential equations if the exponent in (4.89) is changed from 2 to 1, and sign $(\dot{\bar{\varepsilon}}^{\mathrm{tr}*} - \dot{\bar{\varepsilon}}^{\mathrm{tr}}) = 1$. To accommodate this possibility, (4.89) is numerically implemented as

$$F = \exp\left[\text{sign } (\dot{\bar{\varepsilon}}^{\mathrm{tr}*} - \dot{\bar{\varepsilon}}^{\mathrm{tr}})^{\chi-1}\, \kappa \left(1 - \frac{\dot{\bar{\varepsilon}}^{\mathrm{tr}}}{\dot{\bar{\varepsilon}}^{\mathrm{tr}*}}\right)^{\chi}\right] \tag{4.91}$$

where χ is a user specified integer that is equal to 2 by default, but one can set $\chi = 1$ for verification testing.

- Each steady state creep mechanism is implemented with a viscoplastic rate scale factor s, such that (4.88) becomes

$$\begin{aligned}
\dot{\bar{\varepsilon}}^{\mathrm{ss}} &= \sum_{i=0}^{3} \dot{\bar{\varepsilon}}_i^{\mathrm{ss}} \\
\dot{\bar{\varepsilon}}_i^{\mathrm{ss}} &= s\, A_i\, \exp\left(-\frac{Q_i}{R\,\theta}\right) \left(\frac{\bar{\sigma}}{\mu}\right)^{n_i} \qquad \text{for} i = 0, 1, and 2 \\
\dot{\bar{\varepsilon}}_3^{\mathrm{ss}} &= s\, H(\bar{\sigma} - \bar{\sigma}_{\mathrm{g}}) \sum_{i=0}^{2} B_i\, \exp\left(-\frac{Q_i}{R\,\theta}\right) \sinh\left(q \frac{(\bar{\sigma} - \bar{\sigma}_{\mathrm{g}})}{\mu}\right).
\end{aligned}$$

This scale factor can be used to speed up or slow down the equivalent steady-state strain rate and the total equivalent viscoplastic strain rate, because $\dot{\bar{\varepsilon}}^{\mathrm{vp}} = \dot{\bar{\varepsilon}}^{\mathrm{tr}} + \dot{\bar{\varepsilon}}^{\mathrm{ss}} = F\, \dot{\bar{\varepsilon}}^{\mathrm{ss}}$. The default value is $s = 1$, but it can be useful to set s to some small value to "freeze" the material's viscoplasticity for a period of time, or increase s to larger values to squeeze hundreds of years into a few seconds. Speeding up the viscoplasticity can allow one to make quasi-static simulations using explicit dynamics, provided inertial effects are kept to a minimum. The variable s is implemented as an internal state variable, rather than a material parameter, so a user can modify it in the middle of a simulation. Internal state variables can be altered by creating a user variable with the same name as the internal state variable (`viscoplastic_rate_scale_factor` in this case) in a Sierra input deck and modifying the user variable with a user function or user subroutine (see Sections 2.3 and A.2.1 in [87]).

- The MD model is extended into the finite-deformation realm using hypoelasticity. Consistent with the Green-McInnis stress rate, the infinitesimal strain rates are replaced with the corresponding unrotated rates of deformation (i.e. $\dot{\varepsilon}_{ij} \rightarrow D_{ij}$) and the stress is replaced with the unrotated Cauchy stress ($\sigma_{ij} \rightarrow Tij$).

- Following the lead of Scherzinger [88], the model's time derivatives are discretized using the backwards Euler method, and the resulting non-linear algebraic equations are solved with a line search augmented Newton-Raphson method.

A typical user of the model should not need to adjust the routine's default numerical parameters, but the parameters are briefly mentioned here should adjustment become necessary.

- The implementation has some expressions where $\bar{\sigma}$ is in the denominator of a fraction. If an initial calculation of the Hosford stress results in $\bar{\sigma} < \bar{\sigma}_{\min}$, then the initial value is replaced with $\bar{\sigma}_{\min}$. The value of $\bar{\sigma}_{\min}$ should be small enough to have negligible impact, yet still avoid $\bar{\sigma} = 0$.
- Each iteration of the implicit integration routine updates the merit function $\omega^{(k)} = 1/2 \left(\mathcal{R}_{ij}^{(k)} \mathcal{R}_{ij}^{(k)} + r^{(k)^2} \right)$ for iteration k, where $\mathcal{R}_{ij}^{(k)}$ and $r^{(k)}$ are the residuals associated with the differential equations in (4.86) and (4.88), respectively. An iteration is considered converged when $\sqrt{\omega^{(k)}} < \sqrt{\omega_{\max}}$. The value of $\sqrt{\omega_{\max}}$ should be a small positive value close to zero.
- If a Newton iteration (or a line search iteration) does not produce sufficient decrease in $\omega^{(k)}$, a line search iteration is performed. The line search algorithm selects $\zeta^{(j)}$, for each iteration j, to search for a sufficient decrease in $\omega^{(k)}(\zeta^{(j)})$ along the search direction provided by the Newton iteration. The start and end of the last Newton iteration are $\zeta^{(j)} = 0$ and $\zeta^{(j)} = 1$, respectively. A decrease in $\omega^{(k)}(\zeta^{(j)})$ is considered sufficient if $\omega^{(k)}(\zeta^{(j)}) < (1 - 2\,\xi\,\zeta^{(j-1)})\,\omega^{(k)}(0)$, where ξ is a positive value usually set close to zero.
- The minimum allowed value of $\zeta^{(j)}$ is γ.
- The maximum number of Newton iterations is $k_{\max}$.
- The maximum number of line search iterations is $j_{\max}$.

See [86] for further discussion of these numerical parameters.

4.21.3 Verification

The MD model contains ordinary differential equations ((4.86) and (4.88)) that make it non-trivial to verify. A straightforward analytical solution, however, can be constructed to these equations if $\chi = 1$ in (4.91) and if the stresses and temperatures remain piecewise constant in time.

Temporally constant stresses and temperatures allow (4.82), (4.83), (4.84), (4.85), (4.86), (4.87), and (4.88) to be integrated to

$$\varepsilon_{kl} - \varepsilon_{kl}(t_j) = \mathbb{C}^{-1}_{klmn} \left(\sigma_{mn} - \sigma_{mn}(t_j) \right) - \alpha \, \left(\theta - \theta(t_j) \right) \, \delta_{kl} + \varepsilon^{\mathrm{vp}}_{kl} - \varepsilon^{\mathrm{vp}}_{kl}(t_j) \tag{4.92}$$

$$\varepsilon^{\mathrm{vp}}_{kl} - \varepsilon^{\mathrm{vp}}_{kl}(t_j) = \left[\dot{\bar{\varepsilon}}^{\mathrm{tr}} - \dot{\bar{\varepsilon}}^{\mathrm{tr}}(t_j) + \dot{\bar{\varepsilon}}^{\mathrm{ss}} \, (t - t_j) \right] \frac{\partial \bar{\sigma}}{\partial \sigma_{kl}} \tag{4.93}$$

where t_j is the time at the end of the previous time period j. The quantities from the previous time period ($\varepsilon_{kl}(t_j)$, $\sigma_{mn}(t_j)$, $\theta(t_j)$, $\varepsilon^{\mathrm{vp}}_{kl}(t_j)$, and $\dot{\bar{\varepsilon}}^{\mathrm{tr}}(t_j)$) are assumed to be known. Setting $\chi = 1$ in (4.91) enables the following general analytical solution to (4.88):

$$\dot{\bar{\varepsilon}}^{\mathrm{tr}} = \frac{\dot{\bar{\varepsilon}}^{\mathrm{tr}*}}{\kappa} \, \ln \left\{ \exp(\kappa) + \exp \left[\frac{\kappa}{\dot{\bar{\varepsilon}}^{\mathrm{tr}*}} \left(C_1 - \dot{\bar{\varepsilon}}^{\mathrm{ss}} t \right) \right] \right\} . \tag{4.94}$$

One can solve for the integration constant C_1 using the initial condition $\dot{\bar{\varepsilon}}^{\text{tr}} = \dot{\bar{\varepsilon}}^{\text{tr}}(t_j)$ at $t = t_j$. After substituting the result back into (4.94), one obtains

$$\dot{\bar{\varepsilon}}^{\text{tr}} = \frac{\dot{\bar{\varepsilon}}^{\text{tr}*}}{\kappa} \ln\left\{\exp(\kappa) + \left[\exp\left(\frac{\dot{\bar{\varepsilon}}^{\text{tr}}(t_j)\,\kappa}{\dot{\bar{\varepsilon}}^{\text{tr}*}}\right) - \exp(\kappa)\right] \exp\left[-\frac{\kappa}{\dot{\bar{\varepsilon}}^{\text{tr}*}}\,\dot{\bar{\varepsilon}}^{\text{ss}}\,(t - t_j)\right]\right\}. \tag{4.95}$$

Combining (4.92), (4.93), and (4.95) produces the following closed form expression for the total strain change over a time period

$$\begin{aligned}\varepsilon_{kl} - \varepsilon_{kl}(t_j) = \mathbb{C}^{-1}_{klmn}\left(\sigma_{mn} - \sigma_{mn}(t_j)\right) - \alpha\,\left(\theta - \theta(t_j)\right)\,\delta_{kl} + \\ \left[\frac{\dot{\bar{\varepsilon}}^{\text{tr}*}}{\kappa} \ln\left\{\exp(\kappa) + \left[\exp\left(\frac{\dot{\bar{\varepsilon}}^{\text{tr}}(t_j)\,\kappa}{\dot{\bar{\varepsilon}}^{\text{tr}*}}\right) - \exp(\kappa)\right] \exp\left[-\frac{\kappa}{\dot{\bar{\varepsilon}}^{\text{tr}*}}\,\dot{\bar{\varepsilon}}^{\text{ss}}\,(t - t_j)\right]\right\}\right. \\ \left. - \dot{\bar{\varepsilon}}^{\text{tr}}(t_j) + \dot{\bar{\varepsilon}}^{\text{ss}}\,(t - t_j)\right] \frac{\partial \bar{\sigma}}{\partial \sigma_{kl}}.\end{aligned}$$

The next three subsections compare numerical solutions against analytical solutions for axisymmetric compression, pure shear, and unequal biaxial compression. In each case, the numerical solution for the total strain is denoted as ε_{ij}, while the analytical solution for the total strain in (4.96) is denoted as $\hat{\varepsilon}_{ij}$. All the verification tests only involve principal deformations, so hypoelasticity simply reinterprets the stress and strain in Section 4.21.1 as the Cauchy stress and logarithmic strain, respectively. As a reminder, compressive stresses and strains are treated as positive.

All the verification tests utilize Calibration 3B of the MD model. The full parameter set can be found in [86], but Fig. 4.99, Fig. 4.100 and Fig. 4.101 depict much of the calibration graphically. Fig. 4.99 shows the shape of the Hosford equivalent stress surface for $a = 16$. The Hosford surface and the angle ϕ of its normal n_{ij} depend on the Lode angle ϕ of the deviatoric stress $\sigma^{\text{dev}}_{ij} = \sigma_{ij} - 1/3\sigma_{kk}\,\delta_{ij}$. Fig. 4.100 and Fig. 4.101 show the individual mechanisms $\dot{\bar{\varepsilon}}^{\text{tr}*}_i$ and $\dot{\bar{\varepsilon}}^{\text{ss}}_i$, as well as the sums $\dot{\bar{\varepsilon}}^{\text{tr}*} = \sum_{i=0}^{1} \dot{\bar{\varepsilon}}^{\text{tr}*}_i$ and $\dot{\bar{\varepsilon}}^{\text{ss}} = \sum_{i=0}^{3} \dot{\bar{\varepsilon}}^{\text{ss}}_i$, so that one can visualize where each mechanism dominates the total behavior.

4.21.3.1 Triaxial Compression

Triaxial compression tests are frequently used to characterize the creep and strength behavior of geomaterials, such as rock salt. Cylindrical specimens are subjected to a radial confining pressure σ_{rr} and an axial stress σ_{zz}. Axisymmetric compression is perhaps a more appropriate name for these tests, because the hoop stress $\sigma_{\vartheta\vartheta}$ is equal to σ_{rr}, but triaxial compression is the common name.

The applied stress and temperature histories for the test are shown in the top two plots in Fig. 4.102. The test begins with an isothermal, 20 MPa hydrostatic, hold period for 10 days, where the strain is purely elastic. At $t = 0$, σ_{zz} is increased to 35 MPa, while the other stresses are held fixed, causing a 15 MPa equivalent stress. This stress state is held for the next 50 days. The strain evolves quickly at first, but slows down to the steady-state rate as the material work hardens. At

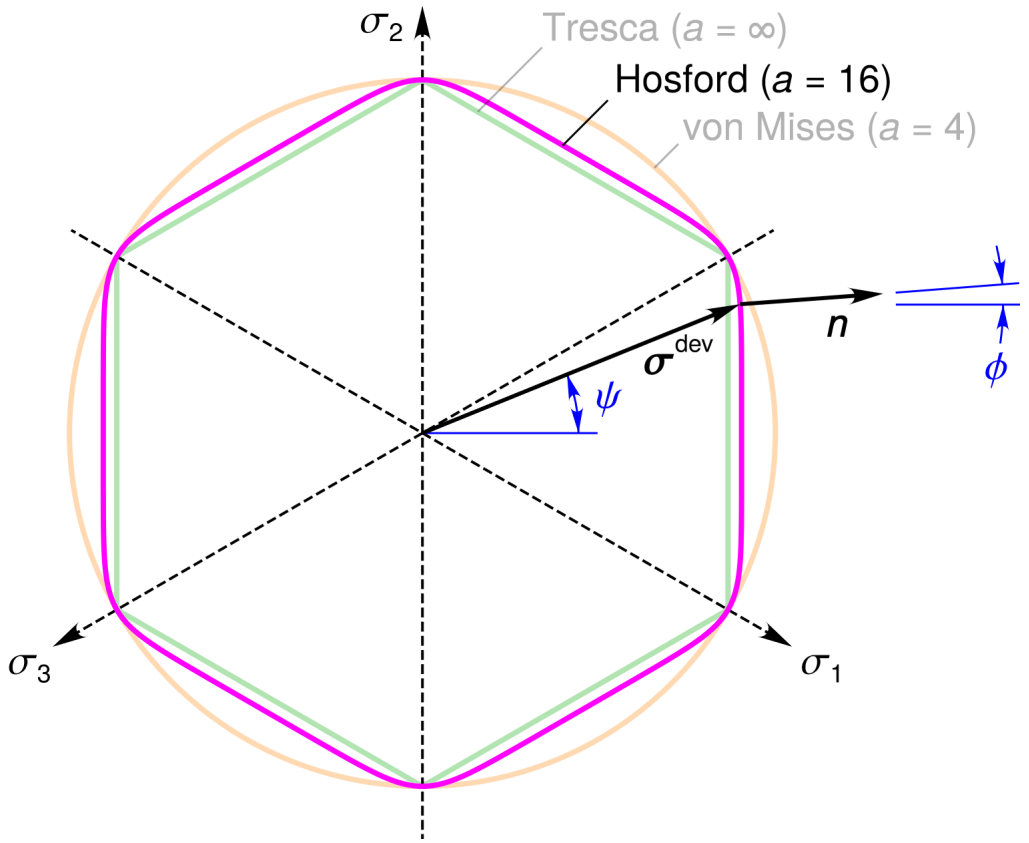

Fig. 4.99 Hosford equivalent stress surface in the π-plane.

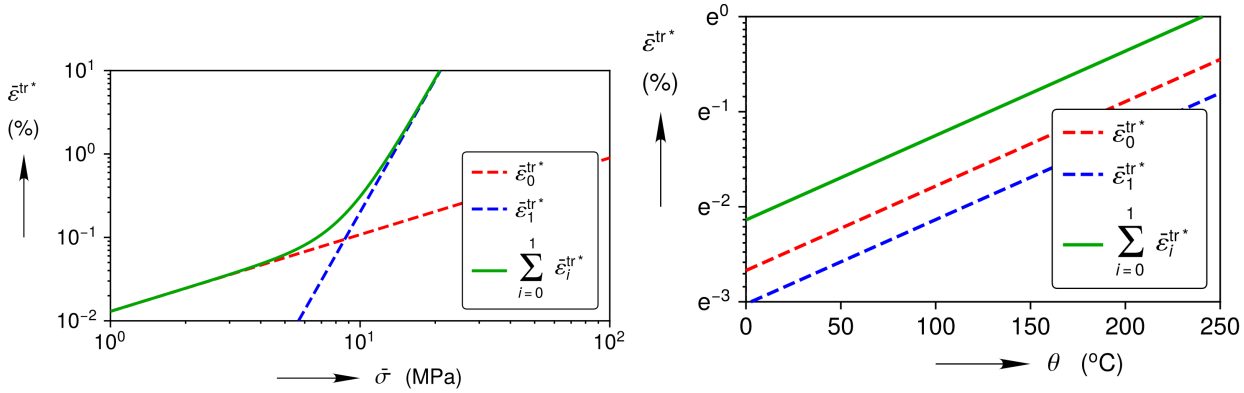

(a) Stress Dependence at 27 C **(b) Temperature Dependence at 8 MPa**

Fig. 4.100 Stress and temperature dependence of the transient strain limit for Calibration 3B.

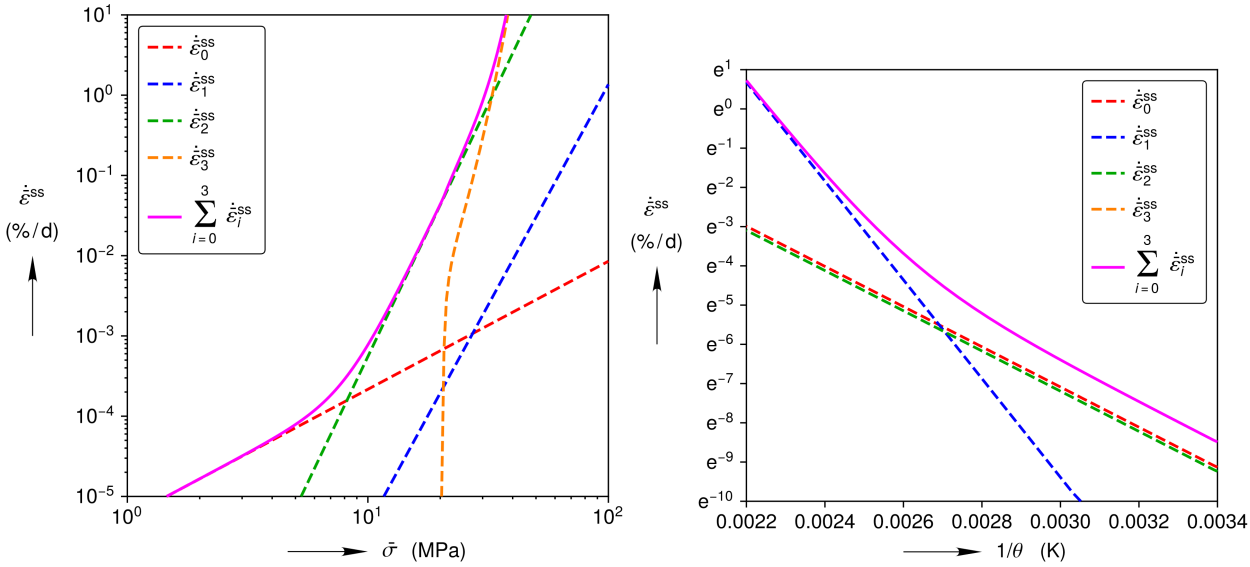

(a) Stress Dependence at 27 C **(b) Temperature Dependence at 8 MPa**

Fig. 4.101 Stress and temperature dependence of the steady-state strain rate for Calibration 3B.

$t = 50$, σ_{zz} is decreased to 33 MPa, while the other stresses are held fixed. The 2 MPa drop in $\bar{\sigma}$ causes the strain rate to slow down markedly, but it gradually builds to a new steady-state rate as the material recovers over the next 50 days.

In summary, the numerical and analytical solutions for the total strain match very well throughout the test, which verifies:

- Linear elasticity under triaxial compression
- Zero viscoplastic strain evolution under hydrostatic loading
- Viscoplastic strain evolution for $\psi = -30°$
- Work hardening ($\dot{\bar{\varepsilon}}^{tr} < \dot{\bar{\varepsilon}}^{tr*}$) dominated by transient strain limit mechanism 1
- Recovery ($\dot{\bar{\varepsilon}}^{tr} > \dot{\bar{\varepsilon}}^{tr*}$) dominated by transient strain limit mechanism 1
- Steady-state strain accumulation dominated by transient strain limit mechanism 2.

4.21.3.2 Pure Shear

The Hosford equivalent stress depends on a for $-30\,\text{deg} < \psi < 30\,\text{deg}$, but it is independent of a for $\psi = -30°$ (triaxial compression) and $\psi = 30°$ (triaxial extension). Pure shear is a simple stress state that exercises the Hosford stress at a Lode angle other than $\psi = \pm 30°$. Pure shear can be expressed in the principal frame as $\sigma_3 = -\sigma_1$ and $\sigma_2 = 0$. In addition to exercising the model under pure shear, this test also varies the temperature to verify thermal expansion and creep at elevated temperatures.

The applied stress and temperature histories for the test are shown in the top two plots in Fig.

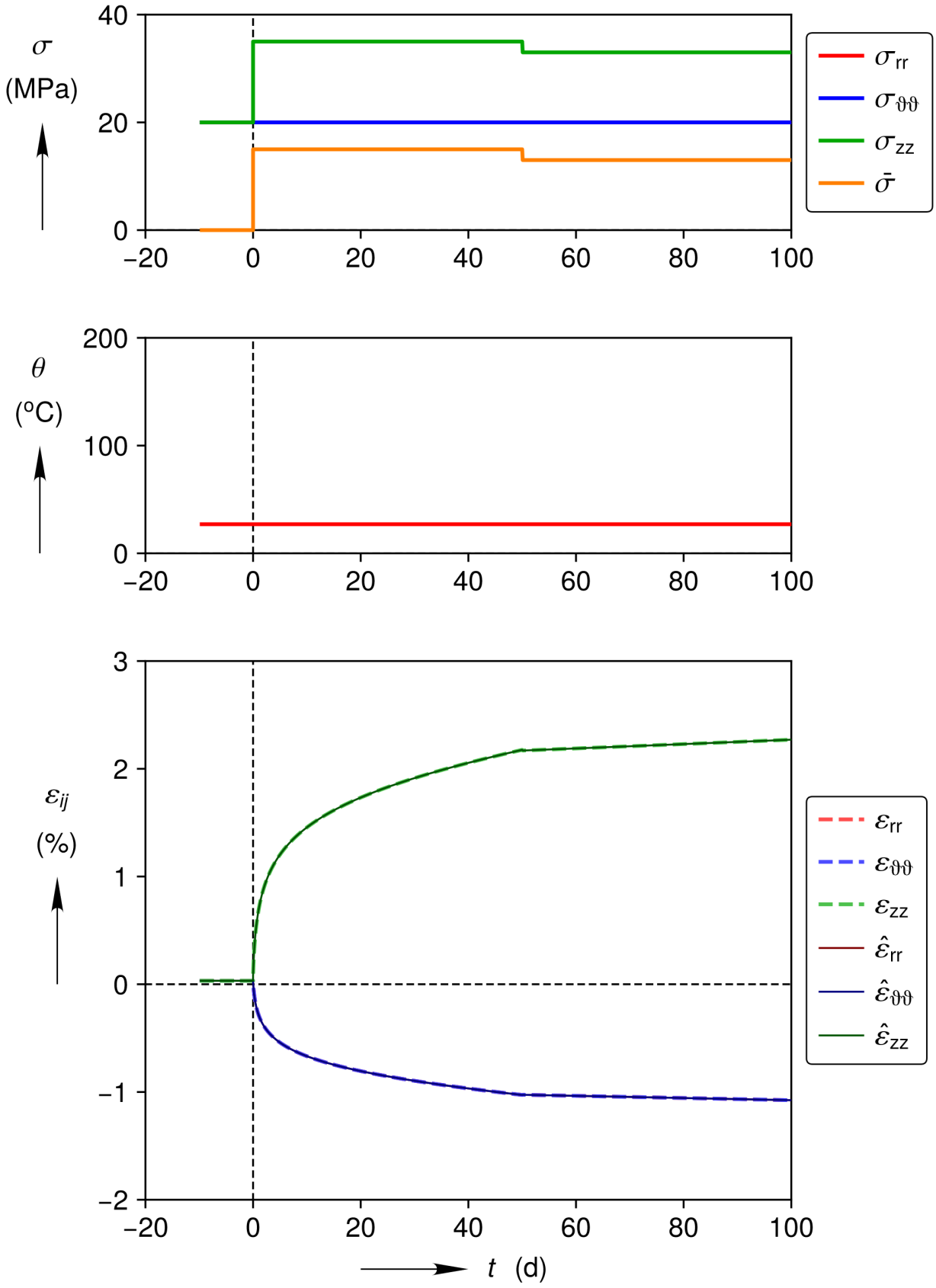

Fig. 4.102 Triaxial Compression Verification Test

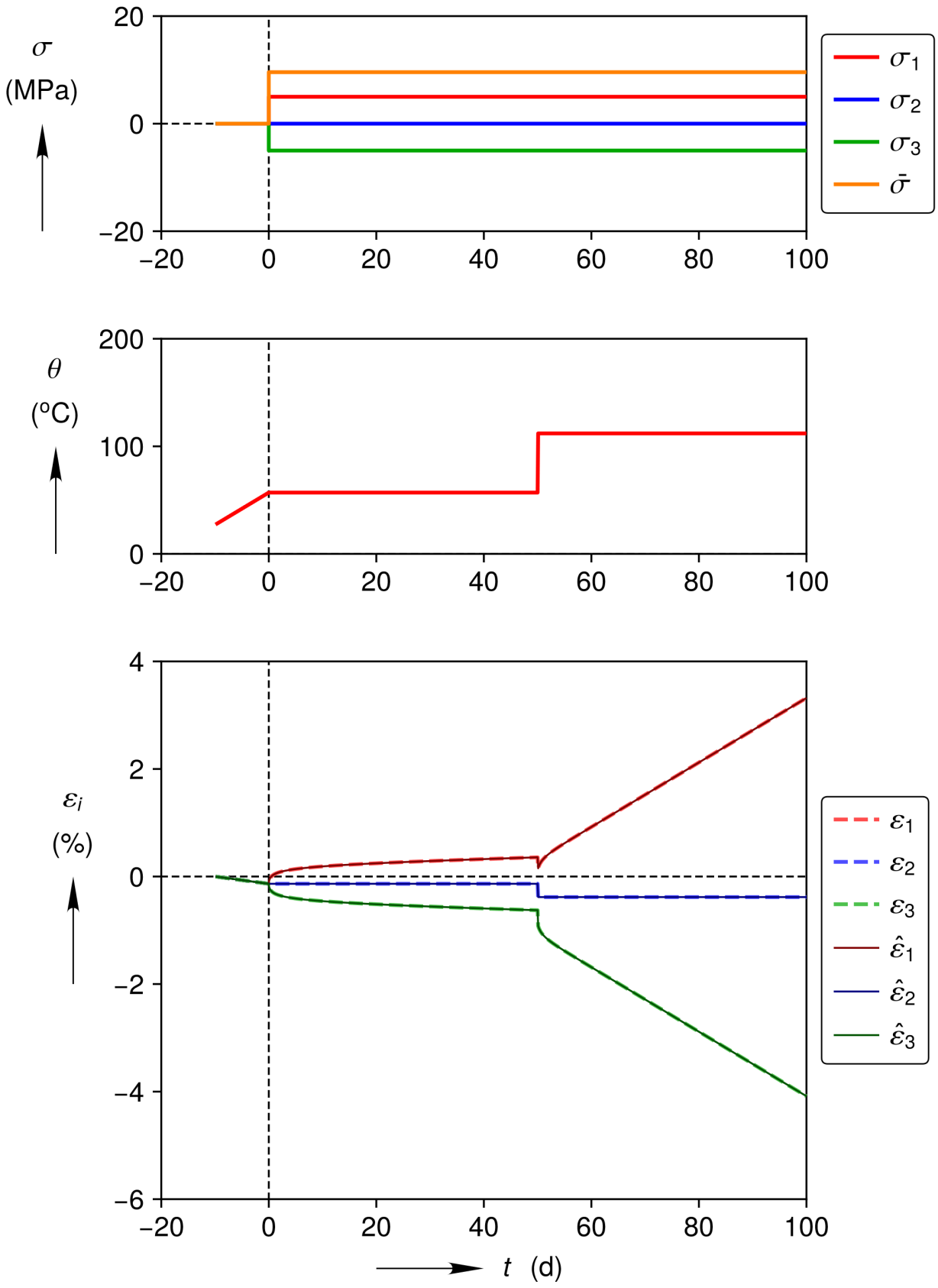

Fig. 4.103 Pure Shear Verification Test

4.103. The test begins with a 0 MPa hydrostatic hold period for 10 days while the temperature is linearly ramped from 27°C to 57°C. Some thermal strains develop during this time. At $t = 0$, the temperature ramp stops, σ_1 is increased to 5 MPa, σ_2 is held at zero, and σ_3 is reduced to -5 MPa. This state is held for the next 50 days, while the material creeps. At $t = 50$, θ is increased to 112°C, but the stresses remain fixed. The sharp increase in θ causes a step change in thermal strain, and then accelerated creep is observed over the over the next 50 days.

In summary, the numerical and analytical solutions for the total strain match very well throughout the test, which verifies:

- Linear elasticity under pure shear
- Thermal expansion
- Viscoplastic strain evolution for $\psi = 0°$
- Temperature dependence of transient strain limit mechanism 1
- Steady-state strain accumulation dominated by mechanism 1
- Steady-state strain accumulation dominated by mechanism 2.

4.21.3.3 Unequal Biaxial Compression

Unequal biaxial compression is another stress state that exercises the Hosford stress at a Lode angle other than $\psi = \pm 30°$. Unequal compressive stresses σ_{xx} and σ_{yy} are applied to two faces of a cube, while $\sigma_{zz} = 0$. This stress state is slightly more complex than triaxial compression or pure shear because all three stress magnitudes are unequal. This test also alters the stress component ratios after 50 days of creep to verify the model's ability to change Lode angle.

The applied stress and temperature histories for the test are shown in the top two plots in Fig. 4.104. The test begins with a stress free hold period for 10 days. At $t = 0$, σ_{xx} is increased to 3.5 MPa, σ_{yy} is increased to 5 MPa, and σ_{zz} is held at zero. In this stress state, $\psi = 13.0°$ and the intermediate principal stress is σ_{xx}. The intermediate principal strain rate $\dot{\varepsilon}_{xx} \approx 0$ and $\dot{\varepsilon}_{yy} \approx -\dot{\varepsilon}_{zz}$ because the flow rule (4.86) causes $\dot{\varepsilon}^{vp}$ to be coaxial with the flow potential normal n_{ij}, and n_{ij} is nearly horizontal at $\phi = 13.0°$ in Calibration 3B (see Fig. 4.99). At $t = 50$, σ_{xx} is increased to 6.0 MPa, while the other stresses remain fixed. The sharp increase in σ_{xx} causes a step change in elastic strain that is visible because the viscoplastic strains are small at these low values of $\bar{\sigma}$. In this stress state, $\psi = 21.1°$ and the intermediate principal stress is σ_{yy}. Accordingly, $\dot{\varepsilon}_{yy} \approx 0$ and $\dot{\varepsilon}_{xx} \approx -\dot{\varepsilon}_{zz}$. If one looks more closely, however, $\dot{\varepsilon}_{yy}$ is slightly positive and $\dot{\varepsilon}_{xx} > -\dot{\varepsilon}_{zz}$ because $\psi = 21.1°$ is beginning to approach the corner of the Tresca hexagon (see again Fig. 4.99).

In summary, the numerical and analytical solutions for the total strain match very well throughout the test, which verifies:

- Linear elasticity under unequal biaxial compression
- Viscoplastic strain evolution for $\psi = 13.0°$ and a subsequent change to $\psi = 21.1°$
- Transient strain accumulation dominated by transient strain limit mechanism 0

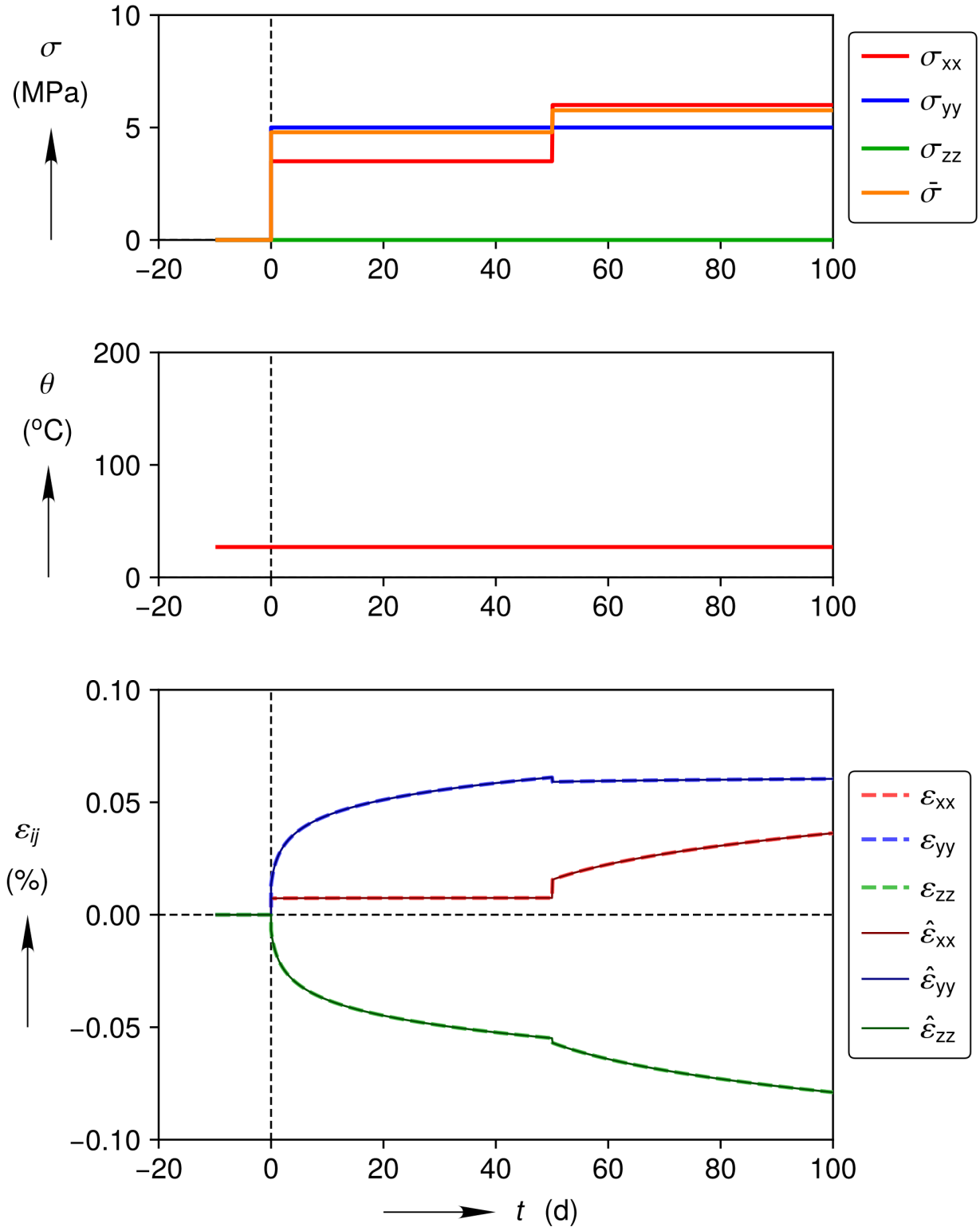

Fig. 4.104 Unequal Biaxial Compression Verification Test

- Steady-state strain accumulation dominated by mechanism 0.

4.21.4 User Guide

```
BEGIN PARAMETERS FOR MODEL MD_VISCOPLASTIC
  # Elastic constants
  YOUNGS MODULUS  = <real>
  POISSONS RATIO  = <real>
  SHEAR MODULUS   = <real>
  BULK MODULUS    = <real>
  LAMBDA          = <real>
  TWO MU          = <real>
  # Steady-state creep parameters
  A0              = <real> (0.0)
  A1              = <real> (0.0)
  A2              = <real> (0.0)
  Q0oR            = <real> (0.0)
  Q1oR            = <real> (0.0)
  Q2oR            = <real> (0.0)
  n0              = <real> (0.0)
  n1              = <real> (0.0)
  n2              = <real> (0.0)
  sigma_g         = <real>
  B0              = <real> (0.0)
  B1              = <real> (0.0)
  B2              = <real> (0.0)
  q               = <real> (0.0)
  # Transient creep parameters
  K0              = <real> (0.0)
  K1              = <real> (0.0)
  c0              = <real> (0.0)
  c1              = <real> (0.0)
  m0              = <real> (0.0)
  m1              = <real> (0.0)
  alpha_h         = <real> (0.0)
  alpha_r         = <real> (0.0)
  beta_h          = <real> (0.0)
  beta_r          = <real> (0.0)
  # Other parameters
  alpha           = <real> (0.0)
  a               = <real> (1000.0)
  # Numerical implementation parameters
  _chi            = <real> (2.0)
  _sigma_min      = <real> (1e-10 * SHEAR_MODULUS)
  _sqrt_omega_max = <real> (1e-11)
```

(continues on next page)

(continued from previous page)

```
  _xi               = <real> (1e-4)
  _gamma            = <real> (0.1)
  _k_max            = <real> (100)
  _j_max            = <real> (10)
END [PARAMETERS FOR MODEL MD_VISCOPLASTIC]
```

Output variables available for this model are listed in Table 4.32.

Table 4.32 State Variables for MD_VISCOPLASTIC Model

Name	Description
EQ_TR_STRAIN	equivalent transient viscoplastic strain, $\bar{\varepsilon}^{\text{tr}}$
EQ_VP_STRAIN	equivalent viscoplastic strain, $\bar{\varepsilon}^{\text{vp}}$
EQ_STRESS	equivalent stress, $\bar{\sigma}$
VP_RATE_SCALE_FACTOR	viscoplastic rate scale factor, s

4.22 Hyperfoam Model

4.22.1 Theory

The hyperfoam model is a hyperelastic model that can be used for modeling elastomeric foams. It is based on a strain energy with a form given by Storakers [95] which is similar to a form presented by Ogden [79]. The strain energy depends on the principal stretch ratios of the material and is given by

$$W(\lambda_k) = \sum_{i=1}^{N} \frac{2\mu_i}{\alpha_i^2}\left[\lambda_1^{\alpha_i} + \lambda_2^{\alpha_i} + \lambda_3^{\alpha_i} - 3 + \frac{1}{\beta_i}\left(J^{-\alpha_i\beta_i} - 1\right)\right] \tag{4.96}$$

where μ_i and α_i are input parameters and J is the determinant of the deformation gradient. The value of β_i is calculated from the parameters ν_i via

$$\beta_i = \frac{\nu_i}{1 - 2\nu_i}.$$

The ν_i can be thought of as Poisson's ratios, however in the context of the summation in (4.96) it is best to consider them as fitting parameters.

The strain energy (4.96) is a sum of N contributions. The principal Kirchoff stresses for the hyperfoam model, τ_k, can be calculated as

$$\tau_k = \lambda_k \frac{\partial W}{\partial \lambda_k}$$

which can be used to calculate the components of the Kirchoff stress, τ_{ij}, through

$$\tau_{ij} = \sum_{k=1}^{3} \tau_k \hat{e}_i^k \hat{e}_j^k.$$

where $\hat{e}_i^k$ are the components of the k^{th} eigenvector of the left stretch tensor in the global Cartesian coordinate system. The components of the Cauchy stress are then

$$\sigma_{ij} = \frac{1}{J}\tau_{ij}. \tag{4.97}$$

Finally, it should be noted that the Hyperfoam model is also capable of reproducing the Blatz-Ko model [10, 11]. If only one term is chosen, $N = 1$, and $\mu_1 = \mu$, $\alpha_1 = -2$, and $\nu_1 = 0.25$ we get the Blatz-Ko strain energy density

$$W = \frac{\mu}{2}\left(\frac{I_2}{I_3} + 2\sqrt{I_3} - 5\right) \quad ,$$

where I_2 and I_3 are the second and third invariants of the right Cauchy-Green tensor.

4.22.2 Implementation

The hyperfoam model is evaluated using the left stretch tensor, V_{ij}. Given the left stretch, the eigenvalues, λ_k, and eigenvectors, $\hat{e}_i^k$, of the stretch are calculated

$$V_{ij}\hat{e}_j^k = \lambda_k \hat{e}_i^k \quad ; \quad V_{ij} = \sum_{k=1}^{3} \lambda_k \hat{e}_i^k \hat{e}_j^k.$$

Next, the determinant of the deformation gradient is calculated

$$J = \lambda_1 \lambda_2 \lambda_3.$$

Then the contribution of each term in the expansion is added to the Kirchoff stress

$$\tau_{ij}^n = \tau_{ij}^{n-1} + \lambda_1 \frac{\partial W^{(n)}}{\partial \lambda_1} \hat{e}_i^1 \hat{e}_j^1 + \lambda_2 \frac{\partial W^{(n)}}{\partial \lambda_2} \hat{e}_i^2 \hat{e}_j^2 + \lambda_3 \frac{\partial W^{(n)}}{\partial \lambda_3} \hat{e}_i^3 \hat{e}_j^3$$

where $\tau_{ij}^0 = 0$ and

$$\lambda_k \frac{\partial W^{(n)}}{\partial \lambda_k} = \frac{2\mu_n}{\alpha_n}\left(\lambda_k^{\alpha_n} - J^{-\alpha_n \beta_n}\right). \tag{4.98}$$

After summing the terms $n = 1, ..., N$ the Kirchoff stress is converted to the Cauchy stress using (4.97). If necessary the Cauchy stress is transformed back into an unrotated configuration to be returned to the host code.

4.22.3 Verification

The hyperfoam model is verified for four loading paths: uniaxial strain, biaxial strain, pure shear, and simple shear. The material parameters used for the verification tests are shown in Table 4.33. For these problems $N = 3$.

Table 4.33 The material properties for the hyperfoam model tested in uniaxial strain.

EQPS	equivalent plastic strain		
SVB	kinematic hardening variable, **B**		
SVB_XX	kinematic h		
μ_i	25.8 MPa	-21.9 MPa	0.0814 MPa
α_i	2.536	2.090	-8.807
ν_i	0.5630	0.5507	0.3662

4.22.3.1 Uniaxial Strain

Since the hyperfoam model is formulated in terms of principal stretches, a uniaxial strain problem is a very simple verification problem that can be run.

In uniaxial strain, the stretch ratio in the direction of straining is $\lambda = \exp(\varepsilon)$, where ε is the applied strain. In a direction orthogonal to the direction of straining the stretch ratios are equal to one. The determinant of the deformation gradient is $J = \lambda$.

Since the deformation is aligned with the global coordinate axes, the eigenvectors of the left stretch are also aligned with the global coordinate axes. Using the derivatives of the strain energy density given in (4.98), the non-zero stress components are

$$\sigma_{11} = \frac{1}{\lambda}\sum_{i=1}^{N}\frac{2\mu_i}{\alpha_i}\left(\lambda^{\alpha_i} - \lambda^{-\alpha_i\beta_i}\right)$$

$$\sigma_{22} = \sigma_{33} = \frac{1}{\lambda}\sum_{i=1}^{N}\frac{2\mu_i}{\alpha_i}\left(1 - \lambda^{-\alpha_i\beta_i}\right)$$

The results of the analysis in tension are shown in Fig. 4.105 to Fig. 4.107.

For the results in Fig. 4.105, a single element is strained to $\varepsilon = 0.6$ which, in uniaxial strain in tension, is very large for this model. At some point the stresses begin to increase rapidly. Since the axial stress and the lateral stresses are both very large, the pressure in uniaxial strain in tension is also very large. For this extreme loading the model in Adagio shows agreement with the analytical solution.

The model is also loaded in uniaxial compression. These results are shown in Fig. 4.106. The model again shows agreement with the analytical solution. The behavior in compression is very different than tension. The maximum stress is an order of magnitude less at a strain of $\varepsilon = -0.6$, where the axial stress is just over 9 MPa, compared to $\varepsilon = 0.6$ in tension where the axial and lateral stresses are nearly 450 MPa. The lateral stresses reach a plateau while the axial stress increases. The stresses in compression also have a different nonlinear form than the stresses in tension.

Finally, both the tension and compression responses are shown in Fig. 4.107. Here the continuity of the behavior at $\varepsilon = 0$ can be seen along with the very different responses in tension and compression.

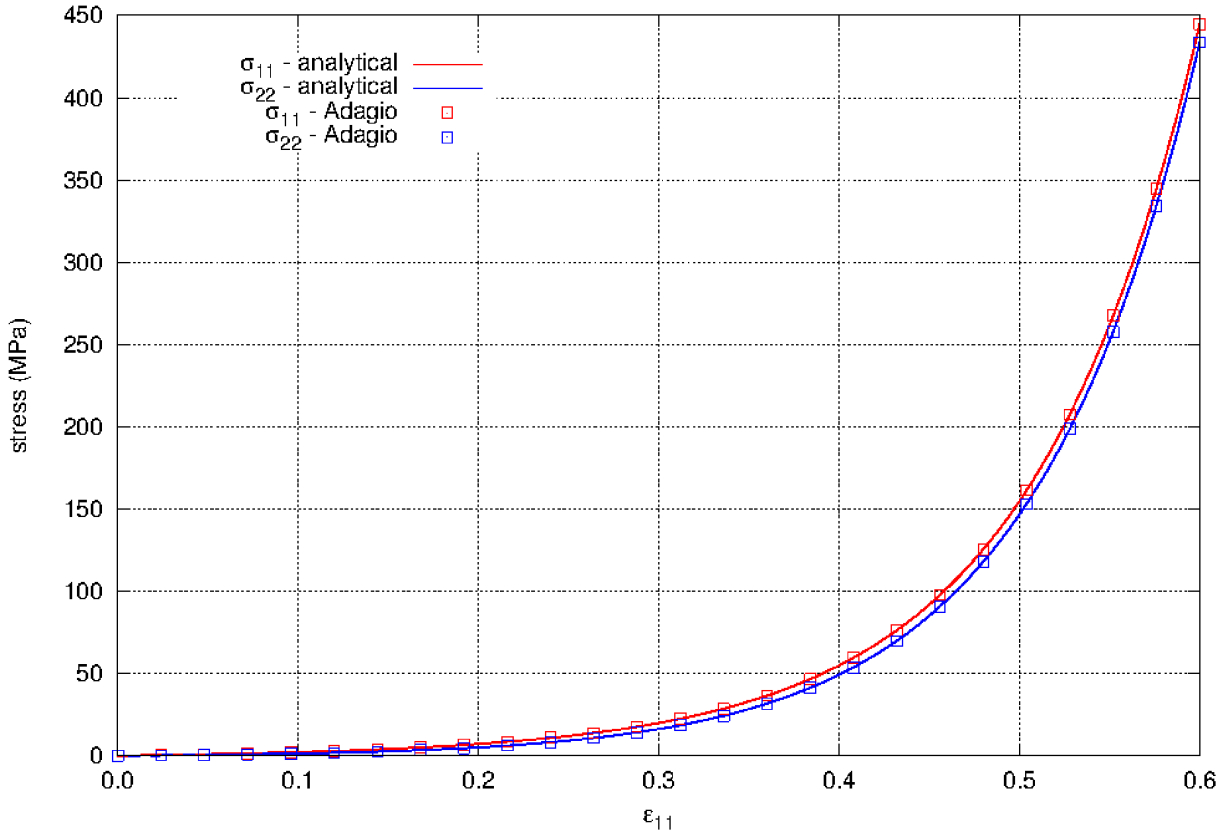

Fig. 4.105 The axial and lateral stresses for uniaxial strain in tension using the hyperfoam model. The results show agreement with the analytical results. The material properties for the model are given in Table 4.33

4.22.3.2 Biaxial Strain

Another simple verification problem for the hyperfoam model is biaxial strain.

In biaxial strain, the stretch ratios are prescribed in two orthogonal directions. For this $\lambda_1 = \exp(\varepsilon_1)$ and $\lambda_2 = \exp(\varepsilon_2)$, where ε_i are the applied strains in the x_1 and x_2 directions. In the third direction orthogonal to the first two, the stretch ratio is one. The determinant of the

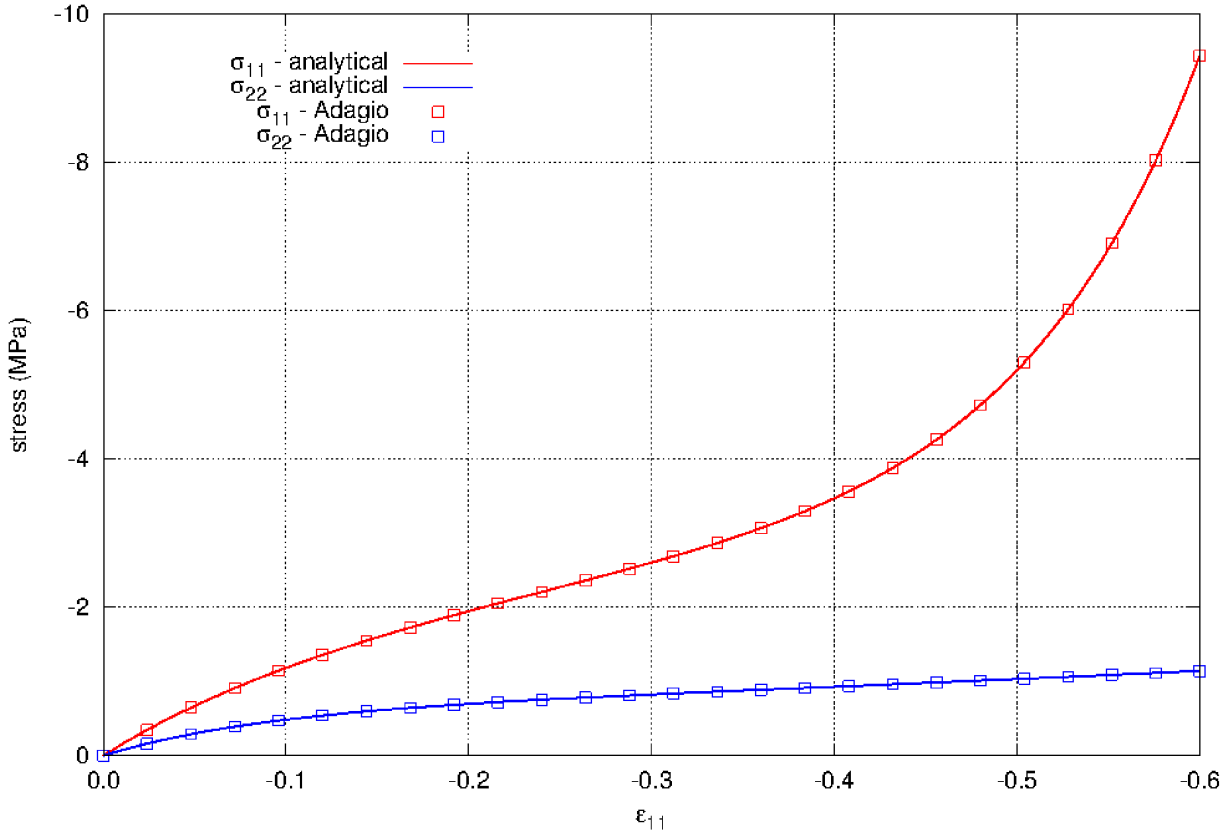

Fig. 4.106 The axial and lateral stresses for uniaxial strain in compression using the hyperfoam model. The results show agreement with the analytical results. The material properties for the model are given in Table 4.33.

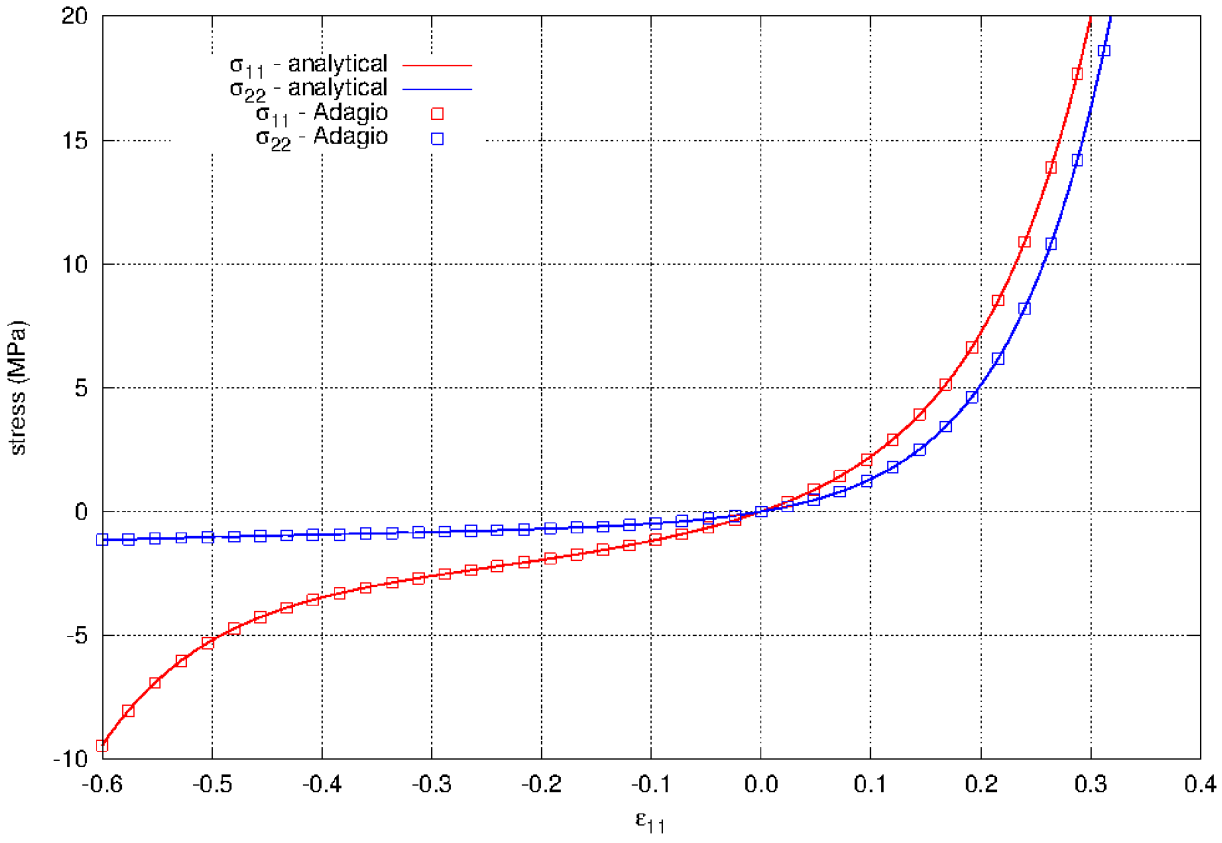

Fig. 4.107 The axial and lateral stresses for uniaxial strain in both tension and compression using the hyperfoam model. The results show agreement with the analytical results and that the response of the material is very different in tension and compression. The material properties for the model are given in Table 4.33.

deformation gradient is $J = \lambda_1\lambda_2$.

$$\sigma_{11} = \frac{1}{\lambda_1\lambda_2}\sum_{i=1}^{N}\frac{2\mu_i}{\alpha_i}\left[\lambda_1^{\alpha_i} - (\lambda_1\lambda_2)^{-\alpha_i\beta_i}\right] \quad ; \quad \sigma_{22} = \frac{1}{\lambda_1\lambda_2}\sum_{i=1}^{N}\frac{2\mu_i}{\alpha_i}\left[\lambda_2^{\alpha_i} - (\lambda_1\lambda_2)^{-\alpha_i\beta_i}\right]$$

$$\sigma_{33} = \frac{1}{\lambda_1\lambda_2}\sum_{i=1}^{N}\frac{2\mu_i}{\alpha_i}\left[1 - (\lambda_1\lambda_2)^{-\alpha_i\beta_i}\right]$$

The results of the analysis in tension are shown in Fig. 4.108 to Fig. 4.110.

For the results in Fig. 4.108, a single element is strained with $\varepsilon_1 = 0.4$ and $\varepsilon_2 = 0.2$ which, in biaxial strain in tension, is very large for this model. At some point the normal stresses begin to increase rapidly. Since the normal stresses are very large, the hydrostatic pressure is also very large. For this extreme loading the model in Adagio shows agreement with the analytical solution.

The model is also loaded in biaxial compression. These results are shown in Fig. 4.109. The model again shows agreement with the analytical solution. The behavior in compression is very different than tension. The maximum stress is orders of magnitude less at a strain of $\varepsilon_1 = -0.4$ and $\varepsilon_2 = -0.3$, where the maximum normal stress is just over 4.5 MPa, compared to $\varepsilon_1 = 0.4$ and $\varepsilon_2 = 0.3$ in tension where the normal stresses from the model are nearly 1.3 GPa. The lateral stress σ_{zz} reaches a plateau while the other two stress increase with increased straining The stresses in compression also have a different nonlinear form than the stresses in tension.

Finally, both the tension and compression responses are shown in Fig. 4.110. Here the continuity of the behavior at $\varepsilon = 0$ can be seen along with the very different responses in tension and compression.

4.22.3.3 Pure Shear

The hyperfoam model is is also tested in pure shear in strain. Note that this is different from pure shear in stress.

In pure shear, the principal stretch ratios are $\lambda_1 = \lambda$, $\lambda_2 = 1$, and $\lambda_3 = \lambda^{-1}$. The determinant of the deformation gradient is $J = 1$, which means the Kirchhoff and Cauchy stress measures are the same.

The principal stresses are

$$\sigma_1 = \sum_{i=1}^{N}\frac{2\mu_i}{\alpha_i}\left(\lambda^{\alpha_i} - 1\right) \quad ; \quad \sigma_2 = 0 \quad ; \quad \sigma_3 = \sum_{i=1}^{N}\frac{2\mu_i}{\alpha_i}\left(\lambda^{-\alpha_i} - 1\right)$$

The principal axes of deformation are aligned at 45° to the coordinate axes. In the global

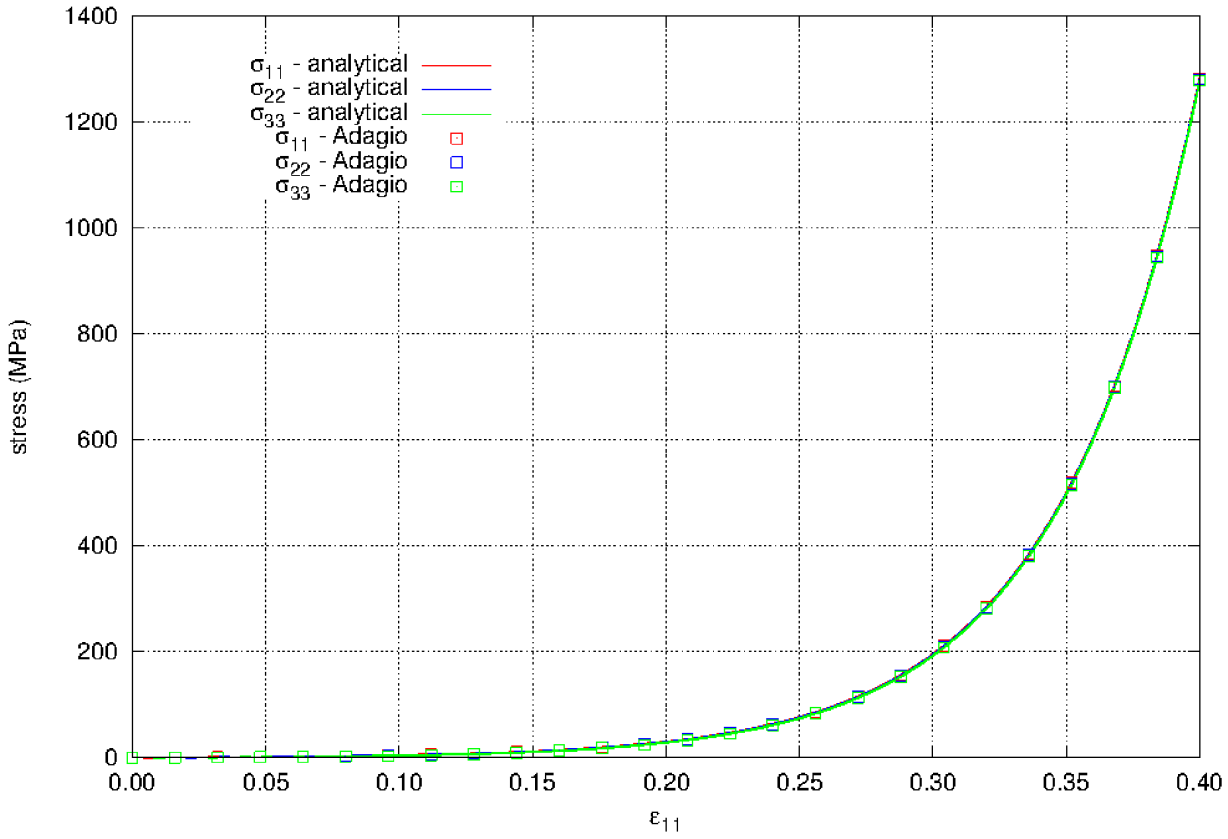

Fig. 4.108 The normal stresses for biaxial strain in tension using the hyperfoam model. The results show agreement with the analytical results. The material properties for the model are given in Table 4.33.

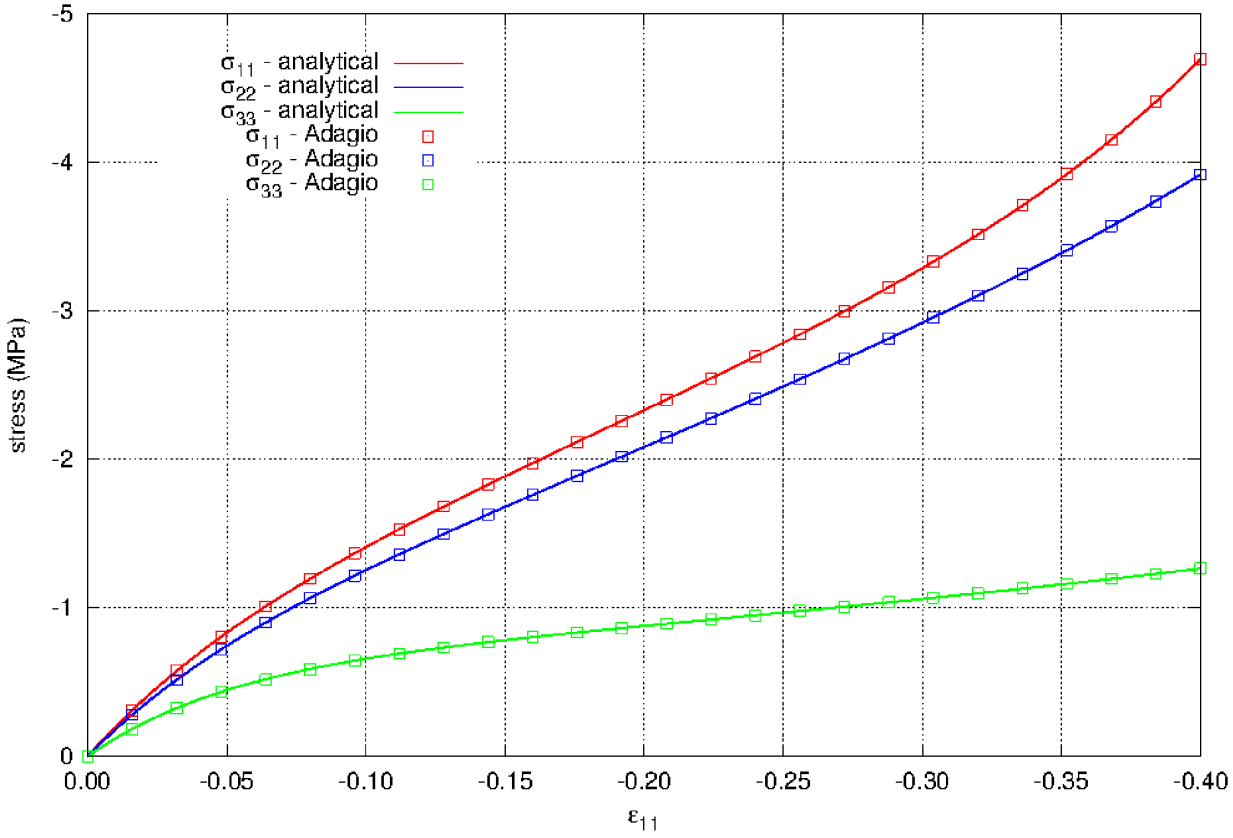

Fig. 4.109 The normal stresses for biaxial strain in compression using the hyperfoam model. The results show agreement with the analytical results. The material properties for the model are given in Table 4.33.

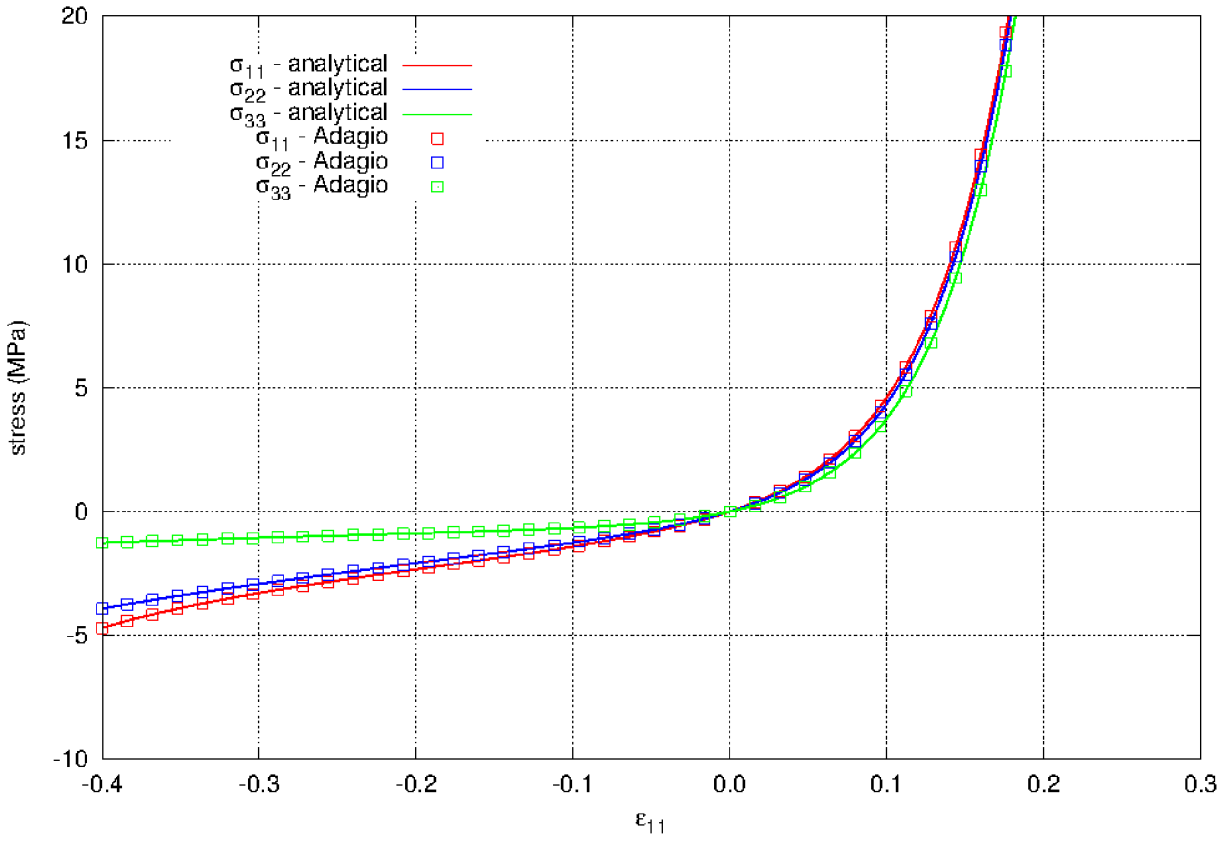

Fig. 4.110 The normal stresses for biaxial strain in both tension and compression using the hyper-foam model. The results show agreement with the analytical results and that the response of the material is very different in tension and compression. The material properties for the model are given in Table 4.33.

coordinate system the non-zero stress components are

$$\sigma_{11} = \sigma_{22} = \sum_{i=1}^{N} \frac{2\mu_i}{\alpha_i} \left(\lambda^{\alpha_i} + \lambda^{-\alpha_i} - 2\right)$$

$$\sigma_{12} = \sum_{i=1}^{N} \frac{2\mu_i}{\alpha_i} \left(\lambda^{\alpha_i} - \lambda^{-\alpha_i}\right)$$

The results of the analysis in pure shear are shown in Fig. 4.111. A single element is strained to a shear strain of $\varepsilon = 0.4$. The model in Adagio shows agreement with the analytical solution presented above. It is interesting to note that pure shear strain produces not only normal stresses with the hyperfoam model, but a non-zero pressure. The deviatoric/volumetric split so often used with our constitutive model does not occur with the hyperfoam model.

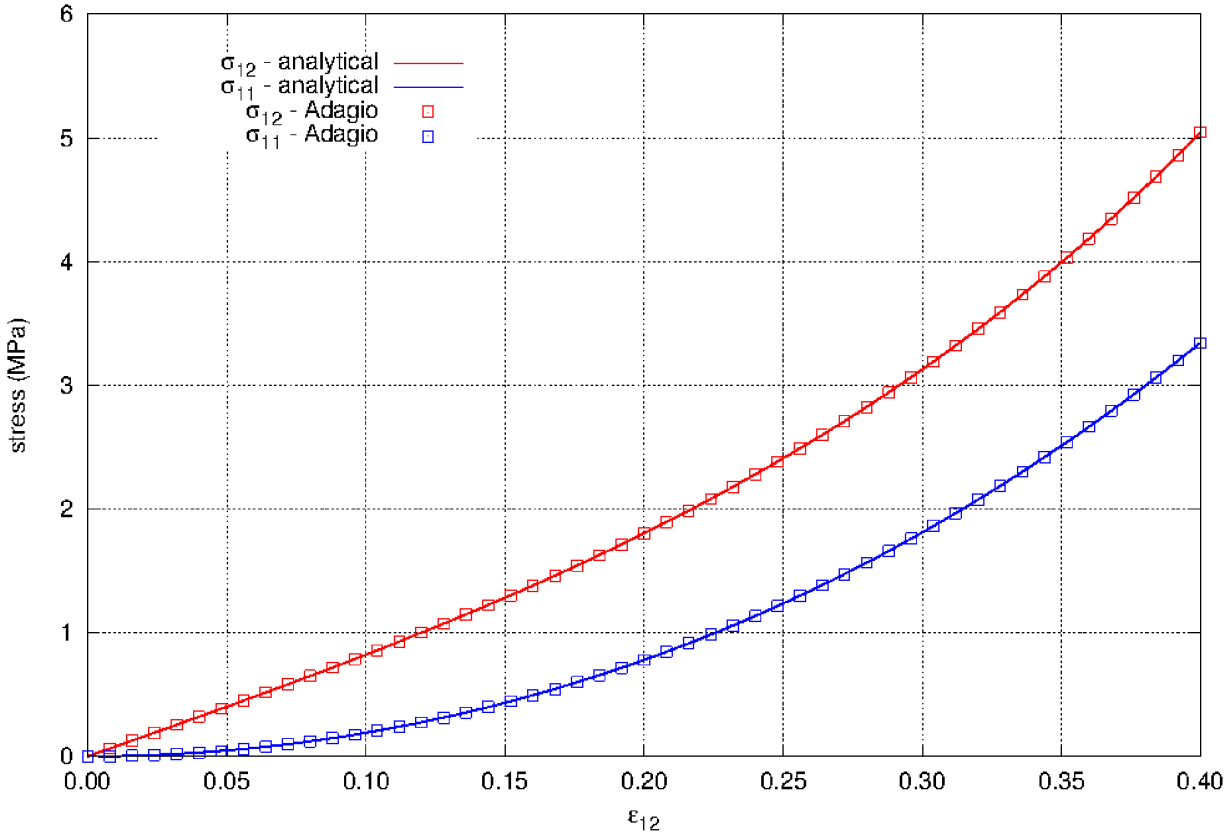

Fig. 4.111 The shear and normal stresses for the hyperfoam model in pure shear. The material properties for the model are given in Table 4.33.

4.22.3.4 Simple Shear

The hyperfoam model is is also tested in simple shear. Note that this is a different deformation path than pure shear. In simple shear the deformation gradient is

$$\left[F_{ij}\right] = \begin{bmatrix} 1 & \gamma & 0 \\ 0 & 1 & 0 \\ 0 & 0 & 1 \end{bmatrix}$$

The principal stretch ratios are $\lambda_1 = \lambda$, $\lambda_2 = 1$, and $\lambda_3 = \lambda^{-1}$. The determinant of the deformation gradient is $J = 1$, which means the Kirchhoff and Cauchy stress measures are the same. This gives the {em same} principal stresses as in pure shear when written in terms of the principal stretch ratio, λ. The principal stresses are

$$\sigma_1 = \sum_{i=1}^{N} \frac{2\mu_i}{\alpha_i} \left(\lambda^{\alpha_i} - 1\right) \quad ; \quad \sigma_2 = 0 \quad ; \quad \sigma_3 = \sum_{i=1}^{N} \frac{2\mu_i}{\alpha_i} \left(\lambda^{-\alpha_i} - 1\right)$$

The principal stretch ratio is

$$\lambda = \frac{1 + \sin\theta}{\cos\theta} \quad ; \quad \theta = \tan^{-1}\left(\frac{\gamma}{2}\right)$$

The principal axes of deformation in the current configuration, i.e. the eigenvectors of the left stretch, are given by

$$\hat{e}_i^1 = \cos\phi\, e_i^1 + \sin\phi\, e_i^2 \quad ; \quad \hat{e}_i^2 = e_i^3 \quad ; \quad \hat{e}_i^3 = -\sin\phi\, e_i^1 + \cos\phi\, e_i^2$$

where $\phi = \pi/4 - \theta/2$.

The results of the analysis in simple shear are shown in Fig. 4.112. A single element is strained to a shear parameter of $\gamma = 0.4$. The model in Adagio shows agreement with the analytical solution presented above. It is interesting to note that simple shear with the hyperfoam model produces different normal stresses than simple shear, i.e. the two non-zero normal stresses are not equal. The difference arises from the fact that the principal axes of deformation in pure shear are fixed, while in simple shear the principal axes rotate. There is still a non-zero pressure which again shows that the deviatoric/volumetric split does not occur with the hyperfoam model.

4.22.4 User Guide

```
BEGIN PARAMETERS FOR MODEL HYPERFOAM
  #
  # Elastic constants
  #
  YOUNGS MODULUS = <real>
  POISSONS RATIO = <real>
```

(continues on next page)

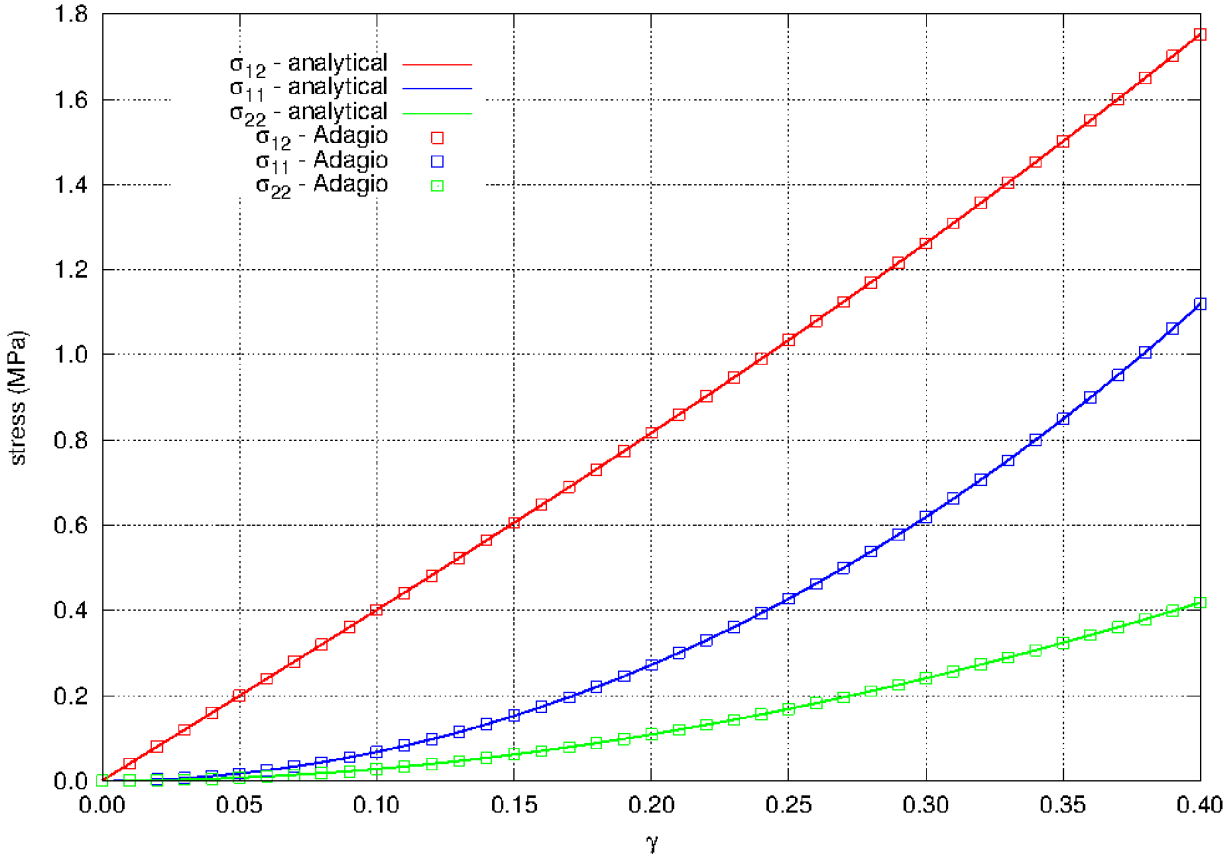

Fig. 4.112 The shear and normal stresses for the hyperfoam model in simple shear. The material properties for the model are given in Table 4.33.

(continued from previous page)

```
  SHEAR MODULUS   = <real>
  BULK MODULUS    = <real>
  LAMBDA          = <real>
  TWO MU          = <real>
  #
  # Strain energy density
  #
  N = <integer>
  SHEAR     = <real_list>
  ALPHA     = <real_list>
  POISSON   = <real_list>
END [PARAMETERS FOR HYPERFOAM]
```

- The number of terms in the expansion of the strain energy is defined with the `N` command line.
- The shear terms in the expansion of the strain energy, μ_i, are defined with the `SHEAR` command line.
- The alpha terms in the expansion of the strain energy, α_i, are defined with the `ALPHA` command line.
- The Poisson ratio terms in the expansion of the strain energy, ν_i, are defined with the `POISSON` command line.

There are no output variables available for this model.

4.23 Hyperelastic Damage Model

4.23.1 Theory

The hyperelastic damage model is an isotropic, strain rate and temperature independent continuum damage formulation. In this case, the specific form is that discussed by Holzapfel [43] and proposed primarily for particulate reinforced (filled) rubber-like materials exhibiting the so called Mullins effect. Specifically, this model utilizes a Kachanov-like effective stress concept to propose an *effective* Helmholtz free energy, W, of the form

$$W = (1 - \zeta)\, W_0 \left(C_{ij}\right),$$

in which $\zeta = [0, 1]$ is the isotropic damage variable and W_0 is the Helmholtz free energy of the *undamaged* material and C_{ij} is the right Cauchy-Green tensor ($C_{ij} = F_{ki}F_{kj}$ with F_{ij} the deformation gradient). The free energy expression of the neo-Hookean model (Section 4.5) is used to describe the undamaged strain energy and is given as,

$$W_0 \left(C_{ij}\right) = \frac{1}{2}K \left[\frac{1}{2}\left(J^2 - 1\right) - \ln J\right] + \frac{1}{2}\mu \left(\bar{C}_{kk} - 3\right),$$

with K and μ the bulk and shear moduli, J the determinant of the deformation gradient and $\bar{C}_{kk}$ the isochoric part of the deformation – $\bar{C}_{ij} = \bar{F}_{ki}\bar{F}_{kj}$ and $\bar{F}_{ij} = J^{-1/3}F_{ij}$. In the undamaged configuration, the second Piola-Kirchoff stress, S^0_{ij}, is the energetic conjugate of the right Cauchy-Green strain such that

$$S^0_{ij} = 2\frac{\partial W_0}{\partial C_{ij}},$$

leading to a *damaged* stress of the form,

$$S_{ij} = (1 - \zeta)\, S^0_{ij}.$$

To describe the softening process, two damage related variables are needed. The first is the previously mentioned smooth, continuous effective damage variable, ζ, while the second is the so-called discontinuous damage variable, α. In essence, this second variable may be considered to be the maximum strain energy in the undamaged material throughout the entire loading history. This statement may be expressed as,

$$\alpha = \max_{s\in[0,t]} W_0\,(s)\,, \tag{4.99}$$

in which s is a history variable representing any time in the loading history and the dependence on s in (4.99) is used to indicate the loading history and not an explicit dependence on time or strain rate. The two damage terms are related by assuming $\zeta = \zeta\,(\alpha)$. To ascertain this dependence, it is noted that $\zeta\,(0) = 0$ and $\zeta\,(\infty) = 1$ the former explicitly stating that the material is initially undamaged and the latter noting in the limit the material is completely damaged the strain energy will go to ∞. These observations lead to an expression of the form,

$$\zeta\,(\alpha) = \zeta_\infty\,[1 - \exp\,(-\alpha/\tau)]\,, \tag{4.100}$$

with τ being a constant referred to as the damage saturation parameter and ζ_∞ being the maximum value of the damage parameter that may be achieved.

The evolution of the damage process is governed by a so-called damage function, $f\,(C_{ij}, \alpha)$ (analogous to the yield function in plasticity), postulated as,

$$f\,(C_{ij}, \alpha) = \phi\,(C_{ij}) - \alpha,$$

where ϕ is the thermodynamic driving of the damage process. In this case, the thermodynamic conjugate of the damage variable ζ is the undamaged strain energy, W_0, such that $\phi\,(C_{ij}) = W_0\,(C_{ij})$. By enforcing the consistency condition during damage ($\dot{f} = 0$), it can be shown that,

$$\dot{\alpha} = \dot{\phi} = \frac{\partial W_0}{\partial C_{ij}}\dot{C}_{ij} = \frac{1}{2}S^0_{ij}\dot{C}_{ij}.$$

4.23.2 Implementation

For the hyperelastic damage model, the first step is to calculate the undamaged second Piola-Kirchoff stress, $S_{ij}^{0(n+1)}$ of the current $(n+1)^{th}$ time step. To this end, the deformation gradient, $F_{ij}^{(n+1)}$, is calculated based on the input stretch, $V_{ij}^{(n+1)}$, and rotation, $R_{ij}^{(n+1)}$, tensors via the polar decomposition. The second Piola-Kirchoff stress may then be determined as,

$$S_{ij}^{0(n+1)} = \left[\frac{1}{2}K\left(\left(J^{(n+1)}\right)^2 - 1\right)I_{il} + \mu\left(J^{(n+1)}\right)^{-2/3}\left(C_{il}^{(n+1)} - \frac{1}{3}C_{kk}^{(n+1)}I_{il}\right)\right]\left(C_{jl}^{(n+1)}\right)^{-1}.$$

To determine the damage state, the undamaged strain energy $W_0^{(n+1)}$, is first calculated as,

$$W_0^{(n+1)} = \frac{1}{2}K\left(\frac{1}{2}\left(\left(J^{(n+1)}\right)^2 - 1\right) - \ln J^{(n+1)}\right) + \frac{1}{2}\mu\left[\left(J^{(n+1)}\right)^{-2/3}C_{kk}^{(n+1)} - 3\right].$$

The current discrete damage variable, $\alpha^{(n+1)}$, may then be determined via,

$$\alpha^{(n+1)} = \max\left[\alpha^{(n)}, W_0^{(n+1)}\right],$$

so that the current continuous damage variable, $\zeta^{(n+1)}$, is,

$$\zeta^{(n+1)} = \zeta_\infty\left[1 - \exp\left(\alpha^{(n+1)}/\tau\right)\right].$$

Finally, these expressions lead to an unrotated Cauchy stress of the form,

$$T_{ij}^{(n+1)} = \frac{1}{J^{(n+1)}}\left(1 - \zeta^{(n+1)}\right)R_{ki}^{(n+1)}F_{km}^{(n+1)}S_{mn}^{0(n+1)}F_{rn}^{(n+1)}R_{rj}^{(n+1)}.$$

4.23.3 Verification

Given the hyperelastic formulation of the hyperelastic damage model, it is possible to find closed form solutions for simple loadings. Two such instances (uniaxial strain and simple shear) are considered here to evaluate and verify the response of this implementation. In this case, the results explored here are extensions of the neo-Hookean verification tests previously discussed in Section 4.5.3 and [91]. One set of material properties was used for all tests and they are given in Table 4.34. The damage parameters are taken from [43].

Table 4.34 The material properties for the hyperelastic damage model used for both the uniaxial and simple shear tests.

Name	Description		
K	0.5 MPa	μ	0.375 MPa
ζ_∞	0.8	τ	0.3 MPa

4.23.3.1 Uniaxial Strain

First, utilizing a displacement condition corresponding to uniaxial strain results in a deformation gradient of the form,

$$F_{ij} = \lambda\delta_{1i}\delta_{1j} + \delta_{2i}\delta_{2j} + \delta_{3i}\delta_{3j}. \tag{4.101}$$

As the undamaged material is neo-Hookean, it is noted that the under these loading conditions the stress field is found by evaluating relation (4.10) and may be written as

$$\begin{aligned}
\sigma^0_{11} &= \frac{1}{2}K\left(\lambda - \frac{1}{\lambda}\right) + \frac{2}{3}\mu\left(\lambda^2 - 1\right)\lambda^{-5/3}, \\
\sigma^0_{22} = \sigma^0_{33} &= \frac{1}{2}K\left(\lambda - \frac{1}{\lambda}\right) - \frac{1}{3}\mu\left(\lambda^2 - 1\right)\lambda^{-5/3}, \\
\sigma^0_{12} = \sigma^0_{23} = \sigma^0_{31} &= 0.
\end{aligned}$$

The damaged, effective stresses are then simply $\sigma_{ij} = (1 - \zeta)\,\sigma^0_{ij}$ and the problem reduces to the determination of ζ. In this case, given the deformation gradient in (4.101), $J = \lambda$ and

$$W_0 = \frac{1}{2}K\left[\frac{1}{2}\left(\lambda^2 - 1\right) - \ln\lambda\right] + \frac{1}{2}\mu\left[\lambda^{-2/3}\left(\lambda^2 + 2\right) - 3\right].$$

During loading, $\alpha = W_0$ while during unloading $\alpha = W_0\,(\lambda^{\max})$ and ζ can be determined from (4.100).

Both the corresponding analytical and numerical solutions are presented in Fig. 4.113 for a complete loading and unloading cycle. Note, the damage parameter, ζ, increases during loading but remains constant during unloading verifying the irreversibility of the proposed model.

4.23.3.2 Simple Shear

For the simple shear case, a deformation gradient of the form,

$$F_{ij} = \delta_{ij} + \gamma\delta_{1i}\delta_{2j},$$

is prescribed. Again, from the neo-Hookean model definitions the undamaged stresses may be determined via (4.10) and noting this is a volume preserving definition ($J = 1$) leading to expressions of the form,

$$\begin{aligned}
\sigma^0_{11} &= \frac{2}{3}\mu\gamma^2, \\
\sigma^0_{22} = \sigma_{33} &= -\frac{1}{3}\mu\gamma^2, \\
\sigma^0_{12} &= \mu\gamma, \\
\sigma^0_{23} = \sigma^0_{31} &= 0.
\end{aligned}$$

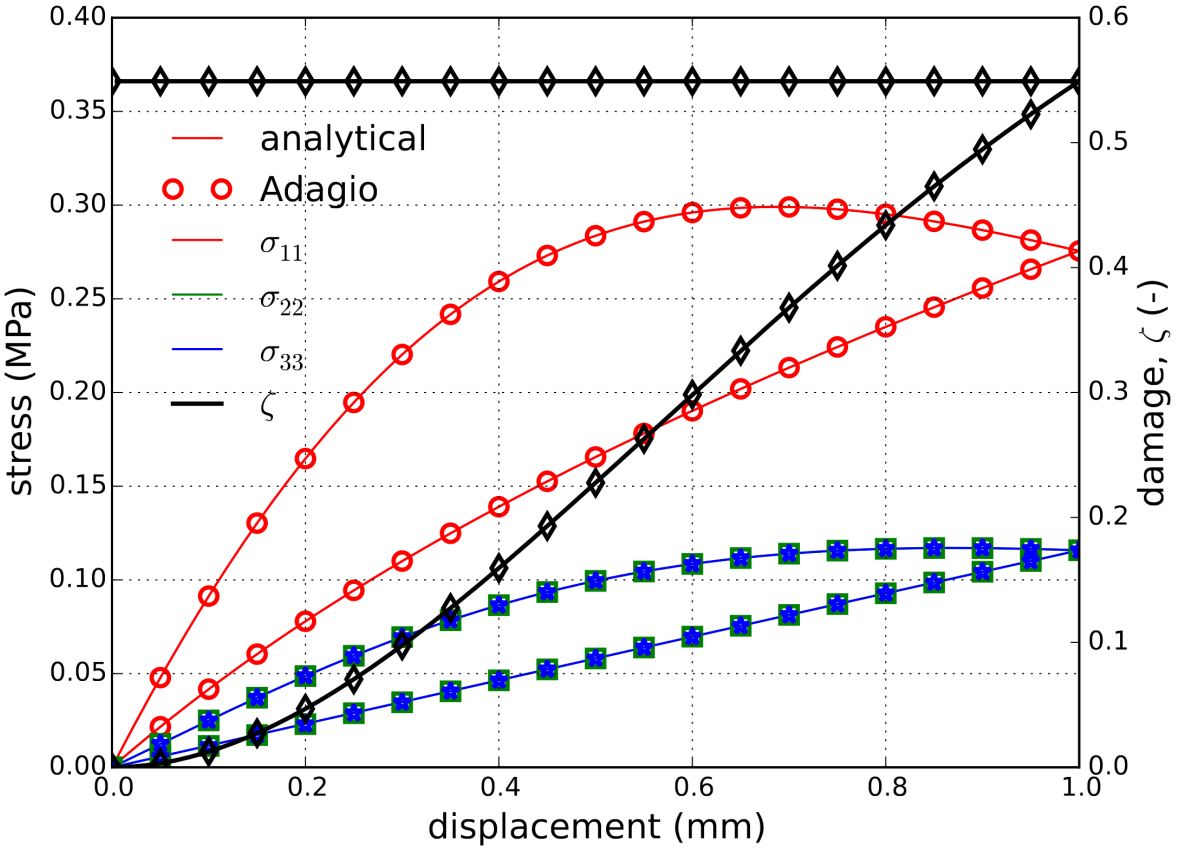

Fig. 4.113 Analytical and numerical results of the stress and damage state for the uniaxial stretch case.

In this case, the undamaged strain energy is simply,

$$W_0 = \frac{1}{2}\mu\gamma^2,$$

and ζ may be evaluated via (4.100). The effective stresses are then $\sigma_{ij} = (1 - \zeta)\,\sigma^0_{ij}$

Both the corresponding analytical and numerical solutions are presented in Figure. Fig. 4.114 for a complete loading and unloading cycle. Note, the damage parameter, ζ, increases during loading but remains constant during unloading given the irreversible form of the damage process.

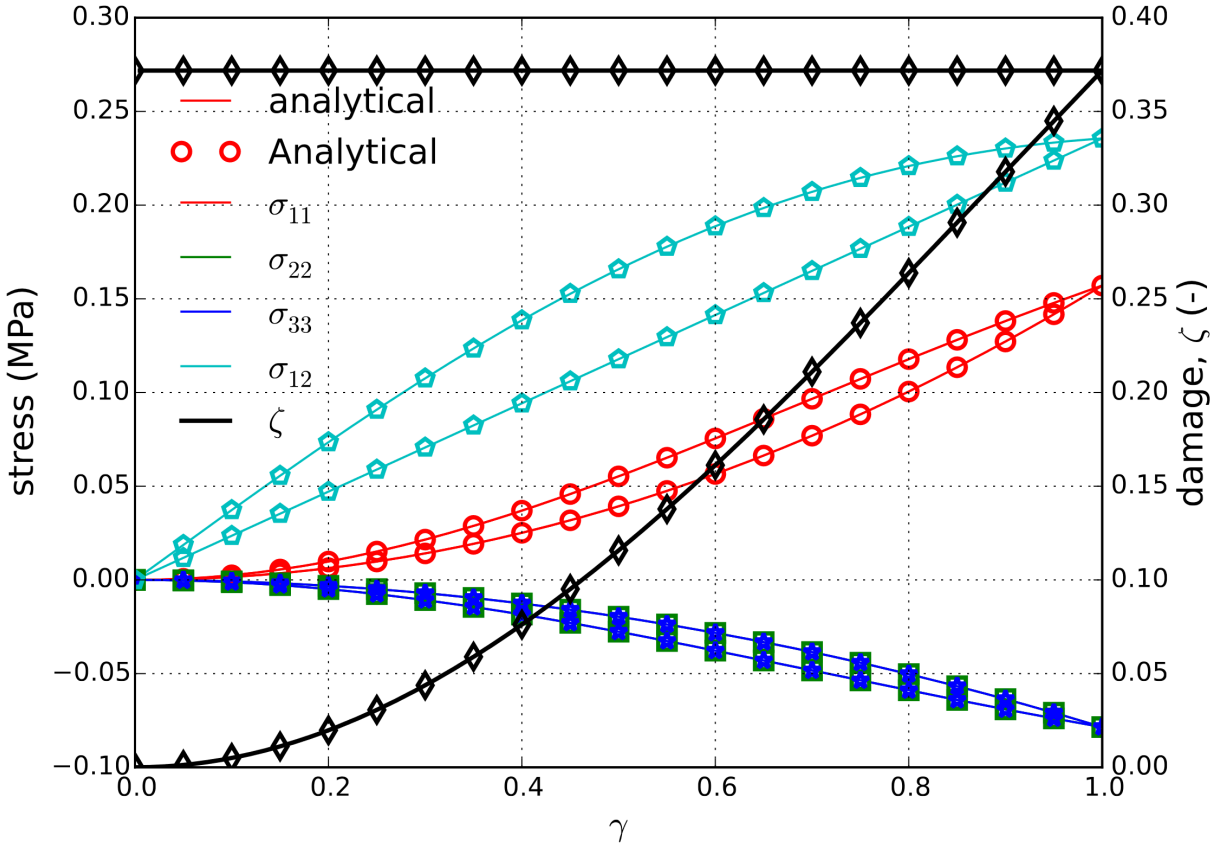

Fig. 4.114 Analytical and numerical results of the stress and damage state for the simple shear case.

4.23.4 User Guide

```
BEGIN PARAMETERS FOR MODEL HYPERELASTIC_DAMAGE
  #
  # Elastic constants
  #
```

(continues on next page)

(continued from previous page)

```
  YOUNGS MODULUS = <real>
  POISSONS RATIO = <real>
  SHEAR MODULUS  = <real>
  BULK MODULUS   = <real>
  LAMBDA         = <real>
  TWO MU         = <real>
  #
  DAMAGE MAX         = <real>
  DAMAGE SATURATION = <real>
END [PARAMETERS FOR MODEL HYPERELASTIC_DAMAGE]
```

Output variables available for this model are listed in Table 4.35. For information about the hyperelastic damage model, consult [43].

Table 4.35 State Variables for HYPERELASTIC DAMAGE Model

Name	Description
DAMAGE	continuous isotropic damage variable, ζ
ALPHA	discontinuous damage variable, α
PRESSURE	reference undamaged tensile pressure, $(1/3)\,(1-\zeta)\,S_{kk}$

4.24 Soil and Foam Model

4.24.1 Theory

The soil and crushable foam model is a plasticity model that can be used for modeling soil, crushable foam, or other highly compressible materials. Given the right input, the model is a Drucker-Prager model.

For the soil and crushable foam model, the yield surface is a surface of revolution about the hydrostat in principal stress space. A planar end cap is assumed for the yield surface so that the yield surface is closed. The yield stress σ_{yd} is specified as a polynomial in pressure p. The yield stress is given as:

$$\sigma_{yd} = a_0 + a_1 p + a_2 p^2 \,, \tag{4.102}$$

where the pressure p is positive in compression. The determination of the yield stress from (4.102) places severe restrictions on the admissible values of a_0, a_1, and a_2. There are three valid cases for the yield surface. In the first case, there is an elastic–perfectly plastic deviatoric response, and the yield surface is a cylinder oriented along the hydrostat in principal stress space. In this case, a_0 is positive, and a_1 and a_2 are zero. In the second case, the yield surface is conical. A conical yield surface is obtained by setting a_2 to zero and using appropriate values for a_0 and a_1. In the third case, the yield surface has a parabolic shape. For the parabolic yield surface, all

three coefficients in (4.102) are nonzero. The coefficients are checked to determine that a valid negative tensile-failure pressure can be derived based on the specified coefficients.

For the case of the cylindrical yield surface (e.g., $a_0 > 0$ and $a_1 = a_2 = 0$), there is no tensile-failure pressure. For the other two cases, the computed tensile-failure pressure may be too low. To handle the situations where there is no tensile-failure pressure or the tensile-failure pressure is too low, a pressure cutoff can be defined. If a pressure cutoff is defined, the tensile-failure pressure is the larger of the computed tensile-failure pressure and the defined cutoff pressure.

The plasticity theories for the volumetric and deviatoric parts of the material response are completely uncoupled. The volumetric response is computed first. The mean pressure p is assumed to be positive in compression, and a yield function ϕ_p is written for the volumetric response as:

$$\phi_p = p - f_p\left(\varepsilon_V\right) , \tag{4.103}$$

where $f_p\left(\varepsilon_V\right)$ defines the volumetric stress-strain curve for the pressure. The yield function ϕ_p determines the motion of the end cap along the hydrostat.

4.24.2 Implementation

The soil and crushable foam model is a rate-independent, hypoelastic model that splits and sequentially evaluates the volumetric and deviatoric response. To determine the inelastic flow, an elastic predictor-inelastic corrector approach is adopted for each of the aforementioned responses.

For the volumetric response, an updated logarithmic volume strain, ε_v^{n+1}, is computed by,

$$\varepsilon_v^{n+1} = \varepsilon_v^n - \Delta t d_{kk}.$$

Note, in this case, the volume strain is defined such that it is positive in compression. This strain value is then used to evaluate the volumetric yield function defined in (4.103) and determine the appropriate pressure, p, the material is subject to.

To evaluate the deviatoric response, a trial deviatoric stress, s_{ij}^{tr}, is defined as,

$$s_{ij}^{tr} = s_{ij}^n + 2\mu\hat{d}_{ij}\Delta t,$$

with $\hat{d}_{ij}$ being the deviatoric part of the unrotated rate of deformation. The deviatoric yield function, f, is then used to evaluate if any deviatoric plastic flow is occurring and is written as,

$$f\left(s_{ij}, p\right) = \phi\left(s_{ij}\right) - \sigma_{yd}\left(p\right),$$

where σ_{yd} is the yield stress given in (4.102) and $\phi\left(s_{ij}\right)$ the effective stress given as,

$$\phi\left(s_{ij}\right) = \sqrt{\frac{3}{2}s_{ij}s_{ij}}.$$

If an elastic response is evident ($f \leq 0$), then the final stress is simply,

$$T_{ij}^{n+1} = s_{ij}^{tr} - p\delta_{ij}.$$

Otherwise, if a plastic response is observed, a radial return approach like that discussed in Section 4.7.2 is utilized to find the equivalent plastic strain increment, $\Delta\bar{\varepsilon}^p$. Unlike that case, given the decoupling between the volumetric and deviatoric behaviors, the hardening component of the yield surface does not change leading to an expression of the form,

$$\Delta\bar{\varepsilon}^p = \frac{f}{3\mu},$$

and the final stress is,

$$T_{ij}^{n+1} = s_{ij}^{tr} - 3\mu\Delta\bar{\varepsilon}^p \frac{s_{ij}^{tr}}{\phi} - p\delta_{ij}.$$

4.24.3 Verification

The soil and foam model is verified for a triaxial compression load path. First the material is biaxially loaded in plane strain using load control, then the prescribed loads are released while the material is compressed in displacement control.

4.24.3.1 Triaxial Compression

The soil and foam model is tested in triaxial compression. For this problem, both lateral stresses, σ_{11} and σ_{33}, are prescribed along with the axial strain, ε_{22}. Furthermore, the lateral stresses are equal, $\sigma_{11} = \sigma_{33}$. For the elastic response, the axial stress is

$$\sigma_{22} = E\varepsilon_{22} + 2\nu\sigma_{11}$$

where E is the elastic modulus and ν is the Poisson's ratio. The lateral strains are

$$\varepsilon_{11} = -\nu\left(\varepsilon_{22} - \sigma_{11}/\lambda\right)$$

where λ is the Lame constant.

4.24.4 User Guide

```
BEGIN PARAMETERS FOR MODEL SOIL_FOAM
  #
  # Elastic constants
  #
```

(continues on next page)

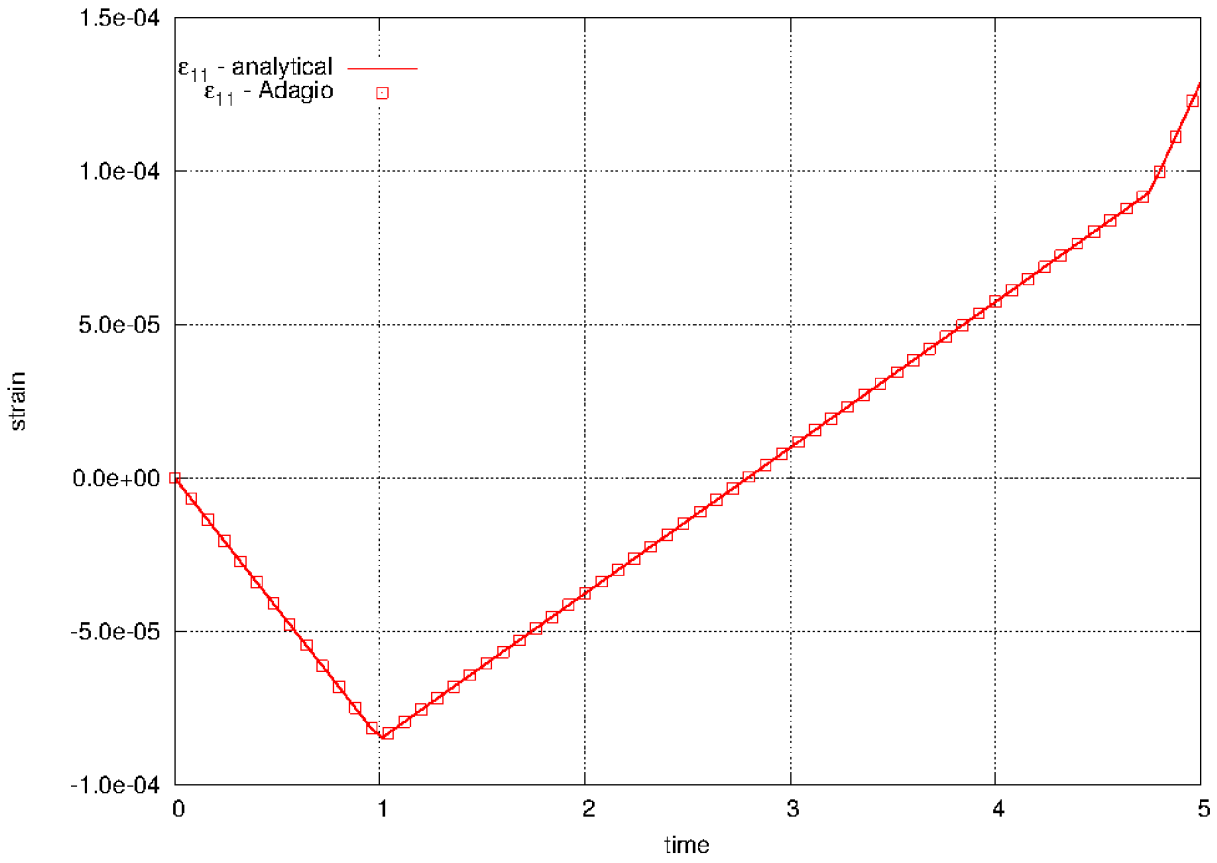

Fig. 4.115 Lateral strain, ε_{11} and ε_{33}, over the course of the prescribed triaxial loading path.

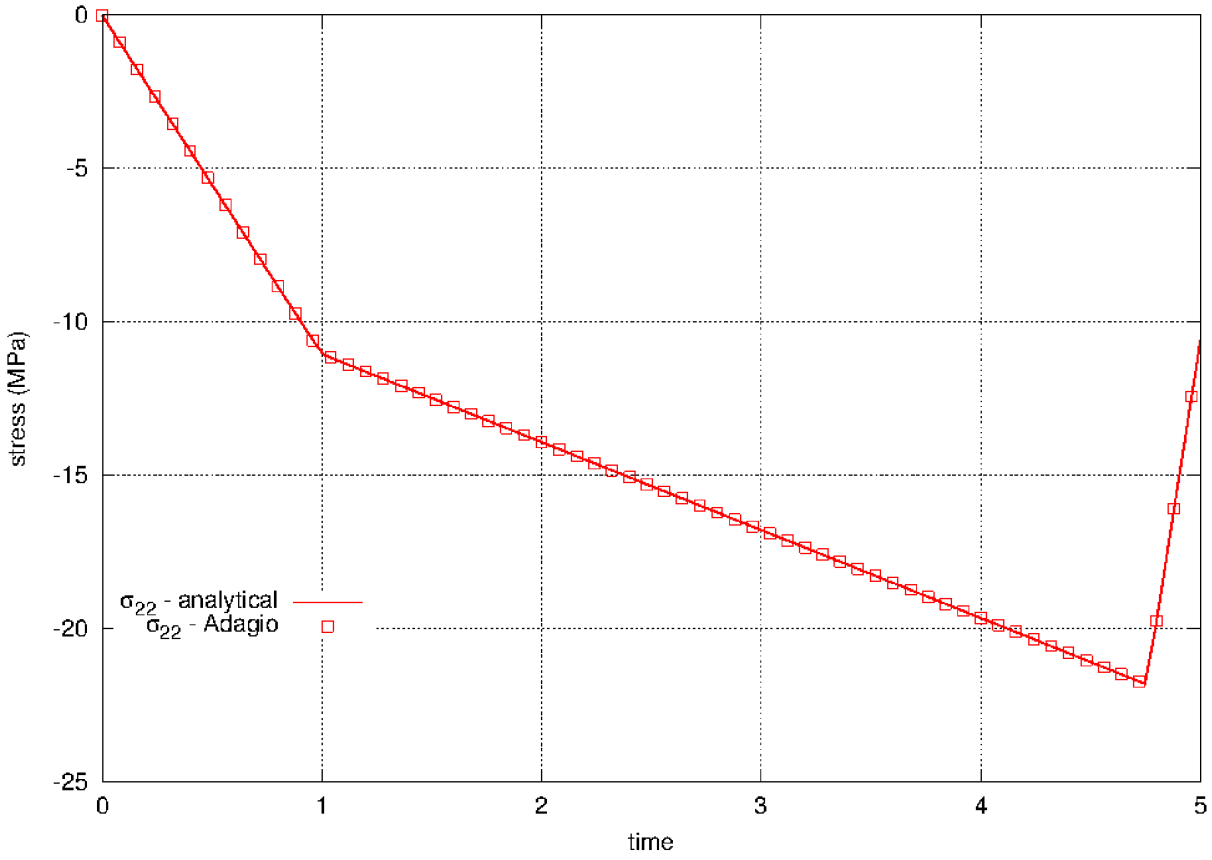

Fig. 4.116 Axial stress, σ_{22}, over the course of the prescribed triaxial loading path.

(continued from previous page)

```
  YOUNGS MODULUS = <real>
  POISSONS RATIO = <real>
  SHEAR MODULUS  = <real>
  BULK MODULUS   = <real>
  LAMBDA         = <real>
  TWO MU         = <real>
  #
  # Yield surface parameters
  #
  A0 = <real>
  A1 = <real>
  A2 = <real>
  PRESSURE CUTOFF   = <real>
  PRESSURE FUNCTION = <string>
END [PARAMETERS FOR MODEL SOIL_FOAM]
```

In the above command blocks:

- The constant coefficient in the equation for the yield surface ((4.102)) is defined with the `A0` command line.
- The coefficient for the linear term in the equation for the yield surface ((4.102)) is defined with the `A1` command line.
- The coefficient for the quadratic term in the equation for the yield surface ((4.102)) is defined with the `A2` command line.
- The user-defined maximum tensile-failure pressure is defined with the `PRESSURE CUTOFF` command line.
- The pressure as a function of volumetric strain is defined with the function named on the `PRESSURE FUNCTION` command line.

For information about the soil and crushable foam model, see the PRONTO3D document listed as Reference [106]. The soil and crushable foam model is the same as the soil and crushable foam model in PRONTO3D. The PRONTO3D model is based on a material model developed by Krieg [52]. The Krieg version of the soil and crushable foam model was later modified by Swenson and Taylor [104]. The soil and crushable foam model developed by Swenson and Taylor is the model in PRONTO3D and is also the shared model for Presto and Adagio.

Output variables available for this model are listed in Table 4.36.

Table 4.36 State Variables for SOIL FOAM Model

Name	Description
EVOL_MAX	maximum volumetric strain seen by the material point
EVOL_FRAC	volumetric strain for tensile fracture
EVOL	current volumetric strain
EQPS	equivalent plastic strain

4.25 Shape Memory Alloy Model

4.25.1 Theory

The shape memory alloy (SMA) model is used to describe the thermomechanical response of intermetallics (e.g. NiTi, NiTiCu, NiTiPd, NiTiPt) that can undergo a reversible, diffusionless, solid-to-solid martensitic transformation. Specifically, the materials have a high-symmetry (typically cubic) austenitic crystallographic structure at high temperature and/or low stress. At lower-temperatures and/or high stress the crystallographic structure is transformed to a lower symmetry (typically orthorhombic or monoclinic) martensitic phase. The change in structure and symmetry may be taken advantage of to produce large inelastic strains of $\approx$ 1-8%. Importantly, this class of materials differentiates itself from TRIP steels in that the transformation is *reversible* and a variety of thermomechanical loading paths have been conceived of to take advantage of this behavior. A notable application of these materials is as an actuator in smart, morphing structures.

Phenomenologically, the macroscopic behavior of SMAs is typically discussed in effective stress-temperature space via a *phase diagram* like in Fig. 4.117. The four lines denoted M_s, M_f, A_s, and A_f indicate the martensitic start, martensitic finish, austenitic start, and austenitic finish transformation surfaces. *Forward transformation* (from an austenitic to a martensitic state) is described by the martensitic start and finish surfaces. Specifically, the former refers to the thermomechanical conditions at which transformation will initiate while the latter corresponds to complete transformation. The difference between the two surfaces is associated with internal hardening effects due to microstructure (i.e. texture, back stresses). Transformation from martensite to austenite is referred to as *reverse* and is characterized by the austenitic start and finish surfaces. Detailed discussion of the crystallography and phenomenology may be found in [55], [82] (In the martensitic configuration, the crystallographic structure can either self-accommodate in a *twinned* configuration producing no macroscopic inelastic strain or an internal or external stress field may be used to *detwin* the microstructure thereby producing the desired inelastic strain. For simplicity, this distinction is bypassed in this brief text and the interested reader should consult the referenced works.).

Two responses characteristic of SMAs may also be represented via the phase diagram. These are the *actuation response* and the *pseudoelastic* (often referred to as *superelastic* in the literature) responses. The first (actuation) is indicated by path A in Fig. 4.117. In this case, a mechanical bias load is applied to the SMA and the material is then thermally cycled through forward and reverse transformation. The resulting transformation first produces and then removes the large

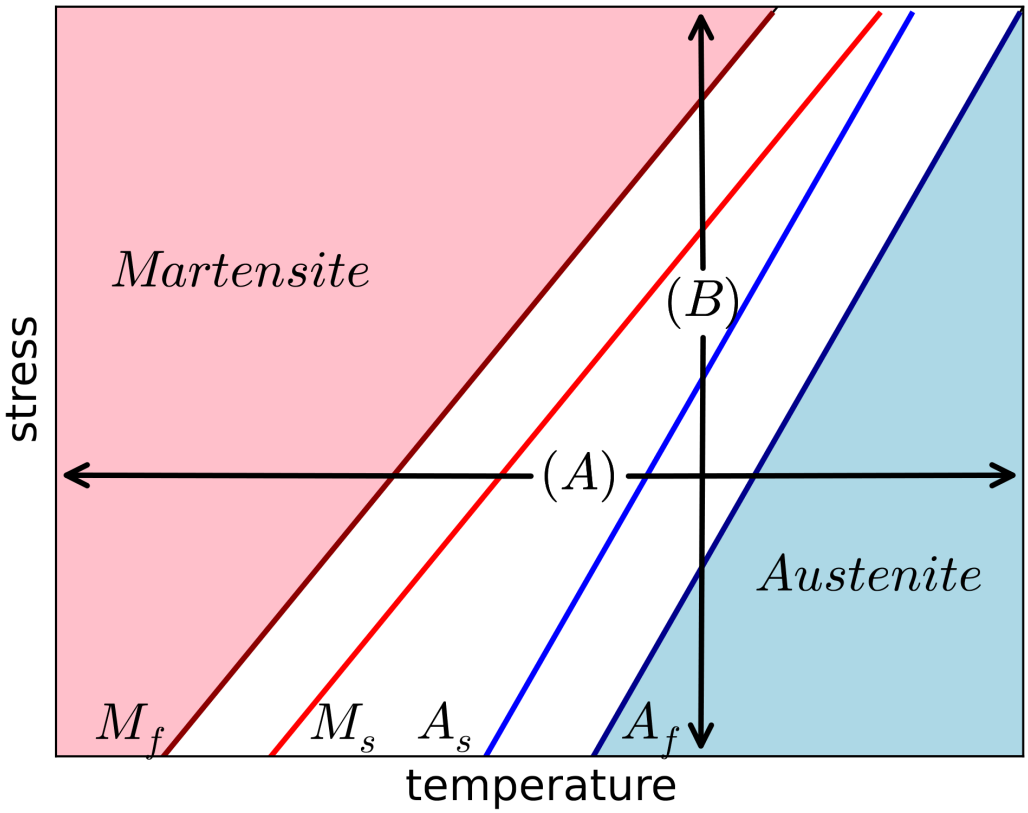

Fig. 4.117 Representative phase diagram of shape memory alloys highlighting characteristic loading paths ((A) and (B)), transformation surfaces, and phases.

transformation strains of SMAs and is commonly used for (surprisingly) actuation applications. At higher temperatures ($T > A_f$), mechanical loading may be used induce forward and, upon unloading, reverse transformation as indicated in path B of Fig. 4.117. Through such a cycle, a distinctive flag shape in the stress strain response is observed through which large amounts of energy may be dissipated while producing no permanent deformations. As such, this loading path is often considered for vibration isolation or damping applications.

In LAME, the response of SMAs is described by the phenomenological model of Lagoudas and coworkers [54]. This model was motivated by actuator applications and it describes the inelastic deformation associated with martensitic transformation through two internal state variables – the scalar martensitic volume fraction, ξ, and tensorial transformation strain tensor, $\varepsilon_{ij}^{\text{tr}}$. Before proceeding it should be noted that the *structural* response of SMA specimens and components exhibit a rate dependency associated with the strong thermomechanical coupling of SMAs. Specifically, the transformation process gives off/absorbs large amounts of energy via the *latent heat of transformation*. The rate dependence observed is a result of the characteristic time scale associated with thermal transport of this heat. In pure mechanical analyses (like Sierra/SM), this means quasistatics loadings are typically considered (a strain rate of $\approx 1x10^{-4}$ and/or heating/cooling rate of $\approx 2°C/\text{min}$). Formulations accounting for the full coupling have been developed but require more complex implementations.

To begin, the model assumes an additive decomposition of the total, elastic, thermal, and transformation deformation (strain) rates respectively denoted by D_{ij}, D_{ij}^{e}, D_{ij}^{th} and D_{ij}^{tr} producing a total deformation rate of the form,

$$D_{ij} = D_{ij}^{\text{e}} + D_{ij}^{\text{th}} + D_{ij}^{\text{tr}}.$$

With respect to the thermoelastic deformations, it is noted that the different crystallographic phases have different thermoelastic constants. Previous studies have demonstrated that a rule of mixtures on the compliance and other material properties of the form,

$$\mathbb{S}_{ijkl} = \mathbb{S}_{ijkl}^{A} + \xi\left(\mathbb{S}_{ijkl}^{M} - \mathbb{S}_{ijkl}^{A}\right) = \mathbb{S}_{ijkl}^{A} + \xi\Delta\mathbb{S}_{ijkl},$$
$$\alpha_{ij} = \alpha^{A}\delta_{ij} + \xi\left(\alpha^{M}\delta_{ij} - \alpha^{A}\delta_{ij}\right) = \alpha^{A}\delta_{ij} + \xi\Delta\alpha\delta_{ij},$$

in which $\mathbb{S}_{ijkl}$ and α_{ij} are the current effective compliance and coefficient of thermal expansion and the superscripts A and M denote thermoelastic properties in the austenitic and martensitic configuration. The symbol Δ is used to indicate the difference in a property between the martensitic and austenitic phases while δ_{ij} is the Kronecker delta. Isotropy is assumed for all these properties and the compliances are determined via the definition of elastic moduli and Poisson's ratio of the two phases – E^A, E^M, ν^M, and ν^M. The two Poisson ratios are often the same and take typical values for metals ($\nu^A \approx \nu^M \approx 0.3$) while the elastic moduli can differ by a factor of more than two. For instance the austenitic modulus of NiTi is typically given as ≈ 70 GPa while the martensitic one is ≈ 30 GPa (Given the lower symmetry of the martensitic phase the determination of an isotropic elastic modulus can vary with characterization methodology. In this case, the apparent elastic modulus measured from macroscopic thermoelastic tests should be used.). Importantly, this difference means that the thermoelastic properties and corresponding

deformations vary with transformation. As such, the corresponding rates of deformation are given as,

$$D_{ij}^{\mathrm{e}} = \dot{\xi}\Delta\mathbb{S}_{ijkl}\sigma_{kl} + \mathbb{S}_{ijkl}\,\overset{\circ}{\sigma}_{kl},$$
$$D_{ij}^{\mathrm{th}} = \dot{\xi}\Delta\alpha\delta_{ij}\left(\theta - \theta_0\right) + \alpha\delta_{ij}\dot{\theta},$$

where θ and θ_0 are the current and reference temperature and σ_{ij} is the symmetric Cauchy stress. Note, in using the SMA model a temperature field *must* be defined. The stress rate may then be shown to be,

$$\overset{\circ}{\sigma}_{ij} = \mathbb{C}_{ijkl}\left(D_{kl} - \alpha\delta_{kl}\dot{\theta} - \dot{\xi}\left(\Delta\mathbb{S}_{klmn}\sigma_{mn} + \Delta\alpha\delta_{kl}\left(\theta - \theta_0\right)\right) - D_{kl}^{\mathrm{tr}}\right),$$

with $\mathbb{C}_{ijkl}$ being the current stiffness tensor defined as $\mathbb{C}_{ijkl} = \mathbb{S}_{ijkl}^{-1}$.

To describe the transformation strain evolution, it is assumed that these deformations evolve with (and only with) the martensitic volume fraction, ξ. The corresponding flow rule is given as,

$$D_{ij}^{\mathrm{tr}} = \dot{\xi}\Lambda_{ij},$$

and Λ_{ij} is the transformation direction tensor assumed to be of the form,

$$\Lambda_{ij} = \begin{cases} H^{\mathrm{cur}}\left(\bar{\sigma}_{vM}\right)\frac{3}{2}\frac{s_{ij}}{\bar{\sigma}_{vM}} & \dot{\xi} \geq 0 \\ \frac{\varepsilon_{ij}^{\mathrm{tr}-rev}}{\xi^{rev}} & \dot{\xi} < 0 \end{cases}. \tag{4.104}$$

In (4.104), H^{cur} is the transformation strain magnitude that is dependent on the von Mises effective stress, $\bar{\sigma}_{vM}$, and s_{ij} is the deviatoric stress. With forward transformation defined in this way, it is assumed that deformation is shear-based and follows a J_2 like flow direction. For reverse transformation ($\dot{\xi} < 0$), the postulated form is utilized to ensure complete recovery of transformation strains with martensitic volume fraction. In other words, all transformation strain components are zero-valued at $\xi = 0$. Without enforcing this condition in this way, non-proportional loading paths could be constructed producing a non-zero transformation strain when the material is austenitic. The transformation strain at load reversal, $\varepsilon_{ij}^{\mathrm{tr}-rev}$, and martensitic volume fraction at load reversal, ξ^{rev}, are then tracked (via the implementation) and used for this purpose.

The transformation strain magnitude, H^{cur}, is a function of the von Mises effective stress ($\bar{\sigma}_{vM}$) and is introduced to incorporate detwinning effects without introducing an additional internal state variable complicating the model. Specifically, at low stress values, this function returns a minimum value. If the microstructure is self-accommodated this value will be zero. A decaying exponential is used such that as the stress increases the value of the strain magnitude becomes that of the maximum value incorporating both crystallographic and texture effects. The given functional form is,

$$H^{\mathrm{cur}} = \begin{cases} H_{\min} & \bar{\sigma}_{vM} \leq \sigma_{\mathrm{crit}} \\ H_{\min} + \left(H_{\mathrm{sat}} - H_{\min}\right)\left(1 - \exp\left(-k\left(\bar{\sigma}_{vM} - \sigma_{\mathrm{crit}}\right)\right)\right) & \bar{\sigma}_{vM} > \sigma_{\mathrm{crit}} \end{cases},$$

where $H_{\min}$, H_{sat}, k, and σ_{crit} are model parameters giving the minimum transformation strain magnitude, maximum transformation strain magnitude, exponential fitting parameter governing the transition zone, and critical stress values (in some ways analogous to the detwinning stress).

The evolution of martensitic transformation process is governed by a transformation function serving an analogous role to the yield function in plasticity. This function is given by,

$$f\left(\sigma_{ij},\theta,\xi\right)=\pm\phi\left(\sigma_{ij},\theta,\xi\right)-\bar{\sigma}\left(\sigma_{ij}\right),$$

with ϕ begin the thermodynamic driving force for transformation and $\bar{\sigma}$ the critical value. The $\pm$ is used to denote either forward (+) or reverse (−) transformation. This transformation function and the associated forms are derived from continuum thermodynamic considerations and the details of that process are neglected here for brevity but may be found in [54]. The functional forms of these variables are given as,

$$\begin{aligned}\phi\left(\sigma_{ij},\theta,\xi\right)&=\sigma_{ij}\Lambda_{ij}+\frac{1}{2}\sigma_{ij}\Delta\mathbb{S}_{ijkl}\sigma_{kl}+\sigma_{ij}\Delta\alpha\delta_{ij}\left(\theta-\theta_0\right)+\rho\Delta s_0\theta-\rho\Delta u_0-f^t\left(\xi\right),\\ \bar{\sigma}\left(\sigma_{ij}\right)&=\sigma_0+D\sigma_{ij}\Lambda_{ij},\end{aligned}$$

in which $\rho\Delta s_0$ and $\rho\Delta u_0$ are the differences in reference entropy and internal energy of the two phases, D is a calibration parameter intended to capture variations in dissipation with stress, and $f^t\left(\xi\right)$ is the hardening function. With respect to this latter term, empirical observations were used to arrive at a postulated form of,

$$f^t\left(\xi\right)=\begin{cases}\frac{1}{2}a_1\left(1+\xi^{n_1}-\left(1-\xi\right)^{n_2}\right)+a_3 & \dot{\xi}\geq 0\\ \frac{1}{2}a_2\left(1+\xi^{n_3}-\left(1-\xi\right)^{n_4}\right)-a_3 & \dot{\xi}<0\end{cases},$$

with $a_1,\ a_2$, and a_3 being fitting parameters and $n_1,\ n_2,\ n_3$, and n_4 are exponents fit to match the smooth transformation from elastic to inelastic deformations at the start of forward, end of forward, start of reverse, and end of reverse transformation respectively.

Before proceeding, one final note should be given in regards to calibration. Specifically, some of the model parameters just listed ($a_1,\ a_2,\ a_3,\ D,\ \sigma_0,\ \rho\Delta s_0$ and $\rho\Delta u_0$) are not easily identified or conceptualized in terms of common thermomechanical experiments. Some easily identifiable parameters ($M_s,\ M_f,\ A_s$, and A_f), however, are not evident in the theoretical formulation. Conditions associated with these terms and some physical constraints may be used to determine the model parameters in terms of these more accessible properties. These relations are,

$$\begin{aligned}\rho\Delta s_0&=\frac{-2\left(C^MC^A\right)\left[H^{\text{cur}}\left(\sigma\right)+\sigma\frac{\partial H^{\text{cur}}}{\partial\sigma}+\sigma\left(\frac{1}{E^M}-\frac{1}{E^A}\right)\right]}{C^M+C^A}\Big|_{\sigma=\sigma^*},\\ D&=\frac{\left(C^M-C^A\right)\left[H^{\text{cur}}\left(\sigma\right)+\sigma\frac{\partial H^{\text{cur}}}{\partial\sigma}+\sigma\left(\frac{1}{E^M}-\frac{1}{E^A}\right)\right]}{\left(C^M+C^A\right)\left[H^{\text{cur}}\left(\sigma\right)+\sigma\frac{\partial H^{\text{cur}}}{\partial\sigma}\right]}\Big|_{\sigma=\sigma^*},\\ a_1&=\rho\Delta s_0\left(M_f-M_s\right),\qquad a_2=\rho\Delta s_0\left(A_s-A_f\right),\\ a_3&=-\frac{a_1}{4}\left(1+\frac{1}{n_1+1}-\frac{1}{n_2+1}\right)+\frac{a_2}{4}\left(1+\frac{1}{n_3+1}-\frac{1}{n_4+1}\right),\\ \rho\Delta u_0&=\frac{\rho\Delta s_0}{2}\left(M_s+A_f\right),\qquad \sigma_0=\frac{\rho\Delta s_0}{2}\left(M_s-A_f\right)-a_3,\end{aligned}\tag{4.105}$$

in which σ^* is the scalar stress measure in which the calibration is performed at. For additional discussion on the characterization of SMAs and calibration of this model, the user is referred to [40], [41].

4.25.2 Implementation

Similar to the various plasticity models in LAMÉ, an elastic predictor-inelastic corrector approach is used to perform the stress updating routine. Unlike the other models, however, in the shape memory alloy routine a convex cutting plane (CCP) return mapping algorithm (RMA) is used in lieu of the closest point projection. This difference essentially simplifies the integration of flow rule and the corresponding problem at the cost of some algorithmic stability. Prior studies [85] have shown that this implementation is sufficient for convergence in most cases while providing a substantial savings in cost. The specific implementation used here is that of [54].

To compute an elastic trial state, a trial stress is determined assuming purely thermoelastic deformations such that,

$$T_{ij}^{tr} = \mathbb{C}_{ijkl}\left(\xi^n\right)\left(d_{kl}\Delta t - \alpha_{kl}\left(\xi^n\right)\Delta\theta\right), \qquad \Delta\theta = \theta^{n+1} - \theta^n.$$

In this case, it is assumed that the temperature fields are known at t_{n+1} and t_n (denoted θ^{n+1} and θ^n, respectively) and the thermoelastic properties are computed using the martensitic volume fraction at the previous time step ξ^n. At this stage, a perturbation stress ($T_{ij}^{per} = T_{ij}^n + \beta\left(T_{ij}^{tr} - T_{ij}^n\right)$ with $\beta << 1$) is computed and used to determine local variations of the thermodynamic driving force, ϕ. This is necessary to determine the direction of transformation (forward or reverse). Using the full trial stress to this end can produce spurious results in some thermally-driven cases. The trial yield function value is then computed as,

$$f^{tr} = f\left(T_{ij}^{tr}, \theta^{n+1}, \xi^n\right) = \pm\phi\left(T_{ij}^{tr}, \theta^{n+1}, \xi^n\right) - \bar{\sigma}\left(T_{ij}^{tr}\right).$$

If $f^{tr} < 0$, no nonlinear deformation occurs and the trial solution is accepted as the material state at $t = t_{n+1}$. When this condition is not satisfied, the CCP-RMA routine is used to correct the trial state and return it to the yield surface.

To perform the inelastic correction, the Newton-Raphson method is iteratively used to update the material state (T_{ij} and ξ) until convergence is achieved. Denoting the current and next iteration by (k) and $(k+1)$, respectively, produces updating expressions of the form,

$$\begin{aligned} T_{ij}^{(k+1)} &= T_{ij}^{(k)} + \Delta T_{ij}, \\ \xi^{(k+1)} &= \xi^{(k)} + \Delta\xi, \end{aligned}$$

with $\xi^{(0)}$ and $T_{ij}^{(0)}$ initialized to ξ^n and T_{ij}^{tr}, respectively. The key difference between the CCP and closest point projection (CPP) methods is associated with how the inelastic strain flow rules are integrated. In the former method, an explicit evaluation of the flow direction is utilized while the latter is associated with a fully implicit expression. For the CPP algorithms, this implicit expression means the flow rule must be solved in a nonlinear system of equations with the consistency equation. Relaxing this assumption via the CCP method, however, produces an explicitly evaluated flow rule of,

$$\varepsilon_{ij}^{t(k+1)} = \varepsilon_{ij}^{t(k)} + \Delta\xi\Lambda_{ij}^{(k)}.$$

Importantly, this means that the only nonlinear equation to be solved is the scalar consistency equation ($f = 0$) which can be linearized such that,

$$\Delta\xi = -\frac{f^{(k)}}{\frac{\partial f^{(k)}}{\partial \xi} - \frac{\partial f^{(k)}}{\partial T_{ij}}\mathbb{C}_{ijkl}\left(\xi^{(k)}\right)\left(\Delta\mathbb{S}_{klmn}T^{(k)}_{mn} + \Delta\alpha_{kl}\Delta\theta + \Lambda^{(k)}_{kl}\right)},$$

and the stress increment is then found as,

$$\Delta T^{(k)} = -\mathbb{C}_{ijkl}\left(\xi^{(n)}\right)\left(\Delta\mathbb{S}_{klmn}T^{(k)}_{mn} + \Delta\alpha_{kl}\Delta\theta + \Lambda^{(k)}_{kl}\right)\Delta\xi.$$

4.25.3 Verification

The shape memory alloy model is verified through a series of thermomechanical loadings. The material properties and model parameters for these investigations are given in Table 4.37. These properties correspond to those given in Table 3.4 in [55] with all $n'`sassumedtobe1andsetting : math : `E^M = E^A$.

Table 4.37 The material and model parameters for the shape memory alloy model used during verification test.

E^A	55 GPa	E^M	55 GPa
ν^A	0.33	ν^M	0.33
α^A	$22.0x10^{-6}\frac{1}{\mathrm{K}}$	α^M	$22.0x10^{-6}\frac{1}{\mathrm{K}}$
M_s	245 K	A_s	270 K
M_f	230 K	A_f	280 K
C^M	$7.4\ \frac{\mathrm{MPa}}{\mathrm{K}}$	C^A	$7.4\ \frac{\mathrm{MPa}}{\mathrm{K}}$
$H_{\min}$	0.056	H_{sat}	0.056

It should also be clear that because $H_{\min} = H_{\mathrm{sat}}$ the model response is independent of the values of σ^{crit} and k. For convenience, values of $k = 1.0x10^6$ and $\sigma^{\mathrm{crit}} = 0$ will be used. Additionally, σ^* will be taken to be zero although inspection of (4.105) and consideration of the relative magnitudes of the transformation strain and the difference in elastic strain similarly indicates an invariance in the model response to this parameter with constant H^{cur}. The default prestrain values are also utilized such that the SMA is initially austenitic.

4.25.3.1 Uniaxial Stress – Pseudoelasticity

First, the isothermal ($\theta > A_f$) pseudoelastic response through a uniaxial stress loading is explored. Importantly, the simplifications and model parameters described above ($E^A = E^M = E$, $H^{\mathrm{cur}}\left(\bar{\sigma}_{vM}\right) = H$, $C^A = C^M = C$, $n_i = 1$) allow for a simple analytical description of the pseudoelastic response (essentially trilinear). For instance, given the constant slopes of the transformation surfaces, the stresses needed to induce or complete transformation are simply given by,

$$\sigma^{\beta}\left(\theta\right) = C\left(\theta - \beta\right), \qquad \beta = M_s,\ M_f,\ A_s,\ A_f,$$

where $\sigma^{M_s}(\theta)$ is the stress needed to start forward transformation at temperature, θ. Given a stress value, the strain and material state may be completely determined by knowing the martensitic volume fraction, ξ. Specifically, the axial (here taken to be the 1 direction) strain is simply,

$$\varepsilon_{11} = \frac{\sigma}{E} + \xi H,$$

and the lateral strains are

$$\varepsilon_{22} = \varepsilon_{33} = -\nu\frac{\sigma}{E} - \frac{1}{2}\xi H,$$

in which the fact that the transformation strain tensor is deviatoric is being leveraged. The martensitic volume fraction may then simply be found by noting that $f = 0$ during transformation. Therefore, for forward transformation,

$$\xi = \begin{cases} 0 & \sigma \leq \sigma^{M_s} \\ \frac{1}{a_1}\left(\sigma H + \rho\Delta s_0\theta - \rho\Delta u_0 - a_3 - \sigma_0\right) & \sigma^{M_s} < \sigma < \sigma^{M_f} \\ 1 & \sigma \geq \sigma^{M_f} \end{cases}. \tag{4.106}$$

A comparable expression is easily determined for reverse transformation.

The results of this simple analytical expression and those determined by Adagio are presented in Fig. 4.118 for three different temperatures. Fig. 4.118(a) presents the stress-strain response under these conditions while Fig. 4.118(b) presents the evolution of the martensitic volume fraction.

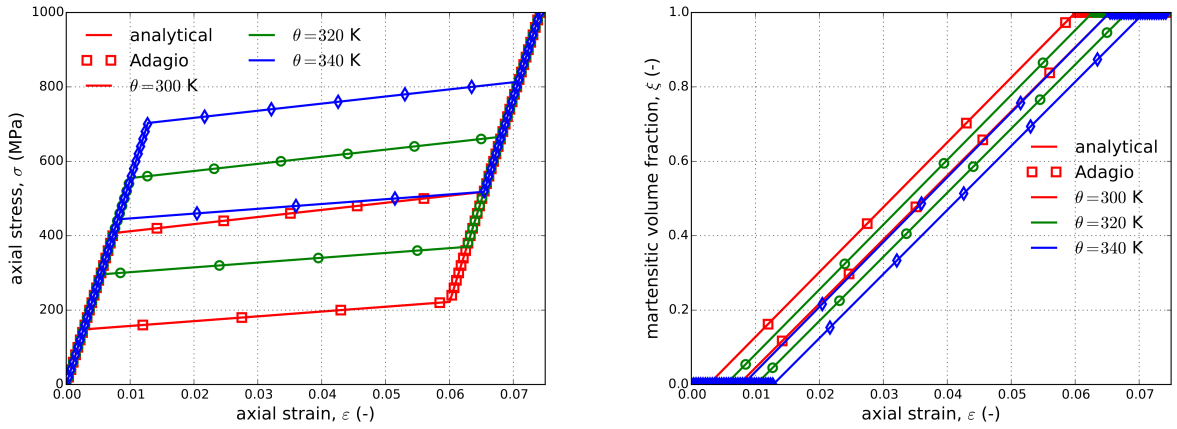

(a) Axial stress-strain **(b) MVF**

Fig. 4.118 Axial stress-strain response (a) and martensitic volume fraction (b), ξ, evolution determined analytically and via adagio for three different ambient temperatures $\theta = 300,\ 320$ and 340 K.

4.25.3.2 Constant Stress Actuation

To consider thermally driven transformation, the constant stress actuation response is investigated. In such a loading, a mechanical load is applied at high temperature ($\theta > A_f$) and held constant while the specimen is cooled through forward transformation and then heated back to its initial state. Given the aforementioned simplifications to the model parameters, the analytical response is determined in a very similar fashion to that of pseudoelasticity. In this instance, critical temperatures needed for transformation are first determined by

$$\beta^\sigma = \beta + \frac{\sigma}{C}, \qquad \beta = M_s,\ M_f,\ A_s,\ A_f,$$

with M_s^σ being the temperature needed to start forward transformation at an effective stress, σ. The zero-stress value is M_s. Similarly, the axial and lateral strains may be adjusted as,

$$\varepsilon_{11} = \frac{\sigma}{E} + \xi H + \alpha\left(\theta - \theta_0\right),$$
$$\varepsilon_{22} = \varepsilon_{33} = -\nu\frac{\sigma}{E} - \frac{1}{2}\xi H + \alpha\left(\theta - \theta_0\right).$$

The martensitic volume fraction is found through relations (4.106) albeit with the piecewise intervals defined in terms of temperature ($e.g\ \sigma^{Ms} < \sigma < \sigma^{M_f} \leftrightarrow M_f^\sigma < \theta < M_s^\sigma$). Results for the axial strain-temperature, lateral strain-temperature, and martensitic volume fraction-temperature as determined analytically and via adagio are presented below in Fig. 4.119(a), Fig. 4.119(b), and Fig. 4.119(c), respectively.

4.25.4 User Guide

```
BEGIN PARAMETERS FOR MODEL SHAPE_MEMORY_ALLOY
  #
  # Elastic constants
  #
  YOUNGS MODULUS = <real>
  POISSONS RATIO = <real>
  SHEAR MODULUS  = <real>
  BULK MODULUS   = <real>
  LAMBDA         = <real>
  TWO MU         = <real>
  #
  # Thermoelastic properties of two crystallographic phases
  #
  ELASTIC MODULUS AUSTENITE  = <real>
  POISSON RATIO AUSTENITE    = <real>
  CTE AUSTENITE              = <real>
  ELASTIC MODULUS MARTENSITE = <real>
  POISSON RATIO MARTENSITE   = <real>
```

(continues on next page)

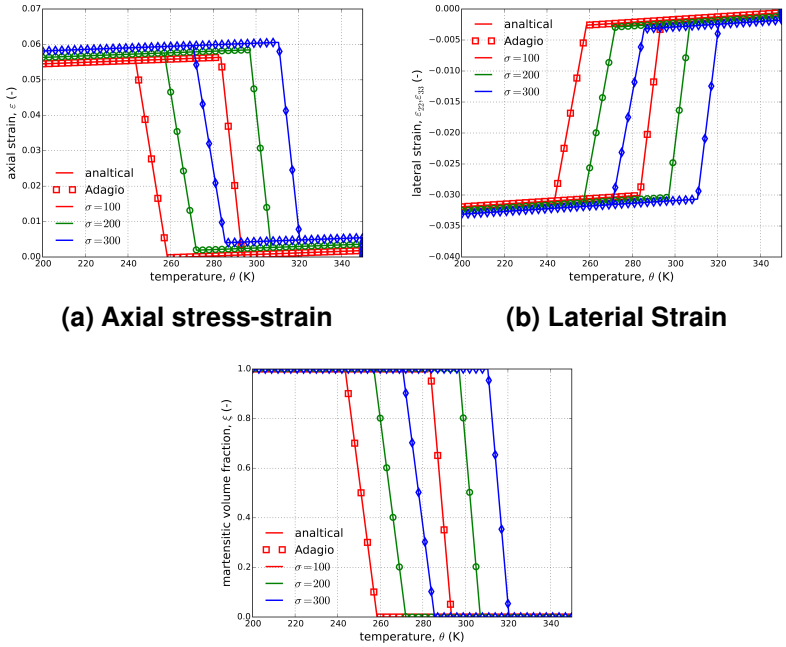

(a) Axial stress-strain **(b) Laterial Strain**

(c) MVF

Fig. 4.119 Axial stress-strain (a), lateral strain (b), and martensitic volume fraction (c), ξ, evolution as a function of temperature as determined analytically and numerically (Sierra/SM). Results are presented for three different applied bias stresses $\sigma = 100,\ 200$ and 300 MPa.

(continued from previous page)

```
CTE MARTENSITE              = <real>
#
# Phase diagram parameters
#
MARTENSITE START                    = <real>
MARTENSITE FINISH                   = <real>
AUSTENITE START                     = <real>
AUSTENITE FINISH                    = <real>
STRESS INFLUENCE COEFF MARTENSITE = <real>
STRESS INFLUENCE COEFF AUSTENITE  = <real>
#
# Transformation strain magnitude parameters
#
H_MIN          = <real>
H_SAT          = <real>
KT             = <real>
SIGMA_CRITICAL = <real>
#
# Calibration parameters
#
N1         = <real>
```

(continues on next page)

(continued from previous page)

```
  N2          = <real>
  N3          = <real>
  N4          = <real>
  SIGMA STAR = <real>
  T0          = <real>
  #
  # Initial phase conditions
  #
  XI0                  = <real> (0.0)
  PRESTRAIN_DIRECTION = <int> (0)
  PRESTRAIN_MAGNITUDE = <real> (0.0)
  #
END [PARAMETERS FOR MODEL SHAPE_MEMORY_ALLOY]
```

In the command blocks that define the Shape Memory Alloy model:

- Although the thermoelastic constants of the phases are defined separately, the definition of these constants in this form is necessary for the global solver. Typical values of the phases should be applied.
- The isotropic elastic moduli of the austenitic (E^A) and martensitic phases (E^M) are defined with the `ELASTIC MODULUS AUSTENITE` and `ELASTIC MODULUS MARTENSITE` command lines, respectively. Note, alternative elastic constants (e.g. bulk or shear moduli) may not be used.
- The isotropic Poisson's ratio of the austenitic (ν^A) and martensitic phases (ν^M) are defined with the `POISSON RATIO AUSTENITE` and `POISSON RATIO MARTENSITE` command lines, respectively. Note, alternative elastic constants (e.g. lame constant) may not be used.
- The isotropic coefficient of thermal expansion of the austenitic (α^A) and martensitic phases (α^M) are defined with the `CTE AUSTENITE` and `CTE MARTENSITE` command lines, respectively. Note, given the phase and history dependence of the material thermal expansion, the use of artificial or thermal strain functions may not lead to desired results. The use of these constants in encouraged instead.
- The zero stress, smooth transformation temperatures corresponding to the start and end of forward transformation (martensitic start M_s and finish M_f, respectively) and start and end of reverse transformation (austenitic start A_s and finish A_f, respectively) are given by the (in order) command lines `MARTENSITE START`, `MARTENSITE FINISH`, `AUSTENITE START`, and `AUSTENITE FINISH`.
- The stress influence coefficients giving the slope of the forward and reverse transformation surfaces (C^M and C^A, respectively) are given by the `STRESS INFLUENCE COEFF MARTENSITE` and `STRESS INFLUENCE COEFF AUSTENITE`, respectively.
- The stress dependence of the transformation strain magnitude requires four coefficients. These are the minimum transformation strain magnitude ($H_{\min}$), the saturation (or

maximum) magnitude (H_{sat}), exponential fitting coefficient (k), and critical effective stress value below which the magnitude is minimum (σ_{crit}). These parameters are defined via the `H_MIN`, `H_SAT`, `KT`, and `SIGMA_CRITICAL` command lines, respectively.

- The smooth hardening fitting constants n_1, n_2, n_3, and n_4 correspond to the degree of smoothness (essentially how gradual the transformation is) of the martensitic start, martensitic finish, austenitic start, and austenitic finish transformation surfaces. They are given by the `N1`, `N2`, `N3`, and `N4` command lines, respectively, and should take values $0 < n_i \leq 1$.
- The stress level of transformation at which calibration is performed is denoted by σ^* and given by the command line `SIGMA STAR`. For thermally induced transformation this corresponds to the bias stress level while in pseudo-elastic loadings it corresponds to the stress level at which the material is roughly evenly split between martensite and austenite.
- The zero-strain reference temperature is denoted θ_0 and prescribed via the `T0` command line.
- Three optional parameters describing the initial state of the material may be input. These parameters are intended for the case in which the material is initially martensite to allow for initial heating and transformation recovery. The first is the initial martensitic volume fraction, $\xi\ (t = 0)$, input via the `XI0` command line. If this parameter is not specified the default value is 0.0 representative of an austenitic material. A value between 0.0 and 1.0 may be entered to initialize the material to partially (or fully) martensitic. Corresponding initial transformation strains may be entered via the `PRESTRAIN_DIRECTION` (n^{ps}) and `PRESTRAIN_MAGNITUDE` $\left(||\varepsilon_{ij}^{\text{tr}}\ (t = 0)\ ||\right)$ commands. The first (an integer between one and three) gives the direction of transformation (in global Cartesian space) and the magnitude of the inelastic strain in that direction is given by a fraction (between 0 and 1) of H_{sat} via the second `PRESTRAIN_MAGNITUDE` line. As the transformation strain tensor is deviatoric, the other two directions are specified by preserving that the tensor be trace less. Note, the `PRESTRAIN_DIRECTION` and `PRESTRAIN_MAGNITUDE` cannot be specified without a non-zero `XI0` definition.
- Thermal strains functions and commands in Sierra should not be used in conjunction with the `shape_memory_alloy` model.
- In order for this material model to function a temperature must be defined on every block that uses the model.

Output variables available for this model are listed in Table 4.38.

Table 4.38 State Variables for SHAPE MEMORY ALLOY Model

Name	Description
`MVF`	martensitic volume fraction, ξ
`TransStrain`	transformation strain tensor, $\varepsilon_{ij}^{\text{tr}}$

4.26 Low Density Foam Model

4.26.1 Theory

The low density foam material model is a phenomenological model for rigid, low density polyurethane foams. Development of this model followed extensive characterization efforts at Sandia National Laboratory with special emphasis placed on hydrostatic and triaxial compression tests [75]. A key observation of this investigation was the impact of trapped air inside the foam on the load bearing capabilities of the material.

In constructing a model describing the response of the low-density foams, Neilsen et al. [75] decomposed the response into that of the polymeric skeleton and the air such that,

$$\sigma_{ij} = \sigma_{ij}^{\text{sk}} + \sigma^{\text{air}}\delta_{ij}, \tag{4.107}$$

where the super script sk is used to refer to variables relating to the skeleton and air to the air. The contribution of the air component is only present, however, in constrained cases when the internal gases are trapped and not allowed to escape. If the foam material in not encased or encapsulated in someway, the air may escape and $\sigma^{\text{air}} = 0$. A model parameter, N_{air}, is included to distinguish between these cases. If N_{air} is set to 0, the air pressure term is set to zero. For any other value, it is included.

Using the ideal gas law, it can be found that for an isothermal case,

$$\sigma^{\text{air}} = \frac{p_0 \varepsilon_{\text{V}}}{\varepsilon_{\text{V}} + 1 - \phi}, \tag{4.108}$$

where p_0, ε_{V}, and ϕ are the initial air pressure, volumetric strain, and the volume fraction of the solid (skeleton) material. Knowing the total stress of the material volume and air contribution, the skeleton stress may be found via (4.107). Furthermore, it should be noted that the foam (total) and skeleton strains are the same.

Based on their experimental observations, Neilsen et al. [75] noted a decoupling between the skeleton principal stresses. Therefore, the Poisson's ratio of the skeleton is zero and that the yielding behavior in each principal direction is independent. A yield function of the form,

$$f_i = \sigma_i^{\text{sk}} - \bar{\sigma},$$

where f_i and σ_i^{sk} are the i^{th} yield function and skeleton principal stress, respectively, and

$$\bar{\sigma} = A \left\langle I_2' \right\rangle + B \left(1.0 + C\varepsilon_V\right) \tag{4.109}$$

with A, B, and C are material parameters, and $\langle \cdot \rangle$ denoting the Heaviside step function where

$$\langle x \rangle = \begin{cases} 0 & \text{if } x \leq 0 \\ 1 & \text{if } x > 0 \end{cases}, \tag{4.110}$$

was proposed. Additionally, I_2' is the second invariant of the deviatoric strain. If a skeleton principal stress indicates yielding, it is set to the effective yield stress value, $\bar{\sigma}$.

4.26.2 Implementation

The low density foam material model is implemented in a hypoelastic fashion. Therefore, a trial material state of,

$$\begin{aligned} T_{ij}^{\mathrm{sk}-tr} &= T_{ij}^{\mathrm{sk}-n} + E\Delta t d_{ij}, \\ \varepsilon_{ij}^{n+1} &= \varepsilon_{ij}^{n} + \Delta t d_{ij}, \end{aligned} \tag{4.111}$$

with d_{ij}, T_{ij}^{sk}, and ε_{ij} are the unrotated rate of deformation, unrotated skeleton stress, and foam strain, respectively, is calculated. The superscript tr denotes a trial stress while E is the Young's Modulus and (4.111) leverages the fact that the Poisson's ratio of the skeleton is zero. The principal stresses of the trial skeleton stress state, $T_i^{\mathrm{sk}-tr}$, are then computed via the algorithm of Scherzinger and Dohrmann [89].

To check the yielding behavior, the (logarithmic) volumetric strain, $\varepsilon_{\mathrm{V}}^{n+1}$, and second invariant of the deviatoric strain, I_2', are needed. These values are simply calculated as,

$$\begin{aligned} \varepsilon_{\mathrm{V}}^{n+1} &= \exp\left(\varepsilon_{kk}^{n+1}\right) - 1, \\ I_2'^{n+1} &= \hat{\varepsilon}_{11}^{n+1}\hat{\varepsilon}_{22}^{n+1} + \hat{\varepsilon}_{11}^{n+1}\hat{\varepsilon}_{33}^{n+1} + \hat{\varepsilon}_{22}^{n+1}\hat{\varepsilon}_{33}^{n+1} - \left[\left(\hat{\varepsilon}_{12}^{n+1}\right)^2 + \left(\hat{\varepsilon}_{23}^{n+1}\right)^2 + \left(\hat{\varepsilon}_{31}^{n+1}\right)^2\right], \end{aligned}$$

with $\hat{\varepsilon}_{ij}^{n+1}$ being the deviatoric strain tensor. The effective yield stress, $\bar{\sigma}^{n+1}$, may be written as,

$$\bar{\sigma}^{n+1} = A\left\langle I_2'^{n+1}\right\rangle + B\left(1 + C\varepsilon_{\mathrm{V}}^{n+1}\right).$$

It should also be noted that a steep sinusoidal approximation of the Heaviside step function to alleviate numerical issues associated with the sharp discontinuity inherit to the use of the Heaviside function. The updated principal stresses may then be determined as,

$$T_i^{\mathrm{sk}-n+1} = \begin{cases} T_i^{\mathrm{sk}-tr}, & |T_i^{\mathrm{sk}-tr}| \le |\bar{\sigma}| \\ \mathrm{sgn}\left(T_i^{\mathrm{sk}-tr}\right)\bar{\sigma}, & |T_i^{\mathrm{sk}-tr}| > |\bar{\sigma}| \end{cases},$$

where $\mathrm{sgn}\,(x)$ denotes the sign of x. An updated air pressure is then computed from (4.108) and the current stress is found to be,

$$T_{ij}^{n+1} = \sum_{k=1}^{3} T_k^{\mathrm{sk}-n+1}\hat{e}_i^k\hat{e}_j^k + \sigma^{\mathrm{air}-n+1}\left(\varepsilon_{\mathrm{V}}^{n+1}\right)\delta_{ij},$$

where $\hat{e}_i^k$ is the eigenvector associated with the k^{th} principal skeleton stress.

4.26.3 Verification

The low density foam model is implemented through two compression tests – uniaxial and hydrostatic. Cases both including ($N_{\mathrm{air}} = 1.0$) and excluding ($N_{\mathrm{air}} = 0.0$) the contribution of the

air are investigated. The rest of the properties and parameters used for these tests are given in Table 4.39 and are originally from [91].

Table 4.39 Material properties and model parameters for the low density foam model used during verification testing.

E	3010 psi	ν	0.0
A	49.2 psi	B	60.8 psi
C	-0.517	p_0	14.7 psi
ϕ	0.09		

4.26.3.1 Uniaxial Compression

First, a uniaxial compression test under displacement control is considered with and without the contribution of air. In this case, a displacement of the form $u_1 = \lambda$ is applied while the other two directions are left traction free. When air pressure does not play a role, the model response reduces to that of the skeleton and the problem becomes one-dimensional. The deformation rate can be easily integrated to find that $\varepsilon_{11} = \ln(1+\lambda)$ and $\varepsilon_{\mathrm{V}} = \lambda$. Additionally, the uniaxial compression loading considered here is obviously deviatoric in nature leading to $\langle I_2' \rangle$ evaluating to 1. Therefore,

$$\begin{aligned} \bar{\sigma} &= A + B\,(1 + C\lambda)\,, \\ \sigma_{11} &= \begin{cases} E\varepsilon_{11} & |\sigma_{11}| \le |\bar{\sigma}| \\ \operatorname{sgn}(\varepsilon_{11})\,\bar{\sigma} & |\sigma_{11}| > |\bar{\sigma}| \end{cases} . \end{aligned} \tag{4.112}$$

The corresponding stress and strain results are presented in Fig. 4.120(a) and Fig. 4.120(b).

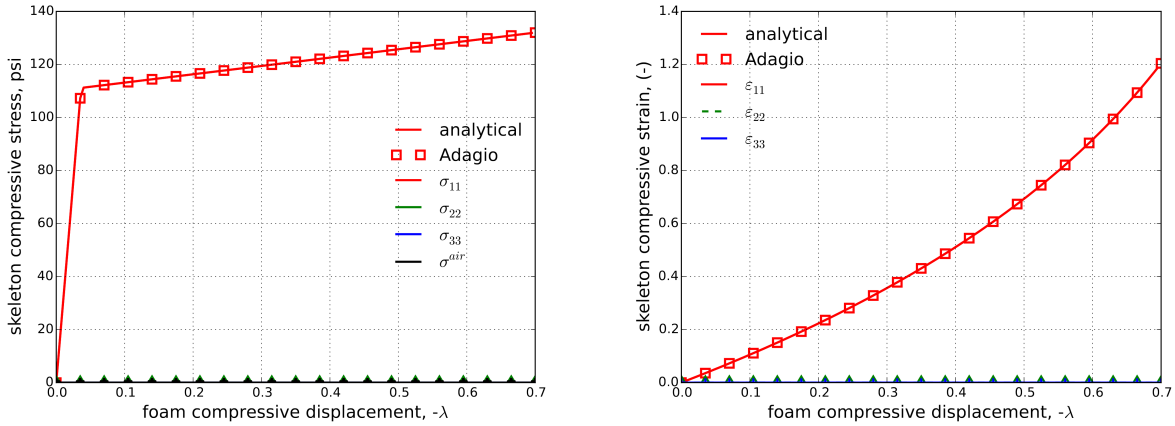

(a) Skeleton stress **(b) Skeleton strain**

Fig. 4.120 Skeleton (a) stress and (b) strain determined analytically and numerically (with $N_{\mathrm{air}} = 0$) with the low density foam model during a displacement controlled uniaxial compression test.

The case of internal air pressure is also considered by setting $N_{\mathrm{air}} = 1$. This, however, complicates the response and turns it into a three-dimensional case given the pressure components in the

off-loading directions. Specifically, it can be found trivially that, $\varepsilon_{22} = \varepsilon_{33} = -\sigma^{\text{air}}/E$. The complication arises as the volumetric strain is now,

$$\varepsilon_{\text{V}} = (1+\lambda)\exp\left(-2\sigma^{\text{air}}/E\right) - 1,$$

leading to an implicit expression for σ^{air}. By evaluating σ^{air} in a forward Euler fashion, noting $\bar{\sigma} = A + B\,(1 + C\varepsilon_{\text{V}})$, and treating (4.112) as an expression for σ_{11}^{sk} the stress and strain responses may be found as given in Fig. 4.121(a) and Fig. 4.121(b). The impact of the air on the model response is clear by comparing the two sets of figures.

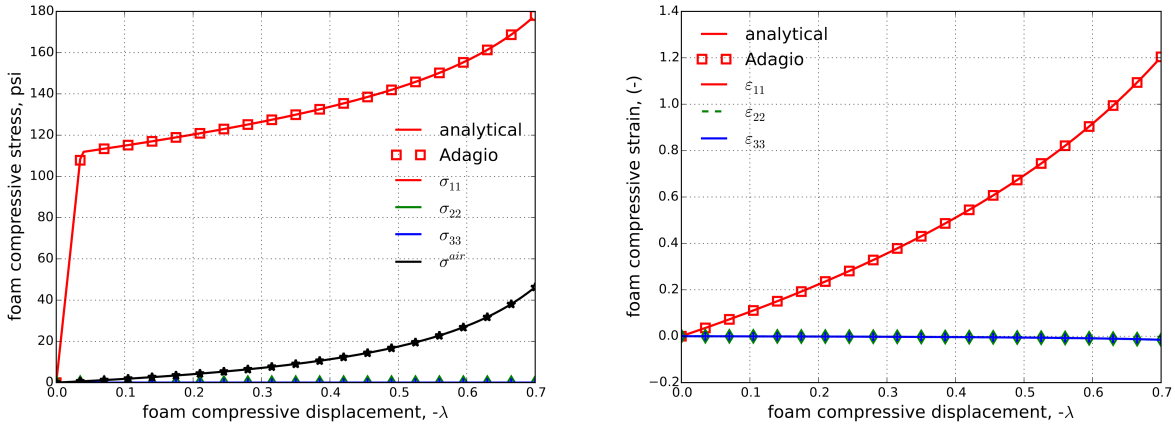

(a) Skeleton stress **(b) Skeleton strain**

Fig. 4.121 Foam (a) stress and (b) strain determined analytically and numerically (with $N_{\text{air}} = 1$) with the load density foam model during a displacement controlled uniaxial compression test.

4.26.3.2 Hydrostatic Compression

The volumetric deformation capabilities of the model are also investigated through displacement controlled hydrostatic compression. Specifically, an imposed displacement of the form $u_i = \lambda$ is considered. The resultant strain field is $\varepsilon_{11} = \varepsilon_{22} = \varepsilon_{33} = \ln(1+\lambda)$ leading to a volumetric strain of the form $\varepsilon_{\text{V}} = (1+\lambda)^3 - 1$. As there is no deviatoric deformation it is apparent that $\langle I_2' \rangle = 0$. Therefore, the effective yield stress is $\bar{\sigma} = B\,(1 + C\varepsilon_{\text{V}})$. Also noting that $\sigma = \sigma_{11} = \sigma_{22} = \sigma_{33}$, the foam response through such a loading may easily be determined. The foam stress for both the with and without air case is presented in Fig. 4.122 along with σ^{air} for the appropriate case.

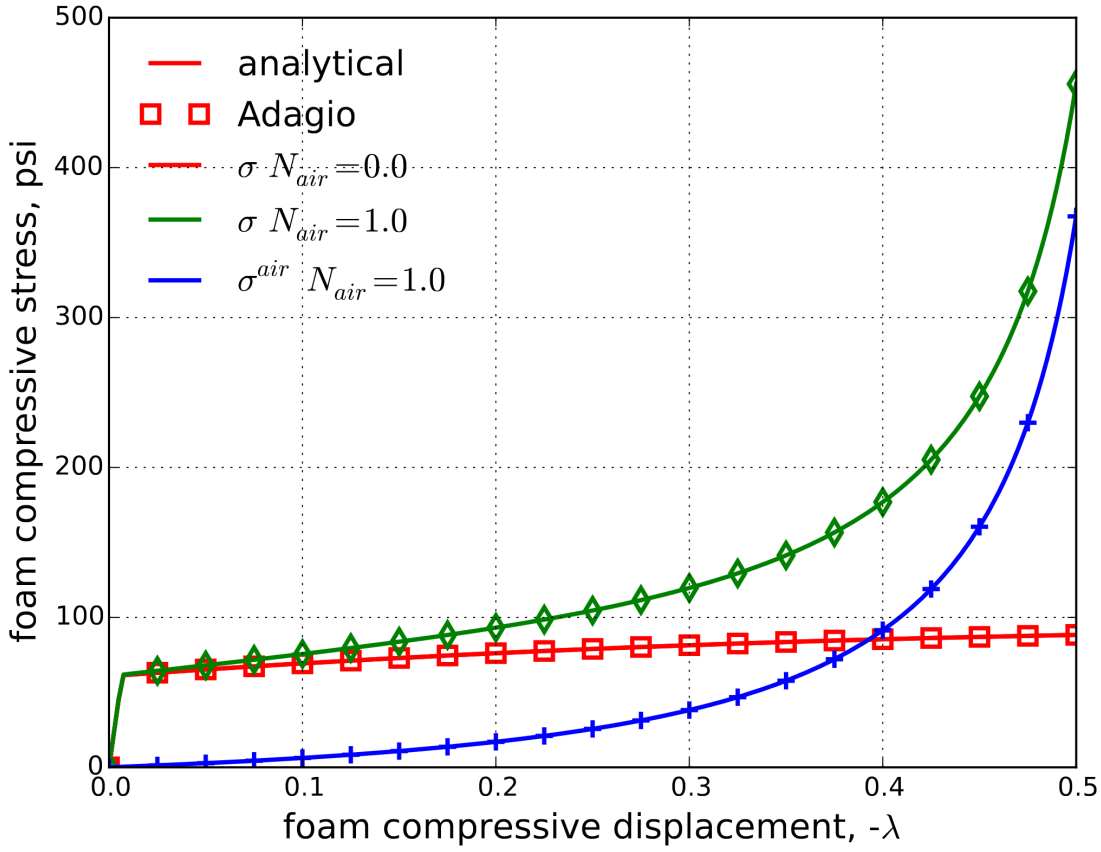

Fig. 4.122 Foam stress determined analytically and numerically for both $N_{air} = 0.0$ and $N_{air} = 1.0$ cases for the low density foam model during displacement controlled hydrostatic compression

4.26.4 User Guide

```
BEGIN PARAMETERS FOR MODEL LOW_DENSITY_FOAM
  #
  # Elastic constants
  #
  YOUNGS MODULUS = <real>
  POISSONS RATIO = <real>
  SHEAR MODULUS  = <real>
  BULK MODULUS   = <real>
  LAMBDA         = <real>
  TWO MU         = <real>
  #
  A    = <real>
  B    = <real>
  C    = <real>
  NAIR = <real>
  P0   = <real>
  PHI  = <real>
END [PARAMETERS FOR MODEL LOW_DENSITY_FOAM]
```

State variables for this model are listed in Table 4.40. For more information on the low density foam material model, see [75].

Table 4.40 State Variables for LOW DENSITY FOAM Model

Name	Description
PAIR	Air pressure

4.27 Foam Plasticity Model

4.27.1 Theory

The foam plasticity model was developed to describe the response of porous materials (like closed-cell polyurethane foams) exhibiting irreversible, elastic-plastic like responses through large deformations. Such foams can exhibit significant plastic deviatoric and volumetric strains leading to permanent shape and volume changes, respectively. The former behavior is quite typical of metals and corresponding theories are well established. The latter response, however, is not typical of metals and a theory combining these two behaviors is needed. Given these responses of interest, the foam plasticity model is well suited to use with metal foams and many closed-cell polymeric foams (e.g. polyurethane, polystyrene bead, etc.) subjected to large deformations. As permanent strains are of interest, this model is not appropriate for use with flexible foams that return to their undeformed shape after loads are removed.

Specifically, the model developed by Neilsen et al. [72] seeks to capture the response associated

with three distinct deformation regimes. First, when foams are initially compressed, they typically exhibit an elastic response. After sufficient load is applied, a plateau of nearly constant stress over a large deformation region is noted as pores start to compress and cell walls undergo substantial deformation. Eventually, the various collapsed cells and walls begin to interact and a densification response with substantial hardening is observed. Details of these deformation processes may be found in the text of Gibson and Ashby [36].

Like other plasticity-based models, the incremental constitutive law for the foam plasticity model is written as,

$$\overset{\circ}{\sigma}_{ij} = \mathbb{C}_{ijkl} D^{\mathrm{e}}_{kl},$$

where an additive decomposition of the strain rates such that $D_{ij} = D^{\mathrm{e}}_{ij} + D^{\mathrm{p}}_{ij}$ is assumed. To describe the inelastic response of the foams of interest, Neilsen and coworkers [72] proposed a yield function of the form

$$f = \frac{\bar{\sigma}^2}{a^2} + \frac{p^2}{b^2} - 1, \tag{4.113}$$

where $\bar{\sigma}$ is the von Mises effective stress ($\bar{\sigma} = \sqrt{(3/2)\, s_{ij} s_{ij}}$ with s_{ij} being the deviatoric stress) and p being the hydrostatic pressure ($p = (1/3)\, \sigma_{kk}$). In such a form, the initial yield surface forms an ellipsoid about the hydrostat. The two denominators, a and b, are state variables capturing hardening effects and have the functional form of,

$$a = A_0 + A_1 \phi^{A_2}, \tag{4.114}$$

$$b = \begin{cases} B_0 + B_1 \phi^{B_2} & p \geq 0 \\ B_0 & p < 0 \end{cases}, \tag{4.115}$$

with A_0, A_1, A_2, B_0, B_1, and B_2 being model parameters and ϕ being the maximum volume fraction of solid material obtained through the loading history and is defined as,

$$\phi = \max\left(\phi_c\right)$$

where,

$$\phi_c = \phi_0 \frac{V_0}{V},$$

in which ϕ_0 is the initial volume fraction of solid material and V_0 and V are the initial volume and current volume, respectively, of the foam. Put in terms of the deformation,

$$\phi_c = \phi_0 \frac{1}{1 + \varepsilon_{\mathrm{V}}},$$

where ε_{V} is the engineering volume strain.

To describe the inelastic plastic deformation, a non-associated flow rule is used. Specifically,

$$D^{\mathrm{p}}_{ij} = \dot{\gamma} g_{ij},$$

where $\dot{\gamma}$ is the consistency multiplier found by enforcing the corresponding condition and

$$g_{ij} = \frac{(1-\beta)\, g^{\mathrm{a}}_{ij} + \beta g^{\mathrm{r}}_{ij}}{|\,(1-\beta)\, g^{\mathrm{a}}_{ij} + \beta g^{\mathrm{r}}_{ij}|}, \tag{4.116}$$

with the superscripts a and r being used to denote associated and radial flow directions, respectively. The model parameter β is introduced in (4.116) to enable associated ($\beta = 0$), radial ($\beta = 1$), or a linear combination of the two flow rules ($0 < \beta < 1$) to be used. The two direction vectors may written as,

$$g^{\mathrm{a}}_{ij} = \frac{\frac{\partial f}{\partial \sigma_{ij}}}{|\frac{\partial f}{\partial \sigma_{kl}}|} = \frac{\frac{3}{a^2} s_{ij} + \frac{2}{3b^2} p\delta_{ij}}{|\frac{3}{a^2} s_{ij} + \frac{2}{3b^2} p\delta_{ij}|}, \tag{4.117}$$

$$g^{\mathrm{r}}_{ij} = \frac{\sigma_{ij}}{|\sigma_{kl}|} = \frac{\sigma_{ij}}{\sqrt{\sigma_{kl}\sigma_{kl}}}. \tag{4.118}$$

In alternative models of foam plasticity, the yield function is offset in the $\bar{\sigma} - p$ plane along the pressure axis. To generalize the model, an offset yield surface centered at pressure p_0 may be used in the form

$$\hat{f} = \frac{\bar{\sigma}^2}{a^2} + \frac{(p - p_0)^2}{b^2} - 1. \tag{4.119}$$

Note that with this form of the yield function, the component of the flow direction g^a_{ij} is now non-associative. This component is associative to the yield surface centered at the origin, but non-associative to the yield surface centered at p_0.

4.27.2 Implementation

Like other more classical rate-independent plasticity models (e.g. Section 4.7.2), the foam plasticity model is implemented in a hypoelastic fashion using an elastic predictor-inelastic corrector scheme. As such, a trial material state is calculated by assuming purely elastic deformations. The trial stress is given by,

$$T^{tr}_{ij} = T^n_{ij} + \Delta t \left(\lambda \delta_{ij} d_{kk} + 2\mu d_{ij}\right),$$

and an updated logarithmic volume strain is given by,

$$\varepsilon^{n+1}_{kk} = \varepsilon^n_{kk} + \Delta t d_{kk}.$$

The engineering volume strain may then be readily computed via $\varepsilon^{n+1}_{\mathrm{V}} = \exp\left(\varepsilon^{n+1}_{kk}\right) - 1$. A trial solid volume fraction is then calculated, $\phi^{tr} = \phi_0 \frac{1}{1+\varepsilon^{n+1}_{\mathrm{V}}}$, and compared to the previous maximum to obtain the maximum solid volume fraction over the loading history,

$$\phi^{n+1}_c = \max\left(\phi^n, \phi^{tr}\right). \tag{4.120}$$

Equations (4.114) and (4.115) are evaluated using the volume fraction found in (4.120). Using invariants of the trial stress state, the yield function (4.113) is calculated. If $f \leq 0$, the loading is elastic and the trial solution is correct. On the other hand, if $f > 0$ a correction scheme is necessary to iterate and determine the inelastic solution. To that end, by noting $\Delta T_{ij} = -\mathbb{C}_{ijkl}\Delta d^{\mathrm{P}}_{kl} = -\Delta\gamma\mathbb{C}_{ijkl}g_{kl}$ (with Δ being a correction increment), the consistency condition may be used to find,

$$\Delta\gamma = \frac{f}{\frac{\partial f}{\partial \sigma_{ij}}\mathbb{C}_{ijkl}g_{kl}},$$

where the fact that the strain (and therefore a and b) do not change over an increment. The correction is repeated until $f < \mathrm{tol}$.

4.27.3 Verification

The foam plasticity model is verified through a hydrostatic compression tests. Material properties used for this test are presented in Table 4.41 and correspond to room temperature properties of the PMDI20 rigid polyurethane foam characterized in [72].

Table 4.41 Material properties and model parameters for the foam plasticity model used during verification testing.

E	22,600 psi	ν	0.343
A_0	513.3 psi	A_1	4,629 psi
A_2	2.90	ϕ_0	0.238
B_0	971 psi	B_1	7,377.5 psi
B_2	4.89	β	0.95

4.27.3.1 Hydrostatic Compression

The response of the foam plasticity model to hydrostatic compression is investigated here. Specifically, a displacement of the form $u_i = \lambda$ is imposed resulting in a total strain field of $\varepsilon_{11} = \varepsilon_{22} = \varepsilon_{33} = \ln(1+\lambda)$ and the engineering volume strain is simply $\varepsilon_{\mathrm{V}} = (1+\lambda)^3 - 1$. Furthermore, the maximum solid volume fraction monotonically increases and may be found to be $\phi = \phi_0 \frac{1}{(1+\lambda)^3}$. The stress state undergoes a similar reduction and is given to $\sigma_{ij} = -p\delta_{ij}$ and $s_{ij} = 0$. Note, in the theory section pressure is defined positive in tension whereas in the current exercise compression is positive. There is no practical impact of this selection and it is done for simplicity of presentation. This simplification leads to a reduced yield function of the form,

$$f = \frac{p^2}{b^2} - 1,$$

where b is evaluated via (4.115) and is a function of the strain. The model may then be simply solved as,

$$p = \begin{cases} -3K\ln(1+\lambda) & f \leq 0 \\ b & f > 0 \end{cases}.$$

The elastic strains then reduce to $\varepsilon^{\mathrm{e}}_{ij} = -\frac{p}{3K}\delta_{ij}$ and the plastic strains computed as $\varepsilon^{\mathrm{p}}_{ij} = \left(\ln\left(1+\lambda\right) + \frac{p}{3K}\right)\delta_{ij}$. The resulting engineering strain vs. pressure results determined numerically and analytically are presented in Fig. 4.123.

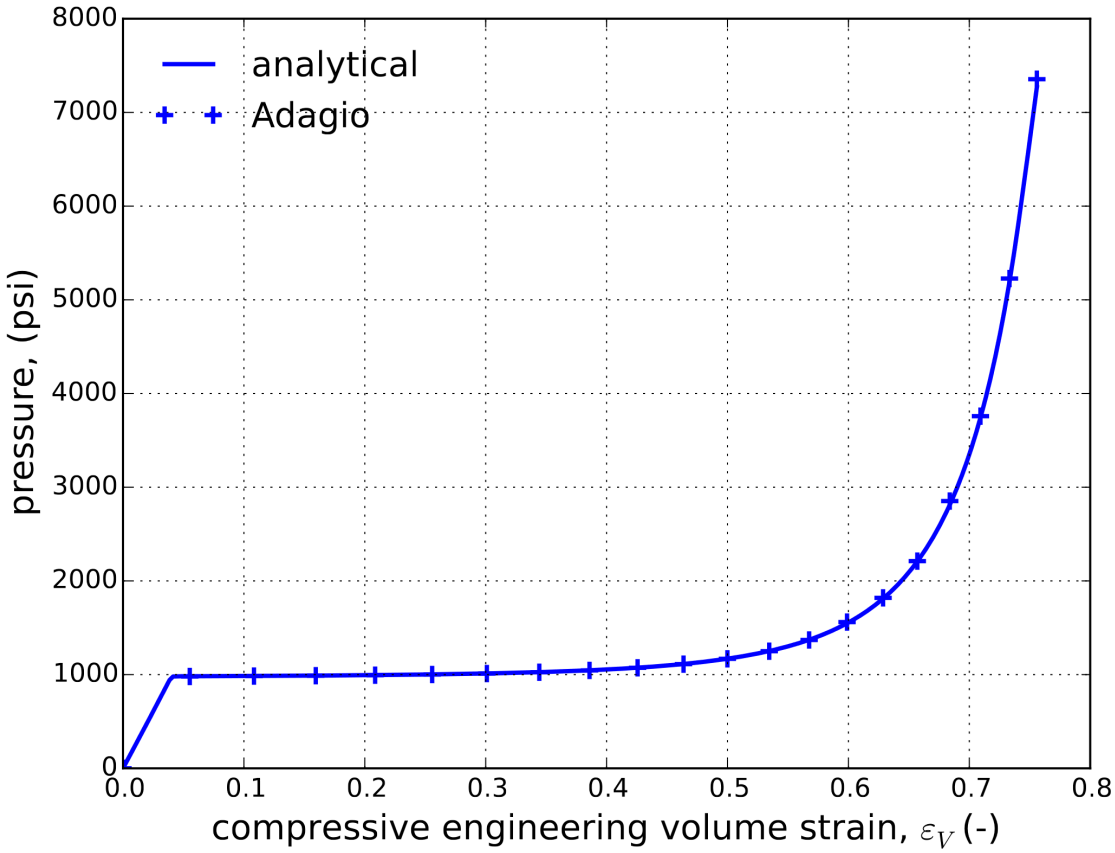

Fig. 4.123 Pressure vs. engineering volume strain (ε_V) response of the foam plasticity model through a hydrostatic compression cycle. For convenience, pressure is defined as positive in compression in the figure.

4.27.4 User Guide

```
BEGIN PARAMETERS FOR MODEL FOAM_PLASTICITY
  #
  # Elastic constants
  #
  YOUNGS MODULUS = <real>
  POISSONS RATIO = <real>
  SHEAR MODULUS  = <real>
  BULK MODULUS   = <real>
```

(continues on next page)

(continued from previous page)

```
  LAMBDA          = <real>
  TWO MU          = <real>
  #
  #
  #
  PHI              = <real>
  SHEAR STRENGTH   = <real>
  SHEAR HARDENING  = <real>
  SHEAR EXPONENT   = <real>
  HYDRO STRENGTH   = <real>
  HYDRO HARDENING  = <real>
  HYDRO EXPONENT   = <real>
  BETA             = <real>
  P0               = <real>
END [PARAMETERS FOR MODEL FOAM_PLASTICITY]
```

In the above command blocks:

- The initial volume fraction of solid material in the foam, φ, is defined with the `PHI` command line. For example, solid polyurethane weighs 75 pounds per cubic foot (pcf); uncompressed 10 pcf polyurethane foam would have a φ of 0.133 = 10/75.
- The shear (deviatoric) strength of uncompressed foam is defined with the `SHEAR STRENGTH` command line.
- The shear hardening modulus for the foam is defined with the `SHEAR HARDENING` command line.
- The shear hardening exponent is defined with the `SHEAR EXPONENT` command line. The deviatoric strength is given by `(SHEAR STRENGTH) + (SHEAR HARDENING) * PHI**(SHEAR EXPONENT).`
- The hydrostatic (volumetric) strength of the uncompressed foam is defined with the `HYDRO STRENGTH` command line.
- The hydrodynamic hardening modulus is defined with the `HYDRO HARDENING` command line.
- The hydrodynamic hardening exponent is defined with the `HYDRO EXPONENT` command line. The hydrostatic strength is given by `(HYDRO STRENGTH) + (HYDRO HARDENING) * PHI**(HYDRO EXPONENT).`
- The prescription for non associated flow, β, is defined with the `BETA` command line. When $\beta = 0.0$, the flow direction is given by the normal to the yield surface (associated flow). When $\beta = 1.0$, the flow direction is given by the stress tensor. It is recommended that associated flow $\beta = 0.0$ be used for most analyses.

Output variables available for this model are listed in Table 4.42.

Table 4.42 State Variables for FOAM PLASTICITY Model

Name	Description
ITER	iterations
EVOL	volumetric strain
PHI	phi, ϕ
EQPS	equivalent plastic strain, $\bar{\varepsilon}^p$
PA	A
PB	B

4.28 Viscoplastic Foam Model

4.28.1 Theory

The viscoplastic foam model is used to model the rate (and temperature) dependent crushing of foams [72]. It is based on an additive split of the rate of deformation into an elastic and plastic portion

$$D_{ij} = D^{\mathrm{e}}_{ij} + D^{\mathrm{p}}_{ij}.$$

The stress in the material is due strictly to the elastic portion of the rate of deformation so that

$$\overset{\circ}{\sigma}_{ij} = \mathbb{C}_{ijkl} D^{\mathrm{e}}_{kl},$$

where $\mathbb{C}_{ijkl}$ are the components of the fourth-order, isotropic elasticity tensor. The stress rate is arbitrary, as long as it is objective. Two objective stress rates are commonly used: the Jaumann rate and the Green-McInnis rate. For problems with fixed principal axes of deformation, these two rates give the same answers. For problems where the principal axes of deformation rotate during deformation, the two rates can give different answers.

To describe the rate-dependent response, an over-stress-type yield function is used. Specifically, the rate-independent foam plasticity yield function

$$f = \frac{\bar{\sigma}^2}{a^2} + \frac{p^2}{b^2} - 1 \tag{4.121}$$

where σ^* is the effective stress given by

$$\sigma^* = \sqrt{\bar{\sigma}^2 + \frac{a^2}{b^2} p^2}. \tag{4.122}$$

In (4.122), $\bar{\sigma}$ is the von Mises effective stress ($\bar{\sigma} = \sqrt{\frac{3}{2} s_{ij} s_{ij}}$) and p is the pressure resulting from a stress decomposition of the form,

$$s_{ij} = \sigma_{ij} - p\delta_{ij}.$$

Furthermore, a and b are state variables that are functions of the absolute temperature, θ, and maximum solid volume fraction, ϕ, and are defined as

$$a\left(\theta,\phi\right)=\left(A_0\left(\theta\right)+A_1\left(\theta\right)\phi^{A_2}\right)f_a\left(\phi\right), \tag{4.123}$$

$$b\left(\theta,\phi\right)=\left(B_0\left(\theta\right)+B_1\left(\theta\right)\phi^{B_2}\right)f_b\left(\phi\right). \tag{4.124}$$

In (4.123) and (4.124), the functional forms are chosen to provide flexibility in terms of representation. To this end, f_a and f_b default to constant values of one and the expression reduce to legacy analytical functions. This both provides for backward compatibility with previous user input decks while allowing for user defined definitions. Further, if $A_1\left(\theta\right)=0$, $a\left(\theta,\phi\right)=A_0\left(\theta\right)f_a\left(\phi\right)$; a multiplicative decomposition of dependencies.

The temperature dependent material properties in the preceding relations are all defined as, $A_0\left(\theta\right)=A_0h_{A_0}\left(\theta\right)$ where A_0 is the reference material parameter and $h_{A_0}\left(\theta\right)$ is the relative value as a function of temperature. In addition to the a and b state variables, the Young's modulus and Poisson's ratio are also functions of the absolute temperature. The latter may be written as $\nu\left(\theta\right)=\nu h_\nu\left(\theta\right)$ while the former is also dependent on the maximum volume fraction of solid material and is given as $E\left(\theta,\phi\right)=Eh_E\left(\theta\right)f_E\left(\phi\right)$.

The maximum volume fraction of solid material, ϕ, is given by

$$\phi=\max_{t>0}\tilde{\phi}\left(t\right)$$

where $\tilde{\phi}\left(t\right)$ is the current volume fraction of solid material and is defined as,

$$\tilde{\phi}\left(t\right)=\frac{\phi_0}{\exp\left(\varepsilon_v^{\mathrm{p}}\right)}$$

with ϕ_0 being the initial solid volume fraction and $\varepsilon_v^{\mathrm{p}}$ is

$$\varepsilon_v^{\mathrm{p}}=\int_0^t D_{kk}^{\mathrm{p}}dt.$$

During inelastic deformation ($f>0$), the corresponding rate of plastic deformation is given in a Perzyna-type form as,

$$D_{ij}^{\mathrm{p}}=\begin{cases}\exp\left(h\left(\theta\right)\right)\left(\dfrac{\sigma^*}{a}-1\right)^{n(\theta)}g_{ij} & \text{if}\quad f>0\\[2ex] 0 & \text{if}\quad f\leq 0\end{cases}$$

where $h\left(\theta\right)$ and $n\left(\theta\right)$ are the flow rate and power exponent respectively. The inelastic flow direction, g_{ij}, is given as a linear combination of the associated (with respect to (4.121)), g_{ij}^{a}, and radial, g_{ij}^{r},

$$g_{ij}=\frac{\left(1-\beta\right)g_{ij}^{\mathrm{a}}+\beta g_{ij}^{\mathrm{r}}}{\left|\left(1-\beta\right)g_{kl}^{\mathrm{a}}+\beta g_{kl}^{\mathrm{r}}\right|} \tag{4.125}$$

The directions g^{a}_{ij} and g^{r}_{ij} are given by

$$g^{\mathrm{a}}_{ij} = \frac{\frac{\partial f}{\partial \sigma_{ij}}}{|\frac{\partial f}{\partial \sigma_{kl}}|} = \frac{\frac{3}{a^2} s_{ij} - \frac{2}{3b^2} p\delta_{ij}}{|\frac{3}{a^2} s_{ij} - \frac{2}{3b^2} p\delta_{ij}|},$$
$$g^{\mathrm{r}}_{ij} = \frac{\sigma_{ij}}{|\sigma_{kl}|} = \frac{\sigma_{ij}}{\sqrt{\sigma_{kl}\sigma_{kl}}},$$

in Equations (4.117) and (4.118),

respectively. In this model, the flow rule weight, β, may be specified as either a constant value or as a function of the maximum solid volume fraction ($\beta = \beta_0 f_\beta(\phi)$).

4.28.2 Implementation

As the viscoplastic foam model is a time-dependent, hypoelastic model it is integrated using an explicit, forward Euler scheme. Given this approach, a critical time step for stability is computed based on the shear strength, current modulus, and deviatoric deformation rate. If the input time step is acceptable, the new material state at time $t = t_{n+1}$ is computed. On the other hand, if the time step is too large a series of sub-increments are used. In this case, the total time step Δt is subdivided into N sub-increments. Each such sub-interval (denoted by k) has a time increment δt^k such that $\Delta t = \sum_{k=1}^{N} \delta t^k$ and the forward Euler time stepping scheme is performed over each sub-interval until the desired material state at time t_{n+1} is determined. For the case of temperature dependent variables (e.g. the Poisson's ratio ν), the value at the start of the sub-increment is determined by linearly interpolating over the total time step,

$$\nu^k = \nu_n + \frac{\Delta t^k}{\Delta t}(\nu_{n+1} - \nu_n),$$

where Δt^k is the current sub-increment time, $\Delta t^k = \sum_{r=1}^{k} \delta t^r$. For simplicity, in the remainder of this section it is assumed that the input time step is acceptable and only a single increment is needed. If additional sub-increments are needed, the below steps would be repeated N times with time intervals of δt^k.

Noting the forward Euler approach adopted in this formulation, the first step is to determine the temperature (and solid volume fraction) dependent model parameters (E, ν, A_0, A_1, B_0, B_1, h and n). With the parameters established, state variables a and b are easily determined through (4.123) and (4.124), respectively, enabling the calculation of the effective stress via (4.122). The effective inelastic (plastic) strain rate, $\dot{\bar{\varepsilon}}^p$, is then given as,

$$\dot{\bar{\varepsilon}}^p = \exp(h(\theta_n)) \left\langle \frac{\sigma^*_n}{a_n} - 1 \right\rangle^{n(\theta_n)},$$

with $\langle\rangle$ being the Macaulay brackets such that,

$$\langle x \rangle = \begin{cases} x & x \geq 0 \\ 0 & x < 0 \end{cases}.$$

Knowing the magnitude of the rate of inelastic deformation, the change in deviatoric and hydrostatic stresses is simply,

$$\dot{s}_{ij} = 2\mu\left(\theta_n, \phi_n\right)\left(\hat{d}_{ij} - \hat{d}^{\mathrm{p}}_{ij}\right),$$
$$\dot{p} = K\left(\theta_n, \phi_n\right)\left(d_{kk} - d^{\mathrm{p}}_{kk}\right),$$

where d_{ij} is the total unrotated rate of deformation, $\hat{x}_{ij}$ denotes the deviatoric portion of tensor x_{ij}, and d^{p}_{ij} is the plastic rate of deformation given by,

$$d^{\mathrm{p}}_{ij} = \dot{\bar{\varepsilon}}^{p} g^{n}_{ij}. \tag{4.126}$$

In (4.126), g_{ij} is the inelastic flow direction and can be calculated via (4.125).

An additional comment is needed with respect to accounting for temperature and solid volume fraction dependence in the shear and bulk moduli. This careful consideration is necessary due to the fact that the temperature dependence is only given with respect to the elastic moduli and Poisson's ratio. As such, the shear and bulk moduli inherit the associated dependencies and are calculated for isotropic elastic relations. For the bulk moduli, this leads to an expression of the form,

$$K\left(\theta, \phi\right) = \frac{E h_E\left(\theta\right) f_E\left(\phi\right)}{3\left(1 - 2\nu h_\nu\left(\theta\right)\right)}.$$

The updated stress state is then easily computed by explicitly integrating the established expressions. Specifically,

$$s^{n+1}_{ij} = \frac{\mu_{n+1}}{\mu_n} s^{n}_{ij} + \dot{s}_{ij}\Delta t,$$
$$p^{n+1} = \frac{K_{n+1}}{K_n} p^{n} + \dot{p}\Delta t,$$
$$T^{n+1}_{ij} = s^{n+1}_{ij} + p^{n+1}\delta_{ij},$$

with μ_n and K_n representing $\mu\left(\theta_n, \phi_n\right)$ and $K\left(\theta_n, \phi_n\right)$, respectively, and T_{ij} being the unrotated stress.

4.28.3 Verification

The viscoplastic foam model was verified in both uniaxial and hydrostatic compression. The material properties and model parameters for both of these investigations are given in Table 4.43. As both loadings are isothermal, temperature dependence is neglected in the relevant model parameters. Furthermore, analytical solutions could not be found directly, so semi-analytical solutions were found.

Table 4.43 The material properties for the viscoplastic foam model tested in uniaxial stress.

E	4,807 psi	A_0	63.03 psi
ν	0.33	A_1	7000 psi
h	-8.12	A_2	3.7878
n	2	B_0	93 psi
β	0.9	B_1	1483.4 psi
ϕ_0	0.1148	B_2	3.7878

4.28.3.1 Uniaxial Compression

To obtain a semi-analytical solution for the uniaxial compression test, the model was reduced to a one-dimensional form and then numerically integrated. The results obtained from the implemented model and the semi-analytical solution are shown below in Fig. 4.124.

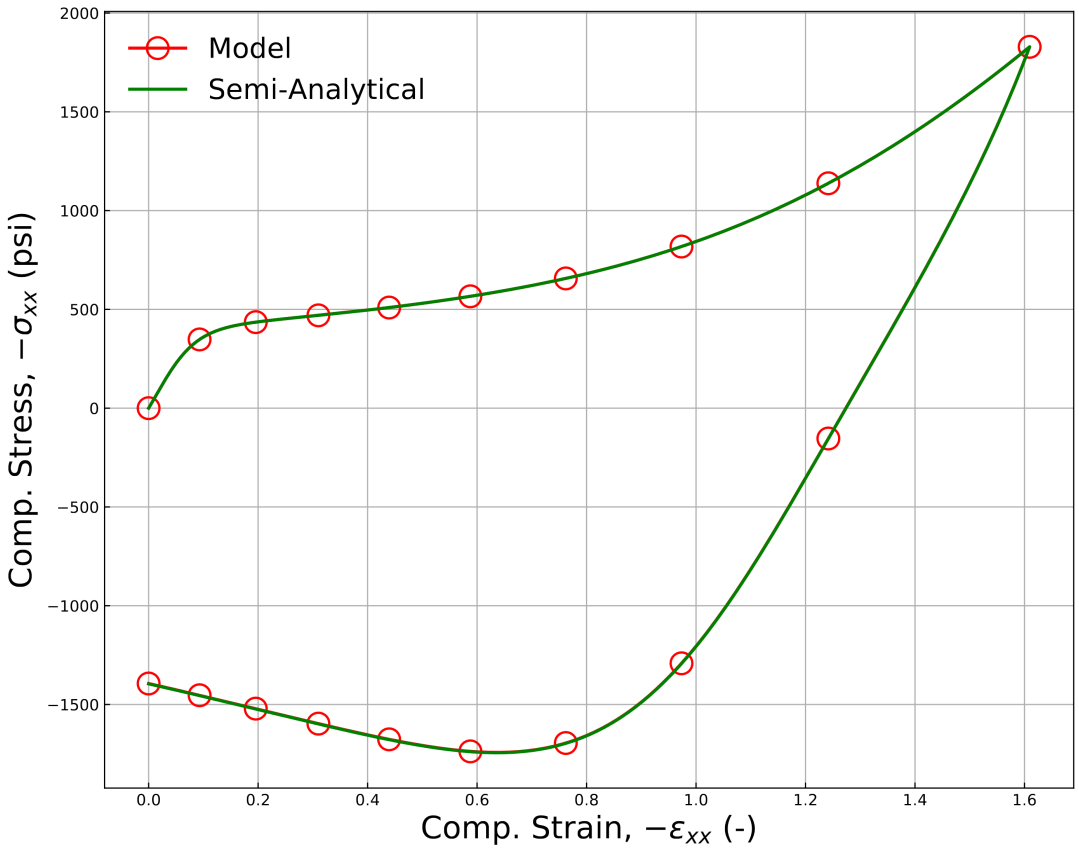

Fig. 4.124 Verification of the viscoplastic foam model in uniaxial compression showing the axial stress as a function of thelogarithmic strain

4.28.3.2 Hydrostatic Compression

The response of the model through hydrostatic compression. To this end, a displacement of the form $u_i = \lambda(t)$ is considered. The applied displacement scales linearly from $\lambda = 0$ at $t = 0.0$ to $\lambda = -0.7$ at $t = t_{\max}$. Rate-dependent effects are considered through the use of two cases each with a different $t_{\max}$. Creatively denoted Fast and Slow, the two cases correspond to $t_{\max} = 1$ s and $t_{\max} = 100$ s, respectively. With such a displacement field, the engineering volume strain, ε_{V}, is simply $\varepsilon_{\mathrm{V}} = (1+\lambda)^3 - 1$. Additionally, the stress state reduces trivially to $\sigma_{ij} = -p\delta_{ij}$.

Given the rate-dependent overstress form of the constitutive model, an analytical solution is not readily available. Therefore, a semi-analytical analysis using a model reduction specialized for hydrostatic loadings is considered. Specifically, noting $s_{ij} = 0$, the overstress reduces to,

$$\sigma^* = \frac{a}{b}|p|.$$

Furthermore, the associated and radial flow direction vectors simplify to the same form and are given as,

$$g^{\mathrm{a}}_{ij} = g^{\mathrm{r}}_{ij} = -\frac{1}{\sqrt{3}}\mathrm{sgn}\,(p)\,\delta_{ij},$$

where $\mathrm{sgn}\,(p)$ is the sign of p. The semi-analytical (integrated in a forward Euler fashion) and numerical results are presented in Fig. 4.125.

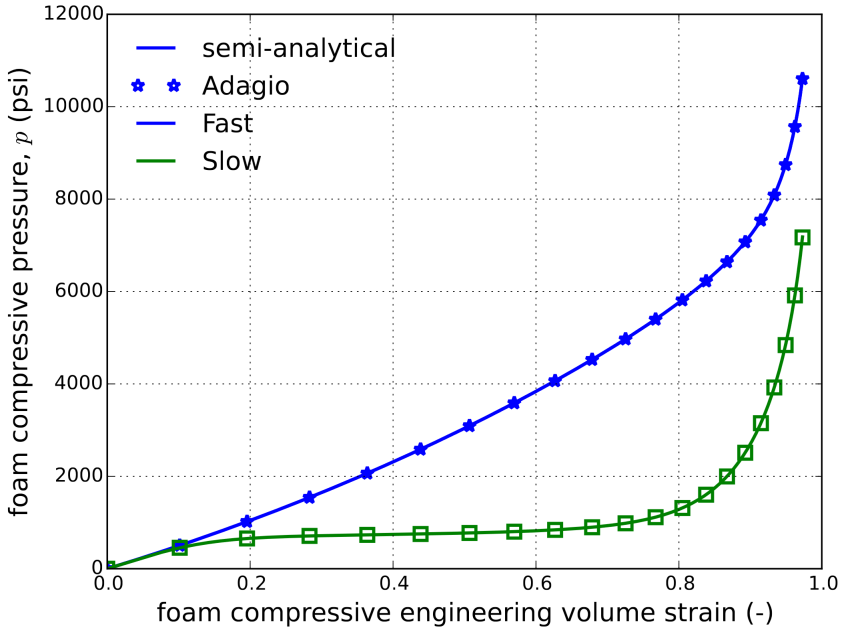

Fig. 4.125 Pressure-engineering volume strain results of viscoplastic foam model subjected to a hydrostatic loading at both fast and slow rates determined semi-analytically and numerically.

4.28.4 User Guide

```
BEGIN PARAMETERS FOR MODEL VISCOPLASTIC_FOAM
  #
  # Elastic constants
  #
  YOUNGS MODULUS = <real>
  POISSONS RATIO = <real>
  SHEAR MODULUS  = <real>
  BULK MODULUS   = <real>
  LAMBDA         = <real>
  TWO MU         = <real>

  FLOW RATE      = <real>
  POWER EXPONENT = <real>
  BETA           = <real> (1.0)
  PHI            = <real>

  SHEAR STRENGTH  = <real> (1.0)
  SHEAR HARDENING = <real> (0.0)
  SHEAR EXPONENT  = <real> (1.0)
  HYDRO STRENGTH  = <real> (1.0)
  HYDRO HARDENING = <real> (0.0)
  HYDRO EXPONENT  = <real> (1.0)

  YOUNGS FUNCTION    = <string>
  POISSONS FUNCTION  = <string>
  SS FUNCTION        = <string>
  SH FUNCTION        = <string>
  HS FUNCTION        = <string>
  HH FUNCTION        = <string>
  RATE FUNCTION      = <string>
  EXPONENT FUNCTION  = <string>
  STIFFNESS FUNCTION = <string>

  SHEAR HARDENING FUNCTION = <string>
  HYDRO HARDENING FUNCTION = <string>
  BETA FUNCTION            = <string>
END [PARAMETERS FOR MODEL VISCOPLASTIC_FOAM]
```

In the above command blocks:

- Since the model requires functions to describe the temperature dependence of the elastic modulus and Poisson's ratio, it is recommended that one inputs these properties at some reference temperature. However, any two of the elastic constants can be used for input.
- The reference value for the flow rate, h, is defined with the `FLOW RATE` command line.

- The reference value of the over-stress exponent, n, is defined with the `POWER EXPONENT` command line.
- The user-defined scalar scaling between associated and radial flow, β, is defined with the `BETA` command line.
- The initial volume fraction of solid material, ϕ_0, is defined with the `PHI` command line.
- The reference value for the shear strength, A_0, is defined with the `SHEAR STRENGTH` command line.
- The reference value for the shear hardening modulus, A_1, is defined with the `SHEAR HARDENING` command line.
- The shear hardening exponent, A_2, is defined with the `SHEAR EXPONENT` command line.
- The reference value for the hydrostatic strength, B_0, is defined with the `HYDRO STRENGTH` command line.
- The reference value for the hydrostatic hardening modulus, B_1, is defined with the `HYDRO HARDENING` command line.
- The hydrostatic hardening exponent, B_2, is defined with the `HYDRO EXPONENT` command line.
- The user-defined and normalized function that gives the elastic modulus as a function of temperature, $h_E(\theta)$, is defined with the `YOUNGS FUNCTION` command line.
- The user-defined and normalized function that gives the Poisson's ratio as a function of temperature, $h_\nu(\theta)$, is defined with the `POISSONS FUNCTION` command line.
- The user-defined and normalized function that gives the shear strength as a function of temperature, $h_{A_0}(\theta)$, is defined with the `SS FUNCTION` command line.
- The user-defined and normalized function that gives the shear hardening modulus as a function of temperature, $h_{A_1}(\theta)$, is defined with the `SH FUNCTION` command line.
- The user-defined and normalized function that gives the hydrostatic strength as a function of temperature, $h_{B_0}(\theta)$, is defined with the `HS FUNCTION` command line.
- The user-defined and normalized function that gives the hydrostatic hardening modulus as a function of temperature, $h_{B_1}(\theta)$, is defined with the `HH FUNCTION` command line.
- The user-defined and normalized function that gives the flow rate as a function of temperature, $h_h(\theta)$, is defined with the `RATE FUNCTION` command line.
- The user-defined and normalized function that gives the over-stress exponent as a function of temperature, $h_n(\theta)$, is defined with the `EXPONENT FUNCTION` command line.
- The user-defined and normalized function that gives the elastic modulus as a function of maximum solid volume fraction, $f_E(\phi)$, is defined with the `STIFFNESS FUNCTION` command line.

- The optional user-defined function that gives the shear strength as a function of the maximum solid volume fraction, $a\,(\phi)$, is defined with the `SHEAR HARDENING FUNCTION` command line. Note, if this function is defined the `SHEAR STRENGTH`, `SHEAR HARDENING`, and `SHEAR EXPONENT` values should not be specified.
- The optional user-defended function that gives the hydrostatic strength as a function of the maximum solid volume fraction, $b\,(\phi)$, is defined with the `HYDRO HARDENING FUNCTION` command line. Note, if this function is defined the `HYDRO STRENGTH`, `HYDRO HARDENING`, and `HYDRO EXPONENT` values should not be specified.
- The optional user-defined function that gives the scaling between associated and radial flow as a function of maximum solid volume fraction, $\beta\,(\phi)$, is defined with the `BETA FUNCTION` command line. Note, if this function is defined the `BETA` value should not be specified.

Output variables available for this model are listed in Table 4.44.

Table 4.44 State Variables for VISCOPLASTIC FOAM Model

Name	Description
`ITER`	number of sub-increments
`EPVOL`	inelastic volumetric strain, $\varepsilon_v^{\mathrm{p}}$
`EDOT`	effective inelastic strain rate, $\dot{\bar{\varepsilon}}^p$
`PHI`	maximum volume fraction of solid material, ϕ
`FA`	shear strength, a
`FB`	hydrostatic strength, b
`STIF`	elastic stiffness as a function of ϕ

4.29 Foam Damage Model

4.29.1 Theory

The foam damage model was developed at Sandia National Laboratories to model the behavior of rigid polyurethane foams under a variety of loading conditions [73]. For instance, temperature, rate, and tension-compression dependencies are all built into this model. This model, leverages previous efforts and experience with other foam models (e.g. low density foam Section 4.26, foam plasticity Section 4.27, and viscoplastic foam Section 4.28). Like those past efforts, this model utilizes an additive decomposition of the strain rates into elastic and inelastic parts,

$$D_{ij} = D_{ij}^{\mathrm{e}} + D_{ij}^{\mathrm{in}}.$$

It is also assumed that the elastic response is linear and isotropic such that the stress rate for isothermal conditions is given by the following equation

$$\overset{\circ}{\sigma}_{ij} = \mathbb{C}_{ijkl} D_{kl}^{\mathrm{e}} = \mathbb{C}_{ijkl} \left(D_{kl} - D_{kl}^{\mathrm{in}} \right),$$

with $\mathbb{C}_{ijkl}$ being the fourth-order, isotropic elasticity tensor. The specific stress rate considered is arbitrary as long as it is object. Two common rates satisfying that constraint are the Jaumann and Green-McInnis rates.

The initial yield surface is assumed to be an ellipsoid about the hydrostat and is described by the function

$$f = \frac{\bar{\sigma}^2}{a^2} + \frac{p^2}{b^2} - 1 = 0, \tag{4.127}$$

where a and b are state variables that define the current deviatoric and volumetric strengths, respectively, of the foam. The von Mises effective stress, $\bar{\sigma}$ is a scalar measure of the deviatoric stress given by

$$\bar{\sigma} = \sqrt{\frac{3}{2} s_{ij} s_{ij}},$$

while p is the pressure, or mean stress, and is defined as

$$p = \frac{1}{3}\sigma_{kk},$$

with σ_{ij} and s_{ij} being the components of the Cauchy and deviatoric stress. This latter tensor may be written as,

$$s_{ij} = \sigma_{ij} - p\delta_{ij},$$

where δ_{ij} are the components of the identity tensor - $\delta_{ij} = 1$ if $i = j$, $\delta_{ij} = 0$ if $i \neq j$.

For this model, the yield function (4.127) is re-written as

$$f = \sigma^* - a = 0$$

with the effective stress, σ^*, being a function of the von Mises effective stress, $\bar{\sigma}$, and the pressure, p, as follows

$$\sigma^* = \sqrt{\bar{\sigma}^2 + \frac{a^2}{b^2} p^2}.$$

Next, using a Perzyna-type formulation, the following expression for the inelastic strain rate, D_{ij}^{in}, is developed

$$D_{ij}^{\text{in}} = \begin{cases} \dot{\bar{\varepsilon}}^p \, g_{ij} = e^h \left(\dfrac{\sigma^*}{a} - 1 \right)^n g_{ij} & \text{if } \dfrac{\sigma^*}{a} - 1 > 0 \\ 0 & \text{if } \dfrac{\sigma^*}{a} - 1 \leq 0, \end{cases}$$

where g_{ij} are the components of a symmetric, second-order tensor that defines the orientation of the inelastic flow. This type of model is sometimes referred to as an over-stress model because the

inelastic rate is a function of the over-stress - the distance outside the yield surface. For associated flow, g_{ij} is simply normal to the yield surface and is given by

$$g_{ij}^{\mathrm{a}} = \frac{\dfrac{\partial f}{\partial \sigma_{ij}}}{\left|\dfrac{\partial f}{\partial \sigma_{kl}}\right|} = \frac{\dfrac{3}{a^2} s_{ij} + \dfrac{2}{3b^2} p\, \delta_{ij}}{\left|\dfrac{3}{a^2} s_{kl} + \dfrac{2}{3b^2} p\, \delta_{kl}\right|}. \tag{4.128}$$

When lower density foams are subjected to a simple load path like uniaxial compression, the inelastic flow direction at moderate strains appears nearly uniaxial. In other words, the flow direction is given by the normalized stress tensor as follows

$$g_{ij}^{\mathrm{r}} = \frac{\sigma_{ij}}{|\sigma_{kl}|}.$$

This type of flow is called radial flow. The foam damage model has another parameter, β, which allows for the flow direction to be prescribed as a linear combination of associated and radial flow such that,

$$g_{ij} = \frac{(1-\beta)\, g_{ij}^{\mathrm{a}} + \beta\, g_{ij}^{\mathrm{r}}}{\left|(1-\beta)\, g_{kl}^{\mathrm{a}} + \beta\, g_{kl}^{\mathrm{r}}\right|}. \tag{4.129}$$

Rigid polyurethane foams have little ductility when they are subjected to tensile stress. For this loading case, the materials behave more like brittle materials and even for uniaxial compression the foams often show cracking at large strains.

The damage surfaces for the foam damage model are simply three orthogonal planes with the normals given by the positive principal stress axes. The damage surfaces are given by the following equation

$$f_{\mathrm{dam}}^{i} = \hat{\sigma}^{i} - c\,(1-w)\,, \quad ; \quad i = 1, 2, 3$$

where $\hat{\sigma}^{i}$ is a principal stress, c is the initial tensile strength which is a material parameter, and w is a scalar measure of the damage. As damage occurs, the damage surface will collapse toward the origin and the foam will lose tensile strength. The foam will, however, still have compressive strength.

Damage is taken to be a positive, monotonically increasing function of the damage strain, $\varepsilon_{\mathrm{dam}}$, and the damage strain is a function of the maximum principal strain, $\varepsilon_{\mathrm{max}}$, and the plastic volume strain, $\varepsilon_{v}^{\mathrm{p}}$, such that

$$w = w\,(\varepsilon_{\mathrm{dam}}) \quad ; \quad \varepsilon_{\mathrm{dam}} = a_{\mathrm{dam}} \varepsilon_{\mathrm{max}} + b_{\mathrm{dam}} \varepsilon_{v}^{\mathrm{p}},$$

with the material parameters a_{dam} and b_{dam} controlling the rate at which damage is generated in tension and compression, respectively. The model does not allow healing, so the damage never decreases even if the damage strain decreases.

To fully capture temperature, strain rate, and lock-up effects, several material parameters are defined as functions of temperature, θ, and/or some measure of the amount of compaction, e.g.

the maximum volume fraction of the solid material obtained during any prior loading, ϕ. For instance,

$$E\left(\theta,\phi\right) = E\, h_E\left(\theta\right)\; f_E\left(\phi\right),$$

$$\nu\left(\theta,\phi\right) = \nu\, h_\nu\left(\theta\right)\; f_\nu\left(\phi\right),$$

and the natural logarithm of the reference flow rate, h, and the power law exponent, n are also functions of temperature

$$h\left(\theta\right) = h\, h_h\left(\theta\right)$$

$$n\left(\theta\right) = n\, h_n\left(\theta\right).$$

The current deviatoric and volumetric strengths are hardening functions of the maximum volume fraction of the solid material obtained during any prior loading, ϕ, as is the parameter that defines the fraction of associated and radial flow, β. Therefore,

$$a = a\left(\phi\right) \quad ; \quad b = b\left(\phi\right)$$

$$\beta = \beta\left(\phi\right).$$

Through the loading cycle, the maximum volume fraction of solid material is written as,

$$\phi = \max_{t>0} \tilde{\phi}\left(t\right)$$

where $\tilde{\phi}\left(t\right)$ is the current volume faction of solid material defined as

$$\tilde{\phi}\left(t\right) = \frac{\phi_0}{\exp\left(\varepsilon_v^{\mathrm{p}}\right)},$$

with ϕ_0 and $\varepsilon_v^{\mathrm{p}}$ being the initial solid volume fraction and plastic volumetric strain, respectively.

The foam damage model, as presented, provides a phenomenological model with enough flexibility to model the observed deformation and failure of rigid polyurethane foams.

4.29.2 Implementation

Like the other foam models, the foam damage model is integrated using an explicit forward Euler scheme. Essentially, this specific form is a combination of a rate-dependent viscoplastic mechanism and a distinct damage element. At the highest level, these two responses are considered independently and sequentially with the viscoplastic behavior being evaluated first. Initially, the damage parameter is set to 0 and is limited to a maximum value of 0.99 to prevent the tensile strength from going to zero or negative due to numerical round-off. Foam material elements that are completely damaged can be removed using element death based approaches in

the case of the damage variable reaching a value close to 1, say 0.99. This topic, however, will not be discussed here as the focus is on the constitutive behavior of the foam model.

To ensure integration stability, an allowable strain increment is first calculated so that a critical time step may be found. Essentially, such a maximum is given by the ratio of shear strength to elastic modulus. If the input time step is sufficiently small to meet this requirement, the material state at time $t = t_{n+1}$ is calculated directly. For unsuitably large time steps, a series of sub-increments are used such that the integration may proceed in a stable fashion. Specifically, a total time step of Δt is subdivided into N sub-increments with the k^{th} such sub-increment having a time interval of δt^k so that $\Delta t = \sum_{k=1}^{N} \delta t^k$. In this case, the same forward Euler scheme is used to integrate successively over the sub-increments. For temperature dependent properties (e.g. the power law exponent n), the value at the start of the sub-increment is determined by linearly interpolating over the total time step,

$$n^k = n_n + \frac{\Delta t^k}{\Delta t}\left(n_{n+1} - n_n\right),$$

with Δt^k begin the current sub-increment time step, $\Delta t^k = \sum_{r=1}^{k} \delta t^r$. For simplicity, in the remainder of this section it is assumed that the input time step is acceptable and only a single increment is needed. If additional sub-increments are needed, the below steps would be repeated N times with time intervals of δt^k.

The rate-dependent plastic response is then calculated in a fashion very similar to that of the viscoplastic foam model (Section 4.28.2). The key differences are primarily the additional, and more complex, dependencies of ν, β, a, and b on the solid volume fraction. As such, first the various material properties and model parameters that are dependent on temperature, θ, or solid volume fraction, ϕ, are determined based on the respective values at $t = t_n$. The effective plastic strain rate, $\dot{\bar{\varepsilon}}^p$, is readily found as,

$$\dot{\bar{\varepsilon}}^p = e^{h(\theta_n)}\left\langle \frac{\sigma_n^*}{a\left(\phi_n\right)} - 1 \right\rangle^{n(\theta_n)},$$

where σ_n^* is given by,

$$\sigma_n^* = \sqrt{\bar{\sigma}_n^2 + \frac{a^2\left(\phi_n\right)}{b^2\left(\phi_n\right)} p_n^2},$$

and $\langle x \rangle$ are the Macaulay brackets evaluated as,

$$\langle x \rangle = \begin{cases} x, & x \geq 0 \\ 0, & x < 0 \end{cases}.$$

Knowing the effective plastic strain increment, corresponding stress increments may be determined. Specifically, the rates of change of the deviatoric stress, $\dot{s}_{ij}$, and pressure, $\dot{p}$, are given for isothermal conditions by

$$\dot{s}_{ij} = 2\mu_n\left(\hat{d}_{ij} - \hat{d}_{ij}^{\mathrm{p}}\right),$$
$$\dot{p} = K_n\left(d_{kk} - d_{kk}^{\mathrm{p}}\right),$$

with d_{ij} and d_{ij}^{p} being the the total and plastic, respectively, rates of deformation, and the symbol $\hat{x}_{ij}$ denoting the deviatoric part of the tensor x_{ij}. The plastic strain rate is given by,

$$d_{ij}^{\mathrm{p}} = \dot{\varepsilon}^{p} g_{ij}^{n},$$

where g_{ij}^{n} is evaluated via relation (4.128)-(4.129) using state variable at time $t = t_n$ and it is noted that $\beta = \beta(\phi_n)$. Elastic constants K_n and μ_n are found through isotropic relations using the values E_n and ν_n so the temperature and solid volume fraction dependencies may be incorporated.

Therefore, after accounting for plastic deformation and any associated temperature changes,

$$\begin{aligned}
\tilde{s}_{ij} &= \frac{\mu_{n+1}}{\mu_n} s_{ij}^{n} + \dot{s}_{ij}\Delta t, \\
\tilde{p}_{ij} &= \frac{K_{n+1}}{K_n} p^{n} + \dot{p}\Delta t, \\
\tilde{T}_{ij} &= \tilde{s}_{ij} + \tilde{p}\delta_{ij},
\end{aligned}$$

where the tilde, $\tilde{x}$, is used to distinguish the fact that the damage response has not yet been evaluated and these are temporary variables. Updated expressions for the state variables are also given as,

$$\begin{aligned}
\varepsilon_{v}^{\mathrm{p}-n+1} &= \varepsilon_{v}^{\mathrm{p}-n} + d_{kk}^{\mathrm{p}}\Delta t, \\
\phi_{n+1} &= \max\left[\frac{\phi_0}{\exp\left(\varepsilon_{v}^{\mathrm{p}-n+1}\right)}, \phi_n\right].
\end{aligned}$$

With the plastic deformations determined, the damage state of the material is evaluated. As a first step, the eigenvalues, $\hat{\sigma}^{i}$, and vectors, $\hat{e}_{i}^{k}$ (where k denotes the corresponding eigenvalue) of the stress state, $\tilde{T}_{ij}$, and eigenvalues, ε_i of the total strain state are determined. Of particular interest is the maximum eigenvalue of the strain tensor, $\varepsilon_{\max}$. The damage strain, $\varepsilon_{\mathrm{dam}}^{n+1}$, is

$$\varepsilon_{\mathrm{dam}}^{n+1} = \left\langle a_{\mathrm{dam}}\varepsilon_{\max} + b_{\mathrm{dam}}\varepsilon_{v}^{\mathrm{p}-n+1} \right\rangle,$$

with $\langle\rangle$ being Macaulay brackets. This value of the damage strain is then used to evaluate the current value of the damage, w^{n+1}, and a check is also imposed to insure that the damage does not decrease. An effective tensile strength, σ^{dam}, may then be calculated as

$$\sigma^{\mathrm{dam}} = c\left(1 - w^{n+1}\right),$$

leading to a damage surface of the form,

$$f_{\mathrm{dam}}^{i} = \hat{\sigma}^{i} - \sigma^{\mathrm{dam}}.$$

The eigenvalues of the updated stress tensor may be written as,

$$\hat{\sigma}_{n+1}^{i} = \begin{cases} \hat{\sigma}^{i}, & f_{\mathrm{dam}}^{i} \leq 0 \\ \sigma^{\mathrm{dam}}, & f_{\mathrm{dam}}^{i} > 0 \end{cases},$$

producing a final updated stress state of the form,

$$T_{ij}^{n+1} = \sum_{k=1}^{3} \hat{\sigma}_{n+1}^{k} \hat{e}_{i}^{k} \hat{e}_{j}^{k}.$$

4.29.3 Verification

Given the complexity and variety of response and features of the foam damage model, a series of verification analyses are performed. Common material properties and model parameters used for these investigations are given in Table 4.45. For these initial studies, isothermal loadings are considered and the solid volume fraction dependence of the elastic properties is neglected ($f_E(\phi) = 1,\ f_\nu(\phi) = 1$). Properties used correspond to those of a FR3712 foam from [73]. In the case of the elastic modulus, flow rate, and exponent, the values correspond those at a temperature of 18.30°C.

Table 4.45 Common material properties and model parameters for the foam damage model used during verification testing.

E	9,240 psi	c	280 psi
ν	0.25	a_{dam}	1.0
h	2.60	b_{dam}	0.55
n	14.0	ϕ_0	0.160

The shear strength, hydrostatic strength, and damage function all require user defined functional forms. For purposes of these tests, simple linear forms are considered for use in the analytical evaluations. Using the data same FR3712 data as before, simplified expressions of the form,

$$\begin{aligned} a(\phi) &= 160 + 2400\phi, \\ b(\phi) &= 160 + 3266.67\phi, \\ w(\varepsilon_{\text{dam}}) &= \frac{10}{3}\varepsilon_{\text{dam}}, \end{aligned}$$

are considered.

4.29.3.1 Uniaxial Compression

First, the behavior of the model subject to a uniaxial compression load is considered. As the loading is purely compressive, no tensile stress is generated and the damage surface is not violated. Therefore, only the rate-dependent plasticity is considered in this section. Given the rate-dependent nature, no analytical solution is readily available and and a semi-analytical approach is developed by specializing the equations to uniaxial compression. Additionally, it is noted that the flow parameter, β, is not specified above and is enabled in this model to be an user-defined function of the solid volume fraction ϕ. Here, to isolate the impact of this parameter, the two extreme cases are considered – fully associated or radial flow with $\beta = 0,\ 1$, respectively.

To induce the uniaxial stress state of interest, a displacement of the form $u_1 = \lambda_1$ is applied while the remaining degrees of freedom (2 and 3) are left traction free. The applied displacement scales linearly from $\lambda_1 = 0$ at $t = 0.0$ to $\lambda_1 = -0.7$ at $t = 1.0$. In this case, the stress state is simply

$\sigma_{ij} = \sigma_{11}\delta_{i1}\delta_{j1}$ leading to an overstress of the form $\sigma^* = |\sigma_{11}|\sqrt{1 + \frac{a^2}{9b^2}}$. For both associated and radial flow, the inelastic flow rate simplifies to,

$$D_{ij}^{\text{in}} = e^h \left\langle \frac{|\sigma_{11}|}{3ab}\sqrt{a^2 + 9b^2} - 1 \right\rangle^n g_{ij},$$

with $\langle\cdot\rangle$ being Macaulay brackets. The total strains may then be written as,

$$\begin{aligned} \varepsilon_{11} &= \ln\left(1 + \lambda_1\right), \\ \varepsilon_{22} = \varepsilon_{33} &= -\nu\left(\ln\left(1 + \lambda_1\right) - \varepsilon_{11}^{\text{in}}\right) + \varepsilon_{22}^{\text{in}}, \end{aligned}$$

where $\varepsilon_{ij}^{\text{in}} = \int_0^t D_{ij}^{\text{in}} d\tau$. The associated and radial flow cases are distinguished by the form of g_{ij}. In the latter case, g_{ij} reduces simply to $g_{ij}^{\text{r}} = \delta_{i1}\delta_{j1}$. The former case, on the other hand, produces a flow direction of the form,

$$\begin{aligned} \hat{g} &= \frac{1}{3\sqrt{\frac{2}{3}\left(2a^4 + 81b^4\right)}}, \\ g_{11}^{\text{r}} &= \hat{g}2\left(a^2 + 9b^2\right), \\ g_{22}^{\text{r}} = g_{33}^{\text{r}} &= \hat{g}\left(2a^2 - 9b^2\right). \end{aligned}$$

The stress evolution for both of these flow cases determined numerically (adagio) and semi-analytically is presented in Fig. 4.126.

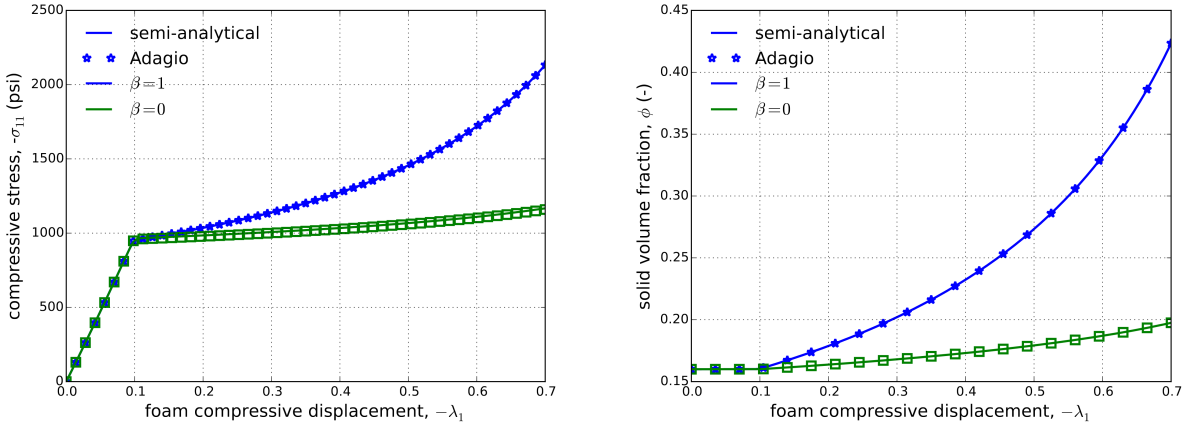

(a) Axial stress **(b) Solid volume fraction**

Fig. 4.126 Axial stress (a) and maximum solid volume fraction (b), ϕ, evolution obtained as a function of applied compressive displacement and determined via the foam damage model considering both associated ($\beta = 0$) and radial($\beta = 1$) flow assumptions semi-analytically and numerically.

From these results, the impact of the flow direction choice can be observed to have a large impact on the model response. Specifically, in the radial case more substantial hardening is seen throughout the entire plastic domain. As the hardening results from the solid volume fraction

(which is a function of volumetric plastic deformation), such a difference may be anticipated. Specifically, given the uniaxial plastic flow in the radial case more pronounced volumetric strains are to be expected. The associated case, on the other hand, has a more deviatoric character leading to lower plastic volume strains. This difference may also be more readily observed in the total strain evolutions of the associated and radial cases in Fig. 4.127(a) and Fig. 4.127(b), respectively.

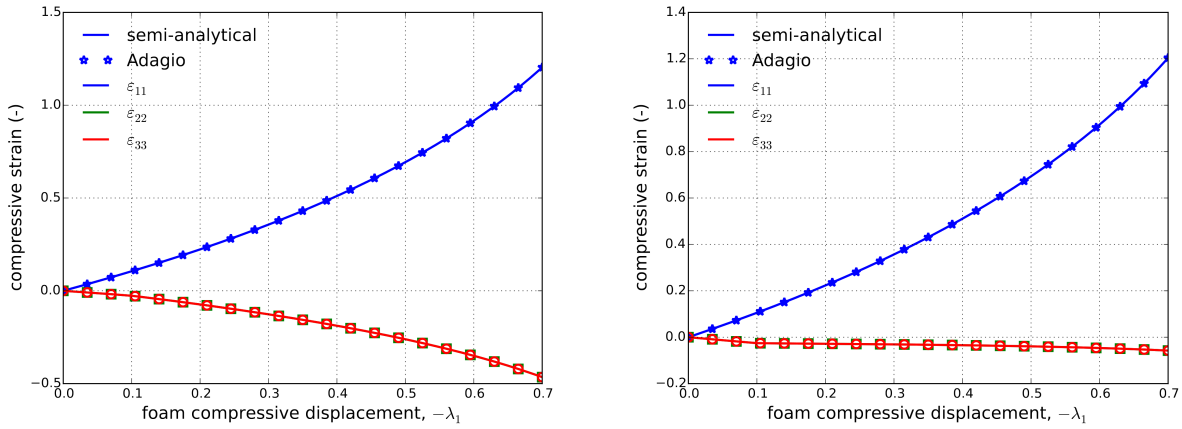

(a) Associated Flow, beta=0 **(b) Radial Flow, beta=1**

Fig. 4.127 Diagon strain evolution through a uniaxial displacement loading of the foam damage model considering (a) associated ($\beta = 0$) and (b) radial ($\beta = 1$) flow determined semi-analytically and numerically.

Specifically, in the radial case, only small off-axis strains are observed while in the associated results much more substantial strains are noted. This difference produces a large impact on the plastic volumetric strain and therefore on the maximum solid volume fraction, ϕ, whose evolution through loading in both cases is presented in Fig. 4.127. To emphasize this point, the radial solid volume fraction is more than double the associated case at the end of loading.

4.29.3.2 Uniaxial Tension

As the compressive and tensile behaviors of the model are different (due to the activation of the damage mechanism), the uniaxial tensile response is also investigated. To this end, a uniaxial displacement is applied, $u_1 = \lambda_1$, while the other off-axis components are kept traction free. For this test, the maximum displacement ($\lambda_1 = 0.2$) is applied linearly from $t = 0.0$ to $t = 1.0$. Use of a displacement condition is essential due to the expected stress degradation. In this case, given the relative values of the strength (a (ϕ_0) versus c) it is clear that no plastic deformations will take place and a purely damage driven response is expected. With this simplification, it is also noted that the rate-dependency of the problem is eliminated. As the stress state is uniaxial, it is clear that the only non-zero eigenvalue of the stress tensor is σ_{11} and that $\varepsilon_{\text{dam}} = a_{\text{dam}}\varepsilon_{11} = a_{\text{dam}} \ln(1 + \lambda_1)$ where the fact that the plastic strain is zero is utilized. Bearing these simplifications in mind, an analytical expression for the stress and strain may be developed. The stress in the axial direction

may be written as,

$$\sigma_{11} = \begin{cases} (\mathbb{C}_{1111} - 2\nu\mathbb{C}_{1122}) \ln(1+\lambda_1), & \lambda_1 < \lambda_{\text{crit}} \\ c\left(1 - \frac{10}{3} a_{\text{dam}} \ln(1+\lambda_1)\right), & \lambda_1 \geq \lambda_{\text{crit}} \end{cases},$$

where

$$\lambda_{\text{crit}} = \exp\left(\frac{c}{\mathbb{C}_{1111} - 2\nu\mathbb{C}_{1122} + \frac{10}{3} a_{\text{dam}} c}\right) - 1.$$

The analytical results along with numerical simulations from adagio are given below in Fig. 4.128.

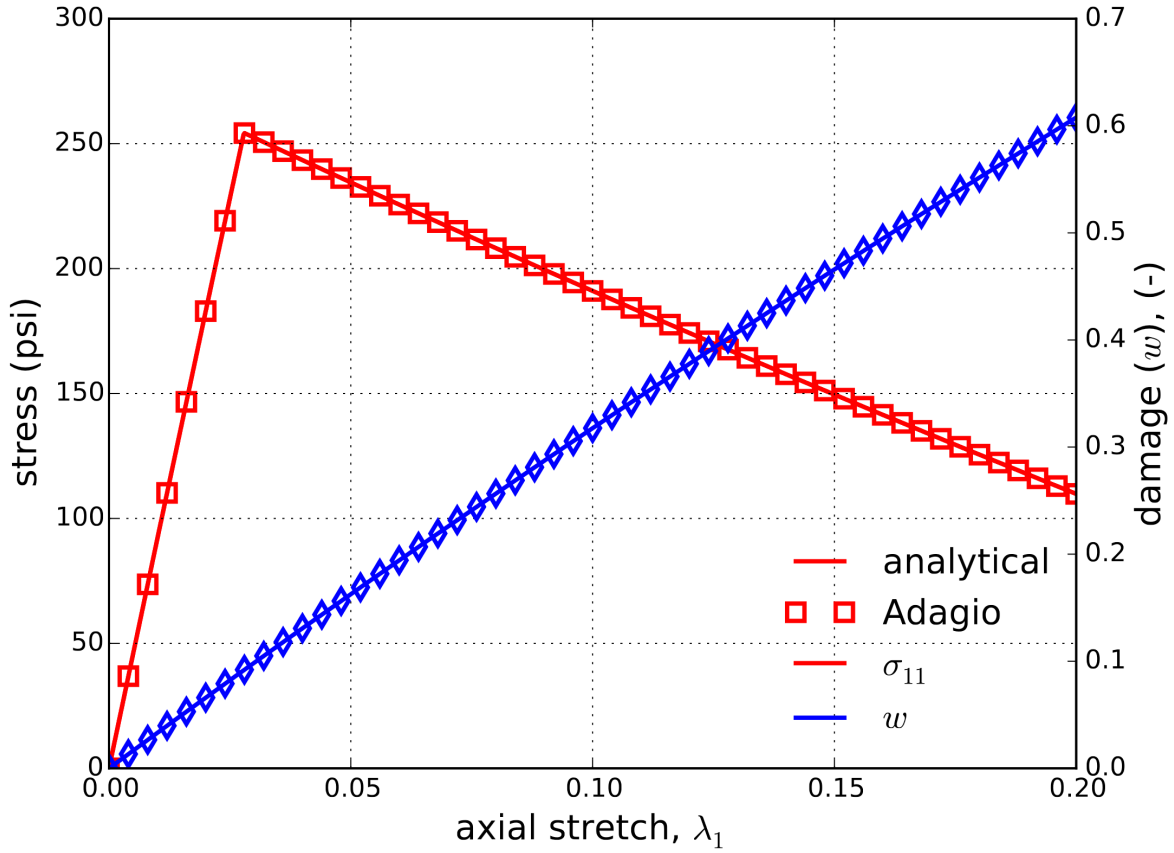

Fig. 4.128 Response of the foam damage model through a uniaxial stress, displacement controlled tension simulation. Stress in the loading direction, σ_{11}, and damage measure, w, against the applied displacement, λ_1, are shown.

4.29.3.3 Hydrostatic Compression

To consider the pressure dependence, the response of this model subject to a hydrostatic compression loading is determined. Specifically, a displacement of the form $u_i = \lambda(t)$ is considered. The applied displacement scales linearly from $\lambda = 0$ at $t = 0.0$ to $\lambda = -0.7$ at $t = t_{\max}$. Two cases are considered to incorporate rate-dependent effects into the analysis. The two tests are denoted fast and slow and are distinguished via $t_{\max}$ values of 1.0 and 100.0, respectively. With this displacement field the engineering volume strain, ε_{V}, is simply $\varepsilon_{\mathrm{V}} = (1+\lambda)^3 - 1$. The stress state reduces trivially to $\sigma_{ij} = -p\delta_{ij}$ and the corresponding (repeated) eigenvalue is compressive. Therefore, damage does not play a role in this analysis.

No direct analytical solution to this problem is readily obtainable. Therefore, a semi-analytical analysis is used. Reducing the foam damage model for the loading described in this section leads to an expression for the overstess of,

$$\sigma^* = \frac{a}{b}|p|,$$

where the fact that $s_{ij} = 0$ is leveraged. Additionally, given this stress state, β becomes an unnecessary parameter as,

$$g_{ij} = g^{\mathrm{a}}_{ij} = g^{\mathrm{r}}_{ij} = -\frac{1}{\sqrt{3}}\mathrm{sgn}(p)\,\delta_{ij},$$

with $\mathrm{sgn}(p)$ being the sign of p. Both the numerical (adagio) and semi-analytical (evaluated in a forward Euler fashion) results are presented in Fig. 4.129.

4.29.3.4 Hydrostatic Tension

A tensile hydrostatic loading provides an interesting possibility for investigating the damage response. Specifically, with the model parameters defined above the damage tensile strength is always less than the hydrostatic strength - $c < b(\phi_0)$. Additionally, given the tensile loading $\phi(t) = \phi_0$ and no plastic deformation occurs. This also removes the rate-dependency form the model enabling an analytical solution to be obtained.

Through a hydrostatic loading, the only stress eigenvalue is $-p$ (noting the convention of p positive in compression) and the corresponding strain eigenvalue is $\varepsilon_{\max} = \ln(1+\lambda)$. As no plastic deformation is occurring, the damage is simply a function of the deformation and is given by,

$$w(\varepsilon_{\mathrm{dam}}) = w(\lambda) = \frac{10}{3}a_{\mathrm{dam}}\ln(1+\lambda).$$

The pressure is then simply given as,

$$p = \begin{cases} 3K\ln(1+\lambda) & \lambda < \lambda_{\mathrm{crit}} \\ c\left(1 - \frac{10}{3}a\ln(1+\lambda)\right) & \lambda \geq \lambda_{\mathrm{crit}} \end{cases},$$

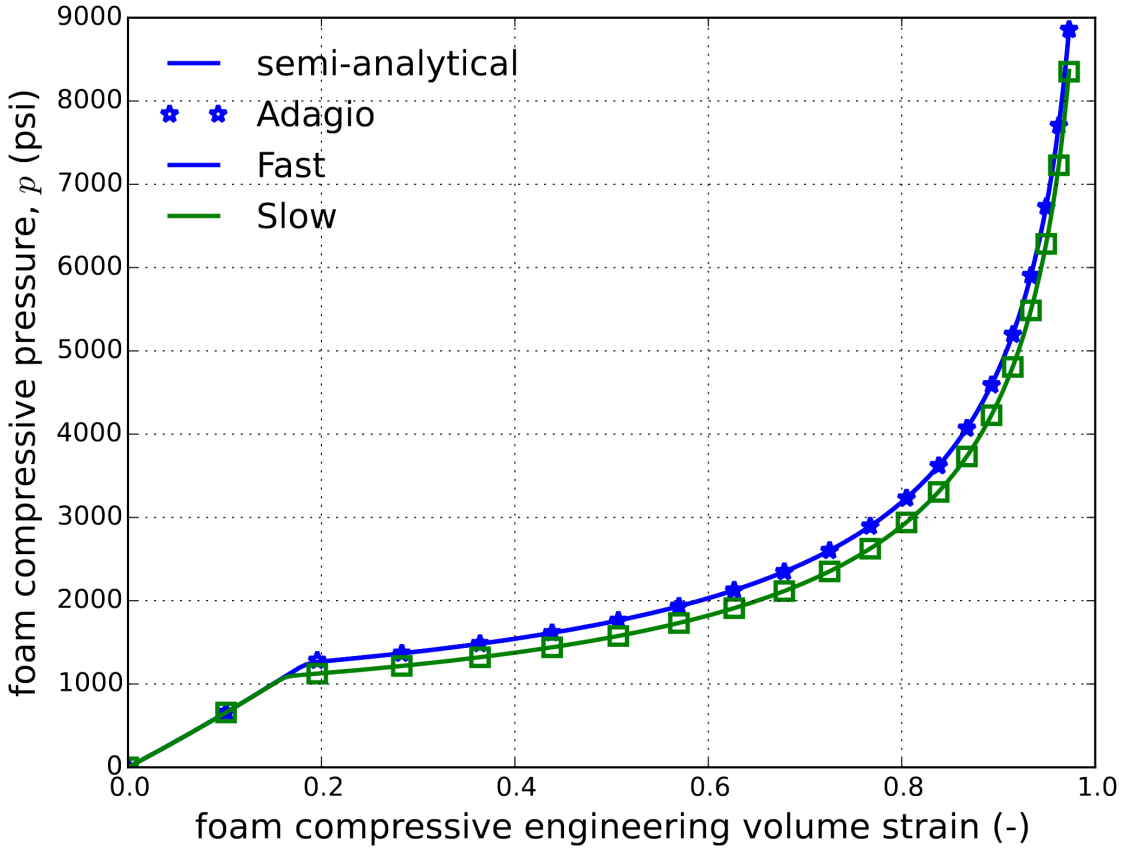

Fig. 4.129 Pressure-engineering volume strain results of the foam damage model subjected to a hydrostatic loading at both fast and slow rates determined semi-analytically and numerically.

where,

$$\lambda_{\text{crit}} = \exp\left(\frac{3c}{9K + 10c}\right) - 1.$$

In the preceding relations, the fact that $\varepsilon_{\text{dam}} = a\varepsilon_{\max}$ is used. The analytical and numerical results are given below for a loading of $\lambda = 0$ to $\lambda = 0.2$ through the time period $t = [0, 1]$ in Fig. 4.130.

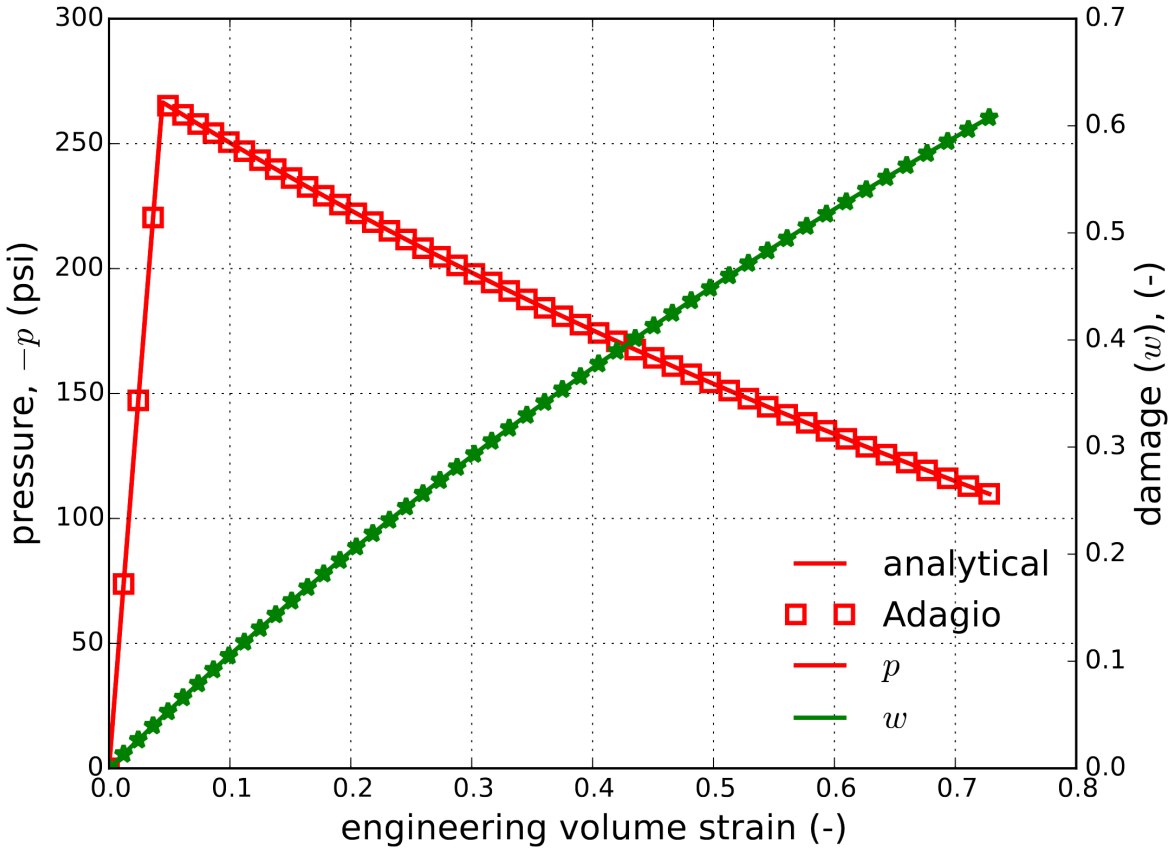

Fig. 4.130 Pressure and damage evolutions as function of engineering volume strain results of the foam damage model subject to a tensile hydrostatic loading determined analytically and numerically. Note, conventionally with this model pressure is defined positive in compression.

4.29.4 User Guide

```
BEGIN PARAMETERS FOR MODEL FOAM_DAMAGE
  #
  # Elastic constants
  #
```

(continues on next page)

(continued from previous page)

```
  YOUNGS MODULUS = <real>
  POISSONS RATIO = <real>
  SHEAR MODULUS  = <real>
  BULK MODULUS   = <real>
  LAMBDA         = <real>
  TWO MU         = <real>
  #
  # Yield behavior
  #
  PHI                = <real>
  FLOW RATE          = <real>
  POWER EXPONENT     = <real>
  TENSILE STRENGTH   = <real>
  ADAM               = <real>
  BDAM               = <real>
  #
  # Functions
  #
  YOUNGS FUNCTION           = <string>
  POISSONS FUNCTION         = <string>
  RATE FUNCTION             = <string>
  EXPONENT FUNCTION         = <string>
  SHEAR HARDENING FUNCTION = <string>
  HYDRO HARDENING FUNCTION = <string>
  BETA FUNCTION             = <string>
  YOUNGS PHI FUNCTION       = <string>
  POISSONS PHI FUNCTION     = <string>
  DAMAGE FUNCTION           = <string>
END [PARAMETERS FOR FOAM_DAMAGE]
```

Output variables available for this model are listed in Table 4.46. For information about the foam damage model, consult [73].

Table 4.46 State Variables for FOAM DAMAGE Model

Name	Description
ITER	number of sub-increments taken in subroutine
EPVOL	plastic volume strain
PHI	maximum volume fraction of solid material
EQPS	equivalent plastic strain
FA	shear strength - a
FB	hydrostatic strength - b
DAMAGE	damage
EMAX	maximum tensile strain
PWORK	plastic work rate

4.30 Orthotropic Crush Model

4.30.1 Theory

The orthotropic crush model in LAMÉ is designed to model the energy absorbing capability of crushable orthotropic materials, e.g. aluminum honeycomb, and is empirically based. The formulation follows that used for metallic honeycomb materials in LS-DYNA [111]. Three response regimes are assumed for this material: (*i*) orthotropic elastic, (*ii*) crush, and (*iii*) complete compaction (fully crushed). During the elastic regime, the model exhibits the response of an elastic, orthotropic material with *all Poisson's ratio equal to zero*. After full compaction, the response is taken to be that of an isotropic, perfectly plastic material and the response between these two stages is tailored to smoothly transition between the two extremes. Crushing, incorporating both nonlinear elastic and plastic-like behaviors, is taken to begin as soon as volumetric contraction is noted ($J = \det\left(F_{ij}\right) < 1$). As such, the purely elastic response is primarily seen during cyclic loadings in which the material is unloaded. An internal state variable, J_c, is introduced to track the crushed state of the material and is defined as the minimum J over the entire deformation history such that,

$$J_c = \min_{t>0} \left[J\left(t\right)\right] .$$

The crushing process manifests through two distinct behaviors: (*i*) the elastic properties scale linearly with the crush state from the initial orthotropic state to the of the final isotropic completely compacted material; and (*ii*) a plastic-like response is observed associated with corresponding crush curves (analogous to hardening curves).

Before complete compaction, the incremental constitutive relation may be written in terms of the rate of deformation tensor, D_{ij}, as,

$$\begin{Bmatrix} \overset{\circ}{\sigma}_{11} \\ \overset{\circ}{\sigma}_{22} \\ \overset{\circ}{\sigma}_{33} \\ \overset{\circ}{\sigma}_{12} \\ \overset{\circ}{\sigma}_{23} \\ \overset{\circ}{\sigma}_{31} \end{Bmatrix} = \begin{bmatrix} \hat{E}_{11} & 0 & 0 & 0 & 0 & 0 \\ 0 & \hat{E}_{22} & 0 & 0 & 0 & 0 \\ 0 & 0 & \hat{E}_{33} & 0 & 0 & 0 \\ 0 & 0 & 0 & 2\hat{G}_{12} & 0 & 0 \\ 0 & 0 & 0 & 0 & 2\hat{G}_{23} & 0 \\ 0 & 0 & 0 & 0 & 0 & 2\hat{G}_{31} \end{bmatrix} \begin{Bmatrix} D_{11} \\ D_{22} \\ D_{33} \\ D_{12} \\ D_{23} \\ D_{31} \end{Bmatrix} \tag{4.130}$$

where $\hat{E}_{11}$, $\hat{E}_{22}$, and $\hat{E}_{33}$ are the normal stiffness and $\hat{G}_{12}$, $\hat{G}_{23}$, and $\hat{G}_{31}$ are the shear stiffness. A clear decoupling between the different directional components is evident in (4.130). All six stiffness components are assumed to be functions of the current compaction level which may be defined as $1 - J_c$ and the evolution of these terms is responsible for crushing behavior ($*i*$) alluded to previously.

The functional forms of the stiffness are given by,

$$\begin{aligned} \hat{E}_\beta &= E_\beta + \alpha\left(E - E_\beta\right) && \beta = 11,\ 22,\ 33 \\ \hat{G}_\gamma &= G_\gamma + \alpha\left(G - G_\gamma\right) && \gamma = 12,\ 23,\ 31, \end{aligned}$$

where E and G are the Young's and shear moduli, respectively, of the fully compacted material while E_β and G_γ are the input orthotropic elastic stiffness components of the virgin, uncompacted material. It is assumed that these stiffness vary linearly between the pre- and post-compacted material such that,

$$\alpha = \frac{(1 - J_c)}{V_{min}},$$

with V_{min} being the minimum relative volume (or maximum compaction).

With respect to the second behavior observed during crushing, a plastic-like response governed by crush curves is observed. Given the decoupling between the different stresses and deformations, a crush curve needs to be defined for each of the six normal and shear stresses. An example of such a curve is presented in Fig. 4.131, and three distinct regions are evident. Initially, at low compaction levels, a plateau is observed. This plateau is essentially an initial crush strength and prior to this stress level all nonlinear deformations associated with material compaction manifest through changes in the respective moduli. When the stress reaches the specified levels, however, the curves play a role analogous to the hardening curve and the material stress follows the curve. Physically, the plateau is associated with crushing the internal honeycomb or foam structure of the material. As the material approaches full compaction and microstructural contact effects become important, a sharp rise in the stress is noted (see $\approx 0.6 \leq 1 - J_c \leq 0.7 = V_{min}$ in Fig. 4.131). After complete compaction another plateau corresponding to perfect plasticity is evident.

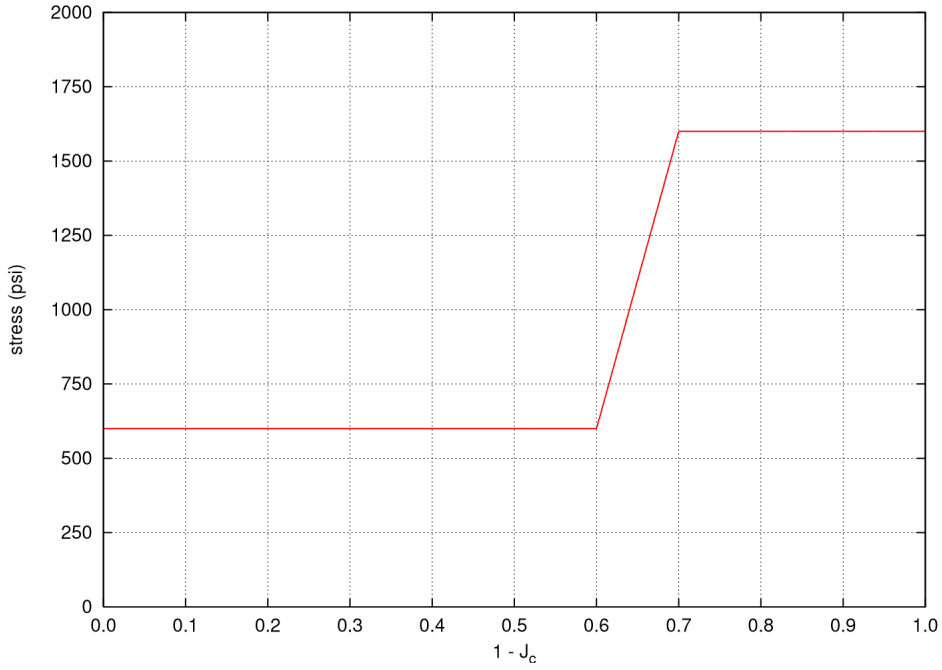

Fig. 4.131 An example of an input crush curve for an aluminum honeycomb.

Above some value of compaction ($1 - J_c = V_{min}$), the material will be fully compacted and behave as an elastic, perfectly plastic material. The fully compacted response is given by the Young's modulus, E, Poisson's ratio, ν, and the yield stress, σ_y. Details of this response may be found in previous sections on the various elastic-plastic models (e.g. Section 4.7.1).

4.30.2 Implementation

Implementation of the orthotropic crush model involves addressing two cases: before and after complete compaction. When the material is fully crushed, the model reduces to that of an isotropic perfectly plastic response. As corresponding isotropic elastic-plastic models with various hardenings have been extensively explored in prior sections, this response will not be discussed here and the reader is referred to those sections (e.g. Section 4.7.2). The two cases are distinguished by the previous compaction state variable, J_c^n, where $J_c^{n+1} = \min\left[J_c^n, J^{n+1}\right]$ with $J^{n+1} = \det\left(F_{ij}^{n+1}\right) = \det\left(V_{ij}^{n+1}\right)$. If $J_c^n > 1 - V_{min}$, the material has not yet fully crushed and the response is evaluated as discussed in the following.

To determine the material state prior to complete compaction, the current values of orthogonal stiffness must be determined via (4.131) noting

$$\alpha^{n+1} = \frac{1 - J_c^n}{V_{min}}.$$

By assuming completely elastic deformation, trial stresses may then be computed as,

$$\begin{aligned}
\sigma_{11}^{tr} &= \sigma_{11}^n + \Delta t \hat{E}_{11}\left(\alpha^{n+1}\right) d_{11}^{n+1}, \\
\sigma_{22}^{tr} &= \sigma_{22}^n + \Delta t \hat{E}_{22}\left(\alpha^{n+1}\right) d_{22}^{n+1}, \\
\sigma_{33}^{tr} &= \sigma_{33}^n + \Delta t \hat{E}_{33}\left(\alpha^{n+1}\right) d_{33}^{n+1}, \\
\sigma_{12}^{tr} &= \sigma_{12}^n + 2\Delta t \hat{G}_{12}\left(\alpha^{n+1}\right) d_{12}^{n+1}, \\
\sigma_{23}^{tr} &= \sigma_{23}^n + 2\Delta t \hat{G}_{23}\left(\alpha^{n+1}\right) d_{23}^{n+1}, \\
\sigma_{31}^{tr} &= \sigma_{31}^n + 2\Delta t \hat{G}_{31}\left(\alpha^{n+1}\right) d_{31}^{n+1},
\end{aligned}$$

with d_{ij}^{n+1} being the unrotated rate of deformation tensor. Given the decoupling between the different stress components, the various trial stresses are considered individually. Specifically, each trial stress must be compared to the crush stress for the current compaction level. Denoting $\sigma_\beta^{crush} = \hat{\sigma}_\beta\left(1 - J_c^{n+1}\right)$ (with $\beta = 11,\ 22,\ 33,\ 12,\ 23,$ or 31) to be the current crush stress specified by the crush curve, the current stress of interest is,

$$\sigma_\beta^{n+1} = \begin{cases} \sigma_\beta^{tr}, & |\sigma_\beta^{tr}| \le \sigma_\beta^{crush} \\ \operatorname{sgn}\left(\sigma_\beta^{tr}\right)\sigma_\beta^{crush}, & |\sigma_\beta^{tr}| > \sigma_\beta^{crush}, \end{cases}$$

where $\operatorname{sgn}(x)$ returns the sign of the argument and is used as σ_β^{crush} is entered as a positive number.

4.30.3 Verification

The orthotropic crush model was verified through a series of uniaxial compression tests. Given the lack of coupling between the different directions, such a variety of tests were performed to test each loading component. One set of material properties was used for all tests and they are given in Table 4.47.

Table 4.47 The material properties for the orthotropic crush model used for the uniaxial crush tests.

E_{11}	50.0 ksi	E	1000.0 ksi
E_{22}	220.0 ksi	ν	0.25
E_{33}	10.0 ksi	σ_y	2.0 ksi
G_{12}	110.0 ksi		
G_{23}	5.0 ksi	V_{min}	0.7
G_{31}	25.0 ksi		

The crush curves used as input for these tests are given in Fig. 4.132.

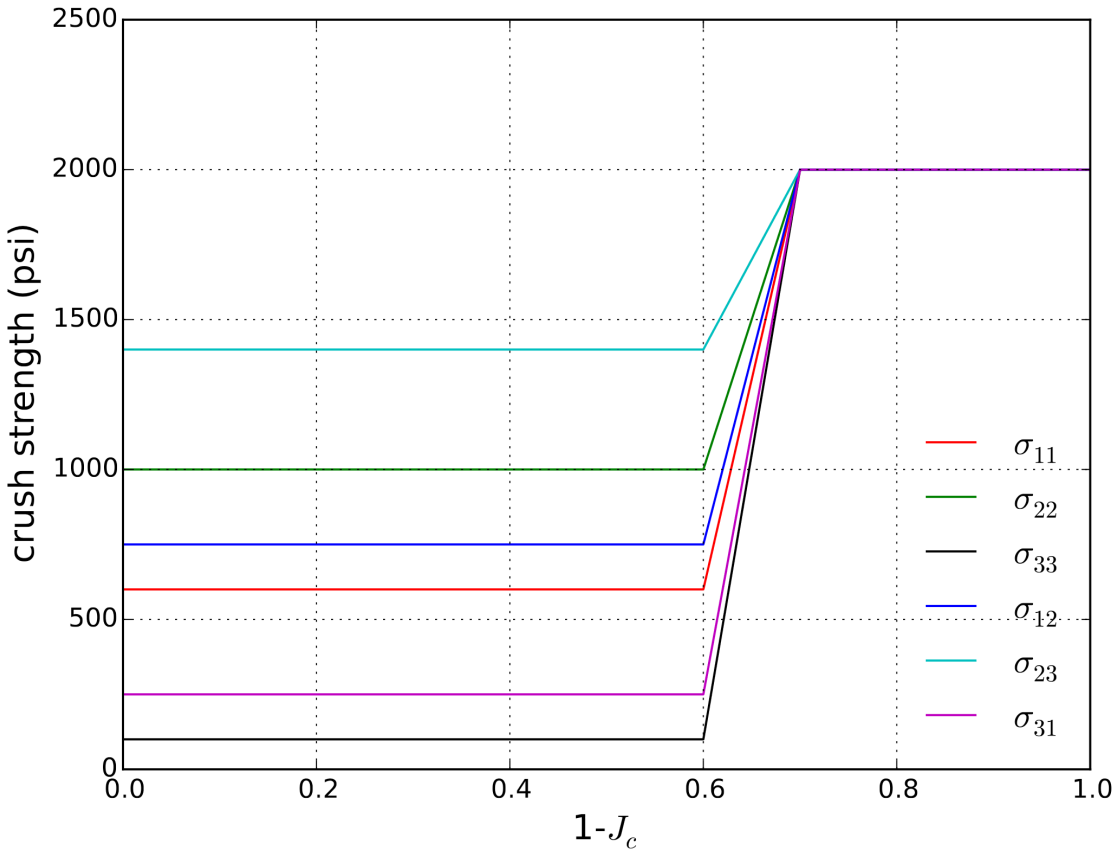

Fig. 4.132 Input crush curves used for uniaxial crush analysis.

To test this model, both the anisotropic nature and different deformation regimes need to be tested.

Therefore, given the decoupled directional nature prior to complete compaction, each component will be tested. For the diagonal stress components, a simple uniaxial displacement of the form,

$$u_i = -\lambda \delta_{i\beta},$$

where $\beta = 1,\ 2$, or 3 corresponding to the directional component being tested is applied. In such cases (with a monotonically increasing λ), $J_c = 1 - \lambda$. The model described in the prior to sections can be easily evaluated analytically under such conditions, and the corresponding analytical and numerical results are presented in Fig. 4.133.

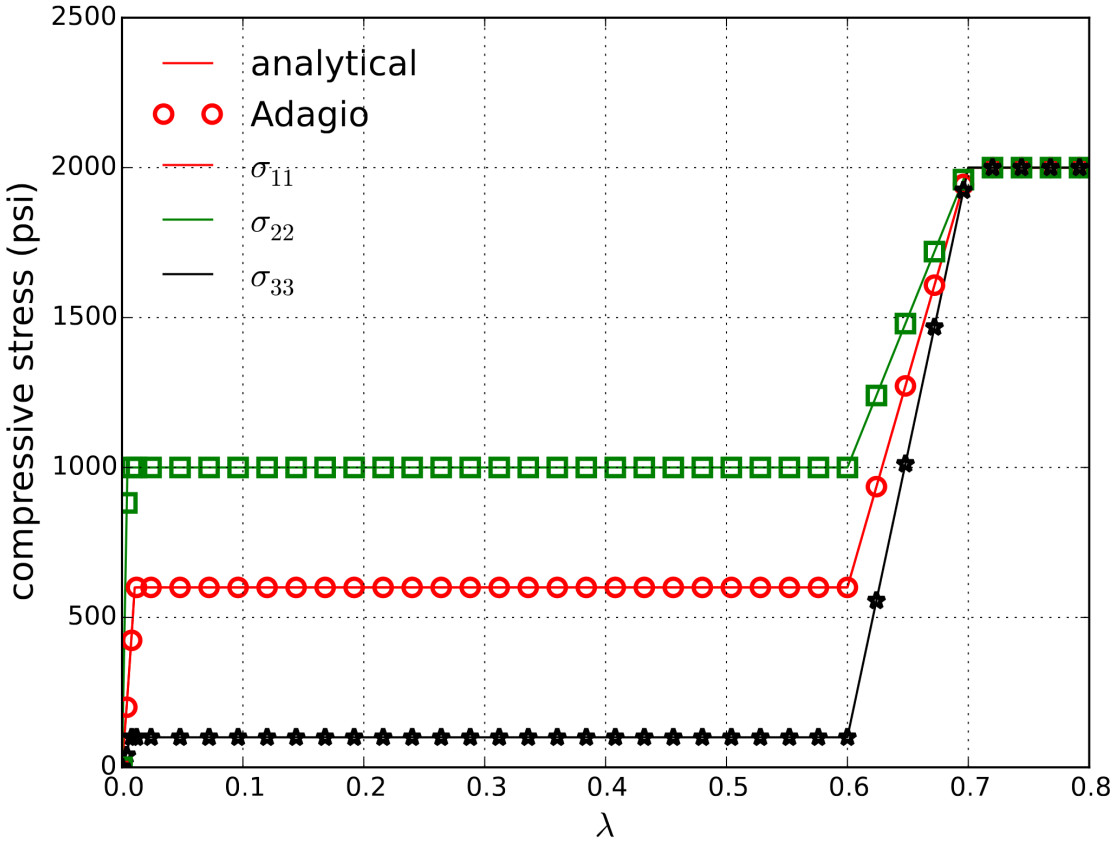

Fig. 4.133 Analytical and numerical results for uniaxial crush cases.

4.30.4 User Guide

```
BEGIN PARAMETERS FOR MODEL ORTHOTROPIC_CRUSH
  #
  # Elastic constants - Post lock-up
  YOUNGS MODULUS = <real>
```

(continues on next page)

(continued from previous page)

```
  POISSONS RATIO = <real>
  SHEAR MODULUS  = <real>
  BULK MODULUS   = <real>
  LAMBDA         = <real>
  TWO MU         = <real>
  #
  # Orthotropic Elastic properties - Pre-Crush
  #
  EX             = <real>
  EY             = <real>
  EZ             = <real>
  GXY            = <real>
  GYZ            = <real>
  GZX            = <real>
  #
  # Crush properties
  #
  CRUSH XX       = <string>
  CRUSH YY       = <string>
  CRUSH ZZ       = <string>
  CRUSH XY       = <string>
  CRUSH YZ       = <string>
  CRUSH ZX       = <string>
  VMIN           = <real>
  #
  # Post lock-up yield properties
  #
  YIELD STRESS   = <real>
  #
END [PARAMETERS FOR MODEL ORTHOTROPIC_CRUSH]
```

In the above command blocks:

- The EX, EY, EZ, GXY, GYZ, and GZX command lines define, respectively, the initial, pre-crush directional moduli E_{xx}, E_{yy}, E_{zz}, G_{xy}, G_{yz}, and G_{zx} from (4.130).
- CRUSH XX, YY, ZZ, XY, YZ, and ZX inputs require the name of a function defined via a FUNCTION command line in the SIERRA scope. These functions describe the directional crush characteristics of the material and give the current stress value (in a direction) as a function of the current compaction $(1 - J_c)$.
- The command VMIN defines the minimum relative volume of the material that is achieved when the material is completely crushed. This parameter may also be considered as the maximum compaction.
- The elastic constant commands refer to the *post lock-up, fully compacted* isotropic response of the material.

- `YIELD STRESS` refers to the plateau stress of the material after lock-up when the response is perfectly plastic.

Output variables available for this model are listed in Table 4.48. For information about the orthotropic crush model, consult [111].

Table 4.48 State Variables for ORTHOTROPIC CRUSH Model

Name	Description
`CRUSH`	current (unrecoverable) compaction/relative volume

4.31 Orthotropic Rate Model

4.31.1 Theory

The orthotropic rate model is an improved version of the orthotropic crush model [7] that incorporates anisotropic elasticity, strain-rate dependence, and the ability to define the material coordinate system. The specific form of this model is motivated by metallic honeycombs and the material coordinate system is usually given in terms of T, L, and W directions. These directions correspond to the strong (T) and ribbon (L) axes depicted in Fig. 4.134. The third component of the coordinate system, W, is the weak direction and is simply the cross-product of the other two directions.

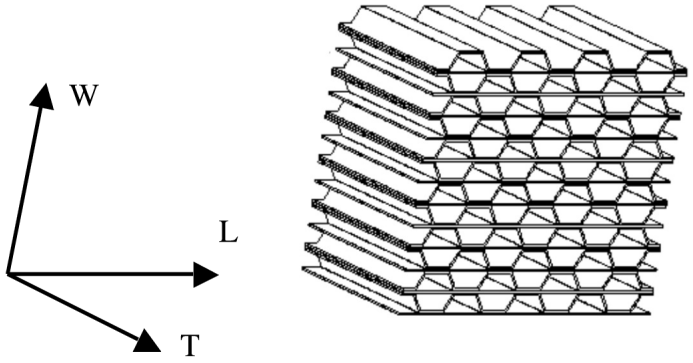

Fig. 4.134 Orientation of the T, L and W vectors for 38 pc aluminum honeycomb.

In terms of expected response, and similar to the orthotropic crush model, the deformation is split into two regimes – uncompacted and compacted. Unlike the crush model, the state of compaction is not determined by the determinant of the deformation gradient but is instead a function of the engineering (not logarithmic) volume strain, ε_V. The degree of compaction, α, is therefore defined as,

$$\alpha = \min_{t>0}\left(\frac{V_0 - V(t)}{V_0}\right) = 1 - \frac{\min_{t>0} V(t)}{V_0} = -\min_{t>0} \varepsilon_V(t),$$

with $V(t)$ and V_0 being the current and original volume of the material. Complete compaction occurs at a user specified value, α_{comp}.

Prior to complete compaction, the elastic stiffness, $\mathbb{C}_{ijkl}$, is taken to exhibit orthotropic symmetry and depends on the compaction state of the material, $\mathbb{C}_{ijkl} = \mathbb{C}_{ijkl}(\alpha)$. In the material frame and in Voigt notation, this stiffness is represented as,

$$[\mathbb{C}(\alpha)] = \begin{bmatrix} E_{TTTT}(\alpha) & E_{TTLL}(\alpha) & E_{TTWW}(\alpha) & 0 & 0 & 0 \\ E_{TTLL}(\alpha) & E_{LLLL}(\alpha) & E_{LLWW}(\alpha) & 0 & 0 & 0 \\ E_{TTWW}(\alpha) & E_{LLWW}(\alpha) & E_{WWWW}(\alpha) & 0 & 0 & 0 \\ 0 & 0 & 0 & G_{TLTL}(\alpha) & 0 & 0 \\ 0 & 0 & 0 & 0 & G_{LWLW}(\alpha) & 0 \\ 0 & 0 & 0 & 0 & 0 & G_{WTWT}(\alpha) \end{bmatrix}. \tag{4.131}$$

Once the material is completely compacted, the elastic stiffness is taken to be isotropic and the evolution of the initially orthotropic components ($E_{TTTT}(\alpha = 0) = E^0_{TTTT}$) to final isotropic, compacted coefficients ($E_{TTTT}\left(\alpha = \alpha_{\text{comp}}\right) = \lambda + 2\mu$ with λ and 2μ being Lam'{e}'s constant and the shear modulus) is given via a common user-defined scaling function, $f_E(\alpha)$. The mechanical stiffness coefficients then scale as,

$$E_{TTTT}(\alpha) = E^0_{TTTT} + \left(\lambda + 2\mu - E^0_{TTTT}\right) f_E(\alpha), \tag{4.132}$$

for the volumetric diagonal terms ($E_{TTTT},\ E_{LLLL},\ E_{WWWW}$),

$$E_{TTLL}(\alpha) = E^0_{TTLL} + \left(\lambda - E^0_{TTLL}\right) f_E(\alpha), \tag{4.133}$$

for the off-diagonal terms ($E_{TTLL},\ E_{TTWW},\ E_{LLWW}$) and

$$G_{TLTL}(\alpha) = G^0_{TLTL} + \left(2\mu - G^0_{TLTL}\right) f_E(\alpha)$$

for the shear terms. From these relations, it is obvious that $f_E(\alpha)$ should be bounded such that $0 \leq f_E(\alpha) \leq 1$ with $f_E(0) = 0$ and $f_E\left(\alpha_{\text{comp}}\right) = 1$.

As was mentioned earlier, the deformation and model response may be readily split between two regimes – the uncompacted and compacted. The behavior during the latter regime is simpler and is assumed to be that of an isotropic elastic-perfectly plastic material characterized by the elastic coefficients ($\lambda,\ 2\mu$) and yield stress (σ_y). During the uncompacted regime the deformation is more complex and typical responses may include elastic bending of cell structures, buckling of cell walls, or densification (see the text of Gibson and Ashby [36] for a complete discussion of these and other mechanisms). In this formulation, however, none of these deformation modes are explicitly modeled. Instead, the response is defined via six independent yield functions (one for

each stress component in the material coordinate system), $\phi_{\beta\gamma}$, that are a function of the corresponding stress, the compaction state, and the current strain rate, $\dot{\bar{\varepsilon}} = \sqrt{d_{ij} d_{ij}}$. Here, d_{ij} is the unrotated rate of deformation in the global (X, Y, Z) coordinate system and β and γ are being used as subscripts to denote variables in the material coordinate system.

The six yield functions are,

$$\begin{aligned}
\phi_{LL} &= \sigma_{LL} - f_{LL}(\alpha)\, h\left(\dot{\bar{\varepsilon}}\right) \\
\phi_{TT} &= \sigma_{TT} - f_{TT}(\alpha)\, h\left(\dot{\bar{\varepsilon}}\right) \\
\phi_{WW} &= \sigma_{WW} - f_{WW}(\alpha)\, h\left(\dot{\bar{\varepsilon}}\right) \\
\phi_{LT} &= \sigma_{LT} - f_{LT}(\alpha)\, h\left(\dot{\bar{\varepsilon}}\right) \\
\phi_{TW} &= \sigma_{TW} - f_{TW}(\alpha)\, h\left(\dot{\bar{\varepsilon}}\right) \\
\phi_{WL} &= \sigma_{WL} - f_{WL}(\alpha)\, h\left(\dot{\bar{\varepsilon}}\right)
\end{aligned},$$

with $\sigma_{\beta\gamma}$ being the current symmetric Cauchy stresses in the material coordinate system, $f_{\beta\gamma}$ are user specified hardening functions defining the maximum stress in that direction for a given compaction state and $h\left(\dot{\bar{\varepsilon}}\right)$ is the strain rate sensitivity function that is common to all the yield functions. With these forms, it is evident that the definition of the different hardening functions dictates the model response through the uncompacted regime. All (or none) of the aforementioned deformation mechanisms may be captured by the appropriate definition of those functions. As such, the response is dictated by the desire of the analyst and appropriate selection of the elastic scaling, hardening, and strain rate sensitivity function – $f_E(\alpha)$, $f_{\beta\gamma}(\alpha)$, and $h\left(\dot{\bar{\varepsilon}}\right)$.

4.31.2 Implementation

Unlike the orthotropic crush model, the rate variant considered here has couplings between the different directional strains and cannot be evaluate numerically as easily. Therefore, the orthotropic rate model is integrated using a hypoelastic formulation. As was discussed in the preceding section, the model is formulated in the T, L, W coordinate system and not the unrotated frame. Therefore, the first step before proceeding is to map strain and stress values from the unrotated to the material frame. To this end, an orthogonal rotation tensor $\tilde{Q}_{ij}$ is constructed from user input vectors $\hat{t}_i$ and $\hat{l}_i$ defining the strong and ribbon directions, respectively. In this case, the $\tilde{}$ is used to differentiate this tensor from that mapping between the rotated and unrotated configurations defined in (4.1). The stress and deformation rates in the material coordinate system, $\tilde{\sigma}_{ij}$ and $\tilde{d}_{ij}$, are determined via,

$$\begin{aligned}
\tilde{\sigma}_{ij}^{n} &= \tilde{Q}_{ki} T_{kl}^{n} \tilde{Q}_{lj}, \\
\tilde{d}_{ij}^{n+1} &= \tilde{Q}_{ki} d_{kl}^{n+1} \tilde{Q}_{lj},
\end{aligned} \tag{4.134}$$

where T_{ij}^{n} and d_{ij}^{n+1} are the unrotated stress and deformation rates, respectively. For convenience, the remainder of this discuss will neglect the $\tilde{}$ notation and all operations will be assumed to be in the material coordinate system unless specifically noted. Additionally, after a converged stress is achieved, the inverse mapping of (4.134) is used to determine T_{ij}^{n+1}.

As the strain increment is fixed for a load step, kinematically defined variables such as α^{n+1} and the strain rate, $\dot{\bar{\varepsilon}}^{n+1}$, may first be determined. The latter term is defined as,

$$\dot{\bar{\varepsilon}}^{n+1} = \sqrt{d_{ij}^{n+1} d_{ij}^{n+1}},$$

with d_{ij}^{n+1} being the strain rate in the global coordinate system. For the former, it must first be noted that the engineering, ε_{V}, and logarithmic, ε_{kk}, volumetric strains are related via $\varepsilon_{\mathrm{V}} = \exp(\varepsilon_{kk}) - 1$. The current state of compaction is then given as,

$$\alpha^{n+1} = 1 - \hat{\varepsilon}_V^{n+1},$$

where $\hat{\varepsilon}_V^{n+1} = \min\left[\hat{\varepsilon}_V^n, \exp\left(\varepsilon_{kk}^{n+1}\right)\right]$.

The material response has two distinct regimes. As discussed in the corresponding theory section, the compacted material behaves as an elastic-plastic material. Such a response and the corresponding numerical analysis has been described in Section 4.7.2. As such, it will not be further presented here and instead the focus is on the behavior during the uncompacted stages.

Earlier, it was mentioned that the response during the compaction process is dictated by three functions – the elastic scaling, hardening, and strain rate sensitivity. These three expressions are dependent on the state of compaction and strain rate. As those kinematic properties have already been calculated, the values of $f_E^{n+1} = f_E\left(\alpha^{n+1}\right)$, $f_{ij}^{n+1} = f_{ij}\left(\alpha^{n+1}\right)$, and $h^{n+1} = h\left(\dot{\bar{\varepsilon}}^{n+1}\right)$ may easily be calculated. In the remainder of this section, the functional dependencies of these terms will not be explicitly presented for ease and brevity. Similarly, the superscript $n+1$ will be dropped and it should be assumed that unless specifically denoted the variable is evaluated at the $n+1$ step. With f_E (and f_E^n) defined, the elastic stiffness, $\mathbb{C}_{ijkl}$ and $\mathbb{C}_{ijk}^n$, and compliance, $\mathbb{S}_{ijkl}$ and $\mathbb{S}_{ijkl}^n$, tensors may also be calculated.

To determine the updated material state, the change in elastic stiffness (associated with the change in compaction) must be determined. To this end,

$$\hat{\sigma}_{ij}^n = \mathbb{C}_{ijkl} \varepsilon_{kl}^{\mathrm{e}-n}$$

where

$$\varepsilon_{ij}^{\mathrm{e}-n} = \mathbb{S}_{ijkl}^n \sigma_{kl}^n.$$

In the previous two relations, it is noted that the respective mechanical tensors are determined at different load steps thus leading to the altered stress state. The tensor σ_{ij}^n refers to the stress determined and stored from the previous load step while $\hat{\sigma}_{ij}^n$ incorporates the change in mechanical stiffness. A trial stress state may be calculated as,

$$\sigma_{ij}^{tr} = \hat{\sigma}_{ij}^n + \mathbb{C}_{ijkl} d\varepsilon_{kl}^{\mathrm{e}-tr},$$

with the trial elastic strain increment, $d\varepsilon_{ij}^{\mathrm{e}-tr}$ being that of the total strain increment, $d_{ij}\Delta t$. The flow (yield) functions, f_{ij}^{tr}, are then calculated. If all $f_{ij}^{tr} < 0$, the solution is elastic and the trial state is accepted. On the other hand, if any $f_{ij}^{tr} > 0$ a correction scheme is needed. This poses a

more complex problem than in the orthotropic crush model given the multiple (six) yield surfaces.

To perform the plastic correction, an approach similar in principle to the return-mapping schemes heavily used in metal plasticity (e.g. Section 4.7.2). Here, however, there is no internal state variable and associated evolution equations to evolve the state. Instead, in this case the elastic strain is iterated over until all the yield conditions are satisfied. Specifically, for the k-th iteration, the stress is calculated as

$$\sigma_{ij}^{k} = \hat{\sigma}_{ij}^{n} + \mathbb{C}_{ijkl} d\varepsilon_{kl}^{\mathrm{e}-k}.$$

Updated yield functions, f_{ij}^{k}, are then calculated and the active flow directions (those with $f_{ij} > 0$) determined. A tangent modulus is then constructed (essentially by turning off components corresponding to inactive directions) and a plastic flow tensor is determined using the tangent compliance and the value of the yield functions. The updated elastic strain increment, $d\varepsilon_{ij}^{\mathrm{e}-k+1}$, is then found by removing the calculated strain. This process is repeated until satisfaction of all the yield functions.

4.31.3 Verification

To verify the orthotropic crush model, a series of uniaxial compression tests are performed. Given the multiple salient features in this model (e.g. strain rate dependence, user-defined coordinate system), the test sequence is constructed to investigate and probe each of the different features to gain confidence in all of the anticipated capabilities. Additionally, the analyzed loading paths correspond to those in which the kinematics are fully prescribed. This is done so that analytical expressions may be found due to the strong coupling between the kinematics and constitutive response through the compaction state, α. The common model parameters used for these tests are given in Table 4.49 and the functional forms of the input strength/hardening curves, $f_{\beta\gamma}$, are presented in Fig. 4.135. It is noted, however, that these properties will take various values during the verification tests to activate and deactivate different responses. Additionally, in Fig. 4.135, two sets of curves are given – the full, complex set of six distinct functions (Fig. 4.135a) and a simpler set (Fig. 4.135b). In the latter, only one curve common to the three diagonal strengths are shown. The other three strength functions are all set artificially high to enable the study of a simpler case.

Table 4.49 Material and model parameters for the orthotropic rate model used for verification

E^0_{TTTT}	2,322.0 ksi	E	4000.0 ksi
E^0_{TTLL}	485.8 ksi	ν	0.3
E^0_{TTWW}	68.8 ksi	σ_y	15.0 ksi
E^0_{LLLL}	1,348.0 ksi	$\hat{t}_x$	1.0
E^0_{LLWW}	121.8 ksi	$\hat{t}_y$	0.0
E^0_{WWWW}	85.0 ksi	$\hat{t}_z$	0.0
G^0_{TLTL}	1,345.0 ksi	$\hat{l}_x$	0.0
G^0_{LWLW}	67.0 ksi	$\hat{l}_y$	1.0
G^0_{WTWT}	260.0 ksi	$\hat{l}_z$	0.0
$h\left(\dot{\bar{\varepsilon}}\right)$	1.0	$f_E\left(\alpha\right)$	α

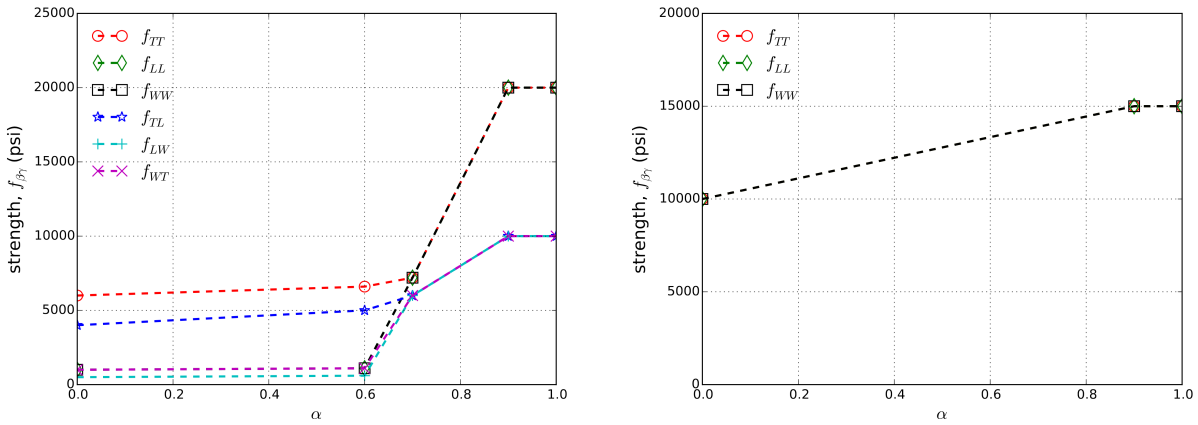

(a) Complex case **(b) Simple case**

Fig. 4.135 Input strength/hardening curves, $f_{\beta\gamma}$, for use in verification tests of the orthotropic rate model.

4.31.3.1 Uniaxial Strain - Isotropic

First, the response of the model with through a uniaxial strain loading is explored. In this case, the prescribed displacement is $u_i = \hat{\lambda}\delta_{i1}$. For this initial study, isotropic elastic constants are assumed leading to $E_L^0 = E_{LLLL}^0 = E_{TTTT}^0 = E_{WWWW}^0 = 5,384.6$ ksi and $E_T^0 = E_{TTLL}^0 = E_{TTWW}^0 = E_{LLWW}^0 = 2,307.7$ ksi. These properties are chosen to match the compacted state and $f_E(\alpha)$ is set to zero. In this way, the elastic properties are constant throughout loading. The shear moduli are scaled accordingly and the remaining properties are left unchanged from Table 4.49. In this case, the model response simplifies to

$$\alpha = -\hat{\lambda},$$

and

$$\sigma_{11} = \begin{cases} \hat{\sigma} & \hat{\sigma} \leq f_{TT}(\alpha) \\ f_{TT} & \hat{\sigma} > f_{TT}(\alpha) \end{cases} \tag{4.135}$$

$$\sigma_{22} = \sigma_{33} = \begin{cases} \lambda \ln\left(1+\hat{\lambda}\right) & \hat{\sigma} \leq f_{TT}(\alpha) \\ \frac{\lambda}{\lambda+2\mu}\sigma_{11} & \hat{\sigma} > f_{TT}(\alpha) \end{cases},$$

where

$$\hat{\sigma} = (\lambda + 2\mu)\ln\left(1+\hat{\lambda}\right).$$

The single linear hardening crush curve given in Fig. 4.135(b) is used for this analysis. The resulting stresses as a function of applied displacement, $\hat{\lambda}$, are given in Fig. 4.136 and good agreement is noted.

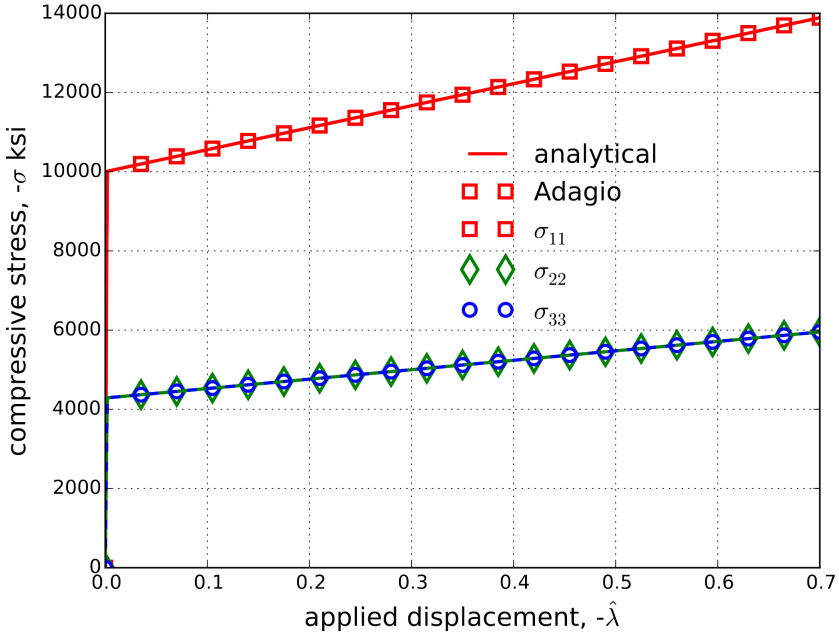

Fig. 4.136 Axial and off-axis stresses determined analytically and numerically via the orthotropic rate model with constant, isotropic elastic properties.

4.31.3.2 Uniaxial Strain - Orthotropic

The uniaxial problem described in the previous section is again studied – although this time using the orthotropic elastic properties listed in Table 4.49. To test the material coordinate system capabilities two cases are considered – essentially with the x_1 axis aligned with the T and L axes. The first case corresponds to the definition of the $\hat{t}_i$ and $\hat{l}_i$ vectors in Table 4.49. Alternatively, the second case is defined by setting the L direction aligned with the x_1 axis ($\hat{l}_x = 1.0,\ \hat{l}_y = 0.0,\ \hat{l}_z = 0.0$ and $\hat{t}_x = 0.0,\ \hat{t}_y = 0.0,\ \hat{t}_z = 1.0$). The stress state evolutions determined via adagio and analytically for the two considered orientations are shown in Fig. 4.137(a) and Fig. 4.137(b), respectively. The analytical solutions are found in the same fashion as (4.135) with the moduli changed for the orthotropic case. Good agreement is observed.

4.31.4 User Guide

```
BEGIN PARAMETERS FOR MODEL ORTHOTROPIC_RATE
  #
  # Elastic constants
  #
  YOUNGS MODULUS = <real>
  POISSONS RATIO = <real>
  SHEAR MODULUS  = <real>
```

(continues on next page)

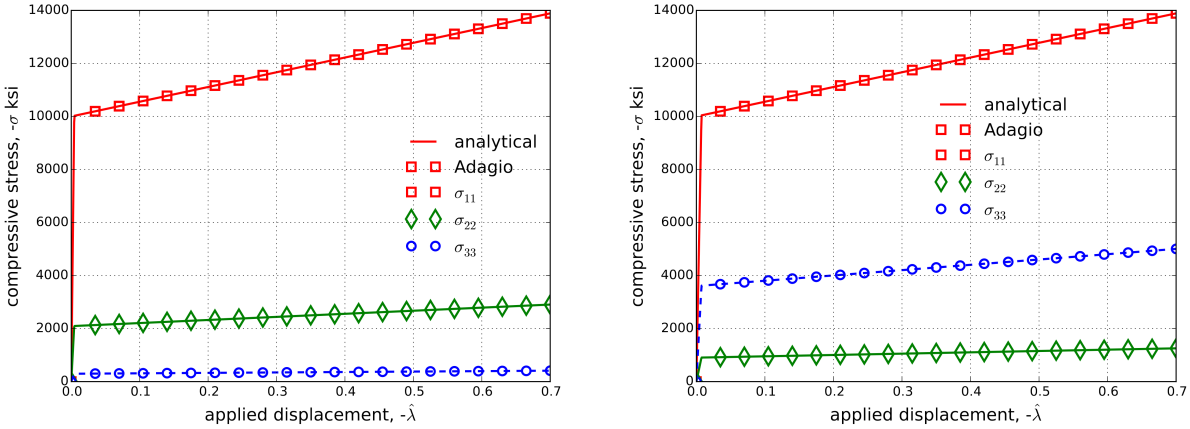

(a) Loading aligned with the T direction

(b) Loading aligned with the W direction

Fig. 4.137 Axial and off-axis stresses determined analytically and numerically via the orthotropic rate model with constant, orthotropic elastic constants. The material coordinate systems is rotated in two different directions with the loading direction always aligned with x_1

(continued from previous page)

```
BULK MODULUS    = <real>
LAMBDA          = <real>
TWO MU          = <real>
#
YIELD STRESS = <real>
#
MODULUS TTTT = <real>
MODULUS TTLL = <real>
MODULUS TTWW = <real>
MODULUS LLLL = <real>
MODULUS LLWW = <real>
MODULUS WWWW = <real>
MODULUS TLTL = <real>
MODULUS LWLW = <real>
MODULUS WTWT = <real>
#
TX = <real>
TY = <real>
TZ = <real>
LX = <real>
LY = <real>
LZ = <real>
#
MODULUS FUNCTION = <string>
RATE FUNCTION    = <string>
#
```

(continues on next page)

(continued from previous page)

```
  T FUNCTION  = <string>
  L FUNCTION  = <string>
  W FUNCTION  = <string>
  TL FUNCTION = <string>
  LW FUNCTION = <string>
  WT FUNCTION = <string>
END [PARAMETERS FOR MODEL ORTHOTROPIC_RATE]
```

The orthotropic rate model extends the functionality of the orthotropic crush constitutive model described in Section 4.30. The orthotropic rate model has been developed to describe the behavior of an aluminum honeycomb subjected to large deformation. The orthotropic rate model, like the original orthotropic crush model, has six independent yield functions that evolve with volume strain. Unlike the orthotropic crush model, the orthotropic rate model has yield functions that also depend on strain rate. The orthotropic rate model also uses an orthotropic elasticity tensor with nine elastic moduli in place of the orthotropic elasticity tensor with six elastic moduli used in the orthotropic crush model.

A honeycomb orientation capability is included with the orthotropic rate model, allowing users to prescribe initial honeycomb orientations that are not aligned with the original global coordinate system. The three material directions are defined as follows: The T-direction is usually associated with the generator axis for the honeycomb, the L-direction is in the ribbon plane (defined by flat sheets used in reinforced honeycomb) orthogonal to the generator axis, and the W-direction is orthogonal to the ribbon plane.

In the above command blocks:

- For the `ORTHOTROPIC_RATE` model, only `YOUNGS MODULUS` needs to be defined; this is the Young's modulus in the fully compacted state. If two other elastic constants are provided, they will be used to define the fully compacted Young's modulus.
- The `YIELD STRESS` command line defines the yield stress of the fully compacted honeycomb.
- The nine elastic moduli for the orthotropic, uncompacted honeycomb are defined with respect to each material direction using the `MODULUS TTTT`, `MODULUS TTLL`, `MODULUS TTWW`, `MODULUS LLLL`, `MODULUS LLWW`, `MODULUS WWWW`, `MODULUS TLTL`, `MODULUS LWLW`, and `MODULUS WTWT` command lines.
- The components of vectors defining the T- and L-directions of the honeycomb are specified using the `TX`, `TY`, and `TZ`, and `LX`, `LY`, and `LZ` command lines, respectively. The vector component values `tx`, `ty`, and `tz` define the orientation of the honeycomb's T-direction (generator axis), while `lx`, `ly`, and `lz` define the orientation of the L-direction. The vectors T and L are defined in the global coordinate system and *must* be orthogonal.
- The function describing the variation in moduli with compaction is given by the `MODULUS FUNCTION` command line. The moduli vary continuously from their initial orthotropic values to isotropic values when full compaction is obtained.

- The function describing the change in strength with strain rate is given by the `RATE FUNCTION` command line. Note that all strengths are scaled with the multiplier obtained from this function.
- The function describing the T-normal strength of the honeycomb as a function of compressive volumetric strain is given by the `T FUNCTION` command line.
- The function describing the L-normal strength of the honeycomb as a function of compressive volumetric strain is given by the `L FUNCTION` command line.
- The function describing the W-normal strength of the honeycomb as a function of compressive volumetric strain is given by the `W FUNCTION` command line.
- The function describing the TL-normal strength of the honeycomb as a function of compressive volumetric strain is given by the `TL FUNCTION` command line.
- The function describing the LW-normal strength of the honeycomb as a function of compressive volumetric strain is given by the `LW FUNCTION` command line.
- The function describing the WT-normal strength of the honeycomb as a function of compressive volumetric strain is given by the `WT FUNCTION` command line.

Note that several of the command lines in this command block reference functions. These functions must be defined in the SIERRA scope.

Output variables for this model are listed in Table 4.50.

Table 4.50 State Variables for ORTHOTROPIC RATE Model

Name	Description	
1	`CRUSH`	minimum volume ratio, crush is unrecoverable ($\hat{\varepsilon}_V$)

4.32 Universal Polymer Model

4.32.1 Theory

The Universal Polymer Model (UPM) is a phenomenological, non-linear viscoelastic (NLVE) model that is, in the literature, named the Simplified Potential Energy Clock (SPEC) [3]. The UPM model is considerably simpler than the parent model, the Potential Energy Clock (PEC) model, labeled the NLVE polymer model in SIERRA, which itself is not phenomenological but requires extensive data and experience to calibrate [21].

The UPM model is suitable for modeling the finite deformation, thermal-mechanical behavior of glassy materials, both organic and inorganic. Successful usage of the model is widespread. Some examples include the modeling of amorphous, thermosetting polymers across and through the glass transition such as epoxies [2]. It is also suitable for modeling thermoplastics from within the melt state and down into the glass transition from polystyrene to polycarbonate. Finally, it has been used to represent inorganic glasses for glass-to-metal seals. The UPM model was developed

for production analyses of encapsulated components. It predicts a full range of behavior including yielding, stress relaxation, volume relaxation, and physical aging.

The key physical principal behind the UPM model is that there exists a material time scale (material clock) separate from the laboratory time scale. If the material time scale is fast, such as in the rubbery state of a polymer, then the UPM model responds instantly to changes in temperature and strain such that the user would observe rate-independent behavior. However, if the material clock is slow relative to the laboratory time scale, viscoelastic memory builds with any process, which causes acute history and thermodynamic path dependent behavior.

The model response is derived from a Helmholtz Free Energy density and takes as an input the unrotated rate of deformation, d_{ij}, the temperature at the start and end of the time step (θ_n and θ_{n+1}, and the time step, Δt. From these inputs, the hereditary integrals within the model are updated, and the unrotated Cauchy stress tensor is returned.

For the UPM model, the strain measure is approximated from the integrated unrotated rate of deformation tensor, which we label ϵ_{ij},

$$\epsilon_{ij} = \int_0^\infty \left(R_{mi} D_{mn} R_{nj}\right) ds, \quad D_{ij} = \frac{1}{2}\left(L_{ij} + L_{ji}\right), \quad F_{ij} = R_{im} U_{mj}. \tag{4.136}$$

Here, F_{ij}, R_{ij}, U_{ij}, L_{ij}, and D_{ij} are the deformation gradient, rotation, material stretch, velocity gradient, and rate of deformation tensors standard in Lagrangian continuum mechanics.

The UPM model allows the user to initiate an analysis from a stress-free temperature, θ_{sf}, that is different from the reference temperature, θ_{ref}, at which all material properties are defined. Here we briefly summarize the constitutive equations. The model is derived from a Helmholtz Free Energy, but we begin directly with the (unrotated) Cauchy Stress and refer the reader to reference [3] for more detail:

$$\begin{aligned}
\sigma_{ij} = &\left(K_G\left(\theta\right) - K_\infty\left(\theta\right)\right) \int_0^t f_v\left(t' - s'\right) \frac{dI_1}{ds} ds \delta_{ij} \\
&- \left(K_G\left(\theta\right) \delta_G\left(\theta\right) - K_\infty\left(\theta\right) \delta_\infty\left(\theta\right)\right) \int_0^t f_v\left(t' - s'\right) \frac{d\theta}{ds} ds \delta_{ij} \\
&+ 2\left(G_G\left(\theta\right) - G_\infty\left(\theta\right)\right) \int_0^t f_s\left(t' - s'\right) \frac{d\left(\text{dev}\epsilon_{ij}\right)}{ds} ds \\
&+ \left(K_\infty\left(\theta\right) I_1 - K_\infty\left(\theta\right) \delta_\infty\left(\theta\right)\left(\theta - \theta_{\text{sf}}\right)\right) \delta_{ij} + 2G_\infty\left(\theta\right) \text{dev}\epsilon_{ij}.
\end{aligned} \tag{4.137}$$

The first three lines of terms in (4.137) represent the time-dependent and dissipative (non-equilibrium) response of the model to volumetric, thermal, and shear deformation histories. Accordingly, K, δ, and G represent a bulk modulus, volumetric thermal expansion coefficient, and shear modulus while subscripts $_G$ or $_\infty$ denote a glassy or rubbery, respectively, properties. The last collection of terms in (4.137) furnish the time-independent rubbery (equilibrium) response.

The variables in (4.137) are:

$$
\begin{aligned}
I_1 &= \delta_{ij}\epsilon_{ij} = \mathrm{tr}\epsilon_{ij}, && \mathrm{dev}\epsilon_{ij} = \epsilon_{ij} - \frac{I_1}{3}\delta_{ij}, \\
G_G(\theta) &= G_G^{\mathrm{ref}} + \frac{dG_G}{d\theta}(\theta - \theta_{\mathrm{ref}}), && G_\infty(\theta) = G_\infty^{\mathrm{ref}} + \frac{dG_\infty}{d\theta}(\theta - \theta_{\mathrm{ref}}), \\
K_G(\theta) &= K_G^{\mathrm{ref}} + \frac{dK_G}{d\theta}(\theta - \theta_{\mathrm{ref}}), && K_\infty(\theta) = K_\infty^{\mathrm{ref}} + \frac{dK_\infty}{d\theta}(\theta - \theta_{\mathrm{ref}}), \\
\delta_G(\theta) &= \delta_G^{\mathrm{ref}} + \frac{d\delta_G}{d\theta}(\theta - \theta_{\mathrm{ref}}), && \delta_\infty(\theta) = \delta_\infty^{\mathrm{ref}} + \frac{d\delta_\infty}{d\theta}(\theta - \theta_{\mathrm{ref}}).
\end{aligned}
\tag{4.138}
$$

The first three terms in (4.137) represent the material's viscoelastic response to changes in volume strain, temperature, and shear deformation. Two relaxation functions are used to characterize the thermal/volumetric (f_v) and shear (f_v) relaxation responses. The model assumes the thermal and volumetric relaxation responses are identical. Otherwise, f_v and f_s are typically quite different and are expressed as a Prony series (Note: to distinguish between indices used with conventional summation convention and those related to Prony series terms, all Prony series summations shall be explicitly written with the relevant index given parenthetically in a superscript.):

$$
f_v(x) = \sum_{k=1}^{N} w^{(k)} \exp\left(-\frac{x}{\tau^{(k)}}\right), \quad f_s(x) = \sum_{l=1}^{M} w^{(l)} \exp\left(-\frac{x}{\tau^{(l)}}\right). \tag{4.139}
$$

These relaxation functions describe the material's response to a suddenly applied volumetric/thermal or shear perturbation at the reference temperature where, under certain conditions, the material and laboratory time scales are equivalent. In (4.137), the viscous terms (non-rubbery) involve hereditary integrals over the difference in material time from $s = 0$ to $s = t$, which is the current laboratory time.

An increment in material time, dt', and the laboratory time, dt, are related through the (highly) history dependent shift factor, a, such that the difference in material time, $t' - s'$, is related to the corresponding difference in laboratory time, $t - s$ through:

$$
a dt' = dt, \quad t' - s' = \int_{u=s}^{u=t} \frac{du}{a(u)}. \tag{4.140}
$$

If the material time scale is very slow compared to the laboratory time, then $a >> 1$, which is often the case inside and below the glass transition for typically glassy materials.

The shift factor is instantaneously defined through:

$$
\begin{aligned}
\log_{10} a &= \frac{-C_1 N}{C_2 + N}, \\
N(t) &= \theta - \theta_{\mathrm{ref}} - \int_0^t f_v(t' - s') \frac{d\theta}{ds} ds \\
&\quad + C_3 \left(I_1 - \int_0^t f_v(t' - s') \frac{dI_1}{ds} ds \right) \\
&\quad + C_4 \int_{u=0}^{u=t} \int_{s=0}^{s=t} \left(f_s(t' - s', t' - u') \frac{d\left(\mathrm{dev}\epsilon_{ij}\right)}{ds} \frac{d\left(\mathrm{dev}\epsilon_{ij}\right)}{du} ds du \right).
\end{aligned}
\tag{4.141}
$$

The key physics in the model comes from (4.141). Temperature rise (generally) causes N to increase, and hence the material shift factor shrinks (the material time scale speeds up). Shrinking the volume generally causes the shift factor to increase as if the temperature had been decreased. Mechanistically, this feature is the manifestation of the trade-off between between mobility and free volume available to polymer chains. Finally, shear deformation can greatly speed up the material clock through the last term. This phenomenon is a direct manifestation of deformation induced mobility, a key mechanism for glassy materials.

Since the shift factor involves hereditary integrals, even at a constant temperature and state of deformation, the material clock will change over time. Under stress-free conditions, the material will creep and densify if the model is out of equilibrium (when any viscous term is non-zero). These phenomena are the model's manifestations of physical aging, time-dependent material change without a change in composition or microstructure. C_1, C_2, C_3, and C_4 are all material constants. We note that the double relaxation function appearing in the last term takes on a slightly different form from f_s:

$$f_s\left(x,y\right)=\sum_{k=1}^{N}w^{(k)}\exp\left(-\frac{x}{\tau^{(k)}}\right)\exp\left(-\frac{y}{\tau^{(k)}}\right) \tag{4.142}$$

It is desirable to relate a special case of the model to the Williams-Landel-Ferry (WLF) form because of how time-temperature superposition fitting is typically performed. Specifically, one can show that the clock parameters, C_1 and C_2, relate to the WLF parameters, $\hat{C}_1$ and $\hat{C}_2$, through the following relationships: $\hat{C}_1=C_1$ and $\hat{C}_2=C_2/\left(1+C_3\delta_\infty^{\text{ref}}\right)$.

For more information about the universal polymer model, consult [3].

4.32.2 Implementation

The hereditary integrals in (4.137) and (4.141) are difficult to evaluate directly. Instead a rate form is pursued than can be integrated straightforwardly over each time step. Consider a typical hereditary integral after the Prony series for its specific relaxation function has been substituted into it. Differentiate the integral with respect to the current time, t, and use the Leibnitz rule to arrive at:

$$\int_{s=0}^{s=t}f_v\left(t'-s'\right)\frac{d\theta}{ds}ds=\sum_{k=0}^{N}w^{(k)}\int_{s=0}^{s=t}\exp\left(-\frac{t'-s'}{\tau^{(k)}}\right)\frac{d\theta}{ds}ds=\sum_{k=0}^{N}w^{(k)}J^{(k)} \tag{4.143}$$

$$\begin{aligned}\frac{dJ^{(k)}}{dt}&=\int_{s=0}^{s=t}\frac{d}{dt}\left(\exp\left(-\frac{t'-s'}{\tau^{(k)}}\right)\frac{d\theta}{ds}\right)ds+\left(\exp\left(-\frac{t'-s'}{\tau^{(k)}}\right)\frac{d\theta}{ds}\right)_{s=t}\frac{d(t)}{dt}\\&=\int_{s=0}^{s=t}\exp\left(-\frac{t'-s'}{\tau^{(k)}}\right)\frac{d\theta}{ds}\left(\frac{-1}{\tau^{(k)}}\right)\frac{dt'}{dt}ds+\frac{d\theta}{dt}\\&=-\frac{1}{a\tau^{(k)}}J^{(k)}+\frac{d\theta}{dt}.\end{aligned}$$

Notice this rate form involves a memory term which decays as well as input from new history, in this case a change in temperature. To integrate this easily, we approximate this rate as constant

over the time step in a constitutive equation update and use the mid-step evaluation to determine the rate. Consider a process in which the temperature changes from θ_n at time t_n to θ_{n+1} at t_{n+1} so that $\Delta t = t_{n+1} - t_n$. Then,

$$\frac{dJ^{(k)}}{dt}|_{t_{n+1/2}} \approx \frac{J^{(k)}\left(t_{n+1}\right) - J^{(k)}\left(t_n\right)}{t_{n+1} - t_n} = -\frac{1}{a_{t_{n+1/2}}\tau^{(k)}} \frac{J^{(k)}|_{n+1} + J^{(k)}|_n}{2} + \frac{\theta_{n+1} - \theta_n}{t_{n+1} - t_n}, \tag{4.144}$$

yielding,

$$J^{(k)}|_{n+1} = \left(\frac{2a_{n+1/2}\tau^{(k)} - \Delta t}{2a_{n+1/2}\tau^{(k)} + \Delta t}\right) J^{(k)}|_n + \left(\frac{2a_{n+1/2}\tau^{(k)}}{2a_{n+1/2}\tau^{(k)} + \Delta t}\right) \left(\theta_{n+1} - \theta_n\right).$$

Stability of (4.144) requires that the first term to remain positive. Hence, the change in time for the purposes of updating these hereditary integrals is:

$$\Delta t = \text{MIN}\left(t_{n+1} - t_n, 2a_{n+1/2}\tau^{(k)}\right). \tag{4.145}$$

The collection of $J^{(k)}$ from $k = 1, N$ are internal state variables associated with this particular hereditary integral. Each Prony term for each distinct hereditary integral must be stored as an internal state variable.

Fortunately, changing from a scalar field to a tensor field (θ to ϵ_{ij}) does not alter the above time integration except that for each Prony term, each component of the tensor must be stored and updated as a state variable. For example, the hereditary integrals associated with deviatoric strain history may be updated by letting,

$$H_{ij} = \int_0^t ds f_s\left(t' - s'\right) \frac{d\left(\text{dev}\epsilon_{ij}\right)}{ds} ds = \sum_{k=1}^{N} w^{(k)} H_{ij}^{(k)}, \tag{4.146}$$

and approximating the time rate of change at the midstep as,

$$\frac{dH_{ij}^{(k)}}{dt}|_{t_{n+1/2}} \approx \frac{H_{ij}^{(k)}\left(t_{n+1}\right) - H_{ij}^{(k)}\left(t_n\right)}{t_{n+1} - t_n} = -\frac{1}{a_{t_{n+1/2}}\tau^{(k)}} \frac{H_{ij}^{(k)}|_{n+1} + H_{ij}^{(k)}|_n}{2} + \frac{H_{ij}^{n+1} - H_{ij}^n}{t_{n+1} - t_n},$$

resulting in,

$$H_{ij}^{(k)}|_{n+1} = \left(\frac{2a_{n+1/2}\tau^{(k)} - \Delta t}{2a_{n+1/2}\tau^{(k)} + \Delta t}\right) H_{ij}^{(k)}|_n + \left(\frac{2a_{n+1/2}\tau^{(k)}}{2a_{n+1/2}\tau^{(k)} + \Delta t}\right) \left(H_{ij}^{n+1} - H_{ij}^n\right).$$

Here, $H_{ij}^{(k)}$ is a collection of six state variables that compose the k^{th} Prony term deviatoric strain history hereditary integral as in (4.137). The superscripts refer to the Prony term number, and each component of these tensors much be updated and stored.

Because of the double hereditary integral in (4.141) associated with shear deformation and shift factor acceleration, a rate form for this kind of term is also needed. Again, differentiate the

integral with respect to the current time, t, and use the Leibnitz rule to arrive at:

$$\int_{u=0}^{u=t}\int_{s=0}^{s=t}\left(f_s\left(t'-s',t'-u'\right)\frac{d\left(\mathrm{dev}\epsilon_{ij}\right)}{ds}\frac{d\left(\mathrm{dev}\epsilon_{ij}\right)}{du}ds\,du\right)$$

$$=\sum_{k=1}^{N}w^{(k)}\int_{u=0}^{u=t}\int_{s=0}^{s=t}\left(\exp\left(-\frac{t'-s'}{\tau^{(k)}}\right)\exp\left(-\frac{t'-u'}{\tau^{(k)}}\right)\frac{d\left(\mathrm{dev}\epsilon_{ij}\right)}{ds}\frac{d\left(\mathrm{dev}\epsilon_{ij}\right)}{du}ds\,du\right)$$

$$=\sum_{k=0}^{N}w^{(k)}Q^{(k)}.$$

$$\frac{dQ^{(k)}}{dt}=\frac{-2Q^{(k)}}{a\tau^{(k)}}+2\frac{d\left(\mathrm{dev}\epsilon_{ij}\right)}{dt}\int_{s=0}^{s=t}\left(\exp\left(-\frac{t'-u'}{\tau^{(k)}}\right)\frac{d\left(\mathrm{dev}\epsilon_{ij}\right)}{du}du\right)$$

$$=\frac{-2Q^{(k)}}{a\tau^{(k)}}+2\frac{d\left(\mathrm{dev}\epsilon_{ij}\right)}{dt}H_{ij}^{(k)}.$$

The variables $J^{(k)}$, $Q^{(k)}$, and all six components of $H_{ij}^{(k)}$ are state variables that are stored and updated through the midstep algorithm presented above.

The actual update of the constitutive equations involves finding the shift factor at $t_{n+1/2}$, which requires Newton's method on (4.141). Using the techniques from (4.143) through (4.147), it is straightforward to chain rule differentiate the term N in (4.141), and that analysis is not reproduced here for brevity.

4.32.3 Verification

Verification for the full non-linear viscoelastic features of the universal polymer model is difficult because analytic solutions are not available. Here we verify that two key parts of the model are working correctly, but at this time not all non-linearities in the material clock are verified. First, we verify that the material clock (shift factor) follows the Williams-Landel-Ferry behavior near and above the glass transition (reference temperature). Then, as the material is cooled below the glass transition, we verify that the thermal hereditary integral in the material clock is working properly. Finally, the specimen is reheated through the glass transition, and the shift factor is again compared between the UPM model and a semi-analytic solution.

Second, with the non-linear portions of the clock turned off and the temperature held fixed, an analytic solution to the uniaxial strain boundary value problem is pursued at three different strain rates. This latter verification exercise demonstrates that the hereditary integrals are updated correctly and that the stress response may be calculated using both the shear and bulk relaxation responses simultaneously even when they have different relaxation functions.

4.32.3.1 Shift Factor During Traction-Free Cooling and Heating

The WLF equation (considering temperature only) provides a simple means of performing time-temperature superposition. It relates the shift factor, a, to the current temperature through,

$$\log_{10} a = -\frac{C_1 \, (\theta - \theta_{\text{ref}})}{C_2 + (\theta - \theta_{\text{ref}})}. \tag{4.147}$$

Near and above θ_{ref}, the UPM model limits to the WLF model, and below the glass transition, the hereditary integral in the clock freezes out further evolution of the shift factor with temperature.

A single element boundary value problem is analyzed in Sierra/SM with the UPM model. A simple temperature sweep is executed under traction free conditions through the glass transition starting from above it at a constant rate of 1°C per minute. The material is then immediately reheated at 1°C per minute to well above the glass transition. The material properties used for this analysis as well as the uniaxial strain problem below are provided in Table 4.51 and reflect a simplified version of the material properties used to represent 828DGEBA / DEA (often called 828DEA) [3].

Table 4.51 The material and model parameters for the Universal Polymer Model used for verification testing. Parameters are approximately based on a fit for 828DEA, but they represent a linear thermal-viscoelastic representation of the model. Both the shear and volumetric Prony series weights come from fitting these 4 relaxation times to stretched exponential series as discussed in that paper. The thermal relaxation and volumetric relaxation functions are the same in the UPM model. All other material and model parameters are unused and set to zero.

θ_{ref}	75°C	θ_{sf}	125°C
$\hat{C}_1$	16.5	$\hat{C}_2$	54.5°C
K_G	4.9 GPa	K_∞	3.2 GPa
G_G	0.75 GPa	G_∞	4.5 MPa
$\{f_1\}$	$\{2.99149 \times 10^{-3}, 6.42966 \times 10^{-2}, 6.49783 \times 10^{-1}, 2.82929 \times 10^{-1}\}$		
$\{f_2\}$	$\{1.00305 \times 10^{-2}, 2.11421 \times 10^{-1}, 7.01534 \times 10^{-1}, 7.70145 \times 10^{-2}\}$		
$\{\tau\}$	$\{1.0 \times 10^{-11}, 1.0 \times 10^{-6}, 1.0 \times 10^{-1}, 1.0 \times 10^{4}\}$ (s)		

For the verification of the time-temperature shift behavior, the model is expected to exactly match the WLF behavior above θ_{ref}, but as the material is cooled below this point, the temperature hereditary integral in the material shift factor definition (4.141) slows further evolution of the shift factor. WLF behavior is observed in the model, which confirms this elementary behavior of the model in Fig. 4.138. Then, as the model is further cooled below the glass transition, the UPM model is compared against a custom Newton-Raphson scheme for this boundary value problem (outside Sierra), and agreement is perfect. During reheat, one sees that the shift factor does not retrace the path through temperature space, and a large hysteresis is observed.

Changing the cooling rate changes the temperature at which the UPM model will depart from WLF behavior with the behavior remaining WLF like at colder temperatures for slower cooling rates and departing at warming temperatures for faster cooling rates.

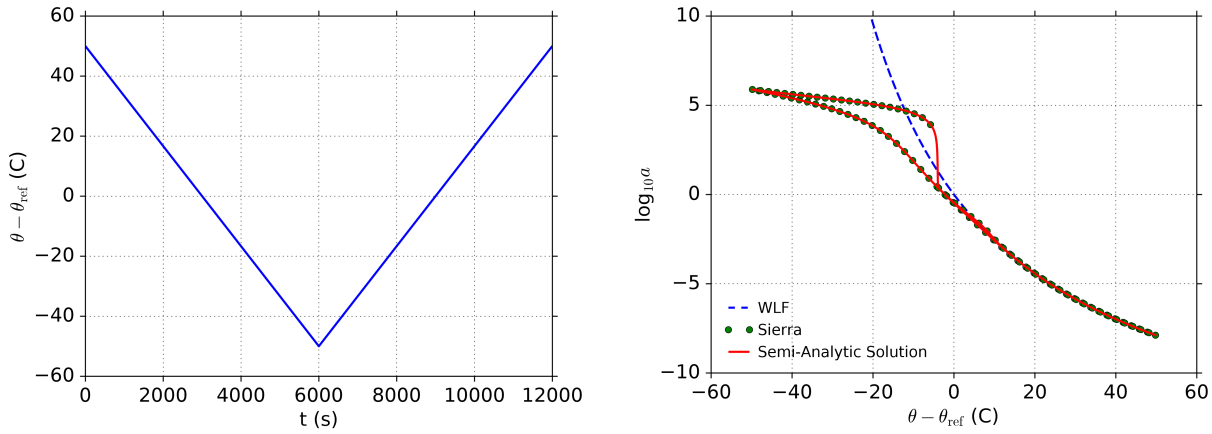

(a) Applied Temperature History **(b) Shift Factor Vs. Temperature**

Fig. 4.138 Time-temperature dependence of the shift factor, a, during cooling through the glass transition and then reheating back through it. The cooling/heating rate is 1°C per minute. FEA (circles) show the expected WLF (blue dashed line) behavior for $\theta - \theta_{\text{ref}} > 0$. The UPM model departs from WLF behavior below the reference temperature as expected, and continues to agree with an external to Sierra numerical scheme (solid line) to simulate this boundary value problem.

4.32.3.2 Uniaxial Strain

The second verification problem considered is uniaxial strain under isothermal conditions wherein the non-linear clock terms are set to zero ($C_3 = 0$ and $C_4 = 0$). Here, the temperature is set to the reference temperature, $\theta = \theta_{\text{ref}}$, and a two stage boundary value problem is simulated. A material point (single 8-node hexahedral element with selective deviatoric spatial integration) is loaded at a constant logarithmic strain rate in uniaxial strain up to a prescribed logarithmic strain (characterized by a loading time, t_{L}). Then, the logarithmic strain rate is fixed to zero. The stress responses in the axial and transverse directions are output over time during this load and hold process. Three logarithmic strain rates are considered: 0.001, 1, and 1000 per second which activate the rubbery, mixed, and glassy responses respectively. For all three cases, the specimen is loaded to 10% axial logarithmic strain, and then the specimen is held for 10 seconds. Uniaxial strain involves finite volume and shape change, and so this boundary value problem tests both relaxation processes simultaneously.

Next we develop the analytic solution for linear thermal-viscoelasticity based on the UPM model. Note that the temperature is fixed to the reference temperature such that the shift factor is 1.0 always. We prescribe the following logarithmic strain rate history on a material point (in a Cartesian frame). Since both the spherical and deviatoric parts of the logarithmic strain history

are needed for the model, we derive them too:

$$\text{for} \quad 0 \le t \le t_{\mathrm{L}}, \qquad \dot{H}_{ij} = \dot{\epsilon} \begin{bmatrix} 1 & 0 & 0 \\ 0 & 0 & 0 \\ 0 & 0 & 0 \end{bmatrix}, \quad \dot{H}^{\mathrm{dev}}_{ij} = \frac{\dot{\epsilon}}{3} \begin{bmatrix} 2 & 0 & 0 \\ 0 & -1 & 0 \\ 0 & 0 & -1 \end{bmatrix},$$

$$\text{otherwise} \qquad \dot{H}_{ij} = \dot{H}^{\mathrm{dev}}_{ij} = \begin{bmatrix} 0 & 0 & 0 \\ 0 & 0 & 0 \\ 0 & 0 & 0 \end{bmatrix},$$

and the associated strain invariants needed for the model are:

$$I_1,\, I_2 : \begin{cases} \text{for} \quad 0 \le t \le t_{\mathrm{L}}, \\ \quad I_1 = \delta_{ij} H_{ij} = \dot{\epsilon} t \\ \quad \dot{I}_1 = \dot{\epsilon} \\ \quad I_2 = H^{\mathrm{dev}}_{ij} H^{\mathrm{dev}}_{ij} = \frac{2}{3} \dot{\epsilon}^2 t^2 \\ \quad \dot{I}_2 = \frac{4}{3} \dot{\epsilon}^2 t \\ \\ \text{for} \quad t_{\mathrm{L}} \le t, \\ \quad I_1 = \dot{\epsilon} t_{\mathrm{L}} \\ \quad \dot{I}_1 = 0 \\ \quad I_2 = \frac{2}{3} \dot{\epsilon}^2 t_{\mathrm{L}}^2 \\ \quad \dot{I}_2 = 0 \end{cases} \tag{4.148}$$

Now, the motion involves a finite volume change, and the Jacobian of the deformation gradient will be needed. It is:

$$J = \begin{cases} \text{for} \quad 0 \le t \le t_{\mathrm{L}}, \\ \quad \exp\left(\dot{\epsilon} t\right) \\ \text{for} \quad t_{\mathrm{L}} \le t, \\ \quad \exp\left(\dot{\epsilon} t_{\mathrm{L}}\right) \end{cases} \tag{4.149}$$

The derivation of the linear viscoelastic response proceeds directly with the stress integral from (4.137) with equivalent laboratory and material time scales since $\theta = \theta_{\mathrm{ref}}$. Using the prescribed strain history from (4.148) and the Jacobian of the deformation gradient (4.149), the Cauchy stress response is given below. Again, there are only two non-zero stress components: the axial stress (σ_{11}) and the transverse stresses ($\sigma_{22} = \sigma_{33}$), which we will label with under score σ_A and σ_T

respectively. These are:

$$\text{for} \quad 0 \le t \le t_{\mathrm{L}} : \begin{cases} J\sigma_A = \exp\left(-\dot{\epsilon}t\right) \\ \qquad \left\{\frac{4\left(G_g - G_\infty\right)\dot{\epsilon}}{3} \sum_{k=1}^{N} w^{(k)}\tau^{(k)} \left(1 - \exp\left(-\frac{t}{\tau^{(k)}}\right)\right)\right. \\ \qquad \left. + \left(K_g - K_\infty\right)\dot{\epsilon} \sum_{l=1}^{M} q^{(l)}\tau^{(l)} \left(1 - \exp\left(-\frac{t}{\tau^{(l)}}\right)\right)\right\} \\ \qquad + \left(K_\infty + \frac{4}{3}G_\infty\right)\dot{\epsilon}t, \\ \\ J\sigma_T = \exp\left(-\dot{\epsilon}t\right) \\ \qquad \left\{-\frac{2\left(G_g - G_\infty\right)\dot{\epsilon}}{3} \sum_{k=1}^{N} w^{(k)}\tau^{(k)} \left(1 - \exp\left(-\frac{t}{\tau^{(k)}}\right)\right)\right. \\ \qquad \left. + \left(K_g - K_\infty\right)\dot{\epsilon} \sum_{l=1}^{M} q^{(l)}\tau^{(l)} \left(1 - \exp\left(-\frac{t}{\tau^{(l)}}\right)\right)\right\} \\ \qquad + \left(K_\infty - \frac{2}{3}G_\infty\right)\dot{\epsilon}t, \end{cases} \tag{4.150}$$

$$\text{for} \quad t_{\mathrm{L}} \le t : \begin{cases} J\sigma_A = \exp\left(-\dot{\epsilon}t_{\mathrm{L}}\right) \\ \qquad \left\{\frac{4\left(G_g - G_\infty\right)\dot{\epsilon}}{3} \sum_{k=1}^{N} w^{(k)}\tau^{(k)} \left(\exp\left(-\frac{t-t_{\mathrm{L}}}{\tau^{(k)}}\right) - \exp\left(-\frac{t}{\tau^{(k)}}\right)\right)\right. \\ \qquad \left. + \left(K_g - K_\infty\right)\dot{\epsilon} \sum_{l=1}^{M} q^{(l)}\tau^{(l)} \left(\exp\left(-\frac{t-t_{\mathrm{L}}}{\tau^{(l)}}\right) - \exp\left(-\frac{t}{\tau^{(l)}}\right)\right)\right\} \\ \qquad + \left(K_\infty + \frac{4}{3}G_\infty\right)\dot{\epsilon}t_{\mathrm{L}}, \\ \\ J\sigma_T = \exp\left(-\dot{\epsilon}t_{\mathrm{L}}\right) \\ \qquad \left\{-\frac{2\left(G_g - G_\infty\right)\dot{\epsilon}}{3} \sum_{k=1}^{N} w^{(k)}\tau^{(k)} \left(\exp\left(-\frac{t-t_{\mathrm{L}}}{\tau^{(k)}}\right) - \exp\left(-\frac{t}{\tau^{(k)}}\right)\right)\right. \\ \qquad \left. + \left(K_g - K_\infty\right)\dot{\epsilon} \sum_{l=1}^{M} q^{(l)}\tau^{(l)} \left(\exp\left(-\frac{t-t_{\mathrm{L}}}{\tau^{(l)}}\right) - \exp\left(-\frac{t}{\tau^{(l)}}\right)\right)\right\} \\ \qquad + \left(K_\infty - \frac{2}{3}G_\infty\right)\dot{\epsilon}t_{\mathrm{L}}, \end{cases} \tag{4.151}$$

Using the two Prony series in Table 4.51, and the three strain rates (0.1, 1, and 10 per second), the analytic model and UPM are directly compared in Fig. 4.139.

4.32.4 User Guide

The UPM model is commonly used in one of two ways. The most general use case is portrayed in full in the following syntax in which the user specifies both Prony series explicitly. That is, the user specifies all Prony relaxation times (τ) and weights for both the thermal/volumetric (f_v) and shear (f_s) relaxation functions. Note that in the UPM model, only a single set of Prony relaxation times can be specified and acts as the basis for both relaxation spectra. In other words, a single set of relaxation times is specified, and both functions use their own (distinct) weights.

Default parameters are not set. Any system of units can be used with the model. There are no internal units assumptions.

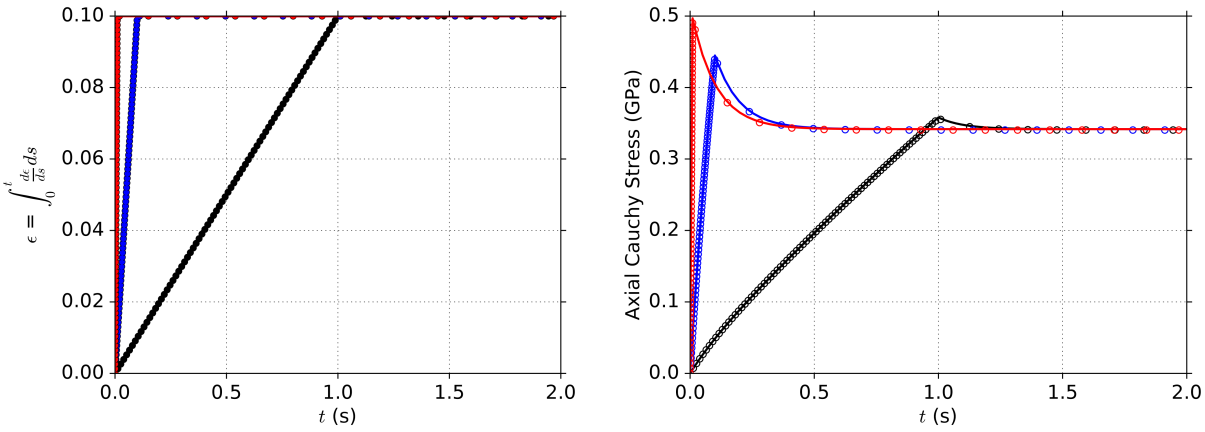

(a) Applied Strain History **(b) Axial Stress History**

Fig. 4.139 Linear viscoelastic response to a two stage uniaxial strain boundary value problem with material and loading properties specified in Table 4.51. Symbols represent FEA simulations with the UPM model while solid lines are the analytic results. The three logarithmic strain rates of 0.1, 1.0, and 10.0 per second are shown, and all cease at 10% strain, and all cases are isothermal at the reference temperature so that the shift factor is unity.

```
BEGIN PARAMETERS FOR MODEL UNIVERSAL_POLYMER
  #
  # Elastic constants: These Should be Set to the Glassy Moduli
  #                    for robustness considerations
  #
  SHEAR MODULUS   = <real>
  BULK MODULUS    = <real>
  #
  ## Reference Temperature and Material CLOCK Parameters
  #
  REFERENCE TEMPERATURE    = <real> # Temperature
  STRESS FREE TEMPERATURE = <real> # Temperature
  #
  WLF C1    = <real>
  WLF C2    = <real> # Temperature
  CLOCK C3 = <real> # Temperature
  CLOCK C4 = <real> # Temperature
  #
  ## Glassy and Rubbery Moduli
  #  and CTE Definitions at the Reference Temperature
  #
  BULK GLASSY 0     = <real> # Units of Pressure
  BULK RUBBERY 0    = <real> # Units of Pressure
  SHEAR GLASSY 0    = <real> # Units of Pressure
  SHEAR RUBBERY 0   = <real> # Units of Pressure
```

(continues on next page)

(continued from previous page)

```
 VOLCTE glassy 0  = <real> # Units of Inverse Temperature
 VOLCTE rubbery 0 = <real> # Units of Inverse Temperature
 #
 FILLER VOL FRACTION = <real>
 #
 ## Relaxation Time Spectra Definitions
 #
 WWBETA 1 = <real>
 WWTAU 1  = <real> # Units of time
 WWBETA 2 = <real>
 WWTAU 2  = <real> # Units of time
 #
 SPECTRUM START TIME = <real>  # Units of time
 SPECTRUM END TIME   = <real>  # Units of time
 LOG TIME INCREMENT  = <real>  # Units of time
 #
 ## Direct Prony Spectra Inputs
 #
 RELAX TIME 1 = <real>  # Unit of time
 RELAX TIME 2 = <real>
 .
 RELAX TIME 30 = <real>
 #
 ## Thermal/Volumetric Relaxation Spectrum Prony Weights
 #
 F1 1 = <real>
 F1 2 = <real>
 .
 F1 30 = <real>
 #
 ## Shear Relaxation Spectrum Prony Weights
 #
 F2 1 = <real>
 F2 2 = <real>
 .
 F2 30 = <real>
END [PARAMETERS FOR MODEL UNIVERSAL_POLYMER]
```

Not all Prony spectra/weight parameter pairs (1-30) need to be specified. Only those specified will be used, and the ones not specified will be set to zero. Prony weights for each relaxation function should sum to 1.0, or the model will rescale the weights so that they do sum to one. This rescaling will change the underlying relaxation response.

When the model is used with both relaxation functions being specified directly, then the parameters: SPECTRUM START TIME, SPECTRUM END TIME, LOG TIME INCREMENT, WW TAU (1,2), and WW BETA (1,2) must be specified as 0 to avoid errors during the model

property check. Note (1) is associated with the thermal/volumetric function, and (2) is associated with the shear relaxation function.

Another common usage of the UPM model is to specify the Williams-Watts (KWW) stretched exponential τ, β parameters for either or both relaxation functions (1 and/or 2) corresponding to the function $f = \exp(-(t/\tau)^{\beta})$. That is, a set of Prony weights, w_i corresponding to a specific set of Prony times, τ_i, will be found during the model property check routine. If the other relaxation function is directly specified as above, then the Prony times from the directly specified relaxation spectrum are used. In this case, the Prony weights for the relaxation function being fit to the KWW function are found through a Least-Squared Error minimization routine built into the UPM model over a discretely sampled set of times between the minimum and maximum Prony times.

When neither Prony spectrum is directly specified (both will be fit to KWW functions), then the Prony times (for both relaxation functions) are determined from an evenly logarithmically spaced set of Prony times beginning with the SPECTRUM START TIME and ending with the SPECTRUM END TIME and spaced with the (base 10) LOG TIME INCREMENT. For each relaxation function that is fit with the UPM model to a KWW function, the WW TAU (1,2) and WW BETA (1,2) parameters must be specified. However, if the user specifies both a KWW form and the same Prony series directly, the model will error out during the property check.

There are many useful optional parameters for the UPM model that generally allow for: temperature dependence of moduli, coefficients of thermal expansion, deformation dependence of moduli, and/or alternative material clock parameter specifications. These parameters may optionally be added to the material input block, but are defaulted to 0.0:

```
### OPTIONAL parameters for the universal_polymer model
 CLOCK C1          = <real> # CLOCK Coef. 1 instead of "WLF C1"
 CLOCK C2          = <real> # CLOCK Coef. 1 instead of "WLF C2"
 BULK GLASSY 1     = <real> # Pressure per Temperature
 BULK RUBBERY 1    = <real> # Pressure per Temperature
 SHEAR GLASSY 1    = <real> # Pressure per Temperature
 SHEAR RUBBERY 1   = <real> # Pressure per Temperature
 VOLCTE GLASSY 1   = <real> # Inverse Temperature Squared
 VOLCTE RUBBERY 1  = <real> # Inverse Temp. Squared
```

Finally, we note that the UPM model may be reduced to a finite deformation, linear thermoviscoelastic model by choosing $C_3 = 0$ and $C_4 = 0$. Under these conditions the material clock is only temperature (history) dependent but involves no deformation dependence. Moreover, if one wants to fix the laboratory and material time scales to be the same, then one should set WLF $C_1 = 0$.

Output variables available for this model are listed in Table 4.52. The user should always output the shift factor $aend$ or $\log_{10} a$ as this variable is critical for interpreting the material behavior.

Table 4.52 State Variables for Universal Polymer Model

Name	Description
`aend`	The shift factor relating increments of material to laboratory time, $a\,dt^* = dt_{\text{lab}}$
`loga`	$\log_{10}$ of the shift factor, $\log_{10} a$
`epsxx`	xx component of the integrated unrotated rate of deformation, ϵ_{xx}
`epsyy`	yy component of the integrated unrotated rate of deformation, ϵ_{yy}
`epszz`	zz component of the integrated unrotated rate of deformation, ϵ_{zz}
`epsxy`	xy component of the integrated unrotated rate of deformation, ϵ_{xy}
`epsyz`	yz component of the integrated unrotated rate of deformation, ϵ_{yz}
`epszx`	zx component of the integrated unrotated rate of deformation, ϵ_{zx}
`effi2`	second (non-Cayley Hamilton) invariant of ϵ providing shear deformation, I_2
`if1p1-30`	volumetric hereditary integrals 1-30
`ikat1-30`	thermal hereditary integrals 1-30
`igxx1-30`	xx component shear hereditary integrals 1-30
`igyy1-30`	yy component shear hereditary integrals 1-30
`igzz1-30`	zz component shear hereditary integrals 1-30
`igxy1-30`	xy component shear hereditary integrals 1-30
`igyz1-30`	yz component shear hereditary integrals 1-30
`igzx1-30`	zx component shear hereditary integrals 1-30

4.33 Linear Thermoviscoelastic Model

4.33.1 Theory

The linear thermoviscoelastic model (LTVE for short) is, as the name implies, a phenomenological thermoviscoelasticity model. This formulation seeks to provide a similar, albeit simpler and more adaptable, form versus the complexity of models like the `UNIVERSAL_POLYMER_MODEL` based on the potential energy clock (PEC) or simplified potential energy clock (SPEC). Further, to aid in the adaptability of the new model a modular shift factor capability is added.

For a general perspective, the LTVE model is a continuum thermodynamics based, hereditary integral viscoelastic formulation. The basic theory is quite similar to that found in Christensen [23] with some extra observations and assumptions found in the PEC/SPEC formalisms [21], [3]. To begin, external state variables of the total strain, ε_{ij}, absolute temperature, θ, and time, t, are used. No additional internal state variables are needed. A Helmholtz free energy, ψ, is introduced such that

$$\psi\left(\varepsilon_{ij},\theta,t\right) = \psi^{\infty}\left(\varepsilon_{ij},\theta\right) + \psi^{\text{neq}}\left(\varepsilon_{ij},\theta,t\right),$$

with ψ^{∞} and ψ^{neq} being the equilibrium energy describing the free-energy of the equilibrium phase and non-equilibrium energy associated with the additional energy of the glassy phase yet to

be relaxed, respectively. The former term may be given as,

$$\psi^{\infty} = \frac{1}{2\rho}\left(\varepsilon_{ij} - \bar{\alpha}^{\infty}\left(\theta - \theta_0\right)\delta_{ij}\right)\bar{\mathbb{C}}^{\infty}_{ijkl}\left(\varepsilon_{kl} - \bar{\alpha}^{\infty}\left(\theta - \theta_0\right)\delta_{kl}\right) + \psi^{\infty}_{\theta}\left(T\right),$$

where ρ, $\bar{\alpha}^{\infty}$, θ_0, and $\bar{\mathbb{C}}^{\infty}_{ijkl}$ are, respectively, the material density, current linear coefficient of thermal expansion, reference temperature, and current equilibrium stiffness tensor. A purely thermal contribution, ψ^{∞}_{θ}, is also included in the free energy but does not contribute to the mechanical response and as such is not explicitly defined at this point. In the previous and following relations, an overbar, $\bar{\cdot}$, denotes a temperature dependent quantity such that $\bar{x} = x f^{x}\left(\theta\right)$ with x being the reference constant value and $f^{x}\left(\theta\right)$ being a temperature dependent multiplier that should be order one. To capture the non-equilibrium contribution, the corresponding free-enery term is written,

$$\begin{aligned}
\psi^{\text{neq}} = &\frac{\Delta\bar{K}}{2\rho}\int_0^t\int_0^t f_v\left(t^* - s^*, t^* - u^*\right)\frac{\partial\varepsilon_{kk}}{\partial s}\frac{\partial\varepsilon_{mm}}{\partial u}dsdu \\
&+ \frac{\Delta\bar{\mu}}{\rho}\int_0^t\int_0^t f_s\left(t^* - s^*, t^* - u^*\right)\frac{\partial\varepsilon'_{ij}}{\partial s}\frac{\partial\varepsilon'_{ij}}{\partial u}dsdu \\
&- \frac{3\Delta\left(\bar{\alpha}\bar{K}\right)}{\rho}\int_0^t\int_0^t f_v\left(t^* - s^*, t^* - u^*\right)\frac{\partial\theta}{\partial s}\frac{\partial\varepsilon_{kk}}{\partial u}dsdu \\
&+ \psi^{\text{neq}}_{\theta}\left(\theta, t\right),
\end{aligned}$$

in which Δ denotes the difference in a glassy and equilibirium property ($\Delta\bar{x} = \bar{x}^{g} - \bar{x}^{\infty}$), K and μ are bulk and shear moduli, and $\psi^{\text{neq}}_{\theta}$ is a purely thermal term that does not currently impact the mechanical theory. The prior relation also included two terms related to viscoelastic spectra – f_v and f_s – with the former being related to volumetric terms and the later shear. Further, a $*$ indicates a quantity taken in the material time that is shifted from the laboratory time. These two scales are related via a shift factor, a, such that,

$$t^* = \int_0^t \frac{ds}{a\left(s\right)}.$$

While different shift factors are allowed via the modular framework, it should be noted they are restricted to those that are a function of temperature (and potentially time) alone. Non-linear shift factors involving things like deformation measures are not permitted.

Following conventional continuum thermodynamic arguments, the Cauchy stress may be determined to be,

$$\begin{aligned}
\sigma_{ij} = &\bar{K}^{\infty}\left(\varepsilon_{kk} - 3\bar{\alpha}^{\infty}\left(\theta - \theta_0\right)\right)\delta_{ij} + 2\bar{\mu}^{\infty}\varepsilon'_{ij} \\
&+ \Delta\bar{K}J^1\delta_{ij} - 3\Delta\left(\bar{\alpha}\bar{K}\right)J^3\delta_{ij} + 2\Delta\bar{\mu}J^2_{ij},
\end{aligned} \tag{4.152}$$

where J^1, J^2_{ij}, and J^3 are representations of the hereditary integrals given by,

$$J^1 = \int_0^t f_v\left(t^* - s^*\right) \frac{\partial \varepsilon_{kk}}{\partial s} ds,$$
$$J^2_{ij} = \int_0^t f_s\left(t^* - s^*\right) \frac{\partial \varepsilon'_{ij}}{\partial s} ds,$$
$$J^3 = \int_0^t f_v\left(t^* - s^*\right) \frac{\partial \theta}{\partial s} ds.$$

4.33.1.1 Modular Shift Factor

To provide enhanced flexibility to the user, the shift factor was implemented in a modular fashion such that four different functional forms can be used. The first two are well-established analytical forms – Williams-Landel-Ferry (WLF) [113] and Arrhenius. These forms are given by,

$$\log_{10} a^{\text{WLF}} = \frac{-C_1\left(\theta - \theta_{\text{ref}}\right)}{C_2 + \left(\theta - \theta_{\text{ref}}\right)},$$
$$\log_{10} a^{\text{Arr}} = \frac{E_a}{R}\left(\log_{10} \text{e}\right)\left(\frac{1}{\theta} - \frac{1}{\theta_{\text{ref}}}\right),$$

with C_1, C_2, and θ_{ref} being fit parameters for the WLF expression and E_a and R are the activation energy and gas constant for the Arrhenius energy, respectively. To enable direct utilization of experimental determination of the shift factor, the third option is a user-defined shift factor that is explicitly a function of temperature such that,

$$a = a^{\text{ud}}\left(\theta\right),$$

in which a^{ud} is any user-defined Sierra scope function. Additionally, to be clear, the Sierra function should define the actual shift factor and not its logarithm.

Finally, the fourth option for the modular shift factor is defined to introduce history dependence in the cooling rate. This shift factor is referred to as `WLF_LAG` and is the WLF term with an extra thermal history dependence integral and is equivalent to the SPEC shift factor with $C_3 = C_4 = 0$ and is written,

$$\log_{10} a^{\text{WLF_LAG}} = \frac{-C_1\left(\theta - \theta_{\text{ref}} - \int_0^{tf_v}\left(t^* - s^*\right)\frac{\partial\theta}{\partial s} ds\right)}{C_2 + \left(\theta - \theta_{\text{ref}} - \int_0^{tf_v}\left(t^* - s^*\right)\frac{\partial\theta}{\partial s} ds\right)}.$$

For more details please see [59]

4.33.2 Implementation

To implement the LTVE model, a fully implicit, backward Euler hypoelastic approach is utilized to integrate the model from a time t_n to a new time t_{n+1} with $\Delta t = t_{n+1} - t_n$. The material state at time t_n is taken to be completely known. Loading is prescribed via a total strain rate, $\dot{\varepsilon}_{ij}^{n+1}$, such that $\varepsilon_{ij}^{n+1} = \varepsilon_{ij}^{n} + \Delta t \dot{\varepsilon}_{ij}^{n+1}$, and prescribed temperature history such that $\theta^{n+1} = \theta\left(t_{n+1}\right)$ is known. Objectivity is satisfied through the standard approaches described in Section 4.1.

In such an implicit form, the updated stress is written

$$\sigma_{ij}^{n+1} = \sigma_{ij}^{n} + \Delta t \dot{\sigma}_{ij}^{n+1}.$$

The rate of change of the stress, $\dot{\sigma}_{ij}$, may be found by differentiating (4.152) and written as,

$$\begin{aligned}
\dot{\sigma}_{ij} = {} & \bar{K}^{\infty} \dot{\varepsilon}_{kk} \delta_{ij} + 2\bar{\mu}^{\infty} \dot{\varepsilon}'_{ij} + \Delta\bar{K} \dot{J}^1 \delta_{ij} - 3\Delta\left(\bar{\alpha}\bar{K}\right) \dot{J}^3 \delta_{ij} - 3\bar{K}^{\infty} \bar{\alpha}^{\infty} \dot{\theta} \delta_{ij} + 2\Delta\bar{\mu} \dot{J}^2_{ij} \\
& - 3\dot{\theta}\delta_{ij} \left(\left(\frac{\partial \bar{K}^{\infty}}{\partial \theta} \bar{\alpha}^{\infty} + \bar{K}^{\infty} \frac{\partial \bar{\alpha}^{\infty}}{\partial \theta} \right) (\theta - \theta_0) + \frac{\partial \left(\Delta\bar{\alpha}\bar{K}\right)}{\partial \theta} J^3 - \frac{1}{3} \frac{\partial \bar{K}^{\infty}}{\partial \theta} \varepsilon_{kk} - \frac{1}{3} \frac{\partial \left(\Delta\bar{K}\right)}{\partial \theta} J^1 \right) \\
& + 2\dot{\theta} \left(\frac{\partial \bar{\mu}^{\infty}}{\partial \theta} \varepsilon'_{ij} + \frac{\partial \left(\Delta\bar{\mu}\right)}{\partial \theta} J^2_{ij} \right)
\end{aligned}$$

In the preceeding relation, the latter two lines pertain purely to changes in temperature dependent thermoelastic properties. With the strain rate, current strain, and current temperature prescribed as inputs, expressions for the temperature rate, hereditary integral rates, and current values of the hereditary integral are needed. The first may be simply numerically approximated via,

$$\dot{\theta}^{n+1} \approx \frac{\theta^{n+1} - \theta^{n}}{\Delta t}.$$

The actual expression for the hereditary integral has not been defined to this point. The choice and selection of these functions has long been studied as the ability to accurately and efficiently numerically integrate them is essential for making the models tractable. This problem has been tackled previously through the judicious use of exponential functions. To this end, the forms proposed by Caruthers *et al.* [21] are used and are written,

$$f_{v,s}\left(t^* - s^*, t^* - u^*\right) = \sum_{k=1}^{n_{v,s}} w_k^{v,s} \exp\left(-\frac{t^* - s^*}{\tau_k^{v,s}}\right) \exp\left(-\frac{t^* - u^*}{\tau_k^{v,s}}\right),$$

where v, s indicate either the volumetric or shear spectra and w_k and τ_k are the corresponding charastic weight and time, respecitvely, of the $k-$th prony term. The number of prony terms is denoted $n_{v,s}$.

The first herediatry integral term may be written,

$$J^1 = \sum_{n=1}^{n_v} w_k^v J^{1(k)}, \qquad J^{1(k)} = \int_0^t \exp\left(-\frac{t^* - s^*}{\tau_k^v}\right) \frac{\partial \varepsilon_{mm}}{\partial s} ds. \tag{4.153}$$

For simplicity in what follows, only the integration of J^1 is presented although similar approaches may be followed for J^2_{ij} and J^3. Differentiating the two expressions in (4.153) yields,

$$\dot{J}^1 = \sum_{k=1}^{n_v} w_k^v \dot{J}^{1(k)}, \tag{4.154}$$

$$\dot{J}^{1(k)} = \dot{\varepsilon}_{mm} - \frac{1}{\tau_k^v}\frac{dt^*}{dt}\int_0^t \exp\left(-\frac{t^*-s^*}{\tau_k^v}\right)\frac{\partial \varepsilon_{mm}}{\partial s}ds = \dot{\varepsilon}_{mm} - \frac{1}{a\tau_k^v}J^{1(k)}. \tag{4.155}$$

With these expressions, it is clear that first step in updating J_1 is updating the various characteristic components. Each of these may be integrated implicitly via,

$$J_{n+1}^{1(k)} = J_n^{1(k)} + \Delta t \dot{J}_{n+1}^{1(k)}.$$

Using (4.155), the updated characteristic component of the hereditary integral is written,

$$J_{n+1}^{1(k)} = \frac{a^{n+1}\tau_k^v}{a^{n+1}\tau_k^v + \Delta t}\left(J_n^{1(k)} + \Delta t \dot{\varepsilon}_{mm}^{n+1}\right).$$

With all of the components identified, the updated stress becomes,

$$\begin{aligned}
\sigma_{ij}^{n+1} = {} & \sigma_{ij}^n + \hat{K} d\varepsilon_{kk}\delta_{ij} + 2\hat{\mu} d\varepsilon'_{ij} - 3\left(\hat{K\alpha}\right) d\theta \delta_{ij} \\
& - \Delta\bar{K}\sum_{k=1}^{n_v}\frac{w_k^v \Delta t}{a\tau_k^v + \Delta t}\left(J_n^{1(k)} + d\varepsilon_{mm}\right)\delta_{ij} - 2\Delta\bar{\mu}\sum_{k=1}^{n_s}\frac{w_k^s \Delta t}{a\tau_k^s + \Delta t}\left(J_{ij}^{2(k)(n)} + d\varepsilon'_{ij}\right) \\
& + 3\Delta\left(\bar{\alpha}\bar{K}\right)\sum_{k=1}^{n_v}\frac{w_k^v \Delta t}{a\tau_k^v + \Delta t}\left(J_n^{3(k)} + d\theta\right) \\
& - 3d\theta\delta_{ij}\left((\theta - \theta_0)\left(\frac{\partial \bar{K}^\infty}{\partial\theta}\bar{\alpha}^\infty + \bar{K}^\infty\frac{\partial\bar{\alpha}}{\partial\theta}\right) + \frac{\partial\left(\Delta\bar{\alpha}\bar{K}\right)}{\partial\theta}\sum_{k=1}^{n_v} w_k^v\left(\frac{a\tau_k^v}{a\tau_k^v + \Delta t}\right)\left(d\theta + J_n^{3(k)}\right)\right) \\
& + d\theta\left(\frac{\partial\bar{K}^\infty}{\partial\theta}\varepsilon_{kk}^{n+1}\delta_{ij} + 2\frac{\partial\bar{\mu}^\infty}{\partial\theta}\varepsilon_{ij}^{\prime(n+1)} + \frac{\partial\left(\Delta\bar{K}\right)}{\partial\theta}\delta_{ij}\sum_{k=1}^{n_v} w_k^v\left(\frac{a\tau_k^v}{a\tau_k^v + \Delta t}\right)\left(J_n^{1(k)} + d\varepsilon_{mm}\right)\right. \\
& \left. + 2\frac{\partial\Delta\bar{\mu}}{\partial\theta}\sum_{k=1}^{n_s} w_k^s\left(\frac{a\tau_k^s}{a\tau_k^s + \Delta t}\right)\left(J_{ij}^{2(k)(n)} + d\varepsilon'_{ij}\right)\right),
\end{aligned}$$

with $d\theta = \theta^{n+1} - \theta^n$, $d\varepsilon_{ij} = \dot{\varepsilon}_{ij}\Delta t$, and

$$\begin{aligned}
\hat{K} &:= \bar{K}^\infty + \Delta\bar{K}\sum_{k=1}^{n_v} w_k^v, \\
\hat{\mu} &:= \bar{\mu}^\infty + \Delta\bar{\mu}\sum_{k=1}^{n_s} w_k^s, \\
\left(\hat{\alpha K}\right) &:= \bar{K}^\infty\bar{\alpha}^\infty + \Delta\left(\bar{\alpha}\bar{K}\right)\sum_{k=1}^{n_v} w_k^v.
\end{aligned}$$

4.33.3 Verification

To verify the LTVE model, a series of verification exercises have been pursued. For these activities the viscoelastic parameterization provided by Kuether [53] are used in which model parameters are given in Table 4.53 and the viscoelastic spectra in Table 4.54. Given the rate-dependent nature of the viscoelastic models, analytical solutions are generally not available. As such, semi-analytic approaches are generally pursued through a variety of loadings.

Table 4.53 Model parameters for the linear thermoviscoelastic model from Kuether.

K^{∞}	3.2 GPa	K^{g}	4.9 GPa
G^{∞}	4.5 MPa	G^{g}	752 MPa
C_1	16.5 (-)	C_2	54.3 (^{o}C)
T_{ref}	75 (^{o}C)	E_a/R	3928 (^{o}C)

Table 4.54 Viscoelastic strectra for the linear thermoviscoelastic model from Kuether.

term	τ_k^v (s)	w_k^v (-)	τ_k^s (s)	w_k^s (-)
1	1.0×10^{-10}	1.06×10^{-2}	1.0×10^{-10}	4.96×10^{-3}
2	1.0×10^{-9}	1.14×10^{-2}	1.0×10^{-9}	6.85×10^{-3}
3	1.0×10^{-8}	1.64×10^{-2}	1.0×10^{-8}	1.14×10^{-2}
4	1.0×10^{-7}	2.27×10^{-2}	1.0×10^{-7}	1.97×10^{-2}
5	1.0×10^{-6}	2.63×10^{-2}	1.0×10^{-6}	2.64×10^{-2}
6	3.16×10^{-6}	8.85×10^{-3}	3.16×10^{-6}	1.13×10^{-2}
7	1.0×10^{-5}	2.52×10^{-2}	1.0×10^{-5}	2.98×10^{-2}
8	3.16×10^{-5}	1.94×10^{-2}	3.16×10^{-5}	2.75×10^{-2}
9	1.0×10^{-4}	2.80×10^{-2}	1.0×10^{-4}	4.02×10^{-2}
10	3.16×10^{-4}	2.83×10^{-2}	3.16×10^{-4}	4.58×10^{-2}
11	1.0×10^{-3}	3.41×10^{-2}	1.0×10^{-3}	5.76×10^{-2}
12	3.16×10^{-3}	3.70×10^{-2}	3.16×10^{-3}	6.74×10^{-2}
13	1.0×10^{-2}	4.19×10^{-2}	1.0×10^{-2}	7.90×10^{-2}
14	3.16×10^{-2}	4.58×10^{-2}	3.16×10^{-2}	8.85×10^{-2}
15	1.0×10^{-1}	5.02×10^{-2}	1.0×10^{-1}	9.56×10^{-2}
16	3.16×10^{-1}	5.39×10^{-2}	3.16×10^{-1}	9.72×10^{-2}
17	1.0×10^{0}	5.71×10^{-2}	1.0×10^{0}	9.17×10^{-2}
18	3.16×10^{0}	5.93×10^{-2}	3.16×10^{0}	7.79×10^{-2}
19	1.0×10^{1}	6.03×10^{-2}	1.0×10^{1}	5.75×10^{-2}
20	3.16×10^{1}	5.97×10^{-2}	3.16×10^{1}	3.49×10^{-2}
21	1.0×10^{2}	5.72×10^{-2}	1.0×10^{2}	1.63×10^{-2}
22	3.16×10^{2}	5.30×10^{-2}	3.16×10^{2}	5.26×10^{-3}
23	1.0×10^{3}	4.66×10^{-2}	1.0×10^{3}	1.05×10^{-3}
24	3.16×10^{3}	3.95×10^{-2}	3.16×10^{3}	8.72×10^{-5}
25	1.0×10^{4}	3.03×10^{-2}	1.0×10^{4}	1.29×10^{-5}

continues on next page

Table 4.54 – continued from previous page

26	3.16×10^4	2.34×10^{-2}	1.0×10^5	2.67×10^{-6}
27	1.0×10^5	1.34×10^{-2}	1.0×10^6	4.17×10^{-7}
28	3.16×10^5	1.12×10^{-2}		
29	1.0×10^6	1.56×10^{-2}		
30	3.16×10^6	4.84×10^{-3}		

4.33.3.1 Balanced Biaxial Creep

For the first test of the LTVE model, the creep response under a balanced biaxial load is investigated. For this case, the stress state reduces to,

$$\sigma_{ij}\left(t\right) = \begin{bmatrix} \sigma\left(t\right) & 0 & 0 \\ 0 & -\sigma\left(t\right) & 0 \\ 0 & 0 & 0 \end{bmatrix}.$$

Under a constant temperature, $\theta\left(t\right) = \theta\left(t_0\right)$, the stress state remains deviatoric through loading such that $\sigma'_{ij}\left(t\right) = \sigma_{ij}\left(t\right)$ thereby reducing the stress tensor to

$$\sigma_{ij} = 2\mu^{\infty}\varepsilon_{ij} + 2\Delta\mu J^2_{ij}. \tag{4.156}$$

With these prescribed, only the strain remains unknown to be determined. Given the assumed stress state, the strains may also be related via $\varepsilon_{yy} = -\varepsilon_{xx}$ reducing the problem to a single unknown. Following the implicit integration approaches discussed in the numerical implementation section, a semi-analytic expression for the strain is written,

$$\varepsilon^{n+1}_{xx} = \frac{\sigma^{n+1}_{xx} - 2\Delta\mu\sum_{i=1}^{n_s} w^s_k \frac{a^{n+1}\tau^s_k}{a^{n+1}\tau^s_k+\Delta t}\left(J^{2(k)(n+1)}_{xx} - \varepsilon^n_{xx}\right)}{2\left(\mu^{\infty} + \Delta\mu\sum_{i=1}^{n_s} w^s_k \frac{a^{n+1}\tau^s_k}{a^{n+1}\tau^s_k+\Delta t}\right)} \tag{4.157}$$

This problem is run with $\theta\left(t=0\right) = 65°\text{C}$ and 75°C and a mechanical load initially at $\sigma\left(t=0\right) = 0$ increasing to 10 MPa in 10 seconds. The load is then held for two hours. To consider the user-defined shift factor, an analytical function of the WLF shift factor is defined and used for the tests. Both the semi-analytic expression of (4.157) and equivalent responses of the LTVE model are considered. As a further test, the `UNIVERSAL_POLYMER` model is reduced to the same response and is also presented in Fig. 4.140. For a final comparison, the viscoelastic capabilities of Sierra/StructuralDynamics (the `Linear Viscoelastic` model) are also considered. However, the shift factor form used in that model uses the WLF expression above θ_{ref} and a different expression below. Therefore, results from that model are only given for the case of $\theta\left(t=0\right) = 75°\text{C}$ case.

Results for the various WLF shift factor cases are given in Fig. 4.140(a) while Arrhenius shift factors are found in Fig. 4.140(b). In all of the analyses, 1000 time steps are used. In all instance, agreement is observed between all the results.

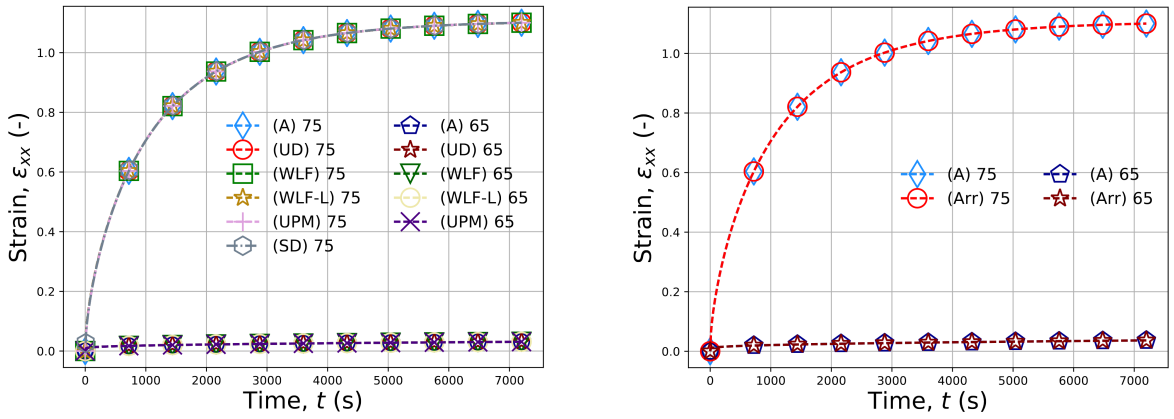

(a) WLF **(b) Arr**

Fig. 4.140 Verification results for the balanced biaxial creep problem for models with (a) WLF and (b) Arrhenius shift factors at 65°C and 75°C. Results labelled with (A), (UPM), and (SD) reflect solutions obtained from (4.157), the `UNIVERSAL_POLYMER` model, and Sierra/SD, respectively. Results from the LTVE model with user-defined, WLF, `WLF_LAG`, and Arrhenius shift factors are denoted, respectively, (UD), (WLF), (WLF-L), and (Arr).

4.33.3.2 Hydrostatic Creep

As the previous balanced biaxial loading produced a purely deviatoric stress state it correspondingly tested only the deviatoric spectra. To probe the volumetric response, a pure hydrostatic creep test is now investigated. For this purpose, a stress state of the form,

$$\sigma_{ij}\left(t\right) = \frac{1}{3}\begin{bmatrix} p\left(t\right) & 0 & 0 \\ 0 & p\left(t\right) & 0 \\ 0 & 0 & p\left(t\right) \end{bmatrix},$$

is assumed. Taking the temperature history to be constant ($\theta\left(t\right) = \theta\left(t = 0\right)$) yields a stress state of the form,

$$\sigma_{ij} = K^{\infty}\varepsilon_{kk}\delta_{ij} + \Delta K J^{1}\delta_{ij}. \tag{4.158}$$

Integrating (4.158) implicitly yields the semi-analytical relation,

$$\varepsilon_{mm}^{n+1} = \frac{p^{n+1} - 3\Delta K\sum_{k=1}^{n_v} w_k^v \frac{a^{n+1}\tau_k^v}{a^{n+1}\tau_k^v + \Delta t}\left(J_n^{1(k)} - \varepsilon_{mm}^n\right)}{3\left(K^{\infty} + \Delta K\sum_{k=1}^{n_v} w_k^v \frac{a^{n+1}\tau_k^v}{a^{n+1}\tau_k^v + \Delta t}\right)}. \tag{4.159}$$

To verify the LTVE model response, the creep problem is solved for temperatures of $\theta\left(t = 0\right) = 65$°C and 75°C with an applied pressure of -30 MPa applied via a linear ramp over 10 s and then held constant for two hours. Results for the semi-analytical model, LTVE model with the WLF, `WLF_LAG` (WLF-L), and user-defined (UD) shift factors as well as the `UNIVERSAL_POLYMER` model at both temperatures as well as the Sierra/StructuralDynamics

(SD) response at 75°C are presented in Fig. 4.141(a). Semi-analytical expressions and LTVE results with the Arhhenius shift factor are given in Fig. 4.141(b). In both figures, semi-analytical results are indicated by an (A) and all simulations use 1,000 time steps during the hold portion of the creep loading.

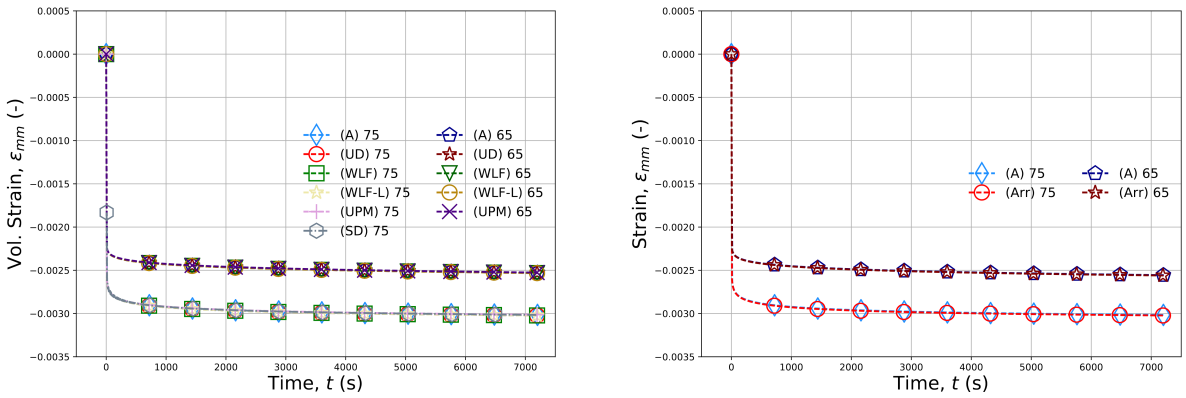

(a) WLF **(b) Arr**

Fig. 4.141 Verification results for the hydrostatic creep problem for models with (a) WLF and (b) Arrhenius shift factors at 65°C and 75°C. Results labelled with (A), (UPM), and (SD) reflect solutions obtained from (4.159), the `UNIVERSAL_POLYMER` model, and Sierra/SD, respectively. Results from the LTVE model with user-defined, WLF, `WLF_LAG`, and Arrhenius shift factors are denoted, respectively, (UD), (WLF), (WLF-L), and (Arr).

From the results in Fig. 4.141, clear agreement is noted across all of the results verifying the implementation of the volumetric hereditary integrals.

4.33.3.3 Pure Shear

The two prior investigations probed the model response under various creep loadings. Such cases neglect to consider regimes with evolving mechanical loads. Further, while both the volumetric and deviatoric spectra were tested, the resulting stress states only had normal components. Therefore, to test both of these limitations, verification exercises with an isothermal, constant strain rate pure shear mechanical loadings are pursued. For these studies, $\varepsilon_{xy}\,(t) = \dot{\varepsilon} t$ and all other strains are zero. With the isothermal profile and pure shear mechanical loadings the volumetric contributions are zero and may be neglected. The only non-zero stress is σ_{xy} which may be described via (4.156). Unlike the previous cases in which the stress was known and the strain found, the current study has a prescribed strain path in which the stress must be determined. Using the previous assumptions and an implicit integration scheme, a semi-analytic expression for the updated stress is given by,

$$\sigma_{xy} = 2\mu^{\infty}\varepsilon_{xy}^{n+1} + 2\Delta\mu \sum_{i=1}^{n_{\text{shear}}} w_k^s \left(\frac{a^{n+1}\tau_k^s}{a^{n+1}\tau_k^s + \Delta t} \right) \left(J_{xy}^{2(k)(n)} + \dot{\varepsilon}_{xy}\Delta t \right). \tag{4.160}$$

To enable comparing the responses across shift factors, the loading is simulated for three different strain rates at $T\,(t) = T_{\text{ref}} = 75°\text{C}$. Responses are presented for the semi-analytical in (4.160) as well as via the LTVE model with various shift factors and the `UNIVERSAL_POLYMER` model in Fig. 4.142. For every case presented in Fig. 4.142, agreement is noted across all responses.

4.33.3.4 No-Load Cooling

All of the previous cases considered isothermal temperature profiles. Differences in the shift factors were introduced via the use of varying constant temperatures and applied strain rates. However, the hereditary integral in the `WLF_Lag` shift factor does not play a role in such cases and therefore is not tested. To alleviate this, a no-load cooling profile is investigated. Specifically, a problem previously considered in [58] is studied here. It consists of cooling a representative inorganic glass (Schott 8061) extensively characterized by Chambers *et al.* [22] from 510°C ($T_{\text{ref}} + 50°\text{C}$) to 150°C (783 K to 423K) at different constant cooling rates. The model parameterizations used in this study may be found in corresponding references [58], [22] and are not repeated here for brevity (for the Arrhenius shift factor, a value of $E_a/R = 23,670$ was found by doing a best fit to the WLF expression). For this test, temperature dependence of thermoelastic constants is neglected to simplify the restrict the impact of cooling to the shift factor. A constant cooling rate of $\dot{T} = 2°\text{C/min}$ is used for all shift factors while additional rates of $\dot{T} = 0.2$ and 20°C/min are also used to assess history dependence.

By implicitly integrating J^1 and noting that the response is purely volumetric, an expression for the volume strain may be given as,

$$\varepsilon_{kk}^{n+1} = \frac{1}{K^\infty + \Delta K \sum_{i=1}^{n_{\text{bulk}}} \frac{a^{n+1}\tau_k^v}{a^{n+1}\tau_k^v + \Delta t}} \left[3K^\infty \alpha^\infty \left(T - T_0\right) + 3\Delta\left(\alpha K\right) J_{n+1}^3 \right.$$
$$\left. -\Delta K \sum_{i=1}^{n_{\text{bulk}}} \frac{a^{n+1}\tau_k^v}{a^{n+1}\tau_k^v + \Delta t} \left(J_n^{1(k)} - \varepsilon_{kk}^n \right) \right].$$

The previous relation assumes that J_{n+1}^3 is known. As this term is purely temperature and history dependent it may be integrated seperately knowing the loading history. For the `WLF_Lag` shift factor this is a non-linear relation. Regardless, for all cases of interest this term is found via implicit integration.

Fig. 4.143 presents results determined semi-analytically via (4.161) and numerically via the LTVE model. Histories for the $(a)\ \log_{10} a$ $(b)\ \varepsilon_{kk}$ $(c)\ J^1$ and $(d)\ J^3$ are presented for all of the shift factors without history dependence. Good agreement is noted across all results.

To consider the impact of the history dependence, results at the three different cooling rates are determined semi-analytically (A), numerically with the LTVE model (N), and numerically with the `UNIVERSAL_POLYMER` model (UPM) in Fig. 4.144. Evolutions for $(a)\ \log_{10} a$ (b) volume strain $(c)\ J_1$ and $(d)\ J_3$. The J_1 and J_3 results are not presented for the UPM case as they are not readily output. Once more, good agreement is noted across all of the results.

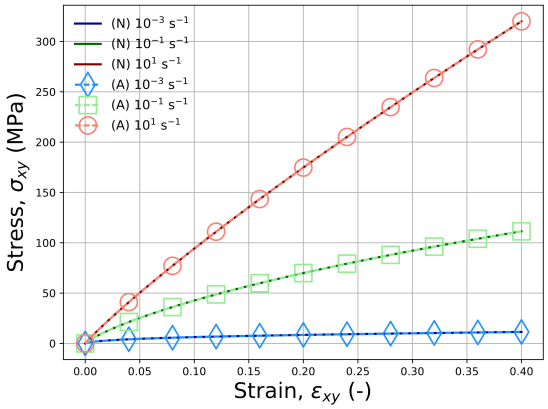

(a) WLF

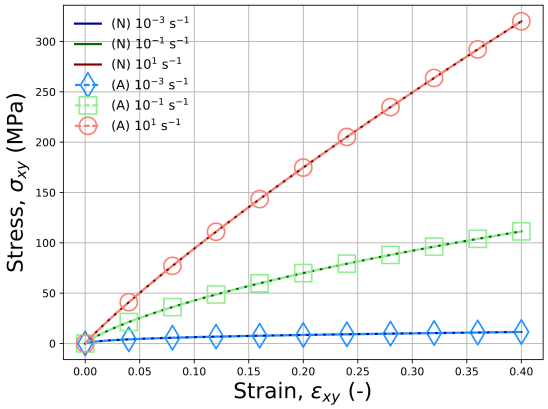

(b) WLF Lag

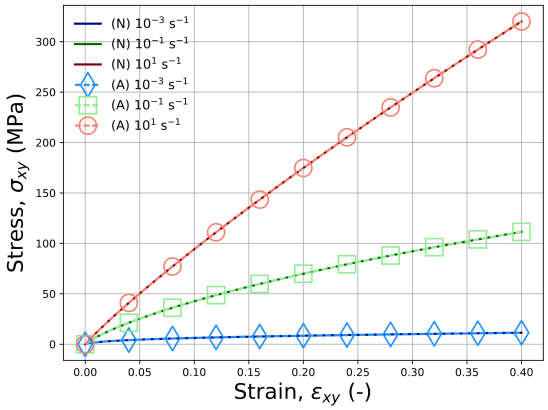

(c) UD

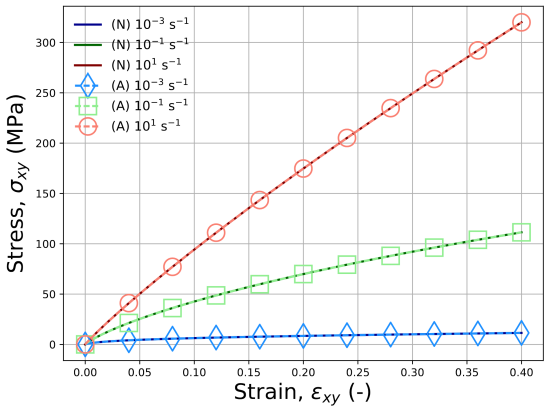

(d) ARR

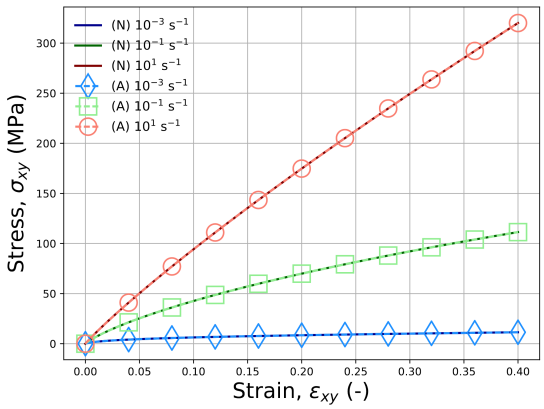

(e) UPM

Fig. 4.142 Verification results for the pure shear, constant strain rate problem for LTVE model with (*a*) WLF, (*b*) `WLF_Lag` (*c*) user-defined (ud), (*d*) Arrhenius (Arr) shift factors and (*e*) `UNIVERSAL_POLYMER` model at 75∘C and shear strain rates of $\dot{\varepsilon}_{xy} = 1 \times 10^{-3},\ 1 \times 10^{-1}$, and 1×10^{1} $\mathbf{s}^{-1}$. Solutions determined through the reduced in (4.160) are (A).

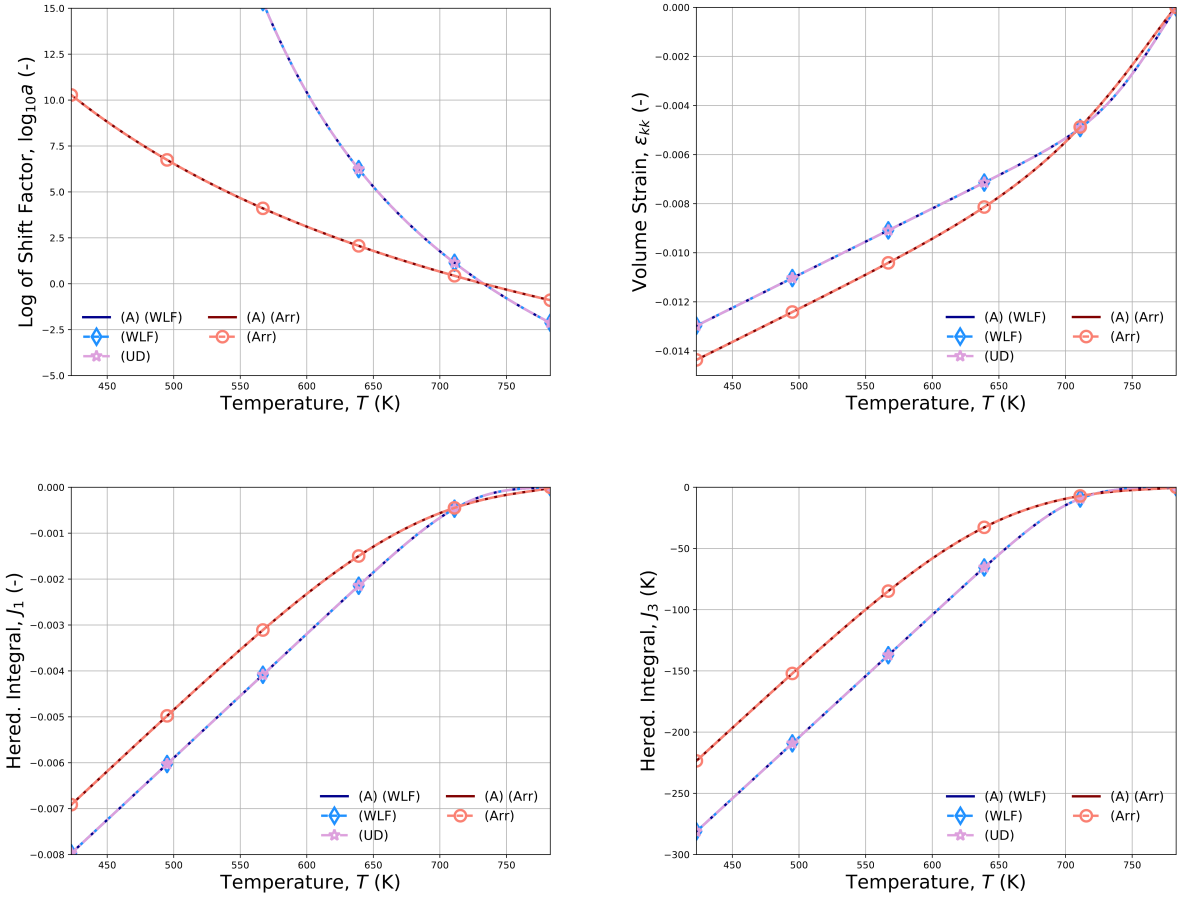

Fig. 4.143 Verification results for the no-load cooling problem for the LTVE model exhibiting analytical and numerical results for (a) $\log_{10}a$, (b) ε_{kk}, (c) J^1, and (d) J^3. Results are obtained (A) semi-analytically and with WLF, (UD) user-defined, and (Arr) Arrhenius shift factors.

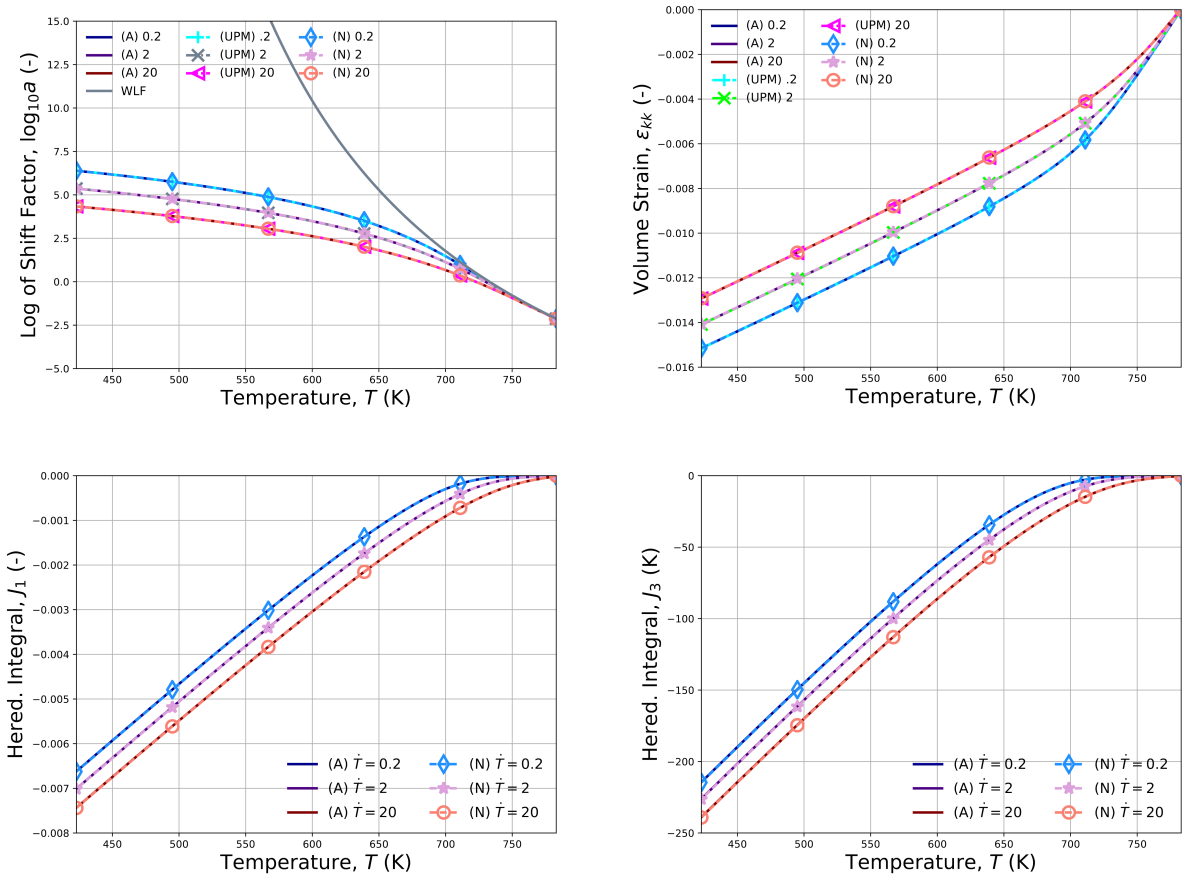

Fig. 4.144 Verification results for the no-load cooling problem for the LTVE and `UNIVERSAL_POLYMER` models exhibiting analytical and numerical results for (a) $\log_{10}a$, (b) ε_{kk}, (c) J^1, and (d) J^3. The numbers in the legend indicate cooling rates of $\dot{T} = 0.2,\ 2,$ and 20 K/min and results are obtained semi-analytically (A), numerically with the LTVE model (N), and numerically with the `UNIVERSAL_POLYMER` (UPM) model.

4.33.4 User Guide

```
BEGIN PARAMETERS FOR MODEL LINEAR_THERMOVISCOELASTIC
  #
  SHEAR MODULUS  = <real>
  BULK MODULUS   = <real>
  #
  BULK RUBBERY 0  = <real>
  SHEAR RUBBERY 0 = <real>
  ALPHA RUBBERY 0 = <real>
  #
  BULK GLASSY 0  = <real>
  SHEAR GLASSY 0 = <real>
  ALPHA GLASSY 0 = <real>
  #
  #  - Optional temperature dependence of thermoelastic constants
  #
  BULK RUBBERY TEMPERATURE DEPENDENCE  = <string>
  SHEAR RUBBERY TEMPERATURE DEPENDENCE = <string>
  ALPHA RUBBERY TEMPERATURE DEPENDENCE = <string>
  #
  BULK GLASSY TEMPERATURE DEPENDENCE  = <string>
  SHEAR GLASSY TEMPERATURE DEPENDENCE = <string>
  ALPHA GLASSY TEMPERATURE DEPENDENCE = <string>
  #
  #  - Reference temperature only needed
  #    if using temperature dependent parameters
  #
  T0 = <real>
  #
  SHIFT FACTOR MODEL = WLF | ARRHENIUS | USER_DEFINED | WLF_LAG
  #
  #  - IF SHIFT FACTOR MODEL = WLF | WLF_LAG
  #
  WLF C1 = <real>
  WLF C2 = <real>
  REFERENCE TEMPERATURE   = <real>
  #
  #  - IF SHIFT FACTOR MODEL = ARRHENIUS
  #
  NORM ACTIVATION ENERGY = <real>
  REFERENCE TEMPERATURE  = <real>
  #
  #  - IF SHIFT FACTOR MODEL = USER_DEFINED
  #
  SHIFT FACTOR FUNCTION = <string>
```

(continues on next page)

(continued from previous page)

```
  #
  NUM BULK PRONY TERMS = <int>
  #
  BULK RELAX TIME 1 = <real>
  BULK RELAX TIME 2 = <real>
  # ...
  BULK RELAX TIME 30 = <real>
  #
  f1 1  = <real>
  f1 2  = <real>
  # ...
  f1 30 = <real>
  #
  NUM SHEAR PRONY TERMS = <int>
  #
  SHEAR RELAX TIME 1 = <real>
  SHEAR RELAX TIME 2 = <real>
  # ...
  SHEAR RELAX TIME 30 = <real>
  #
  f2 1  = <real>
  f2 2  = <real>
  # ...
  f2 30 = <real>
  #
END [PARAMETERS FOR MODEL LINEAR_THERMOVISCOELASTIC]
```

In the command blocks that define the LINEAR_THERMOELASTIC model:

- The bulk and shear moduli of the equilibrium (rubbery) phase are defined by the `BULK RUBBERY 0` and `SHEAR RUBBERY 0` command lines, respectively.
- The bulk and shear moduli of the glassy phase are defined by the `BULK GLASSY 0` and `SHEAR GLASSY 0` command lines, respectively.
- The *linear* coefficients of thermal expansion of the rubbery and glassy phases are given by the `ALPHA RUBBERY 0` and `ALPHA GLASSY 0` command lines, respectively. Note, the UNIVERSAL POLYMER model uses volumetric – not linear – coefficients of thermal expansion.
- The shift factor model is specified via the `SHIFT FACTOR MODEL` command line.
- For the WLF or WLF_LAG shift factor models, the C_1 coefficient, C_2 coefficient, and reference temperature, θ_{ref}, are defined via the `WLF C1`, `WLF C2`, and `REFERENCE TEMPERATURE` command lines.
- For the Arrhenius shift factor model, the normalized activation energy, E_a/R, and reference temperature, θ_{ref}, are specified via the `NORM ACTIVATION ENERGY` and `REFERENCE`

TEMPERATURE command lines.

- For the user-defined shift factor model, the function name is specified via the SHIFT FACTOR FUNCTION command line. Note, any Sierra scope function may be defined and should be specified as a function of temperature. It is also emphasized the actual shift factor – not the logarithm of it – should be directly defined. Care should be taken to ensure the function is defined and admissible over the expected temperature domain.
- The number of terms in the Prony series of the bulk, n_{bulk}, and shear, n_{shear}, are given by the NUM BULK PRONY TERMS and NUM SHEAR PRONY SERIES command lines. These two numbers do not need to be the same and must both be defined. The maximum permissible number is 30 although any lower number is permissible.
- The bulk relaxation spectrum is characterized by a series of times, τ_k^v, and weights, w_k^v. The times are defined via BULK RELAX TIME 1 through BULK RELAX TIME k where k is the number of terms in the spectrum. The same times do not need to be used for the bulk and shear terms. Weights are defined via the f1 1 through f1 k command lines. k should be equal to n_{bulk}.
- The shear relaxation spectrum is characterized by a series of times, τ_k^s, and weights, w_k^s. The times are defined via SHEAR RELAX TIME 1 through SHEAR RELAX TIME k where k is the number of terms in the spectrum. The same times do not need to be used for the bulk and shear terms. Weights are defined via the f2 1 through f2 k command lines. k should be equal to n_{shear}.

Output variables available for this model are listed in Table 4.55. Note, for each of the various hereditary integral individual components may be output by specifying a hereditary integral ..._X where X is an integer term in the spectrum. For instance, the 7^{th} term of the Prony series of the volume strain integral (J_7^1) is output by specifying J1_7.

Table 4.55 State Variables for LINEAR_THERMOVISCOELASTIC Model

Name	Description
a	shift factor, a
J1	volume strain hereditary integral, J^1
J2_XX	XX component of the deviatoric hereditary integral, J^2_{11}
J2_YY	YY component of the deviatoric hereditary integral, J^2_{22}
J2_ZZ	ZZ component of the deviatoric hereditary integral, J^2_{33}
J2_XY	XY component of the deviatoric hereditary integral, J^2_{12}
J2_YZ	YZ component of the deviatoric hereditary integral, J^2_{23}
J2_ZX	ZX component of the deviatoric hereditary integral, J^2_{31}
J3	thermal strain hereditary integral, J^3

4.34 Wire Mesh Model

4.34.1 Theory

The wire mesh model was developed at Sandia National Laboratories for use with layered sequences of metallic wire meshes and cloth fabric. Model development was based on an extensive series of experiments performed on these materials (see [76]) and used an existing model for rigid polyurethane foams as a starting point [75].

To be able to analyze the response of this material, the Cauchy stress tensor is first decomposed into its principal components, σ^i. Each principal stress is evaluated independently and two behaviors are considered depending on whether or not the material is in tension or compression. Under a tensile load, the material is taken to be perfectly plastic above a yield stress, τ. For compressive loads, it is assumed that the materials hardens functionally with the volumetric engineering strain, ε_{V}. In this formulation, an arbitrary form of this hardening function, $\bar{\sigma}\left(\varepsilon_{\mathrm{V}}\right)$ is assumed although in the original work [76],

$$\bar{\sigma}\left(\varepsilon_{\mathrm{V}}\right) = ae^{-b\varepsilon_{\mathrm{V}}}, \tag{4.161}$$

with a and b as material constants, was used.

With these assumptions, the yield function of the i^{th} principal stress, f^i, may be written as,

$$f^i = \begin{cases} \sigma^i - \tau, & \sigma^i \geq 0 \\ -\sigma^i - \bar{\sigma}\left(\varepsilon_{\mathrm{V}}\right) & \sigma^i < 0 \end{cases}.$$

where τ is the isotropic tensile strength of the material.

Similar to the rigid polyurethane foam model [76], the flow rule is defined as:

$$d_{ij}^{\mathrm{p}} = \dot{\gamma}^1 P_{ijkl}^1 \sigma_{kl} + \dot{\gamma}^2 P_{ijkl}^2 \sigma_{kl} + \dot{\gamma}^3 P_{ijkl}^3 \sigma_{kl}$$

with $\dot{\gamma}^i$ being the magnitude of the i^{th} plastic strain increment and P_{ijkl}^r is the fourth-order principal projection operator defined as,

$$P_{ijkl}^r = n_i^r n_j^r n_k^r n_l^r$$

in which n_i^r is the corresponding direction vector of principal stress, σ^r. With this definition,

$$\sigma^r = \sigma_{ij} P_{ijkl}^r \sigma_{kl}.$$

4.34.2 Implementation

The wire mesh model is implemented in a hypoelastic fashion similar to the previous elastic-plastic models. First, a trial (unrotated) stress is calculated assuming a purely elastic deformation increment,

$$T_{ij}^{tr} = T_{ij}^n + \Delta t \left(\lambda \delta_{ij} d_{kk} + 2\mu d_{ij}\right).$$

Corresponding principal stresses and their complementary directions are then found using the robust, analytical algorithm put forth in [89]. The principal stresses are denoted σ^r and their eigenvectors are symbolically represented by $\hat{e}_i^r$. Here, $r = 1, 2,$ or 3 refer to the respective eigenvalue/vector pair and are not summed unless explicitly indicated. Before evaluating the respective yield functions, the current volumetric engineering strain, $\varepsilon_{\mathrm{V}}^{n+1}$, must be determined. To this end, the current strain tensor, ε_{ij}, is determined via,

$$\varepsilon_{ij}^{n+1} = \varepsilon_{ij}^{n} + \Delta t d_{ij},$$

and the volumetric engineering strain is,

$$\varepsilon_{\mathrm{V}}^{n+1} = \exp\left(\varepsilon_{kk}^{n+1}\right) - 1.$$

The yield function for each principal stress, f^γ, may then be computed as,

$$f^\gamma = \begin{cases} \sigma^\gamma - \tau, & \sigma^\gamma \geq 0 \\ -\sigma^\gamma - \bar{\sigma}\left(\varepsilon_{\mathrm{V}}^{n+1}\right), & \sigma^\gamma < 0 \end{cases}.$$

Principal stresses at the current load increment, σ_{n+1}^γ, are then determined via,

$$\sigma_{n+1}^\gamma = \begin{cases} \sigma^\gamma & f^\gamma < 0 \\ \tau & f^\gamma \geq 0 \end{cases},$$

for $\sigma^\gamma > 0$ and,

$$\sigma_{n+1}^\gamma = \begin{cases} \sigma^\gamma & f^\gamma < 0 \\ -\bar{\sigma}\left(\varepsilon_{\mathrm{V}}^{n+1}\right) & f^\gamma \geq 0 \end{cases},$$

for compressive principal stresses. The final Cartesian stress tensor may be determined via,

$$T_{ij}^{n+1} = \sum_{\gamma=1}^{3} \sigma_{n+1}^\gamma \hat{e}_i^\gamma \hat{e}_j^\gamma.$$

4.34.3 Verification

To investigate the performance of the wire mesh model and verify its capabilities, a series analyses are performed considering both the tensile and compressive behavior. The material properties and model parameters come from [76] and are listed in Table Table 4.56 with one difference. Specifically, $\nu \neq 0$ to better test the various code interactions. For the numerical simulations the functional hardening form given in (4.161) (with a and b given in Table Table 4.56) is discretized and entered as a piecewise linear function.

Table 4.56 The material properties and model parameters of the wire mesh model used for verification testing

E	100,000 psi	ν	0.3
a	120 psi	b	8.68
τ	12,000 psi		

4.34.3.1 Uniaxial Compression

First, the case of uniaxial compression is treated to investigate the hardening behavior. As a uniaxial compressive stress state is being explored, the principal stresses are simply $\sigma^1 = \sigma^2 = 0$ and $\sigma^3 = \sigma_{11}$ enabling the development of analytical solutions. To this end, $u_1 = \lambda_1$ and the remaining surfaces are left traction free. The corresponding strain state is then,

$$\begin{aligned} \varepsilon_{11} &= \ln(1+\lambda_1), \\ \varepsilon_{22} = \varepsilon_{33} &= -\nu \ln(1+\lambda_1), \end{aligned}$$

producing a engineering volume strain of,

$$\varepsilon_{\mathrm{V}} = (1+\lambda_1)^{(1-2\nu)} - 1.$$

Noting the elastic uniaxial stress, $\hat{\sigma}_{11}$, is simply,

$$\hat{\sigma}_{11} = [\lambda(1-2\nu) + 2\mu] \ln(1+\lambda_1),$$

the final stress state is simply $\sigma_{22} = \sigma_{33} = 0$ and,

$$\sigma_{11} = \begin{cases} \hat{\sigma}_{11} & \hat{\sigma}_{11} \leq -ae^{-b\varepsilon_{\mathrm{V}}} \\ -ae^{-b\varepsilon_{\mathrm{V}}} & \hat{\sigma}_{11} > -ae^{-b\varepsilon_{\mathrm{V}}} \end{cases}.$$

The analytical and numerical solution (from adagio) of this problem are presented in Fig. 4.145 with the stress and strains given in Fig. 4.145(a) and Fig. 4.145(b), respectively. Excellent agreement is observed verifying the compressive hardening performance.

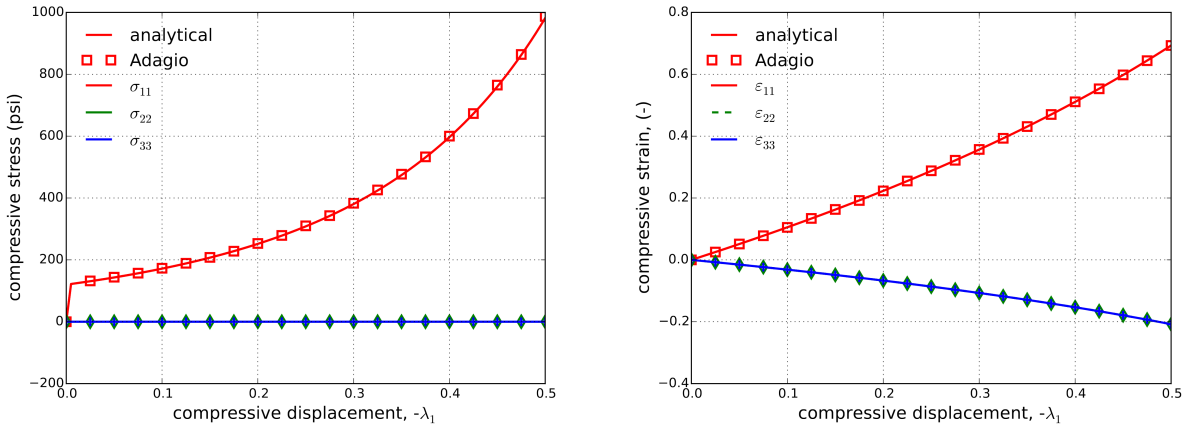

(a) Linear, Johnson-Cook **(b) Linear, Power-Law Breakdown**

Fig. 4.145 Analytical and numerical results of the normal stress and strain components through a compressive uniaxial stress loading path as a function of the applied displacement, λ_1

4.34.3.2 Uniaxial Tension

To consider the tensile behavior, the response of the model under a uniaxial tensile emph{strain} loading is interrogated. In this case the applied displacement is $u_i = \lambda_1 \delta_{i1}$ with the remaining displacements fixed such that $\varepsilon_{22} = \varepsilon_{33} = 0$ and the axial strain is again $\varepsilon_{11} = \ln(1 + \lambda_1)$. Given that the model behavior is perfectly plastic after yield, the axial and off-axis responses both reduce to bilinear forms. As such, the applied deformation necessary to induce the perfectly plastic response in the axial direction, λ_1^{crit}, is simply

$$\lambda_1^{\text{crit}} = e^{\tau/(\lambda+2\mu)} - 1,$$

leading to an expression for the axial stress as,

$$\sigma_{11} = \begin{cases} (\lambda + 2\mu)\ln(1+\lambda_1) & \lambda_1 < \lambda_1^{\text{crit}} \\ \tau & \lambda_1 \geq \lambda_1^{\text{crit}} \end{cases}.$$

For the off-axis behavior, the critical displacement, $\lambda_1^{\text{off-crit}}$, is

$$\lambda_1^{\text{off-crit}} = e^{\tau/\lambda} - 1,$$

producing stresses of the form,

$$\sigma_{22} = \sigma_{33} = \begin{cases} \lambda \ln(1+\lambda_1) & \lambda_1 < \lambda_1^{\text{off-crit}} \\ \tau & \lambda_1 \geq \lambda_1^{\text{off-crit}} \end{cases}.$$

The stress and strain responses (both numerical and analytical) are presented below in Fig. 4.146(a) and Fig. 4.146(b), respectively, and excellent agreement is observed verifying this behavior in this deformation mode.

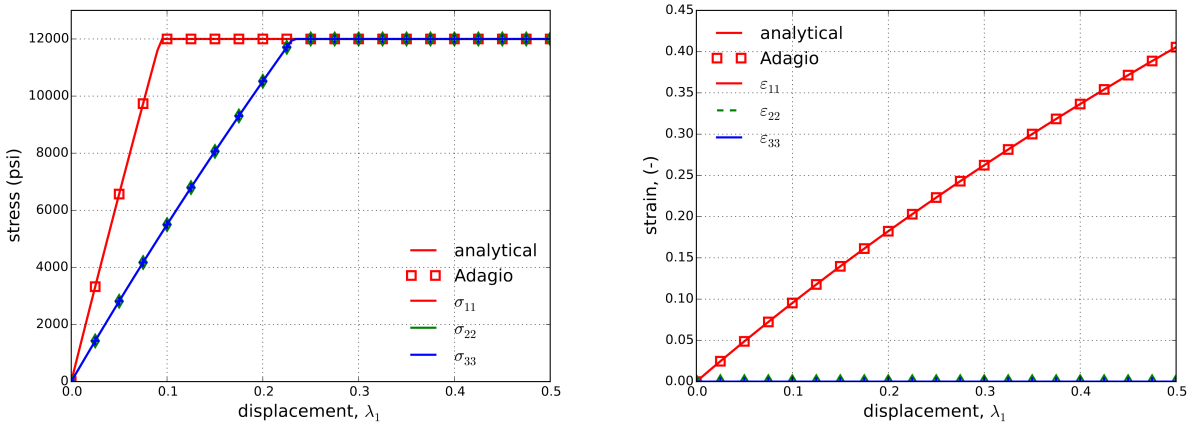

(a) Linear, Johnson-Cook **(b) Linear, Power-Law Breakdown**

Fig. 4.146 Analytical and numerical results of the normal stress and strain components through a tension uniaxial strain loading path as a function of the applied displacement, λ_1.

4.34.3.3 Hydrostatic Compression

To further explore the compressive response, the models behavior under a hydrostatic (compressive) loading is investigated. In this instance, the corresponding stress state produces a single, repeated, principal stress associated with the pressure, $p = -(1/3)\,\sigma_{kk}$ (here defined positively in compression). Details of this loading may be found in *Appendix A*, although in this instance it is important to point out that,

$$\varepsilon_{\mathrm{V}} = (1 + \lambda_1)^3 - 1,$$

and the stress state reduces to,

$$p = -3K \ln (1 + \lambda_1)$$

in the elastic limit and

$$p = ae^{-b\varepsilon_{\mathrm{V}}},$$

during plastic loading. The numerical and analytical results are presented in Fig. 4.147 and excellent agreement in noted.

4.34.4 User Guide

```
BEGIN PARAMETERS FOR MODEL WIRE_MESH
  #
  # Elastic constants
  #
  YOUNGS MODULUS = <real>
  POISSONS RATIO = <real>
  SHEAR MODULUS  = <real>
  BULK MODULUS   = <real>
  LAMBDA         = <real>
  TWO MU         = <real>
  #
  # Yield surface parameters
  #
  YIELD FUNCTION = <string>
  TENSION        = <real>
END [PARAMETERS FOR MODEL WIRE_MESH]
```

- The yield function in compression is defined with the `YIELD FUNCTION` command line.
- The tensile strength is give by the `TENSION` command line.

Output variables available for this model are listed in Table 4.57.

More information on the model can be found in the report by Neilsen, et. al. [76].

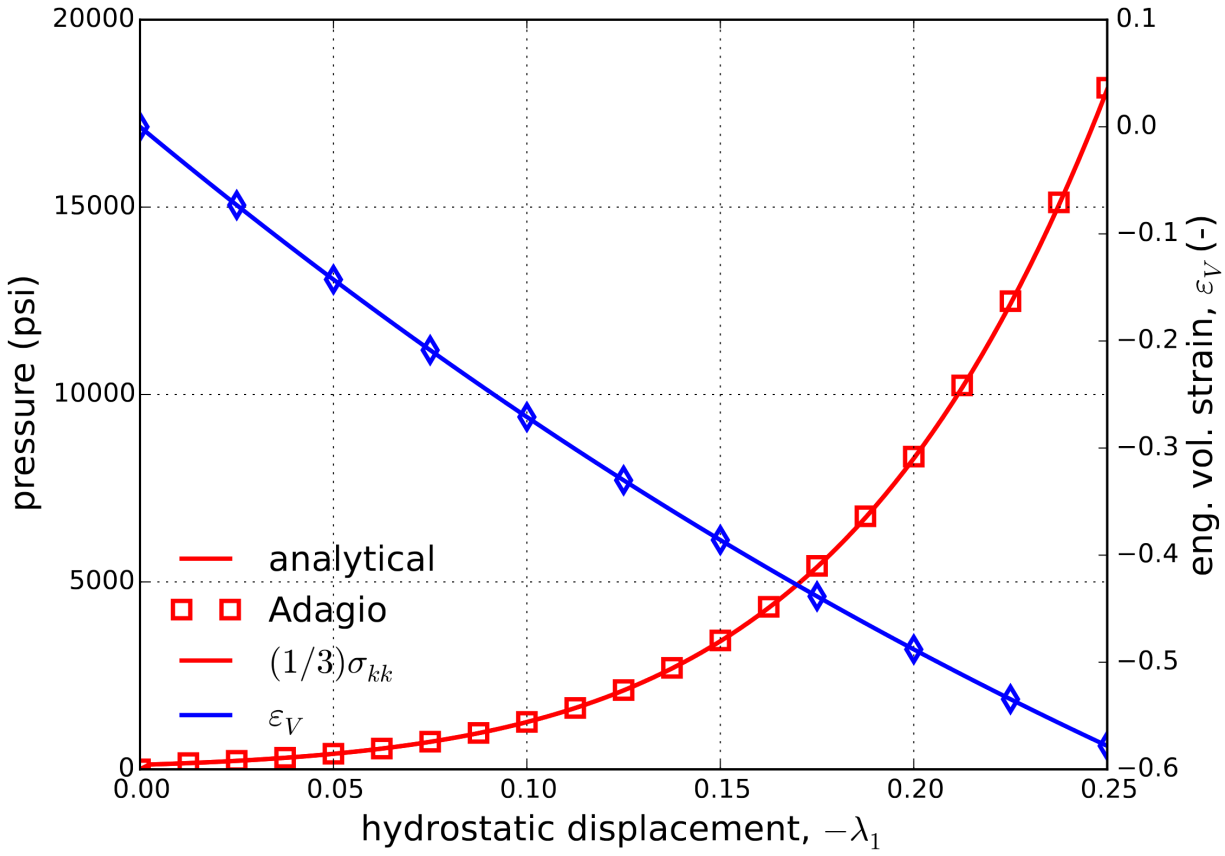

Fig. 4.147 Analytical and numerical pressure-volume strain response of the wire mesh model through a hydrostatic compression loading as a function of the applied displacement, λ_1.

Table 4.57 State Variables for WIRE MESH Model

Name	Description
EVOL	engineering volumetric strain
YIELD	current yield strength in compression

4.35 Viscoplastic-viscoSCRAM Model

4.35.1 Theory

The viscoSCRAM model is an isotropic, linear viscoelasticity model with isotropic damage for modeling particulate composite materials. The bulk material is treated as viscoelastic while damage is governed by a statistical crack mechanics (SCRAM) theory [28] which accounts for material damage from the nucleation and growth of microcracks. Damage can occur from bond breakage within the binder, between the binder and particulates, and within the particulates. The crack growth kinetics assume non-interacting cracks and include no mechanisms for shear dilation such as from particulate debonding and rotation. The viscoSCRAM model captures linear viscoelastic shear rate-dependence and inelastic deformation associated with damage. The viscoSCRAM model is based on the papers by Hackett and Bennett [39] and Buechler and Luscher [20] with a modified implementation.

The viscoplastic-viscoSCRAM model [108] is an extension of the viscoSCRAM model to include pressure-dependent viscoplasticity and volumetric dilation. The linear viscoelasticity and damage mechanics of the viscoSCRAM model remain largely unaltered, but are embedded within a yield surface plasticity model. Prior to plasticity, the model reduces identically to the viscoSCRAM model. The viscoplastic-viscoSCRAM model draws on elements of the papers by Buechler [18], [19] as well as standard viscoplasticity theory from Kojic and Bathe [51].

The deviatoric strain e_{ij} is additively decomposed into a viscoelastic component e^{ve}_{ij}, a damage component e^{D}_{ij}, and a viscoplastic component e^{p}_{ij} as

$$e_{ij} = (e^{ve}_{ij} + e^{D}_{ij}) + e^{p}_{ij}. \tag{4.162}$$

The deviatoric stress s_{ij} depends only on the viscoelastic strain through a generalized Maxwell model as

$$\dot{s}_{ij} = 2G^{\infty}\dot{e}^{ve}_{ij} + \sum_{\kappa=1}^{N}\left(2G^{(\kappa)}\dot{e}^{ve}_{ij} - \frac{s^{(\kappa)}_{ij}}{\tau^{(\kappa)}}\right) \tag{4.163}$$

where G^{∞} is the steady-state (rubbery) shear modulus and $G^{(\kappa)}$, $s^{(\kappa)}_{ij}$, $\tau^{(\kappa)}$ are the shear modulus, deviatoric stress, and relaxation time for the κ^{th} Maxwell element.

The damage strain is given by

$$e^{D}_{ij} = \frac{1}{2G_0}\left(\frac{c}{a}\right)^3 s_{ij} \tag{4.164}$$

where $G_0 = G^\infty + \sum_{\kappa=1}^{N} G^{(\kappa)}$ is the instantaneous shear modulus, c is the damage parameter representing an averaged microcrack size, and a is a crack normalizing factor.

The damage parameter c captures crack growth. It is based on brittle fracture mechanics including stable and unstable crack growth regions. The crack growth rate is

$$\dot{c} = \begin{cases} v_{res}\left(\frac{K_I}{K_1}\right)^m & \text{for } K_I < K' \\ v_{res}\left[1 - \left(\frac{K_{0\mu}}{K_I}\right)^2\right] & \text{otherwise} \end{cases} \tag{4.165}$$

where $v_{res} = min\{v_c \bar{\dot{\varepsilon}}^{v_a} 10^{v_b}, v_{max}\}$ is an empirical relation for the crack speed with fitting parameters v_a and v_b and limited by the Raleigh wave speed v_{max}. The coefficient v_c is included for ease of unit conversion. Here, $\bar{\dot{\varepsilon}} = \sqrt{\frac{2}{3}\dot{\varepsilon}_{ij}\dot{\varepsilon}_{ij}}$ is the effective strain rate. The exponent m is a model parameter controlling the shape of the crack growth rate curve. The stress intensity is

$$K_I = \bar{\sigma}\sqrt{\pi c} \tag{4.166}$$

where the effective stress $\bar{\sigma}$ is computed as

$$\bar{\sigma} = \begin{cases} \left(\frac{3}{2}s_{ij}s_{ij}\right)^{\frac{1}{2}} & \text{for } \sigma_m < 0 \\ \left(\frac{3}{2}\sigma_{ij}\sigma_{ij}\right)^{\frac{1}{2}} & \text{otherwise} \end{cases} \tag{4.167}$$

and $\sigma_m = \sigma_{kk}/3$ is the mean stress. The transition stress intensity K', marking the boundary between stable (slow) crack growth and unstable (rapid) crack growth, is given by

$$K' = K_{0\mu}\left(1 + \frac{2}{m}\right)^{\frac{1}{2}} \tag{4.168}$$

where $K_{0\mu}$ is the frictional threshold stress intensity. $K_{0\mu}$ reflects the frictional resistance to crack growth under compressive loading which inhibits damage evolution. This tensile/compressive frictional asymmetry is given by

$$K_{0\mu} = K_0\left[1 + \frac{\pi\mu'\langle p\rangle\sqrt{c}}{K_0}\left(1 + \frac{\mu'\langle p\rangle\sqrt{c}}{K_0}\right)\right]^{\frac{1}{2}} \tag{4.169}$$

where K_0 is the frictionless threshold stress intensity, a model fitting parameter, μ' is the friction coefficient, and $p = -\sigma_m$ is the pressure. Here, $\langle\cdot\rangle$ are Macaulay brackets.

Finally, the normalizing stress intensity K_1 is defined as

$$K_1 = K'\left(1 + \frac{m}{2}\right)^{\frac{1}{m}}. \tag{4.170}$$

The damage parameter c captures crack growth; however, it is not normalized like a traditional continuum mechanics damage parameter. An alternative damage parameter, D, may be defined as

$$D = \frac{\left(\frac{c}{a}\right)^3}{1 + \left(\frac{c}{a}\right)^3}, \tag{4.171}$$

which is 0 for the undamaged state $c = 0$ and asymptotes to 1 for a fully damaged state.

In the viscoSCRAM model, there is no viscoplasticity; that is, the viscoplastic strain component $e^p_{ij} = 0$ in (4.162). For the viscoplastic-viscoSCRAM model, a viscoplastic constitutive response extends the viscoSCRAM model.

The viscoplastic model is based on an overstress assumption; that is, in stress space, the stress point may lie outside the yield surface and move towards the yield surface with time. Viscoplastic flow occurs until the stress point lies on the yield surface. Let $f(\sigma_{ij}, \varepsilon^p_{ij}, D)$ be the yield surface such that the yield condition is

$$f(\sigma_{ij}, \varepsilon^p_{ij}, D) = 0. \tag{4.172}$$

The total viscoplastic strain rate is prescribed by a Perzyna model as

$$\dot{\varepsilon}^p_{ij} = \dot{\lambda} \frac{\partial g}{\partial \sigma_{ij}}, \tag{4.173}$$

with

$$\dot{\lambda} = \gamma \langle \phi[f] \rangle, \tag{4.174}$$

where $g(\sigma_{ij}, \varepsilon^p_{ij}, D)$ is the flow surface, which is, in general, non-associative. Here γ is a fluidity parameter and ϕ is a functional of the yield surface. The rate of plastic flow is controlled by $\dot{\lambda}$ while the direction of plastic flow is normal to the flow surface.

For particulate composite materials, common choices for the yield surface f and flow surface g are Drucker-Prager forms with potentially different fitting constants. However, the theory is general and allows for any form of yield or flow surface to be prescribed based on the experimental data.

The implemented Drucker-Prager forms for the yield surface and flow surface are defined, respectively, as

$$f(\sigma_{ij}) = \sigma_e + A \cdot \sigma_m - \sigma_y \qquad \text{and} \qquad g(\sigma_{ij}) = \sigma_e + B \cdot \sigma_m - \sigma_y, \tag{4.175}$$

where σ_e is the equivalent stress given by

$$\sigma_e = \sqrt{\frac{3}{2} s_{ij} s_{ij}},$$

σ_m is the mean stress, σ_y is the yield stress, and A and B are fitting constants.

The flow rule is selected to be,

$$\dot{\lambda} = \frac{1}{\tilde{\tau}} \langle \frac{f(\sigma_{ij})}{\sigma_0} \rangle^{\tilde{m}}, \tag{4.176}$$

where $\tilde{\tau}$ is the viscoplastic relaxation time, σ_0 is a normalizing constant, and $\tilde{m}$ is a fitting exponent.

4.35.1.1 Time-Temperature Superposition Principle

The preceding theory embeds the standard mechanical viscoSCRAM theory. The temperature dependent response of viscoelastic materials was not discussed; however, the theory may be extended. The thermo-viscoelastic behavior of a polymer is related to the molecular rearrangement of the material under loading; the speed of this rearrangement is controlled by the temperature [65]. For the class of thermorheologically simple materials, one dominant molecular transition controls the response. For these materials, the time-temperature superposition principle is valid. This principle holds that long time relaxation behavior at low temperatures is equivalent to short term relaxation behavior at high temperatures. This manifests as a simple horizontal time shift of the relaxation modulus curve with temperature change.

The generalized Maxwell model (4.163) may be written equivalently in integral form as

$$s_{ij} = \int_{-\infty}^{t} 2G(t-r)\frac{de_{ij}^{ve}}{dr}dr, \tag{4.177}$$

where $G(t-r) = G^{\infty} + \sum_{\kappa=1}^{N} G^{(\kappa)} e^{\frac{-(t-r)}{\tau^{(\kappa)}}}$ is the relaxation spectra. At a reference temperature T_{ref}, the relaxation spectra in terms of logarithmic time is $G(t-r, T_{ref}) = \hat{G}(log_{10}(t-r))$. For a thermorheologically simple material, time-temperature superposition states that the relaxation spectra at any other temperature T is a horizontal translation of the reference relaxation spectra; that is, $G(t-r, T) = \hat{G}(log_{10}(t-r) - log_{10}(a_T(T)))$ where $a_T(T)$ is the shifting factor. The deviatoric stress at any temperature is then equal to the deviatoric stress at the reference temperature, but at a scaled time; namely, $s_{ij}(t, T) = s_{ij}(\frac{t}{a_T}, T_{ref})$. Reverting to the differential form, the deviatoric stress equation is

$$\dot{s}_{ij} = 2G^{\infty}\dot{e}_{ij}^{ve} + \sum_{\kappa=1}^{N}\left(2G^{(\kappa)}\dot{e}_{ij}^{ve} - \frac{s_{ij}^{(\kappa)}}{\tau^{(\kappa)}}\right), \tag{4.178}$$

where the relaxation times are $\tau^{(\kappa)} = a_T(T)\,\tau_{ref}^{(\kappa)}$ with $\tau_{ref}^{(\kappa)}$ being the relaxation times at the reference temperature.

The generalized Maxwell equations for the standard mechanical model (4.163) have identical form and are recovered by setting the shift factor $a_T(T) = 1$. The crack growth kinetics are assumed to be unaffected by temperature, so both formulations use the same implementation with temperature dependence introduced solely through the shift factor.

The shift factor model is defaulted to none ($a_T = 1$). Available shift factor models are the Williams-Landel-Ferry (WLF) model, the Arrhenius model, and a user defined model. In these models, the shift factors are defined as

$$\begin{aligned} \text{WLF:} \quad & log_{10}(a_T) = \frac{-C_1\,(T - T_{ref})}{C_2 + (T - T_{ref})}, \\ \text{ARRHENIUS:} \quad & log_{10}(a_T) = \frac{E_a}{R}(log_{10}e)\left(\frac{1}{T} - \frac{1}{T_{ref}}\right), \\ \text{USER DEFINED:} \quad & a_T = a^{ud}(T). \end{aligned} \tag{4.179}$$

Here, C_1 and C_2 are fitting constants for the WLF model. For the Arrhenius model, E_a is the activation energy and R is the gas constant.

Note, time-temperature superposition is verified for the viscoSCRAM component of the model with no viscoplasticity. Time-temperature superposition will run with the full viscoplastic-viscoSCRAM model; however, the theoretical basis with viscoplasticity is still under investigation.

4.35.2 Implementation

The viscoplastic-viscoSCRAM model discretization uses a staggered solution scheme. The damage model has both stable and unstable crack growth branches which causes implicit numerical solution schemes to be highly sensitive, unstable, or difficult to converge. For this reason, the time integration of the deviatoric stress is explicit in the damage variable and implicit in the viscoplastic strain. The solution scheme is staggered between the damage update and viscoplastic update; that is, the damage state variable and Maxwell stresses are held fixed at their converged values from the previous timestep, the viscoplastic strain is updated within a solution loop, and finally, the damage state variable and Maxwell stresses are updated with the new viscoplastic strain held fixed.

The viscoSCRAM component is evaluated with an explicit time integration scheme. Substituting the time derivatives of (4.162) and (4.164) into (4.163), the deviatoric strain rate becomes

$$\dot{s}_{ij} = \psi(c)(\dot{e}_{ij} - \dot{e}^p_{ij}) - \theta(c,\dot{c})s_{ij} - \lambda_{ij}(c, s^{(\kappa)}_{ij}) \tag{4.180}$$

where

$$\psi(c) = \frac{2G_0}{1 + (\frac{c}{a})^3} = 2G_0(1 - D) \tag{4.181}$$

and

$$\theta(c,\dot{c}) = \frac{3(\frac{c}{a})^2 \frac{\dot{c}}{a}}{1 + (\frac{c}{a})^3} = \frac{\dot{D}}{1 - D} = \tag{4.182}$$

and

$$\lambda_{ij}(c, s^{(\kappa)}_{ij}) = \frac{\sum_{\kappa=1}^{N} \frac{s^{(\kappa)}_{ij}}{\tau^{(\kappa)}}}{1 + (\frac{c}{a})^3} = (1 - D) \sum_{\kappa=1}^{N} \frac{s^{(\kappa)}_{ij}}{\tau^{(\kappa)}}. \tag{4.183}$$

Integrating (4.180) explicitly, the deviatoric stress update becomes

$$(s_{ij})_{n+1} = (s_{ij})_n + \frac{\Delta t}{(1 + \frac{\Delta t}{2}\theta_n)} \left[\psi_n((\dot{e}_{ij})_n - (\dot{e}^p_{ij})_n) - \theta_n(s_{ij})_n - (\lambda_{ij})_n \right]. \tag{4.184}$$

The mean crack size is updated according to

$$c_{n+1} = c_n + \dot{c}_n \Delta t. \tag{4.185}$$

The Maxwell stress rates can be written in the form

$$\dot{s}_{ij}^{(\kappa)} = 2G^{(\kappa)}(\dot{e}_{ij} - \dot{e}_{ij}^{p}) - \frac{s_{ij}^{(\kappa)}}{\tau^{(\kappa)}} - \frac{G^{(\kappa)}}{G_0}\left[\frac{3}{a}\left(\frac{c}{a}\right)^2 \dot{c} s_{ij} + \left(\frac{c}{a}\right)^3 \dot{s}_{ij}\right] \tag{4.186}$$

which, when treated as a first-order, linear, constant-coefficient ODE in $s_{ij}^{(\kappa)}$, may be solved to provide the Maxwell stress update as

$$(s_{ij}^{(\kappa)})_{n+1} = (s_{ij}^{(\kappa)})_n e^{\frac{-\Delta t}{\tau^{(\kappa)}}} + \left(1 - e^{\frac{-\Delta t}{\tau^{(\kappa)}}}\right)\left(2G^{(\kappa)}\tau^{(\kappa)}((\dot{e}_{ij})_{n+1} - (\dot{e}_{ij})_{n+1}^{p}) - \frac{G^{(\kappa)}}{G_0}\tau^{(\kappa)}\left[\left(\frac{3}{a}\right)\left(\frac{c_{n+1}}{a}\right)^2 \dot{c}_n (s_{ij})_{n+1} + \left(\frac{c_{n+1}}{a}\right)^3 (\dot{s}_{ij})_n\right]\right). \tag{4.187}$$

Here, the relaxation times are $\tau^{(\kappa)} = a_T(T_{n+1})\tau_{ref}^{(\kappa)}$. These times are updated at the start of the time step by computing the shift factor at the new temperature T_{n+1} and then shifting the reference relaxation times.

The mean stress is updated as

$$(\sigma_m)_{n+1} = (\sigma_m)_n + K((\dot{e}_{ii})_{n+1} - (\dot{e}_{ii})_{n+1}^{p})\Delta t \tag{4.188}$$

and finally the Cauchy stress is updated as

$$(\sigma_{ij})_{n+1} = (s_{ij})_{n+1} + (\sigma_m)_{n+1}\delta_{ij}. \tag{4.189}$$

For the viscoSCRAM model, there is no viscoplasticity ($\Delta\varepsilon_{ij}^{p} = \Delta e_{ij}^{p} = 0$); both the deviatoric stress update (4.184) and the mean stress update (4.188) are explicit. For the viscoplastic-viscoSCRAM model, both the deviatoric stress update and the mean stress update are implicit in the plastic strain increment.

The viscoplastic flow rate (4.173) is integrated implicitly as

$$\Delta\varepsilon_{ij}^{p} = \Delta\lambda\left(\frac{\partial g}{\partial \sigma_{ij}}\right)_{n+1}, \tag{4.190}$$

where the viscoplastic flow increment is

$$\Delta\lambda = \gamma\langle\phi[f_{n+1}]\rangle\Delta t. \tag{4.191}$$

The deviatoric viscoplastic flow rate is the projection

$$\Delta e_{ij}^{p} = \Delta\lambda\left[\left(\frac{\partial g}{\partial \sigma_{ij}}\right)_{n+1} - \frac{1}{3}\left(\frac{\partial g}{\partial \sigma_{kk}}\right)_{n+1}\delta_{ij}\right]. \tag{4.192}$$

Defining a trial stress as

$$(\sigma_{ij})_{n+1}^{TR} = (s_{ij})_n + \frac{\Delta t}{(1 + \frac{\Delta t}{2}\theta_n)}\left[\psi_n(\dot{e}_{ij})_n - \theta_n(s_{ij})_n - (\lambda_{ij})_n\right] + [(\sigma_m)_n + K(\dot{e}_{ii})_{n+1}\Delta t]\delta_{ij}, \tag{4.193}$$

the Cauchy stress update is then

$$(\sigma_{ij})_{n+1} = (\sigma_{ij})^{TR}_{n+1} - \Delta\lambda \left[\left(\frac{\psi_n}{(1 + \frac{\Delta t}{2}\theta_n)} \right) \left(\frac{\partial g}{\partial \sigma_{ij}} \right)_{n+1} + \left(K - \frac{\psi_n}{3(1 + \frac{\Delta t}{2}\theta_n)} \right) \left(\frac{\partial g}{\partial \sigma_{kk}} \right)_{n+1} \delta_{ij} \right]. \tag{4.194}$$

The total stress update (4.194), solved in conjunction with the viscoplastic flow update (4.191), provides seven equations in the seven unknowns $\{(\sigma_{ij})_{n+1}, \Delta\lambda\}$. This system of equations is solved with a Newton-Raphson scheme as part of a return map algorithm.

The time integration solution scheme outlined is implicit in the viscoplastic update. For the Perzyna model, this implicit integration is unconditionally stable [47]. However, the time integration is explicit for the viscoSCRAM damage update. If the critical timestep is determined by the viscoplastic update, the unconditionally stable implicit integrator is advantageous. If the critical timestep is determined by the damage update, the additional cost of the implicit viscoplastic update is unnecessary and an explicit viscoplastic time integrator may be used. An explicit viscoplastic time integrator is included as an option.

4.35.3 Verification

The viscoplastic and viscoSCRAM responses of the model are verified independently of each other. Coupled, even simple boundary-value problems do not have analytical solutions for the viscoplastic-viscoSCRAM model, nor is code-to-code verification available. However, given the staggered solution scheme implemented, the viscoplastic response is updated holding fixed the viscoSCRAM response and vice versa. For this scheme, independent verification of the individual responses is sufficient. The viscoSCRAM component is verified for a purely viscoelastic response, for the crack growth kinetics from a spherical loading, and for uniaxial compression. The viscoplastic component of the model is verified for uniaxial tension and simple shear.

4.35.3.1 Viscoelasticity

Standard mechanical model The viscoSCRAM component combines standard viscoelasticity with a crack growth damage parameter c. Zeroing the initial crack size, $c = 0$, reduces the model to a viscoelastic model. The crack growth kinetic parameters do not matter in this case. Two Maxwell elements are used for the verification test and the material parameters used are shown in Table 4.58.

Table 4.58 The material properties for the viscoSCRAM model testing viscoelastic response.

K	5.0 MPa	
G^{∞}	1.0 MPa	
c	0.0 mm	
a	1.0 mm	
K_0	0.03 MPa $\sqrt{\text{mm}}$	
μ'	1.16	
m	10.0	
v_{max}	3.0e5 mm/s	
v_a	0.892	
v_b	2.28	
N	2	
$G^{(\kappa)}$ (MPa)	1.0	2.5
$\tau^{(\kappa)_{ref}}(s)$	1.0	10.0
SHIFT FACTOR MODEL	NONE	

A unit cube is fixed in the normal directions on the sides orthogonal to the x_3-axis and on the bottom in the x_3-direction. A constant logarithmic strain rate ramp load followed by a holding period is applied to the top of the cube in the x_3-direction by specifying the applied displacement field as

$$u_i = \begin{cases} (e^{\dot{\epsilon}t} - 1)X_3\delta_{i3} & \text{for } t < t_L \\ (e^{\dot{\epsilon}t_L} - 1)X_3\delta_{i3} & \text{otherwise} \end{cases} \tag{4.195}$$

where $\dot{\epsilon}$ is the strain rate and t_L is the ramp loading time. Here $\dot{\epsilon} = 1\ \text{s}^{-1}$ and $t_L = 1$ s which corresponds to a 100% logarithmic axial strain. The logarithmic deviatoric strain rate during loading is

$$\dot{e}_{ij} = \frac{1}{3}\dot{\epsilon}(3\delta_{i3}\delta_{j3} - \delta_{ij}). \tag{4.196}$$

The analytical Cauchy stress to this boundary-value problem is then

$$\begin{aligned} \sigma_{ij} = K\dot{\epsilon}t\delta_{ij} - K\dot{\epsilon}(t - t_L)\mathcal{H}(t - t_L)\delta_{ij} + 2G^{\infty}t\dot{e}_{ij} - 2G^{\infty}(t - t_L)\mathcal{H}(t - t_L)\dot{e}_{ij} + \\ \sum_{\kappa=1}^{N} 2G^{(\kappa)}\tau^{(\kappa)}(1 - e^{\frac{-t}{\tau^{(\kappa)}}})\dot{e}_{ij} - \sum_{\kappa=1}^{N} 2G^{(\kappa)}\tau^{(\kappa)}(1 - e^{\frac{-(t-t_L)}{\tau^{(\kappa)}}})\mathcal{H}(t - t_L)\dot{e}_{ij} \end{aligned} \tag{4.197}$$

where $\mathcal{H}$ is the Heaviside function.

The results of the analysis are shown in Fig. 4.148.

The axial stress σ_{33} increases nearly linearly until the end of the ramp loading, $t_L = 1$ s, and then relaxes as the displacement is held fixed. Similarly, the stresses $\sigma_{11} = \sigma_{22}$ increase linearly during ramp loading and then continue to increase as the axial stress relaxes. The Adagio solution shows agreement with the analytical solutions.

Time-Temperature Superposition

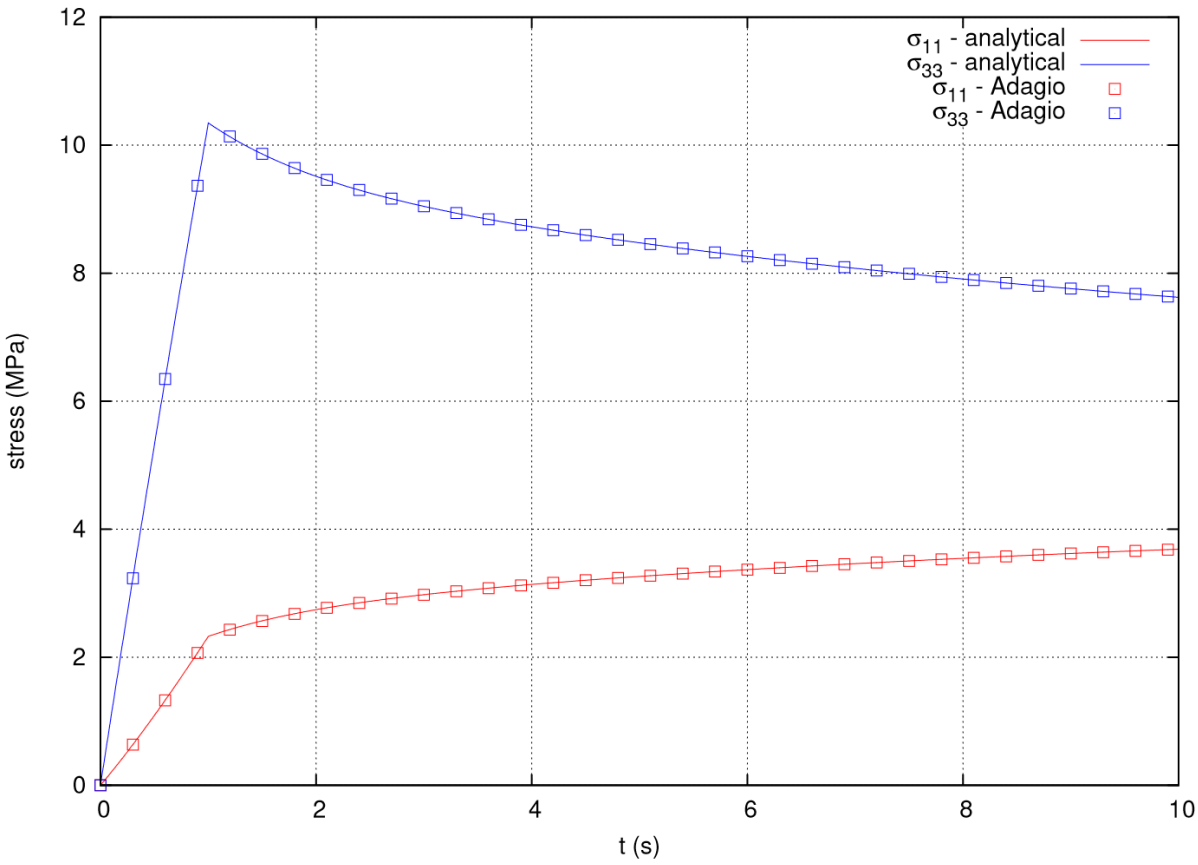

Fig. 4.148 The axial and lateral stresses.

The temperature dependence of the viscoelastic model, via the time-temperature superposition principle, is verified for the same boundary-value problem, viscoelastic parameters, and crack growth kinetic parameters. Only the shift factor model is modified. Here, all three shift factor models are verified for isothermal loading. WLF parameters were selected and then Arrhenius parameters calculated to provide an identical shift factor. The user defined function was defined as the WLF equation. The shift factor model parameters used for the verification test are shown in Table 4.59. The isothermal temperature was set to 305 K.

The results of the analysis are shown in Fig. 4.149.

The axial stress σ_{33} increases nearly linearly until the end of the ramp loading, $t_L = 1$ s, and then relaxes as the displacement is held fixed. Similarly, the stresses $\sigma_{11} = \sigma_{22}$ increase linearly during ramp loading and then continue to increase as the axial stress relaxes. The Adagio solution shows agreement with the analytical solutions.

Table 4.59 The shift factor model properties for the viscoSCRAM model testing viscoelastic response.

SHIFT FACTOR MODEL	WLF
C_1	17.44
C_2	51.6 K
T_{ref}	300 K
SHIFT FACTOR MODEL	ARRHENIUS
E_a/R	6.4918e4 K
T_{ref}	300 K

4.35.3.2 Crack Growth Kinetics

With standard viscoelasticity verified, the second test verifies the crack growth kinetics. By selecting a constant, tensile, volumetric strain rate, the frictional threshold stress intensity $K_{0\mu}$ (4.168) reduces to $K_{0\mu} = K_0$. Further judicious selection of the crack kinetic parameters permits an analytical solution to the crack growth rate (4.165). Note, the volumetric loading results in a linear elastic response, decoupling the viscoelasticity and crack growth kinetics. The Maxwell elements do not matter in this case. The material parameters used are shown in Table 4.60.

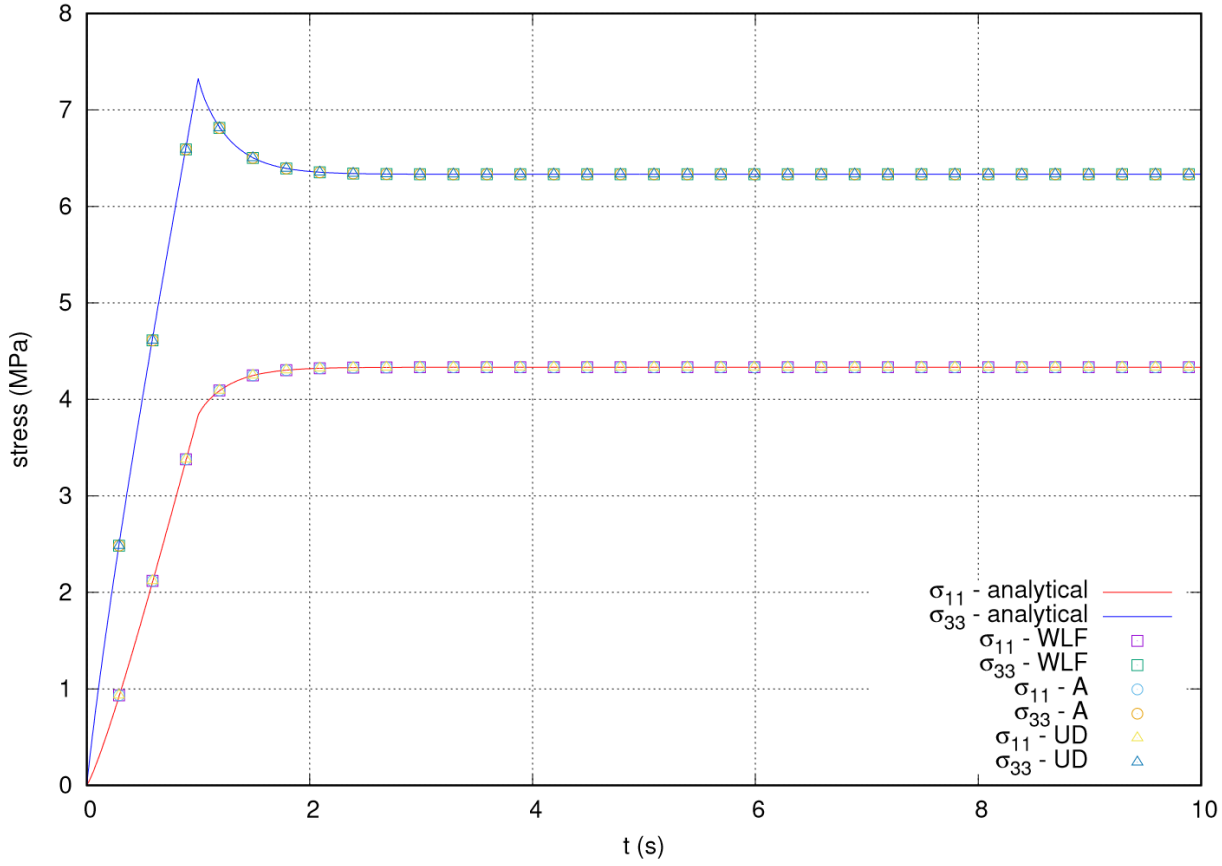

Fig. 4.149 The axial and lateral stresses with the shift factor models. (A) denotes the Arrhenius model and (UD) denotes the user defined model.

Table 4.60 The material properties for the viscoSCRAM model testing crack growth kinetics.

K	3460 MPa									
G^{∞}	404 MPa									
c	3e-3 mm									
a	1.0 mm									
K_0	6920 MPa$\sqrt{\text{mm}}$									
μ'	1.16									
m	2.0									
v_{max}	3.0e5 mm/s									
v_a	0.5									
v_b	2.5									
N	10									
$G^{(\kappa)}$ (MPa)	109	108	139	170	213	267	341	434	581	726
$\tau^{(\kappa)}$ (s)	1e3	1e2	1e1	1e0	1e-1	1e-2	1e-3	1e-4	1e-5	1e-6

Three faces of a unit cube intersecting at the origin are fixed in their normal directions. A constant logarithmic strain rate is applied to the remaining three surfaces by specifying the applied displacement field as

$$u_i = (e^{\dot{\epsilon}t} - 1)X_j\delta_{ij} \tag{4.198}$$

where $\dot{\epsilon}$ is the strain rate. Here $\dot{\epsilon} = 0.1/\sqrt{2}\ \text{s}^{-1}$. The logarithmic strain rate during loading is

$$\dot{\epsilon}_{ij} = \dot{\epsilon}\delta_{ij}. \tag{4.199}$$

The crack growth rate (4.165) becomes

$$\dot{c} = \begin{cases} \left(\frac{9}{4}\frac{K}{K_0}\right)^2 \pi t^2 c & \text{for } K_I < K' \\ 100 - \frac{1}{\pi}\left(\frac{200}{9}\frac{K_0}{K}\right)\left(\frac{1}{t^2 c}\right) & \text{otherwise.} \end{cases} \tag{4.200}$$

During stable crack growth, the analytical solution to the first-order, separable ODE $(4.200)_1$ is

$$c(t) = c_0 e^{\frac{1}{3}\left(\frac{9}{4}\frac{K}{K_0}\right)^2 \pi t^3}. \tag{4.201}$$

During unstable crack growth, the crack growth rate is the Chini ODE $(4.200)_2$ which has no general closed-form solution.

An artificially high frictionless threshold stress intensity is selected, $K_0 = 2K$, to verify crack growth in the stable regime. The results of the analysis are shown in Fig. 4.150.

The crack size increases exponentially and the Adagio solution shows agreement with the analytical solution.

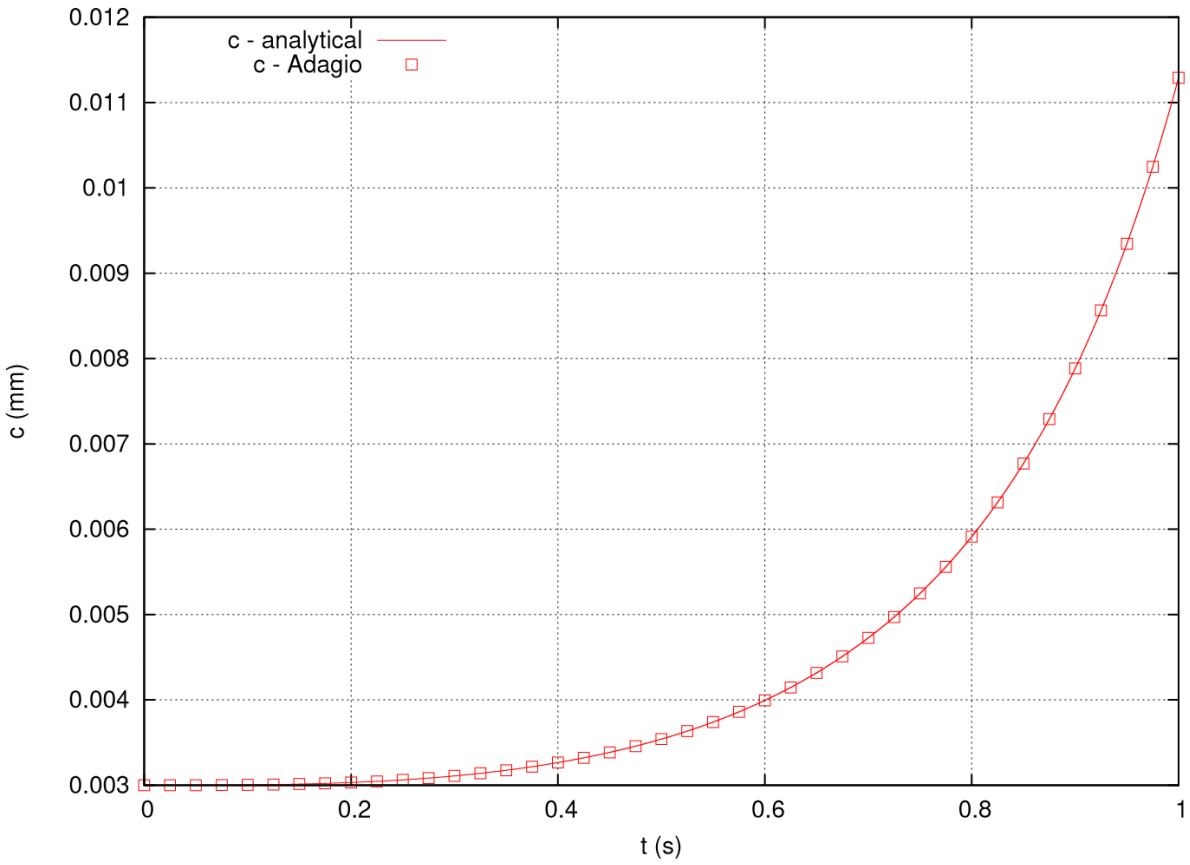

Fig. 4.150 Crack size

4.35.3.3 Uniaxial Compression

Standard viscoelasticity and crack growth during stable fracture have been verified separately. Coupled, even simple boundary-value problems do not have analytical solutions. To verify a general viscoelastic problem with crack growth, the viscoSCRAM model is compared to results from the journal article by Buechler and Luscher [20]. The boundary-value problem is uniaxial compression of a cylinder. The material parameters used for the code-to-code verification test are taken from the article and shown in Table 4.61.

Table 4.61 The material properties for the viscoSCRAM model tested in uniaxial compression.

K	3460 MPa									
G^{∞}	404 MPa									
c	3e-3 mm									
a	1.0 mm									
K_0	0.03 MPa$\sqrt{\text{mm}}$									
μ'	1.16									
m	10.0									
v_{max}	3.0e5 mm/s									
v_a	0.892									
v_b	2.28									
N	10									
$G^{(\kappa)}$ (MPa)	109	108	139	170	213	267	341	434	581	726
$\tau^{(\kappa)}$ (s)	1e3	1e2	1e1	1e0	1e-1	1e-2	1e-3	1e-4	1e-5	1e-6

The results of the analysis are shown in Fig. 4.151. The axial stress increases linearly and then begins to soften due to the accumulation of damage as crack growth occurs. The simulation is for the curve corresponding to the time step $\Delta t = 0.0625$ s in the journal article. The Adagio implementation shows agreement with the journal implementation.

4.35.3.4 Viscoplasticity

Uniaxial tension

For the viscoplastic component of the viscoplastic-viscoSCRAM model, the first verification boundary-value problem is uniaxial tension of a unit cube. Zeroing the initial crack size, $c = 0$, and setting the number of Maxwell elements to zero, reduces the model to the purely viscoplastic model. The crack growth kinetic parameters do not matter in this case. The material parameters used are shown in Table 4.62.

Three faces of a unit cube intersecting at the origin are fixed in their normal directions. A constant logarithmic strain rate ramp load followed by a holding period is applied to the cube in the

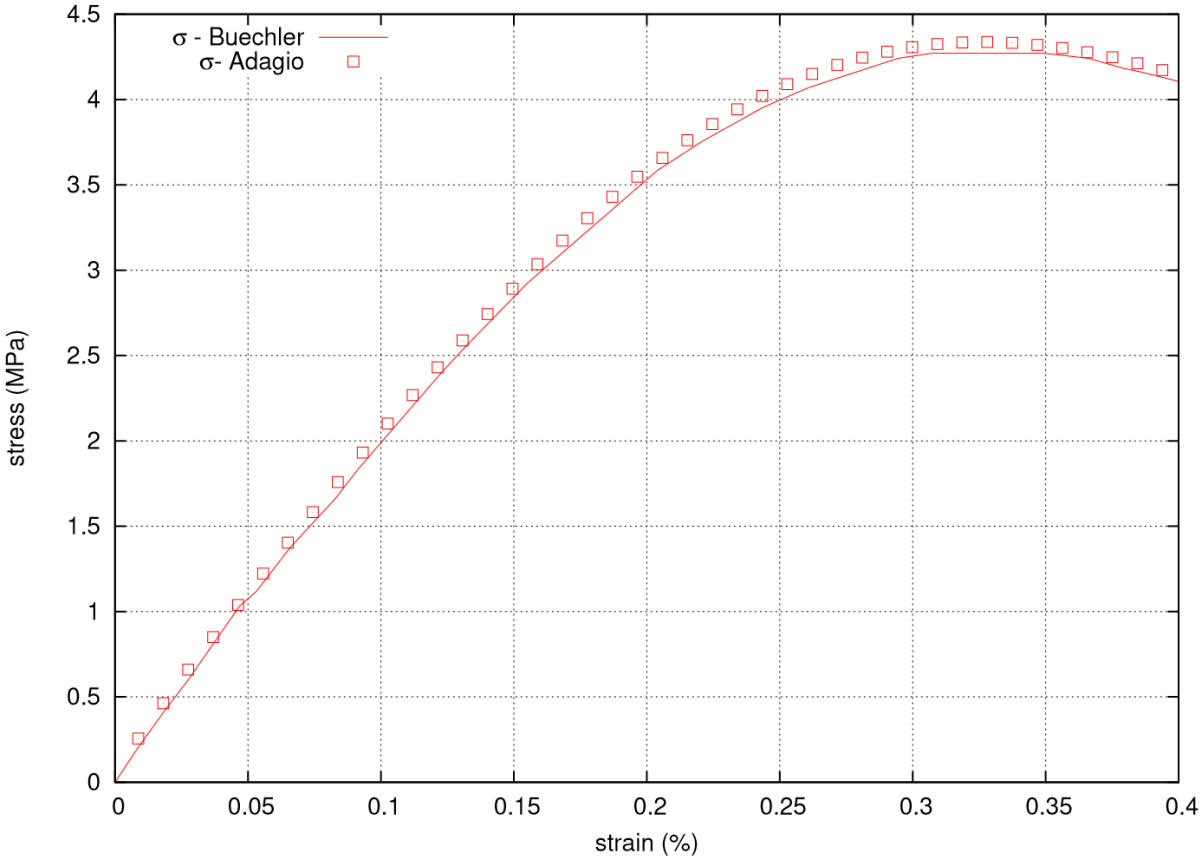

Fig. 4.151 Uniaxial compression

x_1-direction by specifying the applied displacement in this direction as

$$u_1 = \begin{cases} (e^{\beta(\frac{\sigma_y}{E})\left(\frac{t}{t_L}\right)} - 1)X_1 & \text{for } t < t_L \\ (e^{\beta(\frac{\sigma_y}{E})} - 1)X_1 & \text{otherwise} \end{cases} \tag{4.202}$$

where β is a scaling parameter and t_L is the ramp loading time. Here $\beta = \frac{E}{\sigma_y}$ and $t_L = 1$ s which corresponds to a 100% logarithmic axial strain. The logarithmic strain in the applied displacement direction is

$$\epsilon_{11} = \begin{cases} \beta\left(\frac{\sigma_y}{E}\right)\left(\frac{t}{t_L}\right) & \text{for } t < t_L \\ \beta\left(\frac{\sigma_y}{E}\right) & \text{otherwise.} \end{cases} \tag{4.203}$$

Table 4.62 The material properties for the viscoplastic model tested in uniaxial tension.

K	5.0 MPa
G^∞	1.0 MPa
c	0.0 mm
N	0
A	1.0
σ_y	2.0 MPa
B	1.0
$\tilde{\tau}$	0.8 s
σ_0	1.0 MPa
$\tilde{m}$	1.0

In the Drucker-Prager flow rule, set $\tilde{m} = 1$ so that the plastic flow rate is linear in stress and given by

$$\dot{\lambda} = \frac{1}{\tilde{\tau}}\left(\frac{f}{\sigma_0}\right). \tag{4.204}$$

For uniaxial tension, the analytical Cauchy stress in the loading direction is

$$\sigma_{11}(t) = \begin{cases} \frac{\beta\sigma_y}{t_L}t & \text{for } t \le t_y \\ \left(\frac{c_2}{c_1}\right) + \left(\frac{c_3}{c_1}\right) + \left[\frac{3\sigma_y}{(3+A)t_L} - \left(\frac{c_2}{c_1}\right) - \left(\frac{c_3}{c_1}\right)\right] e^{-c_1(t-t_y)} & \text{for } t_y < t < t_L \\ \left(\frac{c_2}{c_1}\right) + \left(\frac{c_3}{c_1}\right) e^{-c_1(t-t_L)} + \left[\frac{3\sigma_y}{(3+A)t_L} - \left(\frac{c_2}{c_1}\right) - \left(\frac{c_3}{c_1}\right)\right] e^{-c_1(t-t_y)} & \text{for } t \ge t_L, \end{cases} \tag{4.205}$$

where

$$\begin{aligned} c_1 &= E\left(\frac{1}{\tilde{\tau}\sigma_0}\right)\left[(1 + \frac{1}{9}A \cdot B) + \frac{1}{3}(A + B)\right] \\ c_2 &= E\left(\frac{1}{\tilde{\tau}\sigma_0}\right)(\sigma_y)(1 + \frac{1}{3}B) \\ c_3 &= \frac{\beta\sigma_y}{t_L}, \end{aligned} \tag{4.206}$$

and

$$t_y = \frac{3t_L}{\beta(3+A)}. \tag{4.207}$$

Here, t_y is the time at yielding.

The results of the analysis, using the implicit solution scheme with a timestep of $\Delta t = 0.025$ s, are shown in Fig. 4.152. The Adagio solition shows agreement with the analytical solution.

The time at yielding is $t_y = 0.5333$ s. The axial stress is linear elastic until this time and then the response is viscoplastic until the end of the loading period, $t_L = 1.0$ s. After the loading period, axial strain is held fixed; stress relaxes asymptotically to

$$\sigma_{11}^{\infty} = \sigma_{11}(t \to \infty) = \frac{c_2}{c_1} = \left(\frac{9+3B}{9+A\cdot B+3(A+B)}\right)\sigma_y, \tag{4.208}$$

or, for the selected material parameters, $\sigma_{11}^{\infty} = 0.75\sigma_y$.

As the relaxation time $\tilde{\tau}$ decreases, the stress relaxes more quickly to σ_{11}^{∞}. In the limit, as $\tilde{\tau} \to 0$, the viscoplastic stress is relaxed immediately and the solution converges to the rate independent plastic solution. Also, as the pressure dependence of the yield surface is reduced, $A \to 0$, the yield surface reduces to the von Mises yield surface where $\sigma_{11}^{\infty} = \sigma_y$. If the pressure dependence of the flow surface is also eliminated; that is, $A = B = 0$, then the flow direction is associative von Mises and as $\tilde{\tau} \to 0$, the solution converges to rate independent J2 plasticity.

Simple shear

For the viscoplastic component of the viscoplastic-viscoSCRAM model, the second verification boundary-value problem is simple shear of a unit cube. Again, zeroing the initial crack size, $c = 0$, and setting the number of Maxwell elements to zero, reduces the model to the purely viscoplastic model. The crack growth kinetic parameters do not matter in this case. The material parameters used are shown in Table 4.63.

The $x_2 = 0$ face of a unit cube is fixed. The faces with x_3-normals are fixed in the normal directions. A constant strain rate ramp load followed by a holding period is applied to the cube in the (x_1x_2)-plane by specifying the applied displacement in the x_1-direction as

$$u_1 = \begin{cases} \beta\left(\frac{t}{t_L}\right)X_2 & \text{for } t < t_L \\ \beta X_2 & \text{otherwise.} \end{cases} \tag{4.209}$$

where β is a scaling parameter and t_L is the ramp loading time. Here $\beta = 0.05$ and $t_L = 1$ s which corresponds to a 2.5% shear strain. These parameters were selected to satisfy the small deformation assumption necessary for the analytical solution. The shear strain is

$$\epsilon_{12} = \begin{cases} \frac{1}{2}\beta\left(\frac{t}{t_L}\right) & \text{for } t < t_L \\ \frac{1}{2}\beta & \text{otherwise.} \end{cases} \tag{4.210}$$

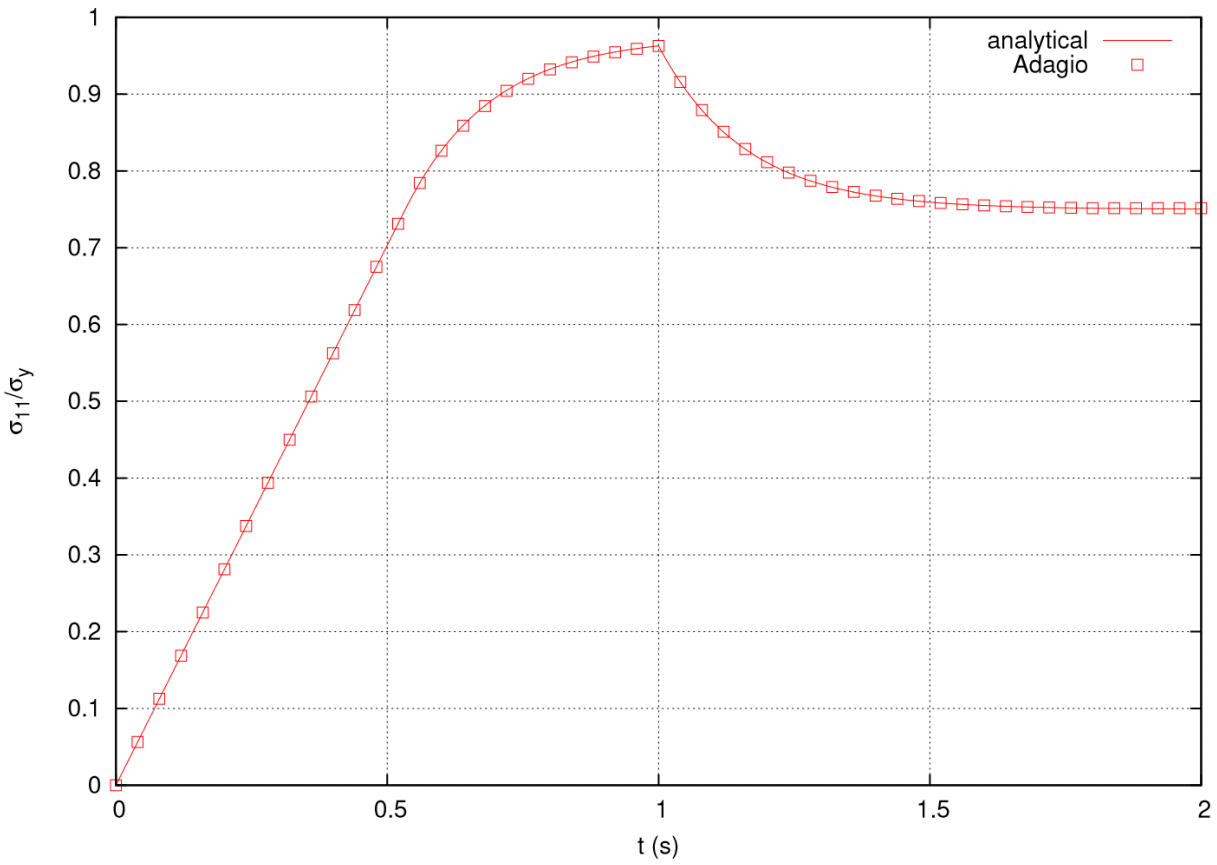

Fig. 4.152 Uniaxial tension

Table 4.63 The material properties for the viscoplastic model tested in simple shear.

K	5.0 MPa
G^∞	1.0 MPa
c	0.0 mm
N	0
A	1.0
σ_y	$\sqrt{3}/40$ MPa
B	0.0
$\tilde{\tau}$	0.8 s
σ_0	1.0 MPa
$\tilde{m}$	1.0

For simple shear, the analytical Cauchy stress in the shear plane is

$$\sigma_{12}(t) = \begin{cases} \frac{\beta G}{t_L} t & \text{for } t \le t_y \\ \left(\frac{c_2}{c_1}\right) + \left(\frac{c_3}{c_1}\right) + \left[\frac{\sigma_y}{\sqrt{3}} - \left(\frac{c_2}{c_1}\right) - \left(\frac{c_3}{c_1}\right)\right] e^{-c_1(t-t_y)} & \text{for } t_y < t < t_L \\ \left(\frac{c_2}{c_1}\right) + \left(\frac{c_3}{c_1}\right) e^{-c_1(t-t_L)} + \left[\frac{\sigma_y}{\sqrt{3}} - \left(\frac{c_2}{c_1}\right) - \left(\frac{c_3}{c_1}\right)\right] e^{-c_1(t-t_y)} & \text{for } t \ge t_L, \end{cases} \tag{4.211}$$

where

$$c_1 = 3G\left(\frac{1}{\tilde{\tau}\sigma_0}\right), \qquad c_2 = \sqrt{3}G\left(\frac{1}{\tilde{\tau}\sigma_0}\right)(\sigma_y), \qquad c_3 = \frac{\beta G}{t_L}, \tag{4.212}$$

and

$$t_y = \frac{\sigma_y t_L}{\sqrt{3}\beta G}. \tag{4.213}$$

Here, t_y is the time at yielding.

The results of the analysis, using the implicit solution scheme, are shown in Fig. 4.153. The Adagio solition shows agreement with the analytical solution.

The time at yielding is $t_y = 0.5$ s. The shear stress is linear elastic until this time and then the response is viscoplastic until the end of the loading period, $t_L = 1.0$ s. After the loading period, shear strain is held fixed; stress relaxes asymptotically to

$$\sigma_{12}^\infty = \sigma_{12}(t \to \infty) = \frac{c_2}{c_1} = \frac{\sigma_y}{\sqrt{3}}. \tag{4.214}$$

As the relaxation time $\tilde{\tau}$ decreases, the stress relaxes more quickly to σ_{12}^∞. In the limit, as $\tilde{\tau} \to 0$, the viscoplastic stress is relaxed immediately and the solution converges to the rate independent plastic solution. For the small deformation simple shear problem, with the flow direction pressure independent ($B = 0$), no normal stresses are developed. The yield surface is then independent of the pressure coefficient A and as $\tilde{\tau} \to 0$, the solution converges to rate independent J2 plasticity.

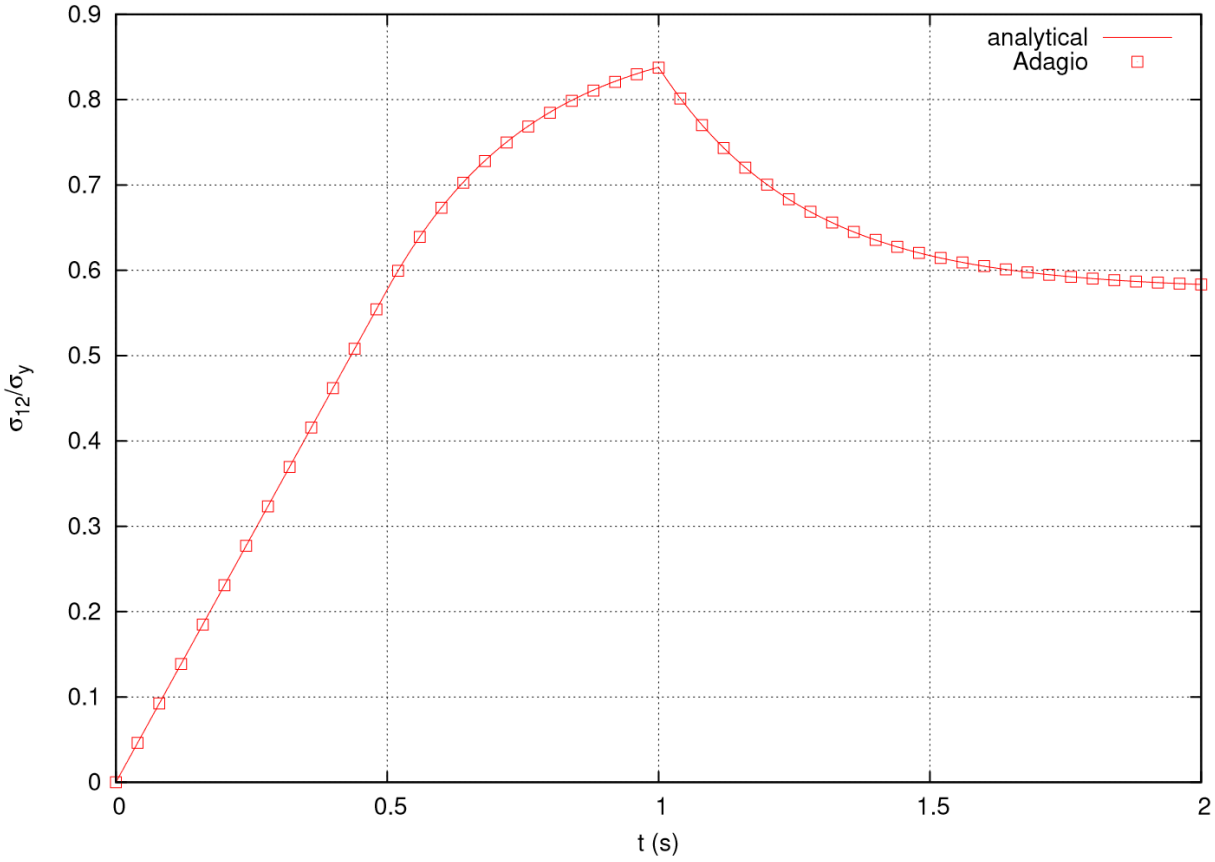

Fig. 4.153 Simple shear

4.35.4 User Guide

```
BEGIN PARAMETERS FOR MODEL VISCOPLASTIC_VISCOSCRAM
  #
  # Elastic constants
  #
  BULK MODULUS    = <real>
  SHEAR MODULUS   = <real>
  #
  # Crack growth kinetics
  #
  CRACK SIZE         = <real>
  CRACK NORM         = <real>
  STRESS INTENSITY   = <real>
  FRICTION           = <real>
  CRACK SHAPE        = <real>
  CRACK SPEED MAX    = <real>
  CRACK SPEED A      = <real>
  CRACK SPEED B      = <real>
  CRACK SPEED C      = <real> (1.0)
  #
  # Viscoelasticity
  #
  NME     = <integer>
  SHEAR   = <real_list>
  TAU     = <real_list>
  #
  # Time-temperature superposition
  #
  SHIFT FACTOR MODEL = <string> NONE | WLF | ARRHENIUS | USER_DEFINED␣
↪(NONE)

  SHIFT FACTOR MODEL = WLF
    WLF C1 = <real>
    WLF C2 = <real>
    REFERENCE TEMPERATURE = <real>

  SHIFT FACTOR MODEL = ARRHENIUS
    NORM ACTIVATION ENERGY = <real>
    REFERENCE TEMPERATURE  = <real>

  SHIFT FACTOR MODEL = USER_DEFINED
    SHIFT FACTOR FUNCTION = <string>
  #
  # Viscoplasticity
  #
```

(continues on next page)

(continued from previous page)

```
  VISCOPLASTIC MODEL = <string> NONE | EXPLICIT | IMPLICIT (NONE)

  VISCOPLASTIC MODEL = EXPLICIT | IMPLICIT
  F A              = <real>
  F YIELD          = <real>
  G B              = <real>
  FLOW TAU         = <real>
  FLOW SIGMA       = <real>
  FLOW M           = <real>

  TOLERANCE NR   = <real> (1.0e-8)

END [PARAMETERS FOR VISCOPLASTIC_VISCOSCRAM]
```

Output variables available for this model are listed in Table 4.64.

The equivalent plastic strain $\bar{\epsilon}^p$, plastic work Q, and plastic work rate $\dot{Q}$ output variables are defined as:

$$\bar{\epsilon}^p = \int_0^t \sqrt{\frac{2}{3}\dot{\epsilon}^p_{ij}\dot{\epsilon}^p_{ij}}\, dt, \qquad Q = \int_0^t \sigma_{ij}\dot{\epsilon}^p_{ij}\, dt, \qquad \dot{Q} = \sigma_{ij}\dot{\epsilon}^p_{ij}.$$

Table 4.64 State Variables for VISCOSCRAM EXPLICIT Model

Name	Description
C	crack size
CDOT	crack velocity
CSTABILITY	crack stability ratio, K_I/K'
DAMAGE	damage, D
ASHIFT	shift factor, $a_T(T)$
EQPS	equivalent plastic strain, $\bar{\epsilon}^p$
PLASTIC_WORK	plastic work, Q
PLASTIC_WORK_RATE	plastic work rate, $\dot{Q}$

4.36 Phase Field F^eF^p Model

Phase Field F^eF^p is an implementation of a cohesive variational phase-field fracture model developed for the purpose of modeling brittle and ductile fracture. The model is based upon the F^eF^p model, a hyperelastic analogue of the J_2 plasticity model, and features a von-Mises yield surface and isotropic hardening. Phase Field F^eF^p is meant to be used in conjunction with a phase-field solver. The use of Sierra/SM's reaction-diffusion solver is strongly recommended. The model leverages several of LAMÉ's modular hardening capabilities, specifically those for which hardening potentials have been defined: linear, power-law, and Voce hardening. Rate-dependent and temperature-dependent plasticity are not yet implemented for this model.

4.36.1 Theory

4.36.1.1 Overview

An overview of the Phase Field F^eF^p model theory is presented in this section. For more comprehensive analytical derivations for this model, we refer the interested reader to the following references: [101], [100], [105].

The phase-field fracture model derives from the Griffith brittle fracture model, characterized by a fracture energy release rate G_c. In that framework, the solution to the fracture mechanics problem can be cast as the minimum of a free energy functional, with displacements u and state variables z:

$$\psi^* = \min_{u,z,\Gamma} \left(\int_\Omega \psi^m(u,z)\, \mathrm{d}\Omega + \int_\Gamma G_c\, \mathrm{d}\Gamma \right), \tag{4.215}$$

where ψ^m is the mechanical energy potential (traditionally elastic strain energy). The phase-field model approximates the discrete crack on surface Γ as a smeared continuum damage field in volume Ω using the phase field ϕ, as illustrated in Fig. 4.154 adapted from [12].

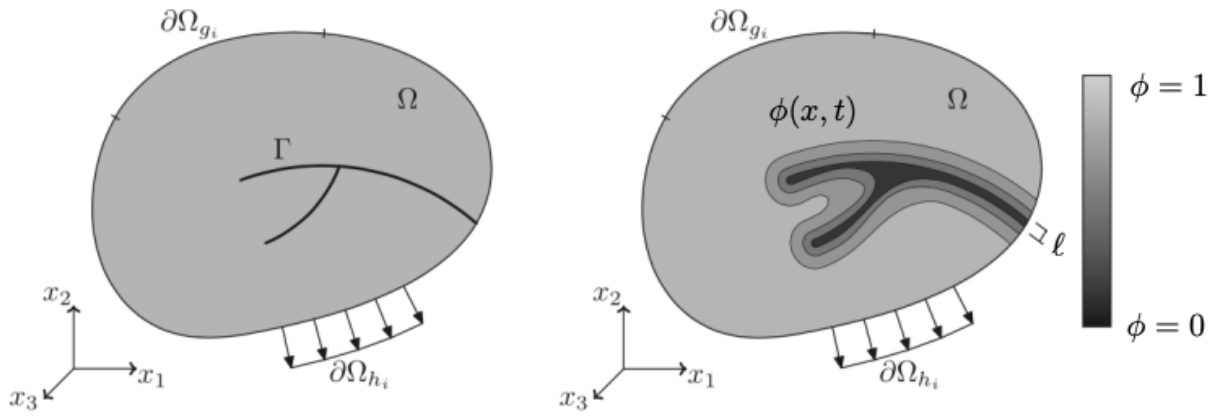

Fig. 4.154 Approximation of sharp crack by smeared phase field.

The material coherence convention is used here, where $\phi = 1$ refers to intact material, and $\phi = 0$ refers to completely damaged material. The mechanical energy potential is degraded through a degradation function $g(\phi)$, defined such that $g(1) = 1$ and $g(0) = 0$. Note that some references use variable c for this interpretation of the phase field; other references interpret the phase field as damage, increasing from zero to one as the material degrades, $d = 1 - \phi$.

We impose the following constraints on the phase field, representing that it remains within the physical range and that damage is irreversible:

$$\begin{cases} 0 \le \phi \le 1 \\ \dot{\phi} \le 0 \end{cases}.$$

The problem solution is therefore recast in terms of this approximation:

$$\psi = \int_\Omega \psi^m(u, z, \phi) + G_c \psi^f(\phi, \nabla\phi, \ell)\, \mathrm{d}\Omega\,, \tag{4.216}$$

$$\psi^* = \min_{u,z,\phi} \psi, \tag{4.217}$$

with ψ^f representing a fracture energy or damage potential that includes a regularizing length scale ℓ. The approximation (4.216) is Γ-convergent to the original functional (4.215) in the limit $\ell \to 0$. The mechanical energy is degraded through the application of individual degradation functions for each the elastic and plastic components:

$$\begin{cases} \psi^m(u, z, \phi) = \psi^e(u, z, \phi) + \psi^p(z, \phi) \\ \psi^e(u, z, \phi) = g^e(\phi)\widetilde{\psi}^e(u, z) \\ \psi^p(z, \phi) = g^p(\phi)\widetilde{\psi}^p(z) \end{cases}.$$

In order to provide an asymmetric response between tension and compression, an additional modification is made to the elastic energy potential $\widetilde{\psi}^e$, decomposing it into a positive portion $\widetilde{\psi}^e_+$ that can damage and a negative portion $\widetilde{\psi}^e_-$ that cannot: $\widetilde{\psi}^e = \widetilde{\psi}^e_+ + \widetilde{\psi}^e_-$. The degradation functions are applied only to the positive portion:

$$\psi^e(u, z, \phi) = g^e(\phi)\widetilde{\psi}^e_+(u, z) + \widetilde{\psi}^e_-(u, z).$$

Details of the elastic potential, plastic potentials, damage potentials, degradation functions, and tension-compression splits are provided in subsequent sections: Section 4.36.1.2, Section 4.36.2, Section 4.36.2.2, Section 4.36.2.3, Section 4.36.2.4.

To provide a direct energetic basis for the phase-field model, the Phase Field $\mathrm{F^eF^p}$ model is implemented with a hyperelastic formulation. Therefore, the kinematics of plastic deformation are written in terms of the deformation gradient F, which is multiplicatively decomposed into elastic (F^e) and plastic (F^p) components:

$$F = F^e F^p.$$

The deformation gradient F_{n+1} at each timestep is taken as an input for the model, while the plastic deformation gradient F^p is initialized as identity and maintained as a state variable. These key variables take the place of the previously-defined displacement u and state variable z, respectively. The elastic deformation gradient is therefore defined as $F^e = FF^{p-1}$, and the plastic flow rule $\dot{F}^p F^{p-1} = \dot{\varepsilon}^p N^p$, with equivalent plastic strain rate $\dot{\varepsilon}^p$ and flow direction tensor N^p.

The equations of motion for this material model derive from the Euler-Lagrange equations that correspond to the stationary point of the energy Lagrangian $\mathcal{L}$ (given the irreversibility of plasticity and damage, the equations of motion actually derive from finding the stationary point of an *incremental* Lagrangian, $(\delta\mathcal{L})_{n+1}(u, z, \phi) = \mathcal{L}_{n+1} - \mathcal{L}_n$, with $\mathcal{L}_n$ fixed and $F_{n+1}(u_{n+1})$ known.). The Lagrangian is formed using the free energy functional ψ and power from applied loads L (b_0 refers to a prescribed body force per unit volume, $\chi = \frac{\partial x}{\partial X}$ is the deformation map, $\bar{t}_0$ is a Neumann

traction boundary condition, and $\bar{\xi}_0$ is Neumann phase boundary condition [not commonly used]):

$$L = \int_\Omega b_0 \cdot \dot{\chi}\, \mathrm{d}\Omega + \int_{\partial_t \Omega} \bar{t}_0 \cdot \dot{\chi}\, \mathrm{d}\partial\Omega + \int_{\partial_\xi \Omega} \bar{\xi}_0 \dot{\phi}\, \mathrm{d}\partial\Omega\,,$$

$$\mathcal{L} = \psi - L,$$

$$\begin{cases} \nabla \cdot \frac{\partial \mathcal{L}}{\partial \nabla u} - \frac{\partial \mathcal{L}}{\partial u} & = 0 \\ \nabla \cdot \frac{\partial \mathcal{L}}{\partial \nabla z} - \frac{\partial \mathcal{L}}{\partial z} & = 0\,. \\ \nabla \cdot \frac{\partial \mathcal{L}}{\partial \nabla \phi} - \frac{\partial \mathcal{L}}{\partial \phi} & = 0 \end{cases} \tag{4.218}$$

The Euler-Lagrange equations (4.218) simplify to the usual balance of linear momentum for solid mechanics with Piola-Kirchoff stress P and boundary normal n_0

$$\begin{cases} \nabla \cdot P + b_0 = 0 & \text{in } \Omega \\ P \cdot n_0 = \bar{t}_0 & \text{on } \partial_t \Omega \end{cases}, \tag{4.219}$$

a plastic yield surface that corresponds to a damaged version of the familiar J_2 von-Mises yield surface with quasistatic flow stress Y^{eq} when corresponding constraints on the flow tensor N^p are applied ($N^p : N^p = \frac{3}{2}$, $\mathrm{tr}(N^p) = 0$)

$$\begin{cases} \left(\bar{\sigma} = \sqrt{\frac{3}{2}} \left\| \mathrm{dev}\sigma \right\| = \sqrt{\frac{3}{2}} g^e(\phi) \left\| \mathrm{dev} \frac{\partial \widetilde{\psi}^e_+}{\partial \varepsilon^e} \right\| \right) = \left(Y^{\mathrm{eq}} = g^p(\phi) \frac{\partial \widetilde{\psi}^p}{\partial \bar{\varepsilon}^p} \right) \\ N^p = \sqrt{\frac{3}{2}} \frac{\mathrm{dev}\sigma}{\left\| \mathrm{dev}\sigma \right\|} \end{cases}, \tag{4.220}$$

and reveal the phase-field update equation

$$\begin{cases} \frac{\partial \psi^f}{\partial \nabla \phi} G_c - \frac{\partial g^e}{\partial \phi} \widetilde{\psi}^e_+ - \frac{\partial g^p}{\partial \phi} \widetilde{\psi}^p - \frac{\partial \psi^f}{\partial \phi} G_c = 0 & \text{in } \Omega \\ \frac{\partial \psi^f}{\partial \nabla \phi} \cdot n_0 = \bar{\xi}_0 & \text{on } \partial_\xi \Omega \end{cases}. \tag{4.221}$$

For the classical phase-field fracture model (AT-2, e.g. [32], [13], [15]), this update equation is

$$2 G_c \ell \Delta\phi - 2\phi \left(\widetilde{\psi}^e_+ + \widetilde{\psi}^p \right) + \frac{G_c}{2\ell}(1 - \phi) = 0, \tag{4.222}$$

and for the threshold model (AT-1, e.g. [84]), the update equation is

$$\frac{3 G_c \ell}{4} \Delta\phi - 2\phi \left(\widetilde{\psi}^e_+ + \widetilde{\psi}^p \right) + \frac{3 G_c}{8\ell} = 0. \tag{4.223}$$

The phase field update is generally a non-linear reaction-diffusion partial differential equation of the form $R(\phi) - D\Delta\phi = S$, whereas (4.222) and (4.223) are linear: $R\phi - D\Delta\phi = S$. Casting the equation into this form enables solution through familiar algorithms in Sierra. This is detailed in Section 4.36.4.2.

Details of the implemented elastic potentials, plastic potentials, damage potentials, and degradation functions follow:

4.36.1.2 Elastic Potential

Isotropic Hencky elasticity using logarithmic strain is selected for the elastic constitutive model. The logarithmic strain tensor is defined from the elastic deformation gradient:

$$\varepsilon^e = \frac{1}{2}\log(F^{eT}F^e).$$

The isotropic Hencky elastic potential is defined in terms of the logarithmic strain, as:

$$\widetilde{\psi}^e = \mu \mathrm{dev}(\varepsilon^e) : \mathrm{dev}(\varepsilon^e) + \frac{\kappa}{2}\left(\mathrm{tr}(\varepsilon^e)\right)^2,$$

and the work-conjugate Mandel stress is defined as (this expression may be later modified by a tension-compression split)

$$\sigma^M = \frac{\partial \psi^e}{\partial \varepsilon^e} = g^e(\phi)\left(2\mu \mathrm{dev}(\varepsilon^e) + \kappa \mathrm{tr}(\varepsilon^e)\right).$$

Cauchy stress can then be defined as:

$$\sigma = \frac{1}{J}F^{e-T}\sigma^M F^{eT}.$$

4.36.2 Plastic Hardening

4.36.2.1 Rate Sensitivity

The variational model proposed by Talamini *et al.* [105] provides for the possibility of rate-dependent plasticity through the inclusion of a dual kinetic potential $\Pi^*(\dot{\bar{\varepsilon}}^p, \phi)$, with the requirement that its derivative approaches zero in the quasistatic limit ($\dot{\bar{\varepsilon}}^p \to 0^+$). The dissipation potential identifies two components Y^{vis} and $\dot{\bar{\varepsilon}}^p$ that define the total dissipation density $\mathcal{D}$:

$$\mathcal{D} = Y^{\mathrm{vis}}\dot{\bar{\varepsilon}}^p,$$

$$Y^{\mathrm{vis}} = \frac{\partial \Pi^*}{\partial \dot{\bar{\varepsilon}}^p}.$$

When rate-dependence is included in the formulation, the viscous over-stress Y^{vis} would be added to the quasistatic flow stress Y^{eq}, replacing (4.220) with the following:

$$\left(\bar{\sigma} = \sqrt{\frac{3}{2}}\left\|\mathrm{dev}\sigma\right\| = \sqrt{\frac{3}{2}}g^e(\phi)\left\|\mathrm{dev}\frac{\partial \widetilde{\psi}^e_+}{\partial \varepsilon^e}\right\|\right) = \left(Y^{\mathrm{eq}} = g^p(\phi)\frac{\partial \widetilde{\psi}^p}{\partial \bar{\varepsilon}^p}\right) + \left(Y^{\mathrm{vis}} = g^p(\phi)\frac{\partial \Pi^*}{\partial \dot{\bar{\varepsilon}}^p}\right). \tag{4.224}$$

As an example, Hu *et al.* [46] proposes a power-law rate-sensitivity dissipation density of the form:

$$\Pi^* = \frac{m}{m+1}Y_0\dot{\epsilon}_0\left(\frac{\dot{\bar{\varepsilon}}^p}{\dot{\epsilon}_0}\right)^{(m+1)/m}$$

Rate-dependent plasticity has not yet been implemented into Phase Field F^eF^p to date.

4.36.2.2 Damage Potentials

The damage potential implemented for Phase Field F^eF^p is the so-called AT-1 potential that includes a linear term in phase:

$$\psi^f = \frac{3}{8\ell}\left((1-\phi) + \ell^2 \nabla\phi \cdot \nabla\phi\right) \tag{4.225}$$

This damage potential was first proposed by Pham *et al.* [84] and is a critical component of the so-called threshold models, named because this potential gives rise to a critical energy threshold ψ_c which must be reached before damage begins evolving. The critical energy threshold can be revealed by substituting this damage potential into (4.221):

$$\frac{3G_c\ell}{4}\Delta\phi - \frac{\partial g^e}{\partial\phi}\widetilde{\psi}^e_+ - \frac{\partial g^p}{\partial\phi}\widetilde{\psi}^p + \frac{3G_c}{8\ell} = 0.$$

For a uniformly intact initial state, the phase field is defined as $\phi = 1$ and $\Delta\phi = 0$. The condition required to evolve beyond this state corresponds to:

$$\frac{\partial g^e}{\partial\phi}\widetilde{\psi}^e_+ + \frac{\partial g^p}{\partial\phi}\widetilde{\psi}^p = \frac{3G_c}{8\ell}. \tag{4.226}$$

When combined with the common quadratic degradation function (4.228), $g^e(\phi) = g^p(\phi) = g^{\mathrm{Q}}(\phi)$, this reduces to

$$\psi_c = \left(\widetilde{\psi}^e_+ + \widetilde{\psi}^p\right)_c = \frac{3G_c}{16\ell} \tag{4.227}$$

4.36.2.3 Degradation Functions

The most common degradation function found in the literature is the quadratic degradation function:

$$g^{\mathrm{Q}}(\phi) = \phi^2 \tag{4.228}$$

When combined with the linear damage potential, this gives rise to the critical energy threshold described above (4.227). For a given load path, the critical energy threshold can be related to a critical failure strength. For example, for an elastic material ($\widetilde{\psi}^p = 0$) under uniaxial tension, the driving energy is a function of the stress $\widetilde{\psi}^e = \frac{\sigma^2}{2E}$, so the failure threshold can be found to be $\sigma_c = \sqrt{\frac{3G_cE}{8\ell}}$. Therefore, the failure threshold (ψ_c or σ_c) depends on the phase field length scale ℓ. The length scale ℓ serves as a *numerical* parameter, with the model convergent to Griffith fracture in the limit as $\ell \to 0$, so the failure threshold approaches infinity. Alternatively, the length scale can be selected so that the critical stress matches the material failure stress [84].

In contrast, when modeling ductile failure, there exists a physical yield stress R. Now, the relationship between σ_c and the yield stress has consequence in terms of model physics. This can be recast in terms of length scales: the interaction between the magnitudes of the phase-field

fracture length scale ℓ and the plastic zone size r_p. This means that the phase-field length scale is now effectively a *material* parameter, rather than a *numerical* one.

This was the motivation for the degradation function proposed by Talamini *et al.* [105]. This degradation function $g^{\mathrm{R}}(\phi)$ takes the form of a rational function and includes ψ_c as a new parameter:

$$g^{\mathrm{R}}(\phi) = \frac{\phi^2}{(1+\gamma(1-\phi))^2}, \tag{4.229}$$

$$\gamma = \frac{3G_c}{16\ell\psi_c} - 1. \tag{4.230}$$

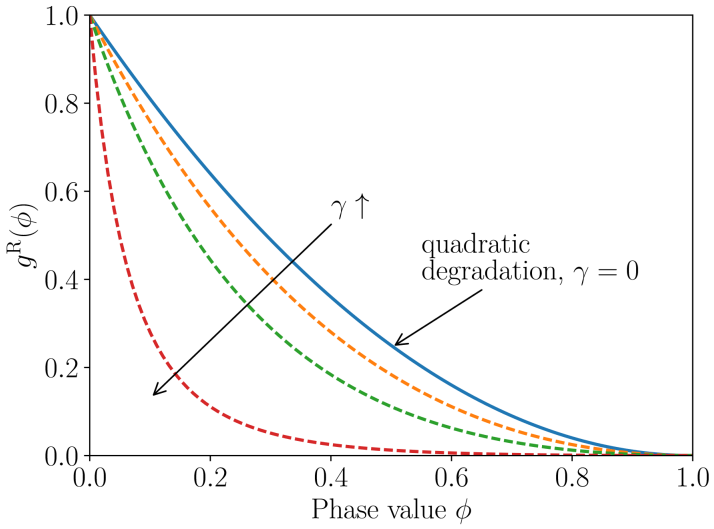

Fig. 4.155 Effect of parameter γ in the rational degradation function. Graphs are shown for $\gamma = \{0, \frac{1}{3}, 1, 7\}$. Increasing γ makes the degradation function (and hence the stress) drop off more quickly with increasing phase value.

The effect of γ on the degradation behavior is shown in Fig. 4.155. In order to ensure convexity of the degradation function and solution uniqueness, a bound of $\gamma \geq -\frac{1}{3}$ is recommended; this corresponds to an upper bound for the threshold parameter: $\psi_c \leq \frac{9G_c}{32\ell}$. The quadratic degradation function exists as a special case of this model, when $\gamma = 0$, $\psi_c = \frac{3G_c}{16\ell}$.

Repeating (4.226) and (4.227) using $g^{\mathrm{R}}(\phi)$ confirms that the new ψ_c parameter is returned as the effective critical energy threshold. This restores the interpretation of ℓ as a numerical parameter. The effect of degradation function parameters ψ_c and γ, is demonstrated on uniaxial constitutive response in Fig. 4.156.

The Lorentz degradation function is the only degradation function currently available in Phase Field $\mathrm{F^eF^p}$, so $g^e = g^{\mathrm{R}}$. The plastic degradation function is assumed to equal the elastic one, with

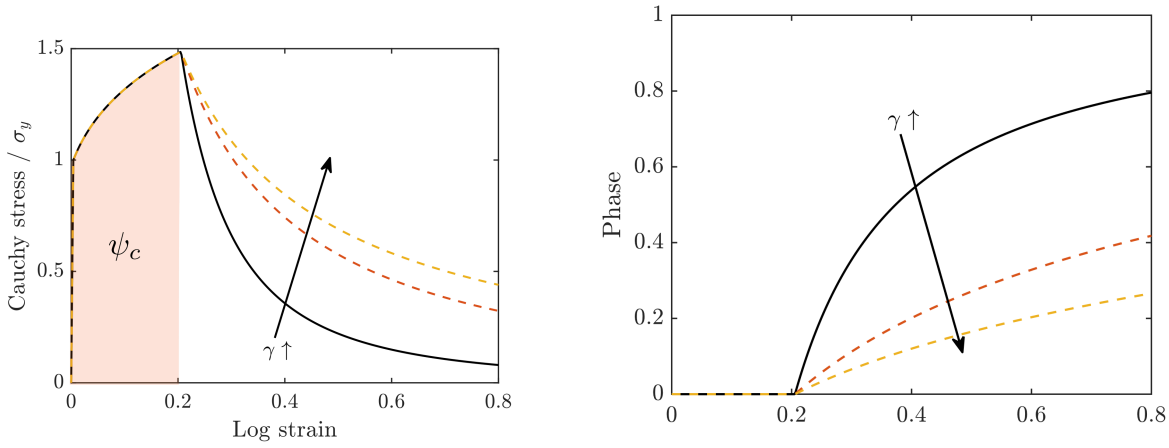

Fig. 4.156 Behavior of the model with the rational degradation function in homogeneous uniaxial tension. Data are shown for $\gamma = \{0, 1, 2\}$. The solid lines are for $\gamma = 0$. (a) Damage nucleates when the free energy density reaches the value of the model parameter ψ_c, regardless of the value of γ. The softening behavior is sensitive to γ. (b) The rate of damage with strain decreases as γ increases.

an additional parameter p_{pl}, which controls the portion of plastic work that contributes to driving fracture:

$$g^p(\phi) = (1 - p_{pl}) + p_{pl} g^e(\phi).$$

Many ductile phase-field references include the plastic work as driving energy ($p_{pl} = 1$, $g^p = g^e$), while others do not ($p_{pl} = 0$, $g^p = 1$). This parameter allows for selection of either convention or an intermediate portion.

4.36.2.4 Tension-Compression Split

Two choices of tension-compression split have been implemented so far: *none* and *volumetric-deviatoric*. The *none* option includes all energy into the positive, damaging portion, holding nothing back in the negative portion:

$$\begin{cases} \widetilde{\psi}^e_+ = \widetilde{\psi}^e \\ \widetilde{\psi}^e_- = 0 \\ \psi^e(u, z, \phi) = g^e(\phi)\widetilde{\psi}^e(u, z) \\ \sigma^M = \frac{\partial \psi^e}{\partial \varepsilon^e} = g^e(\phi)\left(2\mu \mathrm{dev}(\varepsilon^e) + \kappa \mathrm{tr}(\varepsilon^e)\right) \\ \psi^p(z, \phi) = g^p(\phi)\widetilde{\psi}^p(z) \end{cases} .$$

The second option, *volumetric-deviatoric*, divides the elastic potential into volumetric and deviatoric components. The volumetric components contribute to the positive elastic potential only if the trace of the elastic strain tensor is positive (dilatational), while the deviatoric components always contribute. The plastic potential is not divided. The tension-compression split

of the elastic potential also has implications for the definition of the stress:

$$\begin{cases} \widetilde{\psi}^e_+ = \frac{\kappa}{2}\left(\langle \mathrm{tr}(\varepsilon^e)\rangle_+\right)^2 + \mu \mathrm{dev}(\varepsilon^e) : \mathrm{dev}(\varepsilon^e) \\ \widetilde{\psi}^e_- = \frac{\kappa}{2}\left(\langle \mathrm{tr}(\varepsilon^e)\rangle_-\right)^2 \\ \psi^e(u,z,\phi) = g^e(\phi)\widetilde{\psi}^e_+(u,z) + \widetilde{\psi}^e_- \\ \sigma^M = \frac{\partial \psi^e}{\partial \varepsilon^e} = g^e(\phi)\left(2\mu \mathrm{dev}(\varepsilon^e) + \kappa \langle \mathrm{tr}(\varepsilon^e)\rangle_+\right) + \kappa \langle \mathrm{tr}(\varepsilon^e)\rangle_- \\ \psi^p(z,\phi) = g^p(\phi)\widetilde{\psi}^p(z) \end{cases},$$

with Macaulay brackets indicating inclusion of positive $\langle\cdot\rangle_+$ or negative $\langle\cdot\rangle_-$ quantities.

A common third option, a *spectral* split that divides energy based on positive/negative eigenvalues of the strain tensor, has not been implemented to date.

4.36.3 Implementation

Implementational details of Phase Field F^eF^p is included in this section. This includes: (a) deviations between the theory and implementation, (b) an overview of the coupled solution strategy, (c) an overview of the solid mechanics solution, (d) an overview of the phase-field evolution solution.

4.36.3.1 Deviations from theory

Conditioning coefficient

For numerical stability reasons, the degradation function is implemented in the slightly modified form

$$g(\phi) = g^{\mathrm{R}}(\phi)(1 - k_c) + k_c, \tag{4.231}$$

where $k_c \ll 1$ is a small, non-negative parameter called the *conditioning coefficient* that helps to avoid numerical problems such as element inversion in highly damaged material points. This modification directly impacts the stress and the driving energies $g^e\widetilde{\psi}^e_+ + g^p\widetilde{\psi}^p$; neither of these drop to *zero* as ϕ approaches zero. This leaves a small residual stiffness in the material point to resist inversion, but with driving energies still active, the damage may continue to creep outward from fully-damaged areas. The use of conditioning coefficients is widespread throughout the phase-field fracture literature, e.g., [14], [67], [4]. Other techniques, such as removal of highly degraded elements using element death, could be used address this problem, though with a different set of tradeoffs.

Phase-field bound constraint

Examination of the phase-field update equation (4.221) in an unloaded state (i.e., $\{\widetilde{\psi}_+^e, \widetilde{\psi}^p\} = 0$) with a uniform phase field (i.e., $\Delta\phi = 0$) reveals the need for an enforcement strategy for the phase field bound constraint $\phi \leq 1$ in some formulations, such as the threshold model with the AT-1 damage potential (4.225).

The classical phase-field fracture model (AT-2, unimplemented) requires no constraint enforcement, as the solution to this case falls at the bound itself, $\phi = 1$. In contrast, for the threshold model (AT-1, g^{Q}), the update equation (4.223) simplifies to the following solution for a uniform state:

$$\phi = \frac{3G_c}{16\ell\left(\widetilde{\psi}_+^e + \widetilde{\psi}^p\right)}. \tag{4.232}$$

Clearly, when the driving energies are zero the solution of the phase field is infinite. For all values of $\widetilde{\psi}_+^e + \widetilde{\psi}^p$ less than the critical energy $\frac{3G_c}{16\ell}$ will yield a phase field $\phi > 1$, in violation of the phase bound. Enforcement of the phase field constraint is handled by employing a max-function to enforce a sufficient driving energy that guarantees constraint satisfaction. We replace the usage of $\widetilde{\psi}_+^e + \widetilde{\psi}^p$ with ψ_+^D, defined as:

$$\psi_+^D = \max\left(\widetilde{\psi}_+^e + \widetilde{\psi}^p, \frac{3G_c}{16\ell}\right) \tag{4.233}$$

Generalizing this for the rational degradation function $g^{\mathrm{R}}(\phi)$ in the cohesive phase field model yields (derivation omitted):

$$\psi_+^D = \max\left(\widetilde{\psi}_+^e + \widetilde{\psi}^p, \psi_c\right) = \langle\widetilde{\psi}_+^e + \widetilde{\psi}^p - \psi_c\rangle + \psi_c, \tag{4.234}$$

where $\langle\bullet\rangle$ are Macaulay brackets.

This boundary treatment is derived from the homogeneous case ($\phi = 1$); for a phase field that is not spatially uniform, there may be small violations. This approximation is widely used in the literature (e.g., Miehe [67]) and thought to be a reasonable approximation.

While this approach ordinarily provides for satisfaction of the phase-field bound constraint, we note that it does affect the physics of the problem. The resulting phase-field solutions and energy dissipation may differ from analytical solutions that enforce the bound constraint differently.

Phase-field irreversibility constraint

A longstanding strategy for addressing the phase-field irreversibility constraint is to modify the fracture driving energies through the use of a history function, as proposed by Miehe *et al.* [68]:

$$\mathcal{H}(x,t) = \max_{\hat{t}\in[0,t]} \psi_+^D(x,\hat{t}).$$

Practically, this can be enforced by maintaining the history-maximum driving energy as a state variable on the integration points and comparing at each time step:

$$\mathcal{H}(x, t_{n+1}) = \max\left(\psi_+^D(x, t_{n+1}), \mathcal{H}(x, t_n)\right).$$

The monotonicity of the phase-field driving force approximately enforces irreversibility. Together with the bound-constraint modification, the phase-field update equation (formerly (4.221)) now reads:

$$\frac{\partial \psi^f}{\partial \nabla \phi} G_c - \frac{\partial g^e(\phi)}{\partial \phi}\mathcal{H} - \frac{\partial \psi^f}{\partial \phi} G_c = 0. \tag{4.235}$$

For the implemented damage potential implemented (AT-1), this becomes:

$$\frac{3G_c\ell}{4}\Delta\phi - \frac{\partial g^e(\phi)}{\partial \phi}\mathcal{H} + \frac{3G_c}{8\ell} = 0. \tag{4.236}$$

Geelen *et al.* [34] explored the use of an augmented-Lagrangian formulation as an alternative means of enforcing the bound and irreversibility constraints. Their finding was that the history function causes slight increases in global energy dissipation, corresponding to widening of the damage fields around cracks. The additional cost of the augmented-Lagrangian formulation, both in implementation and operation, has been a barrier to its implementation in Sierra so far.

4.36.3.2 Coupled solution strategy for implicit time integration

In order to solve the Euler-Lagrange equations (4.218) for the phase-field fracture model, an *alternating minimization* strategy is employed. In this approach, the conventional balance-of-linear-momentum boundary-value problem is solved in terms of its displacement degrees of freedom, with a return-mapping algorithm for the plastic state variables and the phase field held constant. The phase-field Euler-Lagrange equation (4.221) is then solved with the inputs from the displacement system (driving energies) held constant. Equilibrium between the two fields is achieved by solving the two subproblems repeatedly in a staggered fashion until convergence in both fields is observed. This procedure is illustrated in Fig. 4.157.

This approach is selected primarily due to its consistency with Sierra paradigm for multi-field problems and therefore ease of implementation. Building within the framework of Sierra/SM, it is expedient to leave the traditional displacement system solution as-is, modified only by a damage term relating to the phase-field. This approach is very commonly used in the phase field literature (see, e.g., [14], [68]). Solution of each sub-problem is straightforward, as each is convex; however, with the cross-terms held fixed, the alternating coupled solve may be slow to converge at times.

The alternative approach is a *monolithic* solve, wherein the coupled displacement-phase system is solved as a single matrix system. This approach has been used by several authors (e.g., [34], [46], [105]), and exhibits improved convergence in some cases; however, the solution may stall at saddle points as the convexity of the coupled system is not guaranteed. Monolithic solution is not implemented in Sierra/SM.

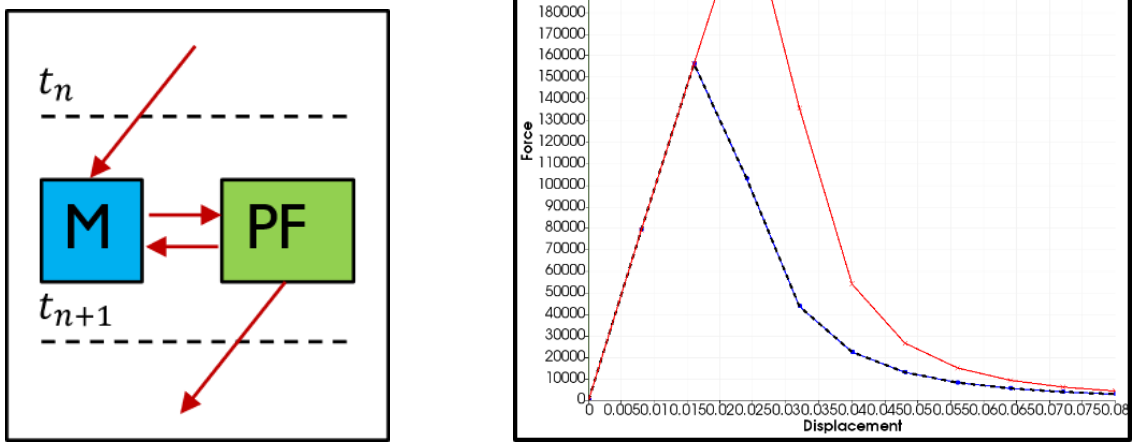

Fig. 4.157 Alternating minimization scheme behavior. (a) Schematic of alternating minimization scheme. At a new time step t_{n+1}, nonlinear solves for mechanics (M) and phase field (PF) are repeated until convergence achieved in both fields. Solver then proceeds to the next time step. (b) Force vs. displacement for a single element uniaxial tension problem with elastic material. The exact solution for the problem is shown with a dotted line. the curve marked "uncoupled" is solved with a single pass at each time step, leading to a solution that is out of equilibrium. The curve "ControlRxnDiff" is solved until convergence, indicating equilibrium. The equilibrium result is seen to agree with the exact solution.

4.36.4 Operator split scheme for explicit time integration

The algorithm for explicit integration is a straightforward extension of the quasi-static scheme outlined above. The major difference is that there is no equilibrium iteration between the fields on a given time step. Iteration is unnecessary given the small size of the time steps dictated by the numerical stability condition. Another consequence of the small time-step size is that the phase field need not be updated at each time step. (An exception to this may be if the loading conditions are in the shock regime.) The phase-field balance equation is also nonlinear, incurring a greater computational cost than an explicit time integration step, and it is therefore desirable to amortize this cost over a number of time steps. The frequency of the phase field update has been made a user-defined choice in the input file.

4.36.4.1 Solid mechanics solution

The full derivation of the solid mechanics solution is provided in the cited references [101], [100], [105]. The return mapping algorithm for the Phase Field F^eF^p constitutive update, which corresponds to the solution of the state-variable Euler-Lagrange equation (4.220) will be specifically described in this section.

The Phase Field F^eF^p uses a radial return predictor-corrector algorithm for the constitutive update. First, an elastic trial stress state is calculated. This is done by assuming that the deformation increment is completely elastic and that the phase field has remained constant:

$$\begin{cases} F^{p,tr} & = F^p{}_n \\ \bar{\varepsilon}^{p,tr} & = \bar{\varepsilon}^p_n \\ F^{e,tr} & = F_{n+1}F^{p,tr-1} \\ \phi_{n+1} & = \phi_n \end{cases}.$$

The trial deformation state is converted to logarithmic strains to compute a conjugate Mandel trial stress (the trial Mandel stress shall be consistent with the tension-compression split, defined in Section 4.36.2.4. The baseline (no tension-compression case) is given here):

$$C^{e,tr} = F^{e,tr^T}F^{e,tr},$$

$$\varepsilon^{e,tr} = \frac{1}{2}\log(C^{e,tr}),$$

$$\sigma^{M,tr} = g^e(\phi_{n+1})\left(2\mu\mathrm{dev}(\varepsilon^{e,tr}) + \kappa\mathrm{tr}(\varepsilon^{e,tr})\right)$$

An effective stress is calculated:

$$\bar{\sigma}^{tr} = \sqrt{\frac{3}{2}}||\mathrm{dev}\sigma^{M,tr}||,$$

and compared to the flow stress, determined by evaluating the hardening model with the trial plastic strain scalar $\bar{\varepsilon}^{p,tr}$ and factoring by the plastic degradation function g^p:

$$\bar{Y}^{\mathrm{eq},tr} = g^p(\phi_{n+1})Y^{\mathrm{eq}}(\bar{\varepsilon}^{p,tr}).$$

If $\bar{\sigma}^{tr} \leq \bar{Y}^{\mathrm{eq},tr}$, then the deformation increment is elastic, and the stress update is finished: $\sigma^m_{n+1} = \sigma^{M,tr}$, $\Delta\bar{\varepsilon}^p = 0$. If instead $\bar{\sigma}^{tr} > \bar{Y}^{\mathrm{eq},tr}$, then plastic deformation had occurred and a radial return algorithm determines the extent of plastic deformation.

The normal to the yield surface is assumed to lie in the direction of the trial stress state. This gives the following expression for the flow tensor N^p_{n+1}, with isotropic hardening assumed:

$$N^p_{n+1} = \sqrt{\frac{3}{2}}\frac{\sigma^{M,tr}}{||\sigma^{M,tr}||} = \frac{3}{2}\frac{\mathrm{dev}\,\sigma^{M,tr}}{\bar{\sigma}^{tr}}.$$

The radial return algorithm seeks to solve the following equation (The first two terms represent the new effective stress $\bar{\sigma}(\varepsilon^e_{n+1})$ evaluated at $\varepsilon^e_{n+1} = \varepsilon^{e,tr} - \Delta\bar{\varepsilon}^p N^p_{n+1}$. This corresponds to

$\frac{\partial \widetilde{\psi}^e_+}{\partial \bar{\varepsilon}^p} = \frac{\partial \widetilde{\psi}^e_+}{\partial \varepsilon^e} - N^p_{n+1}$. The last term represents the new flow stress $Y^{\text{eq}}(\bar{\varepsilon}^p_{n+1})$ evaluated at $\bar{\varepsilon}^p_{n+1} = \bar{\varepsilon}^p_n + \Delta\bar{\varepsilon}^p$.):

$$\bar{\sigma} - 3\mu g^e(\phi_{n+1})\Delta\bar{\varepsilon}^p - g^p(\phi_{n+1})Y^{\text{eq}}(\bar{\varepsilon}^p_n + \Delta\bar{\varepsilon}^p) = 0$$

using a Newton-Raphson algorithm, with residual $\bar{R}$ and iteration denoted by superscript k:

$$\begin{cases} \bar{R} & = \bar{\sigma} - 3\mu g^e(\phi_{n+1})\Delta\bar{\varepsilon}^p - g^p(\phi_{n+1})Y^{\text{eq}}(\bar{\varepsilon}^p_n + \Delta\bar{\varepsilon}^p) \\ \frac{\partial \bar{R}}{\partial \Delta\bar{\varepsilon}^p} & = -3\mu g^e(\phi_{n+1}) - g^p(\phi_{n+1})\frac{\partial Y^{\text{eq}}}{\partial \Delta\bar{\varepsilon}^p}(\bar{\varepsilon}^p_n + \Delta\bar{\varepsilon}^p) \\ (\Delta\bar{\varepsilon}^p)^k & = 0 \\ (\Delta\bar{\varepsilon}^p)^{k+1} & = (\Delta\bar{\varepsilon}^p)^k - \bar{R}/\frac{\partial \bar{R}}{\partial \Delta\bar{\varepsilon}^p} \end{cases}.$$

This equation is iterated until convergence, with a line search algorithm to accelerate convergence. The value $(\Delta\bar{\varepsilon}^p)^{k+1}$ that satisfies the convergence tolerance establishes the solution at time t_{n+1}: $\Delta\bar{\varepsilon}^p_{n+1} = (\Delta\bar{\varepsilon}^p)^{k+1}$. After the plastic update has been solved, the material state fields are updated (the updated Mandel stress shall be consistent with the tension-compression split, defined in Section 4.36.2.4. The baseline (no tension-compression case) is given here):

$$\begin{cases} \bar{\varepsilon}^p_{n+1} & = \bar{\varepsilon}^p_n + \Delta\bar{\varepsilon}^p_{n+1} \\ F^p{}_{n+1} & = \exp(\Delta\bar{\varepsilon}^p_{n+1} N^p_{n+1}) F^p{}_n \\ F^e{}_{n+1} & = F_{n+1} F^{p\,-1}_{n+1} = F^{e,tr} \exp(-\Delta\bar{\varepsilon}^p_{n+1} N^p_{n+1}) \\ C^e_{n+1} & = F^{eT}_{n+1} F^e{}_{n+1} = C^{e,tr} \exp(-2\Delta\bar{\varepsilon}^p_{n+1} N^p_{n+1}) \\ \varepsilon^e{}_{n+1} & = \varepsilon^{e,tr} - \Delta\bar{\varepsilon}^p N^p_{n+1} \\ \sigma^m_{n+1} & = g^e(\phi_{n+1})\,(2\mu \text{dev}(\varepsilon^e{}_{n+1}) + \kappa \text{tr}(\varepsilon^e{}_{n+1})) \\ \bar{\sigma}_{n+1} & = \bar{\sigma}^{tr} - 3\mu g^e(\phi_{n+1})\Delta\bar{\varepsilon}^p_{n+1} \\ \sigma_{n+1} & = \frac{1}{||F_{n+1}||} F^{e-T}_{n+1} \sigma^m_{n+1} F^{eT} \end{cases}.$$

These fields are then used to calculate the driving energies $\{\widetilde{\psi}^e_+, \widetilde{\psi}^p\}$ for the phase-field update solve. The elastic potential is calculated using $F^e{}_{n+1}$, as defined in Section 4.36.1.2; the plastic potential is calculated using $\bar{\varepsilon}^p_{n+1}$, as defined in Section 4.36.2; the final driving energies are created using these potentials, modified by the tension-compression split (Section 4.36.2.4) and the bound-constraint and irreversibility treatments (Section 4.36.3.1).

4.36.4.2 Phase-field evolution solution

The phase-field update equation (4.236) is solved in Sierra/SM's reaction-diffusion solver, using a Galerkin finite element approach to solve the equation in weak form. The same finite element mesh is used for both the displacement solve and the phase-field solve (an alternative solution method is to use Arpeggio to couple with Aria's reaction-diffusion solution capability. Due to the complexity of the input file and the need to compile a custom user-plugin for the source term, this is not recommended. This approach does, however, allow for a different mesh to be used for the phase-field solve).

The weak form is derived by first taking the inner product of the phase-field update equation with a phase variation ω over the domain Ω:

$$\int_\Omega \frac{3G_c\ell}{4}\Delta\phi\omega - \frac{\partial g^e(\phi)}{\partial\phi}\mathcal{H}\omega + \frac{3G_c}{8\ell}\omega \, d\Omega = 0.$$

We linearize the degradation function term $\frac{\partial g^e(\phi)}{\partial\phi} \rightarrow \frac{\partial^2 g^e(\phi)}{\partial\phi^2}\phi$ in order to accommodate the rational degradation function g^{R}, and then integrate by parts and rearrange to achieve a bilinear form:

$$\int_\Omega \frac{3G_c\ell}{4}\nabla\phi\cdot\nabla\omega + \frac{\partial^2 g^e(\phi)}{\partial\phi^2}\mathcal{H}\phi\omega \, d\Omega = \int_\Omega \frac{3G_c}{8\ell}\omega \, d\Omega + \int_{\partial\Omega} \frac{3G_c\ell}{4}\nabla\phi\omega\cdot n_{\partial\Omega} \, d\Gamma.$$

The last term can be omitted as the variation $\omega = 0$ is defined to be zero on the boundary. The phase field and phase variation are discretized using the existing mesh shape functions N_i:

$$\begin{cases} \phi & = \sum_i N_i^A(x)\phi_i \\ \nabla\phi & = \sum_i \nabla N_i^A(x)\phi_i \\ \omega & = \sum_j N_j^B(x)\omega_j \\ \nabla\omega & = \sum_j \nabla N_j^B(x)\omega_j \end{cases},$$

$$\sum_{\{i,j\}}\left(\int_\Omega \frac{3G_c\ell}{4}\nabla N_i^A(x)\phi_i\cdot\nabla N_j^B(x)\omega_j + \frac{\partial^2 g^e(\phi)}{\partial\phi^2}\mathcal{H}N_i^A(x)\phi_i N_j^B(x)\omega_j \, d\Omega = \int_\Omega \frac{3G_c}{8\ell}N_j^B(x)\omega_j \, d\Omega\right).$$

The phase variation nodal field ω_j can then be factored out:

$$\sum_{\{i,j\}}\left(\phi_i\int_\Omega \frac{3G_c\ell}{4}\nabla N_i^A(x)\cdot\nabla N_j^B(x) + \frac{\partial^2 g^e(\phi)}{\partial\phi^2}\mathcal{H}N_i^A(x)N_j^B(x) \, d\Omega = \int_\Omega \frac{3G_c}{8\ell}N_j^B(x) \, d\Omega\right).$$

Gaussian quadrature is used in each element to compute the shape function integrals and then the element systems are assembled into the global system. In the spirit of the reaction-diffusion equation template, we refer to the first term as the diffusion term $D_{ij} = \frac{3G_c\ell}{4}\nabla N_i^A\cdot\nabla N_j^B$, the second as the reaction term $R_{ij} = \frac{\partial^2 g^e(\phi)}{\partial\phi^2}\mathcal{H}N_i^A N_j^B$, and the right-hand side as the source term $S_j = \frac{3G_c}{8\ell}N_j^B$. We note that the diffusion term has the form of a stiffness matrix, while the reaction term has the form of a mass matrix. The system of equations can then be restated as:

$$\left(D_{ij} + R_{ij}\right)\phi_i = S_j.$$

In fact, the phase-field update is solved incrementally; that is to say that we solve for $\Delta\phi$, rather than $\phi_{n+1} = \phi_n + \Delta\phi$ directly. This updates the matrix system to be written as:

$$\left(D_{ij} + R_{ij}\right)(\phi_n + \Delta\phi)_i = S_j.$$

Further, we note that the system of equations is linear for the quadratic degradation function g^{Q} as $\frac{\partial^2 g^{\mathrm{Q}}(\phi)}{\partial\phi^2} = 2$, but is generally nonlinear for the rational degradation function g^{R}, with $R = R(\phi)$. For linear systems ($g^e = g^{\mathrm{Q}} = g^{\mathrm{R}}(\gamma = 0)$), we solve the system for $\Delta\phi$ directly, as:

$$\left(D_{ij} + R_{ij}\right)(\Delta\phi)_i = S_j - \left(D_{ij} + R_{ij}\right)(\phi_n)_i. \tag{4.237}$$

For nonlinear systems ($g^e = g^{\mathrm{R}}(\gamma \neq 0)$), the phase-field increment is solved using an iterative preconditioned conjugate gradient solver that minimizes the residual of (4.237). The nodal preconditioner is established using a probing approach.

Bound constrained solve

While the approaches described in Section 4.36.3.1 tend to enforce the phase field bound and irreversibility constraints fairly well, in practice, there are situations in which they occasionally fail. Assuming that the phase field is properly initialized, the upper bound ($\phi \leq 1$) will be respected as long as the irreversibility constraint $\Delta\phi \leq 0$ is met. This leaves the irreversibility constraint and the lower bound ($\phi \geq 0$) as the relevant bounds.

The phase-field solve is augmented with bound-constraint methods in order to ensure that the constraints are satisfied. For the linear solve, this is implemented by simply restricting the phase field to bounds: $0 \leq \phi_{n+1} \leq \phi_n$; violating values are set to the bound. Further, for the nonlinear solve with conjugate gradient, the conjugate-gradient step size is set to zero at nodes where the bound constraint is active. Details of this algorithm can be found in Vollebregt [109].

While this approach appears to do an adequate job at satisfying the bound constraints on the phase field, we retain the driving energy modifications defined in Section 4.36.3.1 until it is demonstrated that the bound-constrained conjugate gradient solve successfully reproduces known solutions.

4.36.5 Verification

Both single-material point unit tests and full regression tests are used to verify the Phase Field $\mathrm{F^eF^p}$ model.

4.36.5.1 Unit testing

The Phase Field $\mathrm{F^eF^p}$ model is verified through a series of uniaxial stress test considering a variety of load magnitudes and phase-field model forms, loosely based on the boundary value problems of *Appendix A* are used. Throughout these tests, the elastic properties are maintained as $E = 200$ GPa and $\nu = 0.3$, the plasticity is defined as linear hardening with $Y_0 = 180$ MPa and $H = 180$ MPa, the fracture parameters are set to $G_c = 6.2$ J/m ^{2}, $\ell = 1.34‘m, : math : ‘k_c = 1.2 \cdot 10^{-4}$, $p_{pl} = 1$, and a phase field of $\phi = 0.9$. The phase-field model is tested with both the threshold (AT-1) model ($\gamma = 0$, $\psi_c = \frac{3}{16}\frac{G_c}{\ell}$) and the Lorentz model ($\gamma = 2$, $\psi_c = \frac{1}{16}\frac{G_c}{\ell}$) and with the two implemented tension-compression splits (none and volumetric-deviatoric). For these tests, we compare the Cauchy stress (often in the uniaxial component) and plastic strain $\bar{\varepsilon}^p$ as well as the fracture and driving energies.

Uniaxial Tension - Elastic

For this problem, we set the following deformation state, with the applied axial strain to be half of the yield strain to ensure elasticity:

$$\begin{cases} \varepsilon_{11} & = \frac{1}{2}\frac{Y_0}{E} \\ \varepsilon_{22} = \varepsilon_{33} & = -\nu\varepsilon_{11} \\ F_{11} & = \exp(\varepsilon_{11}) \\ F_{22} = F_{33} & = \exp(\varepsilon_{22}) = \exp(-\nu\varepsilon_{11}) \\ \nabla\phi \cdot \nabla\phi & = 0 \end{cases}$$

This is equivalent to $\lambda = \exp(\frac{1}{2}\frac{Y_0}{E}) - 1$. Analytical solutions for the stress, plastic strain, and energies are derived for comparison. The phase-field models considered are the threshold (AT-1) and Lorentz degradation functions. The tension-compression split is not tested as it would not be active in this case. %Begin elastic, the expected stress is $\sigma = \frac{E\varepsilon_{11}}{\exp((1-2\nu)E\varepsilon_{11})}\mathrm{deg}(\phi)$, the plastic strain is $\bar{\varepsilon}^p = 0$

Uniaxial Tension - Plastic

For this problem, we set the following deformation and phase state, with the applied axial strain to be 150% of the yield strain to ensure plasticity:

$$\begin{cases} \varepsilon_{11} & = \frac{3}{2}\frac{Y_0}{E} \\ \varepsilon_{22} = \varepsilon_{33} & = -\nu\varepsilon_{11} \\ F_{11} & = \exp(\varepsilon_{11}) \\ F_{22} = F_{33} & = \exp(\varepsilon_{22}) = \exp(-\nu\varepsilon_{11}) \\ \nabla\phi \cdot \nabla\phi & = 0.1 \end{cases}$$

Analytical solutions for the stress, plastic strain, and energies are derived for comparison. The phase-field models considered are the threshold (AT-1) and Lorentz degradation functions. Additionally, the plastic-work driving energy portion parameter p_{pl} is tested at additional values of $p_{pl} = \{0, 0.5\}$. The tension-compression split is not tested as it would not be active in this case.

Uniaxial Compression - Elastic

For this problem, we set the following deformation and phase state, with the applied axial strain to be negative half of the yield strain to ensure elasticity:

$$\begin{cases} \varepsilon_{11} & = -\frac{1}{2}\frac{Y_0}{E} \\ \varepsilon_{22} = \varepsilon_{33} & = -\nu\varepsilon_{11} \\ F_{11} & = \exp(\varepsilon_{11}) \\ F_{22} = F_{33} & = \exp(\varepsilon_{22}) = \exp(-\nu\varepsilon_{11}) \\ \nabla\phi \cdot \nabla\phi & = 0 \end{cases}$$

Analytical solutions for the stress, plastic strain, and energies are derived for comparison. The phase-field models considered are a matrix of degradation functions (threshold and Lorentz) and the tension-compression splits (none and volumetric-deviatoric).

4.36.5.2 Regression testing

Several tests are implemented in Sierra/SM's regression test library to provide regular testing of the Phase Field F^eF^p in a full finite-element setting. While some of the tests have no analytical solution and are simply compared to an accepted "gold" result file, others include solution verification to known analytical solutions. At a minimum, the former tests include solution verification of the phase bound constraints when the bound-constrained solver is applied.

The tests with solution verification are detailed here:

1D PhaseBC FeFp

% with dimensions $x \in [-0.05, 0.05]$, $y \in [-0.0005, 0.0005]$, $z \in [-0.0005, 0.0005]$ In this test, a 1-D bar is subjected to a Dirichlet phase boundary condition $\phi = 0$ at the center $x = 0$, representing an initial crack. Displacement is fixed on the entire domain, and the nonlinear reaction-diffusion solver solves for the phase-field emanating from the center. This test checks the phase profile against an analytical solution (4.238) both as mesh is refined (successively tighter tolerances) and as Lorentz degradation parameter γ is varied ($\gamma = 0$ and $\gamma \to \infty$). This is critical as single-material-point unit tests cannot verify a spatial phase-field solution.

With no mechanical work, the driving energy relies on the critical energy threshold to satisfy the phase boundary condition: $\mathcal{H} = \psi_c$. Adapting (4.236) for this case reads:

$$\frac{3G_c\ell}{4}\phi_{,xx} - \frac{2\phi(1+\gamma)}{(1+\gamma-\phi\gamma)^3}\frac{3G_c}{16\ell(1+\gamma)} + \frac{3G_c}{8\ell} = 0$$

subject to

$$\begin{cases} 0 \leq \phi \leq 1 \\ \phi(0) = 0 \\ \phi(x_0) = 1 \\ \phi_{,x}(x_0) = 0 \end{cases}.$$

The analytical solution for the cases above is:

$$\phi(x) = \begin{cases} 1 - \exp(-\frac{|x|}{\sqrt{2}\ell}) \text{ with } x_0 = \infty & \text{for } \gamma = 0 \\ 1 - \left(1 - \frac{|x|}{2\ell}\right)^2 \text{ with } x_0 = 2\ell & \text{for } \gamma \to \infty \end{cases}. \tag{4.238}$$

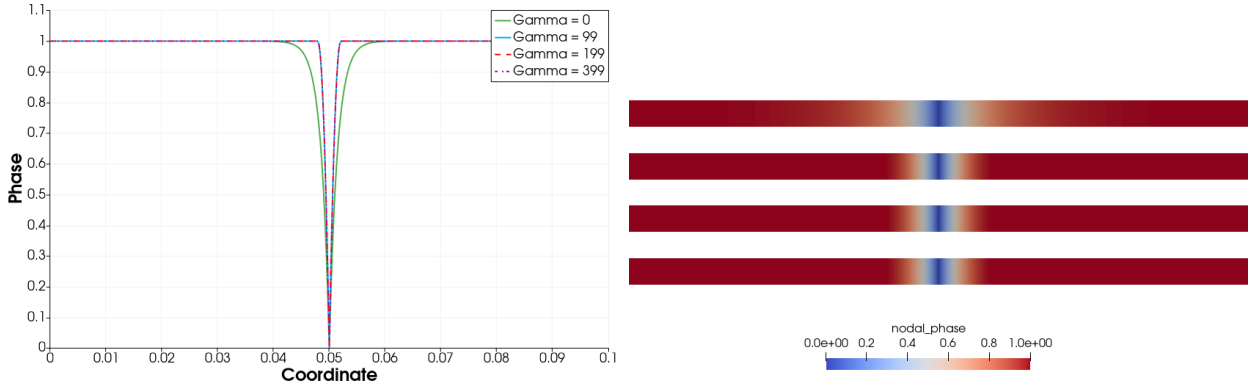

Fig. 4.158 Imagery showing the phase field solutions generated from the *1D PhaseBC FeFp* verification test, with the phase boundary condition placed at $x = 0.5$ and $\ell = 0.001$.

Control 1-D Extension

In this test, a cube is pulled in uniaxial tension with a displacement boundary condition through the elastic, plastic, and damage regimes. The phase-field length scale ℓ is set to be very large compared to the domain, so that the phase-field solution remains uniform and the gradient terms are negligible. The phase-field model form is set to the threshold (AT-1) model with $\gamma = 0$, and the linear reaction diffusion solver is used. The test checks against the reaction force required to assert the boundary condition as well as the phase-field in the body. Both linear-elastic and elastic-plastic materials are considered, each at a single-element and multiple-element mesh.

The analytical solution for the linear-elastic case is

$$\begin{cases} \varepsilon_{11} & = \log(1 + u/L) \\ \varepsilon_{11}^e & = \varepsilon_{11} \\ \widetilde{\psi}^e & = \frac{1}{2} E (\varepsilon_{11}^e)^2 \\ \phi & = \min(1, \psi_c / \widetilde{\psi}^e) \\ P & = \phi^2 \frac{E \varepsilon_{11}^e}{\exp(\varepsilon_{11}^e)} \\ f & = P A_0 \end{cases}, \tag{4.239}$$

while the analytical solution for the elastic-plastic case is

$$\begin{cases} \varepsilon_{11} & = \log(1 + u/L) \\ \varepsilon_{11}^e & = \min(\varepsilon_{11}, \frac{H \varepsilon_{11} + Y_0}{HE}) \\ \varepsilon_{11}^p & = \varepsilon_{11} - \varepsilon_{11}^e \\ \bar{\varepsilon}^p & = \varepsilon_{11}^e \\ \widetilde{\psi}^e & = \frac{1}{2} E (\varepsilon_{11}^e)^2 \\ \widetilde{\psi}^p & = \frac{1}{2} H (\bar{\varepsilon}^p)^2 + Y_0 \bar{\varepsilon}^p \\ \phi & = \min(1, \psi_c / (\widetilde{\psi}^e + \widetilde{\psi}^p)) \\ P & = \phi^2 \frac{E \varepsilon_{11}^e}{\exp(\varepsilon_{11}^e)} \\ f & = P A_0 \end{cases}, \tag{4.240}$$

where P is the first Piola-Kirchhoff stress, A_0 represents the initial cross-sectional area, u represents axial displacement, L represents the initial length of the cube, f represents the reaction force, and H represents the linear hardening slope. The test checks against the reaction force required to assert the boundary condition as well as the phase-field in the body.

Single Element, Linear

This test reproduces a specific case of the *Control 1-D Extension* test (linear-elastic, single element), but adds consideration of the conditioning coefficient k_c. The phase-field model form is set to the threshold (AT-1) model with $\gamma = 0$, and the linear reaction-diffusion solver is used. The test checks against the reaction force required to assert the boundary condition as well as the phase-field in the body.

The analytical solution is

$$\begin{cases} \varepsilon_{11} & = \log(1 + u/L) \\ \varepsilon_{11}^e & = \varepsilon_{11} \\ \widetilde{\psi}^e & = \frac{1}{2} E (\varepsilon_{11}^e)^2 \\ \phi & = \min\left(1, \frac{\psi_c}{\widetilde{\psi}^e (1 - k_c) + \psi_c k_c}\right) \\ P & = (\phi^2 (1 - k_c) + k_c) \frac{E \varepsilon_{11}^e}{\exp(\varepsilon_{11}^e)} \\ f & = P A_0 \end{cases}. \tag{4.241}$$

Single Element, Nonlinear as Linear

This test reproduces a specific case of the *Control 1-D Extension* test (linear-elastic, single element), but adds consideration of the nonlinear reaction diffusion solver. The phase-field model form is set to the threshold (AT-1) model with $\gamma = 0$, but the nonlinear reaction-diffusion solver is used. Additionally, the impact of the tension-compression split is verified by loading in uniaxial tension (no split, volumetric-deviatoric split) and uniaxial compression (no split). The solution for the volumetric-deviatoric split in uniaxial compression is skipped due to its complex derivation, though it is verified numerically in the next test. The test checks against the reaction force required to assert the boundary condition as well as the phase-field in the body. Together with *Single Element, Linear*, this test verifies that the linear and nonlinear reaction-diffusion solvers provide the same result for the linear $\gamma = 0$ case.

Single Element, Nonlinear

This test reproduces a specific case of the *Control 1-D Extension* test (linear-elastic, single element), but adds consideration of the nonlinear reaction diffusion solver. The phase-field model form is set to the Lorentz model with $\gamma = 0.48$. Additionally, the impact of the tension-compression split is verified by loading in uniaxial tension and uniaxial compression, while applying both no split and the volumetric-deviatoric split for each. The test checks against the reaction force required to assert the boundary condition as well as the phase-field in the body. The derivation of a closed-form complex, so a comparison solution has been prepared using symbolic and numerical solution in a Matlab script `solve_Lorentz.m`.

4.36.6 User Guide

```
BEGIN PARAMETERS FOR MODEL PHASE_FIELD_FEFP
  #
  # Elastic constants
  #
  YOUNGS MODULUS = <real>
  POISSONS RATIO = <real>
  SHEAR MODULUS  = <real>
  BULK MODULUS   = <real>
  LAMBDA         = <real>
  TWO MU         = <real>
  #
  # Phase Field parameters
  #
  CONDITIONING COEFFICIENT            = <real>
  CRITICAL ENERGY DENSITY             = <real> (3.0/16.0 * GC / FLS)
  FRACTURE LENGTH SCALE               = <real>
  GC                                  = <real>
```

(continues on next page)

(continued from previous page)

```
  NONLOCAL SOLVER                      = NONE | ARIA | RXNDIFF (RXNDIFF)
  PLASTIC WORK DRIVING ENERGY PORTION = <real> (1.0)
  TENSION COMPRESSION SPLIT            = VOLUMETRIC_DEVIATORIC | NONE␣
↪(NONE)
  #
  # Yield surface parameters
  #
  YIELD STRESS = <real>
```

```
#
  #
  # Hardening model
  #
  HARDENING MODEL = LINEAR | POWER_LAW | VOCE | USER_DEFINED |
  FLOW_STRESS | DECOUPLED_FLOW_STRESS | JOHNSON_COOK |
  POWER_LAW_BREAKDOWN
  #
  # Linear hardening
  #
  HARDENING MODULUS = <real>
  #
  # Power-law hardening
  #
  HARDENING CONSTANT = <real>
  HARDENING EXPONENT = <real> (0.5)
  LUDERS STRAIN      = <real> (0.0)
  #
  # Voce hardening
  #
  HARDENING MODULUS       = <real>
  EXPONENTIAL COEFFICIENT = <real>
  #
  # Johnson-Cook hardening
  #
  HARDENING FUNCTION = <string>hardening_function_name
  RATE CONSTANT      = <real>
  REFERENCE RATE     = <real>
  #
  # Power law breakdown hardening
  #
  HARDENING FUNCTION = <string>hardening_function_name
  RATE COEFFICIENT   = <real>
  RATE EXPONENT      = <real>
  # User defined hardening
  #
```

(continues on next page)

(continued from previous page)

```
  HARDENING FUNCTION = <string>hardening_function_name
  #
```

```
#
  #
  # Following Commands Pertain to Flow_Stress Hardening Model
  #
  #    -  Isotropic Hardening model
  #
  ISOTROPIC HARDENING MODEL = LINEAR | POWER_LAW | VOCE |
                              USER_DEFINED
  #
  # Specifications for Linear, Power-law, and Voce same as above
  #
  # User defined hardening
  #
  ISOTROPIC HARDENING FUNCTION = <string>iso_hardening_fun_name
  #
  #     - Rate dependence
  #
  RATE MULTIPLIER = JOHNSON_COOK | POWER_LAW_BREAKDOWN |
     USER_DEFINED | RATE_INDEPENDENT (RATE_INDEPENDENT)
  #
  # Specifications for Johnson-Cook, Power-law-breakdown
  #     same as before EXCEPT no need to specify a
  #     hardening function
  #
  # User defined rate multiplier
  #
  RATE MULTIPLIER FUNCTION = <string> rate_mult_function_name
  #
  #     - Temperature dependence
  #
  TEMPERATURE MULTIPLIER = JOHNSON_COOK | USER_DEFINED |
     TEMPERATURE_INDEPENDENT (TEMPERATURE_INDEPENDENT)
  #
  #  Johnson-Cook temperature dependence
  #
  MELTING TEMPERATURE   = <real>
  REFERENCE TEMPERATURE = <real>
  TEMPERATURE EXPONENT  = <real>
  #
  #  User-defined temperature dependence
  TEMPERATURE MULTIPLIER FUNCTION = <string>temp_mult_function_name
  #
```

(continues on next page)

(continued from previous page)

```
  # Following Commands Pertain to Decoupled_Flow_Stress Hardening Model
  #
  #    -  Isotropic Hardening model
  #
  ISOTROPIC HARDENING MODEL = LINEAR | POWER_LAW | VOCE | USER_DEFINED
  #
  # Specifications for Linear, Power-law, and Voce same as above
  #
  # User defined hardening
  #
  ISOTROPIC HARDENING FUNCTION = <string>isotropic_hardening_function_
↪name
  #
  #     - Rate dependence
  #
  YIELD RATE MULTIPLIER = JOHNSON_COOK | POWER_LAW_BREAKDOWN |
              USER_DEFINED | RATE_INDEPENDENT (RATE_INDEPENDENT)
  #
  # Specifications for Johnson-Cook, Power-law-breakdown same as before
  #     EXCEPT no need to specify a hardening function
  #     AND should be preceded by YIELD
  #
  #     As an example for Johnson-Cook yield rate dependence,
  #
  YIELD RATE CONSTANT  = <real>
  YIELD REFERENCE RATE = <real>
  #
  # User defined rate multiplier
  #
  YIELD RATE MULTIPLIER FUNCTION = <string>yield_rate_mult_function_
↪name
  #
  HARDENING_RATE MULTIPLIER = JOHNSON_COOK | POWER_LAW_BREAKDOWN |
              USER_DEFINED | RATE_INDEPENDENT (RATE_INDEPENDENT)
  #
  #     Syntax same as for yield parameters but with a HARDENING prefix
  #
  #     - Temperature dependence
  #
  YIELD TEMPERATURE MULTIPLIER = JOHNSON_COOK | USER_DEFINED |
           TEMPERATURE_INDEPENDENT (TEMPERATURE_INDEPENDENT)
  #
  #  Johnson-Cook temperature dependence
  #
  YIELD MELTING TEMPERATURE   = <real>
```

(continues on next page)

(continued from previous page)

```
  YIELD REFERENCE TEMPERATURE = <real>
  YIELD TEMPERATURE EXPONENT  = <real>
  #
  #  User-defined temperature dependence
  YIELD TEMPERATURE MULTIPLIER FUNCTION = <string>yield_temp_mult_fun_
↪name
  #
  HARDENING TEMPERATURE MULTIPLIER = JOHNSON_COOK | USER_DEFINED |
            TEMPERATURE_INDEPENDENT (TEMPERATURE_INDEPENDENT)
  #
  #   Syntax for hardening constants same as for yield but
  #             with HARDENING prefix
```

```
  #
  # Optional Adiabatic Heating / Thermal Softening definitions
  #
  ADIABATIC OPTION      = <bool> (0)
  PLASTIC WORK CONSTANT = <real> (1.0)
  #
  # Optional Functions
  #
  YOUNGS MODULUS FUNCTION = <string> ym_function_name
  POISSONS RATIO FUNCTION = <string> pr_function_name
END [PARAMETERS FOR MODEL PHASE_FIELD_FEFP]
```

Usage of the Phase Field F^eF^p material requires proper usage of the Sierra/SM reaction-diffusion solver. Instructions are located in the Sierra/SM Development Manual.

In the command blocks that define the Phase Field F^eF^p model:

- See the Sierra/SM User's Manual for more information on elastic constants input.
- The reference nominal yield stress, Y_0, is defined with the `YIELD STRESS` command line.
- The type of hardening law is defined with the `HARDENING MODEL` command line, other hardening commands then define the specific shape of that hardening curve.
- The hardening modulus for a linear hardening model is defined with the `HARDENING MODULUS` command line.
- The hardening constant for a power law hardening model is defined with the `HARDENING CONSTANT` command line.
- The hardening exponent for a power law hardening model is defined with the `HARDENING EXPONENT` command line.
- The Luders strain for a power law hardening model is defined with the `LUDERS STRAIN` command line.

- The hardening function for a user defined hardening model is defined with the `HARDENING FUNCTION` command line.
- The shape of the spline for the spline based hardening is defined by the `CUBIC SPLINE TYPE`, `CARDINAL PARAMETER`, `KNOT EQPS`, and `KNOT STRESS` command lines.
- The isotropic hardening model for the flow stress hardening model is defined with the `ISOTROPIC HARDENING MODEL` command line.
- The function name of a user-defined isotropic hardening model is defined via the `ISOTROPIC HARDENING FUNCTION` command line.
- The optional rate multiplier for the flow stress hardening model is defined with the `RATE MULTIPLIER` command line.
- The optional temperature multiplier for the flow stress hardening model is defined via the `TEMPERATURE MULTIPLIER` command line.
- The function name of a user-defined temperature multiplier is defined with the `TEMPERATURE MULTIPLIER FUNCTION` command line.
- For a Johnson-Cook temperature multiplier, the melting temperature, θ_{melt}, is defined via the `MELTING TEMPERATURE` command line.
- For a Johnson-Cook temperature multiplier, the reference temperature, θ_{ref}, is defined via the `REFERENCE TEMPERATURE` command line.
- For a Johnson-Cook temperature multiplier, the temperature exponent, M, is defined via the `TEMPERATURE EXPONENT` command line.

Output variables available for this model are listed in Table 4.65. Those marked with an asterisk * indicates these are *integration-point* values which may differ from input parameters due to temperature changes and/or random-variable assignment.

Table 4.65 State Variables for `PHASE_FIELD_FEFP` Model

Name	Description
YOUNGS_MODULUS	Young's modulus, *, E
POISSONS_RATIO	Poisson's ratio, *, ν
MAX_DRIVING_ENERGY	history-maximum driving energy exceeding threshold, $\mathcal{H} - \psi_c$
FRACTURE_ENERGY	fracture energy, ψ^f
UNDAM-AGED_STRAIN_ENERGY	undamaged elastic strain energy, $\widetilde{\psi}^e$
FRACTURE_LENGTH_SCALE	fracture length scale, ℓ
GC	Griffith fracture energy, *, G_c
CRITI-CAL_ENERGY_DENSITY	critical energy threshold *, ψ_c
PHASE	phase field, ϕ
PHASE_GRAD	phase field gradient, $\nabla\phi$
EQPS	equivalent plastic strain, $\bar{\varepsilon}^p$
EQDOT	equivalent plastic strain, $\dot{\bar{\varepsilon}}^p$
FP	plastic deformation gradient, F^p
ITERATIONS	number of return mapping iterations
UNDAM-AGED_PLASTIC_WORK	undamaged plastic work, $\widetilde{\psi}^p$
DAMAGED_STRAIN_ENERGY	damaged elastic strain energy, ψ^e
DAMAGED_PLASTIC_WORK	damaged plastic work, ψ^p

4.37 Phase Field F^eF^p Modular Model

Phase Field F^eF^p Modular is an implementation of a generalized, modular, cohesive variational phase-field fracture model developed for the purpose of modeling brittle and ductile fracture. The model is based upon the Phase Field F^eF^p model, which in turn is based upon the F^eF^p model, a hyperelastic analogue of the J_2 plasticity model, and features a von-Mises yield surface and isotropic hardening. However, the modular version allows for more generalized hardening models, including rate-dependent and kinematic hardening. As with Phase Field F^eF^p, Phase Field F^eF^p Modular is meant to be used in conjunction with a phase-field solver. The use of Sierra/SM's reaction-diffusion solver is strongly recommended. The model defines several auxiliary classes and departs from the existing LAMÉ hardening capabilities in order to have a unified interface between the elastic, plastic, and damage components of the model.

4.37.1 Theory

As much of the theory and derivation is similar to the Phase Field FeFp theory, interested readers are referred to that model's documentation for more detailed information as well as further references, while deviations will be noted here. As in that model, a multiplicative decomposition of the deformation gradient into elastic and plastic terms ($F_{ij} = F^e_{ik} F^p_{kj}$) is used. The plastic deformation tensor is updated with $\dot{F}^p_{ij} = \dot{Q}_a M_{aik} F^p_{kj}$, where $\dot{Q}_i$ is a vector of internal variables and M_{ijk} is a third-order flow tensor (which can be thought of as a vector of flow tensors, one for each internal variable). Additionally, like in Phase Field FeFp, there is a phase field variable ϕ which tracks the amount of damage; the convention used here is that $\phi = 1$ is intact and $\phi = 0$ is fully damaged.

To further explain the internal variables and flow tensor, this is a generalization of standard plasticity, where there is one internal variable $\bar{\varepsilon}^p$ and a second-order flow tensor N^p_{ij}. The generalization is useful in cases like crystal plasticity, where the existence of multiple slip planes leads to N internal variables, one per slip plane. For more details, consult Ortiz and Stainier [80].

Following similar steps to Phase Field FeFp, the free energy of the system can decomposed into an elastic component ψ^e, a plastic component ψ^p, and a fracture component ψ^f. The total energy ψ can then be written as in (4.242). Further, degradation functions g^e and g^p are introduced to model the effect of damage on the elastic and plastic behavior. Unlike in Phase Field FeFp, these degradation functions are allowed to be different, allowing for more complex modeling of real-world behavior. The elastic and plastic potentials are defined in (4.243) and (4.244), where $\tilde{\psi}^e$ and $\tilde{\psi}^p$ capture the behavior of the undamaged material. We can also define kinetic (rate-dependent) potentials ψ^*_e (elastic kinetic), ψ^*_p (plastic kinetic), and ψ^*_f (damage kinetic) and, similar to the regular potentials, we define the first two using multiplicative decompositions (with respect to phase) in (4.245), (4.246).

$$\psi = \psi^e \left(F^e_{ij}, \phi\right) + \psi^p \left(F^p_{ij}, Q_i, \phi\right) + \psi^f \left(\phi, \phi_{,i}\right) \tag{4.242}$$

$$\psi^e \left(F^e_{ij}, \phi\right) = g^e \left(\phi\right) \tilde{\psi}^e \left(F^e_{ij}\right) \tag{4.243}$$

$$\psi^p \left(F^p_{ij}, Q_i, \phi\right) = g^p \left(\phi\right) \tilde{\psi}^p \left(F^p_{ij}, Q_i\right) \tag{4.244}$$

$$\psi^*_e \left(\dot{F}_{ij}; F_{ij}, \phi\right) = g^e \left(\phi\right) \tilde{\psi}^*_e \left(\dot{F}_{ij}; F_{ij}\right) \tag{4.245}$$

$$\psi^*_p \left(\dot{Q}_i; Q_i, \phi\right) = g^p \left(\phi\right) \tilde{\psi}^*_p \left(\dot{Q}_i; Q_i\right) \tag{4.246}$$

Additionally, we allow most model parameters to vary with temperature and allow for thermal coupling (see "Usage Guide" for details). This means that temperature is an implicit argument to all potentials and kinetic potentials; this can be used to vary material behavior with respect to temperature. Furthermore, the separation of rate-independent behavior (potentials) from rate-dependent behavior (kinetic potentials) is different from other models and should be noted.

4.37.1.1 Notation Simplifications

The theory above uses the general *vector* of internal variables Q_i and third-order flow tensor M_{ijk}. This is with an eye towards future integration of a crystal plasticity-type model with multiple slip planes and multiple internal variables. However, all currently-implemented plasticity models use one internal variable. Accordingly, $Q_0 = \bar{\varepsilon}^p$ and $M_{0ij} = N^p_{ij}$ and the latter notation will be used from here on out when describing model options and the verification tests.

4.37.1.2 Model Options

Unlike in the case of Phase Field F$^{\text{e}}$F$^{\text{p}}$, every component here — the potentials, kinetic potentials, degradation functions, and tension-compression split — is treated as an interface, making it easy to add additional variants of each component without needing to modify the modular framework itself.

The following models are available for each component (the model parameters and state variables are given in the "Usage Guide" section):

- Elastic Potentials
  - Hencky Elastic Potential : $\tilde{\psi}^e = \mu \varepsilon^e_{ij} \varepsilon^e_{ij} + \left(\frac{\kappa}{2} - \frac{\mu}{3}\right) \varepsilon^e_{kk} \varepsilon^e_{\ell\ell}$ where $\varepsilon^e_{ij} = \frac{1}{2}\left[\log[C^e_{mn}]\right]_{ij}$ and $C^e_{ij} = F^e_{ki} F^e_{kj}$
- Plastic Potentials : β_{TQ} is the Taylor-Quinney factor which controls how much plastic energy is dissipated (and therefore does not contribute to the driving force for the phase field evolution)
  - No Plastic Potential : $\tilde{\psi}^p = 0$
  - Linear Plastic Potential : $\tilde{\psi}^p = \left(1 - \beta_{TQ}\right)\left(\sigma_y \bar{\varepsilon}^p + \frac{h \bar{\varepsilon}^{p^2}}{2}\right)$
  - Power Law Plastic Potential : $\tilde{\psi}^p = \left(1 - \beta_{TQ}\right)\left(\sigma_y \bar{\varepsilon}^p + \frac{a}{b+1} \max\left(0, \bar{\varepsilon}^p - \varepsilon_\ell\right)^{b+1}\right)$
  - Power Law Simple Plastic Potential : $\tilde{\psi}^p = \frac{n\left(1-\beta_{TQ}\right)\sigma_y \varepsilon_0}{n+1}\left(\left(1 + \frac{\bar{\varepsilon}^p}{\varepsilon_0}\right)^{(n+1)/n} - 1\right)$
  - Voce Plastic Potential : $\tilde{\psi}^p = \left(1 - \beta_{TQ}\right)\left(\sigma_y \bar{\varepsilon}^p + \sum_{i=0}^{n} h_i \bar{\varepsilon}^p + \frac{h_i}{\alpha_i}\left(\exp\left(-\alpha_i \bar{\varepsilon}^p\right) - 1\right)\right)$
  - Johnson-Cook Plastic Potential : $\tilde{\psi}^p = \left(1 - \beta_{TQ}\right)\left(a \bar{\varepsilon}^p + \frac{b}{n+1} \bar{\varepsilon}^{p^{n+1}}\right)\left(1 - \theta^q\right)$ where $\theta = \frac{T - T_0}{T_m - T_0}$
- Damage Potentials
  - No Damage Potential : $\psi^f = 0$
  - Gradient Damage Potential : $\psi^f = \frac{3 G_c}{8\ell}\left((1 - \phi) + \ell^2 \phi_{,i} a_{ij} \phi_{,j}\right)$
  - Classical Gradient Damage Potential : $\psi^f = \frac{G_c}{4\ell}\left((1 - \phi)^2 + 4\ell^2 \phi_{,i} a_{ij} \phi_{,j}\right)$

  - Wu Damage Potential : $\psi^f = \frac{G_c}{C_0 \ell} \left(\xi \left(1-\phi\right) + \left(1-\xi\right)\left(1-\phi\right)^2 + \ell^2 \phi_{,i} a_{ij} \phi_{,j} \right)$

- Plastic Kinetic Potentials : $\tilde{\sigma}$ and $\tilde{\tau}$ are the Jacobian and Hessian (respectively) of the selected plastic potential with $\beta_{TQ} = 1$ and dt is the instantaneous change in time
  - No Plastic Kinetic Potential : $\tilde{\psi}_p^* = \frac{\beta_{TQ} dt}{2} \tilde{\tau} \left(\dot{\tilde{\varepsilon}}^p\right)^2$ (this is non-zero to ensure that the Tayor-Quinney factor is properly taken into account)
  - Power Law Plastic Kinetic Potential : $\tilde{\psi}_p^* = \frac{\beta_{TQ} dt}{2} \tilde{\tau} \left(\dot{\tilde{\varepsilon}}^p\right)^2 + \frac{m \sigma_y \dot{\varepsilon}_0}{m+1} \left(\frac{\dot{\tilde{\varepsilon}}^p}{\dot{\varepsilon}_0}\right)^{(m+1)/m}$
  - Johnson-Cook Plastic Kinetic Potential : $\tilde{\psi}_p^* = \frac{\beta_{TQ} dt}{2} \tilde{\tau} \left(\dot{\tilde{\varepsilon}}^p\right)^2 + c\tilde{\sigma} \left(\dot{\tilde{\varepsilon}}^p \log \frac{\dot{\tilde{\varepsilon}}^p}{\dot{\varepsilon}_0} - \dot{\tilde{\varepsilon}}^p + \dot{\varepsilon}_0 \right)$
  - Power Law Breakdown Plastic Kinetic Potential : $\tilde{\psi}_p^* = \frac{\beta_{TQ} dt}{2} \tilde{\tau} \left(\dot{\tilde{\varepsilon}}^p\right)^2 + \tilde{\sigma} \dot{\tilde{\varepsilon}}^p \left(\operatorname{asinh}\left(\gamma^{1/m}\right) - \frac{\gamma^{1/m}}{m+1} {}_2F_1\left(g, m\right) \right)$

- Degradation Functions
  - No Degradation Function : $g\left(\phi\right) = 0$
  - Quadratic Degradation Function : $g\left(\phi\right) = \phi^2$
  - Talamini Degradation Function : $g\left(\phi\right) = \left[\frac{\phi}{1 + \left(\frac{3G_0}{16 \ell \psi_c} - 1 \right)\left(1-\phi\right)} \right]^2$
  - Lo Degradation Function : $g\left(\phi\right) = s \left[1 - \left(\frac{s-1}{s} \right)^{\phi^2} \right]$
  - Wu Degradation Function : $g\left(\phi\right) = \frac{\phi^p}{\phi^p + \sum_i a_i (1-\phi)^i}$

- Tension-Compression Split
  - No Tension-Compression Split : Everything is degraded.
  - Deviatoric-Volumetric Tension-Compression Split : Deviatoric part is always degraded. Volumetric part is degraded if the trace of the strain is positive.
  - Star-Convex Tension-Compression Split : Deviatoric part is always degraded. Volumetric part is fully degraded if the trace of the strain is positive; otherwise, the volumetric part is degraded by a factor γ.

4.37.2 Implementation

There are two possible solvers available to solve this minimization problem for Q_i and M_{ijk} (in standard plasticity, these are $\bar{\varepsilon}^p$ and N_{ij}^p): a standard return-mapping algorithm and a sequential quadratic programming (SQP) algorithm. Return-mapping is described in the Phase Field FeFp documentation, while SQP is described below.

The overall approach to the SQP solver is as follows. We first write the discretized difference in total energy density between the state at time t_{n+1} and the state at time t_n (with $dt = t_{n+1} - t_n$) as (4.247), with $\Delta\psi$ given by (4.248). The objective is to find $(Q_{n+1})_i$ and $(M_{n+1})_{ijk}$ such that this functional is minimized, which only requires minimizing the final term (the rest of (4.247) is not dependent on $(Q_{n+1})_i$ and $(M_{n+1})_{ijk}$).

$$W\left((F_{n+1})_{ij}\,;(F_n)_{ij}\,,\phi_n,(Q_n)_i\right) = \Delta t g^e\left(\phi_n\right)\tilde{\psi}_e^*\left(\frac{(F_{n+1})_{ij}-(F_n)_{ij}}{\Delta t};(F_n)_{ij}\right)+\Delta t\psi_f^*\left(\frac{\phi_{n+1}-\phi_n}{\Delta t}\right) + \min_{(Q_{n+1})_i,(M_{n+1})_{ijk}}\left\{\Delta\psi\left(F_{ij},\phi,\phi_{,i},F_{ij}^p,Q_i\right)+\Delta t g^p\left(\phi_n\right)\tilde{\psi}_p^*\left(\frac{(Q_{n+1})_i-(Q_n)_i}{\Delta t};(Q_n)_i\right)\right\} \tag{4.247}$$

$$\begin{aligned}\Delta\psi\left(F_{ij},\phi,\phi_{,i},F_{ij}^p,Q_i\right) &= g^e\left(\phi_{n+1}\right)\tilde{\psi}^e\left((F_{n+1})_{ik}\left(F_{n+1}^{p^{-1}}\right)_{kj}\right)-g^e\left(\phi_n\right)\tilde{\psi}^e\left((F_n)_{ik}\left(F_n^{p^{-1}}\right)_{kj}\right)\\ &+ g^p\left(\phi_{n+1}\right)\tilde{\psi}^p\left(\left(F_{n+1}^p\right)_{ij},(Q_{n+1})_i\right)-g^p\left(\phi_n\right)\tilde{\psi}^p\left(\left(F_n^p\right)_{ij},(Q_n)_i\right)\\ &+\psi^f\left(\phi_{n+1},(\phi_{n+1})_{,i}\right)-\psi^f\left(\phi_n,(\phi_n)_{,i}\right)\end{aligned} \tag{4.248}$$

This leads us to the objective function given in (4.249). All unknowns are grouped into a vector x_i ((4.251) and (4.252)) and all constraints are grouped into a vector c_i (along with associated Lagrange multipliers λ_i); in this notation, the assumption is that there are n internal variables, so $10n$ total unknowns. The Lagrangian is then as (4.250), leading to the optimization problem (4.253). As an aside, taking the derivative of (4.249) with respect to Q_i yields a generalized yield equation (4.254), which is effectively what the radial return method solves[1].

$$\begin{aligned}F &= g^e\left(\phi_{n+1}\right)\tilde{\psi}^e\left(\left(F_{n+1}^e\right)_{ij}\right)+g^p\left(\phi_{n+1}\right)\tilde{\psi}^p\left(\left(F_{n+1}^p\right)_{ij},(Q_{n+1})_i\right)\\ &+\Delta t g^p\left(\phi_{n+\alpha}\right)\tilde{\psi}_p^*\left(\frac{(Q_{n+1})_i-(Q_n)_i}{\Delta t};(Q_{n+1})_i\right)\end{aligned} \tag{4.249}$$

$$\mathcal{L} = F - \lambda_i c_i \tag{4.250}$$

$$x_i = (Q_{n+1})_i \quad i \in \{0..n-1\} \tag{4.251}$$

[1] Hardcoding the constraints and assuming associative flow fixes the flow tensor analytically. Doing this reduces the set of unknowns to Q_i, meaning we can take the derivative of the objective function with respect to Q_i and set it equal to 0 to find the minimizer. Doing this and comparing to the radial return method shows that the equations are identical.

$$x_{n+9a+3b+c} = (M_{n+1})_{abc} \quad a \in \{0..n-1\}, b \in \{0..2\}, c \in \{0..2\} \tag{4.252}$$

$$\min_{x_j} \mathcal{L} = \min_{x_j} (F - \lambda_i c_i) \tag{4.253}$$

$$0 = \left[g^p(\phi) \frac{\partial \tilde{\psi}^p}{\partial F^p_{ij}} + g^e(\phi) \frac{\partial \tilde{\psi}^e}{\partial F^e_{kl}} \frac{\partial F^e_{kl}}{\partial F^p_{ij}} \right] \frac{\partial F^p_{ij}}{\partial \bar{\varepsilon}^p} + g^p(\phi) \frac{\partial \tilde{\psi}^p}{\partial \bar{\varepsilon}^p} + \Delta t g^p(\phi) \frac{d\tilde{\psi}^*_p}{d\bar{\varepsilon}^p} \tag{4.254}$$

A Taylor expansion ((4.255)) is performed around the x_i that minimizes $\mathcal{L}$. Then the original minimization problem ((4.253)) can be converted into a minimum over p_i, the deviation from the minimum ((4.256)). In addition, we perform a Taylor expansion around x_i for the constraint equations as well, leading to the linearized constraint equations given in (4.257) and (4.258). We have introduced the notation here that $\mathcal{E}$ refers to the indices of the equality constraints and $\mathcal{I}$ refers to the indices of the inequality constraints — $\mathcal{E} \cup \mathcal{I} = \{0..M\}$, where M is the total number of constraints.

$$\mathcal{L}(x_i + p_i) \approx \mathcal{L}(x_i) + p_j \frac{\partial \mathcal{L}}{\partial x_j}(x_i) + \frac{1}{2} p_j p_k \frac{\partial^2 \mathcal{L}}{\partial x_j \partial x_k}(x_i) \tag{4.255}$$

$$\min_{x_i} \mathcal{L} = \min_{p_i} \left[\mathcal{L}(x_i) + p_j \frac{\partial \mathcal{L}}{\partial x_j}(x_i) + \frac{1}{2} p_j p_k \frac{\partial^2 \mathcal{L}}{\partial x_j \partial x_k}(x_i) \right] \tag{4.256}$$

$$0 = p_j \frac{\partial c_m}{\partial x_j}(x_i) + c_m(x_i) \quad m \in \mathcal{E} \tag{4.257}$$

$$0 \leq p_j \frac{\partial c_m}{\partial x_j}(x_i) + c_m(x_i) \quad m \in \mathcal{I} \tag{4.258}$$

The SQP algorithm then solves (4.259) iteratively until the unknowns Q_i and M_{ijk} and the Lagrange multipliers λ_i are converged. Inequality constraints are dealt with through an "active-set" approach. More details can be found in Nocedal and Wright [77].

$$\begin{pmatrix} \mathcal{L}_{,xx} & -\boldsymbol{c}_{,x} \\ \boldsymbol{c}_{,x} & \boldsymbol{0} \end{pmatrix} \begin{pmatrix} \boldsymbol{p}_k \\ \boldsymbol{l}_k \end{pmatrix} = \begin{pmatrix} -\mathcal{L}_{,x} \\ -\boldsymbol{c} \end{pmatrix} \tag{4.259}$$

4.37.2.1 Model Options

These model options are related to the solver:

- Plastic Solver
  - Radial Return : Standard J2 associative plasticity solve
  - SQP : Generalized nonlinear fully-coupled solver for internal variables and flow tensors
- Constraints (Only applies to SQP)
  - Flow Tensor Constraint : Set the flow tensor explicitly
  - Flow Tensor Norm Constraint : Set the norm of the flow tensor

  - Flow Tensor Trace Constraint : Set the trace of the flow tensor
  - Flow Tensor Symmetric Constraint (XY, YZ, ZX) : Set the symmetry of the flow tensor across specified components
- Kinetic Constraints (Only applies to SQP)
  - Internal Variable Rate Kinetic Constraint : Ensure that the internal variable can only increase

4.37.3 Verification

We pursue both unit tests and regression tests. Regression tests are actual Sierra runs being tested against known solutions and benchmarks whereas unit tests exercise individual code elements against known solutions and correspond to simple single-element deformations (more information below).

4.37.3.1 Unit testing

In order to ensure thorough verification of all possible combinations of different models in a variety of different regimes, a comprehensive unit testing framework was developed for this model (which can be found with the rest of the LAME unit tests). Every possible combination of different model choices is tested in uniaxial tension, uniaxial compression, and biaxial tension-compression.

The overall test workflow is as follows. For any given test, the inputs are $\bar{\varepsilon}^p$, the flow tensor N_{ij}^p (known from the mechanical configuration), and the desired stress state σ_{ij} (also known from the mechanical configuration). Coupled with the model choices, this allows the calculation of the input elasic deformation tensor F_{ij}^e. Given that the plastic deformation tensor F_{ij}^p is already known from the inputs, this allows the calculation of the total deformation tensor F_{ij}. This deformation tensor is passed as the input to the material model and the calculated stress and $\bar{\varepsilon}^p$ are compared with the reference quantities.

The mechanical configurations tested are:

- Uniaxial tension, elastic regime
- Uniaxial tension, plastic regime
- Uniaxial compression, elastic regime
- Uniaxial compression, plastic regime
- Biaxial tension-compression, elastic regime
- Biaxial tension-compression, plastic regime

Overview

Given the mechanical configuration, the final stress state is known. Coupled with the TCS, this leads to the derivation of effective elastic moduli (such that the desired stress state is achieved even with the degradation function's impact). In the elastic case, $\bar{\varepsilon}^p \equiv 0$ and $F^p_{ij} \equiv \delta_{ij}$. In the plastic case, $\bar{\varepsilon}^p = 0.05$ and $F^p_{ij} = \left[\exp\left(0.05[N^p_{mn}]\right)\right]_{ij}$. All of this is used to solve for the elastic strain such that the generalized yield equation (4.254) is satisfied. A quantity C_p is defined in (4.260) that groups together all of the plastic quantities.

$$C_p = \frac{\partial \tilde{\psi}^p}{\partial F^p_{ij}} \frac{\partial F^p_{ij}}{\partial \bar{\varepsilon}^p} + \frac{\partial \tilde{\psi}^p}{\partial \bar{\varepsilon}^p} + \Delta t \frac{d\tilde{\psi}^*_p}{d\bar{\varepsilon}^p} \tag{4.260}$$

Additionally, there are several code branches which are all tested:

- Radial Return
- SQP with flow tensor norm, trace, and symmetry constraints
- SQP with flow tensor constraint (setting the flow tensor explicitly)

Uniaxial Tension/Compression

In the case of Uniaxial Tension or Compression, the log strain is given in (4.261) and the stress state is given in (4.262), where $\Upsilon > 0$ for uniaxial tension and $\Upsilon < 0$ for uniaxial compression. E^* and ν^* are a modified Young's modulus and Poisson's ratio (respectively) derived based on the specific tension-compression split.

$$[E^e_{ij}] = \begin{pmatrix} \Upsilon & 0 & 0 \\ 0 & -\nu^* \Upsilon & 0 \\ 0 & 0 & -\nu^* \Upsilon \end{pmatrix} \tag{4.261}$$

$$\frac{\partial \tilde{\psi}^e}{\partial [E^e_{ij}]} = E^* \Upsilon \begin{pmatrix} 1 & 0 & 0 \\ 0 & 0 & 0 \\ 0 & 0 & 0 \end{pmatrix} \tag{4.262}$$

The flow tensor N^p_{ij} is given by (4.263) for tension and (4.264) for compression.

$$[N^p_{ij}] = \begin{pmatrix} 1 & 0 & 0 \\ 0 & -0.5 & 0 \\ 0 & 0 & -0.5 \end{pmatrix} \tag{4.263}$$

$$[N^p_{ij}] = \begin{pmatrix} -1 & 0 & 0 \\ 0 & 0.5 & 0 \\ 0 & 0 & 0.5 \end{pmatrix} \tag{4.264}$$

Solving the yield equation yields the value of Υ ((4.265)). As mentioned above, Υ is positive in uniaxial tension and negative in uniaxial compression.

$$\Upsilon = \pm \frac{g^p C_p}{E^*} \tag{4.265}$$

Biaxial Tension-Compression

In the biaxial tension-compression case, the log strain is given by (4.266) and the stress state is given by (4.267), where μ^* is a modified shear modulus derived based on the specific tension-compression split. Likewise, the flow tensor is given by (4.268).

$$[E^e_{ij}] = \begin{pmatrix} \Upsilon & 0 & 0 \\ 0 & -\Upsilon & 0 \\ 0 & 0 & 0 \end{pmatrix} \tag{4.266}$$

$$\frac{\partial \tilde{\psi}^e}{\partial [E^e_{ij}]} = 2\mu^* \Upsilon \begin{pmatrix} 1 & 0 & 0 \\ 0 & -1 & 0 \\ 0 & 0 & 0 \end{pmatrix} \tag{4.267}$$

$$[N^p_{ij}] = \frac{\sqrt{3}}{2} \begin{pmatrix} 1 & 0 & 0 \\ 0 & -1 & 0 \\ 0 & 0 & 0 \end{pmatrix} \tag{4.268}$$

Putting it all together and solving the yield equation yields the value of Υ ((4.269)).

$$\Upsilon = \frac{g^p C_p}{2\sqrt{3}\mu^*} \tag{4.269}$$

4.37.3.2 Regression testing

There are a variety of regression tests for this material model that test different kinds of behavior. The `1d_phaseBC_fefp` and `control_1d_extension` tests are identical to the tests of the same name implemented for Phase Field F^eF^p, so refer to the relevant sections under that documentation for more information.

4.37.4 User Guide

```
BEGIN PARAMETERS FOR MODEL PHASE_FIELD_FEFP_MODULAR
  # Overall options
  ELASTIC POTENTIAL = HENCKY_ELASTIC_POTENTIAL
                    (HENCKY_ELASTIC_POTENTIAL)
  PLASTIC POTENTIAL = NO_PLASTIC_POTENTIAL
                    | LINEAR_PLASTIC_POTENTIAL
                    | POWER_LAW_PLASTIC_POTENTIAL
                    | POWER_LAW_SIMPLE_PLASTIC_POTENTIAL
                    | VOCE_PLASTIC_POTENTIAL
                    | JOHNSON_COOK_PLASTIC_POTENTIAL
  DAMAGE POTENTIAL = NO_DAMAGE_POTENTIAL
                   | GRADIENT_DAMAGE_POTENTIAL
```

(continues on next page)

(continued from previous page)

```
                    | CLASSICAL_GRADIENT_DAMAGE_POTENTIAL
                    | WU_DAMAGE_POTENTIAL
                    (GRADIENT_DAMAGE_POTENTIAL)
  ELASTIC KINETIC POTENTIAL = NO_ELASTIC_KINETIC_POTENTIAL
                             (NO_ELASTIC_KINETIC_POTENTIAL)
  PLASTIC KINETIC POTENTIAL = NO_PLASTIC_KINETIC_POTENTIAL
                             | POWER_LAW_PLASTIC_KINETIC_POTENTIAL
                             | POWER_LAW_BREAKDOWN_PLASTIC_KINETIC_
↪POTENTIAL
                             | JOHNSON_COOK_PLASTIC_KINETIC_POTENTIAL
                             (NO_PLASTIC_KINETIC_POTENTIAL)
  DAMAGE KINETIC POTENTIAL = NO_DAMAGE_KINETIC_POTENTIAL
                            (NO_DAMAGE_KINETIC_POTENTIAL)
  ELASTIC DEGRADATION FUNCTION = NO_DEGRADATION_FUNCTION
                                | QUADRATIC_DEGRADATION_FUNCTION
                                | TALAMINI_DEGRADATION_FUNCTION
                                | LO_DEGRADATION_FUNCTION
                                | WU_DEGRADATION_FUNCTION
                                (TALAMINI_DEGRADATION_FUNCTION)
  PLASTIC DEGRADATION FUNCTION = NO_DEGRADATION_FUNCTION
                                | QUADRATIC_DEGRADATION_FUNCTION
                                | TALAMINI_DEGRADATION_FUNCTION
                                | LO_DEGRADATION_FUNCTION
                                | WU_DEGRADATION_FUNCTION
                                (TALAMINI_DEGRADATION_FUNCTION)
  TENSION COMPRESSION SPLIT = NO_TCS
                             | DEVIATORIC_VOLUMETRIC_TCS
                             | STAR_CONVEX_TCS
                             (NO_TCS)
  THERMAL SOFTENING MODEL = ADIABATIC | COUPLED
  PLASTIC WORK DRIVING ENERGY PORTION = <real> (1.0)
  CONDITIONING COEFFICIENT = <real> (0.0)
  NONLOCAL SOLVER = NONE | ARIA | RXNDIFF (RXNDIFF)
  PLASTIC SOLVER = RADIAL_RETURN | SQP (RADIAL_RETURN)
  CONSTRAINTS = FLOW_TENSOR_CONSTRAINT
              | FLOW_TENSOR_TRACE_CONSTRAINT
              | FLOW_TENSOR_NORM_CONSTRAINT
              | FLOW_TENSOR_SYMMETRIC_CONSTRAINT_XY
              | FLOW_TENSOR_SYMMETRIC_CONSTRAINT_YZ
              | FLOW_TENSOR_SYMMETRIC_CONSTRAINT_ZX
  FLOW TENSOR = <reals>
  KINETIC CONSTRAINTS = INTERNAL_VARIABLE_RATE_KINETIC_CONSTRAINT

  # Hencky Elastic Potential properties
  YOUNGS MODULUS          = <real>
```

(continues on next page)

(continued from previous page)

```
  POISSONS RATIO          = <real>
  BULK MODULUS            = <real>
  SHEAR MODULUS           = <real>
  YOUNGS MODULUS FUNCTION = <string>
  POISSONS RATIO FUNCTION = <string>
  BULK MODULUS FUNCTION   = <string>
  SHEAR MODULUS FUNCTION  = <string>

  # Linear Plastic Potential properties
  YIELD STRESS               = <real>
  HARDENING MODULUS          = <real>
  TAYLOR QUINNEY             = <real>
  YIELD STRESS FUNCTION      = <string>
  HARDENING MODULUS FUNCTION = <string>
  TAYLOR QUINNEY FUNCTION    = <string>

  # Power Law Plastic Potential properties
  YIELD STRESS                = <real>
  HARDENING CONSTANT          = <real>
  HARDENING EXPONENT          = <real>
  LUDERS STRAIN               = <real>
  TAYLOR QUINNEY              = <real>
  YIELD STRESS FUNCTION       = <string>
  HARDENING CONSTANT FUNCTION = <string>
  HARDENING EXPONENT FUNCTION = <string>
  LUDERS STRAIN FUNCTION      = <string>
  TAYLOR QUINNEY FUNCTION     = <string>

  # Power Law Simple Plastic Potential properties
  REFERENCE STRAIN            = <real>
  YIELD STRESS                = <real>
  HARDENING EXPONENT          = <real>
  TAYLOR QUINNEY              = <real>
  REFERENCE STRAIN FUNCTION   = <string>
  YIELD STRESS FUNCTION       = <string>
  HARDENING EXPONENT FUNCTION = <string>
  TAYLOR QUINNEY FUNCTION     = <string>

  # Voce Plastic Potential properties
  YIELD STRESS                     = <real>
  HARDENING MODULUS                = <reals>
  EXPONENTIAL COEFFICIENT          = <reals>
  TAYLOR QUINNEY                   = <real>
  YIELD STRESS FUNCTION            = <string>
  HARDENING MODULUS FUNCTION       = <string>
```

(continues on next page)

(continued from previous page)

```
EXPONENTIAL COEFFICIENT FUNCTION = <string>
TAYLOR QUINNEY FUNCTION          = <string>

# Johnson-Cook Plastic Potential properties
JOHNSON COOK A          = <real>
JOHNSON COOK B          = <real>
JOHNSON COOK N          = <real>
JOHNSON COOK Q          = <real>
JOHNSON COOK T0         = <real>
JOHNSON COOK TM         = <real>
TAYLOR QUINNEY          = <real>
JOHNSON COOK A FUNCTION = <string>
JOHNSON COOK B FUNCTION = <string>
JOHNSON COOK N FUNCTION = <string>
JOHNSON COOK Q FUNCTION = <string>
TAYLOR QUINNEY FUNCTION = <string>

# Gradient Damage Potential properties
GC                              = <real>
FRACTURE LENGTH SCALE           = <real>
ANISOTROPY TENSOR 11            = <real> (1.0)
ANISOTROPY TENSOR 12            = <real> (0.0)
ANISOTROPY TENSOR 13            = <real> (0.0)
ANISOTROPY TENSOR 21            = <real> (0.0)
ANISOTROPY TENSOR 22            = <real> (1.0)
ANISOTROPY TENSOR 23            = <real> (0.0)
ANISOTROPY TENSOR 31            = <real> (0.0)
ANISOTROPY TENSOR 32            = <real> (0.0)
ANISOTROPY TENSOR 33            = <real> (1.0)
GC FUNCTION                     = <string>
FRACTURE LENGTH SCALE FUNCTION = <string>

# Classical Gradient Damage Potential properties
GC                              = <real>
FRACTURE LENGTH SCALE           = <real>
ANISOTROPY TENSOR 11            = <real> (1.0)
ANISOTROPY TENSOR 12            = <real> (0.0)
ANISOTROPY TENSOR 13            = <real> (0.0)
ANISOTROPY TENSOR 21            = <real> (0.0)
ANISOTROPY TENSOR 22            = <real> (1.0)
ANISOTROPY TENSOR 23            = <real> (0.0)
ANISOTROPY TENSOR 31            = <real> (0.0)
ANISOTROPY TENSOR 32            = <real> (0.0)
ANISOTROPY TENSOR 33            = <real> (1.0)
GC FUNCTION                     = <string>
```

(continues on next page)

(continued from previous page)

```
  FRACTURE LENGTH SCALE FUNCTION = <string>

  # Wu Damage Potential properties
  GC                             = <real>
  FRACTURE LENGTH SCALE          = <real>
  WU XI                          = <real>
  ANISOTROPY TENSOR 11           = <real> (1.0)
  ANISOTROPY TENSOR 12           = <real> (0.0)
  ANISOTROPY TENSOR 13           = <real> (0.0)
  ANISOTROPY TENSOR 21           = <real> (0.0)
  ANISOTROPY TENSOR 22           = <real> (1.0)
  ANISOTROPY TENSOR 23           = <real> (0.0)
  ANISOTROPY TENSOR 31           = <real> (0.0)
  ANISOTROPY TENSOR 32           = <real> (0.0)
  ANISOTROPY TENSOR 33           = <real> (1.0)
  GC FUNCTION                    = <string>
  FRACTURE LENGTH SCALE FUNCTION = <string>
  WU XI FUNCTION                 = <string>

  # Power Law Plastic Kinetic Potential properties
  REFERENCE STRAIN RATE          = <real>
  YIELD STRESS                   = <real>
  RATE EXPONENT                  = <real>
  TAYLOR QUINNEY                 = <real>
  REFERENCE STRAIN RATE FUNCTION = <string>
  YIELD STRESS FUNCTION          = <string>
  RATE EXPONENT FUNCTION         = <string>
  TAYLOR QUINNEY FUNCTION        = <string>

  # Johnson-Cook Plastic Kinetic Potential properties
  REFERENCE STRAIN RATE          = <real>
  JOHNSON COOK C                 = <real>
  TAYLOR QUINNEY                 = <real>
  REFERENCE STRAIN RATE FUNCTION = <string>
  JOHNSON COOK C FUNCTION        = <string>
  TAYLOR QUINNEY FUNCTION        = <string>

  # Power Law Breakdown Plastic Kinetic Potential properties
  RATE COEFFICIENT          = <real>
  RATE EXPONENT             = <real>
  TAYLOR QUINNEY            = <real>
  RATE COEFFICIENT FUNCTION = <string>
  RATE EXPONENT FUNCTION    = <string>
  TAYLOR QUINNEY FUNCTION   = <string>
```

(continues on next page)

(continued from previous page)

```
  # Talamini Degradation Function properties
  GC                                = <real>
  FRACTURE LENGTH SCALE             = <real>
  CRITICAL ENERGY DENSITY           = <real>
  GC FUNCTION                       = <string>
  FRACTURE LENGTH SCALE FUNCTION    = <string>
  CRITICAL ENERGY DENSITY FUNCTION = <string>

  # Lo Degradation Function properties
  LO S          = <real>
  LO S FUNCTION = <string>

  # Wu Degradation Function properties
  WU P            = <real>
  WU COEFFICIENTS = <reals>
  WU P FUNCTION   = <string>

  # Star-Convex TCS properties
  STAR CONVEX GAMMA = <real>

END [PARAMETERS FOR MODEL PHASE_FIELD_FEFP_MODULAR]
```

4.37.4.1 Model Parameters

Elastic Potentials

Table 4.66 Property Inputs for `HENCKY_ELASTIC_POTENTIAL`

Name	Description
YOUNGS_MODULUS	Young's modulus E
POISSONS_RATIO	Poisson's ratio ν
BULK_MODULUS	Bulk modulus κ
SHEAR_MODULUS	Shear modulus μ
YOUNGS_MODULUS_FUNCTION	E's temperature-dependent function
POISSONS_RATIO_FUNCTION	ν's temperature-dependent function
BULK_MODULUS_FUNCTION	κ's temperature-dependent function
SHEAR_MODULUS_FUNCTION	μ's temperature-dependent function

Notes:

- Any two of the above four properties can be specified.
- If temperature-dependent functions are specified, two of the four should be specified; the other properties' temperature dependence will be automatically calculated.

Plastic Potentials

Table 4.67 Property Inputs for `LINEAR_PLASTIC_POTENTIAL`

Name	Description
YIELD_STRESS	Yield stress σ_y
HARDENING_MODULUS	Hardening modulus h
TAYLOR_QUINNEY	Taylor-Quinney factor β_Q
YIELD_STRESS_FUNCTION	σ_y's temperature-dependent function
HARDENING_MODULUS_FUNCTION	h's temperature-dependent function
TAYLOR_QUINNEY_FUNCTION	β_Q's temperature-dependent function

Table 4.68 Property Inputs for `POWER_LAW_PLASTIC_POTENTIAL`

Name	Description
YIELD_STRESS	Yield stress σ_y
HARDENING_CONSTANT	Hardening constant a
HARDENING_EXPONENT	Hardening exponent b
LUDERS_STRAIN	Lüder's strain ε_ℓ
TAYLOR_QUINNEY	Taylor-Quinney factor β_Q
YIELD_STRESS_FUNCTION	σ_y's temperature-dependent function
HARDENING_CONSTANT_FUNCTION	a's temperature-dependent function
HARDENING_EXPONENT_FUNCTION	b's temperature-dependent function
LUDERS_STRAIN_FUNCTION	ε_ℓ's temperature-dependent function
TAYLOR_QUINNEY_FUNCTION	β_Q's temperature-dependent function

Table 4.69 Property Inputs for `POWER_LAW_SIMPLE_PLASTIC_POTENTIAL`

Name	Description
REFERENCE_STRAIN	Reference strain ε_0
YIELD_STRESS	Yield stress σ_y
HARDENING_EXPONENT	Hardening exponent n
TAYLOR_QUINNEY	Taylor-Quinney factor β_Q
REFERENCE_STRAIN_FUNCTION	ε_0's temperature-dependent function
YIELD_STRESS_FUNCTION	σ_y's temperature-dependent function
HARDENING_EXPONENT_FUNCTION	n's temperature-dependent function
TAYLOR_QUINNEY_FUNCTION	β_Q's temperature-dependent function

Table 4.70 Property Inputs for `VOCE_PLASTIC_POTENTIAL`

Name	Description
YIELD_STRESS	Yield stress σ_y
HARDENING_MODULUS	Hardening moduli h_i
EXPONENTIAL_COEFFICIENT	Exponential coefficients α_i
TAYLOR_QUINNEY	Taylor-Quinney factor β_Q
YIELD_STRESS_FUNCTION	σ_y's temperature-dependent function
HARDENING_MODULUS_FUNCTION	h_i's temperature-dependent function
EXPONENTIAL_COEFFICIENT_FUNCTION	α_i's temperature-dependent function
TAYLOR_QUINNEY_FUNCTION	β_Q's temperature-dependent function

Table 4.71 Property Inputs for JOHNSON_COOK_PLASTIC_POTENTIAL

Name	Description
JOHNSON_COOK_A	Johnson-Cook yield stress a
JOHNSON_COOK_B	Johnson-Cook hardening modulus b
JOHNSON_COOK_N	Johnson-Cook hardening exponent n
JOHNSON_COOK_Q	Johnson-Cook thermal exponent q
JOHNSON_COOK_T0	Johnson-Cook reference temperature T_0
JOHNSON_COOK_TM	Johnson-Cook melting temperature T_m
TAYLOR_QUINNEY	Taylor-Quinney factor β_Q
JOHNSON_COOK_A_FUNCTION	a's temperature-dependent function
JOHNSON_COOK_B_FUNCTION	b's temperature-dependent function
JOHNSON_COOK_N_FUNCTION	n's temperature-dependent function
JOHNSON_COOK_Q_FUNCTION	q's temperature-dependent function
TAYLOR_QUINNEY_FUNCTION	β_Q's temperature-dependent function

Notes:

- If the Taylor-Quinney factor is not explicitly set, it defaults to 0.
- If the Lüder's strain is not explicitly set, it defaults to 0.
- In the Voce case, HARDENING_MODULUS and EXPONENTIAL_COEFFICIENT can be *lists* of parameters to add multiple Voce hardening terms, but they should both have the same length (if HARDENING_MODULUS has 3 terms, you *must* also have 3 terms for EXPONENTIAL_COEFFICIENT). The HARDENING_MODULUS_FUNCTION is *one* function (as is EXPONENTIAL_COEFFICIENT_FUNCTION) and is applied to *all* Voce hardening terms.

Damage Potentials

Table 4.72 Property Inputs for `GRADIENT_DAMAGE_POTENTIAL`

Name	Description
`GC`	Griffith fracture energy G_c
`FRACTURE_LENGTH_SCALE`	Fracture length scale ℓ
`ANISOTROPY_TENSOR_{1..3}{1..3}`	Components of anisotropy tensor a_{ij}
`GC_FUNCTION`	G_c's temperature-dependent function
`FRACTURE_LENGTH_SCALE_FUNCTION`	ℓ's temperature-dependent function

Table 4.73 Property Inputs for `CLASSICAL_GRADIENT_DAMAGE_POTENTIAL`

Name	Description
`GC`	Griffith fracture energy G_c
`FRACTURE_LENGTH_SCALE`	Fracture length scale ℓ
`ANISOTROPY_TENSOR_{1..3}{1..3}`	Components of anisotropy tensor a_{ij}
`GC_FUNCTION`	G_c's temperature-dependent function
`FRACTURE_LENGTH_SCALE_FUNCTION`	ℓ's temperature-dependent function

Table 4.74 Property Inputs for `WU_DAMAGE_POTENTIAL`

Name	Description
`GC`	Griffith fracture energy G_c
`FRACTURE_LENGTH_SCALE`	Fracture length scale ℓ
`WU_XI`	ξ parameter
`ANISOTROPY_TENSOR_{1..3}{1..3}`	Components of anisotropy tensor a_{ij}
`GC_FUNCTION`	G_c's temperature-dependent function
`FRACTURE_LENGTH_SCALE_FUNCTION`	ℓ's temperature-dependent function
`WU_XI_FUNCTION`	ξ's temperature-dependent function

Plastic Kinetic Potentials

Table 4.75 Property Inputs for `POWER_LAW_PLASTIC_KINETIC_POTENTIAL`

Name	Description
REFERENCE_STRAIN_RATE	Reference strain rate $\dot{\varepsilon}_0$
YIELD_STRESS	Yield stress σ_y
RATE_EXPONENT	Rate exponent m
TAYLOR_QUINNEY	Taylor-Quinney factor β_Q
REFERENCE_STRAIN_RATE_FUNCTION	$\dot{\varepsilon}_0$'s temperature-dependent function
YIELD_STRESS_FUNCTION	σ_y's temperature-dependent function
RATE_EXPONENT_FUNCTION	m's temperature-dependent function
TAYLOR_QUINNEY_FUNCTION	β_Q's temperature-dependent function

Table 4.76 Property Inputs for `JOHNSON_COOK_PLASTIC_KINETIC_POTENTIAL`

Name	Description
REFERENCE_STRAIN_RATE	Reference strain rate $\dot{\varepsilon}_0$
JOHNSON_COOK_C	Johnson-Cook rate dependence strength c
TAYLOR_QUINNEY	Taylor-Quinney factor β_Q
REFERENCE_STRAIN_RATE_FUNCTION	$\dot{\varepsilon}_0$'s temperature-dependent function
JOHNSON_COOK_C_FUNCTION	c's temperature-dependent function
TAYLOR_QUINNEY_FUNCTION	β_Q's temperature-dependent function

Table 4.77 State Variables for `POWER_LAW_BREAKDOWN_PLASTIC_KINETIC_POTENTIAL`

Name	Description
RATE_COEFFICIENT	Rate coefficient γ
RATE_EXPONENT	Rate exponent m
TAYLOR_QUINNEY	Taylor-Quinney factor β_Q
RATE_COEFFICIENT_FUNCTION	γ's temperature-dependent function
RATE_EXPONENT_FUNCTION	m's temperature-dependent function
TAYLOR_QUINNEY_FUNCTION	β_Q's temperature-dependent function

Degradation Functions

Table 4.78 Property Inputs for `TALAMINI_DEGRADATION_FUNCTION`

Name	Description
GC	Griffith fracture energy G_c
FRACTURE_LENGTH_SCALE	Fracture length scale ℓ
CRITICAL_ENERGY_DENSITY	Critical energy density ψ_c
GC_FUNCTION	G_c's temperature-dependent function
FRACTURE_LENGTH_SCALE_FUNCTION	ℓ's temperature-dependent function
CRITICAL_ENERGY_DENSITY_FUNCTION	ψ_c's temperature-dependent function

Table 4.79 Property Inputs for LO_DEGRADATION_FUNCTION

Name	Description
LO_S	Lo s parameter
LO_S_FUNCTION	s's temperature-dependent function

Table 4.80 Property Inputs for WU_DEGRADATION_FUNCTION

Name	Description
WU_P	Wu p parameter
WU_COEFFICIENTS	Wu degradation function coefficients a_i
WU_P_FUNCTION	p's temperature-dependent function

Notes:

- If CRITICAL_ENERGY_DENSITY is not defined, it is defaulted to $\frac{3G_c}{16\ell}$.

Tension-Compression Splits

Table 4.81 Property Inputs for STAR_CONVEX_TCS

Name	Description
STAR_CONVEX_GAMMA	Star-Convex γ parameter

4.37.4.2 State Variables

Elastic Potentials

Table 4.82 State Variables for HENCKY_ELASTIC_POTENTIAL

Name	Description
YOUNGS_MODULUS	E
POISSONS_RATIO	ν
BULK_MODULUS	κ
SHEAR_MODULUS	μ

Plastic Potentials

Table 4.83 State Variables for `LINEAR_PLASTIC_POTENTIAL`

Name	Description
YIELD_STRESS	σ_y
HARDENING_MODULUS	h
TAYLOR_QUINNEY	β_Q
EQPS	$\bar{\varepsilon}^p$
EQPSDOT	$\dot{\bar{\varepsilon}}^p$
FP	F^p_{ij}

Table 4.84 State Variables for `POWER_LAW_PLASTIC_POTENTIAL`

Name	Description
YIELD_STRESS	σ_y
HARDENING_CONSTANT	a
HARDENING_EXPONENT	b
LUDERS_STRAIN	ε_ℓ
TAYLOR_QUINNEY	β_Q
EQPS	$\bar{\varepsilon}^p$
EQPSDOT	$\dot{\bar{\varepsilon}}^p$
FP	F^p_{ij}

Table 4.85 State Variables for `POWER_LAW_SIMPLE_PLASTIC_POTENTIAL`

Name	Description
REFERENCE_STRAIN	ε_0
YIELD_STRESS	σ_y
HARDENING_EXPONENT	n
TAYLOR_QUINNEY	β_Q
EQPS	$\bar{\varepsilon}^p$
EQPSDOT	$\dot{\bar{\varepsilon}}^p$
FP	F^p_{ij}

Table 4.86 State Variables for `VOCE_PLASTIC_POTENTIAL`

Name	Description
YIELD_STRESS	σ_y
HARDENING_MODULUS_*	h_i
EXPONENTIAL_COEFFICIENT_*	α_i
TAYLOR_QUINNEY	β_Q
EQPS	$\bar{\varepsilon}^p$
EQPSDOT	$\dot{\bar{\varepsilon}}^p$
FP	F_{ij}^p

Table 4.87 State Variables for JOHNSON_COOK_PLASTIC_POTENTIAL

Name	Description
JOHNSON_COOK_A	a
JOHNSON_COOK_B	b
JOHNSON_COOK_N	n
JOHNSON_COOK_Q	q
JOHNSON_COOK_THETA	θ
JOHNSON_COOK_DTHETADT	$\frac{\mathrm{d}\theta}{\mathrm{d}T}$
TAYLOR_QUINNEY	β_Q
EQPS	$\bar{\varepsilon}^p$
EQPSDOT	$\dot{\bar{\varepsilon}}^p$
FP	F_{ij}^p

Damage Potentials

Table 4.88 State Variables for GRADIENT_DAMAGE_POTENTIAL

Name	Description
GC	G_c
FRACTURE_LENGTH_SCALE	ℓ

Table 4.89 State Variables for CLASSICAL_GRADIENT_DAMAGE_POTENTIAL

Name	Description
GC	G_c
FRACTURE_LENGTH_SCALE	ℓ

Table 4.90 State Variables for WU_DAMAGE_POTENTIAL

Name	Description
GC	G_c
FRACTURE_LENGTH_SCALE	ℓ
XI	ξ

Plastic Kinetic Potentials

Table 4.91 State Variables for POWER_LAW_PLASTIC_KINETIC_POTENTIAL

Name	Description
REFERENCE_STRAIN_RATE	$\dot{\varepsilon}_0$
YIELD_STRESS	σ_y
RATE_EXPONENT	m
TAYLOR_QUINNEY	β_Q
EQPS	$\bar{\varepsilon}^p$
EQPSDOT	$\dot{\bar{\varepsilon}}^p$
FP	F_{ij}^p

Table 4.92 State Variables for JOHNSON_COOK_PLASTIC_KINETIC_POTENTIAL

Name	Description
REFERENCE_STRAIN_RATE	$\dot{\varepsilon}_0$
JOHNSON_COOK_C	c
TAYLOR_QUINNEY	β_Q
EQPS	$\bar{\varepsilon}^p$
EQPSDOT	$\dot{\bar{\varepsilon}}^p$
FP	F_{ij}^p

Table 4.93 State Variables for POWER_LAW_BREAKDOWN_PLASTIC_KINETIC_POTENTIAL

Name	Description
RATE_COEFFICIENT	γ
RATE_EXPONENT	m
TAYLOR_QUINNEY	β_Q
EQPS	$\bar{\varepsilon}^p$
EQPSDOT	$\dot{\bar{\varepsilon}}^p$
FP	F_{ij}^p

Degradation Functions

Table 4.94 State Variables for TALAMINI_DEGRADATION_FUNCTION

Name	Description
GC	G_c
FRACTURE_LENGTH_SCALE	ℓ
CRITICAL_ENERGY_DENSITY	ψ_c

Table 4.95 State Variables for `LO_DEGRADATION_FUNCTION`

Name	Description
LO_S	s

Table 4.96 State Variables for `WU_DEGRADATION_FUNCTION`

Name	Description
WU_P	p

4.38 Modular Failure

The modular failure capability consists of a suite of failure models (Tearing Parameter, Johnson-Cook Failure, Wilkins, Modular Failure, Modular BCJ Failure) that are available to several of modular material models. These failure models are briefly defined in this chapter, but other references (e.g. [27], [61], [62]) provide a more complete description. Modular failure is currently available to the following material models: J_2 plasticity, Hosford plasticity, Hill plasticity, and Barlat plasticity.

Additionally, an anisotropic failure capability has been implemented (Section 4.38.6). This is compatible with the modular failure models listed here, plus several additional models in development.

```
#
# Optional Failure Definitions
#    Following only need to be defined if intend to use failure model
#
FAILURE MODEL = TEARING_PARAMETER | JOHNSON_COOK_FAILURE | WILKINS
                | MODULAR_FAILURE | MODULAR_BCJ_FAILURE

CRITICAL FAILURE PARAMETER = <real>
```

4.38.1 Tearing Parameter

The tearing parameter model, proposed by Wellman [110], is implemented with the form,

$$d = \frac{1}{d_{\text{crit}}} \int_0^{\bar{\varepsilon}^p} \left\langle \frac{2\sigma_{\max}}{3\left(\sigma_{\max} - p\right)} \right\rangle^m d\bar{\varepsilon}^p, \tag{4.270}$$

where σ_{ij} is the Cauchy stress tensor, $p = \frac{1}{3}\sigma_{kk}$ is the mean hydrostatic stress, σ_{max} is the maximum principal stress, and $\bar{\varepsilon}^p$ is the equivalent plastic strain. The two parameters of the model as m, a fit exponent, and the critical failure (tearing) parameter, d_{crit}. The angle brackets $\langle \cdot \rangle$, denoting Macaulay brackets,

$$\langle x \rangle = \begin{cases} 0 & \text{if } x \leq 0 \\ x & \text{if } x > 0 \end{cases},$$

are used to ensure that the failure process occurs only with tensile stress states and prevent "damage healing". The failure process initiates once the integral term reaches the critical tearing parameter, such that $d = 1$.

4.38.1.1 User Guide

```
#
# TEARING_PARAMETER Failure model definitions
#
TEARING PARAMETER EXPONENT = m
```

4.38.2 Johnson-Cook Failure

The Johnson-Cook model [49] is implemented with the form,

$$d = \int_0^{\bar{\varepsilon}^p} \frac{d\bar{\varepsilon}^p}{(D_1 + D_2 \exp(D_3\eta)) \left(1 + D_4 \langle \ln \frac{\dot{\bar{\varepsilon}}^p}{\dot{\varepsilon}_0} \rangle\right) (1 + D_5 T^*)}, \tag{4.271}$$

where $\{D_1, D_2, D_3, D_4, D_5\}$ are fitting constants and $\dot{\varepsilon}_0$ is a reference strain rate. The term η represents stress triaxiality, the ratio of mean hydrostatic stress to von-Mises stress: $\eta = \frac{p}{\sigma_{vm}}$. The term T^* represents the homologous temperature, given as a function of the temperature T by,

$$T^* = \frac{T - T_{\text{ref}}}{T_{\text{melt}} - T_{\text{ref}}},$$

where T_{ref} is a reference temperature and T_{melt} is the melting temperature.

The Johnson-Cook failure model form (4.271) is formulated as a multiplicative combination of triaxiality, strain-rate, and temperature effects, and the denominator may be interpreted as the critical failure strain. The failure process initiates once the total quantity reaches $d = 1$.

4.38.2.1 User Guide

```
#
# JOHNSON_COOK_FAILURE Failure model definitions
#
JOHNSON COOK D1        = <real>
JOHNSON COOK D2        = <real>
JOHNSON COOK D3        = <real>
JOHNSON COOK D4        = <real>
JOHNSON COOK D5        = <real>
#
```

(continues on next page)

(continued from previous page)

```
#Following Johnson-Cook parameters can only be defined once.  As such,␣
↪only
#  needed if not previously defined via Johnson-Cook multipliers
#  w/ flow-stress hardening.  Does need to be defined
#  w/ Decoupled Flow Stress
#
REFERENCE RATE        = <real>
REFERENCE TEMPERATURE = <real>
MELTING TEMPERATURE   = <real>
```

4.38.3 Wilkins

The Wilkins failure model, proposed by Wilkins [112] is implemented with the form:

$$d = \frac{1}{d_{\text{crit}}} \int_0^{\bar{\varepsilon}^p} w_1 w_2 d\bar{\varepsilon}^p, \tag{4.272}$$

where w_1 represents a pressure-dependent term defined as,

$$w_1 = \left(\frac{1}{1 - \frac{p}{B}} \right)^{\alpha},$$

with α and B as fitting parameters and p is mean hydrostatic stress, and w_2 represents a Lode-angle-related term defined as,

$$w_2 = (2 - A)^{\beta},$$

with β as fitting parameter, and A defined as a function of deviatoric principal stresses ($s_1 \geq s_2 \geq s_3$),

$$A = \max\left(\frac{s_2}{s_3}, \frac{s_2}{s_1} \right).$$

The failure process initiates once the integral term reaches the critical failure parameter, such that $d = 1$.

4.38.3.1 User Guide

```
#
# WILKINS Failure model definitions
#
WILKINS ALPHA    = <real>
WILKINS BETA     = <real>
WILKINS PRESSURE = <real>
```

4.38.4 Modular Failure

The "modular failure" model extends the multiplicative framework set out by the Johnson-Cook and Wilkins models to create a more customizable failure model. This model includes five individual terms that capture effects due to pressure, Lode angle, stress triaxiality, strain rate, and temperature. The "modular failure" model is implemented as,

$$d = \frac{1}{d_{\text{crit}}} \int_0^{\bar{\varepsilon}^p} w_1(p) w_2(\theta) w_3(\eta) w_4(\dot{\bar{\varepsilon}}^p) w_5(T) d\bar{\varepsilon}^p, \tag{4.273}$$

where p is the mean hydrostatic stress, θ is the Lode angle, η is the stress triaxiality, and T is temperature. Mean hydrostatic stress p is defined as,

$$p = \frac{1}{3}\sigma_{kk}.$$

Lode angle θ is defined in terms of deviatoric stress invariants tensor $\{J_2, J_3\}$ as,

$$\cos 3\theta = \sqrt{\frac{27}{4}\frac{{J_3}^2}{{J_2}^3}}.$$

Stress triaxiality η is defined as the ratio of mean hydrostatic stress to von-Mises stress,

$$\eta = \frac{p}{\sigma_{vm}}$$

Each of the multiplicative terms w_i can be independently specified; user-defined functions can be provided, and several presets are provided. Implemented possibilities are,

$$\begin{aligned}
w_1(p) &= 1, w_1^{\text{w}}, w_1^{\text{ud}}, \\
w_2(\theta) &= 1, w_2^{\text{w}}, \\
w_3(\eta) &= 1, w_3^{\text{jc}}, w_3^{\text{ud}}, \\
w_4(\dot{\bar{\varepsilon}}^p) &= 1, w_4^{\text{jc}}, w_4^{\text{ud}}, \\
w_5(T) &= 1, w_5^{\text{jc}}, w_5^{\text{ud}},
\end{aligned}$$

where superscripts {jc, w, ud} represent Johnson-Cook model terms, Wilkins model terms, or user-defined functions, respectively. Refer to Section 4.38.2 and Section 4.38.3 for these function definitions. Leaving a function unspecified defines the function as 1, indicating independence with respect to that variable. The failure process initiates once the integral term reaches the critical failure parameter, such that $d = 1$.

4.38.4.1 User Guide

```
#
#  MODULAR_FAILURE Failure model definitions
#
PRESSURE MULTIPLIER         = PRESSURE_INDEPENDENT | WILKINS
                              | USER_DEFINED (PRESSURE_INDEPENDENT)
LODE ANGLE MULTIPLIER       = LODE_ANGLE_INDEPENDENT |
                              WILKINS (LODE_ANGLE_INDEPENDENT)
TRIAXIALITY MULTIPLIER      = TRIAXIALITY_INDEPENDENT | JOHNSON_COOK
                              | USER_DEFINED (TRIAXIALITY_INDEPENDENT)
RATE FAIL MULTIPLIER        = RATE_INDEPENDENT | JOHNSON_COOK
                              | USER_DEFINED (RATE_INDEPENDENT)
TEMPERATURE FAIL MULTIPLIER = TEMPERATURE_INDEPENDENT | JOHNSON_COOK
                              | USER_DEFINED (TEMPERATURE_INDEPENDENT)
#
# Individual multiplier definitions
#
PRESSURE MULTIPLIER = WILKINS
WILKINS ALPHA       = <real>
WILKINS PRESSURE    = <real>
#
PRESSURE MULTIPLIER = USER_DEFINED
PRESSURE MULTIPLIER FUNCTION = <string> pressure_multiplier_fun_name
#
LODE ANGLE MULTIPLIER = WILKINS
WILKINS BETA          = <real>
#
TRIAXIALITY MULTIPLIER = JOHNSON_COOK
JOHNSON COOK D1        = <real>
JOHNSON COOK D2        = <real>
JOHNSON COOK D3        = <real>
#
TRIAXIALITY MULTIPLIER = USER_DEFINED
TRIAXIALITY MULTIPLIER FUNCTION = <string> triaxiality_multiplier_fun_
 ↪name
#
RATE FAIL MULTIPLIER = JOHNSON_COOK
JOHNSON COOK D4      = <real>
# REFERENCE RATE should only be added if not previously defined
REFERENCE RATE       = <real>
#
RATE FAIL MULTIPLIER = USER_DEFINED
RATE FAIL MULTIPLIER FUNCTION = <string> rate_fail_multiplier_fun_name
#
TEMPERATURE FAIL MULTIPLIER = JOHNSON_COOK
JOHNSON COOK D5             = <real>
# JC Temperatures should only be defined if not previously given
```

(continues on next page)

(continued from previous page)

```
REFERENCE TEMPERATURE        = <real>
MELTING TEMPERATURE          = <real>
#
TEMPERATURE FAIL MULTIPLIER           = USER_DEFINED
TEMPERATURE FAIL MULTIPLIER FUNCTION = <string> temp_multiplier_fun_
↪name
```

4.38.5 Modular BCJ Failure

The modular BCJ (Bammann-Chiesa-Johnson [8]) failure model develops the damage variable through a micromechanical representation of the void evolution process. In this model, damage is defined as void volume fraction as function of void size v_v and count f in a nominal unit volume V_0 [50]:

$$d = \frac{v_v f V_0}{V_0 + v_v f V_0} = \frac{v_v f}{1 + v_v f}.$$

Void evolution is determined by incrementation of *void nucleation* and *void growth* models. Implemented void nucleation models include Horstemeyer-Gokhale (HG) [44] and Chu-Needleman strain distribution (CNSD) [24]:

$$(\dot{f})^{\mathrm{HG}} = f\dot{\bar{\varepsilon}}^p N_4 \left(N_1 \left[\frac{4}{27} - \frac{{J_3}^2}{{J_2}^3} \right] + N_2 \left[\frac{J_3}{{J_2}^{\frac{3}{2}}} \right] + N_3 \left[\frac{|p|}{\sigma_{vm}} \right] \right), \tag{4.274}$$

where $\{N_1, N_2, N_3, N_4\}$ are fitting constants, $\{J_2, J_3\}$ are deviatoric stress tensor invariants, p is the mean hydrostatic stress, and σ_{vm} is the von-Mises stress. The N_1 term premultiplies a term indicating a shear-dominated stress state (maximal in torsion); the N_2 term premultiplies a term indicating uniaxial stress state (maximal in uniaxial tension); the N_3 term premultiplies a term indicating stress triaxiality (maximal in hydrostatic tension/compression).

$$(\dot{f})^{\mathrm{CNSD}} = \frac{1}{(1-d)^2} \left[\frac{\psi}{s v_0 \sqrt{2\pi}} \right] \exp\left(-\frac{1}{2} \left(\frac{\bar{\varepsilon}^p - \varepsilon_N}{s} \right)^2 \right),$$

where ψ is the void amplitude, ε_N is the mean of the nucleation strain distribution, and s is the standard deviation of the nucleation strain distribution.

The Cocks-Ashby (CA) model [25] is the only growth model implemented to date:

$$(\dot{v}_v)^{\mathrm{CA}} = \sqrt{\frac{2}{3}} \dot{\bar{\varepsilon}}^p \left(\frac{1 - (1-d)^{m+1}}{(1-d)^m} \right) \sinh\left[\frac{2(2m-1)}{2m+1} \frac{p}{\sigma_{vm}} \right], \tag{4.275}$$

where m is the damage growth exponent.

The void nucleation and growth models are combined to develop the full expression for void evolution,

$$\dot{d} = \dot{v}_v w_1^G(\dot{\bar{\varepsilon}}^p) w_2^G(T) + (1-d)^2 \dot{f} v_0 w_1^N(\dot{\bar{\varepsilon}}^p) w_2^N(T), \tag{4.276}$$

where optional functions w_i^X are introduced to account for strain-rate and temperature effects. Implemented functions provide for strain-rate and temperature effects using the D_4 and D_5 terms of the Johnson-Cook failure model (4.271).

Note that the void evolution equation is defined implicitly, as void nucleation and growth expressions may each depend on damage. A model parameter β exposes the option to control the temporal integration of (4.276), with $\beta = 0$ representing forward Euler integration (explicit), $\beta = 1$ representing backward Euler integration (implicit), and $\beta = 0.5$ (default) representing trapezoidal integration (implicit). Other common parameters include the initial damage d_0 and initial void size v_0.

4.38.5.1 User Guide

```
#
# MODULAR_BCJ_FAILURE Failure model definitions
#
INITIAL DAMAGE     = <real>
INITIAL VOID SIZE  = <real>
DAMAGE BETA        = <real> (0.5)
GROWTH MODEL       = COCKS_ASHBY | NO_GROWTH (NO_GROWTH)
NUCLEATION MODEL   = HORSTEMEYER_GOKHALE | CHU_NEEDLEMAN_STRAIN
                     | NO_NUCLEATION (NO_NUCLEATION)
#
GROWTH RATE FAIL MULTIPLIER         = JOHNSON_COOK | USER_DEFINED
                                      | RATE_INDEPENDENT
                                      (RATE_INDEPENDENT)
GROWTH TEMPERATURE FAIL MULTIPLIER = JOHNSON_COOK | USER_DEFINED
                                      | TEMPERATURE_INDEPENDENT
                                      (TEMPERATURE_INDEPENDENT)
#
NUCLEATION RATE FAIL MULTIPLIER         = JOHNSON_COOK | USER_DEFINED
                                          | RATE_INDEPENDENT
                                          (RATE_INDEPENDENT)
NUCLEATION TEMPERATURE FAIL MULTIPLIER = JOHNSON_COOK | USER_DEFINED
                                          | TEMPERATURE_INDEPENDENT
                                          (TEMPERATURE_INDEPENDENT)
#
# Definitions for individual growth and nucleation models
#
GROWTH MODEL = COCKS_ASHBY
DAMAGE EXPONENT = <real> (0.5)
#
NUCLEATION MODEL      = HORSTEMEYER_GOKHALE
NUCLEATION PARAMETER1 = <real> (0.0)
NUCLEATION PARAMETER2 = <real> (0.0)
```

(continues on next page)

(continued from previous page)

```
NUCLEATION PARAMETER3 = <real> (0.0)
#
NUCLEATION MODEL          = CHU_NEEDLEMAN_STRAIN
NUCLEATION AMPLITUDE      = <real>
MEAN NUCLEATION STRAIN    = <real>
NUCLEATION STRAIN STD DEV = <real>
#
# Definitions for rate and temperature fail multiplier
#   Note: only showing definitions for growth.
#    Nucleation terms are the same just with NUCLEATION instead
#    of GROWTH
#
GROWTH RATE FAIL MULTIPLIER = JOHNSON_COOK
GROWTH JOHNSON COOK D4      = <real>
GROWTH REFERENCE RATE       = <real>
#
GROWTH RATE FAIL MULTIPLIER          = USER_DEFINED
GROWTH RATE FAIL MULTIPLIER FUNCTION = <string> growth_rate_fail_mult_
 ↪func
#
GROWTH TEMPERATURE FAIL MULTIPLIER = JOHNSON_COOK
GROWTH JOHNSON COOK D5             = <real>
GROWTH REFERENCE TEMPERATURE       = <real>
GROWTH MELTING TEMPERATURE         = <real>
#
GROWTH TEMPERATURE FAIL MULTIPLIER          = USER_DEFINED
GROWTH TEMPERATURE FAIL MULTIPLIER FUNCTION = <string> temp_fail_mult_
 ↪func
#
```

4.38.6 Anisotropic Failure

4.38.6.1 Background

A common feature of many of the modular failures model available in LAMÉ is damage accumulation through integration by a scalar equivalent plastic strain rate variable, e.g. (4.270), (4.271), (4.272), (4.273), (4.274), (4.275). This anisotropic failure approach leverages that common form to introduce a heuristic anisotropic dependence.

The plastic strain rate tensor $\dot{\varepsilon}^p_{ij}$ is defined through the flow rule deriving from the normality principle of associated plasticity, by scalar plasticity rate variable $\dot{\gamma}$, effective stress $\sigma_\star$, and stress tensor σ_{ij}:

$$\dot{\varepsilon}^p_{ij} = \dot{\gamma}\frac{\partial \sigma_\star}{\partial \sigma_{ij}}$$

This relation can be expressed equivalently as an equivalent plastic strain rate scalar $\dot{\varepsilon}^p$ and a flow direction tensor N. The LAMÉ implementation defines the flow tensor as the effective stress derivative with respect to the stress tensor, without any further normalization:

$$\dot{\varepsilon}^p_{ij} = \dot{\varepsilon}^p N_{ij}$$

$$\dot{\varepsilon}^p = \dot{\gamma}, \quad N_{ij} = \frac{\partial \sigma_\star}{\partial \sigma_{ij}} \tag{4.277}$$

$$\dot{\varepsilon}^p = \frac{\sqrt{\dot{\varepsilon}^p_{ij}\dot{\varepsilon}^p_{ij}}}{\sqrt{N_{ij}N_{ij}}} \tag{4.278}$$

For example, in J_2 plasticity, $N_{ij} = \frac{3}{2}\frac{s_{ij}}{\sigma_\star} = \sqrt{\frac{3}{2}}\frac{s_{ij}}{\sqrt{s_{ij}s_{ij}}}$, so $N_{ij}N_{ij} = \frac{3}{2}$. The plastic strain rate scalar is then the familiar $\dot{\varepsilon}^p = \sqrt{\frac{2}{3}\dot{\varepsilon}^p_{ij}\dot{\varepsilon}^p_{ij}}$.

4.38.6.2 Anisotropic Weighting Concept

In order to create anisotropic failure behavior, the plastic strain rate scalar used for failure model integration is weighted using an *anisotropic weight tensor*; the weighted equivalent plastic strain scalar is denoted as $\hat{\dot{\varepsilon}}^p$. Crucially, the weighting is *not* intended to modify the material constitutive (i.e. plasticity, non-failure) model in any way.

Second-order and fourth-order anisotropic weighting is proposed, using symmetric second-order A_{ij} or fourth-order B_{ijkl} symmetric weighting tensors [98], [99]:

2nd-order formulation:

$$\hat{\dot{\varepsilon}}^p = \sqrt{\frac{\dot{\varepsilon}^p_{ik}A_{ij}\dot{\varepsilon}^p_{jl}\delta_{kl}}{N_{mn}N_{mn}}} = \dot{\varepsilon}^p\sqrt{\frac{N_{ik}A_{ij}N_{jl}\delta_{kl}}{N_{mn}N_{mn}}} \tag{4.279}$$

4th-order formulation:

$$\hat{\dot{\varepsilon}}^p = \sqrt{\frac{\dot{\varepsilon}^p_{ij}B_{ijkl}\dot{\varepsilon}^p_{kl}}{N_{mn}N_{mn}}} = \dot{\varepsilon}^p\sqrt{\frac{N_{ij}B_{ijkl}N_{kl}}{N_{mn}N_{mn}}} \tag{4.280}$$

4.38.6.3 Symmetry

As stress tensors and plastic flow direction tensors are assumed to be symmetric, the anisotropic weight tensors are constrained to have major ($A_{ij} = A_{ji}$; $B_{ijkl} = B_{klij}$) and minor ($B_{ijkl} = B_{jikl} = B_{ijlk} = B_{jilk}$) symmetries. This reduces the number of unique parameters to six for the 2nd-order tensor A_{ij} and 21 for the 4th-order tensor B_{ijkl}.

4.38.6.4 Mandel Notation

It is convenient to express the fourth-order tensor B_{ijkl} in Mandel notation as a 6x6 matrix B_{IJ}. The conversion between the full forms of the flow tensor (N_{ij}) and weight tensor (B_{ijkl}) to Mandel notation $\{N_I, B_{IJ}\}$ are as follows:

$$N_I = \begin{bmatrix} N_{11} \\ N_{22} \\ N_{33} \\ \sqrt{2}N_{12} \\ \sqrt{2}N_{23} \\ \sqrt{2}N_{31} \end{bmatrix}$$

$$B_{IJ} = \begin{bmatrix} B_{1111} & B_{1122} & B_{1133} & \sqrt{2}B_{1112} & \sqrt{2}B_{1123} & \sqrt{2}B_{1131} \\ B_{1122} & B_{2222} & B_{2233} & \sqrt{2}B_{2212} & \sqrt{2}B_{2223} & \sqrt{2}B_{2231} \\ B_{1133} & B_{2233} & B_{3333} & \sqrt{2}B_{3312} & \sqrt{2}B_{3323} & \sqrt{2}B_{3331} \\ \sqrt{2}B_{1112} & \sqrt{2}B_{2212} & \sqrt{2}B_{3312} & 2B_{1212} & 2B_{1223} & 2B_{1231} \\ \sqrt{2}B_{1123} & \sqrt{2}B_{2223} & \sqrt{2}B_{3323} & 2B_{1223} & 2B_{2323} & 2B_{2331} \\ \sqrt{2}B_{1131} & \sqrt{2}B_{2231} & \sqrt{2}B_{3331} & 2B_{1231} & 2B_{2331} & 2B_{3131} \end{bmatrix}$$

The anisotropic weighting can now be expressed in terms of the Mandel-converted tensors.

$$\hat{\dot{\varepsilon}}^p = \dot{\varepsilon}^p \sqrt{\frac{N_{ij}B_{ijkl}N_{kl}}{N_{mn}N_{mn}}} = \dot{\varepsilon}^p \sqrt{\frac{N_I B_{IJ} N_J}{N_K N_K}} \tag{4.281}$$

Note that the anisotropic failure model parameters are specified as individual entries of the fourth-order tensor - not as entries of the equivalent Mandel matrix.

4.38.6.5 Weighting Tensor Forms

Common forms for the anisotropic weighting tensors are as follows:

Isotropic, Second-Order:

$$A_{ij}^{iso} = \begin{bmatrix} 1 & 0 & 0 \\ 0 & 1 & 0 \\ 0 & 0 & 1 \end{bmatrix}$$

Coordinate-Axis Aligned, Second-Order:

$$A_{ij}^{diag} = \begin{bmatrix} A_{11} & 0 & 0 \\ 0 & A_{22} & 0 \\ 0 & 0 & A_{33} \end{bmatrix}$$

General (Rotated), Second-Order:

$$A_{ij}^{gen} = \begin{bmatrix} A_{11} & A_{12} & A_{13} \\ A_{12} & A_{22} & A_{23} \\ A_{13} & A_{23} & A_{33} \end{bmatrix} = A_{kl}^{diag} R_{ik} R_{lj}$$

Note that the rotation matrix can equivalently be applied to the weighting tensor (shown here) or to the flow direction tensor.

Fourth-Order Equivalence to Second-Order

$$B_{IJ} = \begin{bmatrix} A_{11} & 0 & 0 & \frac{1}{\sqrt{2}}A_{12} & 0 & \frac{1}{\sqrt{2}}A_{13} \\ 0 & A_{22} & 0 & \frac{1}{\sqrt{2}}A_{12} & \frac{1}{\sqrt{2}}A_{23} & 0 \\ 0 & 0 & A_{33} & 0 & \frac{1}{\sqrt{2}}A_{23} & \frac{1}{\sqrt{2}}A_{13} \\ \frac{1}{\sqrt{2}}A_{12} & \frac{1}{\sqrt{2}}A_{12} & 0 & \frac{1}{2}(A_{11}+A_{22}) & \frac{1}{2}A_{13} & \frac{1}{2}A_{23} \\ 0 & \frac{1}{\sqrt{2}}A_{23} & \frac{1}{\sqrt{2}}A_{23} & \frac{1}{2}A_{13} & \frac{1}{2}(A_{22}+A_{33}) & \frac{1}{2}A_{12} \\ \frac{1}{\sqrt{2}}A_{13} & 0 & \frac{1}{\sqrt{2}}A_{13} & \frac{1}{2}A_{23} & \frac{1}{2}A_{12} & \frac{1}{2}(A_{33}+A_{11}) \end{bmatrix}$$

This tensor form allows for a second-order weighting while using the fourth-order tensor. Any deviation from this tensor form necessarily induce a fundamentally fourth-order weighting.

Isotropic, Fourth-Order:

$$B_{IJ}^{iso} = \begin{bmatrix} 1 & 0 & 0 & 0 & 0 & 0 \\ 0 & 1 & 0 & 0 & 0 & 0 \\ 0 & 0 & 1 & 0 & 0 & 0 \\ 0 & 0 & 0 & 1 & 0 & 0 \\ 0 & 0 & 0 & 0 & 1 & 0 \\ 0 & 0 & 0 & 0 & 0 & 1 \end{bmatrix}$$

Coordinate-Axis Aligned, Fourth-Order:

$$B_{IJ}^{diag} = \begin{bmatrix} A_{11} & 0 & 0 & 0 & 0 & 0 \\ 0 & A_{22} & 0 & 0 & 0 & 0 \\ 0 & 0 & A_{33} & 0 & 0 & 0 \\ 0 & 0 & 0 & \frac{1}{2}(A_{11}+A_{22}) & 0 & 0 \\ 0 & 0 & 0 & 0 & \frac{1}{2}(A_{22}+A_{33}) & 0 \\ 0 & 0 & 0 & 0 & 0 & \frac{1}{2}(A_{33}+A_{11}) \end{bmatrix}$$

Coordinate-Axis Aligned Rotated, Fourth-Order:

$$B_{IJ}^{diag} = B_{KL}M_{IK}M_{LJ} = B_{ijkl}^{diag,rot} = B_{mnpq}^{diag}R_{im}R_{jn}R_{kp}R_{lq}$$

where M is a Mandel-notation rotation tensor [1], [66].

General, Fourth-Order:

$$B_{IJ} = \begin{bmatrix} B_{1111} & B_{1122} & B_{1133} & \sqrt{2}B_{1112} & \sqrt{2}B_{1123} & \sqrt{2}B_{1131} \\ B_{1122} & B_{2222} & B_{2233} & \sqrt{2}B_{2212} & \sqrt{2}B_{2223} & \sqrt{2}B_{2231} \\ B_{1133} & B_{2233} & B_{3333} & \sqrt{2}B_{3312} & \sqrt{2}B_{3323} & \sqrt{2}B_{3331} \\ \sqrt{2}B_{1112} & \sqrt{2}B_{2212} & \sqrt{2}B_{3312} & 2B_{1212} & 2B_{1223} & 2B_{1231} \\ \sqrt{2}B_{1123} & \sqrt{2}B_{2223} & \sqrt{2}B_{3323} & 2B_{1223} & 2B_{2323} & 2B_{2331} \\ \sqrt{2}B_{1131} & \sqrt{2}B_{2231} & \sqrt{2}B_{3331} & 2B_{1231} & 2B_{2331} & 2B_{3131} \end{bmatrix}$$

4.38.6.6 Calibration

For simple loading states, it may be possible to determine the anisotropic weighting tensor entries analytically, using experimentally observed failure strains and presumed plastic strain flow directions for several different loading directions. Examples of this are included in references [98], [99]. For more complex load paths or rate-dependence and temperature effects included, analytical calibration may be intractable, and a numerical optimization approach should be used instead.

4.38.6.7 Permissive Option

Note that the numerator of the anisotropic weighting relations (4.279) and (4.280) include a square root of the tensor products. With no constraints imposed on A_{ij} and B_{ijkl}, this creates the possibility of having a negative argument to the square root, implying a weighting with imaginary terms. By default, LAMÉ will error out if a negative argument is passed to the square root. As an alternative, the `ANISOTROPIC_EQPS_WEIGHT_PERMISSIVE = 1` option allows the failure model to continue in these cases, by setting the argument (and weighting) to zero.

Choosing a positive-semi-definite weighting tensor would ensure that this issue is prevented. Further, since the weighting tensors are contracted with traceless flow direction *tensors* rather than vectors, the positive-semi-definite requirement can be weakened. For second-order tensors, it is only required for tensor invariant $I_1(A) \geq 0$ and $I_2(A) \geq 0$, but $I_3(A)$ may be negative. LAMÉ returns a *warning* when the minimum eigenvalue of A_{ij} is negative and returns an *error* if $I_2(A)$ is negative.

This approach is difficult to generalize for the fourth-order weighting tensor, so no warnings or errors based on the structure of B_{ijkl} are provided.

4.38.6.8 Material Coordinate Rotation

When performing the anisotropic weighting, the failure model first rotates the flow direction tensors from the global coordinate system to a material coordinate system, if one is provided. This is the same material coordinate system used by anisotropic plasticity models like Hill Plasticity. This is performed by applying the rotation matrices to the plastic flow direction tensor: $N^{\text{matl}} = R^T N^{\text{global}} R$. The weighting is then done using N^{matl} and anisotropic weight tensors, which are presumed to be in the material coordinates (i.e. $A = A^{\text{matl}}$).

Equivalently, the rotation matrices could be applied to the weighting tensor, e.g. $A^{\text{global}} = R A^{\text{matl}} R^T$, which could be done either every timestep or even during user parameter specification. While the latter would be more efficient, it limits the use cases to those where the coordinate transformation is invariant in time and space (e.g. not a cylindrical coordinate system).

4.38.6.9 User Guide

```
#
# Anisotropic Failure model definitions
#
ANISOTROPIC_EQPS_WEIGHT_ORDER      = <int> 0 | 2 | 4 (0)
ANISOTROPIC_EQPS_WEIGHT_PERMISSIVE = <bool> 0 | 1 (0)
#
# Definitons for second-order anisotropic weighting
# (symmetric, 6 unique)
ANISOTROPIC_EQPS_WEIGHT_XX = <real> (1.0)
ANISOTROPIC_EQPS_WEIGHT_YY = <real> (1.0)
ANISOTROPIC_EQPS_WEIGHT_ZZ = <real> (1.0)
ANISOTROPIC_EQPS_WEIGHT_XY = <real> (0.0)
ANISOTROPIC_EQPS_WEIGHT_YZ = <real> (0.0)
ANISOTROPIC_EQPS_WEIGHT_ZX = <real> (0.0)
#
# Definitons for fourth-order anisotropic weighting
# (major/minor symmetric, 21 unique)
ANISOTROPIC_EQPS_WEIGHT_XXXX = <real> (1.0)
ANISOTROPIC_EQPS_WEIGHT_YYYY = <real> (1.0)
ANISOTROPIC_EQPS_WEIGHT_ZZZZ = <real> (1.0)
ANISOTROPIC_EQPS_WEIGHT_XXYY = <real> (0.0)
ANISOTROPIC_EQPS_WEIGHT_YYZZ = <real> (0.0)
ANISOTROPIC_EQPS_WEIGHT_ZZXX = <real> (0.0)
#
ANISOTROPIC_EQPS_WEIGHT_XXXY = <real> (0.0)
ANISOTROPIC_EQPS_WEIGHT_XXYZ = <real> (0.0)
ANISOTROPIC_EQPS_WEIGHT_XXZX = <real> (0.0)
ANISOTROPIC_EQPS_WEIGHT_YYXY = <real> (0.0)
ANISOTROPIC_EQPS_WEIGHT_YYYZ = <real> (0.0)
ANISOTROPIC_EQPS_WEIGHT_YYZX = <real> (0.0)
ANISOTROPIC_EQPS_WEIGHT_ZZXY = <real> (0.0)
ANISOTROPIC_EQPS_WEIGHT_ZZYZ = <real> (0.0)
ANISOTROPIC_EQPS_WEIGHT_ZZZX = <real> (0.0)
#
ANISOTROPIC_EQPS_WEIGHT_XYXY = <real> (0.5)
ANISOTROPIC_EQPS_WEIGHT_XYYZ = <real> (0.0)
ANISOTROPIC_EQPS_WEIGHT_XYZX = <real> (0.0)
ANISOTROPIC_EQPS_WEIGHT_YZYZ = <real> (0.5)
ANISOTROPIC_EQPS_WEIGHT_YZZX = <real> (0.0)
ANISOTROPIC_EQPS_WEIGHT_ZXZX = <real> (0.5)
```

Output variables available for this model are listed in *State Variables for Anisotropic Failure Model*.

Table 4.97 State Variables for Anisotropic Failure Model

Name	Description
FAILURE_ROT_XX	material rotation tensor, R_{11}
FAILURE_ROT_YY	material rotation tensor, R_{22}
FAILURE_ROT_ZZ	material rotation tensor, R_{33}
FAILURE_ROT_XY	material rotation tensor, R_{12}
FAILURE_ROT_YZ	material rotation tensor, R_{23}
FAILURE_ROT_ZX	material rotation tensor, R_{31}
FAILURE_ROT_YX	material rotation tensor, R_{21}
FAILURE_ROT_ZY	material rotation tensor, R_{32}
FAILURE_ROT_XZ	material rotation tensor, R_{13}

This page left blank

A. Common Boundary Value Problems

Throughout this effort, a wide variety of boundary value problems have been used to verify the various model responses investigated. Although some of these are specially tailored to a model, many of the loading paths and problems are common. As such, these repeated tests are presented and discussed here in this appendix. Emphasis is placed on the boundary conditions and kinematic descriptions that do not depend on the constitutive behavior and are therefore similar for all models. Details on how to produce these paths in a finite element problem are also discussed. For details on the various problems considered, the reader is referred to various texts [43], [56] on the subject.

A.1 Uniaxial Stress

In all likelihood, the most common test (experimentally or numerically) is that of uniaxial stress. Such a state may be produced via either stress or displacement control. Here, the latter case is discussed as displacement control can be essential when considering model responses that soften through damage or other mechanisms. To produce the uniaxial stress of interest, a displacement of the form $u_1 = \lambda(t)$ is applied along the x_1 edge. In three dimensional finite element cases, it is also essential to leave the x_2 and x_3 surfaces with a traction free condition. With elastically isotropic materials, this produces a strain field of the form,

$$\varepsilon_{ij} = \left[\delta_{i1}\delta_{j1} - \nu\left(\delta_{i2}\delta_{j2} + \delta_{i3}\delta_{i3}\right)\right]\ln\left(1+\lambda\right),$$

which produces σ_{11} as the only non-zero stress.

A.2 Simple Shear

An alternative, and often simpler to implement, shear problem is that of simple shear. With such a deformation field, only one shear stress component is non-zero (like the pure shear case). The difference arises in that given a simple shear loading the diagonal stresses are not necessarily zero. This state may be produced by a motion, $\chi(X_i, t)$ of the form $\chi(X_i, t) = X_i + \gamma(t)X_2\delta_{i1}$. The resultant deformation gradient, F_{ij}, takes the form,

$$F_{ij} = \delta_{ij} + \gamma\left(t\right)\delta_{i1}\delta_{j2}$$

and it is noted that this deformation is volume preserving ($J = \det F_{ij} = 1$). Numerically, such a deformation field results from applying a displacement in the x direction along the y surface.

A.3 Pure Shear

To consider shear-based responses and behaviors of a model, uniaxial loadings are often insufficient. One problem, however, that does investigate shear deformations is that of a pure shear problem. In such problems, only a single shear strain and stress component are non-zero. Such a material state results from a deformation gradient of the form,

$$F_{ij} = \frac{1}{2}\left(\lambda + \lambda^{-1}\right)\left(\delta_{i1}\delta_{j1} + \delta_{i2}\delta_{j2}\right) + \frac{1}{2}\left(\lambda - \lambda^{-1}\right)\left(\delta_{i1}\delta_{j2} + \delta_{i2}\delta_{j1}\right) + \delta_{i3}\delta_{j3},$$

where the shear loading is relative to the $x_1 - x_2$ axis. The logarithmic strain tensor is then simply $\varepsilon_{ij} = \ln\lambda(\delta_{i1}\delta_{j2} + \delta_{i2}\delta_{j1})$. With such a strain tensor, it is trivial to note that σ_{12} is the only non-zero stress.

A.4 Hydrostatic Compression

In many cases, it is preferable to interrogate the pressure-dependent response of various models independently of any deviatoric deformations. To consider such purely volumetric loadings, hydrostatic (almost always compression) problems are invoked. Such loadings are often also referred to as uniform dilation as the volumetric change is the same in all three directions. Specifically, in these cases a purely volumetric response is investigated by applying a deformation of the form $u_i = \lambda(t)$. In a finite element problem, such a deformation field is reproduced by applying the displacement components onto the corresponding edges. With such applied displacement fields, the resulting logarithmic strain tensor is simply,

$$\varepsilon_{ij} = \ln\left[1 + \lambda\left(t\right)\right]\delta_{ij},$$

and the corresponding (elastic) stress field is simply $\sigma_{ij} = -p\delta_{ij}$ where,

$$p = -3K\ln\left(1 + \lambda\right).$$

Note, in the preceding relation p is defined as positive in compression.

A.5 Constant Equivalent Plastic Strain Rate

Typically, for a given boundary value problem it is desirable to know either the stress or deformation (strain) state and solve for the complementary response functions. In the case of rate-dependent hardening, or often rate-independent, it is preferable to prescribe a constant *equivalent plastic strain rate*, $\dot{\bar{\varepsilon}}^p$. Knowing, and controlling, this variable is often essential to finding and solving analytical solutions to verify hardening models.

As the equivalent plastic strain, $\bar{\varepsilon}^p$, is the internal (hidden) state variable corresponding to isotropic hardening, it is counterintuitive to think of prescribing it's value. Nonetheless, for many plasticity models such a case is not only possible but relatively simple. Details of this approach

may be found in [81], but are repeated here for convenience and completeness. In the following, two cases are treated – uniaxial stress and pure shear. For either problem, it is assumed that the stress state is initially at yield $\phi[\sigma_{ij}(t=0,\bar{\varepsilon}^p=0)]=\sigma_y^0$ and a constant equivalent plastic strain rate is prescribed such that,

$$\bar{\varepsilon}^p\,(t)=\dot{\bar{\varepsilon}}^p t.$$

Furthermore, it is recalled that the yield surface, f, is written as,

$$f\left(\sigma_{ij},\bar{\varepsilon}^p,\dot{\bar{\varepsilon}}^p\right)=\phi\left(\sigma_{ij}\right)-\bar{\sigma}\left(\bar{\varepsilon}^p,\dot{\bar{\varepsilon}}^p\right),$$

where,

$$\bar{\sigma}\left(\bar{\varepsilon}^p,\dot{\bar{\varepsilon}}^p\right)=\tilde{\sigma}_y\left(\bar{\varepsilon}^p\right)\hat{\sigma}_y\left(\dot{\bar{\varepsilon}}^p\right).$$

Note, throughout this section function forms for $\tilde{\sigma}_y$ and $\hat{\sigma}_y$ are not given. For the purposes of the developed problem, the specific forms are unnecessarily as long as $\tilde{\sigma}_y$ depends only on $\bar{\varepsilon}^p$ and $\hat{\sigma}_y$ on the corresponding rate.

A.5.1 Uniaxial Stress

During uniaxial stress, the state of stress reduces to,

$$\sigma_{ij}=\sigma\delta_{i\eta}\delta_{j\eta}\quad(\text{no sum on }\eta)$$

where η is the direction of loading (taken to align with one of the material principal axes) and

$$\sigma=\Gamma_{\eta\eta}\bar{\sigma}\,(t)\,, \tag{4.282}$$

with $\Gamma_{\eta\eta}$ being a constant associated with and dependent on the model parameters of the plasticity model. Specific forms for the various yield surfaces are given later in this section. Given this stress state, the axial elastic strain is simply,

$$\varepsilon_{\eta\eta}^{\mathrm{el}}=\frac{\Gamma_{\eta\eta}\bar{\sigma}\,(t)}{E}.$$

To determine the plastic state of the material, the equivalency of plastic work ($\sigma_{ij}\dot{\varepsilon}_{ij}^p=\bar{\sigma}\dot{\bar{\varepsilon}}^p$) is invoked enabling the axial plastic strain to be given as,

$$\dot{\varepsilon}_{\eta\eta}^p=\frac{\bar{\sigma}}{\sigma}\dot{\bar{\varepsilon}}^p=\frac{1}{\Gamma_{\eta\eta}}\dot{\bar{\varepsilon}}^p.$$

Integrating,

$$\varepsilon_{\eta\eta}^p\,(t)=\frac{1}{\Gamma_{\eta\eta}}\bar{\varepsilon}^p.$$

The total strain is found simply as the sum of elastic and plastic components,

$$\varepsilon_{\eta\eta}(t) = \varepsilon_{\eta\eta}^{\mathrm{el}} + \varepsilon_{\eta\eta}^{p} = \frac{\Gamma_{\eta\eta}\bar{\sigma}(t)}{E} + \frac{1}{\Gamma_{\eta\eta}}\dot{\bar{\varepsilon}}t. \tag{4.283}$$

For this boundary value problem, only the axial displacement need be prescribed as zero traction conditions are required on the remaining surfaces to achieve the uniaxial stress state. As the equivalent plastic strain rate is constant, the flow stress, $\bar{\sigma}(t)$, is known and the total strain of (4.283) is only a function of time. Therefore, the desired displacement boundary condition may be prescribed as a function of time alone and is simply,

$$u_{\eta}(t) = \exp\left(\varepsilon_{\eta\eta}(t)\right) - 1.$$

J_2 Plasticity

In the case of an isotropic J_2 effective stress definition, for a uniaxial state of stress,

$$\Gamma_{\eta\eta} = 1 \quad (\text{no sum on } \eta).$$

Hosford Plasticity

As the Hosford effective stress definition is isotropic, for a uniaxial state of stress the coefficients $\Gamma_{\eta\eta}$ are simply,

$$\Gamma_{\eta\eta} = 1 \quad (\text{no sum on } \eta).$$

Hill Plasticity

For a Hill effective stress definition, by inspection of (4.282) it is clear that,

$$\Gamma_{\eta\eta} = R_{\eta\eta} \quad (\text{no sum on } \eta).$$

Barlat Plasticity

With a Barlat effective stress definition, the anisotropy coefficients are,

$$\Gamma_{\eta\eta} = \frac{1}{\omega_{\eta}} \quad (\text{no sum on } \eta),$$

where

$$\begin{aligned}\omega_1 =& \frac{1}{3}\left\{\frac{1}{4}\left[|c'_{12} + c'_{13} - c''_{12} - c''_{13}|^a + |c'_{12} + c'_{13} + 2c''_{21} - c''_{23}|^a + |c'_{12} + c'_{13} + 2c''_{31} - c''_{32}|^a \right.\right.\\ &+ |c'_{23} - 2c'_{21} - c''_{12} - c''_{13}|^a + |c'_{23} - 2c'_{21} + 2c''_{21} - c''_{23}|^a + |c'_{23} - 2c'_{21} + 2c''_{31} - c''_{32}|^a \\ &\left.\left. + |c'_{32} - 2c'_{31} - c''_{12} - c''_{13}|^a + |c'_{32} - 2c'_{31} + 2c''_{21} - c''_{23}|^a + |c'_{32} - 2c'_{31} + 2c''_{31} - c''_{32}|^a\right]\right\}^{1/a},\end{aligned}$$

$$\omega_2 = \frac{1}{3}\left\{\frac{1}{4}\left[|c'_{13} - 2c'_{12} - c''_{13} + 2c''_{12}|^a + |c'_{13} - 2c'_{12} - c''_{21} - c''_{23}|^a + |c'_{13} - 2c'_{12} - c''_{31} + 2c''_{32}|^a \right.\right.$$
$$+ |c'_{21} + c'_{23} - c''_{13} + 2c''_{12}|^a + |c'_{21} + c'_{23} - c''_{21} - c''_{23}|^a + |c'_{21} + c'_{23} - c''_{31} + 2c''_{32}|^a$$
$$\left.\left. + |c'_{31} - 2c'_{32} - c''_{13} + 2c''_{12}|^a + |c'_{31} - 2c'_{32} - c''_{21} - c''_{23}|^a + |c'_{31} - 2c'_{32} - c''_{31} + 2c''_{32}|^a\right]\right\}^{1/a},$$

$$\omega_3 = \frac{1}{3}\left\{\frac{1}{4}\left[|c'_{12} - 2c'_{13} - c''_{12} + 2c''_{13}|^a + |c'_{12} - 2c'_{13} - c''_{21} + 2c''_{23}|^a + |c'_{12} - 2c'_{13} - c''_{31} - c''_{32}|^a \right.\right.$$
$$+ |c'_{21} - 2c'_{23} - c''_{12} + 2c''_{13}|^a + |c'_{21} - 2c'_{23} - c''_{21} + 2c''_{23}|^a + |c'_{21} - 2c'_{23} - c''_{31} - c''_{32}|^a$$
$$\left.\left. + |c'_{31} + c'_{32} - c''_{12} + 2c''_{13}|^a + |c'_{31} + c'_{32} - c''_{21} + 2c''_{23}|^a + |c'_{31} + c'_{32} - c''_{31} - c''_{32}|^a\right]\right\}^{1/a}.$$

A.5.2 Pure Shear

To produce a pure shear stress state, the pure shear conditions discussed in Section A.3 are utilized. In this case, for pure shear in the $\hat{e}_\eta - \hat{e}_\zeta$ plane, a deformation gradient of the form,

$$F_{ij} = \frac{1}{2}\left(\lambda + \lambda^{-1}\right)\left(\delta_{i\eta}\delta_{j\eta} + \delta_{i\zeta}\delta_{j\zeta}\right) + \frac{1}{2}\left(\lambda - \lambda^{-1}\right)\left(\delta_{i\eta}\delta_{j\zeta} + \delta_{i\zeta}\delta_{j\eta}\right) + \delta_{i\theta}\delta_{j\theta}, \quad (\text{no sum on } \eta,\ \zeta,\ \theta),$$

with $\hat{e}_\theta$ being the cross-product of $\hat{e}_\eta$ and $\hat{e}_\zeta$. With such a deformation,

$$\varepsilon_{ij} = \ln\lambda\left(\delta_{i\eta}\delta_{j\zeta} + \delta_{i\zeta}\delta_{j\eta}\right),$$

meaning the appropriate displacement boundary conditions may be applied if the total shear strain is known.

For the pure shear strain case, the stress tensor is simply $\sigma_{ij} = \tau\left(\delta_{i\eta}\delta_{j\zeta} + \delta_{i\zeta}\delta_{j\eta}\right)$ and may be equated to the shear stress as,

$$\tau = \Gamma_{\eta\zeta}\bar{\sigma}(t) \qquad (\eta \neq \zeta).$$

The elastic strain may then simply be written as

$$\varepsilon^{\text{el}}_{\eta\zeta} = \frac{\tau}{2\mu} = \frac{\Gamma_{\eta\zeta}}{2\mu}\bar{\sigma}(t).$$

To find the plastic strain rate, the plastic work equivalency is recalled such that,

$$\sigma_{ij}\dot{\varepsilon}^p_{ij} = 2\sigma_{\eta\zeta}\dot{\varepsilon}^p_{\eta\zeta} = \bar{\sigma}\dot{\bar{\varepsilon}}^p, \quad (\eta \neq \zeta)$$

which produces an expression for the plastic strain rate as,

$$\dot{\varepsilon}^p_{\eta\zeta} = \frac{1}{2\Gamma_{\eta\zeta}}\dot{\bar{\varepsilon}}^p, \quad (\eta \neq \zeta). \tag{4.284}$$

Integrating (4.284) yields,

$$\varepsilon_{\eta\zeta}^{p}(t) = \frac{1}{2\Gamma_{\eta\zeta}}\bar{\varepsilon}^{p}, \quad (\eta \neq \zeta)$$

leading to a total strain of the form,

$$\varepsilon_{\eta\zeta}(t) = \frac{\Gamma_{\eta\zeta}}{2\mu}\bar{\sigma}(t) + \frac{1}{2\Gamma_{\eta\zeta}}\dot{\bar{\varepsilon}}^{p}t, \quad (\eta \neq \zeta)$$

and

$$\lambda(t) = \exp\left(\varepsilon_{\eta\zeta}(t)\right), \quad (\eta \neq \zeta).$$

J_2 Plasticity

In the case of a isotropic J_2 effective stress, the pure shear coefficients are,

$$\Gamma_{\eta\zeta} = \frac{1}{\sqrt{3}} \quad (\eta \neq \zeta).$$

Hosford Plasticity

Although isotropic, the Hosford effective stress definition is non-quadratic leading to a stress multiplier of,

$$\Gamma_{\eta\zeta} = \frac{1}{\left[1 + 2^{a-1}\right]^{1/a}} \quad (\eta \neq \zeta).$$

Hill Plasticity

Like the uniaxial case, for the pure shear response a direct connection may be made between the R stress ratios and $\Gamma_{\eta\zeta}$ such that,

$$\Gamma_{\eta\zeta} = \frac{R_{\eta\zeta}}{\sqrt{3}} \quad (\eta \neq \zeta).$$

Barlat Plasticity

The Barlat effective stress definition produces stress relationships of the form,

$$\Gamma_{\eta\zeta} = \frac{1}{\xi_{\eta\zeta}} \quad (\eta \neq \zeta),$$

where,

$$\xi_{12} = \left\{ \frac{1}{2} \left[|c'_{44} - c''_{44}|^a + |c'_{44} + c''_{44}|^a + |c'_{44}|^a + |c''_{44}|^a \right] \right\}^{1/a},$$

$$\xi_{23} = \left\{ \frac{1}{2} \left[|c'_{55} - c''_{55}|^a + |c'_{55} + c''_{55}|^a + |c'_{55}|^a + |c''_{55}|^a \right] \right\}^{1/a},$$

$$\xi_{31} = \left\{ \frac{1}{2} \left[|c'_{66} - c''_{66}|^a + |c'_{66} + c''_{66}|^a + |c'_{66}|^a + |c''_{66}|^a \right] \right\}^{1/a}.$$

This page left blank

References

[1] Auld B. A. *Acoustic Fields and Waves in Solids*. John Wiley & Sons Inc., 1973.

[2] D. B. Adolf, R. S. Chambers, and J. M. Caruthers. Extensive validation of a thermodynamically consistent, non-linear viscoelastic model for glassy polymers. *Polymer*, 45:4599–4621, 2004.

[3] D. B. Adolf, R. S. Chambers, and M. A. Neidigk. A simplified potential energy clock model for glassy polymers. *Polymer*, 50:4257–4269, 2009.

[4] M. Ambati, T. Gerasimov, and L. De Lorenzis. Phase-field modeling of ductile fracture. *Computational Mechanics*, 55(5):1017–1040, May 2015. URL: https://link.springer.com/article/10.1007/s00466-015-1151-4 (visited on 2017-09-05), doi:10.1007/s00466-015-1151-4.

[5] F. Armero and A. Pèrez-Foguet. On the formulation of closes-point projection algorithms in elastoplasticity – part I: The variational structure. *International Journal for Numerical Methods in Engineering*, 53:297–329, 2002.

[6] Ellen M Arruda and Mary C Boyce. A three-dimensional constitutive model for the large stretch behavior of rubber elastic materials. *Journal of the Mechanics and Physics of Solids*, 41(2):389–412, 1993. doi:10.1016/0022-5096(93)90013-6.

[7] S.W. Attaway. Orthotropic crush constitutive relation for PRONTO. Technical Report Memo, Sandia National Laboratories, Albuquerque, NM, September 29, 1992.

[8] D.J. Bammann, M.L. Chiesa, and G.C. Johnson. Modelling large deformation and failure in manufacturing processes. In T. Tatsumi, E. Watanabe, and T. Kambe, editors, *Proceedings of the 19th International Congress of Theoretical and Applied Mechanics*, 359–376. Amsterdam, 1997. Elsevier Science Publishers.

[9] F. Barlat, H. Aretz, J. W. Yoon, J. C. Brem, and R. E. Dick. Linear transformation-based anisotropic yield functions. *International Journal of Plasticity*, 21:1009–1039, 2005.

[10] P. J. Blatz and W. L. Ko. Application of finite elasticity theory to the deformation of rubbery materials. *Transactions of the Society of Rheology*, 6:223–251, 1962.

[11] G. Bolzon and R. Vitaliani. The blatz-ko model and homogenization. *Archive of Applied Mechanics*, 63:228–241, 1993.

[12] M.J Borden, C.V. Verhoosel, M.A. Scott, T.J.R. Hughes, and C.M. Landis. A phase-field description of dynamic brittle fracture. *Computer Methods in Applied Mechanics and Engineering*, pages 77–95, January 2012. URL: http://dx.doi.org/10.1016/j.cma.2012.01.008 (visited on 2012-01-26), doi:10.1016/j.cma.2012.01.008.

[13] B. Bourdin, G.A. Francfort, and J-J. Marigo. Numerical experiments in revisited brittle fracture. *Journal of the Mechanics and Physics of Solids*, 48(4):797–826, April 2000. URL:

http://www.sciencedirect.com/science/article/pii/S0022509699000289, doi:10.1016/S0022-5096(99)00028-9.

[14] Blaise Bourdin. Numerical implementation of the variational formulation for quasi-static brittle fracture. *Interfaces and Free Boundaries*, 9:411–430, 2007. doi:10.4171/IFB/171.

[15] Blaise Bourdin, Gilles A Francfort, and Jean-Jacques Marigo. The variational approach to fracture. *Journal of Elasticity*, 91:5–148, 2008.

[16] A.A. Brown and D.J. Bammann. Validation of a model for static and dynamic recrystallization in metals. *International Journal of Plasticity*, 32–33:17–35, 2012.

[17] Michael R. Buche and Meredith N. Silberstein. Statistical mechanical constitutive theory of polymer networks: The inextricable links between distribution, behavior, and ensemble. *Phys. Rev. E*, 102:012501, Jul 2020. doi:10.1103/PhysRevE.102.012501.

[18] M.A. Buechler. Viscoelastic-viscoplastic combined hardening constitutive model based on the Drucker Prager yield and flow potentials. Technical report, LA-UR-12-24895, Los Alamos National Laboratory, Los Alamos, New Mexico 87545, 2012.

[19] M.A. Buechler. Viscoelastic viscoplastic damage model development, parameter estimation, and comparison to PBX9501 experimental data. Technical report, LA-UR-13-27547, Los Alamos National Laboratory, Los Alamos, New Mexico 87545, 2013.

[20] M.A. Buechler and D.J. Luscher. A semi-implicit integration scheme for a combined viscoelastic-damage model of plastic bonded explosives. *Int. J. Numer. Meth. Engng.*, 99:54–78, 2014.

[21] J. M. Caruthers, D. B. Adolf, R. S. Chambers, and P. Shrikhande. A thermodynamically consistent, nonlinear viscoelastic approach for modeling glassy polymers. *Polymer*, 45:4577–4597, 2004.

[22] R. Chambers, R. Tandon, and M. Stavig. Characterization and calibration of a viscoelastic simplified potential energy clock model for inorganic glasses. *Journal of Non-Crystalline Solids*, 432:545–555, 2016.

[23] R.M. Christensen. *Theory of Viscoelasticity*. Dover Publications, Inc., Mineola, NY, second edition, 2003.

[24] C. C. Chu and A. Needleman. Void nucleation effects in biaxially stretched sheets. *Journal of Engineering Materials and Technology*, 102(3):249–256, 07 1980.

[25] A. Cocks and M. Ashby. Intergranular fracture during power-law creep under multiaxial stresses. *Metal Sci.*, 14(8–9):395–402, 1980.

[26] E. Corona and G. E. Orient. An evaluation of the Johnson-Cook model to simulate puncture of 7075 aluminum plates. Technical Report SAND2014-1550, Sandia National Laboratories, Albuquerque, NM, 2014. \href http://infoserve.sandia.gov/sand_doc/2014/141550.pdfpdf.

[27] Edmundo Corona and Benjamin Reedlunn. A review of macroscopic ductile failure criteria. Technical Report SAND2013-7989, Sandia National Laboratories, Albuquerque, NM and Livermore, CA, 2013.

[28] J.K. Dienes. A statistical-theory of fragmentation processes. *Mechanics of Materials*, 4(3-4):325–335, 1985.

[29] D.P. Flanagan and L. M. Taylor. An accurate numerical algorithm for stress integration with finite rotations. *Computer Methods in Applied Mechanics and Engineering*, 62:305–320, 1987.

[30] P.S. Follansbee and U.F. Kocks. A constitutive description of the deformation of copper based on the use of the mechanical threshold stress and an internal state variable. *Acta Metallurgica*, 36(1):81–93, 1988.

[31] P.S. Follansbee and G.T. Gray III. An analysis of the low temperature, low and high strain-rate deformation of Ti-6Al-4V. *Metallurgical Transactions A*, 20A:863–874, 1989.

[32] G. Francfort and J. Marigo. Revisiting brittle fracture as an energy minimization problem. *Journal of the Mechanics and Physics of Solids*, 46(8):1319–1342, 1998. doi:10.1016/S0022-5096(98)00034-9.

[33] H. J. Frost and M. F. Ashby. *Deformation Mechanism Maps: the Plasticity and Creep of Metals and Ceramics*. Pergamon Press, 1982.

[34] Rudy J.M. Geelen, Yingjie Liu, Tianchen Hu, Michael R. Tupek, and John E. Dolbow. A phase-field formulation for dynamic cohesive fracture. *Computer Methods in Applied Mechanics and Engineering*, 348:680–711, 2019. doi:10.1016/j.cma.2019.01.026.

[35] A.N. Gent. A new constitutive relation for rubber. *Rubber Chemistry and Technology*, 69(1):59–61, 1996.

[36] L.J. Gibson and M.F. Ashby. *Cellular Solids: Structure and Properties*. Cambridge Solid State Science Series. Cambridge University Press, Cambridge, UK, second edition, 1997.

[37] A. Graf and W. Hosford. Calculations of forming limit diagrams. *Metallurgical Transactions A*, 21A:87–94, 1990.

[38] A.E. Green and W. Zerna. *Theoretical Elasticity, 2nd Edition*. Clarendon Press, Oxford, 1968.

[39] R.M. Hackett and J.G. Bennett. An implicit finite element material model for energetic particulate composite materials. *Int. J. Numer. Meth. Engng.*, 49:1191–1209, 2000.

[40] D. J. Hartl, D. C. Lagoudas, F. T. Calkins, and J. H. Mabe. Use of a Ni60Ti shape memory alloy for active jet engine chevron application: I. thermomechanical characterization. *Smart Materials and Structures*, 19:015020, 2010.

[41] D. J. Hartl, J. T. Mooney, D. C. Lagoudas, F. T. Calkins, and J. H. Mabe. Use of a Ni60Ti shape memory alloy for active jet engine chevron application: II. experimentally validated numerical analysis. *Smart Materials and Structures*, 19:015021, 2010.

[42] R. Hill. *The Mathematical Theory of Plasticity*. Oxford University Press, 1950.

[43] G. A. Holzapfel. *Nonlinear Solid Mechanics: A Continuum Approach For Engineering*. John Wiley & Sons, Ltd, 2000.

[44] Mark F. Horstemeyer and Arun M. Gokhale. A void–crack nucleation model for ductile metals. *International Journal of Solids and Structures*, 36(33):5029–5055, 1999.

[45] W.F. Hosford. A generalized isotropic yield criterion. *Journal of Applied Mechanics*, 39:607–609, 1972.

[46] Tianchen Hu, Brandon Talamini, Andrew J Stershic, Michael R Tupek, and John E Dolbow. A variational phase-field model for ductile fracture with coalescence dissipation. *Computational Mechanics*, 68(2):311–335, 2021.

[47] T.J.R Hughes and R.L. Taylor. Unconditionally stable algorithms for quasi-static elasto/visco-plastic finite element analysis. *Comput Struct*, 8:169–173, 1978.

[48] G.R. Johnson and W.H. Cook. A constitutive model and data for metals subjected to large strains, high strain rates and high temperatures. In *Proc. 7th. Int. Symp. on Ballistics*, 541–547. The Hague, The Netherlands, 1983.

[49] G.R. Johnson and W.H. Cook. Fracture characteristics of three metals subjected to various strains, strain rates, temperatures and pressures. *Engineering Fracture Mechanics*, 21(1):31–48, 1985.

[50] Kyle N. Karlson, Coleman Alleman, James W. Foulk III, Kevin L. Manktelow, Jakob T. Ostien, Michael E Stender, Andrew J. Stershic, and Michael G. Veilleux. Sandia Fracture Challenge 3: detailing the Sandia Team Q failure prediction strategy. *International Journal of Fracture*, 218(1):149–170, 2019.

[51] M. Kojić and K.J. Bathe. *Inelastic Analysis of Solids and Structures*. Springer, 2005.

[52] R.D. Krieg. A simple constitutive description for cellular concrete. Technical Report SAND SC-DR-72-0883, Sandia National Laboratories, Albuquerque, NM, 1978. \href http://infoserve.sandia.gov/sand_doc/1972/720883.pdfpdf.

[53] R.J. Kuether. Two-tier model reduction of viscoelastically damped finite element models. *Computers and Structures*, 219:58–72, 2019.

[54] D. Lagoudas, D. Hartl, Y. Chemisky, L. Machado, and P. Popov. Constitutive model for the numerical analysis of phase transformation in polycrystalline shape memory alloys. *International Journal of Plasticity*, 32-33:155–183, 2012.

[55] D. C. Lagoudas, editor. *Shape Memory Alloys: Modeling and Engineering Application*. Springer, New York, NY USA, 2008.

[56] W.M. Lai, D. Rubin, and E. Krempl. *Introduction to Continuum Mechanics*. Pergamon Press, 3rd edition, 1993.

[57] J. Lemaitre and J.-L. Chaboche. *Mechanics of Solid Materials*. Cambridge University Press, 1990.

[58] B.T. Lester and K.N. Long. Numerical integration of viscoelastic models. Memo to distribution SAND2019-11472R, Sandia National Laboratories, Albuquerque, NM and Livermore, CA, 2019.

[59] B.T. Lester and K.N. Long. Modular linear thermoviscoelastic model. Memo to distribution SAND2020-4973R, Sandia National Laboratories, Albuquerque, NM and Livermore, CA, 2020.

[60] B.T. Lester and W.M. Scherzinger. Adiabatic heating in modular plasticity models. Memo to distribution SAND2019-15003R, Sandia National Laboratories, Albuquerque, NM and Livermore, CA, 2019.

[61] B.T. Lester and W.M. Scherzinger. Failure formulations in modular plasticity models. Memo to distribution SAND2019-9678R, Sandia National Laboratories, Albuquerque, NM and Livermore, CA, 2019.

[62] B.T. Lester and W.M. Scherzinger. Modular growth and nucleation formulations in modular plasticity models. Memo to distribution SAND2020-7404R, Sandia National Laboratories, Albuquerque, NM and Livermore, CA, 2020.

[63] A. E. H. Love. *A Treatise on the Mathematical Theory of Elasticity*. Dover, 4th edition, 1944.

[64] J. Lubliner. *Plasticity Theory*. Dover, 2008.

[65] S. Marques and G.J. Creus. *Computational Viscoelasticity*. Springer, 2012.

[66] Morteza M. Mehrabadi and Stephen C. Cowin. Eigentensors of linear anisotropic elastic materials. *Quarterly Journal of Mechanics and Applied Mathematics*, 43(1):15–41, February 1990. doi:10.1093/qjmam/43.1.15.

[67] C. Miehe, M. Hofacker, L. -M. Schänzel, and F. Aldakheel. Phase field modeling of fracture in multi-physics problems. Part II. Coupled brittle-to-ductile failure criteria and crack propagation in thermo-elastic–plastic solids. *Computer Methods in Applied Mechanics and Engineering*, 294:486–522, September 2015. URL: http://www.sciencedirect.com/science/article/pii/S0045782514004435 (visited on 2017-09-05), doi:10.1016/j.cma.2014.11.017.

[68] Christian Miehe, Martina Hofacker, and Fabian Welschinger. A phase field model for rate-independent crack propagation: Robust algorithmic implementation based on operator splits. *Computer Methods in Applied Mechanics and Engineering*, 199(45-48):2765–2778, November 2010. URL: http://linkinghub.elsevier.com/retrieve/pii/S0045782510001283 (visited on 2018-04-27), doi:10.1016/j.cma.2010.04.011.

[69] Darrell E Munson and PR Dawson. Constitutive model for the low temperature creep of salt (with application to WIPP). Technical Report SAND79-1853, Sandia National Laboratories, Albuquerque, NM, 1979.

[70] Darrell E Munson and PR Dawson. Transient creep model for salt during stress loading and unloading. Technical Report SAND82-0962, Sandia National Laboratories, Albuquerque, NM, 1982.

[71] Darrell E Munson, Arlo F Fossum, and Paul E Senseny. Advances in resolution of discrepancies between predicted and measured in situ WIPP room closures. Technical Report SAND88-2948, Sandia National Laboratories, Albuquerque, NM, 1989.

[72] M. K. Neilsen, W. Y. Lu, B. Olsson, and T. Hinnerichs. A viscoplastic constitutive model for polyurethane foams. In *Proceedings ASME 2006 International Mechanical Engineering Congress and Exposition*. Chicago, IL, 2006. ASME.

[73] M. K. Neilsen, W. Y. Lu, W. M. Scherzinger, T. D. Hinnerichs, and C. S. Lo. Unified creep plasticity damage (UCPD) model for rigid polyurethane foams. Technical Report SAND2015-4352, Sandia National Laboratories, Albuquerque, NM, 2015.

[74] M.K. Neilsen, S. N. Burchett, C. M. Stone, and J. J. Stephens. A viscoplastic theory for braze alloys. Technical Report SAND96-0984, Sandia National Laboratories, Albuquerque, NM, 1996. \href http://infoserve.sandia.gov/sand_doc/1996/960984.pdfpdf.

[75] M.K. Neilsen, H.S. Morgan, and R.D. Krieg. A phenomenological constitutive model for low density polyurethane foams. Technical Report SAND86-2927, Sandia National Laboratories, Albuquerque, NM, April 1987. \href http://infoserve.sandia.gov/sand_doc/1986/862927.pdfpdf.

[76] M.K. Neilsen, J.D. Pierce, and R.D. Krieg. A constitutive model for layered wire mesh and aramid cloth fabric. Technical Report SAND91-2850, Sandia National Laboratories, Albuquerque, NM, 1993. \href http://infoserve.sandia.gov/sand_doc/1991/912850.pdfpdf.

[77] Jorge Nocedal and Stephen J. Wright. *Numerical Optimization*. Springer, 2006.

[78] F.K.G. Odqvist. *Mathematical theory of creep and creep rupture*. Clarendon Press, Oxford, 1966.

[79] R. W. Ogden. *Non-Linear Elastic Deformaitons*. Dover, New York, 1984.

[80] M. Ortiz and L. Stainier. The variational formulation of viscoplastic constitutive updates. *Computer Methods in Applied Mechanics and Engineering*, 171(3):419–444, April 1999. URL: http://www.sciencedirect.com/science/article/pii/S0045782598002199 (visited on 2017-11-10), doi:10.1016/S0045-7825(98)00219-9.

[81] J. T. Ostien and W. M. Scherzinger. Verification of select rate dependent models coupled to a Hill yield surface. Memoraundum, 2017.

[82] K. Otsuka and X. Ren. Physical metallurgy of Ti-Ni-based shape memory alloys. *Progress in Materials Science*, 50:511–678, 2005.

[83] A. Pèrez-Foguet and F. Armero. On the formulation of closest-point projection algorithms in elastoplasticity – part II: Globally convergent schemes. *International Journal for Numerical Methods in Engineering*, 53:331–374, 2002.

[84] Kim Pham, Hanen Amor, Jean-Jacques Marigo, and Corrado Maurini. Gradient Damage Models and Their Use to Approximate Brittle Fracture. *International Journal of Damage Mechanics*, 20(4):618–652, May 2011. URL:

http://journals.sagepub.com/doi/10.1177/1056789510386852 (visited on 2018-03-13), doi:10.1177/1056789510386852.

[85] M. A. Qidwai and D. C. Lagoudas. Numerical implementation of a shape memory alloy thermomechanical constitutive model using return mapping algorithms. *International Journal for Numerical Methods in Engineering*, 47:1123–1168, 2000.

[86] Benjamin Reedlunn. Enhancements to the munson-dawson model for rock salt. Technical Report SAND2018-12601, Sandia National Laboratories, Albuquerque, NM, 2018.

[87] Benjamin Reedlunn, James Bean, John Wilkes, and John Bignell. Simulations of criticality control overpack container compaction at the waste isolation pilot plant. Technical Report SAND2019-3106 O, Sandia National Laboratories, Albuquerque, NM, 2019.

[88] W. M. Scherzinger. A return mapping algorithm for isotropic and anisotropic plasticity models using a line search method. *Computer Methods in Applied Mechanics and Engineering*, 317:526–553, 2017.

[89] W.M. Scherzinger and C.R. Dohrmann. A robust algorithm for finding the eigenvalues and eigenvectors of 3x3 symmetric matrices. *Computer Methods in Applied Mechanics and Engineering*, 197(45-48):4007–4015, 2008.

[90] W.M. Scherzinger and D.C. Hammerand. Library of advanced materials for engineering (LAMÉ). Technical Report SAND2007-5515, Sandia National Laboratories, Albuquerque, NM, August 2007. \href http://infoserve.sandia.gov/sand_doc/2007/075515.pdfpdf.

[91] W.M. Scherzinger and D.C. Hammerand. Testing of constitutive models in LAME. Technical Report SAND2007-5872, Sandia National Laboratories, Albuquerque, NM, September 2007. \href http://infoserve.sandia.gov/sand_doc/2007/075872.pdfpdf.

[92] J. C. Simo and R. L. Taylor. A return mapping algorithm for plane stress elastoplasticity. *International Journal for Numerical Methods in Engineering*, 22:649–670, 1986.

[93] J.C. Simo and T.J.R. Hughes. *Computational Inelasticity*. Springer-Verlag, New York, NY, 1998.

[94] I. S. Sokolnikoff. *Mathematical Theory of Elasticity*. Krieger Publishing Company, 1956.

[95] B. Störakers. On material representation and constitutive branching in finite compressible elasticity. *Journal of the Mechanics and Physics of Solids*, 34:125–145, 1986.

[96] D.J. Steinberg, S.G. Cochran, and M.W. Guinan. A constitutive model for metals applicable at high-strain rate. *Journal of Applied Physics*, 51:1498–1504, 1980.

[97] D.J. Steinberg and C.M. Lund. A constitutive model for strain rates from 10$^-4$ to 10^6 s$^-1$. *Journal of Applied Physics*, 65:1528–1533, 1989.

[98] Andrew Stershic. Simplified mechanism for anisotropic failure in modular material models. Technical Report SAND2023-10653CTF, Sandia National Laboratories, Albuquerque, NM and Livermore, CA, 2021.

[99] Andrew Stershic, Brian Lester, and Kevin Long. Simplified mechanism for anisotropic failure in modular material models. Technical Report SAND2022-8237C, Sandia National Laboratories, Albuquerque, NM and Livermore, CA, 2022.

[100] Andrew J. Stershic, Brandon L. Talamini, Kyle N. Karlson, Bonnie R. Antoun, Sharlotte L.B. Kramer, Jakob T. Ostien, Vincente Pericoli, and Brian Phung. FY20 ASC P&EM L2 Milestone #7182: Ductile failure capability demonstration for nuclear safety assessment. SAND Report SAND2020-9054, Sandia National Laboratories, Livermore, CA, 2020.

[101] Andrew J. Stershic, Brandon L. Talamini, and Jakob T. Ostien. Ductile fracture - gradient regularization. SAND Report SAND2018-13260, Sandia National Laboratories, Livermore, CA, 2018.

[102] C. M. Stone, G. W. Wellman, and R. D. Krieg. A vectorized elastic/plastic power law hardening material model including Lüders strains. Technical Report SAND90-0153, Sandia National Laboratories, Albuquerque, NM, March 1990. \href http://infoserve.sandia.gov/sand_doc/1990/900153.pdfpdf.

[103] C.M. Stone. SANTOS – a two-dimensional finite element program for the quasistatic, large deformation, inelastic response of solids. Technical Report SAND90-0543, Sandia National Laboratories, Albuquerque, NM, 1996. \href http://infoserve.sandia.gov/sand_doc/1990/900543.pdfpdf.

[104] D.V. Swenson and L. M. Taylor. A finite element model for the analysis of tailored pulse stimulation of boreholes. *International Journal for Numerical and Analytical Methods in Geomechanics*, 7:469–484, 1983. \href http://dx.doi.org/10.1002/nag.1610070408doi.

[105] Brandon Talamini, Michael R. Tupek, Andrew J. Stershic, Tianchen Hu, James W. Foulk, Jakob T. Ostien, and John E. Dolbow. Attaining regularization length insensitivity in phase-field models of ductile failure. *Computer Methods in Applied Mechanics and Engineering*, 384:113936, 2021. doi:https://doi.org/10.1016/j.cma.2021.113936.

[106] L.M. Taylor and D.P. Flanagan. Pronto3D: a three-dimensional transient solid dynamics program. Technical Report SAND87-1912, Sandia National Laboratories, Albuquerque, NM, March 1989. \href http://infoserve.sandia.gov/sand_doc/1987/871912.pdfpdf.

[107] S. Timoshenko and J.N. Goodier. *Theory of Elasticity*. McGraw Hill Book Company, 3rd edition, 1970.

[108] C. Vignes and K. Long. Viscoplastic-viscoSCRAM model for particulate composite materials. Technical report, SAND2021- In review., Sandia National Laboratories, Albuquerque, New Mexico 87185 and Livermore, California 94550, September 2021.

[109] Edwin A.H. Vollebregt. The bound-constrained conjugate gradient method for non-negative matrices. *Journal of Optimization Theory and Applications*, 162(3):931–953, 2014.

[110] G. W. Wellman. A simple approach to modeling ductile failure. Technical Report SAND2012-1343, Sandia National Laboratories, Albuquerque, NM, June 2012. \href http://infoserve.sandia.gov/sand_doc/2012/121343.pdfpdf.

[111] R.G. Whirley, B.E. Engelmann, and J.O. Halquist. DYNA3D user's manual. 1991.

[112] M.L. Wilkins, Streit, R.D., and J.E. Reaugh. Cumulative-strain-damage model of ductile fracture: simulation and prediction of engineering fracture tests. Technical Report UCRL-53058, Lawrence Livermore National Laboratory, Livermore, CA, 1980.

[113] M.L. Williams, R.F. Landel, and J.D. Ferry. The temperature dependence of relaxation mechanisms in amorphous polymers and other glass-forming liquids. *Journal of the American Chemical Society*, 77:3701–3707, 1955.

[114] F.J. Zerilli and R.W. Armstrong. Dislocation-mechanics-based constitutive relations for material dynamics calculations. *Journal of Applied Physics*, 61:1816–1825, 1987.

[115] Sierra/SolidMechanics Team. Sierra/SolidMechanics VOTD User's Guide. Technical Report In draft, Sandia National Laboratories, Albuquerque, NM, 2019.

This page left blank

DISTRIBUTION

Email—Internal

Name	Org.	Sandia Email Address
Technical Library	1911	sanddocs@sandia.gov

Sandia National Laboratories is a multimission laboratory managed and operated by National Technology & Engineering Solutions of Sandia LLC, a wholly owned subsidiary of Honeywell International Inc., for the U.S. Department of Energy's National Nuclear Security Administration under contract DE-NA0003525.